THE EFFECTS OF TRANSVERSE REINFORCEMENT ON THE STRENGTH AND DEFORMABILITY OF REINFORCED CONCRETE ELEMENTS

by

Kinsey C. Skillen

A Dissertation

Submitted to the Faculty of Purdue University

In Partial Fulfillment of the Requirements for the degree of

Doctor of Philosophy

Lyles School of Civil Engineering

West Lafayette, Indiana

December 2020

THE PURDUE UNIVERSITY GRADUATE SCHOOL
STATEMENT OF COMMITTEE APPROVAL

Dr. Santiago Pujol, Co-Chair
Lyles School of Civil Engineering

Dr. Ayhan Irfanoglu, Co-Chair
Lyles School of Civil Engineering

Dr. Julio Ramirez
Lyles School of Civil Engineering

Dr. Robert Frosch
Lyles School of Civil Engineering

Dr. Ken Ridgway
Department of Earth, Atmospheric and Planetary Sciences

Approved by:
Dr. Dulcy Abraham

ACKNOWLEDGEMENTS

I express my most sincere appreciation to my advisor Santiago Pujol. I cannot thank him enough for the invaluable experiences he provided me with at Purdue. Whether in the classroom or on the lab floor much of what I know about engineering, research, and teaching is credited to him.

I thank Mete Sozen for the judgement and insight he provided throughout this research program. I am very fortunate to have worked with him and cherish the learning experiences he provided.

I thank Damon Fick for introducing me to research during my time at Montana State University. He is a great mentor, friend and colleague.

I thank Prateek Shah for his willingness to help at a moment's notice and for all the hours he contributed to helping me on the lab floor and in the classroom.

I thank fellow staff and students at Bowen Laboratory for their efforts in completing this research, namely, Harold Tidrick, Molly Stetler, Kevin Brower, William Pollalis, Jonathan Monical, Ash Puranam, and Lucas Laughery.

I thank Robert Frosch, Julio Ramirez, Ken Ridgway, and Ayhan Irfanoglu for taking the time to serve on my committee.

I thank my family and friends for their constant support and encouragement. I am forever indebted to my late grandparents Charles and Francine Skillen for their decency, love, and virtue.

TABLE OF CONTENTS

LIST OF TABLES 7
LIST OF FIGURES 8
ABSTRACT 26
1. INTRODUCTION 27
1.1 Background 27
1.2 Lessons Learned from Previous Earthquakes and Experimental Investigations 28
1.2.1 Past Performance of Reinforced Concrete Structures 28
1.2.2 Review of Past Experimental Investigations Involving Shear Strength of Columns 29
1.2.3 Review of Past Experimental Investigations Involving Lap Splices 30
1.2.4 Review of Investigations Involving Strengthening of Columns 31
1.2.5 Review of Investigations Involving Strengthening of Existing Lap Splices 34
1.2.6 Use of External Stirrups on Reinforced Concrete Beams Without Transverse Reinforcement 35
1.3 Research Objectives 35
1.4 Scope of Research 36
2. EXPERIMENTAL PROGRAM 38
2.1 Introduction 38
2.2 Series One: Unconfined Lap Splices 38
2.2.1 Specimen Description 38
2.2.2 Test Setup and Procedure 39
2.3 Series Two: Lap Splices Confined by Post-Installed Epoxied Anchors 41
2.3.1 Specimen Description 41
2.3.2 Test Setup and Procedure 43
2.4 Series Three: Lap Splices Confined with Spiral Reinforcement 44
2.4.1 Specimen Description 44
2.4.2 Test Setup and Procedure 45
2.5 Series Four: Lap Splices Confined with Post-Tensioned Transverse Reinforcement 45
2.5.1 Specimen Description 45
2.5.2 Test Setup and Procedure 46

2.6 Series Five: Columns with Post-Tensioned Transverse Reinforcement 46
2.6.1 Specimen Description 46
2.6.2 Test Setup and Procedure 49
3. EXPERIMENTAL RESULTS 51
3.1 Introduction 51
3.2 Series One: Unconfined Lap Splices 51
3.2.1 Beam Tests: Maximum Steel Stress, Steel Strain, and Mean Bond Strength 51
3.2.2 Beam Tests: Distribution of Concrete Surface Deformations 53
3.2.3 Coupon Tests: Maximum Steel Stress, Steel Strain, and Mean Bond Strengths 54
3.2.4 Coupon Tests: Distribution of Concrete Surface Deformations 55
3.3 Series Two: Lap Splices Confined with Epoxied Anchors 56
3.3.1 Maximum Steel Stress, Steel Strain, and Mean Bond Strengths 56
3.3.2 Distribution of Concrete Surface Deformations 56
3.4 Series Three: Lap Splices Confined with Spiral Reinforcement 57
3.4.1 Maximum Steel Stress, Steel Strain, and Mean Bond Strengths 57
3.4.2 Distribution of Concrete Surface Deformations 57
3.5 Series Four: Lap Splices Confined with Post-Tensioned Transverse Reinforcement 58
3.5.1 Maximum Steel Stress, Steel Strain and Mean Bond Strength 58
3.5.2 Distribution of Concrete Surface Deformations 58
3.6 Series Five: Columns Strengthened with Post-Tensioned Transverse Reinforcement 59
3.6.1 Force Displacement Response 59
3.6.2 Reinforcing Steel Strains 59
4. DISCUSSION OF RESULTS 61
4.1 Introduction 61
4.2 Series One: Unconfined Lap Splices 61
4.2.1 Splice Strength 62
4.2.2 Splice Deformability 65
4.3 Series Two: Lap Splices Confined by Epoxied Anchors 68
4.3.1 Splice Strength 69
4.3.2 Splice Deformability 70
4.4 Series Three: Lap Splices Confined by Spiral Transverse Reinforcement 71

4.4.1 Splice Strength ... 71
4.4.2 Splice Deformability ... 72
4.5 Series Four: Lap Splices Confined by Post-Tensioned Transverse Reinforcement ... 72
4.5.1 Splice Strength ... 72
4.5.2 Splice Deformability ... 73
4.6 Series Five: Columns with Post-Tensioned Transverse Reinforcement ... 74
4.6.1 Effects of Post-Tensioned Transverse Reinforcement on Strength ... 75
4.6.2 Effects of Post-Tensioned Transverse Reinforcement on Deformability ... 77
5. SCOPE AND CONCLUSIONS ... 83
5.1 Research Objectives ... 83
5.2 Scope of Research ... 83
5.3 Conclusions ... 85
TABLES ... 90
FIGURES ... 103
REFERENCES ... 332
APPENDIX A ... 336

LIST OF TABLES

Table 2-1: Selected Properties from Series-One beams 90

Table 2-2: Selected properties from Series-One coupons... 91

Table 2-3: Selected properties from Series-Two coupons... 92

Table 2-4: Selected properties from Series-Three coupons... 93

Table 2-5: Selected properties from Series-Four coupons... 94

Table 2-6: Selected properties from Series-Five Columns.. 95

Table 3-1: Series-One beam test summary 96

Table 3-2: Series-One coupon test summary 97

Table 3-3: Series-Two coupon test summary 98

Table 3-4: Series-Three coupon test summary 99

Table 3-5: Series-Four coupon test summary 100

Table 3-6: Series-Five column test summary 101

Table 4-1: Test results of columns tested by Yamakawa et al. 102

Table A-1: Concrete mix design for Series One through Series Four 342

Table A-2: Concrete mix design for Series Five 342

Table A-3: Concrete properties for Series One beams 342

Table A-4: Concrete properties for Series One and Series Two.. 343

Table A-5: Concrete properties for Series Three.. 344

Table A-6: Concrete properties for Series Four.. 344

Table A-7: Concrete properties for Series Five 345

Table A-8: Reinforcement summary for all test series 345

Table A-9: Sensors used in Series One beam tests... 346

Table A-10: Sensors used in Series One, Series Two and Series Three 347

Table A-11: Sensors used in Series Four.. 347

Table A-12: Sensors used in Series Five 347

LIST OF FIGURES

Figure 1-1: Reinforcement detailing of beam-column joint in the Van Nuys Holiday Inn building (Seismic Safety Commission (SSC), 1994) 103

Figure 1-2: Failure of exterior reinforced concrete column in the Van Nuys Holiday Inn building during the 1994 Northridge Earthquake (Earthquake Engineering Field Investigation Team (EEFIT), 1994) 104

Figure 1-3: Close-up shear failure of a reinforced concrete column located in the Van Nuys Holiday Inn building during the 1994 Northridge Earthquake (Comartin, Elwood, & Faison, 2004) 105

Figure 1-4: Tests photos of columns with FRP jacketing adapted from Zoppo et al. (2017) 106

Figure 1-5: Drawing of steel jacket used to repair columns adapted from Aboutaha et al. (1999) 107

Figure 1-6: Tests of prestressed strands as transverse reinforcement adapted from Yarandi et al. (2004) 108

Figure 1-7: External transverse reinforcement used by (Richter, 2012) 109

Figure 1-8: External transverse reinforcement used by (Daluga, 2015) 110

Figure 2-1: Typical cross-section of Series One through Series Four specimens (See Table 2-1 through Table 2-4 for definitions) Adapted from Richter (2012) 111

Figure 2-2: Cross-section for Series-one and Series-Two specimens. 112

Figure 2-3: Series-One beam test setup 113

Figure 2-4: Series-One beam instrumentation location 113

Figure 2-5: Shear and moment diagrams for Series-One beam specimens 114

Figure 2-6: Series-One beam specimen optical target layout along spliced bars 115

Figure 2-7: Series-One beam specimen testing setup. 116

Figure 2-8: Series-One through Series-Four coupon specimen test setup 117

Figure 2-9: Series-One and Series-Two coupon specimen optical target layout 118

Figure 2-10: Testing setup for tension coupon specimens (Series One through Series Three). . 119

Figure 2-11: Specimen D4 (configuration 1) and D6 (configuration 2) cross section and anchor depth 120

Figure 2-12: Anchor dimension for specimen D4 (configuration 1) and D6 (configuration 2). Dimension B = 40 in. and A = 20 in. for D4, Dimension B = 53.3 in. and A = 13.3 in. for D6 120

Figure 2-13: Specimen D5 and D7 cross section and anchor depth (configuration 3) 121

Figure 2-14: Anchor dimension for specimen D5 and D7 (configuration 3) 121

Figure 2-15: Specimen cross section and anchor depth for specimens D8, D10, D12-D16, D18 (configuration 4) 122

Figure 2-16: Anchor dimension for specimen D8, D10, D12-D16, D18 (configuration 4) 122

Figure 2-17: Anchor plate assembly for specimens D8, D10, D12-D16, D18 (configuration 4)123

Figure 2-18: Series-Three specimen cross-section 124

Figure 2-19: Series-Three plan view.. 125

Figure 2-20: Series-Three elevation view and target layout 125

Figure 2-21: Series-Four specimen cross-section with post-tensioned transverse reinforcement installed.. 126

Figure 2-22: Series Four elevation view and target layout with post-tensioned transverse reinforcement spaced at 3.5 in. 127

Figure 2-23: Series Four elevation view and target layout with post-tensioned transverse reinforcement spaced at 5 in. 128

Figure 2-24: Series-Four testing setup. 129

Figure 2-25: Series-Five column reinforcement layout 130

Figure 2-26: Series-Five column post-tensioned clamp layout (specimen C1) 131

Figure 2-27: Series-Five plan view with post-tensioned transverse reinforcement.................... 132

Figure 2-28: Series-Five elevation view of one post-tensioned transverse reinforcement tie.... 132

Figure 2-29: Specimen C1 installed with post-tensioned transverse reinforcement.................. 133

Figure 2-30: Specimen C1 elevation view and target layout 134

Figure 2-31: Specimen C2 elevation view and target layout 135

Figure 2-32: Specimen C1 testing setup. 136

Figure 2-33: Specimen C2 testing setup. 137

Figure 3-1: Load vs. midspan deflection for specimen C1 138

Figure 3-2: Load vs. midspan deflection for specimen C2... 139

Figure 3-3: Load vs. midspan deflection for specimen C3... 140

Figure 3-4: Load vs. midspan deflection for specimen C4... 141

Figure 3-5: Load vs. midspan deflection for specimen C5... 142

Figure 3-6: Load vs. midspan deflection for specimen C6... 143

Figure 3-7: Crack pattern for specimen C1, South support (top) and North support (bottom) (Applied load at overhang = 37.5 kip, midspan deflection = 0.4 in.) 144

Figure 3-8: Crack pattern for specimen C2, South support (top) and North support (bottom) (Applied load at overhang = 37.1 kip, midspan deflection = 0.4 in.) 145

Figure 3-9: Crack pattern for specimen C3, South support (top) and North support (bottom) (Applied load at overhang = 37.5 kip, midspan deflection = 0.4 in.) 146

Figure 3-10: Crack pattern for specimen C4, South support (top) and North support (bottom) (Applied load at overhang = 39 kip, midspan deflection = 0.5 in.) 147

Figure 3-11: Crack pattern for specimen C5, South support (top) and North support (bottom) (Applied load at overhang = 37.2 kip, midspan deflection = 0.4 in.) 148

Figure 3-12: Crack pattern for specimen C6, South support (top) and North support (bottom) (Applied load at overhang = 38.5 kip, midspan deflection = 0.5 in.) 149

Figure 3-13: Grid station used for calculating horizontal and vertical deformations for Test Series One, Two, and Three 150

Figure 3-14: Horizontal deformations of concrete surface along splice length of specimen C1, initial loading and reload (data series are labeled using midspan deflection and average load applied at ends) 151

Figure 3-15: Horizontal deformations of concrete surface along splice length of specimen C2, initial loading and reload (data series are labeled using midspan deflection and average load applied at ends) 152

Figure 3-16: Horizontal deformations of concrete surface along splice length of specimen C3, initial loading and reload (data series are labeled using midspan deflection and average load applied at ends) 153

Figure 3-17: Horizontal deformations of concrete surface along splice length of specimen C4, initial loading and reload (data series are labeled using midspan deflection and average load applied at ends) 154

Figure 3-18: Horizontal deformations of concrete surface along splice length of specimen C5, initial loading and reload (data series are labeled using midspan deflection and average load applied at ends) 155

Figure 3-19: Horizontal deformations of concrete surface along splice length of specimen C6, initial loading and reload (data series are labeled using midspan deflection and average load applied at ends) 156

Figure 3-20: Vertical deformations of concrete surface along splice length of specimen C1, initial loading and reload (data series are labeled using midspan deflection and average load applied at ends) 157

Figure 3-21: Vertical deformations of concrete surface along splice length of specimen C2, initial loading and reload (data series are labeled using midspan deflection and average load applied at ends) 158

Figure 3-22: Vertical deformations of concrete surface along splice length of specimen C3, initial loading and reload (data series are labeled using midspan deflection and average load applied at ends) 159

Figure 3-23: Vertical deformations of concrete surface along splice length of specimen C4, initial loading and reload (data series are labeled using midspan deflection and average load applied at ends) 160

Figure 3-24: Vertical deformations of concrete surface along splice length of specimen C5, initial loading and reload (data series are labeled using midspan deflection and average load applied at ends) 161

Figure 3-25: Vertical deformations of concrete surface along splice length of specimen C6, initial loading and reload (data series are labeled using midspan deflection and average load applied at ends 162

Figure 3-26: Spliced region of specimen C5 during testing 163

Figure 3-27: Splice failure of specimen C5. All beams in Series One failed in a similar manner 164

Figure 3-28: Specimen D1 load versus specimen elongation 165

Figure 3-29: Specimen D2 load versus specimen elongation 165

Figure 3-30: Specimen D3 load versus specimen elongation 166

Figure 3-31: Specimen D4 load versus specimen elongation 166

Figure 3-32: Specimen D5 load versus specimen elongation 167

Figure 3-33: Specimen D6 load versus specimen elongation 167

Figure 3-34: Specimen D7 load versus specimen elongation 168

Figure 3-35: Specimen D8 load versus specimen elongation 168

Figure 3-36: Specimen D9 load versus specimen elongation 169

Figure 3 37: Specimen D10 load versus specimen elongation 169

Figure 3-38: Specimen D11 load versus specimen elongation 170

Figure 3-39: Specimen D12 load versus specimen elongation 170

Figure 3-40: Specimen D13 load versus specimen elongation 171

Figure 3-41: Specimen D14 load versus specimen elongation 171

Figure 3-42: Specimen D15 load versus specimen elongation 172

Figure 3-43: Specimen D16 load versus specimen elongation 172

Figure 3-44: Specimen D17 load versus specimen elongation 173

Figure 3-45: Specimen D18 load versus specimen elongation 173

Figure 3-46: Horizontal deformations of concrete surface along splice length of specimen D1, initial loading (data series are label using the average load applied to the splice ends)............. 174

Figure 3-47: Horizontal deformations of concrete surface along splice length of specimen D1, reload (data series are label using the average load applied to the splice ends)......................... 174

Figure 3-48: Horizontal deformations of concrete surface along splice length of specimen D2, initial loading (data series are label using the average load applied to the splice ends)............. 175

Figure 3-49: Horizontal deformations of concrete surface along splice length of specimen D2, reload (data series are label using the average load applied to the splice ends)......................... 175

Figure 3-50: Horizontal deformations of concrete surface along splice length of specimen D3, initial loading (data series are label using the average load applied to the splice ends)............. 176

Figure 3-51: Horizontal deformations of concrete surface along splice length of specimen D3, reload (data series are label using the average load applied to the splice ends)......................... 176

Figure 3-52: Horizontal deformations of concrete surface along splice length of specimen D4, initial loading (data series are label using the average load applied to the splice ends)............. 177

Figure 3-53: Horizontal deformations of concrete surface along splice length of specimen D4, reload (data series are label using the average load applied to the splice ends)......................... 177

Figure 3-54: Horizontal deformations of concrete surface along splice length of specimen D5, initial loading (data series are label using the average load applied to the splice ends)............. 178

Figure 3-55: Horizontal deformations of concrete surface along splice length of specimen D5, reload (data series are label using the average load applied to the splice ends)......................... 178

Figure 3-56: Horizontal deformations of concrete surface along splice length of specimen D6, initial loading (data series are label using the average load applied to the splice ends)............. 179

Figure 3-57: Horizontal deformations of concrete surface along splice length of specimen D6, reload (data series are label using the average load applied to the splice ends)......................... 179

Figure 3-58: Horizontal deformations of concrete surface along splice length of specimen D7, initial loading (data series are label using the average load applied to the splice ends)............. 180

Figure 3-59: Horizontal deformations of concrete surface along splice length of specimen D7, reload (data series are label using the average load applied to the splice ends)......................... 180

Figure 3-60: Horizontal deformations of concrete surface along splice length of specimen D8, initial loading (data series are label using the average load applied to the splice ends)............. 181

Figure 3-61: Horizontal deformations of concrete surface along splice length of specimen D8, reload (data series are label using the average load applied to the splice ends)......................... 181

Figure 3-62: Horizontal deformations of concrete surface along splice length of specimen D9, initial loading (data series are label using the average load applied to the splice ends)............. 182

Figure 3-63: Horizontal deformations of concrete surface along splice length of specimen D10, initial loading (data series are label using the average load applied to the splice ends)............. 183

Figure 3-64: Horizontal deformations of concrete surface along splice length of specimen D10, reload (data series are label using the average load applied to the splice ends) 183

Figure 3-65: Horizontal deformations of concrete surface along splice length of specimen D11, initial loading (data series are label using the average load applied to the splice ends)............. 184

Figure 3-66: Horizontal deformations of concrete surface along splice length of specimen D12, initial loading (data series are label using the average load applied to the splice ends)............. 185

Figure 3-67: Horizontal deformations of concrete surface along splice length of specimen D12, reload (data series are label using the average load applied to the splice ends) 185

Figure 3-68: Horizontal deformations of concrete surface along splice length of specimen D13, initial loading (data series are label using the average load applied to the splice ends)............. 186

Figure 3-69: Horizontal deformations of concrete surface along splice length of specimen D13, reload (data series are label using the average load applied to the splice ends) 186

Figure 3-70: Horizontal deformations of concrete surface along splice length of specimen D14, initial loading (data series are label using the average load applied to the splice ends)............. 187

Figure 3-71: Horizontal deformations of concrete surface along splice length of specimen D14, reload (data series are label using the average load applied to the splice ends) 187

Figure 3-72: Horizontal deformations of concrete surface along splice length of specimen D15, initial loading (data series are label using the average load applied to the splice ends)............. 188

Figure 3-73: Horizontal deformations of concrete surface along splice length of specimen D15, reload (data series are label using the average load applied to the splice ends) 188

Figure 3-74: Horizontal deformations of concrete surface along splice length of specimen D16, initial loading (data series are label using the average load applied to the splice ends)............. 189

Figure 3-75: Horizontal deformations of concrete surface along splice length of specimen D16, reload (data series are label using the average load applied to the splice ends) 189

Figure 3-76: Horizontal deformations of concrete surface along splice length of specimen D17, initial loading (data series are label using the average load applied to the splice ends)............. 190

Figure 3-77: Horizontal deformations of concrete surface along splice length of specimen D18, initial loading (data series are label using the average load applied to the splice ends)............. 191

Figure 3-78: Horizontal deformations of concrete surface along splice length of specimen D18, reload (data series are label using the average load applied to the splice ends) 191

Figure 3-79: Vertical deformations of concrete surface along splice length of specimen D1, initial loading (data series are label using the average load applied to the splice ends) 192

Figure 3-80: Vertical deformations of concrete surface along splice length of specimen D1, reload (data series are label using the average load applied to the splice ends) 192

Figure 3-81: Vertical deformations of concrete surface along splice length of specimen D2, initial loading (data series are label using the average load applied to the splice ends) 193

Figure 3-82: Vertical deformations of concrete surface along splice length of specimen D1, reload (data series are label using the average load applied to the splice ends) 193

Figure 3-83: Vertical deformations of concrete surface along splice length of specimen D3, initial loading (data series are label using the average load applied to the splice ends) 194

Figure 3-84: Vertical deformations of concrete surface along splice length of specimen D3, reload (data series are label using the average load applied to the splice ends) 194

Figure 3-85: Vertical deformations of concrete surface along splice length of specimen D4, initial loading (data series are label using the average load applied to the splice ends) 195

Figure 3-86: Vertical deformations of concrete surface along splice length of specimen D4, reload (data series are label using the average load applied to the splice ends) 195

Figure 3-87: Vertical deformations of concrete surface along splice length of specimen D5, initial loading (data series are label using the average load applied to the splice ends) 196

Figure 3-88: Vertical deformations of concrete surface along splice length of specimen D5, reload (data series are label using the average load applied to the splice ends) 196

Figure 3-89: Vertical deformations of concrete surface along splice length of specimen D6, initial loading (data series are label using the average load applied to the splice ends) 197

Figure 3-90: Vertical deformations of concrete surface along splice length of specimen D6, reload (data series are label using the average load applied to the splice ends) 197

Figure 3-91: Vertical deformations of concrete surface along splice length of specimen D7, initial loading (data series are label using the average load applied to the splice ends) 198

Figure 3-92: Vertical deformations of concrete surface along splice length of specimen D7, reload (data series are label using the average load applied to the splice ends) 198

Figure 3-93: Vertical deformations of concrete surface along splice length of specimen D8, initial loading (data series are label using the average load applied to the splice ends) 199

Figure 3-94: Vertical deformations of concrete surface along splice length of specimen D8, reload (data series are label using the average load applied to the splice ends) 199

Figure 3-95: Vertical deformations of concrete surface along splice length of specimen D9, initial loading (data series are label using the average load applied to the splice ends) 200

Figure 3-96: Vertical deformations of concrete surface along splice length of specimen D10, initial loading (data series are label using the average load applied to the splice ends) 201

Figure 3-97: Vertical deformations of concrete surface along splice length of specimen D10, reload (data series are label using the average load applied to the splice ends) 201

Figure 3-98: Vertical deformations of concrete surface along splice length of specimen D11, initial loading (data series are label using the average load applied to the splice ends) 202

Figure 3-99: Vertical deformations of concrete surface along splice length of specimen D12, initial loading (data series are label using the average load applied to the splice ends) 203

Figure 3-100: Vertical deformations of concrete surface along splice length of specimen D12, reload (data series are label using the average load applied to the splice ends) 203

Figure 3-101: Vertical deformations of concrete surface along splice length of specimen D13, initial loading (data series are label using the average load applied to the splice ends)............. 204

Figure 3-102: Vertical deformations of concrete surface along splice length of specimen D13, reload (data series are label using the average load applied to the splice ends) 204

Figure 3-103: Vertical deformations of concrete surface along splice length of specimen D14, initial loading (data series are label using the average load applied to the splice ends)............. 205

Figure 3-104: Vertical deformations of concrete surface along splice length of specimen D14, reload (data series are label using the average load applied to the splice ends) 205

Figure 3-105: Vertical deformations of concrete surface along splice length of specimen D15, initial loading (data series are label using the average load applied to the splice ends)............. 206

Figure 3-106: Vertical deformations of concrete surface along splice length of specimen D15, reload (data series are label using the average load applied to the splice ends) 206

Figure 3-107: Vertical deformations of concrete surface along splice length of specimen D16, initial loading (data series are label using the average load applied to the splice ends)............. 207

Figure 3-108: Vertical deformations of concrete surface along splice length of specimen D16, reload (data series are label using the average load applied to the splice ends) 207

Figure 3-109: Vertical deformations of concrete surface along splice length of specimen D17, initial loading (data series are label using the average load applied to the splice ends)............. 208

Figure 3-110: Vertical deformations of concrete surface along splice length of specimen D18, initial loading (data series are label using the average load applied to the splice ends)............. 209

Figure 3-111: Vertical deformations of concrete surface along splice length of specimen D18, reload (data series are label using the average load applied to the splice ends) 209

Figure 3-112: Crack pattern for specimen D1, southeast corner (average bar stress = 69 ksi) .. 210

Figure 3-113: Crack pattern for specimen D2, northeast corner (average bar stress = 58 ksi) .. 211

Figure 3-114: Crack pattern for specimen D3, northwest corner (average bar stress = 69 ksi) . 212

Figure 3-115: Crack pattern for specimen D4, northwest corner (average bar stress = 78 ksi) . 213

Figure 3-116: Crack pattern for specimen D5, southeast corner (average bar stress = 69 ksi) .. 214

Figure 3-117: Crack pattern for specimen D6, southwest corner (average bar stress = 70 ksi) . 215

Figure 3-118: Crack pattern for specimen D7, southwest corner (average bar stress = 70 ksi) . 216

Figure 3-119: Crack pattern for specimen D8, southeast corner (average bar stress = 81 ksi) .. 217

Figure 3-120: Crack pattern for specimen D9, northwest corner (average bar stress = 74 ksi) . 218

Figure 3-121: Crack pattern for specimen D10, southwest corner (average bar stress = 77 ksi) 219

Figure 3-122: Crack pattern for specimen D11, northwest corner (average bar stress = 70 ksi) 220

Figure 3-123: Crack pattern for specimen D12, northeast corner (average bar stress = 77 ksi) 221

Figure 3-124: Crack pattern for specimen D13, southwest corner (average bar stress = 77 ksi) 222

Figure 3-125: Crack pattern for specimen D14, southeast corner (average bar stress = 77 ksi) 223

Figure 3-126: Crack pattern for specimen D15, southwest corner (average bar stress = 77 ksi) 224

Figure 3-127: Crack pattern for specimen D16, northeast corner (average bar stress = 77 ksi) 225

Figure 3-128: Crack pattern for specimen D17, northeast corner (average bar stress = 70 ksi) 226

Figure 3-129: Crack pattern for specimen D18, northeast corner (average bar stress = 77 ksi) 227

Figure 3-130: Unconfined specimen D1 during testing 228

Figure 3-131: Splice failure of specimen D1 229

Figure 3-132: Confined specimen D4 (anchor configuration 1) during testing. Anchors under plywood cover which prevent concrete from damaging test equipment 230

Figure 3-133: Splice failure of specimen D4 (plywood removed to show anchor).................... 231

Figure 3-134: Confined specimen D7 (anchor configuration 3) during testing.......................... 232

Figure 3-135: Splice failure of specimen D7 233

Figure 3-136: Confined specimen D8 (anchor configuration 4) during testing.......................... 234

Figure 3-137: Splice failure of specimen D8 235

Figure 3-138: Specimen H1 load versus specimen elongation 236

Figure 3-139: Specimen H2 load versus specimen elongation 236

Figure 3-140: Specimen H3 load versus specimen elongation 237

Figure 3-141: Specimen H4 load versus specimen elongation 237

Figure 3-142: Specimen H5 load versus specimen elongation 238

Figure 3-143: Specimen H6 load versus specimen elongation 238

Figure 3-144: Specimen H7 load versus specimen elongation 239

Figure 3-145: Specimen H8 load versus specimen elongation 239

Figure 3-146: Specimen H9 load versus specimen elongation 240

Figure 3-147: Horizontal deformations of concrete surface along splice length of specimen H1 (data series are label using the average load applied to the splice ends) 241

Figure 3-148: Horizontal deformations of concrete surface along splice length of specimen H2 (data series are label using the average load applied to the splice ends) 241

Figure 3-149: Horizontal deformations of concrete surface along splice length of specimen H3 (data series are label using the average load applied to the splice ends) 242

Figure 3-150: Horizontal deformations of concrete surface along splice length of specimen H4 (data series are label using the average load applied to the splice ends) 242

Figure 3-151: Horizontal deformations of concrete surface along splice length of specimen H5 (data series are label using the average load applied to the splice ends) 243

Figure 3-152: Horizontal deformations of concrete surface along splice length of specimen H6 (data series are label using the average load applied to the splice ends) 243

Figure 3-153: Horizontal deformations of concrete surface along splice length of specimen H7 (data series are label using the average load applied to the splice ends) 244

Figure 3-154: Horizontal deformations of concrete surface along splice length of specimen H8 (data series are label using the average load applied to the splice ends) 244

Figure 3-155: Horizontal deformations of concrete surface along splice length of specimen H9 (data series are label using the average load applied to the splice ends) 245

Figure 3-156: Vertical deformations of concrete surface along splice length of specimen H1 (data series are label using the average load applied to the splice ends) 246

Figure 3-157: Vertical deformations of concrete surface along splice length of specimen H2 (data series are label using the average load applied to the splice ends) 246

Figure 3-158: Vertical deformations of concrete surface along splice length of specimen H3 (data series are label using the average load applied to the splice ends) 247

Figure 3-159: Vertical deformations of concrete surface along splice length of specimen H4 (data series are label using the average load applied to the splice ends) 247

Figure 3-160: Vertical deformations of concrete surface along splice length of specimen H5 (data series are label using the average load applied to the splice ends) 248

Figure 3-161: Vertical deformations of concrete surface along splice length of specimen H6 (data series are label using the average load applied to the splice ends) 248

Figure 3-162: Vertical deformations of concrete surface along splice length of specimen H7 (data series are label using the average load applied to the splice ends) 249

Figure 3-163: Vertical deformations of concrete surface along splice length of specimen H8 (data series are label using the average load applied to the splice ends) 249

Figure 3-164: Vertical deformations of concrete surface along splice length of specimen H9 (data series are label using the average load applied to the splice ends) 250

Figure 3-165: Specimen H1 during testing.. 251

Figure 3-166: Splice failure of specimen H1 252

Figure 3-167: Specimen H4 during testing.. 253

Figure 3-168: Splice failure of specimen H4 254

Figure 3-169: Specimen H8 during testing 255

Figure 3-170: Splice failure of specimen H8 256

Figure 3-171: Grid station used for calculating vertical and horizontal deformations in Series-Four 257

Figure 3-172: Horizontal deformations of concrete surface along splice length of specimen PTR20-3.5-5K (data series are label using the average load applied to the splice ends) 258

Figure 3-173: Horizontal deformations of concrete surface along splice length of specimen PTR20-3.5-10K (data series are label using the average load applied to the splice ends) 258

Figure 3-174: Horizontal deformations of concrete surface along splice length of specimen PTR20-3.5-15K (data series are label using the average load applied to the splice ends) 259

Figure 3-175: Horizontal deformations of concrete surface along splice length of specimen PTR20-5-5K (data series are label using the average load applied to the splice ends) 259

Figure 3-176: Horizontal deformations of concrete surface along splice length of specimen PTR20-5-10K (data series are label using the average load applied to the splice ends) 260

Figure 3-177: Horizontal deformations of concrete surface along splice length of specimen PTR20-5-15K (data series are label using the average load applied to the splice ends) 260

Figure 3-178: Horizontal deformations of concrete surface along splice length of specimen PTR20-NC (data series are label using the average load applied to the splice ends) 261

Figure 3-179: Vertical deformations of concrete surface along splice length of specimen PTR20-3.5-5K (data series are label using the average load applied to the splice ends) 262

Figure 3-180: Vertical deformations of concrete surface along splice length of specimen PTR20-3.5-10K (data series are label using the average load applied to the splice ends) 262

Figure 3-181: Vertical deformations of concrete surface along splice length of specimen PTR20-3.5-15K (data series are label using the average load applied to the splice ends) 263

Figure 3-182: Vertical deformations of concrete surface along splice length of specimen PTR20-5-5K (data series are label using the average load applied to the splice ends) 263

Figure 3-183: Vertical deformations of concrete surface along splice length of specimen PTR20-5-10K (data series are label using the average load applied to the splice ends) 264

Figure 3-184: Vertical deformations of concrete surface along splice length of specimen PTR20-5-15K (data series are label using the average load applied to the splice ends) 264

Figure 3-185: Vertical deformations of concrete surface along splice length of specimen PTR20-NC (data series are label using the average load applied to the splice ends) 265

Figure 3-186: Specimen PTR20-3.5-5K during testing 266

Figure 3-187: Splice failure of specimen PTR20-3.5-5K 267

Figure 3-188: Specimen PTR20-5-10K during testing 268

Figure 3-189: Splice failure of specimen PTR20-5-10K 269

Figure 3-190: Shear cone failure of specimen PTR20-3.5-15K 270

Figure 3-191: Column C1 loading history (markers indicate measurement recordings)............ 271

Figure 3-192: Column C2 loading history (markers indicate measurement recordings)............ 271

Figure 3-193: Lateral load versus top drift ratio for column C1... 272

Figure 3-194: Lateral load versus top drift ratio for column C2... 273

Figure 3-195: Axial load versus top drift ratio for column C1. 274

Figure 3-196: Axial load versus top drift ratio for column C2. 275

Figure 3-197: Grid station for calculating horizontal and vertical strains in series five............ 276

Figure 3-198: Column C1 drift ratio vs. tensile strain (recorded at the column base in the outermost layer of steel in tension)... 277

Figure 3-199: Column C2 drift ratio vs. tensile strain (recorded at the column base in the outermost layer of steel in tension)... 277

Figure 3-200: Reinforcement strain distribution over height of column C1 (south bars indicate outermost steel layer in tension, markers indicate the drift ratio when strain was recorded)..... 278

Figure 3-201: Reinforcement strain distribution over height of column C2 (south bars indicate outermost steel layer in tension, markers indicate the drift ratio when strain was recorded)..... 278

Figure 3-202: Comparisons of column C1 and C2 at the labeled drift ratio.............................. 279

Figure 3-203: Comparisons of column C1 and C2 at the labeled drift ratio.............................. 280

Figure 3-204: Comparisons of column C1 and C2 at the labeled drift ratio.............................. 281

Figure 3-205: Inclined Shear cracking of column C2 at a drift ratio of 1% 282

Figure 3-206: Shear failure of column C2 resulting from large inclined crack......................... 283

Figure 3-207: Concrete compression zone in column C1 at a drift ratio of 5% 284

Figure 4-1: Mean bond strength versus splice length from unconfined lap splice tests 285

Figure 4-2: Mean bond strength versus splice length from unconfined lap splice tests containing #11 reinforcing bars and larger 286

Figure 4-3: Mean bond strength versus splice length from unconfined lap splice tests with data representing yielding and no yielding... 287

Figure 4-4: Mean bond strength versus splice length from unconfined lap splice tests containing #11 reinforcing bars and larger with data representing yielding and no yielding 288

Figure 4-5: Maximum steel stress versus splice length from unconfined lap splice tests 289

Figure 4-6: Maximum steel stress versus splice length from unconfined lap splice tests containing #11 reinforcing bars and larger 290

Figure 4-7: Maximum steel stress versus splice length from unconfined lap splice tests with data representing yielding and no yielding 291

Figure 4-8: Maximum steel stress versus splice length from unconfined lap splice tests containing #11 reinforcing bars and larger with data representing yielding and no yielding 292

Figure 4-9: Idealized diagram showing the distribution of tensile and bond stresses in a simple reinforced concrete beam reprinted from Abrams (1913) 293

Figure 4-10: Distribution of bar stress along lapped bars reprinted from Kluge and Tuma (1945) 294

Figure 4-11: Force in bar and bond distribution reprinted from Mains (1951). 295

Figure 4-12: Idealized strain and stress distribution for unconfined lap splices reprinted from Richter (2012) 296

Figure 4-13: Trend of bar stress versus splice length for unconfined splice database proposed by Fleet 2019........ 297

Figure 4-14: Ratios of measured steel stress to measured yield stress versus splice length........ 298

Figure 4-15: Ratios of measured steel stress to measured yield stress versus splice length of bars of #11 and larger 299

Figure 4-16: Surface tensile strain versus drift ratio adapted from Wang (2014) 300

Figure 4-17: Measured bar strain versus drift ratio 301

Figure 4-18: Peak bar stress values for Series One and Series Two coupon tests........ 302

Figure 4-19: Mean bond strength versus splice length from Series Two 303

Figure 4-20: (Magnified view) Mean bond strength versus splice length from Series Two 304

Figure 4-21: Maximum steel stress versus splice length from Series Two 305

Figure 4-22: (Magnified view) Maximum steel stress versus splice length from Series Two ... 306

Figure 4-23: Mean bond strength versus TRI from Series One and Series Two........ 307

Figure 4-24: Maximum inferred bar strain versus values of TRI for Series One and Series Two 308

Figure 4-25: Mean bond strength versus splice length from Series Three 309

Figure 4-26: Maximum steel stress versus splice length from Series Three 310

Figure 4-27: Mean bond strength versus TRI from Series Three 311

Figure 4-28: Maximum inferred bar strain versus values of TRI for Series One through Series Three 312

Figure 4-29: Mean bond strength versus splice length from Series Four 313

Figure 4-30: Maximum steel stress versus splice length from Series Four 314

Figure 4-31: Mean bond strength versus TRI from Series Four 315

Figure 4-32: Maximum bar strain versus values of lateral confining pressure for Series Four.. 316

Figure 4-33: Crack map of column C2 at a drift ratio of 0.5%, Lateral load equal to 34.4 kips 317

Figure 4-34: Crack map of column C2 at a drift ratio of 1%, Lateral load equal to 57.8 kips ... 318

Figure 4-35: Crack map of column C2 at a drift ratio of 2%, Lateral load equal to 56.1 kips ... 319

Figure 4-36: Crack map of column C1 at a drift ratio of 0.5%, Lateral load equal to 31.1 kips 320

Figure 4-37: Crack map of column C1 at a drift ratio of 1%, Lateral load equal to 53 kips 321

Figure 4-38: Crack map of column C1 at a drift ratio of 2%, Lateral load equal to 56 kips 322

Figure 4-39: Crack map of column C1 at a drift ratio of 3%, Lateral load equal to 56.2 kips ... 323

Figure 4-40: Geometry of specimens and post-tensioned transverse reinforcement adapted from (Yamakawa, 2000) 324

Figure 4-41: Testing protocol and loading setup used in column test by Yamakawa et al. Adapted from (Yamakawa, 2000) 324

Figure 4-42: Summary of selected test specimens by Yamakawa et al. Adapted from (Yamakawa, 2000) 325

Figure 4-43: (Transverse reinforcement shear contribution / nominal shear demand)(shear span/effective depth) versus drift ratio for columns from Yamakawa et al., Series Five, and selected columns from the ACI 369 database. Data points with red border indicate specimens that did not failure in shear... 326

Figure 4-44: (Transverse reinforcement shear contribution / nominal shear demand)(shear span/effective depth) versus drift ratio for columns from Yamakawa et al., Series Five, and selected columns from the ACI 369 database. Data points with red border indicate specimens that did not failure in shear... 327

Figure 4-45: Post-tensioned transverse reinforcement ratio versus drift ratio for columns from Yamakawa et al. and Series Five 328

Figure 4 46: Post-tensioned transverse reinforcement spacing ratios versus drift ratio for columns from Yamakawa et al. and Series Five 329

Figure 4-47: Shear strength contribution from initial post-tensioning stress to nominal shear demand versus drift ratio for columns from Yamakawa et al. and Series Five 330

Figure 4-48: Shear strength contribution from post-tensioning stress equal at yield to nominal shear demand versus drift ratio for columns from Yamakawa et al. and Series Five 331

Figure A-1: Measured stress-strain curves for #11 Gr. 60 A615 bars used in Test Series One through Series Four 348

Figure A-2: Tri-linear stress strain curve used to estimate bar strains in Eq. 3-1 through Eq. 3-3 349

Figure A-3: Parameters for stress-strain relationship for reinforcing steel in Series One through Series Four 350

Figure A-4: Measured stress-strain curves for ¾ in. Gr. B7 threaded rod used as anchors in Series Two 351

Figure A-5: Measured stress-strain curves for ¼ in. C1018 smooth rod used as spirals in Series Three 352

Figure A-6: Measured stress-strain curves for 1/2 in. Gr. B7 threaded rod used as post-tensioning rods in Series Four and Series Five 353

Figure A-7: Measured stress-strain curves for #8 Gr. 60 A615 bars used as longitudinal reinforcement in Series Five 354

Figure A-8: Measured stress-strain curves for #3 Gr. 60 A615 bars used as transverse reinforcement in Series Five 355

Figure A-9: Series One formwork (beams) 356

Figure A-10: Spliced region prior to casting Series-One beams 357

Figure A-11: Placement of concrete in formwork for beams C1-C6........ 358

Figure A-12: Formwork used to cast coupons in Series One and Series Two 359

Figure A-13: Casting of coupons D13 and D14 tested in Series Two........ 360

Figure A-14: Series Three formwork........ 361

Figure A-15: Specimen H3 prior to casting (splice length = 18 in.)........ 362

Figure A-16: Specimen H6 prior to casting (splice length = 24 in.)........ 363

Figure A-17: Specimen H8 prior to casting (splice length = 30 in.)........ 364

Figure A-18: Reinforcing cage for specimens C1 and C2 in Series Five........ 365

Figure A-19: Spacing of ties along the shear span of specimens C1 and C2 (s=12in.)........ 366

Figure A-20: Depths to longitudinal bars in specimens C1 and C2 367

LIST OF SYMBOLS

a	:	Shear span length
A_{pt}	:	Total tensile area of post-tensioning rod within spacing s
A_{st}	:	Total cross-section area of steel reinforcement at a section
A_{tr}	:	Total cross-sectional area of transverse reinforcement perpendicular to spliced bars being developed at a spacing *s*
b	:	Width of rectangular concrete compression zone
d	:	Effect depth or distance from outermost fiber in compression to centroid of steel reinforcement group
d_b	:	Nominal bar diameter of spliced reinforcement
d_{eff}	:	Effective embedment depth of epoxied anchors
E_c	:	Modulus of concrete
E_s	:	Elastic modulus of steel
f_c	:	Concrete stress
f''_c	:	Peak concrete stress
f_{pt}	:	Tensile stress in post-tensioning rods
f_{pti}	:	Initial tensile stress in post-tensioning rods
f_{pty}	:	Tensile stress in post-tensioning rods corresponding to yielding
f_s	:	Steel stress
f_{su}	:	Maximum estimated steel tensile stress
f_y	:	Steel stress corresponding to yield
f_{yt}	:	Yield stress of transverse reinforcement

f_2 : Steel stress used to define slope of strain hardening region

i : Target station number

j : Load step

l_s : Lap splice length

N : Number of bars being spliced by transverse reinforcement

s : Spacing of conventional transverse reinforcement

s_{pt} : Spacing of post-tensioned transverse reinforcement

TRI : Transverse Reinforcement Index

V_{max} : Maximum shear demand

v_{max} : Maximum shear stress demand

v_{pt} : Shear resistance of post-tensioned transverse reinforcement

v_s : Shear resistance of transverse reinforcement

v_{tr} : Shear resistance of conventional transverse reinforcement

x_i^j : Length of target station *i* at load step *j*

x_i^0 : Undeformed length of target station *i* at load step *j*

y_i^j : Length of target station *i* at load step *j*

y_i^0 : Undeformed length of target station *i* at load step *j*

ε_c : Concrete strain

ε_o : Concrete strain at peak stress

ε_s : Steel strain

ε_{sh}	:	Steel strain at the onset of strain hardening
ε_2	:	Steel strain used to define slope of strain hardening region
$\varepsilon_{y_i}^{j}$	:	Vertical deformation at target station *i* at load step *j*
$\delta_{x_i}^{j}$	:	Horizontal deformation at target station *i* at load step *j*
$\delta_{y_i}^{j}$	:	Vertical deformation at target station *i* at load step *j*
δ_{max}	:	Maximum displacement in the direction of applied load
μ	:	Mean bond strength
ρ	:	Longitudinal reinforcement ratio
ρ_{tr}	:	Transverse reinforcement ratio of conventional ties
ρ_{pt}	:	Post-tensioned transverse reinforcement ratio
ρ_{pti}	:	Post-tensioned transverse reinforcement ratio corresponding to the initial prestressing
ρ_{pty}	:	Post-tensioned transverse reinforcement ratio corresponding to yielding of the threaded rods

ABSTRACT

Post-earthquake examinations of reinforced concrete structures often show structural damage resulting from bond and shear failures. Such failures typically occur in reinforced concrete elements with details known to cause problems, such as widely spaced transverse reinforcement and/or lap splices located in regions of flexural yielding. These details are common in older reinforced concrete buildings (built before 1970) that have reinforced concrete columns with longitudinal reinforcement spliced just above the floor level, and transverse reinforcement spaced at a distance of $d/2$ or longer. This investigation focused on means to increase the deformability of existing reinforced concrete elements susceptible to bond and shear failures during a seismic event or other applications requiring toughness. The effects of confinement provided by epoxied anchors, spiral transverse reinforcement, and post-tensioned external clamps were investigated. Emphasis was placed on producing a strengthening device that can be sized, fabricated, and installed with ease because most of the existing strengthening techniques require specialized labor, tools, and materials. The observations collected support the idea that active confinement provided by post-installed and post-tensioned transverse reinforcement was the most effective method to improve structural deformability among the methods studied and within the ranges considered.

1. INTRODUCTION

1.1 Background

Poor performance of reinforced concrete buildings during the 1960 Agadir, Morocco Earthquake is said to be the genesis for seismic design recommendations of reinforced concrete structures (Sozen, 2012). Such recommendations were first introduced in the seminal 1961 publication "*Design of Multistory Reinforced Concrete Buildings for Earthquake Motions*" (Blume, Newmark, & Corning, 1961). This document made seismic design recommendations based on post-earthquake reconnaissance observations and experimental investigations performed by C. P. Siess, M. A. Sozen, and N. M. Newmark. Subsequent shear and bond failures of columns during the 1963 Skopje, 1964 Anchorage, and 1967 Caracas earthquakes resulting from widely spaced transverse reinforcement and bars spliced at column ends motivated the 1971 American Concrete Institute Committee 318 to introduce seismic design provisions for shear reinforcement and lap splices in accordance to Blume et al. (ACI Committee 318, 1971). These provisions required increased lap splice lengths, lap splices placed away from locations of flexural yielding, and confinement of lap splices. It was also determined that the maximum shear force expected in columns was equal to the shear force required to cause flexural yielding at column ends. This design methodology became known later as capacity-based design.

The work of Blume et al. (1961) stood the test of time, becoming the basis of reinforced concrete seismic design codes for decades to come. The recommended details provided structural members with the strength and toughness required to withstand earthquake demands. As a result, buildings built today are less susceptible to brittle failures. But what about buildings built prior to or without these recommendations? With hundreds of thousands of existing vulnerable buildings in seismically active cities such as Istanbul, Athens, Los Angeles, Napoli, Tokyo and many others (fib, 2003), replacement is unfeasible. Strengthening of vulnerable reinforced concrete elements is possible through retrofitting but common techniques used today often require specialized labor, costly materials, and difficult application.

1.2 Lessons Learned from Previous Earthquakes and Experimental Investigations

The objective of this research program was to evaluate the effects of post-installed transverse reinforcement on concrete elements with vulnerable lap splice and shear reinforcement details. In this report, vulnerable reinforcement detailing refers to reinforced concrete elements containing widely spaced transverse reinforcement (such as traditional stirrups or ties), lap splices of inadequate length and/or located in regions of flexural yielding. Such detailing is most common in reinforced concrete columns, often occurring in unison. These details are often the culprit of shear and bond failures during earthquakes. A review of previous experimental investigations which evaluated the performance of poor reinforcement details is discussed. Finally, a review of current strengthening techniques such as steel jacketing, fiber reinforced polymer (FRP) wrapping, and other forms of external confinement are discussed.

1.2.1 Past Performance of Reinforced Concrete Structures

Well documented structural damage to the seven-story reinforced concrete Holiday Inn building located in Van Nuys, CA following the 1994 Northridge Earthquake made apparent the critical consequences of detailing practice in reinforced concrete structures constructed prior to 1971 (Figure 1-1). Constructed in 1966, the Van Nuys building had two common failures during this earthquake: shear failures of reinforced concrete columns, and bond failures of lap splices located near column ends. Shear failures of columns occurred due to a lack of transverse reinforcement also known as ties. The tie spacing s exceeded the quantity $d/2$. Where the effective depth d represents the distance from the outermost concrete fiber in compression to the centroid of the outermost reinforcing steel layer in tension. Reconnaissance reports illustrated the actual spacing of transverse reinforcement to be equal to or greater than the effective depth (Earthquake Spectra, 1996). With this spacing, the transverse reinforcement was believed to have been nearly ineffective in contributing to the shear strength, resulting in a shear failure of the concrete as shown in Figure 1-2 and Figure 1-3.

Prior to the 1994 Northridge Earthquake, the Van Nuys building was instrumented with three strong motion accelerographs located at the roof, third, and ground level floors (Lepage, 1997). Lepage (1997) ran linear and non-linear dynamic analyses to estimate the maximum story drift demands during the earthquake. The story drift ratio is defined as the maximum relative lateral displacement in a given story divided by the story height. Lepage estimated the maximum drift demands to be 1.8%, with yielding of the columns occurring at 1.3%. These numerical estimates assume that bond and shear failures do not occur, suggesting that the bond and shear failures observed likely occurred at drift ratios smaller than 1 to 2%. Clearly, reinforced concrete structures which fail in bond or shear before or even soon after yielding are unreliable.

1.2.2 Review of Past Experimental Investigations Involving Shear Strength of Columns

Sezen and Moehle (2006) investigated reinforced concrete columns containing widely spaced transverse reinforcement or ties typical of that used in buildings not designed for seismic demands (Van Nuys Holiday Inn building). No lap splices were present in these columns. Four full-scale columns were tested with the following range of measured material properties: 1) concrete compressive strengths f_c` of 3 to 3.2 ksi, 2) a mean longitudinal reinforcement yield stress of 63 ksi, and 3) a mean transverse reinforcement yield stress of 69 ksi. The applied axial load ranged from $0.15f_c`A_g$ to $0.6f_c`A_g$, where A_g refers to the gross cross-sectional area of the column (18 in. x 18 in.). The longitudinal reinforcement ratio (for #9 deformed bars) was 2.5%. The aspect ratio was 3.9 for all columns.

The tie spacing s was 12 in. with 90-degree hooks. This resulted in a s/d ratio of 0.8, where d refers to the effective depth of the outermost layer of longitudinal reinforcement in tension. In each spacing, two #3 ties (one perimeter and one diamond) were used as transverse reinforcement. This resulted in a transverse reinforcement ratio ρ_{tr} = 0.18%. The columns were cycled laterally with increasing drift ratios. Results indicated flexural yielding occurring at a drift ratio of approximately 1% followed by shear failure at a drift ratio of approximately 2.5%. The lateral resistance of the columns was effectively zero at drift ratios exceeding 3%. The shear failures were consistent to what was observed in the reconnaissance literature (Earthquake Spectra, 1996).

Henkhaus (2010) tested columns similar to Sezen et al. (2006). Eight full-scale columns were tested with the following range of measured material properties: 1) concrete compressive strengths f_c` of 3 to 4.5 ksi, 2) a mean longitudinal reinforcement yield stress of 67 ksi, and 3) a mean transverse reinforcement yield stress of 60 ksi. The applied axial load ranged from $0.15f_c`A_g$ to

$0.5f_c`A_g$, where A_g = 18 in. x 18 in. The longitudinal reinforcement ratio ranged from 1.5% (for #7 deformed bars) to 2.5% (for #9 deformed bars). The column aspect ratios ranged from 2 to 4.

Henkhaus (2010) tested four tie spacings: 1) #3 tie spaced at 18 in. (ρ_{tr} = 0.07%), 2) #2 tie spaced at 8 in. (ρ_{tr} = 0.07%), 3) two #3 ties (one perimeter and one diamond) spaced at 12 in. (ρ_{tr} = 0.18%), and 4) #3 tie spaced at 12 in. (ρ_{tr} = 0.10%). The resulting *s/d* ratios were 1.2, 0.44, 0.67, and 0.67, respectively. The columns were cycled laterally with increasing drift ratios. Using smaller ties at smaller spacings, while maintaining a constant transverse reinforcement ratio ρ_{tr}, increased the maximum drift ratio. Specimens with a #3 tie spaced at 18 in. (ρ_{tr} = 0.07%) reached a maximum drift ratio of 1.3%, while specimens with a #2 tie spaced at 8 in. (ρ_{tr} = 0.07%) reached a maximum drift ratio of 2.3%. Increasing the total amount of transverse reinforcement ρ_{tr} was also shown to increase the maximum drift ratio. Specimen with two #3 ties spaced at 12 in. (ρ_{tr} = 0.18%) reached a maximum drift ratio of 2.8%, while specimens with #3 tie spaced at 12 in. (ρ_{tr} = 0.10%) reached a maximum drift ratio of 2.0%. The maximum drift ratio was taken as ¾% of the drift ratio at shear failure.

1.2.3 Review of Past Experimental Investigations Involving Lap Splices

Kilic and Sozen (2003) reported the collapse of a 115-meter smokestack during the 1999 Marmara Earthquake in Turkey. Collapse was caused by failure of lap splices located in regions of flexural yielding. Splice lengths in the smokestack were approximately 50-bar diameters, demonstrating that code-conforming splice lengths may not always lead to satisfactory performance during earthquakes. Laboratory tests of unconfined tension lap splices exceeding 50-bar diameters by Richter (2012) showed that bond stresses concentrated within 20-bar diameters from the loaded splice end. It was concluded that increasing splice lengths beyond 40-bar diameters does not produce a proportional increase in splice strength.

Lynn, Moehle, Mahin, and Holmes (1996) previously tested column specimens identical to those tested by Sezen et al. (2006) previously mentioned (replicating columns in the Van Nuys Holiday Inn building.). These columns, however, contained 20-bar diameter lap splices at the base of the column. Results showed yielding of the column occurred at a drift ratio of approximately 1%. Although sudden splice failure did not occur, decay in bond strength caused by load reversals resulted in approximately 50% reduction in moment capacity at a drift ratio of approximately 2%. The authors concluded that the lack of transverse reinforcement prevented the splice from maintaining yield forces through increasing cycles of larger displacements.

1.2.4 Review of Investigations Involving Strengthening of Columns

Shear strengthening of reinforced columns using Fiber Reinforced Polymer (FRP) was tested by Zoppo, Ludovico, Balsamo, and Prota (2017). Seven full-scale columns were tested with the following range of measured material properties: 1) concrete compressive strengths f_c` of 2 to 5 ksi, 2) a mean longitudinal reinforcement yield stress of 67 ksi, and 3) a mean transverse reinforcement yield stress of 68 ksi. The applied axial load was equal to $0.1f_c$`A_g, where A_g refers to the gross cross-sectional area of the column (12 in. x 12 in.). The longitudinal reinforcement ratio was 4.2%. The aspect ratio was 3 for all columns.

Columns tested by Zoppo et al. (2017) contained widely spaced transverse reinforcement $s/d = 1.0$. This resulted in a transverse reinforcement ratio ρ_{tr} = 0.11%. Columns were cycled laterally with increasing drift ratios. Two columns tested without FRP wrapping reached a maximum drift ratio of approximately 2%. The maximum drift ratio was taken as 0.7% of the drift ratio at shear failure. Five columns with FRP had transverse reinforcement ratios ρ_{fr} ranging from 0.06% to 0.67%. Columns with an FRP transverse reinforcement ratio ρ_{fr} of 0.06% maintained their flexural capacity up to a drift ratio of 4%. The flexural capacity was reduced by 50% at a drift ratio of 6%. Columns with an FRP transverse reinforcement ratio ρ_{fr} of 0.3% to 0.67% maintained flexural capacities up to drift ratios of 6%. Maintaining flexural capacity was attributed to the FRP sheets maintaining the integrity of the concrete core. Although effective at preventing shear failure, the failure modes of columns installed with FRP were brittle fracture and sudden debonding of the FRP sheets (Figure 1-4). The authors also noted that estimation of shear strength attributed to FRP is difficult. This leads to expensive, unnecessary and undesirable strengthening.

Columns susceptible to shear failures were repaired using steel jacketing in tests by Aboutaha, Engelhardt, Jirsa, Kreger (1999). Steel jacketing was provided by steel angles and plates that were field-welded, bolted, and connected to each face of the column using adhesive anchor bolts (Figure 1-5). Non-shrink grout was also injected between the face of the specimen and the steel jacketing.

Eleven full-scale columns were tested with the following range of measured material properties: 1) concrete compressive strengths f_c` of 2.4 to 5 ksi, 2) a mean longitudinal reinforcement yield stress of 65 ksi, and 3) a mean transverse reinforcement yield stress of 60 ksi. The applied axial load was equal to $0.1f_c$` A_g, where A_g = 36 in. x 18 in. The longitudinal reinforcement ratio was 2.5%. The aspect ratio was 3 for all columns.

Columns tested by Aboutaha et al. (1999) contained widely spaced transverse reinforcement $s/d = 0.9$. This resulted in a transverse reinforcement ratio ρ_{tr} = 0.05%. Four columns without steel jacketing failed in shear at drift ratios of approximately 2%. The seven columns strengthened with steel jacketing maintained their flexural capacity at drift ratios exceeding 5%. Failure of columns with steel jacketing was not observed at drift ratios beyond 6% as the tests were limited by the stroke of the lateral actuators. While the performance of the steel jacket was impressive, the authors warned that the use of the jacket led to a 40% increase in the flexural strength of the column. This increase could inadvertently increase the shear demands on the column during a strong ground motion. It should also be noted that the installation of the steel jacket was also a meticulous task, requiring specialized labor (for welding and epoxied anchor installation).

Yarandi, Saatcioglu and Foo (2004) tested columns with similar geometries as Aboutaha et al. (1999). Yarandi et al. (2004) used external prestressing to strengthen columns susceptible to shear failures (Figure 1-6). Six full-scale columns were tested with the following range of measured material properties: 1) concrete compressive strengths f_c` of 5 to 6 ksi, 2) a mean longitudinal reinforcement yield stress of 58 ksi and 3) a mean transverse reinforcement yield stress of 58 ksi. The applied axial load was equal to $0.1f_c$` A_g, where A_g = 14 in. x 28 in. The longitudinal reinforcement ratio was 2.4%. The aspect ratio was 2.1 for all columns.

Columns tested by Yarandi et al. (2004) contained transverse reinforcement spaced at $s/d = 0.45$. This resulted in a transverse reinforcement ratio ρ_{tr} = 0.09%. External prestressing was provided by mounting prestressing strands on the column face spaced at d/4. The tensile strength of the strands was 270 ksi. Prestressing was performed through dilating specially manufactured adjustable spacers placed between the prestressing strand and the column face. The initial prestress (prior to testing) in the strands was reported as 25% of tensile strength of the strand. Columns were cycled laterally with increasing drift ratios. Columns without prestressing failed in shear at a drift ratio of 1% while columns with prestressing failed in shear at a drift ratio of 4%. The drift capacity increase attributed to the prestressing was proposed to be proportional to the initial prestressing force in the strand. Nevertheless, it is difficult to estimate initial prestressing in this method as varying prestress exists in between the adjustable spacers.

In tests by Yamakawa, Kamogawa, and Kurashige (2000) columns vulnerable to shear failures were repaired using post-tensioned transverse reinforcing ties. The post-tensioned transverse reinforcing ties consisted of 4 corner blocks which bared against the corners of the square column. Four post-tensioning rods connected each corner block to the column. Post-tensioning stress of approximately 1/3 of the yield stress of the post-tensioning rod was induced into each rod prior to testing. The yield stress of the post-tensioned rod was reported as 180 ksi. In tests done by Yamakawa et al. (2000) the following parameters were used:

- Aspect ratios a/d ranging from 1 to 2
- Concrete compressive strengths f_c' ranging from 2 ksi to 4.5 ksi
- Longitudinal reinforcement with a yield stress f_y of 53 ksi
- Conventional transverse reinforcement with a yield stress f_{yt} of 48 ksi
- Longitudinal reinforcement ratios ρ of 1.38% to 2.53%
- Conventional transverse reinforcement ratio ρ_{tr} of 0.08% to 0.21%
- Post-tensioned transverse reinforcement ratios ρ_{tr} of 0.06% to 0.54%
- Post-tensioned transverse reinforcement yield stress f_{pty} not exceeding 180 ksi

Yamakawa et al. (2000) tested 31 reinforced concrete columns in double curvature using a cyclic loading protocol. An applied axial load of $0.2f_c'A_g$ was used for all specimens. Spacing of the conventional ties ranged from *d/4 to d/2*. Of the 31 columns, 22 columns were installed with post-tensioned transverse reinforcement, the remaining 9 were not. Of the 22 columns tested with post-tensioned transverse reinforcement, only 20 columns failed in flexure or shear. The other two columns (*R99M-P41'R, R99M-P41'pw*) failed prematurely in bond. All 9 columns tested without post-tensioned transverse reinforcement failed in shear.

Columns without post-tensioned transverse reinforcement failed at drift ratios of 0.5% to 1%. The drift ratio at failure was reported as the drift ratio corresponding to 80% of the peak lateral load V_{exp}. Column (*R99L-P0pw*) had conventional ties with a spacing of *d/4*, transverse reinforcement ratio ρ_{tr} of 0.21%, and failed in shear at a drift ratio of 1%. All other columns (*R99L-P0, R99M-P0R*, *R99M-P0L*, *R99M-P0H*, *R99M-P0, R98M-P0, R99S-P0*, *and R98S-P0*) with conventional tie spacings of *d/2* and ρ_{tr} of 0.08% failed at drift ratios around 0.5%.

Columns with post-tensioned transverse reinforcement failed at measured drift ratios ranging from 1.5% to at least 5% (tests were not continued beyond drift ratios of 5%). Columns with reported drift ratios of 5% had post-tensioned transverse reinforcement ratios ρ_{pt} greater than 0.45%, yielded in flexure, and did not suffer shear or bond failure. Columns with post-tensioned transverse reinforcement ratios less than 0.21% reached maximum drift ratios ranging from 1.5% to at least 3.5%. In general, post-tensioned transverse reinforcement resulted in drift capacities equal to that provided by conventional transverse reinforcement for similar transverse reinforcement ratios (ρ_{pt} ~ ρ_{tr}). A detailed discussion of tests by Yamakawa et al. (2000) is presented in Chapter 4 in comparison to columns in Series Five tested in this report.

1.2.5 Review of Investigations Involving Strengthening of Existing Lap Splices

The steel jacketing methods used to increase shear strength of columns by Aboutaha et al.(2000) were also previously examined to increase the strength of columns containing 24-bar diameter lap splices (Aboutaha, Engelhardt, Jirsa, & Kreger, 1996). Specimen geometries and material properties were similar to those mentioned in section 1.2.4. Six steel jacketing configurations were tested on identical columns. Strengthening of the short lap splice consisted of a steel jacket fastened to the column along the length of the lap splice with adhesive anchor bolts. Specimen without steel jacketing suffered abrupt splice failure occurring at a drift ratio of 1% . Specimen with steel jacketing suffered abrupt splice failures at drift ratios ranging from 1.5% to 4%. The control of splitting cracks attributed to the steel jacket resulted in increased deformability of the lap splice. Given the scatter in the drift ratios at bond failure, and limited testing, alternative method to increase the deformability of lap splices should be investigated.

1.2.6 Use of External Stirrups on Reinforced Concrete Beams Without Transverse Reinforcement

External transverse reinforcement was used as shear reinforcement in beam specimens tested by Richter (2012) and Daluga (2015). Richter (2012) tested beam specimens containing lap splices that were subjected to four-point bending. No shear reinforcement was provided in the beams. External transverse reinforcement was provided to prevent shear failure as shown in Figure 1-7. Daluga (2015) tested beams without shear reinforcement. Once shear failure occurred, beams where stitched together using the same external transverse reinforcement used by Richter (2012) and retested (Figure 1-8). The external transverse reinforcement consisted of high-strength threaded rod and steel channels that clamped around the beam. In tests by Richter (2012) and Daluga (2015) the external transverse reinforcement was tightened against the beam using an impact wrench or snugged by hand. In both series of tests, the contribution of shear strength attributed to the external transverse reinforcement was not quantified. The effectiveness of the external transverse reinforcement was consistent in preventing shear failure compared to post-tensioned transverse reinforcing ties installed on columns tested by Yamakawa et al. (2000). Further discussion on the use of external transverse reinforcement (referred to as post-tensioned transverse reinforcement in this report) is available in Chapter Four – Series Five.

1.3 Research Objectives

The objective of this research program was to understand the effects of post-installed transverse reinforcement on both the strength and deformability of reinforced concrete elements containing vulnerable seismic reinforcement details related to bond and shear. This objective was accomplished through forty-two large-scale laboratory experiments on the following five series of tests:

1) Series One – to study the tensile strength and deformability of unconfined tension lap splices.
2) Series Two – to study the effects of post-installed epoxied anchors on the tensile strength and deformability of tension lap splices.
3) Series Three – to study the effects of spiral transverse reinforcement on the tensile strength and deformability of tension lap splices.

4) Series Four – to study the effects of post-tensioned transverse reinforcement on the tensile strength and deformability of tension lap splices.
5) Series Five – to study the effects of post-tensioned transverse reinforcement on the shear strength and drift capacity of reinforced concrete columns.

1.4 Scope of Research

The first objective was pursued by testing twelve specimens with unconfined lap splices (Series One). All specimens contained a pair of spliced Gr. 60 #11 reinforcing bars. A splice length of 56-bar diameters, and the same cross-section were used in all twelve specimens. In Series One, six specimens were tested as beams, and six specimens were tested as tension coupons. In the beam specimens, tensile forces were generated in the splice through bending. In the coupon specimens, tensile forces were applied directly to the splice ends. All splices were loaded monotonically until splice failure occurred. Peak bar stresses, bar strains and deformations of the splice were measured.

The second objective was pursued by testing twelve specimens with lap splices confined by epoxied anchors (Series Two). Specimens in Series Two were cast identical to coupons in Series One. Epoxied anchors were installed along the splice length and embedded perpendicular to the plane producing splitting cracks. Splices were loaded, unloaded, installed with anchors, and then monotonically loaded until bond failure occurred. Peak bar stresses, bar strains and deformations of the splice were measured.

The third objective was pursued by testing nine specimens with lap splices confined by spiral transverse reinforcement (Series Three). The same reinforcement as coupons in Series One and Two was used. However, splice lengths ranged from 12 to 20-bar diameters. The cross section was modified to have equal cover above and below the spliced bars. All other dimensions were identical to Series One and Two. A smooth steel wire, fabricated in the shape of a helical coil (referred to as spiral reinforcement), was placed concentrically around the splice. Splices were monotonically loaded until bond failure occurred. Peak bar stresses, bar strains and deformations of the splice were measured.

The fourth objective was pursued by testing seven specimens with lap splices confined by post-tensioned transverse reinforcement (Series Four). Specimens in Series Four were cast identical to specimens in Series Three. All specimens had a splice length of 20-bar diameters. The post-installed transverse reinforcement was installed on the specimen prior to testing. The spacing and level of post-tensioning stress were varied. Splices were monotonically loaded until bond failure occurred. Peak bar stresses, bar strains and deformations of the splice were measured.

The fifth objective was pursued by testing two columns specimens with poor shear reinforcement detailing (Series Five). Two columns nearly identical were cast. One column was tested with post-tensioned transverse reinforcement, the other was tested without them as reference. Each column was cycled at increasing drift ratios until shear failure was observed. Load versus displacement histories and concrete surface strains were measured.

2. EXPERIMENTAL PROGRAM

2.1 Introduction

Five series of tests (for a total of forty-two specimens) were conducted at Purdue University's Robert L. and Terry L. Bowen Laboratory for Large-Scale Civil Engineering Research in West Lafayette, IN to evaluate the effects of post-installed transverse reinforcement on the strength and deformability of reinforced concrete elements. The focus of the tests was on mechanism of resistance related to bond and shear. This chapter describes the test specimens, testing setup, and testing procedure.

2.2 Series One: Unconfined Lap Splices

2.2.1 Specimen Description

In test Series One, twelve specimens were tested. All specimens contained a pair of unconfined lap splices. Six of the twelve specimens were tested as beams, and the remaining six were tested as coupons. In beam specimens, tensile forces were generated in the splice through bending. In coupon specimens, tensile forces were applied directly to the splice ends. Specimens named C1-C6 were beams. Specimens named D1, D2, D3, D9, D11, and D17 were coupons. All specimens in Series One contained a pair of 56 bar-diameter (79 in.) unconfined lap splices of #11 Gr. 60 reinforcing bars. The nominal specimen cross section for all splice tests is shown in Figure 2-1. The specific cross-section dimensions for Series One is shown in Figure 2-2. Concrete was cast with the bars near the bottom of the formwork to avoid top-casting effects for all specimens. The measured concrete cylinders strengths f_c' ranged from 5.2 ksi to 5.9 ksi for beams, and 4 ksi to 4.5 ksi for coupons at the time of testing. All reinforcing bars were Gr. 60 A615 steel with measured tensile yield stresses f_y of 65 ksi (beams) and 67 ksi (coupons). Reinforcement for all beams was from a single heat. This was the case for coupons, too. Table 2-1 and Table 2-2 list the properties of beam and coupon specimens.

All specimens in Series One had a minimum clear cover c_{so} of 2-1/8 bar diameters (3 in.) as shown in Figure 2-1. The rectangular width b of Series-One specimens was 17-5/8 in. and the height of the section h was 30 in. The resulting effective depth d to the spliced bars was 24-1/4 in. This resulted in a beam longitudinal reinforcement ratio ρ of approximately 1.5% in the spliced region and 0.75% outside of the spliced region. Specimens in Series One contained no transverse reinforcement to serve as reference for Series Two through Series Four. The longitudinal reinforcement ratio ρ is calculated as:

$$\rho = \frac{A_{st}}{b \cdot d} \qquad (2\text{-}1)$$

where:

A_{st} : Total cross-sectional area of steel reinforcement at a section

b : Width of rectangular concrete compression zone

d : Effect depth or distance from outermost fiber in compression to centroid of steel reinforcement group

2.2.2 Test Setup and Procedure

The profile of the test beams and their test setup are shown in Figure 2-3. Each beam was rotated 180-degrees (along its longitudinal axis) from its casting position so that the spliced bars were at the top of the beam. This allowed for crack mapping and observations of the specimen to be documented more easily throughout the test. The beam was then placed on two simple supports in the form of 2.5 in. diameter steel pins resting on smooth plates at each support. Load was applied to each overhang by two 30-ton center-hole hydraulic rams which reacted against high-strength steel threaded rods fastened to the laboratory floor (Figure 2-4). This loading resulted in a region of nearly constant moment over the splice length (Figure 2-5). The hydraulic rams were manually controlled by hand pumps using a single manifold to 1) maintain equal loads in shear spans and 2) prevent rapid loading which may damage or fail the splice. In order to prevent failure of the shear spans, which were cast without conventional transverse reinforcement (stirrups), external shear reinforcement was added. The external shear reinforcement consisted of 11 evenly spaced clamps. The clamps consisted of double steel channels (C3x5) placed on the top and bottom of the beam and fastened together using high-strength threaded rod (ASTM A193 B7). The rods were tightened together with the effort of an air impact driver. This was the same external shear reinforcement used by Richter (2012).

Load was measured using load cells placed in-line with the hydraulic ram at each overhang. The total load was reported at each end was twice the reading of a single load cell. String potentiometers were located at the north overhang, north splice end, midspan, south splice end and south overhang to measure deflections. Dial gauges were also used to supplement deflection measurements at the north overhang, midspan, and south overhang. Linear Variable Differential Transformers (LVDTs) were used to measure north and south support displacements to correct for settlement at the supports. Horizontal and vertical deformations of the concrete surface at the level of the lap splice were measured using an optical target tracking system. Optical targets were placed on the east beam face along the length of the lap splice. The target layout is shown in Figure 2-6. Figure 2-7 shows a photograph of the test setup for beam tests. A summary of the sensors used for the beam specimens is listed in the Appendix.

A plan view of the coupon specimens (D1, D2, D3, D9, D11, D17) test setup is shown in Figure 2-8. Similar to beam specimens (C1-C6), coupon specimens were rotated 180-degrees along their longitudinal axis so that the spliced bars were at the top of the specimen. Each coupon specimen was tested in a self-reacting load frame consisting of two steel columns and channels. Tensile forces were applied to the ends of the spliced bars by using ERICO Lenton headed bar attachments (Terminators) threaded to the ends of each bar. Similar to beams, this loading resulted in a nearly constant moment along the length of the splice. On one end, the headed bar bore against the surface of the channel of the reaction frame. On the other end, load was applied to the headed bars through a transfer beam consisting of double channels. The transfer beam was loaded using two 1-3/8 in. diameter post-tensioning rods. The rods were loaded using two 60-ton hydraulic rams which reacted against the end of the frame. The pressure in each ram was controlled by an independent manifold in effort to keep the transfer beam from rotating excessively, and to maintain approximately equal tensile forces in each splice.

A through-hole load cell placed in-line with each hydraulic ram was used to measure load in each spliced bar. Concrete surface deformations were measured using a layout of optical targets shown in Figure 2-9. A photograph of the test setup is shown in Figure 2-10. A list of the sensors and their accuracies used for coupon specimens are given in the Appendix.

Beam specimens were loaded in increments of 0.08 in. of midspan deflection. Crack maps were drawn at each load step. Optical target readings were recorded after each load step. When the midspan deflection reached 0.4 in., the specimen was unloaded, and optical targets were removed to prevent damage during splice failure. The beam was then reloaded until splice failure occurred. Applied load was monitored continuously. The load steps when optical target readings were recorded are shown in figures presented in Chapter 3.

Coupon specimens were loaded monotonically until splice failure occurred. Splitting crack widths at the splice ends were continuously monitored. Optical target readings, photos, and crack maps were recorded throughout the test. Load and specimen deformations were measured throughout the test. Optical targets were left on the specimen up to splice failure which allowed for measurements of peak surface strains. The load steps when optical target readings were recorded are shown in figures presented in Chapter 3.

2.3 Series Two: Lap Splices Confined by Post-Installed Epoxied Anchors

2.3.1 Specimen Description

Twelve tension coupons were tested in Series Two. Specimens were named D4-D8, D10, D12-D16, and D18. These specimens were cast identical and at the same time as coupons from Series One. However, coupons in Series Two contained four configurations of transverse reinforcement in the form of epoxied anchors. Epoxied anchors consisted of ¾ in. high-strength Gr. B7 threaded rods. The anchors were inserted into 7/8 in. holes drilled into the top surface of the specimen perpendicular to the plane of the spliced bars. The holes were then thoroughly cleaned and filled with Hilti HIT-RE500 V3 epoxy. The anchors were carefully inserted into the fresh epoxy and allowed to cure. Spliced #11 reinforcement was from the same heat as Series One tests. Table 2-3 lists properties of specimen in Series Two.

The first anchor configuration (specimen D4) contained two anchors with a spacing of 40 in. and an effective embedment depth d_{eff} of 5 in. as shown in Figure 2-11 and Figure 2-12. The second anchor configuration (specimen D6) contained two anchors with a spacing of 53 in. and an effective embedment depth d_{eff} of 5 in. as shown in Figure 2-11 and Figure 2-12. The third anchor configuration (specimens D5 and D7) contained 3 anchors with a spacing of 26.5 in. and an effective embedment depth d_{eff} of 5 in. as shown in Figure 2-13 and Figure 2-14. The fourth anchor configuration (specimens D8, D10, D12-D16 and D18) contained 3 anchors with a spacing of 26.5 in. and an effective embedment depth d_{eff} of 12 in. as shown in Figure 2-15 and Figure 2-16. The effective embedment depth d_{eff} of the anchor refers to the distance the anchor extends below the bottom plane of the spliced reinforcing bars. In anchor configuration four, the exposed threaded rod on top of the specimen was furnished with a plate, washer, and nut which was snugged against the concrete surface after curing of the epoxy (Figure 2-17).

In order to quantify the effects of the anchor on bond, the term *TRI* developed by Sozen and Moehle (1990) was used in this report. The term *TRI* is referred to as the "Transverse Reinforcement Index" or "Confining Reinforcement Index". This term was originally developed to quantify the increase in bond strength of spliced bars confined by traditional forms of transverse reinforcement (stirrups or ties). In this report, the use of *TRI* will serve a similar purpose, but it is also used to quantify the effects of transverse reinforcement on splice deformability.

The Transverse Reinforcement Index *TRI* is calculated as:

$$TRI = \frac{A_{tr} \cdot f_{yt}}{N \cdot d_b \cdot s} \qquad (2\text{-}2)$$

where:

A_{tr} : Total cross-sectional area of transverse reinforcement perpendicular to spliced bars being developed at a spacing s

f_{yt} : Yield stress of transverse reinforcement

N : Number of bars being spliced by transverse reinforcement

d_b : Nominal bar diameter of spliced reinforcement

s : Spacing of transverse reinforcement

For Series Two, the value of A_{tr} was taken as the effective tensile area of a ¾ in. threaded rod equal to 0.334 in^2. The value f_{yt} was taken as the minimum specified yield stress of 105 ksi for Gr. B7 threaded rod. Two splices were being confined by the anchors, therefore the value of N equaled 2. The spacing s was equal to the values listed in the anchor configurations above. Values of *TRI* have units of stress.

2.3.2 Test Setup and Procedure

The testing setup and instrumentation was identical to coupons in Series One. Specimens were first loaded until splitting crack widths reached a value of 0.06 inches at the splice ends. After the formation of these splitting cracks, the specimen was unloaded, installed with epoxied anchors, and reloaded to splice failure. Optical targets were left on the specimen until failure. Load and specimen deformations were measured continuously throughout the test. The load steps when specimen deformations were recorded are shown in figures presented in Chapter 3.

An industrial hammer drill was used to drill holes for the epoxied anchors. The drill bit diameter was ⅞ in. Drilled holes were cleaned using compressed air, a steel wire brush, and a vacuum cleaner. Epoxy was injected into each hole, starting from the bottom of the hole and withdrawing the epoxy dispenser. The hole was filled to mid-height before insertion of the ¾ inch threaded rod. Threaded rods were given a half turn once they contacted the bottom of the hole. Epoxy was cured for at least 24 hours in laboratory conditions prior to reloading, except in specimen D7, in which epoxy was cured for 48 hours. In specimens D8, D10, D12-D16, and D18 (configuration four) steel bearing plates (4 in. x 4in. x ¾ in.) were placed over the anchor after the anchor was placed into the fresh epoxy. After curing the epoxy for at least 24 hours, a nut with a washer was torqued to 100 ft-lbf. In specimens D4-D8, D10, and D12, anchors were installed at an ambient temperature of approximately 55° F. In specimens D13-D16, and D18, anchors were installed at an ambient temperature of approximately 75° F.

2.4 Series Three: Lap Splices Confined with Spiral Reinforcement

2.4.1 Specimen Description

In Series Three, nine coupon specimens were tested. Specimens were named H1-H9. These specimens had similar cross-sectional properties as coupon specimens in Series One and Series Two. Nevertheless, in Series Three the cover values c_t and c_b were equal to 5 in. above and below the spliced bars as shown in Figure 2-18. The values of c_{si} and c_o remained unchanged. This change in the cross section was done to conserve material and was not expected to affect factors related to bond, allowing comparison with Series One and Two. The same heat of #11 Gr. 60 A615 steel used in Series One and Two coupons was used in Series Three. In Series Three, transverse reinforcement was provided in the form of ¼ in. diameter C1018 smooth steel rod. This rod was wound and placed concentrically around each splice over its entire length as shown in Figure 2-19 and Figure 2-20. The arrangement resulted in a helical coil with a nominal diameter of 6 in. The smooth rod was cleaned using brake cleaner to remove any manufacturing grease or debris that would affect bond prior to casting. In this report as in engineering practice, the helical coil will be referred to as spiral reinforcement. Table 2-4 lists the specimen properties for Series Three.

Three configurations of spiral reinforcement were used in Series Three. Splice lengths were 12-bar diameters (H1-H3), 16-bar diameters (H4-H6) and 20-bar diameters (H7-H9). The spacing or pitch of the spiral s was 2 in., 3in., and 4 in. respectively. The spiral diameter remained a constant 6 in. for all splice lengths. At the ends of the splice, an extra coil was added to ensure the ends of the spiral had sufficient anchorage. All specimens were cast from the same batch of concrete. The measured concrete cylinder strength f_c' averaged 5.2 ksi. The value of f_{yt} was taken as the minimum specified yield stress of 54 ksi for C1018 rod.

It should be noted that the spiral reinforcement was cast within the specimen, and not post-installed like other forms of transverse reinforcement tested in this study. The use of the Transverse Reinforcement Index TRI was used to quantify the effects of spirals for Series Three using Eq. (2-2). The value of the spacing s and the transverse reinforcement yield stress f_{yt} are listed above. The value of A_{tr} was taken as twice the tensile area of a ¼ in. diameter rod ($2 \times 0.05 \text{ in}^2 = 0.1 \text{ in}^2$)

because each spiral intersected the splitting plane twice within a spacing *s*. The value of *N* was taken as 1 since each spiral surrounded one splice.

2.4.2 Test Setup and Procedure

The testing setup was identical to coupons in Series One and Series Two. The spacing of the optical targets is shown in Figure 2-20. Load was applied to the splice ends until failure. Similar to Series Two, optical targets remained on the specimen all the way to failure. Crack maps, photos and optical target readings were recorded at each load step. Load and specimen deformations were measured at each load step throughout the test. On the final load step the optical tracking system was set to record continuously to capture deformations up to failure. The load steps when specimen deformations were recorded are shown in figures presented in Chapter 3.

2.5 Series Four: Lap Splices Confined with Post-Tensioned Transverse Reinforcement

2.5.1 Specimen Description

In Series Four, seven coupons were tested. All seven specimens in Series Four contained 20-bar diameter lap splices. Specimens in Series Four were installed with post-tensioned transverse reinforcement prior to testing. One specimen did not contain post-tensioned transverse reinforcement to serve as reference. The same Gr. 60 reinforcement was used as in Series One through Series Three. Specimens in this series were named with the following convention: “PTRX-Y-Z”, where X represented the splice length in inches, Y represented the spacing of the post-tensioned transverse reinforcement in inches, and Z represented the post-tensioning force in each threaded rod. The post-tensioning consisted of ½ in. Gr. B7 threaded rods and (2) L3x3x3/8 steel angles at each corner of the specimen as shown in Figure 2-21. The value of f_{yt} was taken as the minimum specified yield stress of 105 ksi. Two spacings of the post-tensioned transverse reinforcement were used, 3.5 in. and 5 in. For each spacing, a post-tensioning force of approximately 5, 10, and 15 kips was applied to all threaded rods (Figure 2-22 and Figure 2-23). These forces corresponded to tensile stresses in the threaded rod of $f_{yt}/3$, $2f_{yt}/3$, and f_{yt}. A calibrated torque wrench was used to apply the post-tensioning force in the threaded rods. The torque corresponding to the desired post-tensioning force was determined using a calibrated bolttensioning indicator before installation. All material properties for Series Four are listed in Table 2-5.

The Transverse Reinforcement Index TRI was used again to quantify the post-tensioned transverse reinforcement in Series Four using Eq. (2-2). Values spacing s between the post-tensioned transverse reinforcement are listed above. The value of A_{tr} was taken as twice the effective tensile area of a ½ in. diameter treaded rod (2 x 0.141 in^2 = 0.282 in^2) as two of the post-tensioning rods are effective in applying force perpendicular to the potential splitting crack that can be generated by bursting stresses caused by bond. The value of N was taken as 2 because the post-tensioned transverse reinforcement surrounds both splices. The transverse reinforcement yield stress f_{yt} was taken as the minimum specified yield stress of 105 ksi for Gr. B7 threaded rod.

2.5.2 Test Setup and Procedure

Coupons in Series Four were tested statically in tension using a 660-kip MTS tensile testing machine (Figure 2-24). Post-tensioned transverse reinforcement was installed on the specimen in an upright position allowing each rod to be easily accessed and post-tensioned. Horizontal and vertical deformations of the concrete surface along the length of the splice were measured using infrared optical targets as shown in Figure 2-22 and Figure 2-23. Coupons in Series Four were loaded in monotonically until splice failure occurred. Crack maps, photos, and optical target readings were recorded at each load step. The load steps when specimen deformations were recorded are shown in figures presented in Chapter 3.

2.6 Series Five: Columns with Post-Tensioned Transverse Reinforcement

2.6.1 Specimen Description

In Series Five, two similar reinforced concrete columns with a square cross section were tested. Columns were named C1 and C2. Figure 2-25 shows the reinforcement layout of both columns. The cross-sectional width b was 18 in. The gross area A_g was (18 in. x 18 in. = 324 in.^{2}). Longitudinal reinforced was provided by (8) #8 Gr. 60 bars for a longitudinal steel area of (8 x 0.79 in.^{2} = 6.32 in.^{2}). The resulting column longitudinal reinforcement ratio was approximately 2%. Transverse reinforcement in the form of conventional rectilinear ties fabricated using #3 Gr.

60 A615 deformed bars with 90-degree hooks. The transverse reinforcement ratio of the conventional ties ρ_{tr} is calculated as:

$$\rho_{tr} = \frac{A_{tr}}{b \cdot s} \tag{2-3}$$

where:

A_{tr}	:	Total cross-sectional area of web or transverse reinforcement (ties)
b	:	Width of rectangular concrete compression zone
s	:	Spacing of conventional transverse reinforcement (ties)

Tie spacing s was 12 in. along the entire column height. The value of A_{tr} was taken as twice the cross-sectional area of a #3 tie (2 x 0.11 in.^{2} = 0.22 in.^{2}). This resulted in a transverse reinforcement ratio ρ_{tr} = 0.1% using Eq. (2-3). The ratio of the tie spacing s to the effective depth d of the column was 0.8. The measured concrete cylinders strength f_c' was 7 ksi for both specimens at the time of testing. All reinforcing bars were Gr. 60 A615 steel with measured reinforcement yield stresses f_y of 70 ksi (longitudinal reinforcement) and 68 ksi (ties). Table 2-6 lists the properties of specimens in Series Five.

For a column subject to lateral loading in single curvature, the maximum shear stress v_{max} that can be applied to the column can be computed as:

$$v_{max} = \frac{V_{max}}{b \cdot d} \tag{2-4}$$

where:

V_{max}	:	Maximum shear demand or (plastic moment capacity of column divided by the shear span)
b	:	Width of rectangular concrete compression zone
d	:	Depth to outermost longitudinal reinforcement layer of steel in tension

The post-tensioned transverse reinforcement was designed to resist v_{max}. The post-tensioned transverse reinforcement was assumed to resist shear force in a similar fashion to that of conventional ties or stirrups. The shear strength contribution of the post-tensioned transverse reinforcement v_{pt} (in terms of stress) is computed as:

$$v_{pt} = \rho_{pt} \cdot f_{pt} \qquad (2\text{-}5)$$

$$\rho_{pt} = \frac{A_{pt}}{b \cdot s_{pt}} \qquad (2\text{-}6)$$

where:

A_{pt}	:	Total tensile area of post-tensioning rod within spacing s
f_{pt}	:	Initial tensile stress in post-tensioning rods
ρ_{pt}	:	Transverse reinforcement ratio of post-tensioning rods
d	:	Effective depth of column section
s_{pt}	:	Spacing of post-tensioned transverse reinforcement
b	:	Width of column perpendicular to the direction of loading

In Eq. (2-5) it is implied that the stress in post-tensioning rods is not expected to increase much from its initial value as observed by Yamakawa et al. (2000). This was shown when columns installed with post-tensioned transverse reinforcement had ratios of ρ_{pt} greater than 0.2% or ratios of v_{pt} / v_{max} greater than 0.4. Therefore, the required post-tensioning stress in the rods can be estimated as:

$$f_{pt} = \frac{v_{max}}{\rho_{pt}} \qquad (2\text{-}7)$$

where:

f_{pt}	:	Initial tensile stress applied to post-tensioning rods
ρ_{pt}	:	Transverse reinforcement ratio of post-tensioning rods

In Series Five, the same post-tensioning geometry was used as in Series Four and installed on column C1 as shown in Figure 2-26 through Figure 2-29. The spacing s_{pt} was chosen to be 5 in.

The value of A_{tr} was taken as twice the effective tensile area of a ½ in. diameter rod (2 x 0.141 in^2 = 0.282 in^2) as only two of the four rods surrounding the column are effective in resisting shear in the direction of the applied lateral load. Using Eq. 2-7 the required stress in each threaded rod was calculated to be approximately 70 ksi (corresponding to 10 kips of force per rod). V_{max} was calculated by obtaining the maximum moment from a moment-curvature analysis of the column. Force in the post-tensioned transverse reinforcement was applied using the same process as in Series Four.

Column C2 did not contain post-tensioned transverse reinforcement. The specimen geometry and reinforcement of columns C1 and C2 were nearly identical to test done by Lynn (2001) and Sezen and Moehle (2006). In these tests, columns failed in shear prior to or at the onset of flexural yielding.

2.6.2 Test Setup and Procedure

Compressive axial load was applied independently with manually controlled hydraulic rams by two high strength threaded rods fastened to the strong floor at the laboratory. Load was applied to each high strength rod through a center-hole 60-ton ram pressurized with the same manifold. The rams reacted against a loading beam resting on the top of the column. Load was measured using load cells placed in-line with the hydraulic rams. The total axial load was a sum of the two load cell readings. Axial load was applied and held nearly constant during the test using a pressure relief valve and electric hydraulic pump. A nearly constant uniaxial force of 150 kips ($0.1f_c{'}A_g$) was applied to each column throughout the test as was done by Lynn (2001) and Sezen and Moehle (2006). Lateral load was applied a distance (H = 58 in.) above the column foundation. The lateral load was controlled using a two-way-acting actuator, controlled manually. Lateral load was measured using a load cell placed in-line with the actuator. Out-of-plane movement of the specimen was prevented by bracing the actuator at the mounting location to the specimen. Slip of the specimen was prevented by clamping the base to the strong floor.

Displacements of each column were measured using an optical tracking system with the layout shown in Figure 2-30 and Figure 2-31. Optical targets were placed along the column height at the level of each longitudinal reinforcement layer. The purpose of the optical tracking system was to infer tensile bars strains, as well as lateral displacements. The top and mid-height displacements of the column were also measured using string potentiometers. Displacements, lateral load, and axial load were measured continuously throughout the test. Optical readings were taken at the drift ratio steps discussed in Chapter 3. Each column was loaded cyclically with increasing lateral displacements. The column was cycled three times at a target drift ratio. Crack maps, photos, and optical target readings were recorded at each load step.

3. EXPERIMENTAL RESULTS

3.1 Introduction

The experimental results from the five series of tests are described in this chapter.

3.2 Series One: Unconfined Lap Splices

3.2.1 Beam Tests: Maximum Steel Stress, Steel Strain, and Mean Bond Strength

For test beams the maximum bar stress f_{su} ranged from 73 ksi to 75 ksi and maximum estimated bar strain ε_{su} of 1.6% to 1.8% respectively. The mean bond strength μ ranged from $4.3\sqrt{f_c'}$ to $4.6\sqrt{f_c'}$. Table 3-1 shows the maximum applied load P_{su}, maximum moment M_u, steel tensile stress f_{su}, tensile bar strain ε_{su}, and mean bond strength μ obtained from each of the six beam tests. The maximum applied load P_{su} was calculated by averaging the applied loads acting on the beam overhangs. The maximum applied moment M_u corresponds to the moment at the end of the lap splice included the effects of self-weight and all loading hardware. The maximum average applied load was obtained from load versus deflection plots recorded during testing (Figure 3-1 through Figure 3-6). The self-weight of the beam was assumed to be 150 pcf. The maximum steel tensile stress f_{su} was calculated at the splice end using a moment-curvature analysis of the beam cross section. The maximum bar strain ε_{su} corresponding to the maximum bar stress was determined from the following tri-linear stress-strain relationship defined by Eqs. (3-3) to (3-5). The mean bond strengths μ were computed using Eq. (3-6). The following assumptions were made in the moment-curvature analysis:

1) Normal strain caused by bending is linearly proportional to distance to neutral axis.
2) Stress-strain relationship for concrete in compression defined by Hognestad (1951) in Eq. (3-1) and Eq. (3-2).
3) Stress-strain relationship defined by Eq. (3-3) to (3-5) which represents the response of bars used.

The stress-strain relationship defined by Hognestad (1951) was defined by Eq. (3-1) and (3-2):

$$f_c = f''_c \cdot \left[2 \cdot \frac{\varepsilon_c}{\varepsilon_o} - \left(\frac{\varepsilon_c}{\varepsilon_o}\right)^2\right] \; (if\ \varepsilon_s \leq \varepsilon_o) \tag{3-1}$$

$$f_c = f''_c \cdot \left[1 - \frac{\varepsilon_c - \varepsilon_o}{0.004 - \varepsilon_o} \cdot 0.15\right] \; (if\ \varepsilon_s \geq \varepsilon_o) \tag{3-2}$$

where:

f_c	:	Concrete stress (psi)
f''_c	:	Peak stress of ($0.85f'_c$) (psi)
ε_c	:	Concrete strain
ε_o	:	Concrete strain at peak stress (approximated as $2f''_c/E_c$)
E_c	:	Modulus (psi) of concrete ($57000\sqrt{f''_c}$ with f''_c in psi)

The maximum bar strain ε_{su} corresponding to the maximum bar stress was determined from the following tri-linear stress-strain relationship defined by Eq. (3-3) to (3-5):

$$f_s = \varepsilon_s \cdot E_s \; (if\ \varepsilon_s < \frac{f_y}{E_s}) \tag{3-3}$$

$$f_s = f_y \; (if\ \frac{f_y}{E_s} \leq \varepsilon_s \leq \varepsilon_{sh}) \tag{3-4}$$

$$f_s = \frac{f_2 - f_y}{\varepsilon_2 - \varepsilon_{sh}} \cdot (\varepsilon_s - \varepsilon_{sh}) + f_y \; (if\ \varepsilon_s > \varepsilon_{sh}) \tag{3-5}$$

where:

f_s	:	Steel stress (ksi)
ε_s	:	Steel strain (in/in)
E_s	:	Elastic modulus of steel (29000 ksi)
f_y	:	Steel stress corresponding to yield (ksi)
ε_{sh}	:	Steel strain at the onset of strain hardening (in/in)
f_2	:	Steel stress used to define slope of strain hardening region (ksi)
ε_2	:	Steel strain used to define slope of strain hardening region (in/in)

For simplicity, a tri-linear stress-strain relationship was used. With the range of bar stress and strains tested, the tri-linear relationship is nearly identical to the measured stress-strain curves listed in the Appendix. The values of f_y, ε_{sh} , f_2, and ε_2 were determined from tensile tests of reinforcement samples described in the Appendix.

The reported mean bond strength μ was computed as:

$$\mu = \frac{A_{st} \cdot f_{su}}{\pi \cdot d_b \cdot l_s} \tag{3-6}$$

where:

A_{st}	:	Nominal cross-sectional area of one #11 reinforcing bar
f_{su}	:	Maximum estimated steel tensile stress
d_b	:	Nominal diameter of one #11 reinforcing bar
l_s	:	Lap splice length (56-bar diameters)

3.2.2 Beam Tests: Distribution of Concrete Surface Deformations

Concrete surface deformations were recorded for all specimens in Series One. These measurements were made using an optical tracking system that records the three-dimensional coordinates of the optical targets which were placed along the length of the lap splice (on the concrete surface of the specimen). Horizontal and vertical deformations of the concrete surface were measured along the length of the lap splice. Horizontal deformations were used to infer bar stress distributions along the length of the lap splice. Vertical deformations were used to infer bond stress distributions based on the formation of splitting cracks. Figure 3-7 through Figure 3-12 show test photos of the beam specimen in a deformed state.

The horizontal concrete surface deformations were measured in the direction parallel to the applied load, or the x-direction based on the coordinate system shown in Figure 3-13. Horizontal deformations were calculated using the following expression:

$$\delta_{x_i}^{\,j} = x_i^j - x_i^0$$

(3-7)

where:

i	:	Target station number
j	:	Load step
${\delta_x}_i^j$	:	Horizontal deformation at target station *i* at load step *j*
x_i^j	:	Length of target station *i* at load step *j*
x_i^0	:	Undeformed length of target station *i* at load step *j*

Horizontal deformation measurements for beam specimens are shown in Figure 3-14 through Figure 3-19.

The vertical concrete surface deformations were measured in the direction perpendicular to the applied load, or the y-direction based on the coordinate system shown in Figure 3-13. Vertical deformations were calculated using the following expression:

$${\delta_y}_i^j = y_i^j - y_i^0 \tag{3-8}$$

where:

i	:	Target station number
j	:	Load step
${\delta_y}_i^j$	:	Vertical deformation at target station *i* at load step *j*
y_i^j	:	Length of target station *i* at load step *j*
y_i^0	:	Undeformed length of target station *i* at load step *j*

Vertical deformation measurements for beam specimens are shown in Figure 3-20 through Figure 3-25. A photo of a beam specimen before and after failure is shown in Figure 3-26 and Figure 3-27.

3.2.3 Coupon Tests: Maximum Steel Stress, Steel Strain, and Mean Bond Strengths

For coupon specimens the maximum bar stress ranged from 71 ksi to 81 ksi and maximum estimated bar strains of 1.2% to 2.3% respectively. The mean bond strengths ranged from $4.8\sqrt{f_c'}$ to $5.8\sqrt{f_c'}$. Table 3-2 shows the maximum applied load P_{su}, steel tensile stress f_{su}, tensile bar strain

ε_{su}, and mean bond strength μ obtained for coupon specimens. The maximum applied load P_{su} was calculated by averaging the maximum loads applied directly to the splice ends. The maximum steel tensile stress f_{su} was computed as:

$$f_{su} = \frac{P_{su}}{A_{st}} \quad (3\text{-}9)$$

where:

P_{su} : Maximum load applied to one lap splice

A_{st} : Cross-sectional area of #11 reinforcing bar (1.56 in.^{2})

The maximum bar strain ε_{su} corresponding to the maximum bar stress was determined from the following tri-linear stress-strain relationship defined by Eq. (3-3) to (3-5). The mean bond strengths μ were computed using Eq. (3-6). The maximum applied load P_{su} was obtained from load versus specimen elongation plots for Series One specimen as shown in Figure 3-28 through Figure 3-45.

3.2.4 Coupon Tests: Distribution of Concrete Surface Deformations

Specimen elongations in Figure 3-28 to Figure 3-45 were produced using Eq. (3-7) from optical measurements made from optical target stations located near ends of the lap splice. They refer to the elongation of the specimen at the level of the spliced bars. The solid black line in these figures represents the load and displacement at a static load step. In order to capture the maximum load and elongation of the specimen, the optical tracking system was set to a continuous measuring mode that captured load and displacement readings up to splice failure. Continuous recording measurements are shown by the dashed line in these figures. Using the maximum elongation at failure from Figure 3-28 through Figure 3-45, an average specimen strain ε_{sa} was computed as:

$$\varepsilon_{sa} = \frac{\delta_{max}}{l_s} \quad (3\text{-}10)$$

where:

δ_{max} : Maximum displacement in the direction of applied load

l_s : Splice length

In this report the value of ε_{sa} was computed for coupon specimens in Series One through Series Four. In Series One coupons, the values of ε_{sa} ranged from 0.4 to 0.9% as compared to 1.2 to 2.3% from estimated bar strains. The average specimen strain ε_{sa} value is expected to be less than the value of the maximum tensile bar strain ε_{su}. Maximum bar strain deformations take place outside of the splice region (this could be thought to be similar to measuring bar strain at a crack) while average bar strains are computed over the entire splice length where cracking does not exist everywhere. Horizontal and vertical deformations of the concrete surface on coupons specimens were calculated using the Eq. (3-7) and Eq. (3-8). Horizontal deformation measurements for coupon tests are shown in Figure 3-46 through Figure 3-78. Vertical deformation measurements for coupons test are shown in Figure 3-79 through Figure 3-111. Test photos showing deformations of the test coupons in Series One are shown in Figure 3-112 Figure 3-129. A photo of a coupon specimen before and after testing (failure) is shown in Figure 3-130 and Figure 3-131.

3.3 Series Two: Lap Splices Confined with Epoxied Anchors

3.3.1 Maximum Steel Stress, Steel Strain, and Mean Bond Strengths

For coupon specimens confined by epoxied anchors the maximum bar stress ranged from 73 ksi to 83 ksi and maximum estimated bar strains of 1.4% to 2.5% respectively. The maximum bond strengths ranged from $5\sqrt{f_c'}$ to $5.8\sqrt{f_c'}$. Table 3-3 shows the maximum applied load (P_{su}), steel tensile stress f_{su}, tensile bar strain ε_{su}, and mean bond strength μ obtained for the twelve specimens containing epoxied anchors. Estimates for maximum applied load, steel tensile stress, steel strain and mean bond strength were calculated similar to coupons in Series One.

3.3.2 Distribution of Concrete Surface Deformations

Values of ε_{sa} ranged from 0.5% to 1% as compared to maximum strain values ε_{su} of 1.4 to 2.5%. Specimen elongation from Figure 3-28 through Figure 3-45 was calculated by using Eq. (3-7) using optical target stations located near the loaded ends of the lap splice. Horizontal and vertical deformations of the concrete surface on coupons specimens was calculated using the Eq. (3-7) and Eq. (3-8). Horizontal deformation measurements for coupon tests are shown in Figure 3-46 through

Figure 3-78. Vertical deformation measurements for coupons test are shown in Figure 3-79 through Figure 3-111. Test photos showing deformations of the test coupons are shown in Figure 3-112 Figure 3-129. Photos of coupon specimens before and after testing (failure) in Series Two are shown in Figure 3-132 through Figure 3-137.

3.4 Series Three: Lap Splices Confined with Spiral Reinforcement

3.4.1 Maximum Steel Stress, Steel Strain, and Mean Bond Strengths

For coupon specimens confined by spiral transverse reinforcement the maximum bar stress ranged from 44 ksi to 61 ksi and estimated maximum bar strains of 0.15% to 0.21% respectively. The maximum bond strengths ranged from $9.9\sqrt{f_c'}$ to $14.6\sqrt{f_c'}$. Table 3-4 shows the maximum applied load P_{su}, steel tensile stress f_{su}, tensile bar strain ε_{su}, and mean bond strength μ obtained from each of the specimens confined with spiral transverse reinforcement. Calculations for maximum applied load, steel tensile stress, steel strain, and mean bond strength were calculated similar to Series One.

3.4.2 Distribution of Concrete Surface Deformations

Values of ε_{sa} ranged from 0.06% to 0.3% compared to estimated maximum strain values ε_{su} of 0.15 to 0.21%. All measurements indicated these specimens did not yield, therefore less concentration of strain took place outside the splice region. This would explain why estimated maximum bar strains were closer in value to average strains. As a results values of Specimen elongation from Figure 3-138 to Figure 3-146 was calculated by using Eq. (3-7) using optical target stations located near the loaded ends of the lap splice. Horizontal and vertical deformations of the concrete surface on coupons specimens were calculated using the Eq. (3-7) and Eq. (3-8). Horizontal deformation measurements for coupon tests are shown in Figure 3-147 though Figure 3-155. Vertical deformation measurements for coupons test are shown in Figure 3-156 through Figure 3-164. Photos of coupon specimens before and after testing (failure) in Series Three are shown in Figure 3-165 through Figure 3-170.

3.5 Series Four: Lap Splices Confined with Post-Tensioned Transverse Reinforcement

3.5.1 Maximum Steel Stress, Steel Strain and Mean Bond Strength

For specimens confined by post-tensioned transverse reinforcement with a spacing of 3.5 in., the maximum bar stress ranged from 74 ksi to 87 ksi and the mean bond strengths ranged from $13.4\sqrt{f_c'}$ to $15.6\sqrt{f_c'}$. For specimens with a spacing of 5 in., the maximum bar stress ranged from 69 ksi to 84 ksi and the mean bond strengths ranged from $12.4\sqrt{f_c'}$ to $15.2\sqrt{f_c'}$. The unconfined specimen achieved a bar stress of 37 ksi and a bond strength of $6.6\sqrt{f_c'}$. Table 3-5 shows the maximum applied load, steel tensile stress, steel strain, and average bond strength. Values for maximum applied load, steel tensile stress and mean bond strength were calculated similar to coupons in Series One.

3.5.2 Distribution of Concrete Surface Deformations

Unlike coupons in Series One through Series Three, coupons in Series Four were tested upright (vertical), therefore the coordinate system shown in Figure 3-171 was used. Here, horizontal deformations were used to infer bond stress distributions along the length of the lap splice, while vertical deformations were used to infer bar stress distributions. Therefore, horizontal deformations were calculated using Eq. (3-8) and vertical deformations were calculated using Eq. (3-7).

Values of (ε_{sa}) could not be calculated as deformations of the concrete surface were within the accuracy of the OptiTrack system. Horizontal deformation measurements for coupon tests are shown in Figure 3-172 through Figure 3-178. Vertical deformation measurements for coupon test are shown in Figure 3-179 through Figure 3-185. Photos of coupon specimens before and after testing (failure) in Series Four are shown in Figure 3-186 through Figure 3-190.

3.6 Series Five: Columns Strengthened with Post-Tensioned Transverse Reinforcement

3.6.1 Force Displacement Response

The loading history for columns C1 and C2 are shown in Figure 3-191 and Figure 3-192. The column was cycled three times at the drift ratios shown. Lateral and axial load versus lateral displacement was recorded continuously throughout the test. Plots of lateral force versus drift ratios for each column are shown in Figure 3-193 and Figure 3-194. Plots of axial force versus lateral drift for each column are shown in Figure 3-195 and Figure 3-196. The axial load was held nearly constant throughout the test. Drift ratios were computed by dividing the column displacement at the level of the lateral load by the column shear span (H). The results indicated both columns developed their flexural capacity at a drift ratio of approximately 1%, but column C2 (without post-tensioned transverse reinforcement) failed in shear and lost axial load carrying capacity at a drift ratio of approximately 1.5%. Column C1 (installed with post-tensioned transverse reinforcement) did not fail in shear and attained a drift ratio of 7% while maintaining its flexural capacity.

3.6.2 Reinforcing Steel Strains

Reinforcement strains were inferred from optical target measurements. Targets were placed on the concrete surface similar to Series One through Series Four. Longitudinal surface strains were calculated along the height of the column at the location of the two outermost layers of longitudinal reinforcement. The surface strain at these locations was used to infer longitudinal bar strain. Using the coordinate system in Figure 3-197, the longitudinal bar strains were approximated using the following expression:

$$\varepsilon_{y}{}_{i}^{j} = \frac{y_i^j - y_i^0}{y_i^0} \qquad (3\text{-}11)$$

where:

i	:	Target Station number
j	:	Load step
$\varepsilon_{y}{}_{i}^{j}$	:	Vertical deformation at target station *i* at load step *j*

y_i^j : Length of target station *i* at load step *j*

y_i^0 : Undeformed length of target station *i* at load step *j*

Targets were placed 5 in. apart along the height of both columns at the level of the longitudinal reinforcement. Therefore, the gage length or value of y_i^0 is taken as 5 in. Figure 3-198 and Figure 3-199 show the maximum inferred bar strain versus drift ratio along the height of each column. Figure 3-200 and Figure 3-201 show the distribution of bar strains along the column height for a given drift ratio. Figure 3-202 through Figure 3-207 show photos of both columns during testing.

4. DISCUSSION OF RESULTS

4.1 Introduction

This chapter contains a discussion of the results presented in Chapter 3 on the basis of strength and deformability. Test Series One through Series Four dealt with bond caused by tensile forces. Test specimens in Series One served as reference as these specimens contained unconfined lap splices. Specimens in Series Two through Series Four addressed the effects of post-installed transverse reinforcement. Of the types of post-installed transverse reinforcement investigated, post-tensioned transverse reinforcement was deemed most effective for improving the strength and deformability related to bond. Because the post-tensioned transverse reinforcement was effective for bond, it was also used in Series Five to investigate its effects on shear strength. In Series Five, two columns were tested. One column was tested with post-tensioned transverse reinforcement, and one column was tested without it as reference. The results are discussed in detail in this chapter.

4.2 Series One: Unconfined Lap Splices

In Series One, all specimens failed in bond. It is crucial to recognize this because 1) the tested splice lengths (56-bar diameters) would have been deemed sufficient by current design standards (ACI 318-19, 2019) and 2) failure was brittle, abrupt, and resulted in a complete loss of resistance. Bond failure is as sudden and catastrophic as steel fracture. Much is said and done to prevent steel fracture, but the same concern does not always seem to exist for bond failure. Yet, their consequences are in essence the same.

In Series One, specimens contained a pair of unconfined 56-bar diameter lap splices of #11 reinforcing bars. The yield stress of the bars was approximately 65 ksi for beam specimens, and 67 ksi for tension coupons. In all six test beams and six tension coupons (for a total of 12 specimens), the spliced reinforcing bars yielded as illustrated in the load versus displacement plots (Figure 3-1 through Figure 3-6 and Figure 3-28 through Figure 3-45). Often, in investigations of bond strength, specimens that reach yielding are deemed not useful to quantify strength. For instance, Orangun, Jirsa and Breen (1977) stated “if a bar yields and the test is stopped without splitting of the concrete, the same anchorage strength (i.e., yield of bar) will be recorded as for a companion specimen with twice the development or anchorage length". While the design objective of a lap splice is bar yielding, no explicit effort is placed on splice deformability. This investigation took a different look at the problem. The objective of a lap splice should not be only to reach yield, but to produce adequate ductility or deformability. What determines adequacy is driven by the structural application, but without question, structural members which fail in bond as soon as yielding occurs are not reliable. Reinforced concrete structures and the design process rely on the ability for reinforcement to yield and maintain yield or larger stresses through increases in displacements during earthquakes, blasts, or foundation settlement. A reinforced concrete structure without deformability is prone to severe damage. For these reasons, the discussion below gives attention to bond from the perspective of both strength and deformability.

4.2.1 Splice Strength

Figure 4-1 through Figure 4-4 show measured mean bond strength plotted against splice length. Figure 4-5 through Figure 4-8 show bar stresses plotted against splice length. Data in these figures had the following properties:

1) bottom-cast spliced bars with the depth of concrete cast below bars not exceeding 12 inches,
2) clear cover equal to or exceeding 1 bar diameter,
3) clear spacing between spliced bars equal to or exceeding 2 bar diameters,
4) no transverse reinforcement (unconfined splices),
5) strength of concrete not exceeding 10 ksi,
6) bar yield stresses ranging from 50 ksi to 120 ksi,
7) conventional black bars (no epoxy coating),
8) lap-splice lengths ranging from 9 to 85-bar diameters

To facilitate comparisons with this study, data plotted in Figure 4-2 represent splices of #11 and larger bars. The mean bond strengths in Figure 4-1 through Figure 4-4 are calculated as the ratio of peak bar force to the bar surface area along the splice (Eq. 3-6). The descending trend in Figure 4-1 is the result of this definition. Notice that the data from Series One does not deviate considerably from the data available from previous investigations. This is of interest because the yielding that occurred in Series One resulted in mean bond strengths similar to previous tests where yielding did not occur. Currently, the square root of concrete compressive strength is an accepted relationship between concrete and bond strength (Ferguson & Thompson, 1962). Frosch and Canbay (2005) found that bond strength can also be described using the fourth root of the concrete compressive strength. For concrete compressive strengths ranging from 3 ksi to 16 ksi, Frosch et al. (2005) concluded that the fourth root provided a better correlation of bond strength than the square root. Nevertheless, the square root of concrete compressive strength is used in this report for comparison to previous investigations which use the square root (ACI 408R-03, 2003).

Abrams (1913), Kluge and Tuma (1945), Mains (1951), and Richter (2012) have all reported clear evidence showing bond stress concentrating near the loaded end of the bar embedded in concrete. Figure 4-9 illustrates measurements made by Abrams (1913). The figure shows variations in axial bar stresses measured along the shear span of beams under four-point bending. The slope of the bar stress distribution curve is proportional to bond stress. Notice that for smaller loads bond is high near the loading point and low elsewhere. This is far from the linear variation in axial bar stress that would be expected from simple mechanics. A comparable variation in axial bar stress was observed by Kluge and Tuma (1945), Mains (1951) in lap splices (Figure 4-10 and Figure 4-11). Notice from Mains (1951), bar stresses are highest near the loaded end of the splice and are reduced to zero near the unloaded end. In a lap splice, as one bar unloads the other is loaded. Equilibrium, therefore, requires concentrations of bond stress near the loaded end and the free end of the bar. The result is the stress distribution as idealized in Figure 4-12 (Richter, 2012). In summary, bond strength is quantified assuming bond stress is uniform, and lap splices are sized using the same assumption, but the evidence shows clearly that bond distribution is far from uniform and that causes the apparent reduction in bond strength and the nonlinearity in the trends in Figure 4-1 through Figure 4-4.

Richter (2012) saw the same phenomenon as Kluge and Tuma (1945). Richter (2012) used instrumentation similar to what was used in Series One. Unlike Kluge and Tuma (1945), who left openings in concrete surrounding the splice to make direct measurements, tests in Series One used optical targets which were placed on the concrete surrounding the lap splice and therefore did not disturb bond. That came with a price, as concrete surface measurements (that are less reliable than measurements made directly on the bar) were made to infer bar and bond stress distributions. Nevertheless, Figure 3-14 through Figure 3-19 show horizontal deformations, or deformations on the concrete surface parallel to the spliced bar at the level of the splice. Figures of horizontal deformations obtained from beams tests in Series One resemble Richter's measurements idealized in Figure 4-12, and the direct measurements shown by Kluge and Tuma (1945). Horizontal deformations in tension coupons were not similar to those from beam tests. Horizontal deformations near the splice ends in tension coupons could not be calculated because the specimen was only an inch longer than the splice making it difficult to capture horizontal deformations from concrete surface strains near the loaded end. In other words, all of the deformations on the splice ends took place outside of the specimen, unlike beam specimens which had concrete outside of the splice region that could be used to make measurements.

The magnitude of bond stress and its distribution were also inferred (at least in qualitative form) from vertical deformations, or deformations perpendicular to the splice bars at the level of the splice. Figure 3-20 through Figure 3-25 and Figure 3-79 through Figure 3-111 also show a concentration of deformations near the loaded ends of the splice. These vertical deformations are the results of what Abrams (1913) referred to as "bursting stress" caused by bond. From Figure 3-20 through Figure 3-25 and Figure 3-79 through Figure 3-111 two key observations can be made: 1) higher bond stresses occurred near the ends of the splices resulting in larger splitting crack widths, and 2) these larger stresses and cracks concentrated within 20-bar diameters from splice ends. This is a rather puzzling observation because how can bond stress occur (in absence of transverse reinforcement) after the formation of splitting cracks? It is not evident what mechanism helps the concrete transfer stresses to and from the bar after the concrete has burst off. Evidence does support that bond is being transferred, however, in the lengths affected by the mentioned splitting cracks. For specimens in Series One, splitting cracks were observed within the first 20 bar diameters from each end of the loaded splice. If bond stress was not transferred there, it is unlikely that the remaining 16 bar diameters which remained uncracked in the center of the splice could carry the entire force reached in the spliced bars. Sim (2014) also noticed that splice failure does not occur immediately after the first formation of splitting cracks. Splices of 28-bar diameters tested by Richter (2012) also suggested this observation to be true.

Figure 4-5 through Figure 4-8 show how peak bar stress (achieved at splice failure) varies with lap splice length. Based on statistical regression, Fleet (2019) suggested that peak bar stress is nearly proportional to the square root of splice length as shown in Figure 4-13. Figure 4-7 and Figure 4-8 show that bars that yielded do not deviate dramatically from the general trend that suggests that maximum bar stress does not increase in direct proportion to increases in lap splice length. For example, doubling the lap splice length does not double the maximum bar stress that can be achieved, and this trend seems not to be critically sensitive to the occurrence of yielding. The relationship between bar stress and lap length does seem to flatten out and it would be prudent to ask to what extent that is the result of yielding versus nonuniformity in the bond stress distribution. The data in Figure 4-14 and Figure 4-15 also include high strength bars that did not yield before bond failure, and those data indicate that the mentioned 'flattening' was not necessarily caused by yielding.

All the evidence discussed indicates that in a long splice (with lengths exceeding 40-bar diameters) the middle region of the splice contributes little to mean bond strength. As a result, mean bond strength does not increase in direct proportion to lap length. Kluge and Tuma (1945) said so, and so did Richter (2012). That is why Figure 4-1 resembles the function 1/x. This is the main reason 1) lap splices need strengthening (i.e. they do not work as assumed in design where extra length is believed to provide room for safety), and 2) lap splices should be avoided in critical regions where yielding is expected. For splices, strength is essential and otherwise unimportant. In other words, while strength is required, lap splices need to be designed for deformability and strength will be satisfied by default.

4.2.2 Splice Deformability

It is evident that splices which fail prior to, or soon after yielding are not reliable. Demands from earthquake, blast, wind or settlement can result in bar strains that exceed the yield strain by large margin. The reliability of the splice should not be based on stress values alone, but rather strains. Achieving large strains, or adequate deformability without splice failure should be the emphasis for design. In this section observations on the deformability of beam and coupons are made on the basis of maximum bar strains inferred from stress, and average strains along the splice.

Current design provisions were not conceived to produce lap splices with deformability. They were conceived to produce splices that can reach the strength associated with the nominal yield stress of the reinforcement. Yet, these provisions and their results are used for and/or affect a number of applications requiring deformation capacity such as:

- structural walls not classified as ‘special’ in the design process (even if allowed only in regions with moderate seismicity)
- older structures with lap splices near critical sections
- applications in which load redistribution is expected (e.g. structures prone to foundation settlement)
- conventional design for demands caused by gravity load for which longitudinal reinforcement ratios are controlled through providing limits on expected strain values to produce ductility
- new practices for the design of structures to resist wind loading that allow yielding of elements under dynamic oscillation produced by wind (ASCE/SEI, 2019)
- protective structures required to resist impulsive loading

The design of lap splices for strength is unlikely to produce ample ductility or deformation capacity for the applications listed above. For example, current design provisions require proportioning lap splices to yield in tension. In critical applications, such as lap splices permitted at the base of structural walls not classified as ‘special’, the nominal yield stress is increased by a factor equal to 1.25 (ACI Committee 318, 2019) with the unstated intent to produce ductile splices. But much of this 25% increase in target stress is offset by differences between actual and nominal yield stress that often amount to 20% or more of the nominal value. Figure 4-7 suggests that plastic strain does not always play a critical role affecting bond strength. Unconfined splices in which bars yielded were observed to be nearly as strong as lap splices in which bars remained linear up to splice failure. From that point of view, it could be argued that all is needed is a larger factor to be applied to the nominal yield stress to produce requisite ductility. But if the intent is to achieve deformation capacity, which can be quantified directly in terms of strain, addressing the problem through stress instead of strain seems to miss the mark.

The real question is how much deformability a lap splice should have. Observations by Wang (2014) are useful in estimating strains reached in reinforced concrete walls as a result of lateral displacements. In cantilever structural walls with the following properties listed by Wang (2014):

- aspect ratios *a/d* = 5
- concrete compressive strengths f_c' ranging from 4 to 5 ksi
- yield stress of longitudinal reinforcement f_y in the boundary element of 80 ksi
- longitudinal reinforcement ratio ρ in the boundary element 2.8%

it was observed that maximum surface tensile strains (near the wall base) and drift ratio were nearly proportional to each other, with strain ranging from 1.5 to 2.5 times the drift ratio (Figure 4-16). Similar tests by Pollalis and Pujol (2020) on walls with the following ranges:

- aspect ratio *a/d* = 5
- measured longitudinal reinforcement yield stresses f_y ranging from 60 to 93 ksi
- concrete compressive strengths f_c' ranging from 5.2 to 6.2 ksi
- splice lengths ranging from 40 to 90-bar diameters
- clear bar cover of either 1.5 or 0.75-bar diameters (measured to the outer edge of transverse reinforcement
- clear bar spacing along the splice length was either 1 or 2.25-bar diameters

showed that surface strain is highly sensitive to gage length, an observation also made by Puranam (2018). For a gage length of 1/7 = 0.14 times the wall length and longitudinal bar diameters, Pollalis et al. (2020) observed peak surface strain in structural walls close to two times drift ratio. For a gage length half as long, surface strain at a given drift ratio was nearly half as large. Surface strain is also sensitive to moment gradient, with smaller gradients producing smaller ratios of strain to drift ratio. The surface strains obtained in test Series Five (with a gage length of 5 in. or 5-bar diameters) were nearly equal to drift ratio (Figure 3-198 and Figure 3-199).

The mentioned questions about gage length apply again, and so do questions about the effect of reinforcement slip (occurring in the foundation) on the apparent surface strain. Measurements obtained by strain gages by Pujol (2002) in columns with the ranges listed below are illustrated in Figure 4-17.

- aspect ratio a/d = 2.6
- concrete compressive strengths $f_c{}'$ ranging from 4.1 to 5.2 ksi
- longitudinal reinforcement yield stresses f_y of 65.7 ksi
- longitudinal reinforcement ratio ρ of 2.4%
- transverse reinforcement ratios ρ_{tr} ranging from 0.6% to 1.1%
- axial load of $0.08f_c`A_g$ to $0.21f_c`A_g$

The measurements in Figure 4-17 suggest that the observations made for columns in Test Series Five are plausible. All the evidence considered suggests that it would be prudent to expect strain demand to exceed drift ratio. Given a) current design target drift ratios as high as 2.5% (ASCE, 2017), b) uncertainties involved in estimating drift demands for phenomena that require the most ductility (earthquake and blast) and c) the potential fatal consequences of splice failure, it is hard to envision situations in which drift or rotation targets would not exceed 2 or 3%. In contrast, consider again the values of strain reported in Chapter 3. Local strains inferred to occur at the splice ends at failure from 1.2 to 2.3%. Average strains measured to occur along the length of the splice (excluding its ends) ranged from 0.4 to 0.9%. considering the scatter in the measurements of strain capacity and the mentioned uncertainties related to strain demand, none of these listed provides any confidence for splices similar to those tested, which were proportioned to meet current standards. The conclusion is simple: unconfined lap splices in critical regions of critical structural elements pose high risk and need strengthening and/or retrofit. Experiments in Series Two through Series Four were meant to test alternatives.

4.3 Series Two: Lap Splices Confined by Epoxied Anchors

In test Series Two, epoxied anchors were installed along the lap splice in an effort to increase the deformability and strength of the splice. Confinement provided by these post-installed epoxied anchors was hypothesized to be as effective in increasing the strength and deformability of the splice as conventional transverse reinforcement (stirrups or ties). The effects of confinement on bond strength of lap splices has been studied extensively in the past: Orangun, Jirsa and Breen (1977); Sozen and Moehle (1990) and others as summarized by Joint ACI-ASCE Committee 408 (2012), but with no emphasis on deformability. In these studies, confinement was provided by conventional transverse reinforcement. The increase in bond strength attributed to conventional transverse reinforcement (in the shape of stirrups and ties) was quantified by Sozen and Moehle (1990) using an index referred to as the Transverse Reinforcing Index (*TRI)* discussed in Ch. 2 (Eq. 2-2). The same index is used in the following discussion to organize the test results from Series Two. The effects of the described anchors on splice strength and deformability are discussed next through comparison between specimens in Series Two and tension coupons in Series One (that had no transverse reinforcement).

4.3.1 Splice Strength

As detailed in Chapter 2, four configurations of epoxied anchors were used. Unlike stirrups which 'bend' around the spliced bars, the epoxy anchors were installed in between the two pairs of spliced bars. As in Series One, all specimens in Series Two yielded as illustrated in Figure 3-28 through Figure 3-45 and failed as a result of bond. The abrupt bond splitting failures observed in Series Two, were similar to the failures observed in Series One: the cover spalled abruptly after initial splitting cracks propagated suddenly along the splice. Specimens with 3 anchors with effective embedment depth (past the splitting plane) of 12 in. (Specimens D8-D18, configuration four), on average, achieved a maximum bar stress of 80 ksi. All other configurations (used in D4-D7) which had 2 to 3 anchors with effective depth of 5 in., on average, reached 75ksi. For comparison, consider that tension coupons from Series One (that had no transverse reinforcement), on average, reached the same peak bar stress of 75 ksi (Figure 4-18). These results suggest that epoxied anchors were effective in increasing splice strength only with embedment depths (beyond the potential plane of splitting) of 16 times their nominal diameter (3/4 in.). The embedment length recommended by the epoxy manufacturer is 10 in. (13-bar diameters). But in initial trials in which test anchors with 10-in. embedment were pulled from the surface of unreinforced concrete blocks (using a jack supported by a chair with a span of ~10-bar diameters) not every test anchor reached yield. For this reason, the embedment length in configuration four in Test Series Two exceeded manufacturer recommendations, and the exposed anchor end near the concrete surface was furnished with a plate and nut.

The better performance of configuration four is likely attributable to two factors:

1) The location of the outer anchors (within 10-bar diameters from the splice end) that control the larger bond stresses and wider splitting cracks occurring in those locations (Figure 3-112 through Figure 3-129) preventing the "unzipping" of the entire splice.
2) Their increased embedment length relative to the manufacturer's recommendations, the embedment in Configurations 1 to 3, and the location of the splitting plane.

In relation to the first attribute, consider Figure 3-20 through Figure 3-25 that show vertical deformations concentrated near the splice ends in Test Series One. These deformations are the results of splitting cracks which form because of bursting stresses caused by bond. As bond stresses increase, so do splitting crack widths and lengths. This eventually leads to unzipping of the concrete surrounding the bar along the entire splice, resulting in total loss of resistance. Transverse reinforcement can be used to control these vertical deformations by intercepting the splitting crack. Transverse reinforcement is most effective near the splice ends because vertical deformations (and bond) concentrate there. In test beams in Series One, vertical deformations and bond stress were observed to concentrate within 20-bar diameters of splice ends. For this reason, the outer anchors in Series Two (configuration 4) were placed at 10-bar diameters from splice ends.

Yet another observation made during the test was the mechanism by which the epoxied anchors controlled the formation of splitting cracks. Unlike traditional forms of transverse reinforcement such as stirrups or ties, the epoxy anchors required large vertical deformations in order to engage. When confined with traditional stirrups, the legs of the reinforcement intercept the splitting crack at the location of the bar (i.e. where bursting stresses are largest and where the splitting crack forms) and directly oppose bursting stresses. The anchors however were placed away from the bar and required more vertical deformations to take place in order to oppose bursting stresses. Because such large deformations were needed to engage the epoxied anchors they were not as successful in increasing the mean bond strengths as compared to unconfined lap splices shown in Figure 4-19 to Figure 4-22, and compared with traditional transverse reinforcement (Figure 4-23).

4.3.2 Splice Deformability

Confinement is typically used to increase strength of splices. But similar to other phenomena affecting reinforced concrete elements, confinement can also improve the deformability or toughness of a splice. For lack of a better measure, (*TRI*) the index used above to quantify effects on strength is used here also to quantify the effects of confinement on deformability. Figure 4-24 shows bar strains (inferred from stress-strain curves) versus values of TRI for test Series One and Two. The plot suggests that the relative increase in strain at failure (from 1.5% to 2% or 33% on average) was much larger than the relative increase in peak stress (from 75 ksi to 80 ksi or 7%). Although the observed increase in strength is within the scatter observed in tests of specimens without confinement, the inferred larger relative increase in strain that can occur after yield is a positive indication that improving deformability may be easier than improving strength. While this increase in deformability may be beneficial for elements with no moment gradient (as tested), the same benefit does not exist in elements with a large moment gradient (such as walls) as observed by Sozen and Wight (1975).

4.4 Series Three: Lap Splices Confined by Spiral Transverse Reinforcement

Spiral reinforcement was investigated in Series Three. Although repair of splices using spiral reinforcement requires invasive removal of concrete around spliced bars, this method of repair was investigated because spirals have been observed to be quite effective as confinement (Richart, Brandtzaeg, & Brown, 1929). Unlike Test Series One and Series Two which contained lap splices which would conform for design standards, Test Series Three investigated splice strength and deformability of admittedly short splices with lengths ranging from 12 to 16-bar diameters. These shorter lengths were used as they provide a more demanding test.

4.4.1 Splice Strength

All splices in Series Three did not yield and failed abruptly in bond similar to Series One and two Coupons. Figure 3-156 through Figure 3-164 suggests that, near failure, bond stress in Series Three tended to be nearly uniform along the entire length of the splice. In Series One and Two, bond stress was observed to be concentrated within 20-bar diameters of the splice ends. In these tests splice lengths were 56-bar diameters. (Richter, 2012) saw the same uniform distribution of bond stress (within 20-bar diameters) on shorter splices (40-bar diameters). The uniform distribution of bond stress along the lap length in Series Three likely resulted from the short splice length.

Figure 4-25 and Figure 4-26 show measurements from Series Three along with test data compile by Richter (2012) containing unconfined lap splices. Results in Series Three fall within the scatter of unconfined specimens. Also, splices with spiral reinforcement did not provide a considerable increase in bond strength in comparison to splice confined by traditional transverse reinforcement as shown in Figure 4-27. This would suggest that with the configuration of spirals and lap splice length tested, the use of spiral reinforcement has no clear improvement on splice strength.

4.4.2 Splice Deformability

Figure 4-28 shows a comparison of *TRI* versus bar strain in Series Three. Bar strains in Series Three were considerably lower than unconfined splices because the splices did not yield. It is interesting that the effect of the spirals was not observed to be more dominant. Spirals have been observed to be quite effective in confining concrete in concentric compression (Richart, Brandtzaeg, & Brown, 1929). In the case of compression, the effects of the spiral are achieved after the concrete undergoes large changes in volume as it exceeds its limit in its unconfined state. In the case of lap splices, such expansion does not occur, and the effect of spirals seems to be as passive as that of traditional transverse reinforcement reacting only at locations where they cross splitting cracks. These cracks do not propagate in the concrete in directions other than the direction of the splice. This may be the reason why the spiral does not seem to be as effective as in the mentioned case of the spiral columns tested in concentric compression by Richart et al. (1929). The spiral becomes active in compression but remained passive in the tested short lap splice.

4.5 Series Four: Lap Splices Confined by Post-Tensioned Transverse Reinforcement

Test Series One through Series Three clearly showed that splices failed abruptly because of splitting of concrete around the bars. Unlike in previous test series, Test Series Four used an active form of confinement. Active confinement was used because it was thought to prevent or delay the formation of splitting cracks and prevent abrupt bond failures.

4.5.1 Splice Strength

All specimens in Series Four provided with post-tensioned transverse reinforcement yielded. The unconfined specimen (PTR20-NC) did not yield and failed abruptly in bond similar to specimens in Series One through Series Three. Bond splitting failures were observed in specimens PTR20-3.5-5K, PTR20-5-5K, and PTR20-5-10K. While the cover did not blow off, a sudden loss of load carrying capacity of the splice was still observed. Specimens PTR20-3.5-10K, PTR20-3.5-15K, and PTR20-5-15K failed as a result of concrete breakout failures at the splice ends.

Figure 4-29 and Figure 4-30 show plots of mean bond strength and bar stress versus splice length for specimens in Series Four as well as unconfined lap splices. Specimen PTR20-NC with no confinement fell within the scatter as expected. Specimens in Series Four with post-tensioned transverse reinforcement produced mean bond strengths and bar stresses that lied near the upper bound of the scatter of data from unconfined lap splices. Specimens with combinations of small spacings and high post-tensioning force produced larger bond and bar stresses. In comparison to lap splices confined using conventional transverse reinforcement, specimens in Series Four with post-tensioned transverse reinforcement produced increases in mean unit bond strength that lied near the upper bound of the scatter of data. Based on results from Series Four, post-tensioned transverse reinforcement seemed similar or marginally better than lap splices confined with conventional forms of transverse reinforcement (Figure 4-31).

4.5.2 Splice Deformability

Figure 4-32 shows a plot of maximum bar strain versus confining pressure values tested for Series One through Series Four. As expected for specimen PTR20-NC (20-bar diameters long), which did not yield, bar strains were low (0.15%). This was consistent with results from specimens in Series Three which did not yield either and were of similar lengths (12 to 20-bar diameters). Nevertheless, specimens installed with post-tensioned transverse reinforcement did not only yield but achieved inferred bar strains ranging from 1.5% to 3%. Average bar strains could not be made for specimens in Series Four as surface deformations were within the accuracy of the OptiTrack system. It was also observed that specimens with a smaller spacing and higher post-tensioning force reached larger bar strains.

For specimens with post-tensioned transverse reinforcement increases in bar stress and bar strain were considerable in comparison to the unconfined specimen. In these specimens an average increase in bar stress of approximately 110% (from 37 ksi to 78 ksi) an average increase in bar strain of approximately 1200% (0.15% to 2%) was observed. This shows that 1) increases in deformability are easier to achieve using confinement rather than increases in bar stress and 2) post-tensioned transverse reinforcement is an effective method of increasing both the maximum bar stress and bar strain at failure. However, it does seem that even with an abundance of confinement ($\rho \cdot f_{pt}$ > 30 ksi) maximum bar strain is limited to 2.5% on average. It appears that the use of post-tensioned transverse reinforcement, at least for short splices, can help but does not cure the lack of deformability inherent in a splice. Despite the relative increases in deformability, all specimens in Series Four failed abruptly and near strain values that may still be insufficient for projected drift demands by Wang (2014) and Pollalis et al. (2020).

4.6 Series Five: Columns with Post-Tensioned Transverse Reinforcement

The results from Test Series One through Series Four show the strength and deformability of lap splices susceptible to bond failures can be improved by providing confinement in the form of transverse reinforcement. Reinforced concrete elements that are susceptible to bond failures are also likely to be vulnerable to shear failures in part because bond and shear are closely related. Where there is shear, there is bond. Lack of confinement can not only lead to bond failures, but shear failures as well. Bond and shear failures are arguably equal in severity. For this reason, the improvement that post-tensioned transverse reinforcement could provide to reinforced concrete elements susceptible to shear failures was also examined in this report. This was done by testing two reinforced concrete columns with widely spaced conventional ties one of which was retrofitted with post-tensioned transverse reinforcement. It was hypothesized that the addition of the post-tensioned transverse reinforcement which provides a lateral pressure equal in magnitude to the maximum expected nominal shear stress would 1) preclude shear failure from occurring before flexural yielding and 2) reduce the number and slope of inclined cracks improving the integrity of the concrete core therefore increasing drift capacity.

Current methods of strengthening columns vulnerable to shear failure require specialized tools, labor and materials, making them unfeasible as a widespread repair method. In Series Five, an alternative method of strengthening columns using post-tensioned transverse reinforcement was investigated. This method was chosen because it was expected to produce beneficial effects similar to or better than confinement provided by traditional forms of transverse reinforcement (stirrups, ties, spirals). In addition, the post-tensioned transverse reinforcement was simple to design, fabricate and install.

4.6.1 Effects of Post-Tensioned Transverse Reinforcement on Strength

Figure 3-194 shows the lateral load vs. drift ratio for column C2 which did not have post-tensioned transverse reinforcement. Column C2 yielded and reached its plastic shear capacity of approximately 58 kips during cycles at a drift ratio of 1%. In the first cycle to a target drift ratio of 2%, the column failed abruptly in shear at a drift ratio of approximately 1.5%. Nevertheless, the column was able to carry the applied axial load of ($0.1f_c{}'A_g$) in that cycle. In subsequent cycles of a drift ratio of 2%, the lateral load carrying capacity of the column reduced to approximately 22 kips. In the first cycle to a drift ratio of 3%, the column abruptly lost its ability to carry any applied axial load (Figure 3-196).

By contrast, column C1 which had post-tensioned transverse reinforcement installed, was able to maintain both its lateral and axial-load carrying capacity without failure to a drift ratio of 7% (Figure 3-193 and Figure 3-195). Column C1 did not fail in shear because confinement provided by the post-tensioned transverse reinforcement controlled the formation of inclined shear cracks. In addition, the column was able to maintain more than 80% of its flexural capacity even at a drift ratio as high as 7% because the post-tensioned transverse reinforcement delayed spalling and crushing of concrete near the base of the column thus maintaining integrity of the compression zone. Yet another benefit of maintaining the compression zone was that the narrowing of the load versus deflection loops called "pinching" was not observed for column C1. At drift ratios of approximately 5%, spalling was observed at the base of the column, between the foundation and closest post-tensioned transverse reinforcing tie, followed by buckling of the outermost layer of longitudinal reinforcement. A drift capacity of 7% is certainly sufficient for even extreme drift demands.

The confinement provided by the transverse reinforcement did not result in an increase in the plastic moment capacity of the column section. It is also plausible that the addition of the post-tensioned transverse reinforcement did not lead to a large increase in compressive strength of the concrete core as it was observed by Roy and Sozen (1965) who tested concrete prisms with conventional hoop reinforcement. This observation is convenient because it would suggest that plastic shear demands (for columns with low axial force demands) would not increase because of additional confinement as feared by Aboutaha et al. (1999). In contrast the use of the post-tensioned transverse reinforcement caused an increase in the shear capacity of the column. This increase in the shear capacity could not be quantified because the shear demands were limited by flexural yielding. Nevertheless, the near absence of inclined cracking observed indicated that designing the post-tensioning clamps to resist the entire shear demand is feasible and enough to prevent the disintegration of concrete described by Wight (1975), in relation to the effects of the post-tensioning crossing the inclined cracks.

Crack maps shown in Figure 4-33 Figure 4-39 compare the progression of cracks at similar drift ratios for columns C1 and C2. In column C2, the first flexural-shear crack was observed at the first cycle of 0.5% drift ratio near the base of the column. In subsequent cycles at 1% drift ratio, multiple shear cracks formed along the height of the column extending along approximately 80% of the shear span. In addition to shear cracks, the formation of bond-shear cracks was also observed along the height of the column. At approximately 1.5% drift ratio (during the first cycle at a target drift ratio of 2%) the column suffered an abrupt shear failure resulting from a crack extending from the load point to the base of the column. This observation was interesting because the shear crack which caused failure formed over a distance equal to 4 times the effective depth of the column section as opposed to in between ties (when spaced at a distance, d) as it could have been expected.

In column C1 flexural cracks were observed at drift ratios up to 3% with limited shear cracking. All flexural cracks initiated between the locations of where post-tensioned transverse reinforcement was installed. Flexural cracking only extended approximately along half the height of the column. Minimal shear cracking was observed in column C1. The lack of shear cracking indicates that the precompression provided by the post-tensioning altered the state of stress in the concrete core. This allowed the entire concrete cross-section to work in shear rather than just the compression zone and surface along the shear crack. At drift ratios exceeding 3%, flexural cracking was mostly concentrated in between the base of the column and the first level of post-tensioned transverse reinforcement. It was estimated that the region of inelasticity (plastic hinge length) extended above the base of the columns by approximately two-thirds of its effective depth

(10 in.). This observation is supported by the plot of inferred surface strains at the location of the outermost layer of longitudinal reinforcement (Figure 3-200 and Figure 3-201) which shows that at increasing drift ratios, longitudinal strains concentrated within the first 10 in. of the base of the column. Deformations past yield of the column concentrated in this region of inelasticity. Quantitative measures of the contributions to the total deformations attributed to shear could not be obtained because the precision of the optical measurement system was insufficient to do so. Refer to Appendix for OptiTrack system details.

4.6.2 Effects of Post-Tensioned Transverse Reinforcement on Deformability

As mentioned in the previous section, column C2 (without post-tensioned transverse reinforcement) failed in shear at a drift ratio of 1.5%, whereas column C1 (with post-tensioned transverse reinforcement) was able to undergoes drift ratios as high as 7% without a loss in lateral or axial load carrying capacity. In order to understand the key parameters contributing to the increase in the deformation capacity of columns with post-tensioned transverse reinforcement, a set of 31-column tests done by Yamakawa et al. (2000) were studied. In these tests, columns vulnerable to shear failures were repaired using post-tensioned transverse reinforcing ties. The ties consisted of 4 corner blocks which bared against the corners of the square column (Figure 4-40). Four post-tensioning rods connected each corner block to the column. Post-tensioning stress of approximately 1/3 of the yield stress of the post-tensioning rods was induced into each rod prior to testing. The yield stress of the post-tensioned rod was reported as 180 ksi. The setup used by Yamakawa et al. (2000) was similar to that used in Series Five. This allowed for direct comparisons and conclusions to be made. In tests done by Yamakawa et al. (2000) the following parameters were included:

- Concrete compressive strengths $f_c{}'$ ranging from 2 ksi to 4.5 ksi
- Longitudinal reinforcement with a yield stress f_y of 53 ksi
- Conventional transverse reinforcement with a yield stress f_{yt} of 48 ksi
- Longitudinal reinforcement ratios ρ of 1.38% to 2.53%
- Conventional transverse reinforcement ratios ρ_{tr} of 0.08% to .21%
- Post-tensioning transverse reinforcement ratios ρ_{tr} of 0.06% to 0.54%
- Post-tensioned transverse reinforcement yield stress f_{pty} not exceeding 180 ksi
- Column aspect ratios *a/d* of 1 to 2

Yamakawa et al. (2000) tested 31 reinforced concrete columns in double curvature using a cyclic loading protocol (Figure 4-41) similar to that used in Series Five. An applied axial load of $0.2f_c'A_g$ was used for all specimens. The conventional transverse reinforcement ratios ρ_{tr} were comparable to those in Series Five. The ties were spaced at *d/4 to d/2* as compared to approximately *d* in Series Five. Of the 31 columns, 22 columns were strengthened with post-tensioned transverse reinforcement, the remaining 9 were not. Of the 22 columns tested with post-tensioned transverse reinforcement, only 20 columns failed in flexure or shear. The other two columns (*R99M-P41'R, R99M-P41'pw*) failed in bond. All 9 columns tested without post-tensioned transverse reinforcement failed in shear. Table 4-1 summarizes the key parameters for each of the specimens tested by Yamakawa et al. (2000).

Columns without post-tensioned transverse reinforcement failed at drift ratios of 0.5% to 1%. The drift ratio at failure reported by Yamakawa et al. (2000) was taken as the drift ratio corresponding to 80% of the peak lateral load V_{exp}. Column (*R99L-P0pw*) had conventional ties with a spacing of *d/4*, transverse reinforcement ratio ρ_{tr} of 0.21%, and failed at a drift ratio of 1%. All other columns without post-tensioning (*R99L-P0, R99M-P0R, R99M-P0L, R99M-P0H, R99M-P0, R98M-P0, R99S-P0, and R98S-P0*) with tie spacings of *d/2* and ρ_{tr} of 0.08% failed at drift ratios around 0.5%. Figure 4-42 shows results of column *R99M-P0*. This column did not reach the shear force corresponding to flexural yielding and the crack pattern (on the depth side, D) at failure showed a shear crack spanning the entire height of the column. This cracking pattern was similar to the pattern in column C2 in Series Five. As in the case of Series Five, columns without post-tensioned transverse reinforcement tested by Yamakawa et al. (2000) would have likely been insufficient to sustain drift demands from even the most extreme case.

Columns strengthened with post-tensioned transverse reinforcement tested by Yamakawa et al. (2000) failed at measured drift ratios from 1.5% to at least 5%. Columns with reported drift ratios of 5% had post-tensioned transverse reinforcement ratios ρ_{pt} greater than 0.45%, yielded in flexure, and did not have shear or bond failure. Had testing not been stopped at 5%, it is likely that these columns would have reached higher drift ratios. Columns with post-tensioned transverse reinforcement ratios less than 0.21% reached maximum drift ratios ranging from 1.5% to at least

3.5%. In general columns with lower values of ρ_{pt} and larger spacing of post-tensioned transverse reinforcement s_{pt} resulted in lower drift capacities.

Yamakawa et al. (2000) reported detailed measurements and observations for columns tested with post-tensioned transverse reinforcement (*R99M-P150, R99M-P41'R, R99M-P41', and R99M-*P_H*34'*) as shown in Figure 4-42. All four of these columns tested had similar aspect ratios, longitudinal reinforcement ratios, and a transverse reinforcement ratio ρ_{tr} of 0.08%. Column *R99M-P150* had a post-tensioned transverse reinforcement ratio ρ_{pt} of 0.06% and failed in shear at a maximum drift ratio of 2%. From Figure 4-42 the following observations were made: 1) The column (*R99M-P150*) yielded in flexure but gradually lost its lateral-load carrying capacity at higher drift ratios, 2) the cracking pattern at failure was similar to that of the column specimen without post-tensioned transverse reinforcement (*R99M-P0*) and 3) the post-tensioning rods yielded at large drift ratios.

Columns (*R99M-P41' and R99M-*P_H*34')* had post-tensioned transverse reinforcement ratios ρ_{pt} of 0.45% and 0.54% respectively. No failure was observed up to a drift ratio of 5%. Unlike in the case of column (*R99M-P150),* these columns 1) maintained their lateral-load carrying capacity at high drift ratios, 2) did not have a considerable increase in post-tensioning stress beyond initial post-tensioning, and 3) had similar cracking patterns to column C1 in Series Five. The stress in the post-tensioned rods did not likely increase considerably as a result of the higher value of ρ_{pt}. In column C1 in Series Five, the ratio ρ_{pt} was approximately 0.41%.

Column (*R99M-P41'*) also had a ρ_{pt} of 0.45%. Yet this column lost its lateral-load carrying capacity at cycles greater than 2% drift ratio. Yamakawa et al. (2000) attributed this loss in lateral-load carrying capacity to bond-slip. This observation suggests that at even high post-tensioned transverse ratios may not be effective in increasing bond strength for longitudinal bars located in columns. This is worth noting because tests in Series Four showed an increase in bond strength attributed to post-tensioned transverse reinforcement installed on short lap splices. In Series Four, all spliced bars were confined by the addition of post-tensioned transverse reinforcement. In columns tests by Yamakawa et al. (2000), the layout of post-tensioned transverse reinforcement may not have been effective at confining longitudinal reinforcement towards the center of the column, which may have resulted in the bond-slip failure reported. Further testing is needed to determine the effectiveness of post-tensioned transverse reinforcement on bond in columns.

Based on the test done by Yamakawa et al. (2000), the spacing of the post-tensioned transverse reinforcement s_{pt}, the post-tensioned transverse reinforcement ratio ρ_{pt}, and the initial post-tensioning stress in the post-tensioning rods were found to be the key parameters affecting deformability of columns. Figure 4-43 through Figure 4-48 show the relationship between the parameters discussed above and measured drift capacities of the columns. Keep in mind that reported values of 5% drift to not correspond to drift capacity. In these tests, columns were not tested beyond a drift ratio of 5%. From these figures, it was concluded that:

1) Columns with larger values of ρ_{pt} reached higher drift capacities. Columns with ρ_{pt} values of 0.2% or greater had a drift capacity of at least 3%.
2) Columns with larger ratios of post-tensioned transverse reinforcement spacing to effective depths ratios s_{pt}/d are more likely to have lower drift capacities. Columns with s_{pt}/d ratios less than 0.2 had drift capacities of at least 3%.
3) Columns where the shear contribution of post-tensioned transverse reinforcement (v_{pt} - expressed as a fraction of the maximum nominal shear stress v_{exp}) was larger than 0.2 had drift capacities greater than 3%. (where v_{pt} is based on the initial post-tensioning stress)
4) Increases in the confinement provided by post-tensioned transverse reinforcement requiring yielding of the post-tensioning bars (for specimens with values of ρ_{pt} < 0.2%), did not have a clear positive effect on drift capacity. It is likely that yielding of the post-tensioning bars did not improve drift capacity because the concrete core had to expand for yielding to occur. This suggests that it would be safer to assume the contribution of the post-tensioned transverse reinforcement to shear resistance is provided by the initial post-tensioning and does not increase.
5) Strains measured in specimens in which yielding of the post-tensioning did not occur suggest that no or little expansion of the concrete core, which is a desirable outcome for earthquake performance.

Results from test Series Five and Yamakawa et al. (2000) were also compared against test results from specimens with conventional forms of transverse reinforcement as shown in Figure 4-43. Test data for the conventional forms of transverse reinforcement were obtained from the database of rectangular reinforced concrete column tests compiled by (ACI Committee 369). To make objective comparison between the two types of reinforcement, only tests with the following critical parameters from the (ACI Committee 369) database were used:

- Concrete compressive strengths f_c' ranging from 2 ksi to 12 ksi
- Yield stress of longitudinal reinforcement f_y ranging from 46 to 74 ksi
- Yield stress of transverse reinforcement ranging f_{yt} from 36 to 95 ksi
- Longitudinal reinforcement ratios ranging ρ from 1.2% to 6.9%
- Conventional transverse reinforcement ratios ρ_{tr} ranging from 0.1% to 1.6%
- Aspect ratios a/d not exceeding 4
- s/d values less than 0.5
- s/d_b values less than 8
- No lap splices
- axial load less than $0.2f_c`A_g$

Figure 4-43 shows drift capacity versus $(v_s/v_{exp})(a/d)$. Here v_s refers to the transverse reinforcement shear resistance and v_{exp} refers to the nominal shear stress demand. For columns without post-tensioned transverse reinforcement, the ratio v_s refers to the transverse reinforcement provided by conventional ties. For columns with post-tensioned transverse reinforcement the value of v_s is taken as initial prestress v_{pti}. Despite the scatter, the results indicate that drift capacity of reinforced concrete columns increases with an increase in the ratio v_s / v_{exp}. The results also suggest that 1) the use of post-tensioned transverse reinforcement tended to produce similar or larger drift capacity in comparison with conventional ties and 2) selecting post-tensioned transverse reinforcement such that the quantity ($v_{pt} > v_{exp}$) is a safe design assumption that should help avoid shear failure before flexural yielding. Figure 4-44 shows again drift capacity versus $(v_s/v_{exp})(a/d)$. This figure is similar to Figure 4-43, however, for specimens with post-tensioned transverse reinforcement the value of v_s is taken as either the initial prestress v_{pti} or the yield stress v_{pty}. The yield stress v_{pty} was used if Yamakawa et al. (2000) reported post-tensioning rods to have yielded during testing. If no yielding was reported the initial prestress v_{pti} was used. Although yielding results in a larger contribution to shear strength, the drift capacity does not increase. This would suggest that the initial stress in the post-tensioning rod contributes to the increase in drift capacity (relative to the bare column) and the observed yielding of the rods is a result of core expansion rather than an increase in confinement. Figure 4-44 may be regarded as a more objective representation of the data because even in columns with conventional ties, yielding of said ties is not always reached (especially for columns with large transverse reinforcement ratios). In both Figure 4-43 and Figure 4-44 the data suggest the columns strengthened with post-tensioned transverse reinforcement were at least as deformable as columns with conventional transverse reinforcement.

The ease of installing, design, and fabrication the post-tensioned transverse reinforcement makes them an attractive alternative for retrofit and repair. Their simplicity has been largely overlooked and by industry so far. To help engineers intending to use them, tests are needed to explore the effects of the initial post-tensioning on column deformability (drift capacity). With the available data, no definitive conclusions can be made on how a column with higher initial post-tensioning differs from a column with lower initial post-tensioning. One could argue that the perceived advantages of the columns with post-tensioned transverse reinforcement are a result of the exceptionally high strength bars used to make them, and that the post-tensioning force may not prevent the cracking and core expansion as suspected. Even then, the use of post-tensioned transverse reinforcement provides a safe and simple alternative worth considering for column strengthening.

5. SCOPE AND CONCLUSIONS

5.1 Research Objectives

The objective of this research program was to understand the effects of post-installed transverse reinforcement on both the strength and deformability of reinforced concrete elements containing vulnerable seismic reinforcement details related to bond and shear. This objective was accomplished through forty-two large-scale laboratory experiments on the following five series of tests:

1) Series One – to study the tensile strength and deformability of unconfined tension lap splices.
2) Series Two – to study the effects of post-installed epoxied anchors on the tensile strength and deformability of tension lap splices.
3) Series Three – to study the effects of spiral transverse reinforcement on the tensile strength and deformability of tension lap splices.
4) Series Four – to study the effects of post-tensioned transverse reinforcement on the tensile strength and deformability of tension lap splices.
5) Series Five – to study the effects of post-tensioned transverse reinforcement on the shear strength and drift capacity of reinforced concrete columns.

5.2 Scope of Research

The first objective was pursued by testing twelve specimens with unconfined lap splices (Series One). All specimens contained a pair of spliced Gr. 60 #11 reinforcing bars. A splice length of 56-bar diameters, and the same cross-section were used in all twelve specimens. In Series One, six specimens were tested as beams, and six specimens were tested as tension coupons. In the beam specimens, tensile forces were generated in the splice through bending. In the coupon specimens, tensile forces were applied directly to the splice ends. All splices were loaded monotonically until splice failure occurred. Peak bar stresses, bar strains and deformations of the splice were measured.

The second objective was pursued by testing twelve specimens containing with lap splices confined by epoxied anchors (Series Two). Specimens in Series Two were cast identical to coupons in Series One. Epoxied anchors were installed along the splice length and embedded perpendicular to the plane producing splitting cracks. Splices were loaded, unloaded, installed with anchors, and then monotonically loaded until bond failure occurred. Peak bar stresses, bar strains and deformations of the splice were measured.

The third objective was pursued by testing nine specimens with lap splices confined by spiral transverse reinforcement (Series Three). The same reinforcement as coupons in Series One and Two was used. However, splice lengths ranged from 12 to 20-bar diameters. The cross section was modified to have equal cover above and below the spliced bars. All other dimensions were identical to Serie One and Two. A smooth steel wire, fabricated in the shape of a helical coil (referred to as spiral reinforcement), was placed concentrically around the splice. Splices were monotonically loaded until bond failure occurred. Peak bar stresses, bar strains and deformations of the splice were measured.

The fourth objective was pursued by testing seven specimens with lap splices confined by post-tensioned transverse reinforcement (Series Four). Specimens in Series Four were cast identical to specimens in Series Three. All specimens had a splice length of 20-bar diameters. The post-installed transverse reinforcement was installed on the specimen prior to testing. The spacing and level of post-tensioning stress were varied. Splices were monotonically loaded until bond failure occurred. Peak bar stresses, bar strains and deformations of the splice were measured.

The fifth objective was pursued by testing two columns specimens with poor shear reinforcement detailing. (Series Five). Two columns nearly identical were cast. One column was tested with post-tensioned transverse reinforcement, the other was tested without them as reference. Each column was cycled at increasing drift ratios until failure or shear failure was observed. Load versus displacement histories and concrete surface strains were measured.

5.3 Conclusions

In Test Series One through Series Four, test data compiled by Richter (2012), Sozen and Moehle (1990), and Pollalis (2020) of deformed-bar lap splices with the following dimensions and parameters were selected:

- Uncoated straight deformed bars in tension
- Short-time load increased monotonically to failure
- Concrete compressive strength f_c' not exceeding 10 ksi
- Yield stress of longitudinal reinforcement f_y less than 120 ksi
- Clear spacing between spliced bars $2c_{si}$ equal to or exceeding 2-bar diameters
- Clear cover equal to or exceeding 1-bar diameter
- Bottom-cast (depth of concrete below bars not exceeding 12 in.)

In test Series Five, the column test database (ACI Committee 369) with the following parameters were used:

- Concrete compressive strengths f_c' ranging from 2 ksi to 12 ksi
- Yield stress of longitudinal reinforcement f_y ranging from 46 to 74 ksi
- Yield stress of transverse reinforcement ranging f_{yt} from 36 to 95 ksi
- Longitudinal reinforcement ratios ranging ρ from 1.2% to 6.9%
- Conventional transverse reinforcement ratios ρ_{tr} ranging from 0.1% to 1.6%
- Aspect ratios a/d not exceeding 4
- s/d values less than 0.5
- s/d_b values less than 8
- No lap splices
- axial load less than $0.2f_c`A_g$

In addition, comparisons were made to column tests performed by Yamakawa et al. (2000) with the following parameters:

- Concrete compressive strengths f_c' ranging from 2 ksi to 4.5 ksi
- Longitudinal reinforcement with a yield stress f_y of 53 ksi
- Conventional transverse reinforcement with a yield stress f_{yt} of 48 ksi

- Longitudinal reinforcement ratios ρ of 1.38% to 2.53%
- Conventional transverse reinforcement ratios ρ_{tr} of 0.08% to .21%
- Post-tensioning transverse reinforcement ratios ρ_{tr} of 0.06% to 0.54%
- Post-tensioned transverse reinforcement yield stress f_{pty} not exceeding 180 ksi
- Column aspect ratios *a/d* of 1 to 2
- axial load less than $0.2f_c`A_g$

The conclusions presented below are valid within the domain of experimental variables and ranges evaluated in this study:

1) In absence of transverse reinforcement, increases in splice length beyond 40-bar diameters, as often produced by current design standards, did not result in proportional increases in splice strength or ductility. These results agree with previous studies by Richter (2012) and Kluge and Tuma (1945).

2) Lap splices confined by post-installed epoxied anchors had bond strengths similar to the strengths of unconfined splices of the same geometry. The addition of anchors, on average, resulted in a larger relative increase in bar strain as compared with bar stress. (7% increase in peak bar stress, compared with a 33% increase in bar strain). The large relative increase in bar strain associated with a smaller increase in peak bar stress after yielding is a result of bar deformations occurring within the yield plateau of the stress-strain curve of the reinforcing steel used. While this increase in deformability may be beneficial for elements with no moment gradient (as those tested), the same benefit is unlikely to exist in elements with a large moment gradient (such as walls and columns) as observed and explained by Sozen and Wight (1975).

3) Lap splices confined by spiral reinforcement had bond strengths similar to what can be achieved with traditional forms of transverse reinforcement (stirrups and ties). The benefits of spiral reinforcement in compression, first reported by Richart (1929), did not translate to bond. The large volumetric expansion that results in large benefits from spirals confining concrete in compression did not seem occur (at least prior to splice failure) in the reported tests of lap splices in which bursting stresses caused by bond were dominant. In the case

of compression, the spiral is ‘active’ after large expansion of the concrete and before failure, but for bond it remains ‘passive’ up to failure similar to traditional forms of confinement.

4) Confinement provided by post-tensioned transverse reinforcement produced bond strengths similar to those observed in past investigations on lap splices confined by conventional stirrups. Its effects on deformability were more profound, as a 500% average relative increase in bar strain was observed when post-tensioned transverse reinforcement was used on 20-bar diameter lap splices. For short lap splices, increases in confining pressure did not lead to proportional increases in bar strain. Maximum bar strain (observed to be 2.5% at failure in the reported tests) was limited by concrete breakout.

5) Considering the data obtained from Test Series Five, and results reported by Yamakawa et al. (2000), which lie within the following ranges of parameters listed below, allowed quantification of the effects of confinement provided by post-tensioned transverse reinforcement on the response of RC columns to lateral displacement reversals.

- Aspect ratios *a/d* ranging from 1 to 4
- Concrete compressive strengths f_c' ranging from 2 ksi to 4.5 ksi
- Longitudinal reinforcement with a yield stress f_y of 53 ksi
- Conventional transverse reinforcement with a yield stress f_{yt} of 48 ksi
- Longitudinal reinforcement ratios ρ of 1.4% to 2.5%
- Conventional transverse reinforcement ratios ρ_{tr} of 0.08% to 0.21%
- Post-tensioning transverse reinforcement ratios ρ_{pt} of 0.06% to 0.54%
- axial load less than $0.2f_c`A_g$

Post-tensioning resulting in a transverse stress (v_{pt} = product of transverse reinforcement ratio and initial stress in tensioning rods) larger than 100% of the nominal unit shear stress demand (v_{max} = maximum shear force divided by product of cross-sectional width b and effective depth d) prevented shear failure prior to flexural yielding of columns repaired with post-tensioned transverse reinforcement.

6) Considering the data obtained in this investigation and the results by Yamakawa et al. (2000) that lie within the ranges listed in bullet 5, the drift capacity of columns strengthened with post-tensioned transverse reinforcement was observed to be as large or larger than the drift capacity of columns provided by conventional rectilinear ties for similar values of the ratio $\frac{v_s}{v_{max}}\frac{a}{d}$. Here, v_s is the unit lateral pressure estimated as the product of the transverse reinforcement ratio, of either conventional ties or post-tensioning rods, and stress (yield stress for conventional ties and initial prestress in the threaded rods f_{pt}). Maximum unit shear demand v_{max} is the maximum shear force divided by product of cross-sectional width b and effective depth d.

7) With the limited data obtained in this investigation and the results by Yamakawa et al. (2000) that lie within the ranges listed in bullet 5, drift capacities of elements reinforced with post-tensioned transverse reinforcement were observed to be nearly proportional to the ratio of initial post-tensioning lateral stress in the concrete to the nominal unit shear demand $\frac{v_{pt}}{v_{max}}\frac{a}{d}$. Here, v_{pt} is the product of the transverse reinforcement ratio (ρ_{pt}) and initial stress f_{pt} in each post-tensioning rod and v_{max} is the maximum nominal unit shear stress. For columns tested by Yamakawa et al. (2000) and in Series Five, column drift capacity could be approximated as:

$$Drift\ Ratio = \frac{v_{pt}}{v_{max}} \cdot \frac{a}{d} \cdot \frac{7\%}{4} = \frac{\rho_{pt} \cdot f_{pt}}{\frac{M_p}{a} \cdot \frac{1}{bd}} \cdot \frac{a}{d} \cdot \frac{7\%}{4}$$

a = shear span (distance from column end to point of inflection)

b = cross-sectional width

d = cross-sectional effective depth

M_p= expected column flexural capacity

This rather generous estimate is likely to be sensitive to other variables not included in this expression (Eberhard and Berry, 2003; Elwood and Moehle, 2005; Ghannoum and Matamoros, 2014), and should not be extrapolated beyond the stated ranges listed in bullet 5 without support from additional data, especially for columns with high axial loads. Its use should require a factor of safety commensurate with the consequences of column failure and the uncertainties related to estimation of drifts caused by dynamic demands.

TABLES

Table 2-1: Selected Properties from Series-One beams

Specimen	l_s / d_b	d_b in.	c_{si} in.	c_{so} in.	c_b in.	c_t in.	b in.	h in.	f_y ksi	f'_c psi
C1	56	1.41	3	3	5	24.25	17.625	30	65	5300
C2										5200
C3										5900
C4										5700
C5										5600
C6										5300

l_s	:	Splice length
d_b	:	Diameter of longitudinal reinforcing bar
c_{si}	:	One-half clear spacing between bars
c_{so}	:	Side cover in same plane as c_{si}
c_b	:	Cover perpendicular to c_{si} and c_{so} cast below the bars
c_t	:	Cover perpendicular to c_{si} and c_{so} cast above the bars
f_y	:	Measured yield stress of longitudinal reinforcement
f'_c	:	Concrete compressive strength
b	:	Width of concrete prism
h	:	Depth of concrete prism

Table 2-2: Selected properties from Series-One coupons

Specimen	l_s / d_b	d_b *in.*	c_{si} *in.*	c_{so} *in.*	c_b *in.*	c_t *in.*	b *in.*	h *in.*	f_y ksi	f'_c psi
D1	56	1.41	3	3	5	24.25	17.625	30	67	3900
D2										3900
D3										3900
D9										4100
D11										4300
D17										4400

l_s	:	Splice length
d_b	:	Diameter of longitudinal reinforcing bar
c_{si}	:	One-half clear spacing between bars
c_{so}	:	Side cover in same plane as c_{si}
c_b	:	Cover perpendicular to c_{si} and c_{so} cast below the bars
c_t	:	Cover perpendicular to c_{si} and c_{so} cast above the bars
f_y	:	Measured yield stress of longitudinal reinforcement
f'_c	:	Concrete compressive strength
b	:	Width of concrete prism
h	:	Depth of concrete prism

Table 2-3: Selected properties from Series-Two coupons

Specimen	l_s / d_b	d_b *in.*	c_{si} *in.*	c_{so} *in.*	c_b *in.*	c_t *in.*	b *in.*	h *in.*	f_y ksi	f'_c psi	*TRI* psi
D4										4000	310
D5										4000	470
D6										4000	240
D7										4200	470
D8										4100	470
D10	56	1.41	3	3	5	24.25	17.625	30	67	4200	470
D12										4100	470
D13										4400	470
D14										4300	470
D15										4500	470
D16										4300	470
D18										4300	470

l_s : Splice length

d_b : Diameter of longitudinal reinforcing bar

c_{si} : One-half clear spacing between bars

c_{so} : Side cover in same plane as c_{si}

c_b : Cover perpendicular to c_{si} and c_{so} cast below the bars

c_t : Cover perpendicular to c_{si} and c_{so} cast above the bars

f_y : Measured yield stress of longitudinal reinforcement

f'_c : Concrete compressive strength

b : Width of concrete prism

h : Depth of concrete prism

Table 2-4: Selected properties from Series-Three coupons

Specimen	l_s / d_b	d_b *in.*	c_{si} *in.*	c_{so} *in.*	c_b *in.*	c_t *in.*	b *in.*	h *in.*	f_y ksi	f'_c psi	*TRI* psi
H1											1880
H2	12										1880
H3											1880
H4											1250
H5	16	1.41	3	3	5	5	17.625	11.41	67	5200	1250
H6											1250
H7											940
H8	20										940
H9											940

l_s : Splice length
d_b : Diameter of longitudinal reinforcing bar
c_{si} : One-half clear spacing between bars
c_{so} : Side cover in same plane as c_{si}
c_b : Cover perpendicular to c_{si} and c_{so} cast below the bars
c_t : Cover perpendicular to c_{si} and c_{so} cast above the bars
f_y : Measured yield stress of longitudinal reinforcement
f'_c : Concrete compressive strength
b : Width of concrete prism
h : Depth of concrete prism

Table 2-5: Selected properties from Series-Four coupons

Specimen	l_s/d_b	d_b (in.)	c_{si} (in.)	c_{so} (in.)	c_b (in.)	c_t (in.)	b (in.)	h (in.)	f_y (ksi)	f'_c (psi)	TRI (psi)
PTR20-NC											0
PTR20-3.5-5K											3000
PTR20-3.5-10K											3000
PTR20-3.5-15K	20	1.41	3	3	5	5	17.625	11.41	67	4800	3000
PTR20-5-5K											2100
PTR20-5-10K											2100
PTR20-5-15K											2100

l_s : Splice length
d_b : Diameter of longitudinal reinforcing bar
c_{si} : One-half clear spacing between bars
c_{so} : Side cover in same plane as c_{si}
c_b : Cover perpendicular to c_{si} and c_{so} cast below the bars
c_t : Cover perpendicular to c_{si} and c_{so} cast above the bars
f_y : Measured yield stress of longitudinal reinforcement
f'_c : Concrete compressive strength
b : Width of concrete prism
h : Depth of concrete prism

Table 2-6: Selected properties from Series-Five Columns

Specimen	H in.	d_b in.	h in.	b in.	d_1 in.	d_2 in.	d_3 in.	ρ_t %	ρ_l %	f_y psi	f_{yt} psi	f'_c psi
C1 *C2*	58	1	18	18	15.5	9	2.5	0.1	2	70	65	7

H	:	Column height or shear span
d_b	:	Diameter of longitudinal reinforcing bars
h	:	Column depth
b	:	Column width
d_1	:	Depth to first layer of steel from top of section
d_2	:	Depth to second layer of steel from top of section
d_3	:	Depth to third layer of steel from top of section
ρ_t	:	Transverse reinforcement ratio
ρ_l	:	Longitudinal reinforcement ratio
f_{yt}	:	Yield stress of longitudinal reinforcement
f_y	:	Yield stress of transverse reinforcement
f'_c	:	Concrete compressive strength

Table 3-1: Series-One beam test summary

Specimen	d_b in	l_s d_b	f'_c psi	M_u[1] kip-ft	f_{su} ksi	f_{su}/f_y	ε_{su} %	μ $\sqrt{f'_c}$ psi	Avg. μ $\sqrt{f'_c}$ psi
C1	1.41	56	5300	419	73	1.12	1.5	4.5	4.5
C2			5200	422	74	1.14	1.6	4.6	
C3			5900	426	74	1.14	1.6	4.3	
C4			5700	431	75	1.15	1.7	4.4	
C5			5600	424	74	1.14	1.7	4.4	
C6			5300	429	75	1.15	1.7	4.6	

[1]	:	From average load of applied to overhangs
l_s	:	Splice length
d_b	:	Diameter of #11 longitudinal reinforcing bar (1.41in)
f_c'	:	Concrete compressive strength
M_{su}	:	Maximum moment at splice end
f_{su}	:	Maximum steel stress
ε_{su}	:	Maximum steel strain
μ	:	Mean bond strength

Table 3-2: Series-One coupon test summary

Specimen	d_b *in*	l_s d_b	f'_c *psi*	P_{su}^1 *kip*	f_{su} *ksi*	f_{su}/f_y	ε_{su} %	ε_{sa} %	μ $\sqrt{f'_c}$ psi	Avg. μ $\sqrt{f'_c}$ psi
D1	1.41	56	3900	114	73	1.09	1.4	0.6%	5.2	5.2
D2			3900	111	71	1.06	1.2	0.4%	5.1	
D3			3900	126	81	1.20	2.3	0.9%	5.8	
D9			4100	119	76	1.14	1.8	0.5%	5.3	
D11			4300	111	71	1.06	1.2	0.4%	4.8	
D17			4400	120	77	1.15	1.9	0.5%	5.2	

1	:	From average load of applied to bar ends
l_s	:	Splice length
d_b	:	Diameter of #11 longitudinal reinforcing bar (1.41 in.)
f_c'	:	Concrete compressive strength
P_{su}	:	Maximum Applied load
f_{su}	:	Maximum steel stress
ε_{su}	:	Maximum steel strain
ε_{sa}	:	Average surface strain of specimen at level of spliced reinforcement
μ	:	Mean bond strength

Table 3-3: Series-Two coupon test summary

Specimen	d_b in	l_s d_b	f'_c psi	P_{su}[1] kip	f_{su} ksi	f_{su}/f_y	ε_{su} %	ε_{sa} %	μ $\sqrt{f'_c}$ psi	Avg. μ $\sqrt{f'_c}$ psi
D4	1.41	56	4000	123	79	1.18	2.1	0.71	5.6	5.4
D5			4000	115	74	1.10	1.5	0.77	5.2	
D6			4000	117	75	1.12	1.6	0.53	5.3	
D7			4200	114	73	1.09	1.4	0.54	5.0	
D8			4100	129	83	1.23	2.5	0.96	5.8	
D10			4200	123	79	1.18	2.1	0.86	5.4	
D12			4100	122	78	1.17	2.0	0.77	5.4	
D13			4400	125	80	1.19	2.2	0.87	5.4	
D14			4300	123	79	1.18	2.1	0.79	5.4	
D15			4500	126	81	1.20	2.3	1.01	5.4	
D16			4300	125	80	1.19	2.2	0.90	5.4	
D18			4300	125	80	1.19	2.2	0.91	5.4	

[1]	:	From average load of applied to bar ends
l_s	:	Splice length
d_b	:	Diameter of #11 longitudinal reinforcing bar (1.41 in.)
$f_c^{'}$	:	Concrete compressive strength
P_{su}	:	Maximum Applied load
f_{su}	:	Maximum steel stress
ε_{su}	:	Maximum steel strain
ε_{sa}	:	Average surface strain of specimen at level of spliced bars
μ	:	Mean bond strength

Table 3-4: Series-Three coupon test summary

Specimen	d_b in	l_s d_b	f'_c psi	P_{su}[1] kip	f_{su} ksi	f_{su}/f_y	ε_{su} %	ε_{sa} %	μ $\sqrt{f'_c}$ psi	Avg. μ $\sqrt{f'_c}$ psi
H1	1.41	12	5200	70	45	0.67	0.15	-	12.9	13.8
H2				69	44	0.66	0.15	-	12.8	
H3				79	51	0.76	0.17	-	14.6	
H4		16		87	56	0.83	0.19	-	12.1	11.5
H5				86	55	0.82	0.19	-	12.0	
H6				79	51	0.76	0.18	-	11.0	
H7		20		96	61	0.91	0.21	-	10.6	10.3
H8				89	57	0.85	0.20	-	9.9	
H9				91	58	0.87	0.20	-	10.0	

[1]	:	From average load of applied to bar ends
l_s	:	Splice length
d_b	:	Diameter of #11 longitudinal reinforcing bar (1.41in)
f_c'	:	Concrete compressive strength
P_{su}	:	Maximum Applied load
f_{su}	:	Maximum steel stress
ε_{su}	:	Maximum steel strain
ε_{sa}	:	Average surface strain of specimen at level of spliced bars
μ	:	Mean bond strength

Table 3-5: Series-Four coupon test summary

Specimen	d_b in	l_s d_b	f'_c psi	P_{su}[1] kip	f_{su} ksi	f_{su}/f_y	ε_{su} %	ε_{sa} %	μ $\sqrt{f'_c}$ psi	Avg. μ $\sqrt{f'_c}$ psi
PTR-20-0	1.41	20	4800	58	37	0.55	0.13	0.7	6.6	6.6
PTR-20-3.5-5				116	74	1.10	1.5	2.0	13.3	14.2
PTR-20-3.5-10				136	87	1.30	3.0	3.0	15.7	
PTR-20-3.5-15				130	83	1.24	2.6	3.4	15.0	
PTR-20-5-5				107	69	1.02	0.9	1.4	12.4	13.8
PTR-20-5-10				128	82	1.22	2.4	2.9	14.8	
PTR-20-5-15				132	84	1.26	2.7	3.3	15.2	

[1]	:	From average load of applied to bar ends
l_s	:	Splice length
d_b	:	Diameter of #11 longitudinal reinforcing bar (1.41 in.)
f_c'	:	Concrete compressive strength
P_{su}	:	Maximum Applied load
f_{su}	:	Maximum steel stress
ε_{su}	:	Maximum steel strain
ε_{sa}	:	Average surface strain of specimen at level of spliced bars
μ	:	Mean bond strength

Table 3-6: Series-Five column test summary

Specimen	f_c' *ksi*	a/d	s_{pt}/d	ρ_{pt} *%*	ρ_{tr} *%*	v_{pt} *ksi*	v_{tr} *ksi*	V_{exp} *kip*	v_{exp} *ksi*	v_{pt}/v_{exp}	DR_{max} %	*Yield of PT*	*Failure Mode*
C1	7	3.9	0.31	0.313	0.1	0.2	0.060	61	0.23	0.97	> 7	-	*F(Y)*
C2			-	-	0.1	-	0.060	61	0.22	-	1.5	-	*S*

f_c'	:	Concrete cylinder compressive strength
s_{pt}/d	:	Ratio of spacing of post-tensioned ties to outermost later of long. Steel
ρ_{pt}	:	Reinforcement ratio of post-tensioned transverse reinforcement
ρ_{tr}	:	Reinforcement ratio of conventional transverse reinforcement (ties)
v_{pt}	:	Shear strength contribution of post-tensioned tranverse reinforcement corresponding to f_{pt} = 70 ksi
v_{tr}	:	Shear strength contribution of conventional tranverse reinforcement
V_{exp}	:	Maximum applied lateral shear force
v_{exp}	:	Maximum shear stress demand corresponding to V_{exp}
DR_{max}	:	Maximum drift ratio corresponding to 80% of V_{exp}

Table 4-1: Test results of columns tested by Yamakawa et al.

Specimen	f_c'	a/d	s_{pt}/d	ρ_{pt}	ρ_{tr}	v_{pt}	v_{tr}	V_{exp}	v_{exp}	v_{pt}/v_{exp}	DR_{max}	*Yield of PT*	*Failure Mode*
	ksi			%	%	*ksi*	*ksi*	*kip*	*ksi*		%		
R98S-P0	4.6	1	0.00	0	0.08	0.0	0.038	40.70	0.47	0	0.6	-	*S*
R98S-P41			0.18	0.21	0.08	0.1	0.038	61.26	0.71	0.1778	3.2	*Y*	*FC(Y)*
R98-P41'			0.18	0.45	0.08	0.3	0.038	64.04	0.74	0.3644	3.4	*Y*	*FC(Y)*
R98-P41'H	4.5		0.18	0.45	0.08	0.3	0.038	63.44	0.73	0.3679	4.6	*N*	*F(Y)*
R99S-P0	3		0.00	0	0.08	0.0	0.038	26.79	0.31	0	0.5	-	*S*
R99S-P105			0.47	0.08	0.08	0.0	0.038	35.53	0.41	0.1168	1.8	*Y*	*S-B*
R99S-P41			0.18	0.45	0.08	0.3	0.038	48.49	0.56	0.4812	5.0	*N*	*F(Y)*
R98M-P0	4	1.5	0.00	0	0.08	0.0	0.038	38.79	0.45	0	0.5	-	*S*
R98M-P105			0.47	0.08	0.08	0.0	0.038	38.97	0.45	0.1065	1.5	*Y*	*SC*
R98M-P65N			0.29	0.14	0.08	0.1	0.038	40.11	0.46	0.181	3.0	*Y*	*F-B(Y)*
R98M-P65N			0.29	0.14	0.08	0.1	0.038	44.07	0.51	0.1648	3.5	*N*	*F(Y)*
R99M-P0	2.7		0.00	0	0.08	0.0	0.038	27.10	0.31	0	0.5	-	*S*
R99M-P150			0.67	0.06	0.08	0.0	0.038	34.61	0.40	0.0899	2.0	*Y*	*S-B*
R99M-P105			0.47	0.08	0.08	0.0	0.038	33.03	0.38	0.1256	2.1	*N*	*S-B*
R99M-P41'			0.18	0.45	0.08	0.3	0.038	40.18	0.46	0.5808	5.0	*N*	*F-B(Y)*
R99M-P$_H$34'	3.5		0.15	0.54	0.08	0.3	0.038	46.58	0.54	0.6012	5.0	*N*	*F(Y)*
R99M-P0H	3.9		0.00	0	0.08	0.0	0.038	33.17	0.38	0	0.5	-	*S*
R99M-P105H			0.67	0.06	0.08	0.0	0.038	39.10	0.45	0.0796	1.7	*Y*	*S-B*
R99M-P41'H			0.18	0.45	0.08	0.3	0.038	45.62	0.53	0.5116	5.0	*N*	*F-B(Y)*
R99M-P0L	2.1		0.00	0	0.08	0.0	0.038	21.66	0.25	0	0.5	-	*S*
R99M-P150L			0.67	0.06	0.08	0.0	0.038	23.87	0.28	0.1304	1.6	*N*	*S-B*
R99M-P41'L			0.00	0.45	0.08	0.3	0.038	31.12	0.36	0.7498	4.6	*N*	*Bond Slip*
R99M-P0R	3.4		0.00	0	0.08	0.0	0.038	28.49	0.33	0	0.6	-	*S*
R99M-P150R			0.67	0.06	0.08	0.0	0.038	32.31	0.37	0.0963	1.6	*N*	*S-B*
R99M-P41'R			0.00	0.45	0.08	0.3	0.038	36.99	0.43	0.6309	2.0	*N*	*Bond Slip*
R99M-P0pw	3.3		0.00	0	0.21	0.0	0.101	29.30	0.34	0	1.0	-	*S*
R99M-P150pw			0.67	0.06	0.21	0.0	0.101	35.82	0.41	0.0869	2.1	*N*	*S-B*
R99M-P41'pw			0.18	0.45	0.21	0.3	0.101	41.10	0.48	0.5678	4.0	*N*	*F-B(Y)*
R99L-P0	3.1	2	0.00	0	0.08	0.0	0.038	23.19	0.27	0	0.5	-	*S*
R99L-P150			0.67	0.06	0.08	0.0	0.038	29.89	0.35	0.1041	2.4	*N*	*S-B*
R99L-P41'			0.18	0.45	0.08	0.3	0.038	31.35	0.36	0.7445	5.0	*N*	*F(Y)*

f_c'	:	Concrete cylinder compressive strength
s_{pt}/d	:	Ratio of spacing of post-tensioned ties to outermost later of long. Steel
ρ_{pt}	:	Reinforcement ratio of post-tensioned transverse reinforcement
ρ_{tr}	:	Reinforcement ratio of conventional transverse reinforcement (ties)
v_{pt}	:	Shear strength contribution of post-tensioned tranverse reinforcement corresponding to initial PT = 70 ksi
v_{tr}	:	Shear strength contribution of conventional tranverse reinforcement
V_{exp}	:	Maximum applied lateral shear force
v_{exp}	:	Maximum shear stress demand corresponding to V_{exp}
DR_{max}	:	Maximum drift ratio corresponding to 80% of V_{exp}

FIGURES

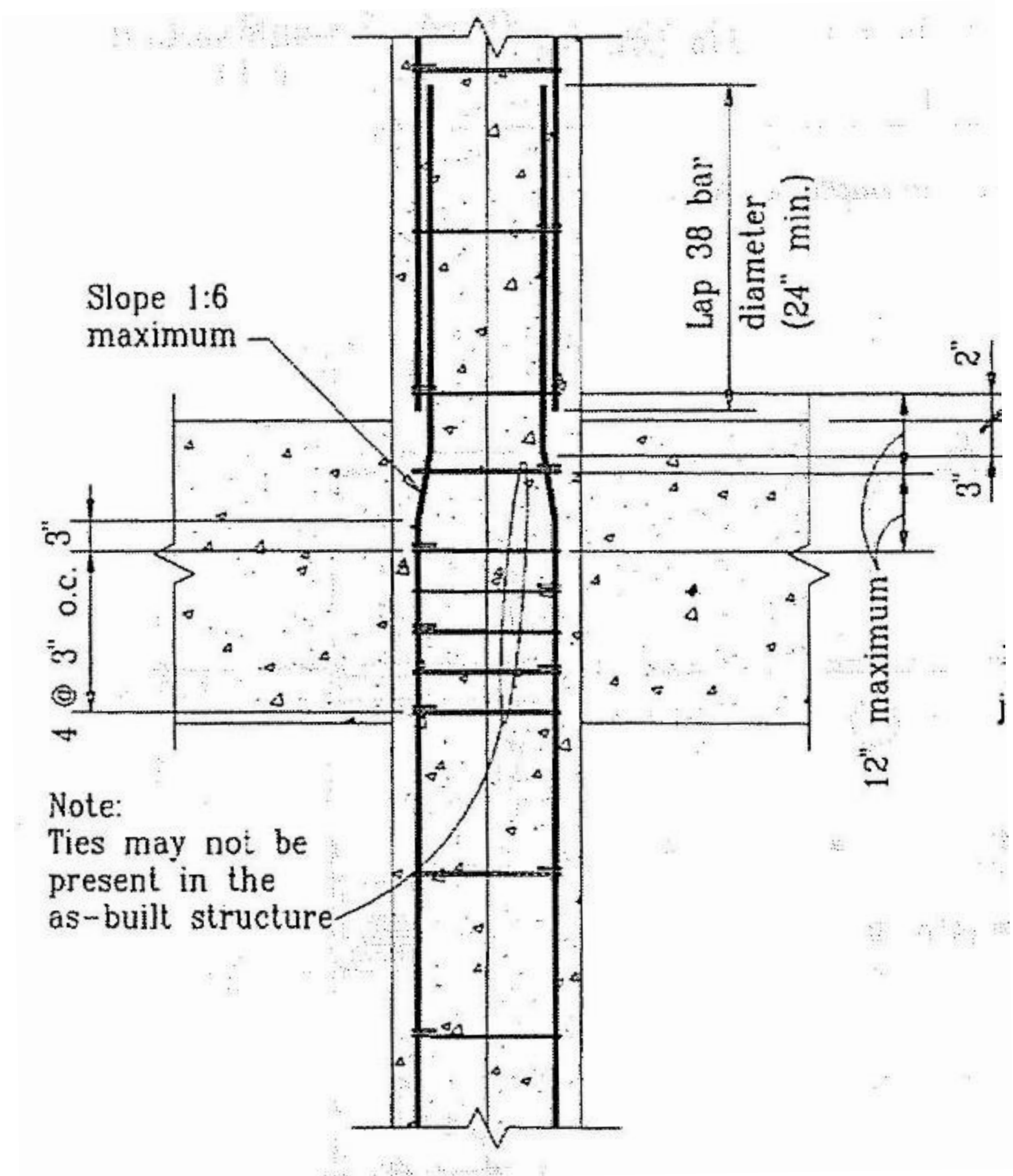

Figure 1-1: Reinforcement detailing of beam-column joint in the Van Nuys Holiday Inn building (Seismic Safety Commission (SSC), 1994)

Figure 1-2: Failure of exterior reinforced concrete column in the Van Nuys Holiday Inn building during the 1994 Northridge Earthquake (Earthquake Engineering Field Investigation Team (EEFIT), 1994)

Figure 1-3: Close-up shear failure of a reinforced concrete column located in the Van Nuys Holiday Inn building during the 1994 Northridge Earthquake (Comartin, Elwood, & Faison, 2004)

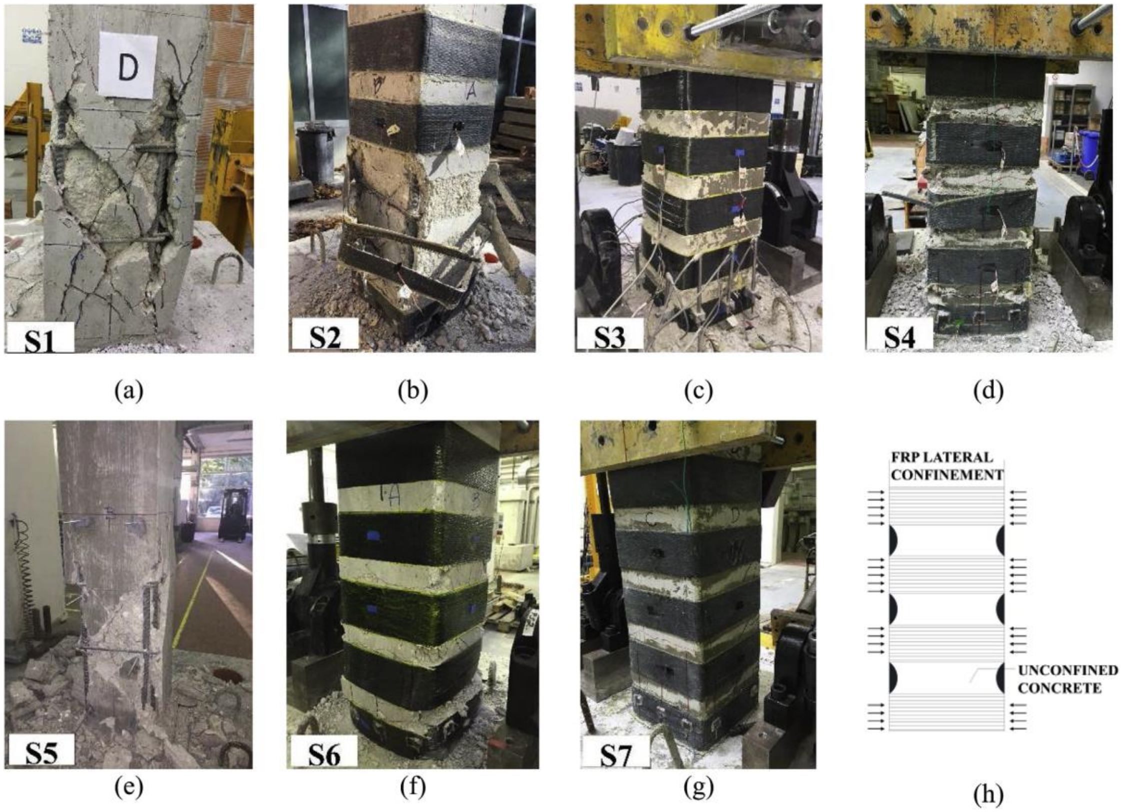

Figure 1-4: Tests photos of columns with FRP jacketing adapted from Zoppo et al. (2017)

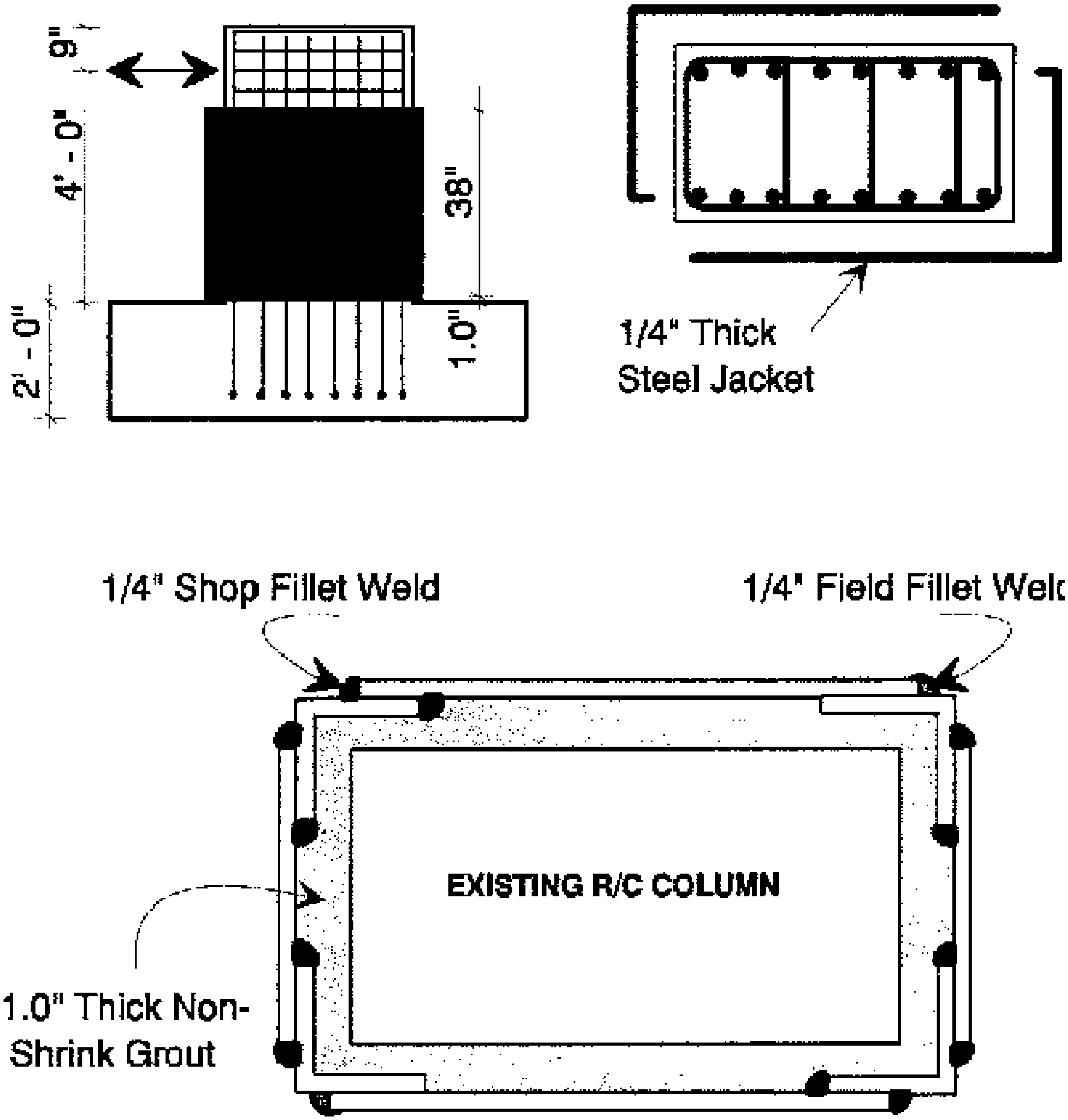

Figure 1-5: Drawing of steel jacket used to repair columns adapted from Aboutaha et al. (1999)

Figure 1-6: Tests of prestressed strands as transverse reinforcement adapted from Yarandi et al. (2004)

Figure 1-7: External transverse reinforcement used by (Richter, 2012)

0

Figure 1-8: External transverse reinforcement used by (Daluga, 2015)

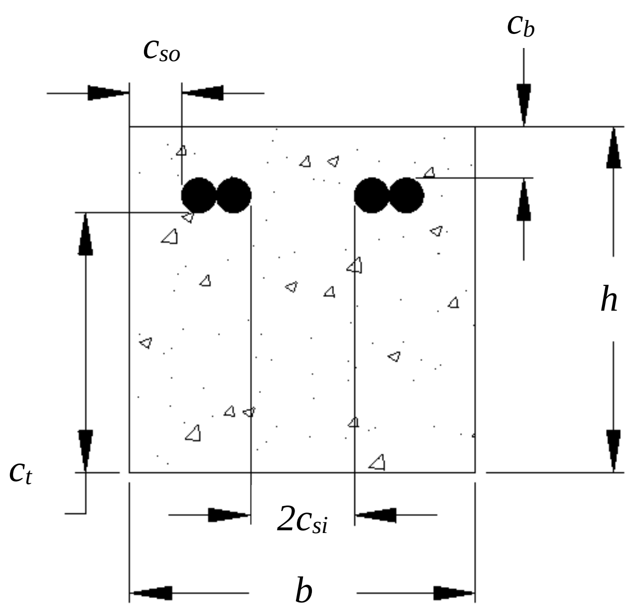

Figure 2-1: Typical cross-section of Series One through Series Four specimens (See Table 2-1 through Table 2-4 for definitions) Adapted from Richter (2012)

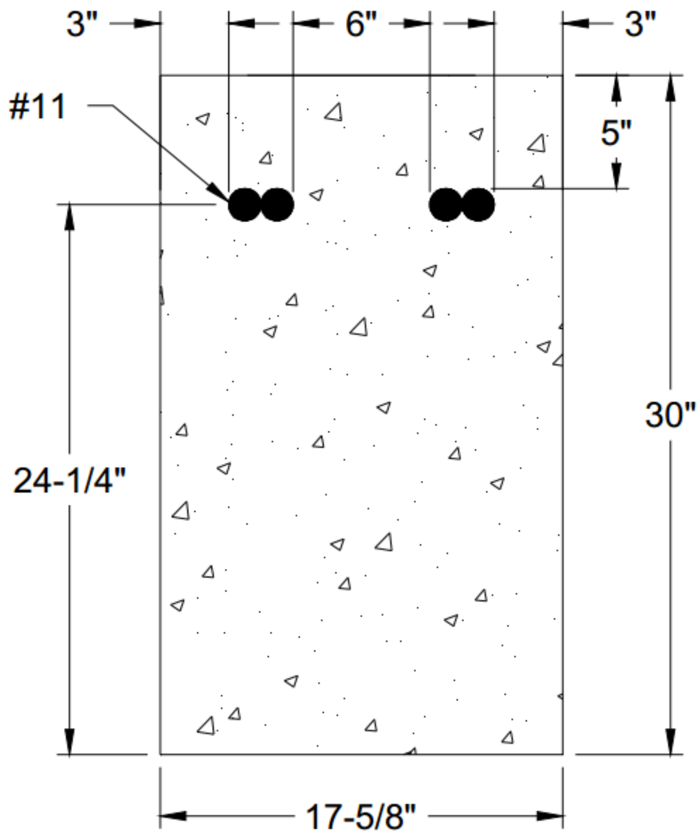

Figure 2-2: Cross-section for Series-one and Series-Two specimens.

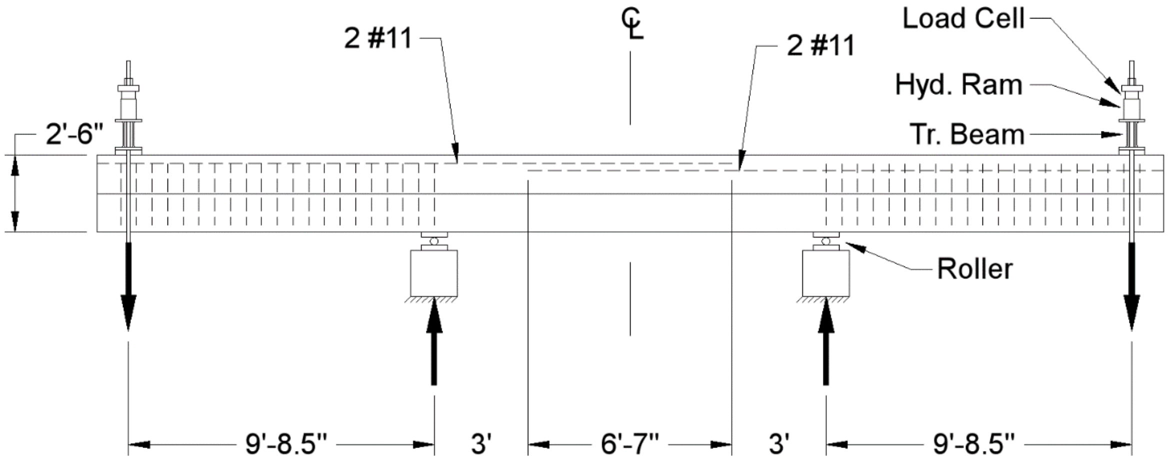

Figure 2-3: Series-One beam test setup

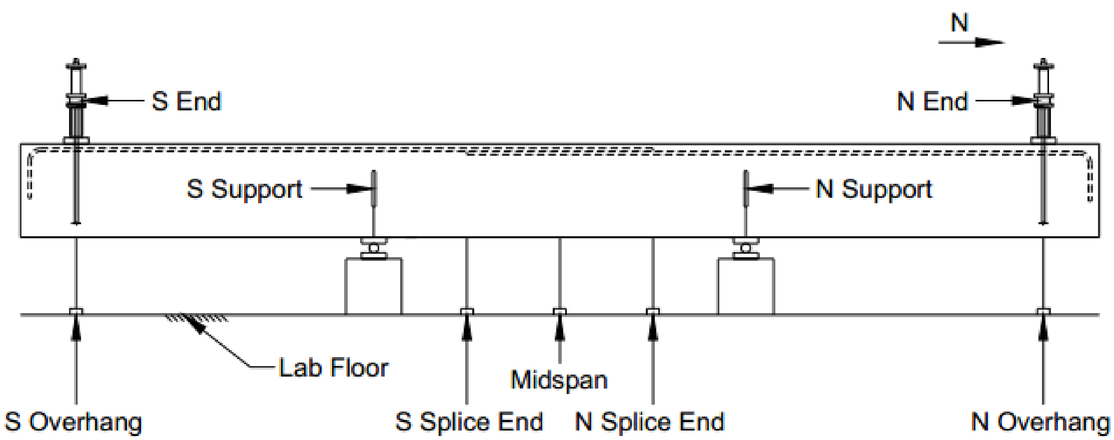

Figure 2-4: Series-One beam instrumentation location

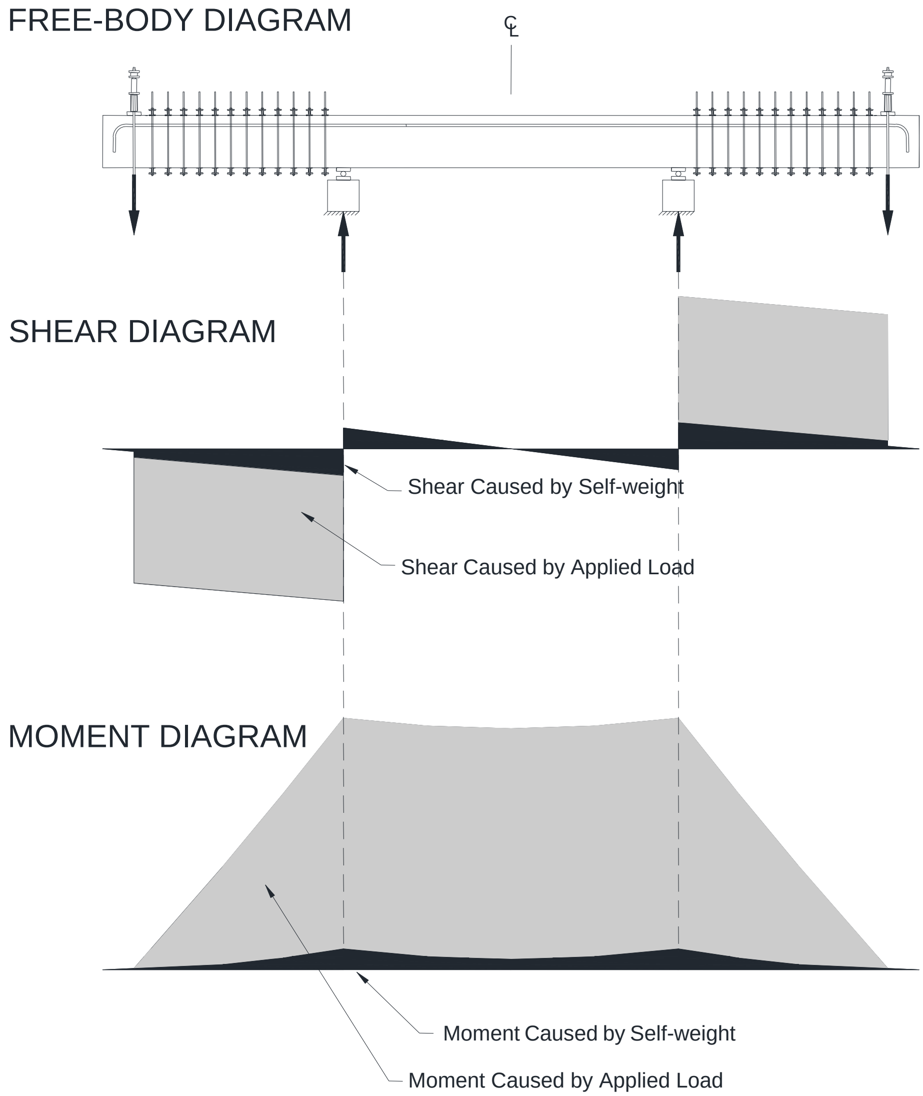

Figure 2-5: Shear and moment diagrams for Series-One beam specimens

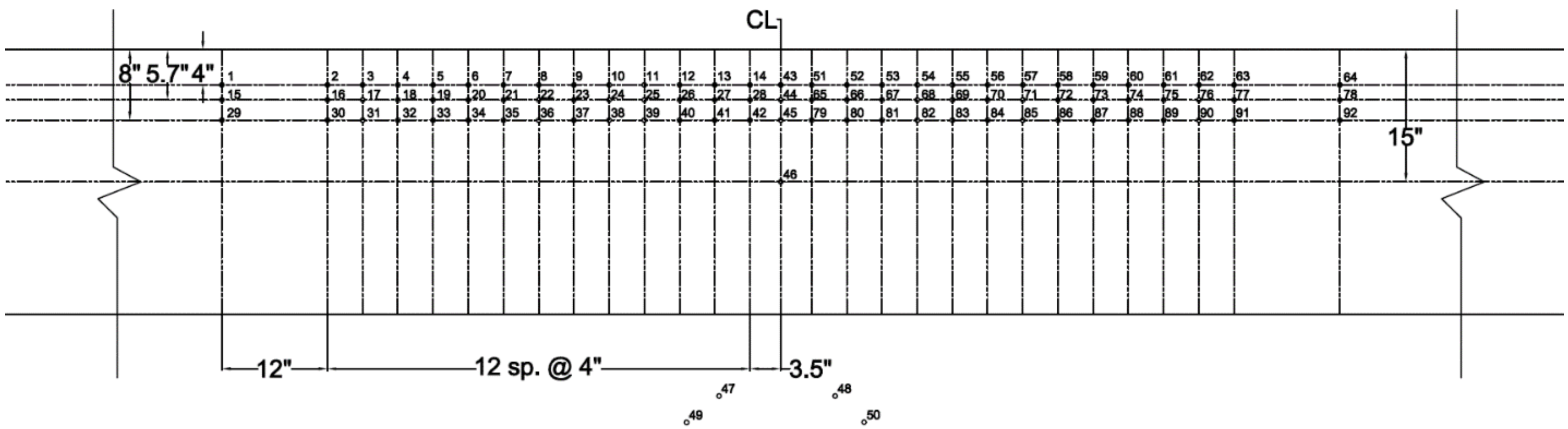

Figure 2-6: Series-One beam specimen optical target layout along spliced bars

Figure 2-7: Series-One beam specimen testing setup.

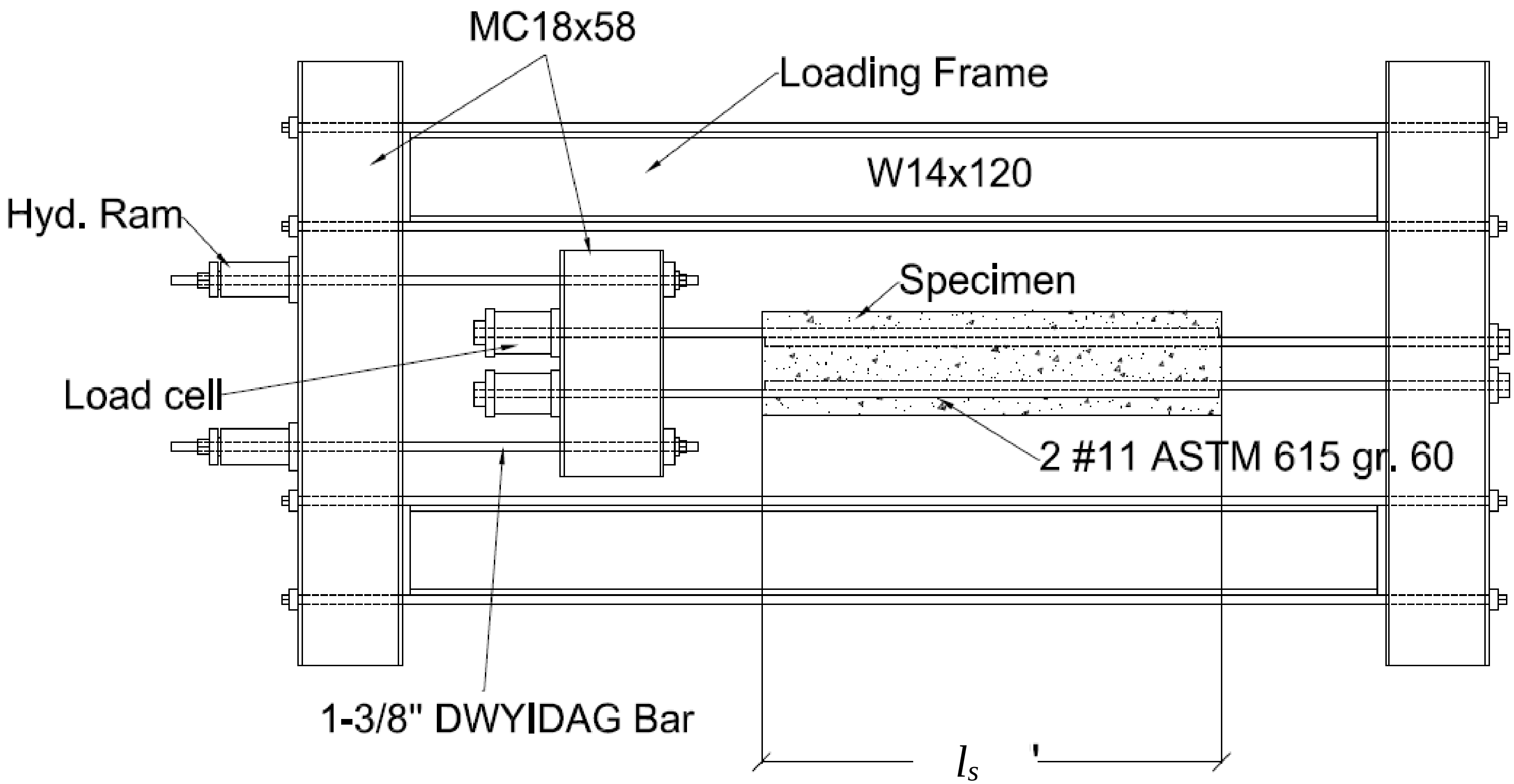

Figure 2-8: Series-One through Series-Four coupon specimen test setup

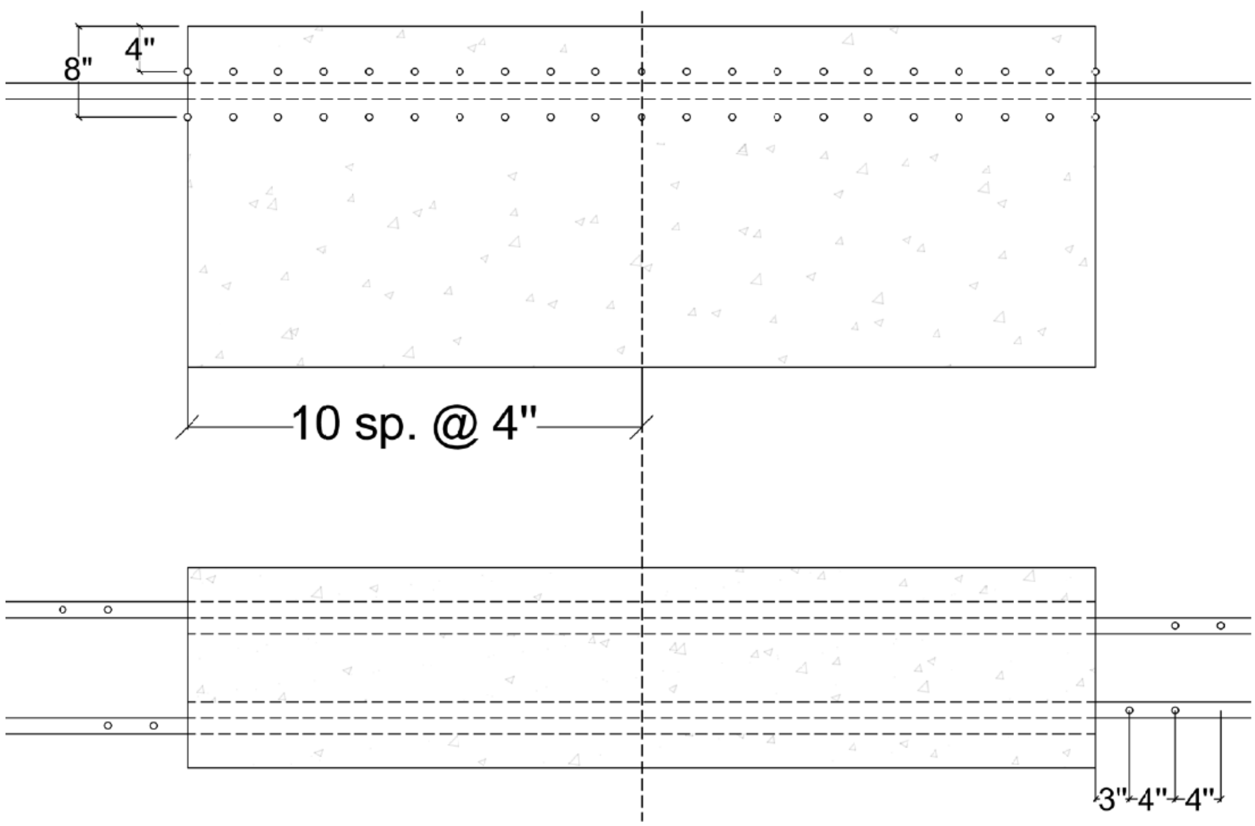

Figure 2-9: Series-One and Series-Two coupon specimen optical target layout

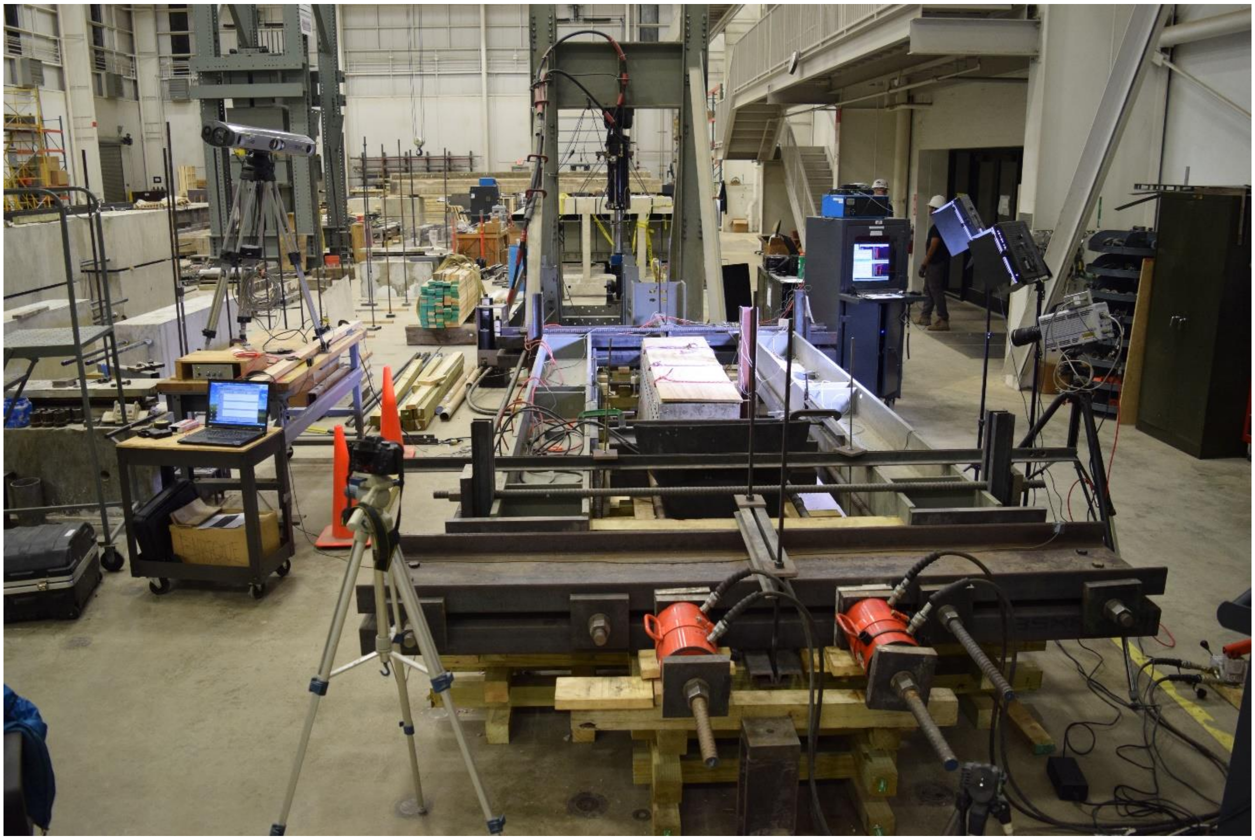

Figure 2-10: Testing setup for tension coupon specimens (Series One through Series Three).

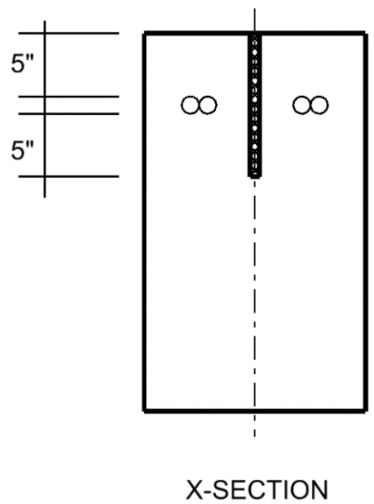

Figure 2-11: Specimen D4 (configuration 1) and D6 (configuration 2) cross section and anchor depth

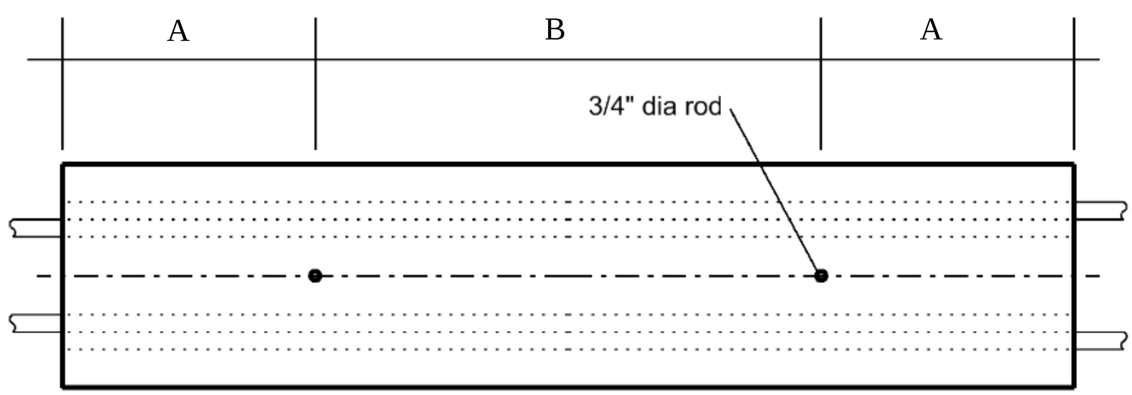

Figure 2-12: Anchor dimension for specimen D4 (configuration 1) and D6 (configuration 2). Dimension B = 40 in. and A = 20 in. for D4, Dimension B = 53.3 in. and A = 13.3 in. for D6

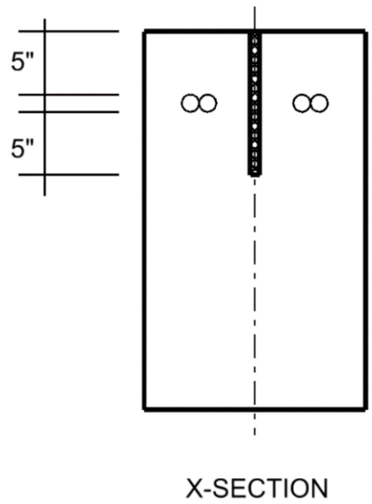

Figure 2-13: Specimen D5 and D7 cross section and anchor depth (configuration 3)

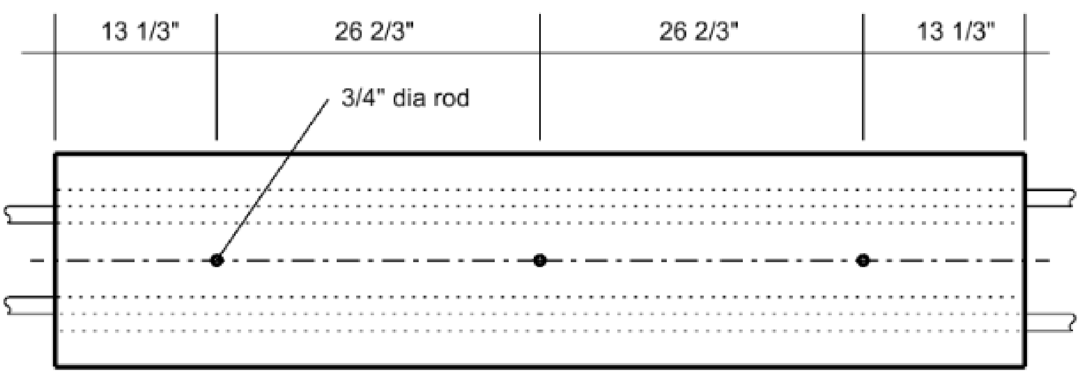

Figure 2-14: Anchor dimension for specimen D5 and D7 (configuration 3)

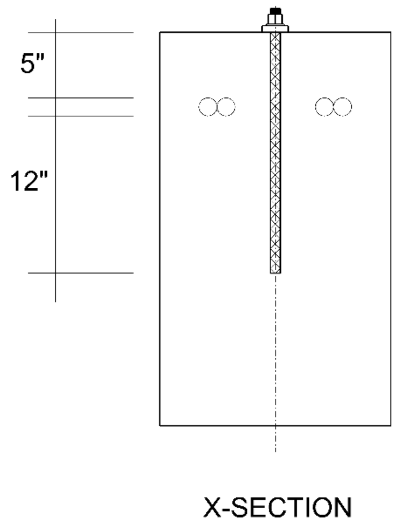

Figure 2-15: Specimen cross section and anchor depth for specimens D8, D10, D12-D16, D18 (configuration 4)

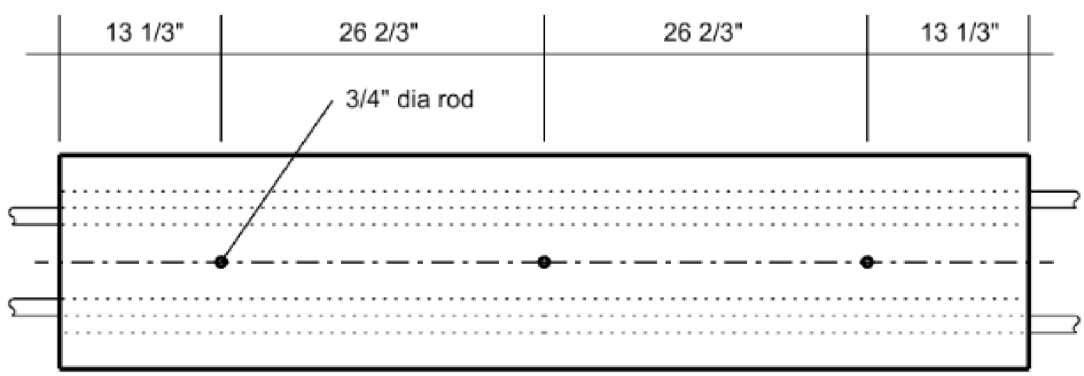

Figure 2-16: Anchor dimension for specimen D8, D10, D12-D16, D18 (configuration 4)

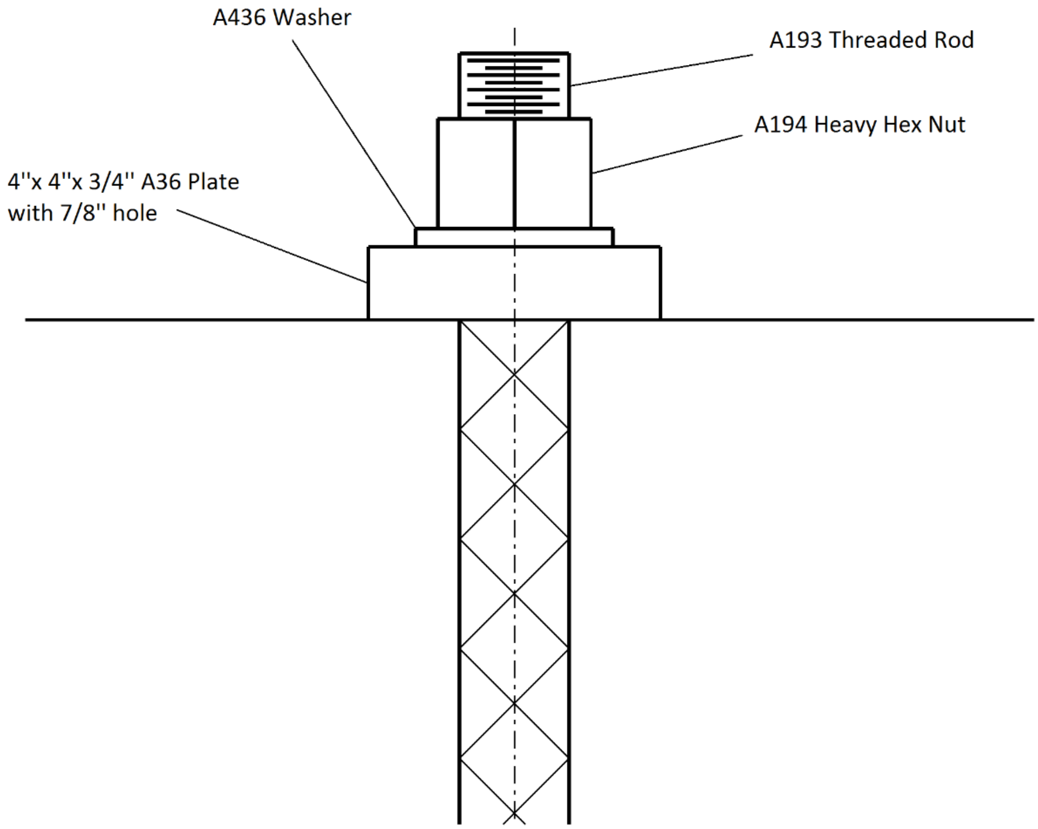

Figure 2-17: Anchor plate assembly for specimens D8, D10, D12-D16, D18 (configuration 4)

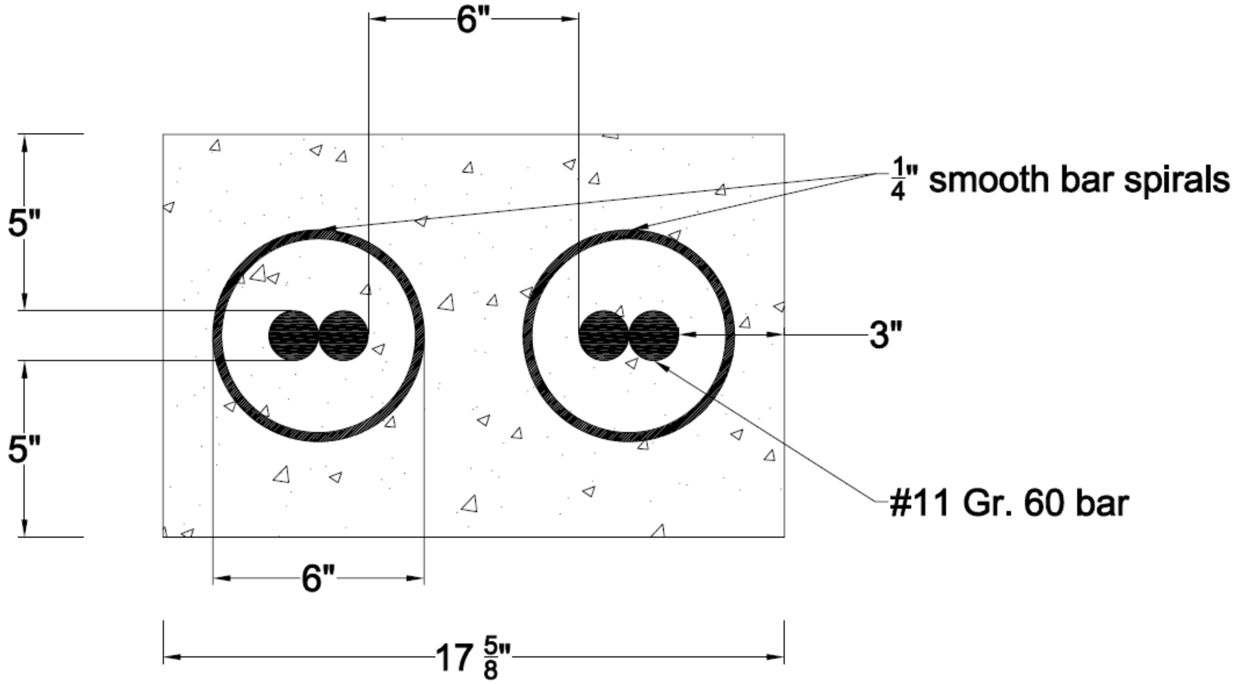

Figure 2-18: Series-Three specimen cross-section

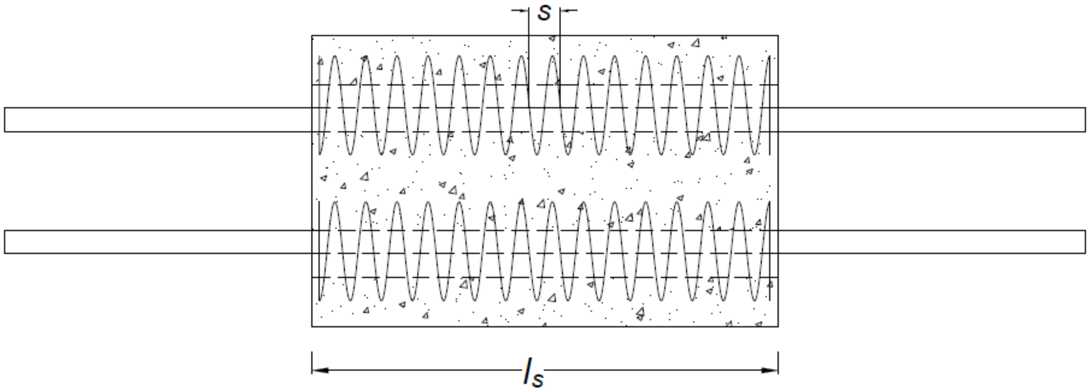

Figure 2-19: Series-Three plan view

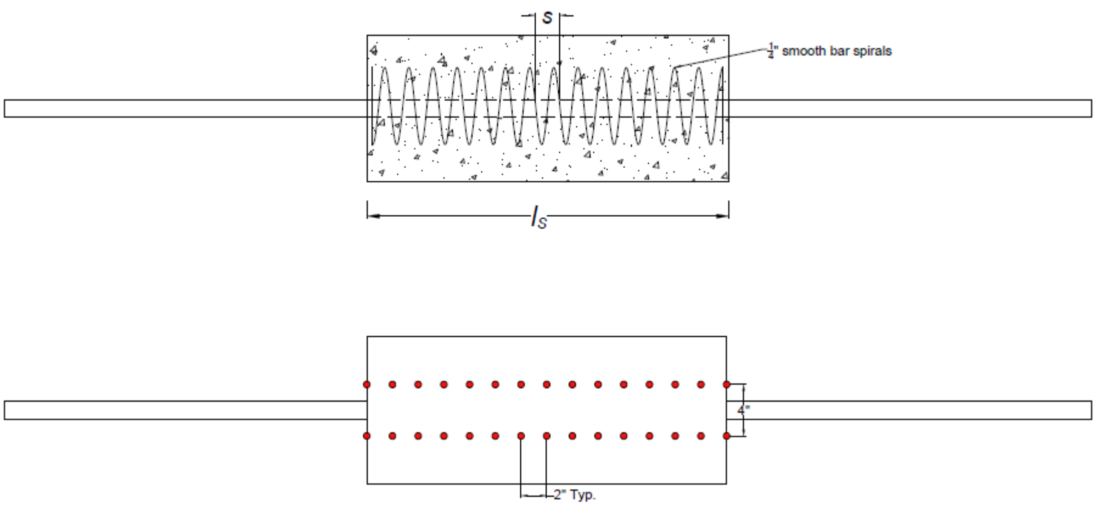

Figure 2-20: Series-Three elevation view and target layout

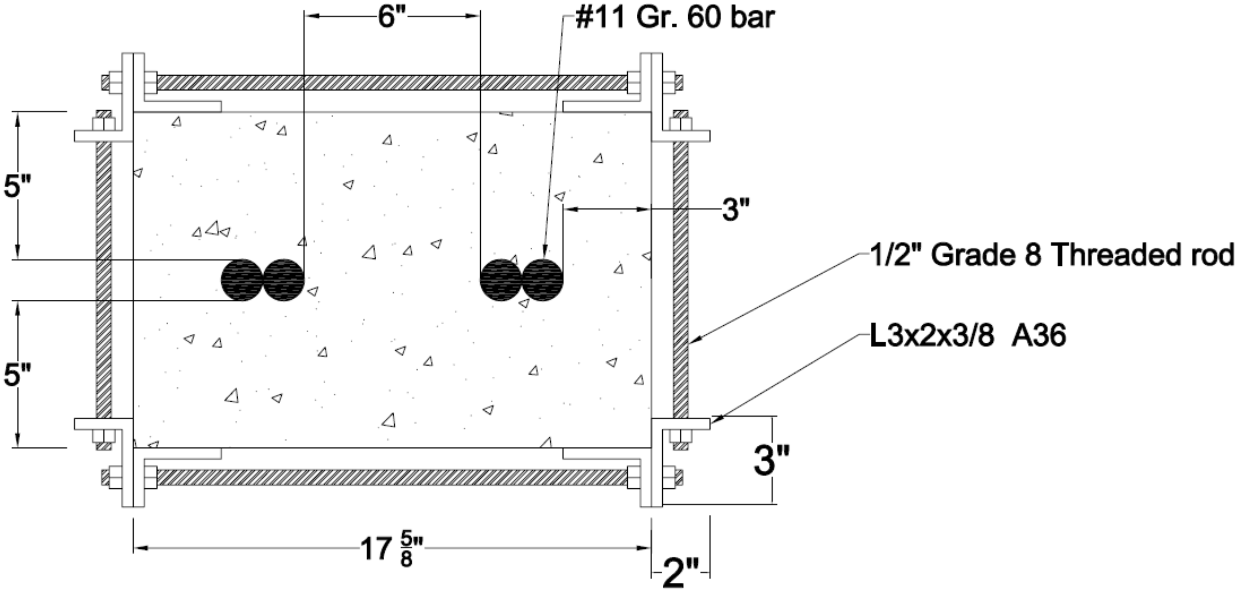

Figure 2-21: Series-Four specimen cross-section with post-tensioned transverse reinforcement installed

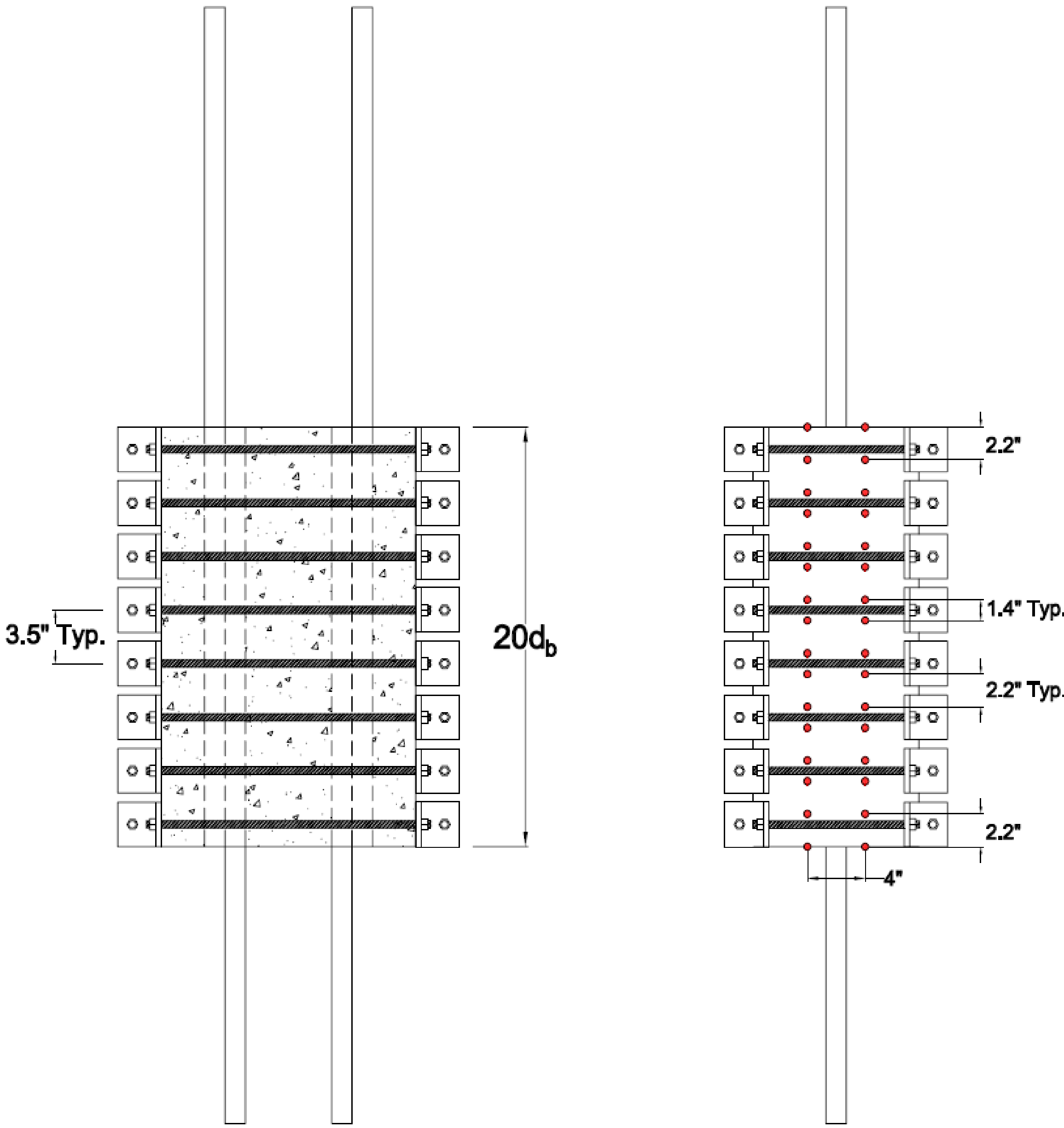

Figure 2-22: Series Four elevation view and target layout with post-tensioned transverse reinforcement spaced at 3.5 in.

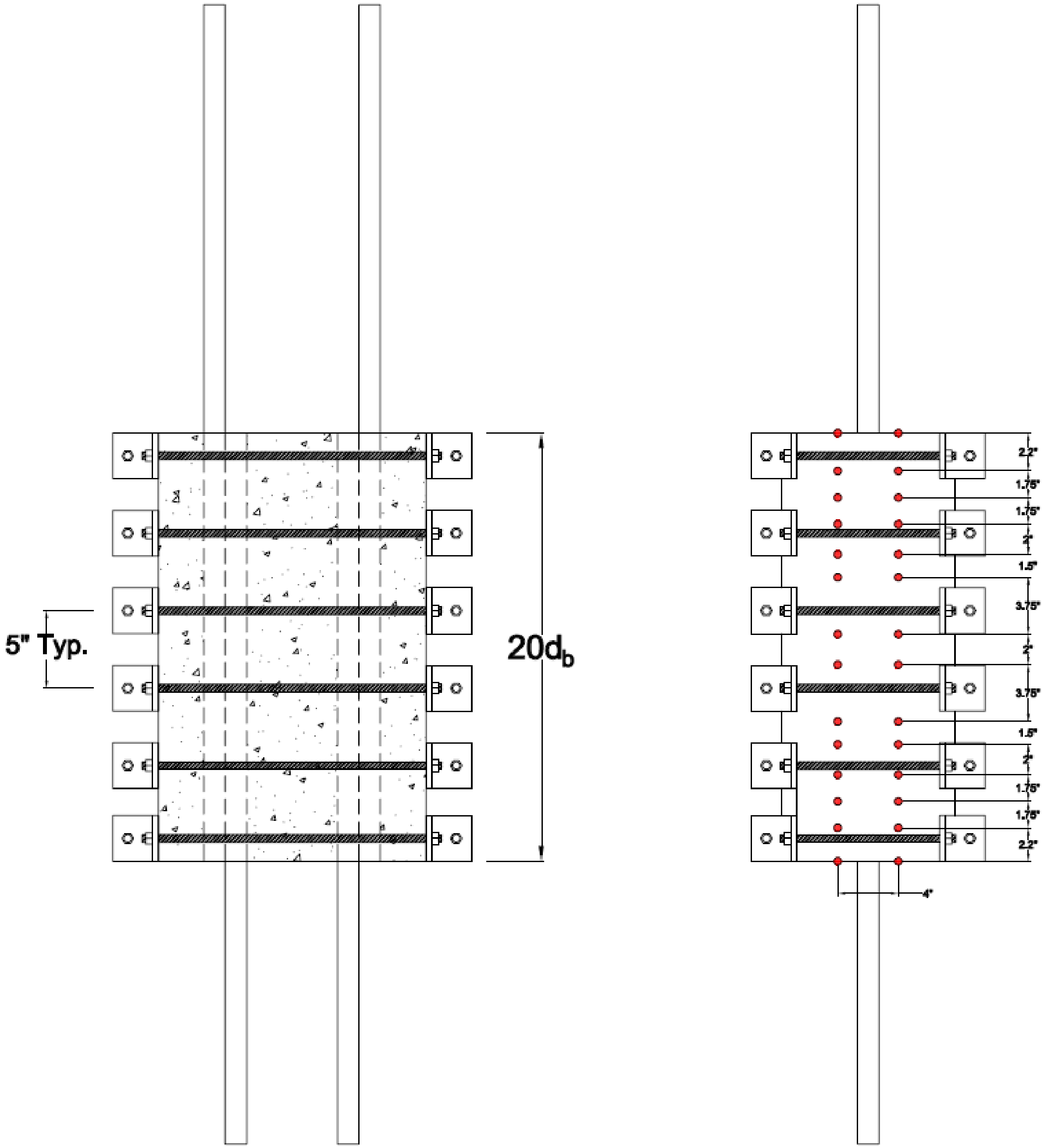

Figure 2-23: Series Four elevation view and target layout with post-tensioned transverse reinforcement spaced at 5 in.

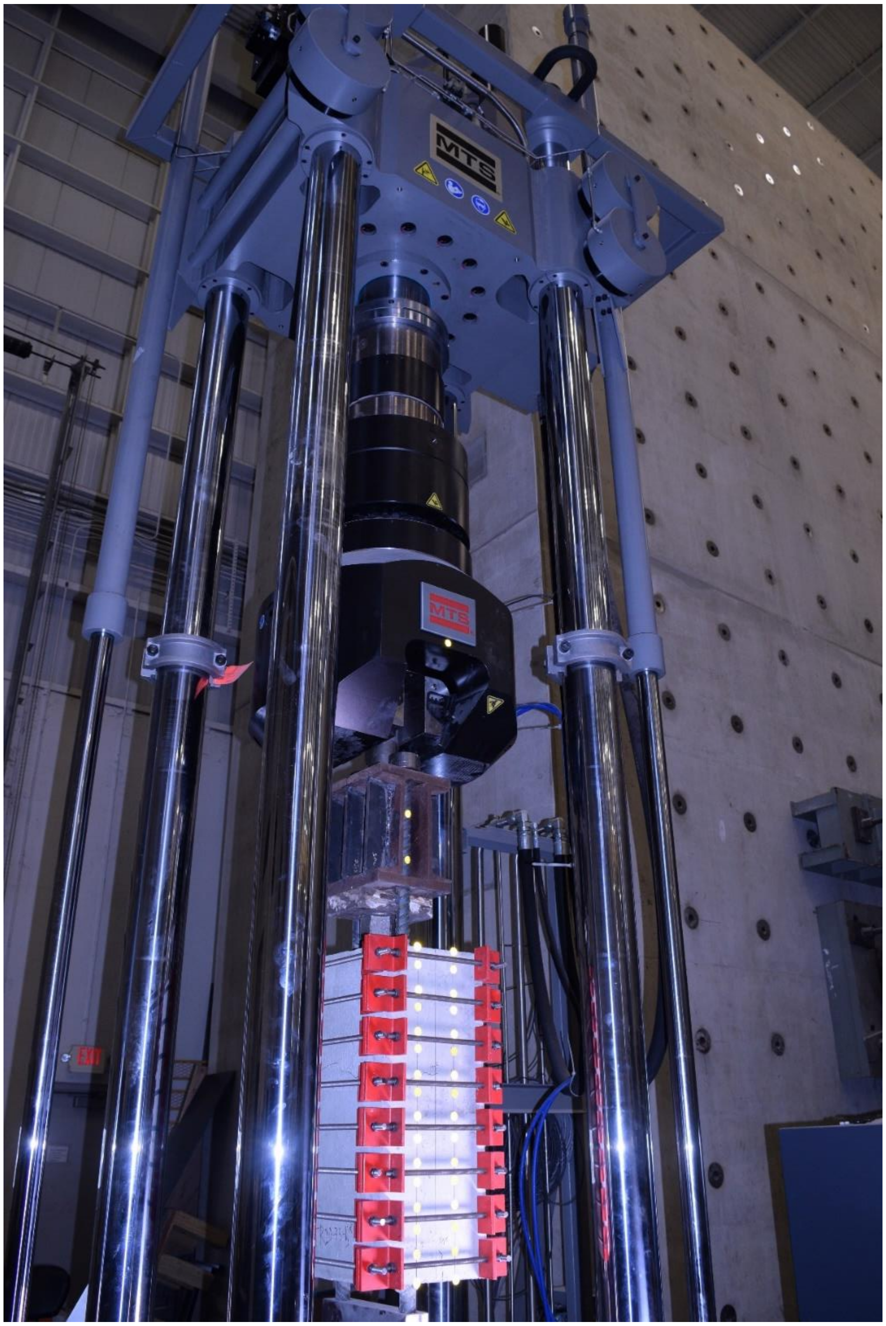

Figure 2-24: Series-Four testing setup.

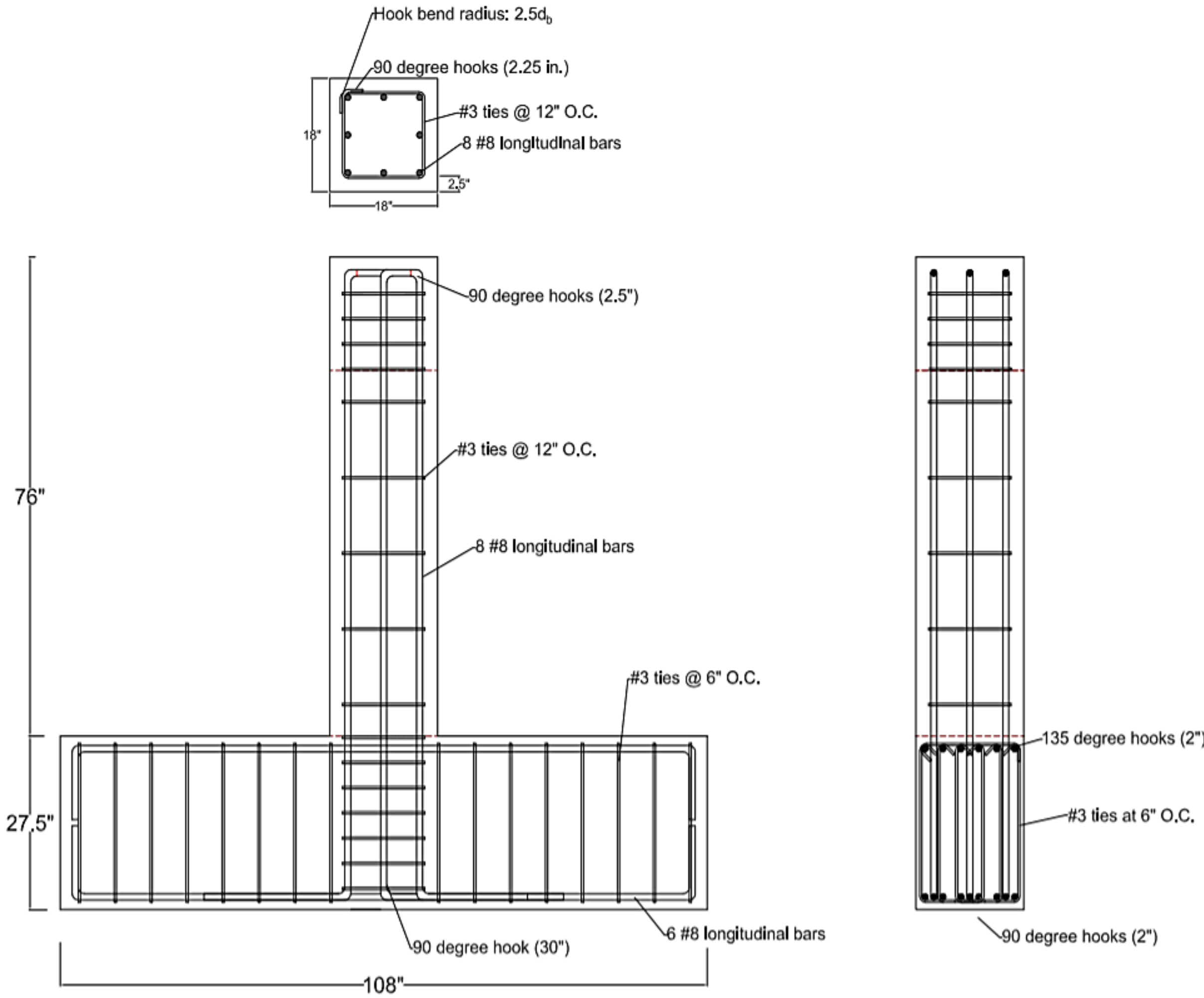

Figure 2-25: Series-Five column reinforcement layout

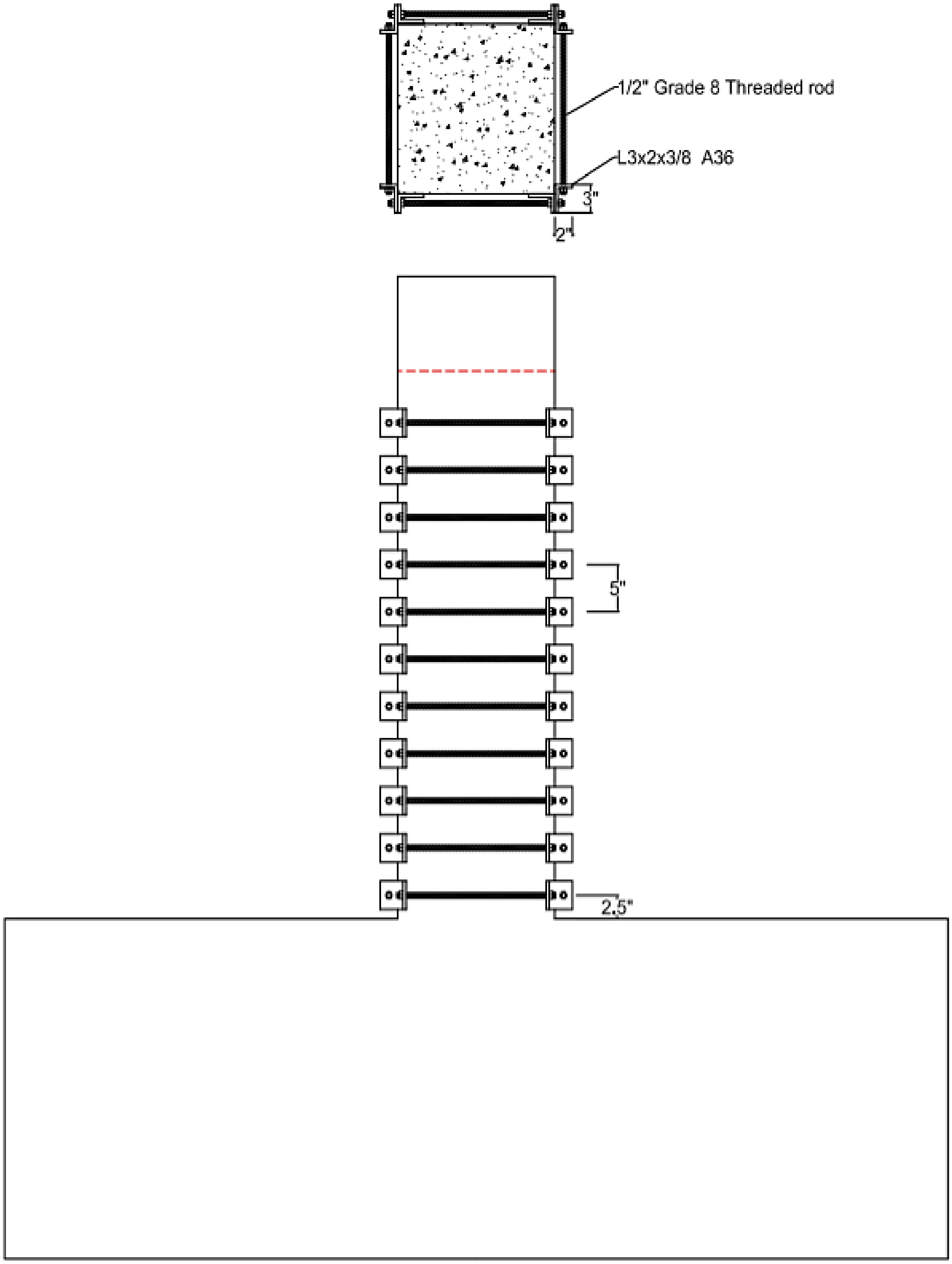

Figure 2-26: Series-Five column post-tensioned clamp layout (specimen C1)

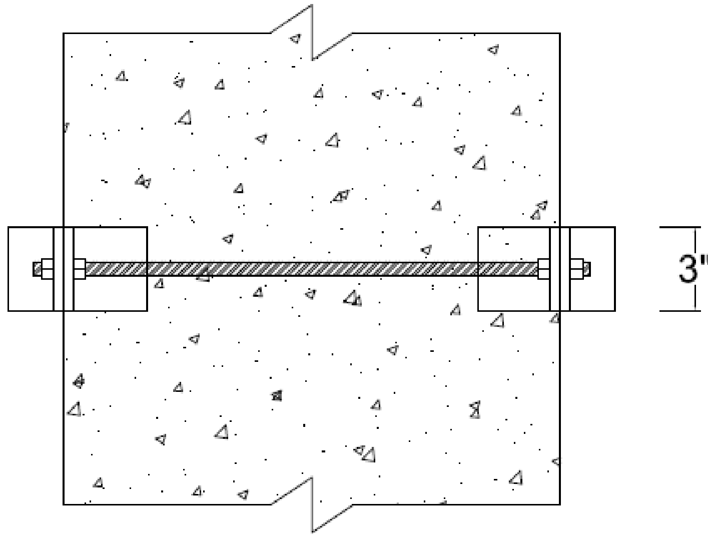

Figure 2-27: Series-Five plan view with post-tensioned transverse reinforcement

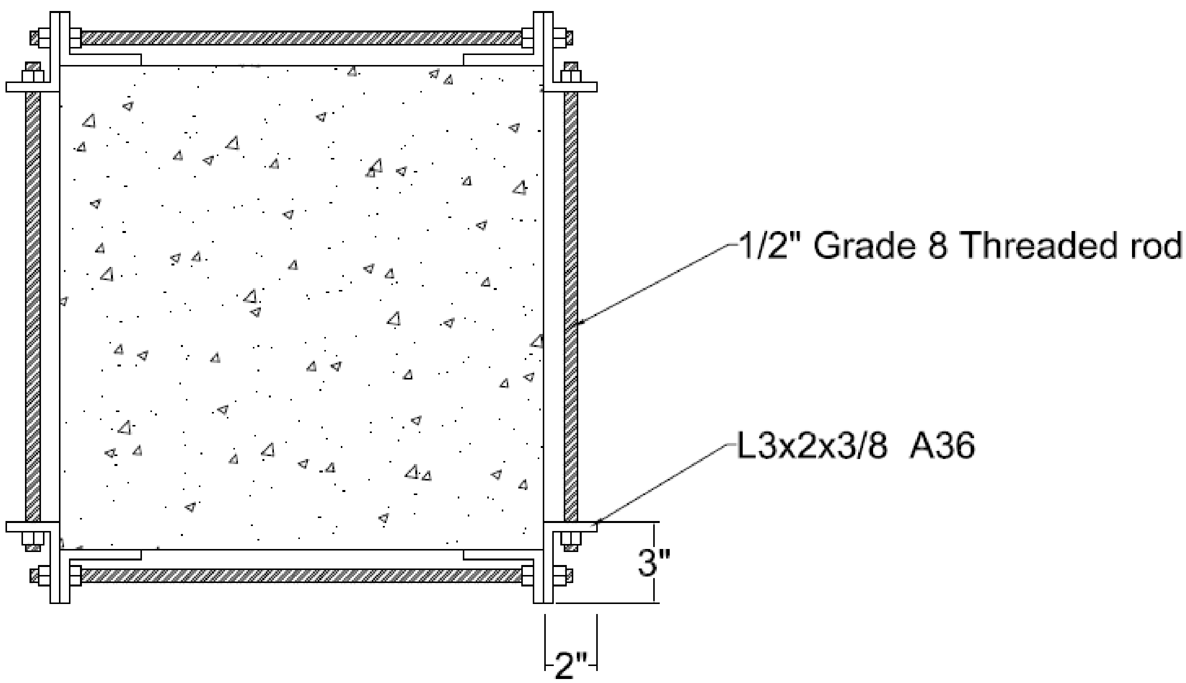

Figure 2-28: Series-Five elevation view of one post-tensioned transverse reinforcement tie

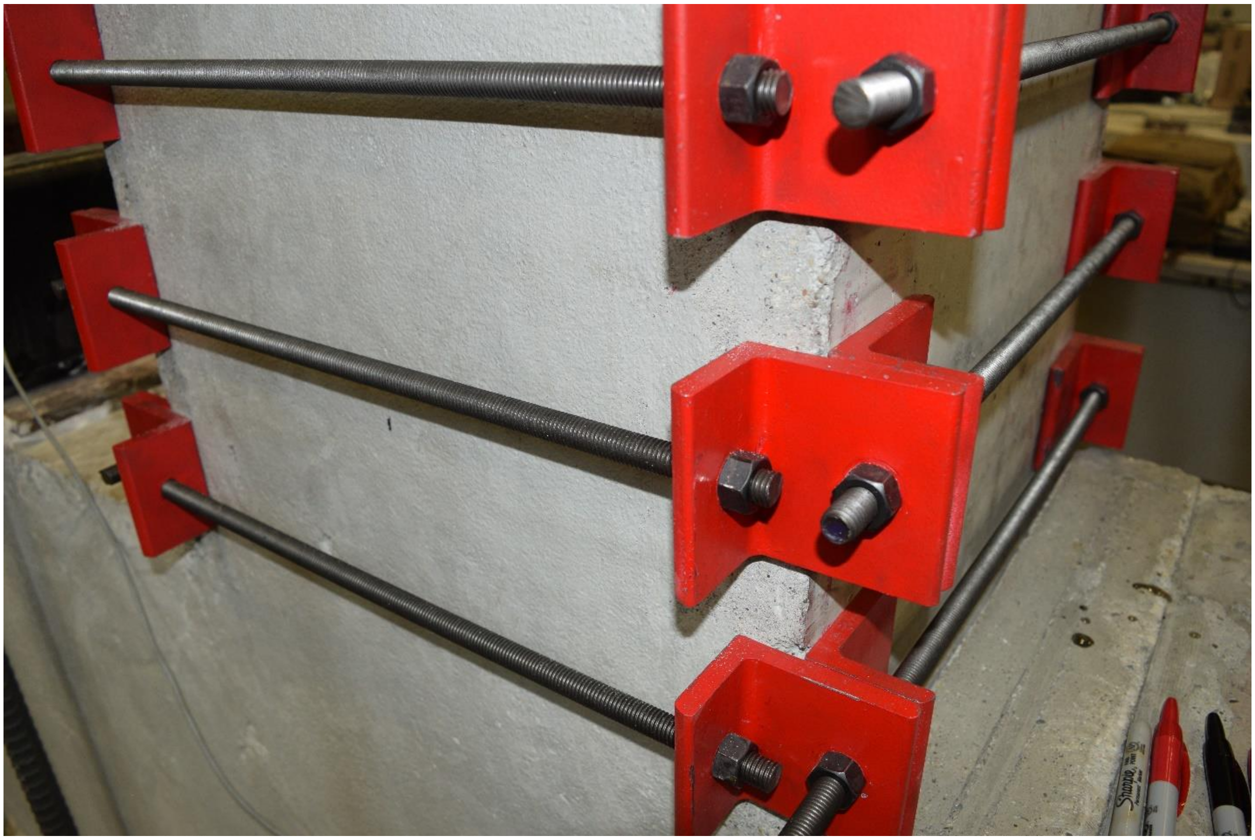

Figure 2-29: Specimen C1 installed with post-tensioned transverse reinforcement

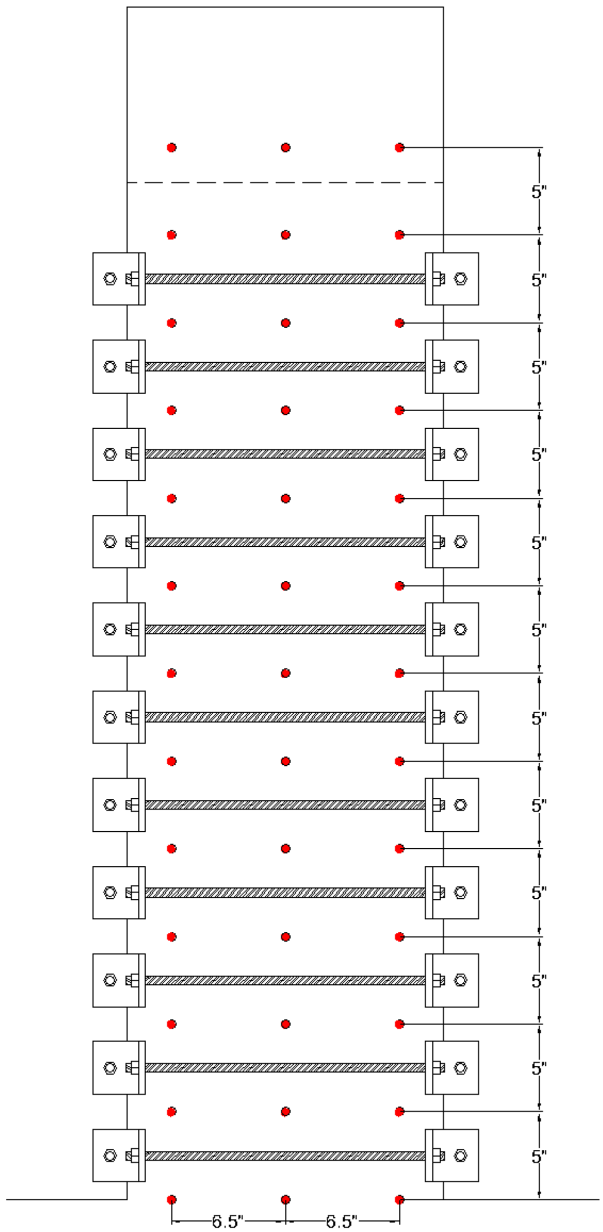

Figure 2-30: Specimen C1 elevation view and target layout

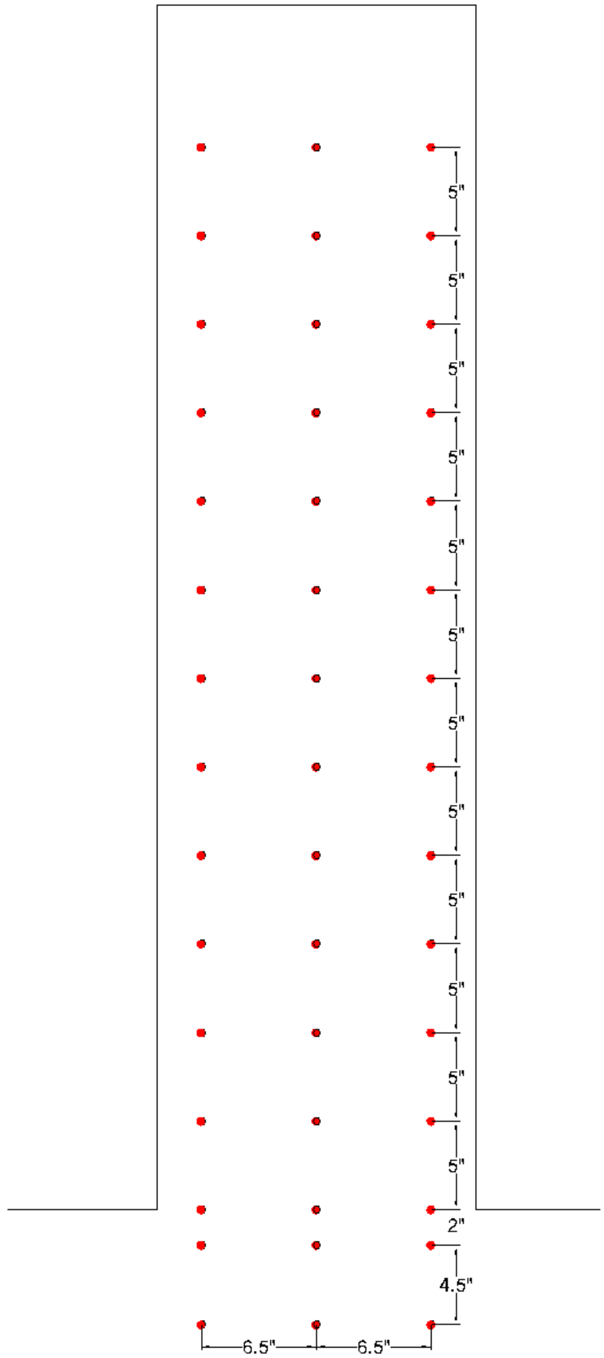

Figure 2-31: Specimen C2 elevation view and target layout

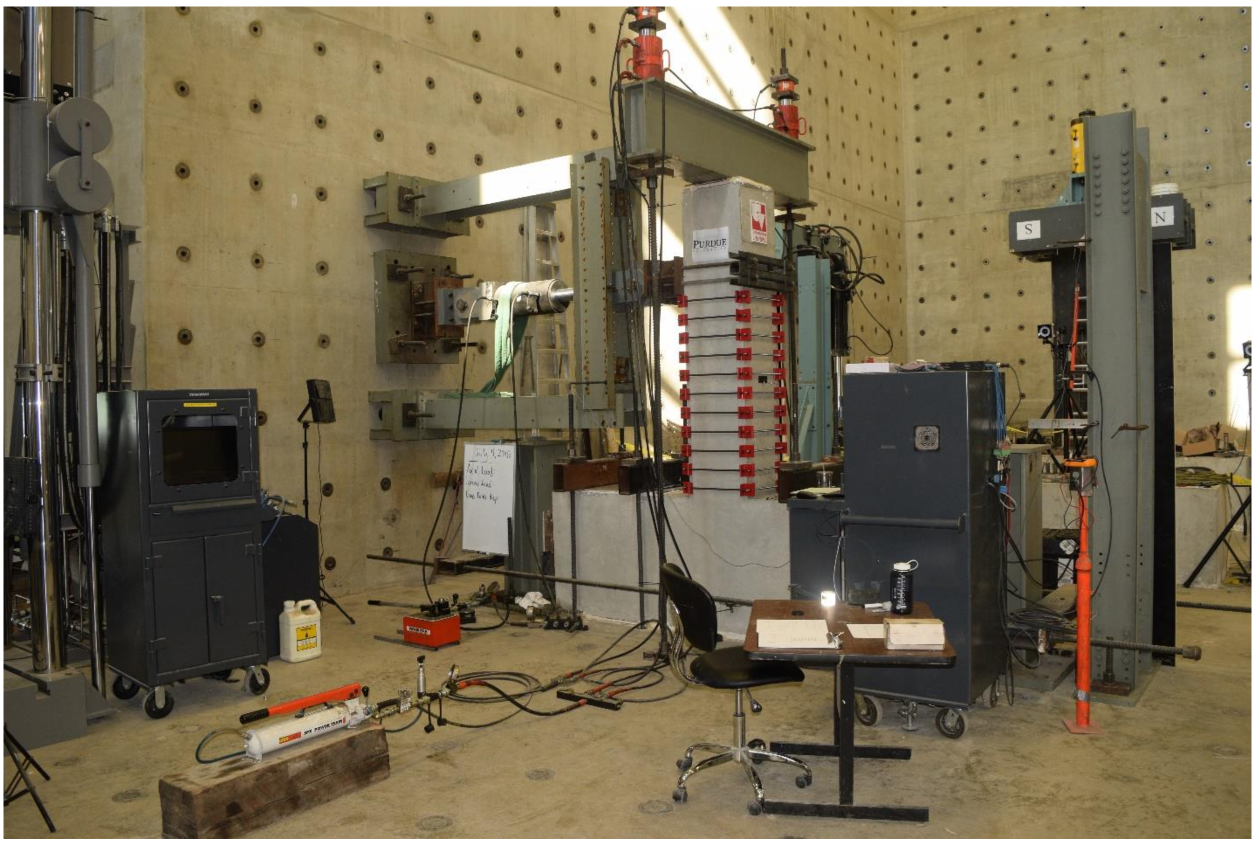

Figure 2-32: Specimen C1 testing setup.

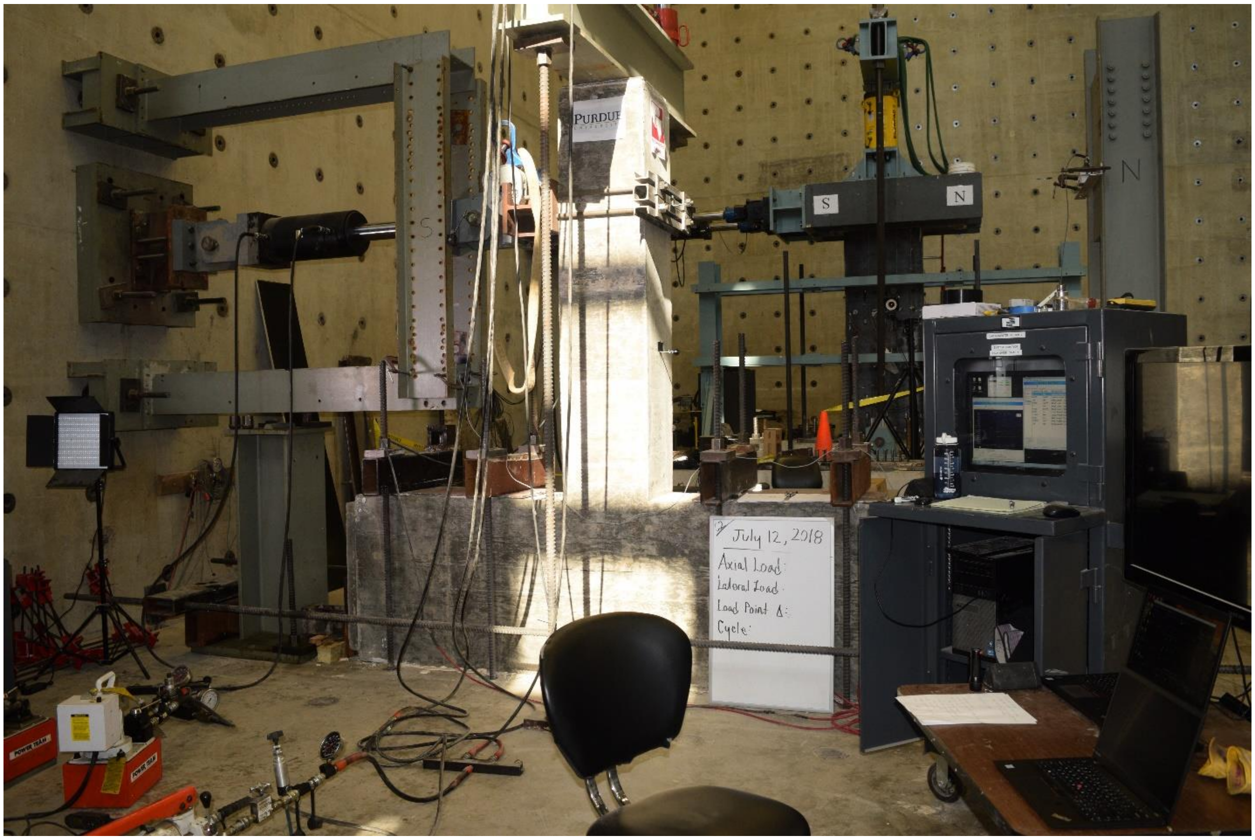

Figure 2-33: Specimen C2 testing setup.

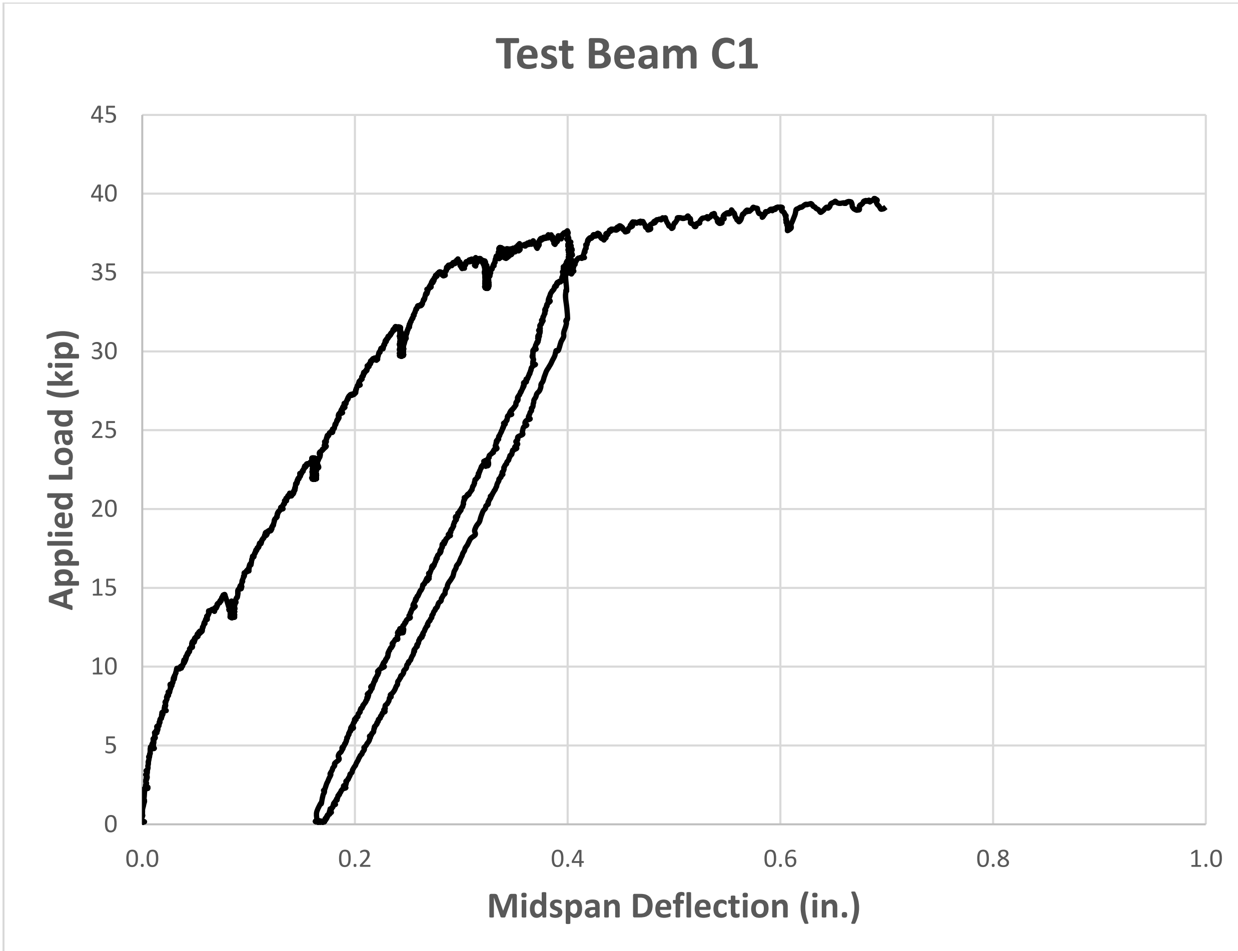

Figure 3-1: Load vs. midspan deflection for specimen C1

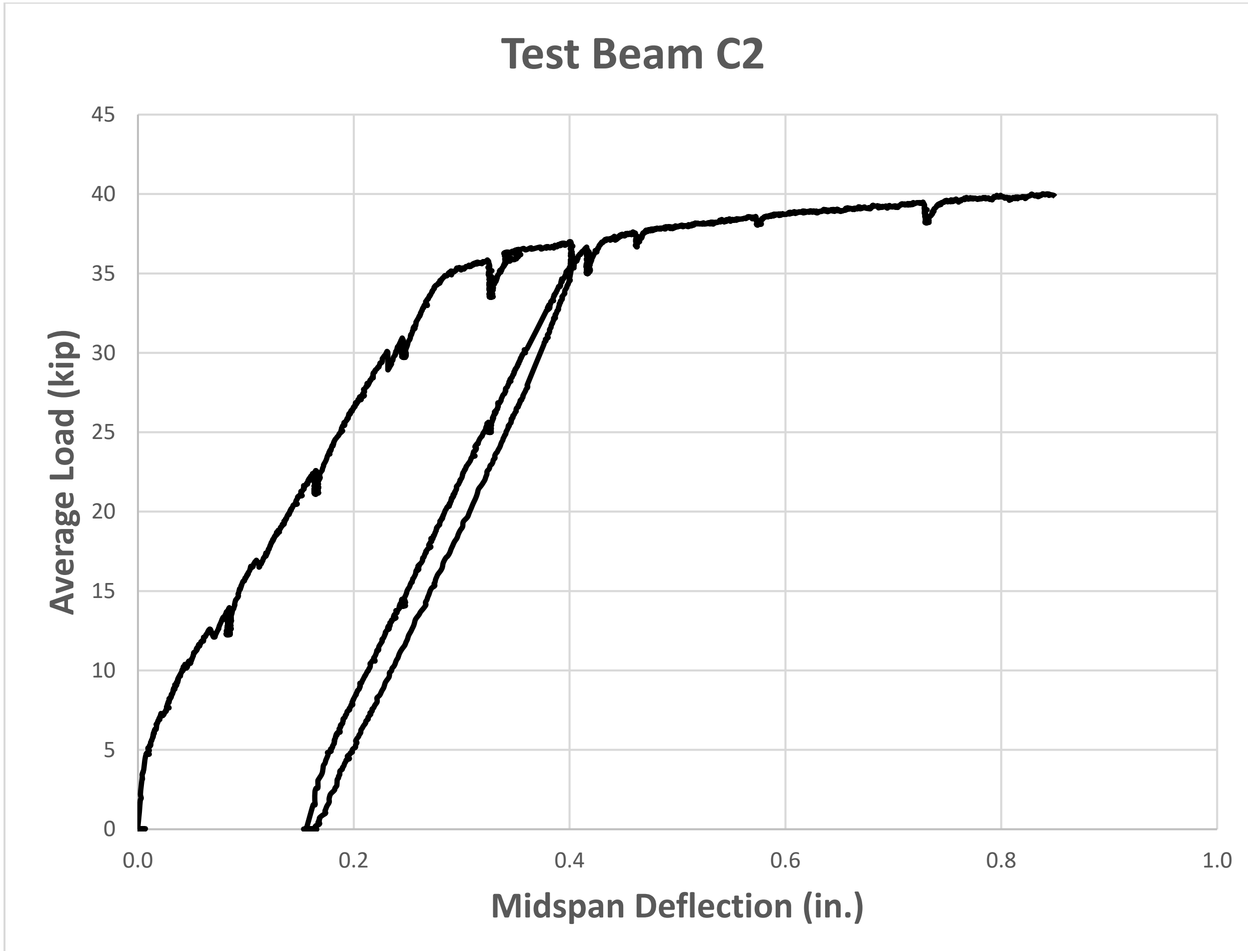

Figure 3-2: Load vs. midspan deflection for specimen C2

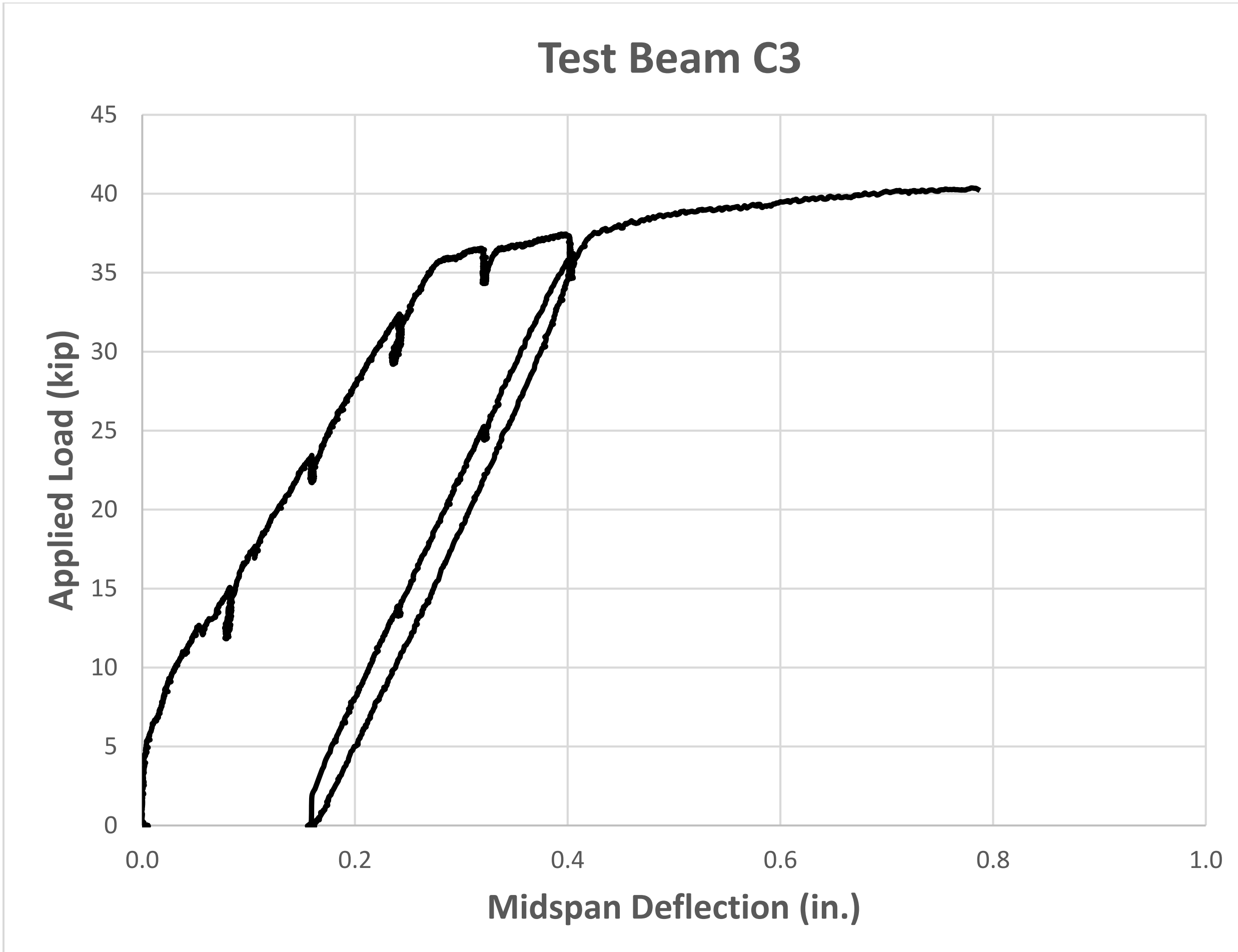

Figure 3-3: Load vs. midspan deflection for specimen C3

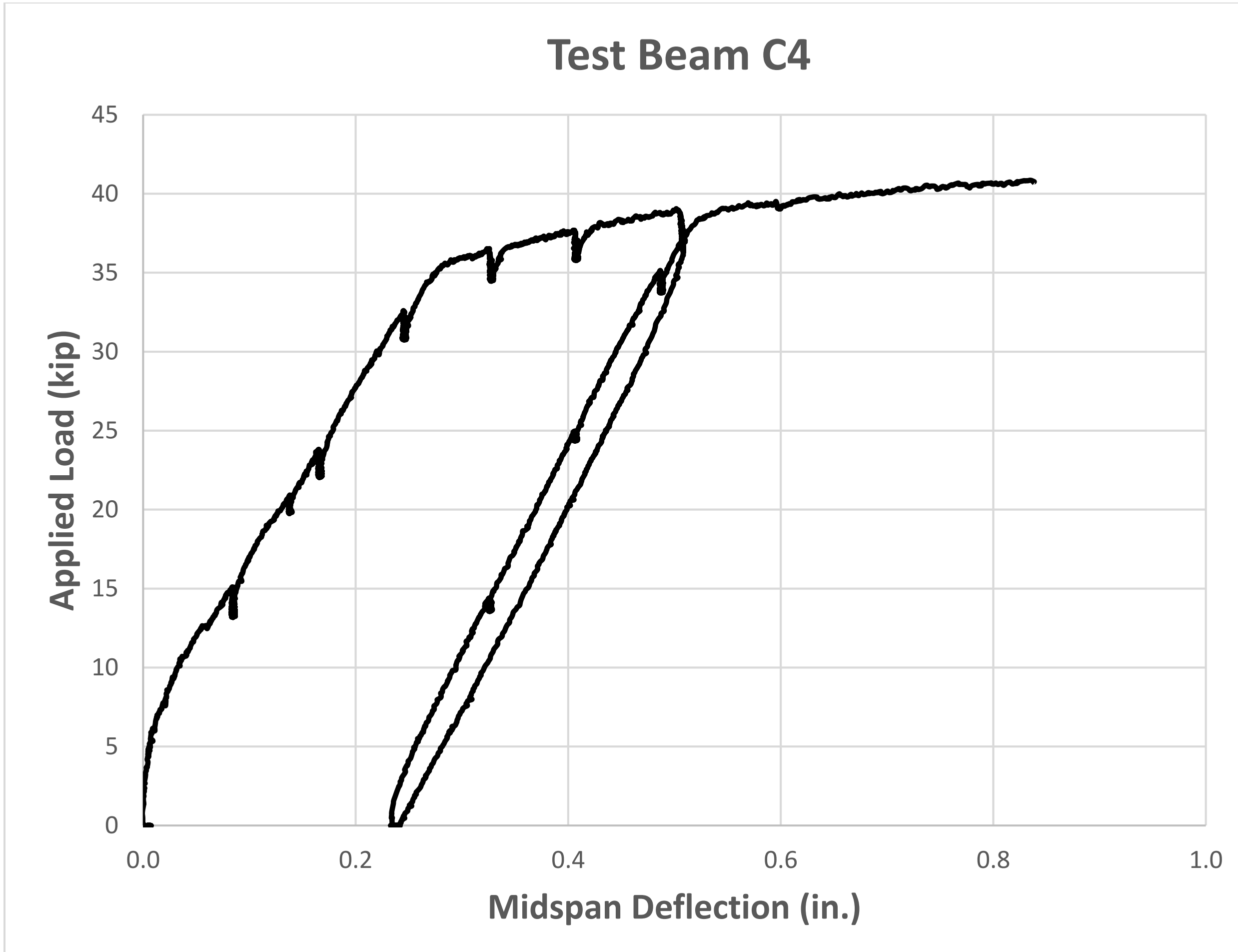

Figure 3-4: Load vs. midspan deflection for specimen C4

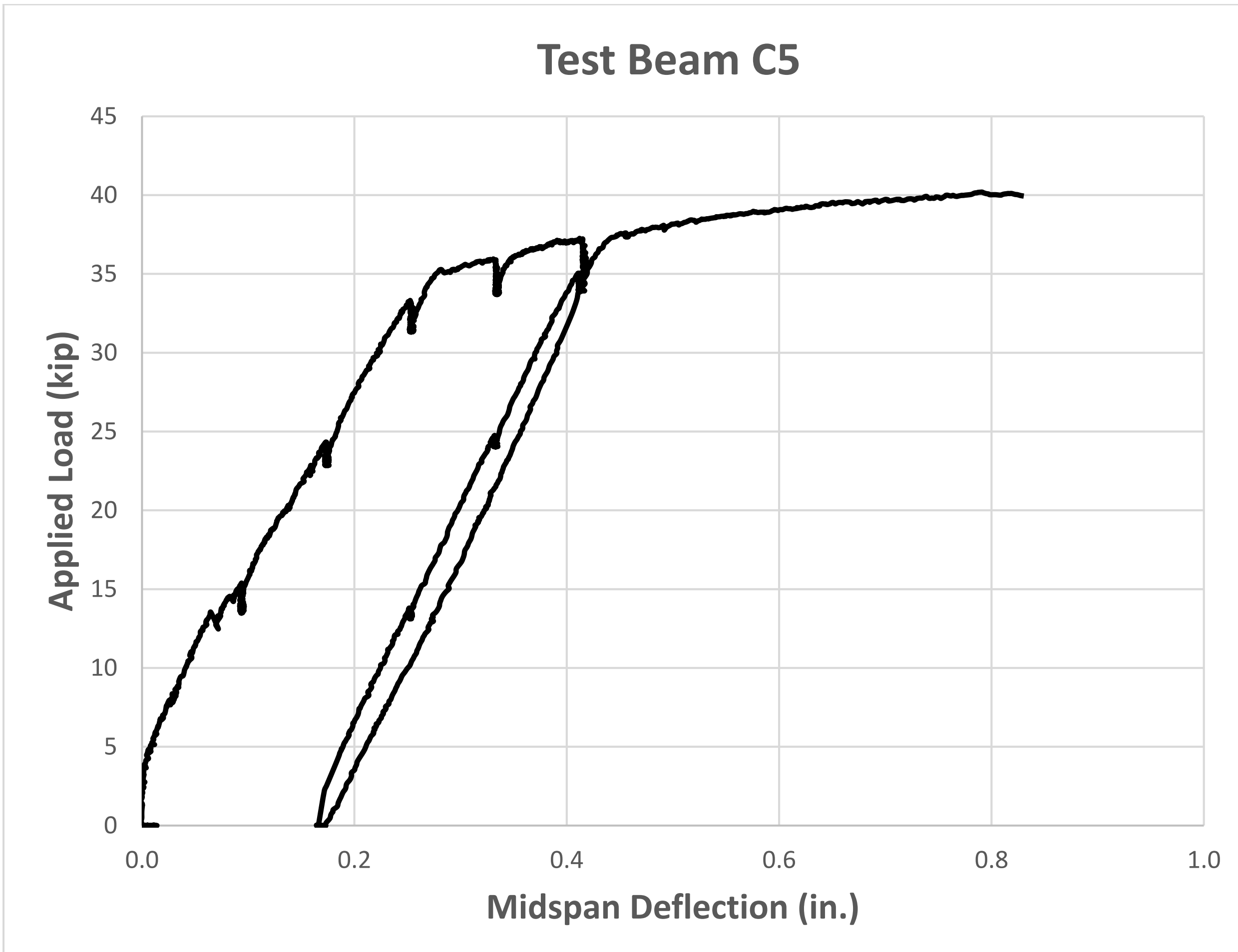

Figure 3-5: Load vs. midspan deflection for specimen C5

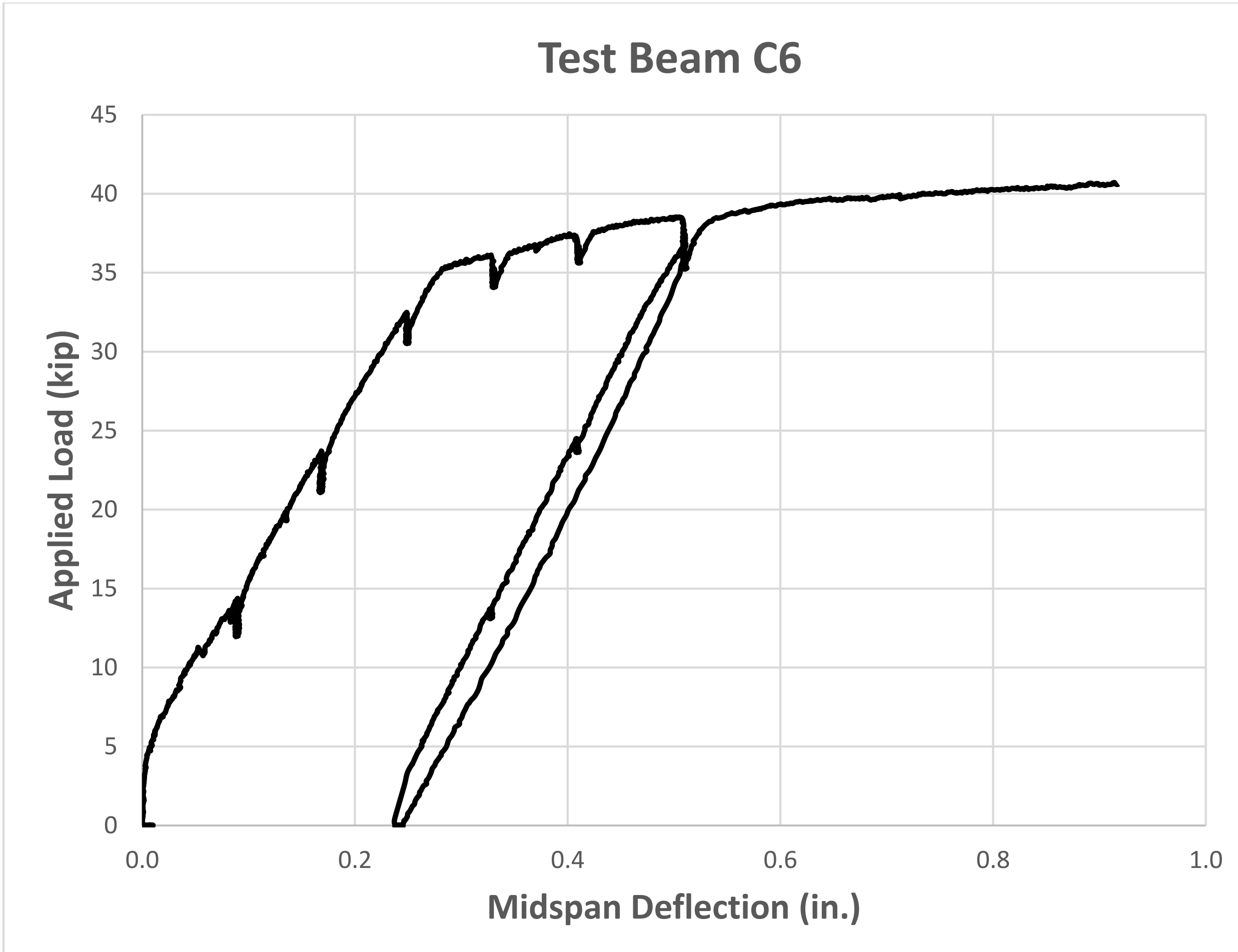

Figure 3-6: Load vs. midspan deflection for specimen C6

Figure 3-7: Crack pattern for specimen C1, South support (top) and North support (bottom) (Applied load at overhang = 37.5 kip, midspan deflection = 0.4 in.)

Figure 3-8: Crack pattern for specimen C2, South support (top) and North support (bottom) (Applied load at overhang = 37.1 kip, midspan deflection = 0.4 in.)

Figure 3-9: Crack pattern for specimen C3, South support (top) and North support (bottom) (Applied load at overhang = 37.5 kip, midspan deflection = 0.4 in.)

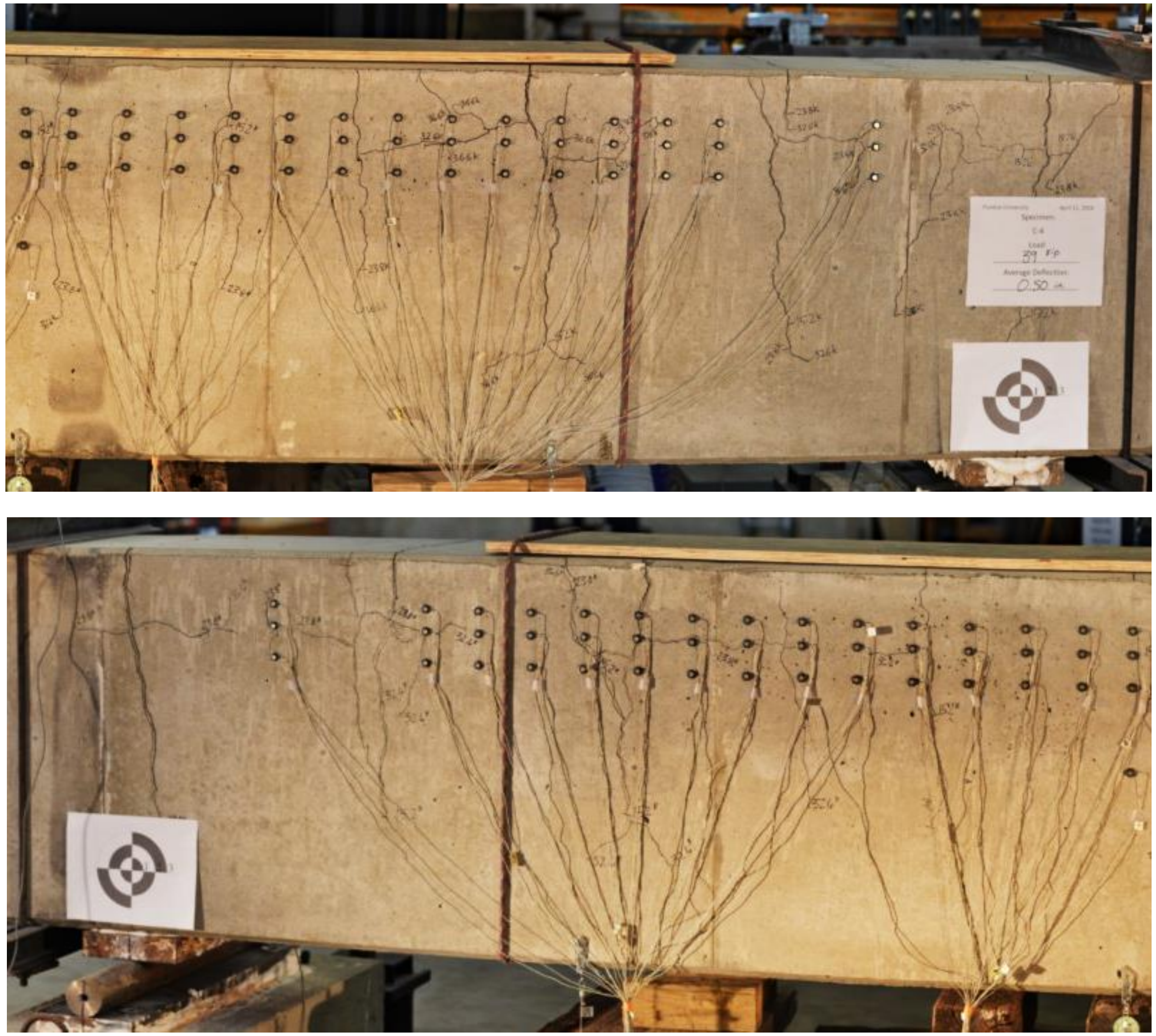

Figure 3-10: Crack pattern for specimen C4, South support (top) and North support (bottom) (Applied load at overhang = 39 kip, midspan deflection = 0.5 in.)

Figure 3-11: Crack pattern for specimen C5, South support (top) and North support (bottom) (Applied load at overhang = 37.2 kip, midspan deflection = 0.4 in.)

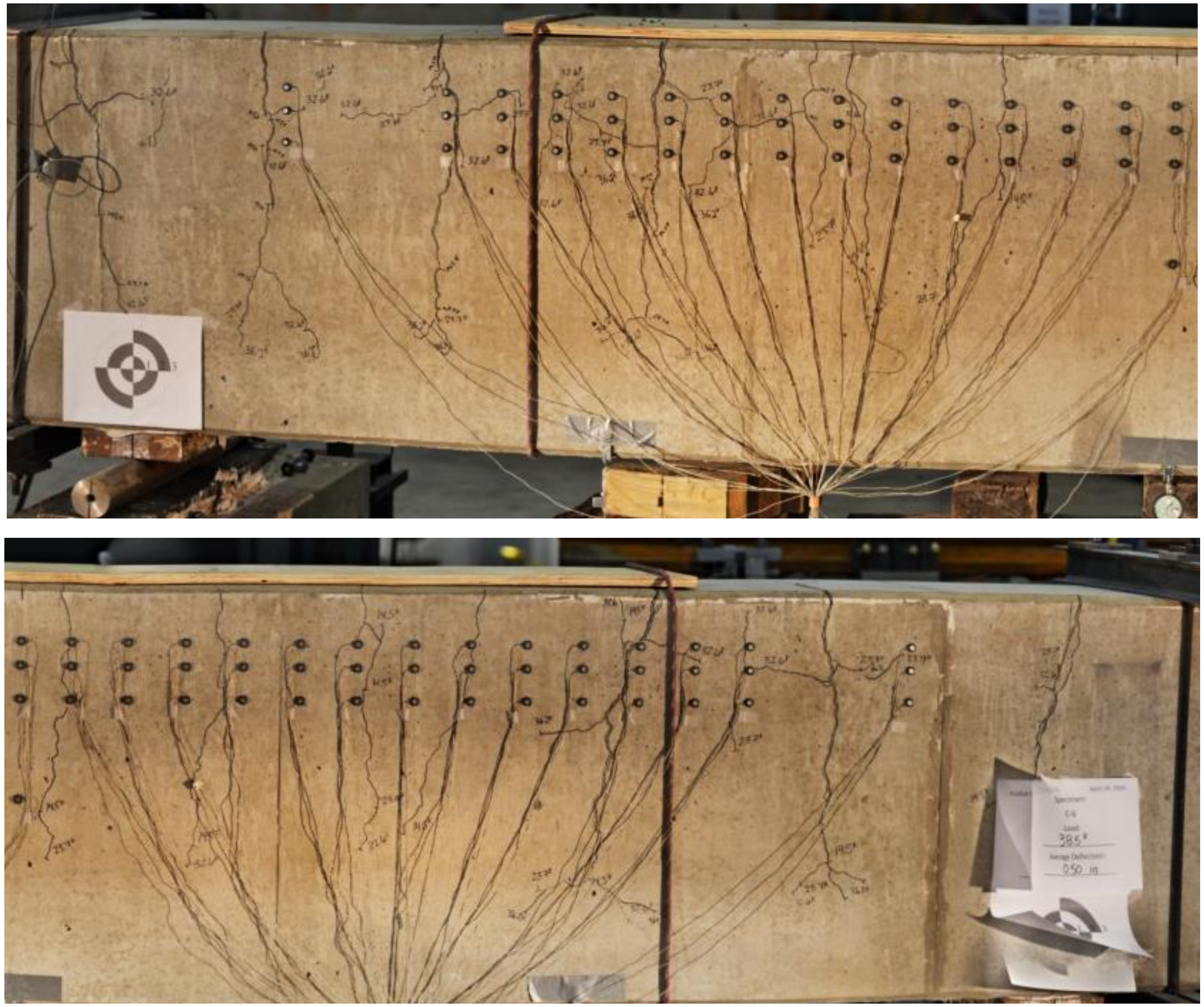

Figure 3-12: Crack pattern for specimen C6, South support (top) and North support (bottom) (Applied load at overhang = 38.5 kip, midspan deflection = 0.5 in.)

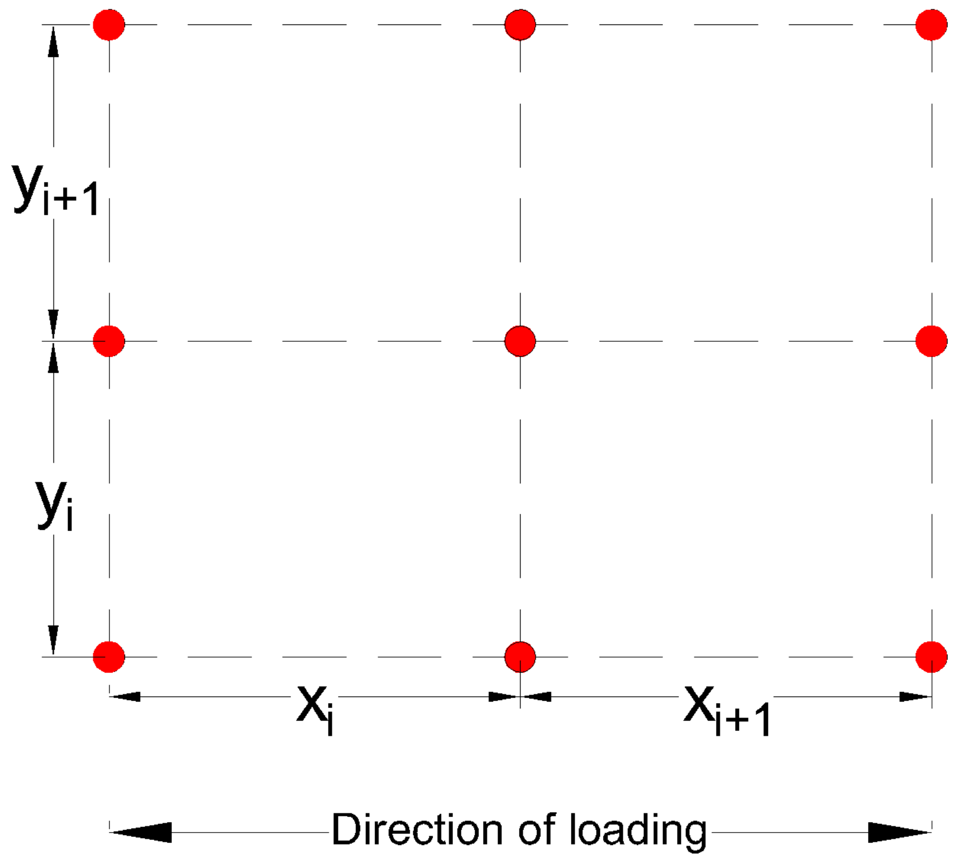

Figure 3-13: Grid station used for calculating horizontal and vertical deformations for Test Series One, Two, and Three

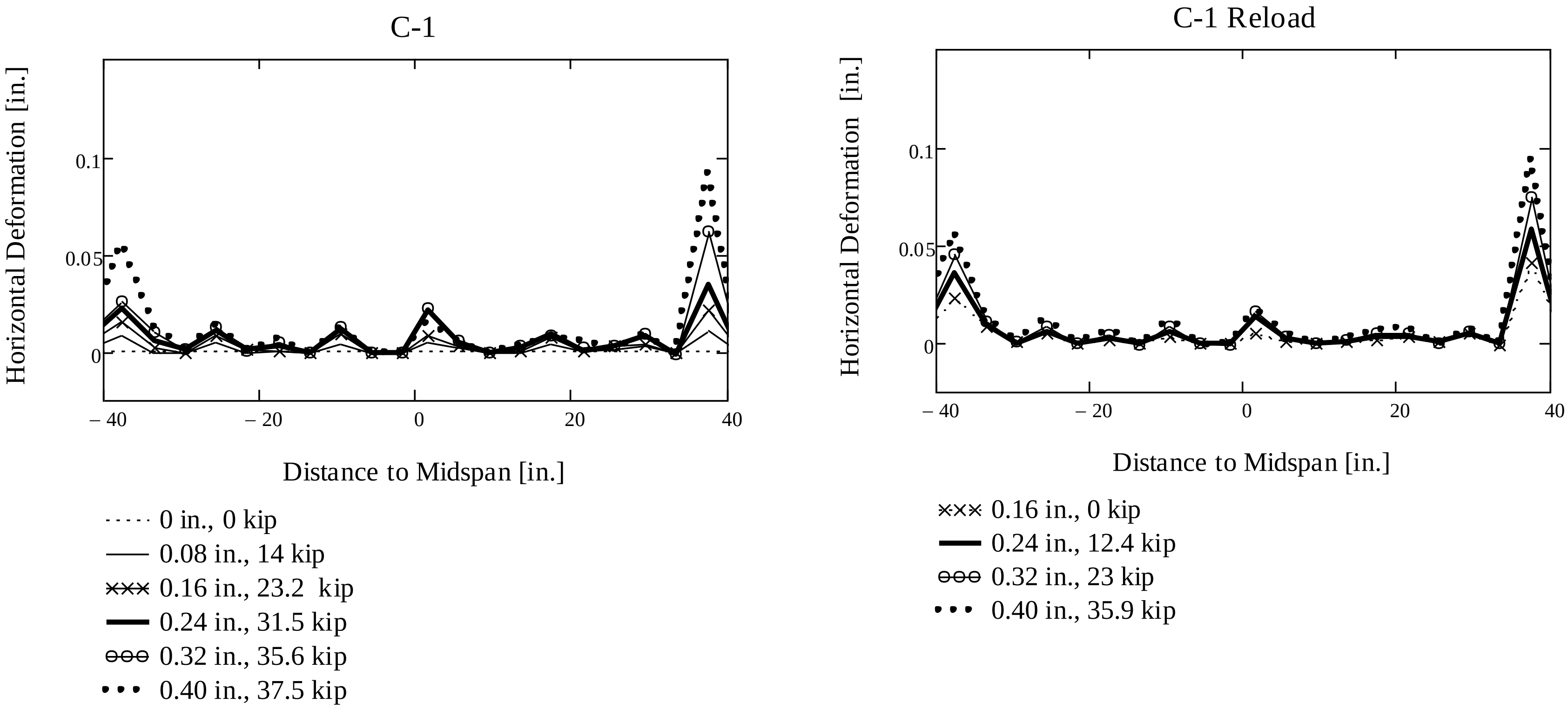

Figure 3-14: Horizontal deformations of concrete surface along splice length of specimen C1, initial loading and reload (data series are labeled using midspan deflection and average load applied at ends)

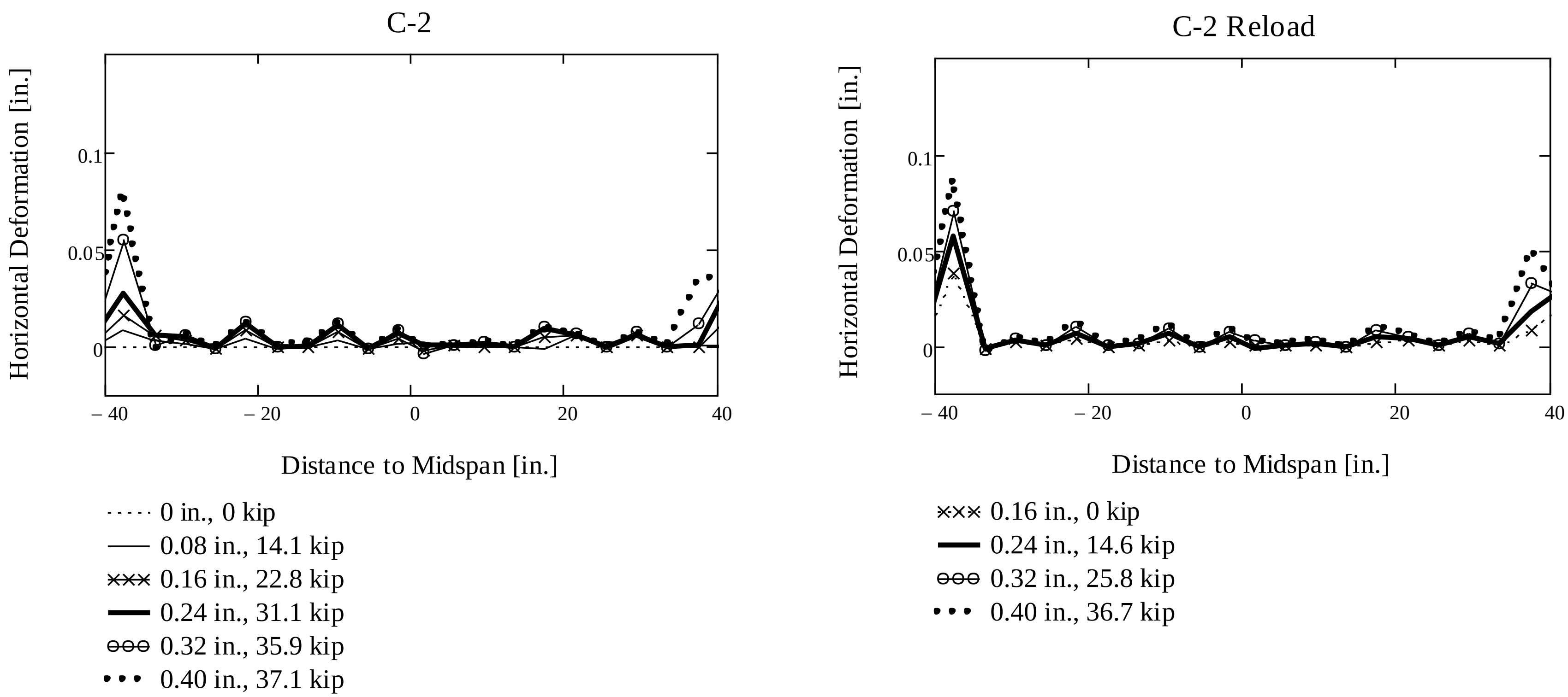

Figure 3-15: Horizontal deformations of concrete surface along splice length of specimen C2, initial loading and reload (data series are labeled using midspan deflection and average load applied at ends)

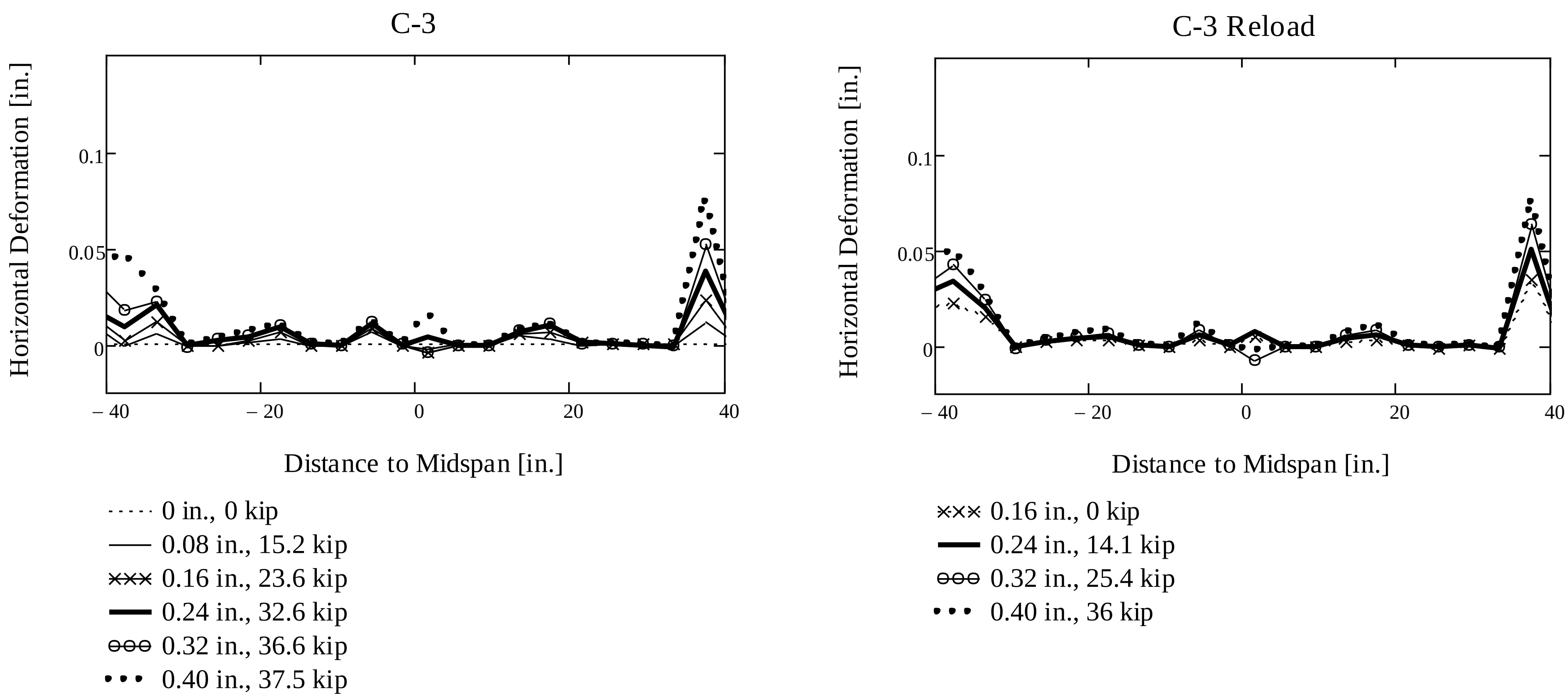

Figure 3-16: Horizontal deformations of concrete surface along splice length of specimen C3, initial loading and reload (data series are labeled using midspan deflection and average load applied at ends)

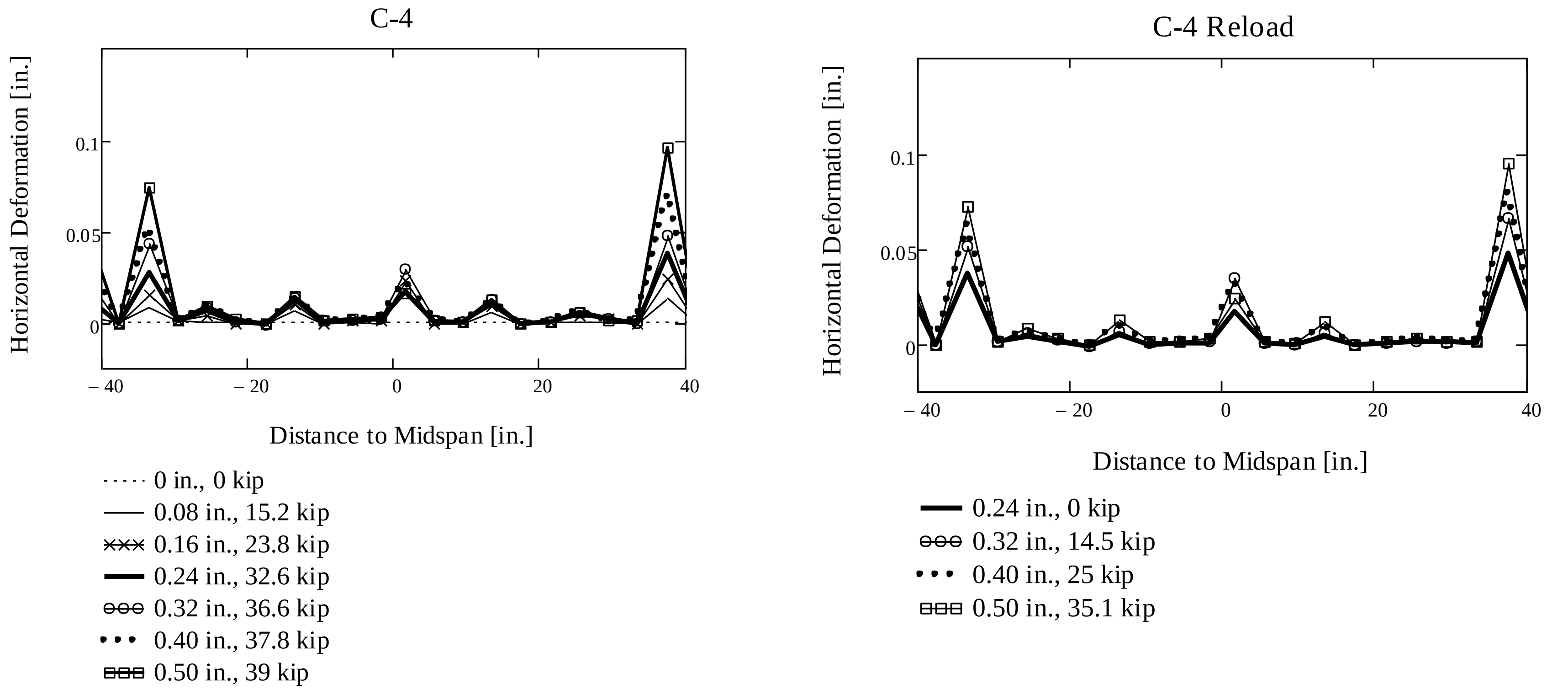

Figure 3-17: Horizontal deformations of concrete surface along splice length of specimen C4, initial loading and reload (data series are labeled using midspan deflection and average load applied at ends)

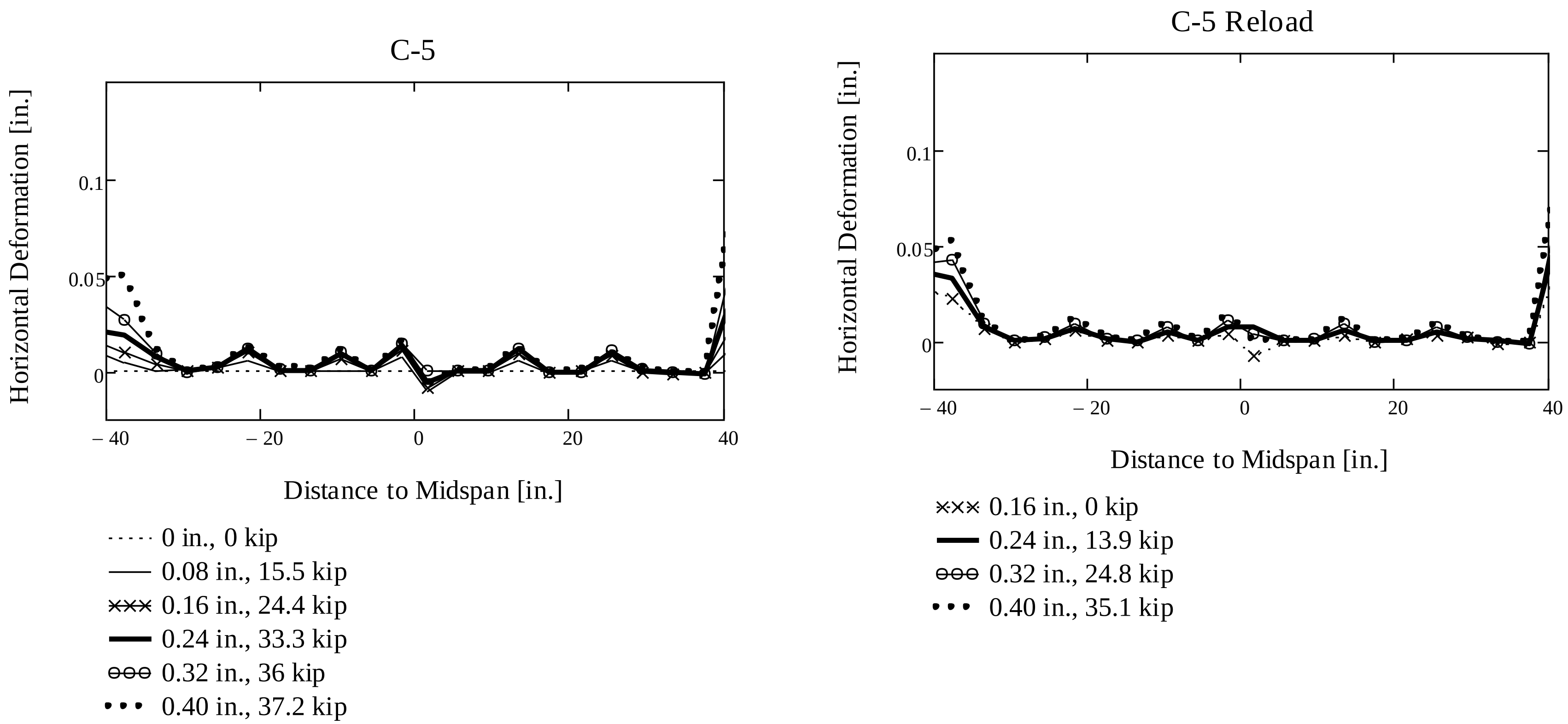

Figure 3-18: Horizontal deformations of concrete surface along splice length of specimen C5, initial loading and reload (data series are labeled using midspan deflection and average load applied at ends)

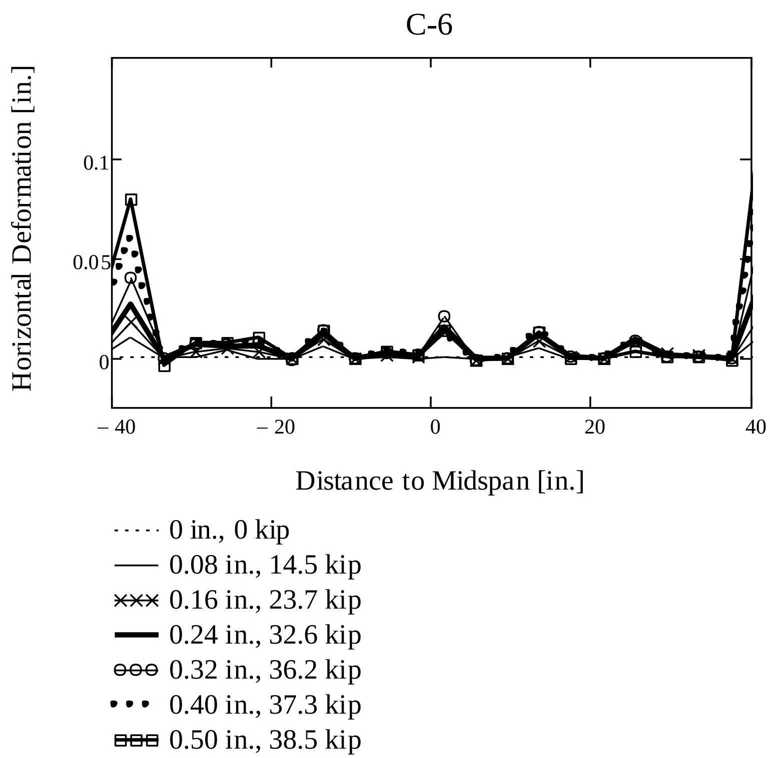

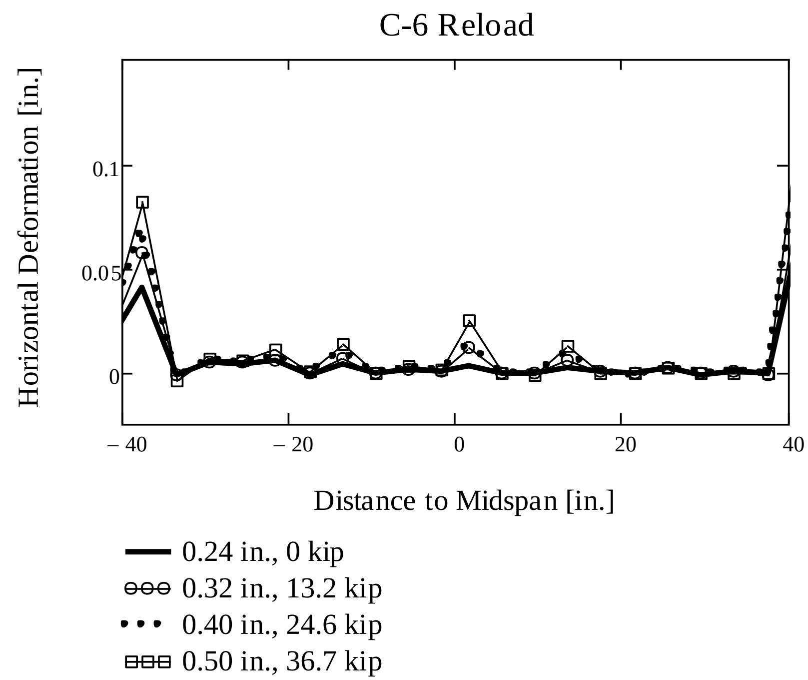

Figure 3-19: Horizontal deformations of concrete surface along splice length of specimen C6, initial loading and reload (data series are labeled using midspan deflection and average load applied at ends)

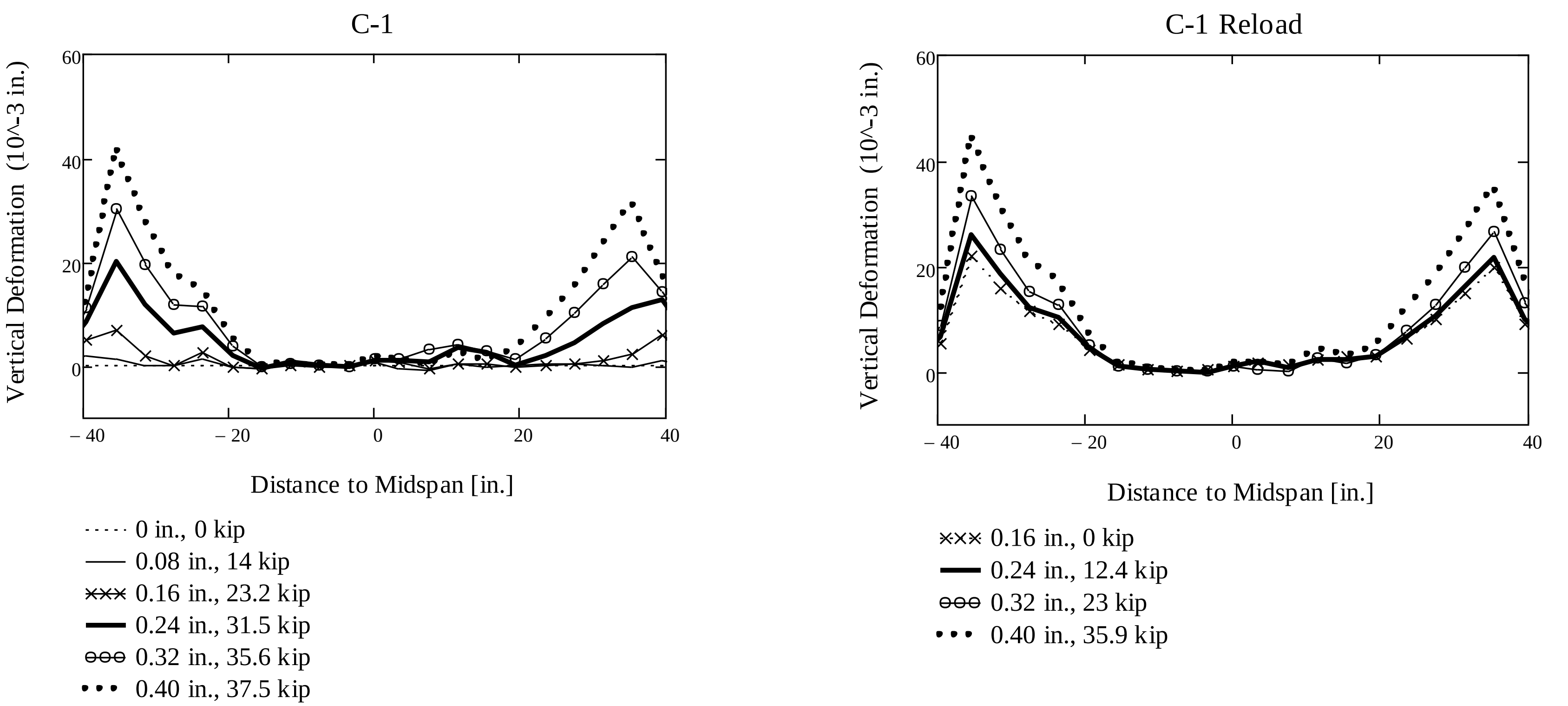

Figure 3-20: Vertical deformations of concrete surface along splice length of specimen C1, initial loading and reload (data series are labeled using midspan deflection and average load applied at ends)

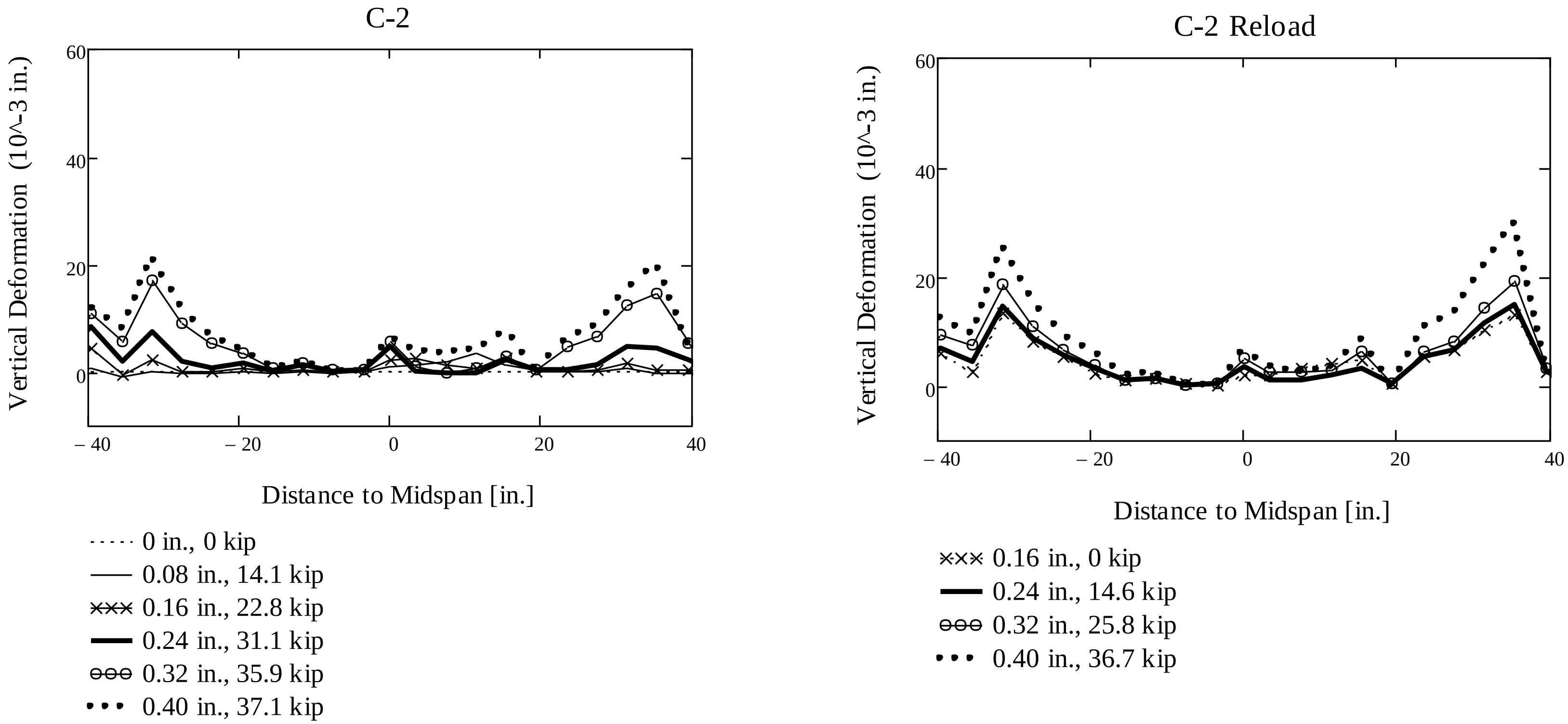

Figure 3-21: Vertical deformations of concrete surface along splice length of specimen C2, initial loading and reload (data series are labeled using midspan deflection and average load applied at ends)

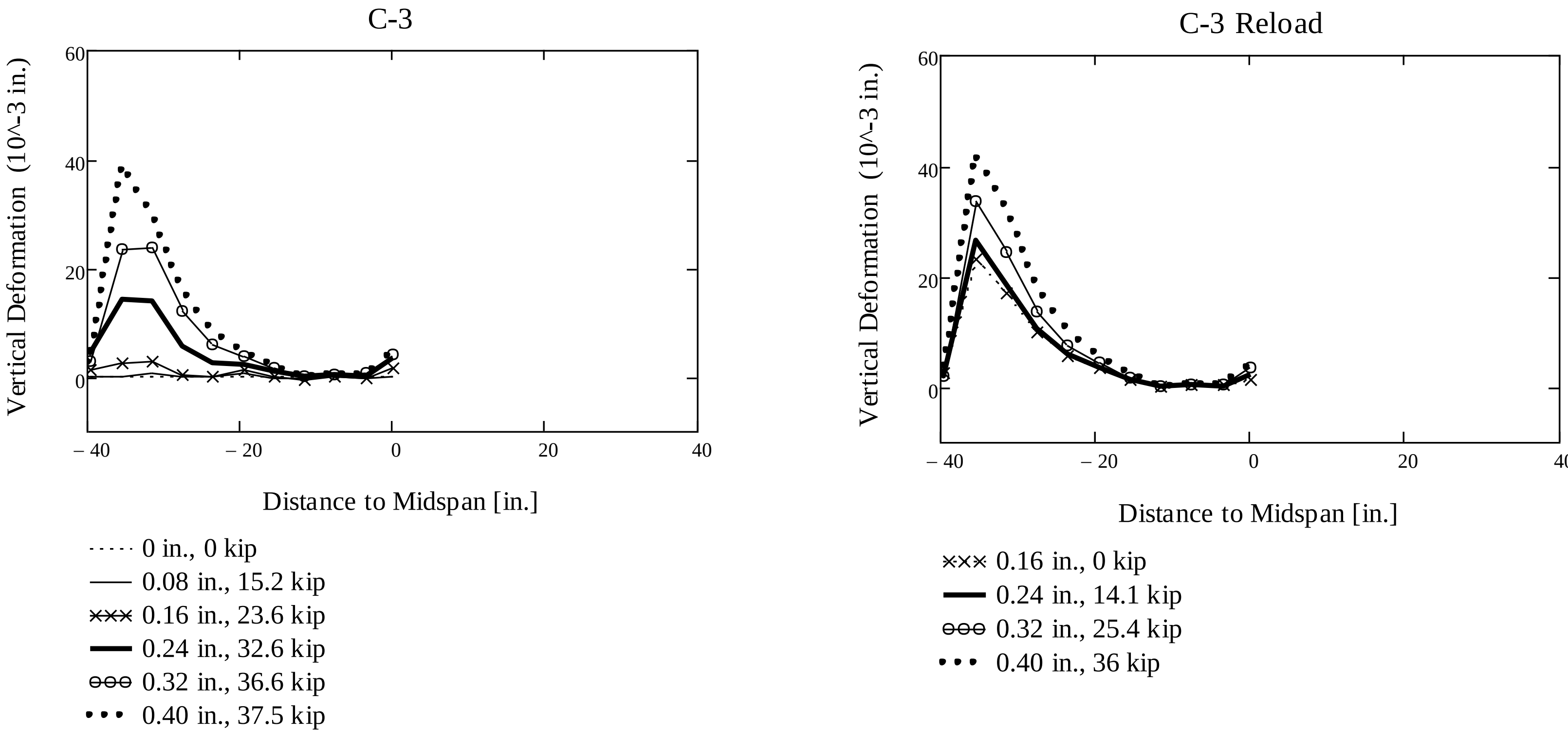

Figure 3-22: Vertical deformations of concrete surface along splice length of specimen C3, initial loading and reload (data series are labeled using midspan deflection and average load applied at ends)

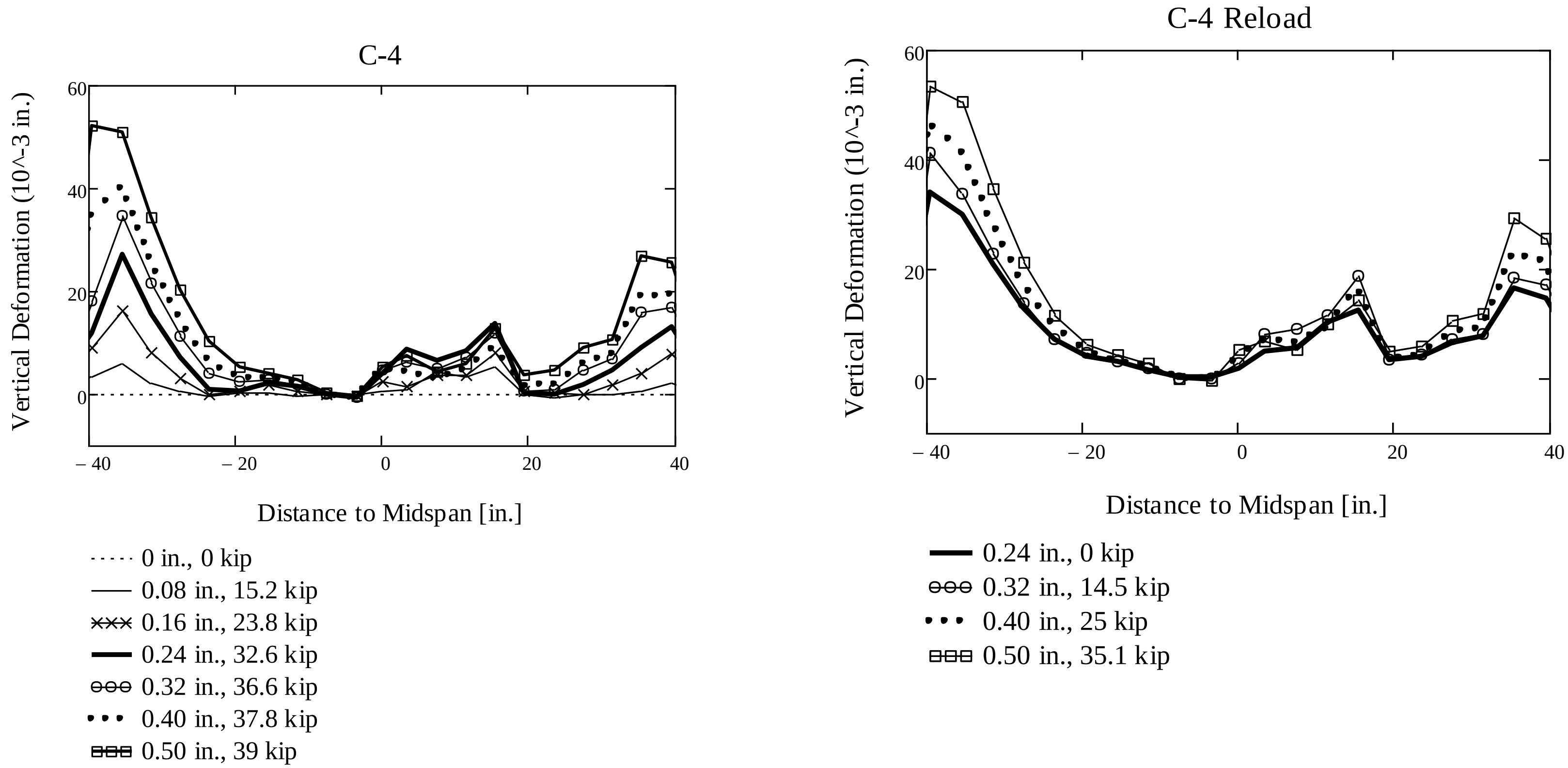

Figure 3-23: Vertical deformations of concrete surface along splice length of specimen C4, initial loading and reload (data series are labeled using midspan deflection and average load applied at ends)

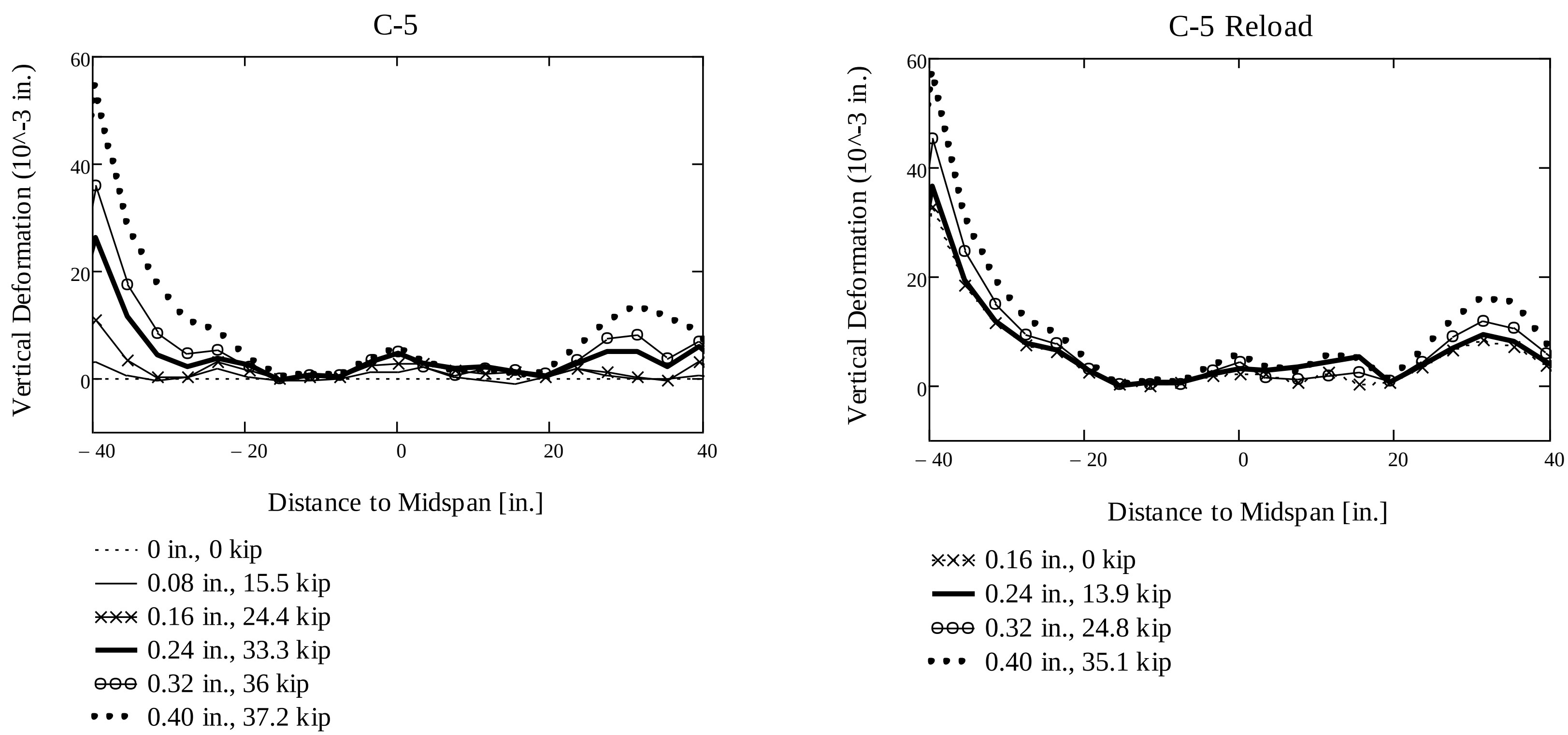

Figure 3-24: Vertical deformations of concrete surface along splice length of specimen C5, initial loading and reload (data series are labeled using midspan deflection and average load applied at ends)

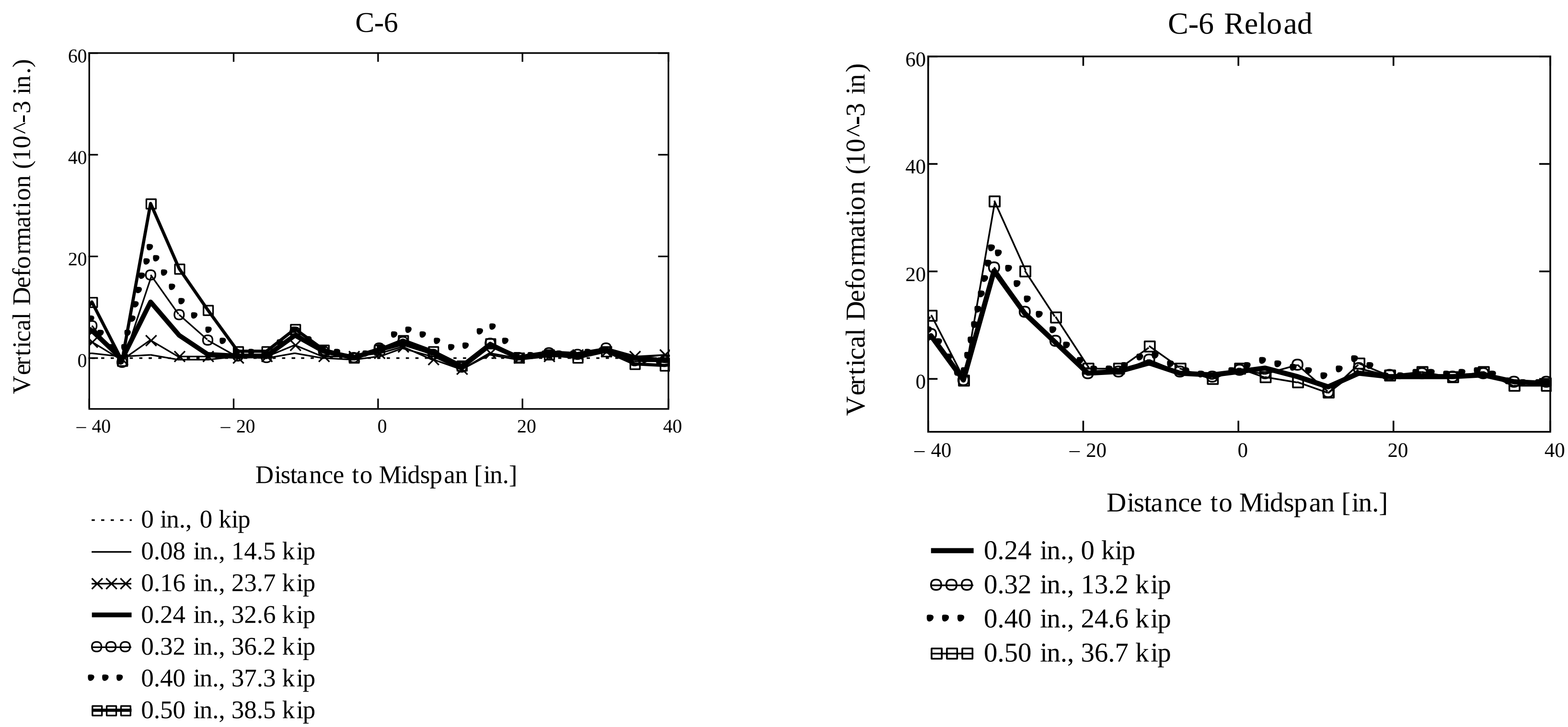

Figure 3-25: Vertical deformations of concrete surface along splice length of specimen C6, initial loading and reload (data series are labeled using midspan deflection and average load applied at ends

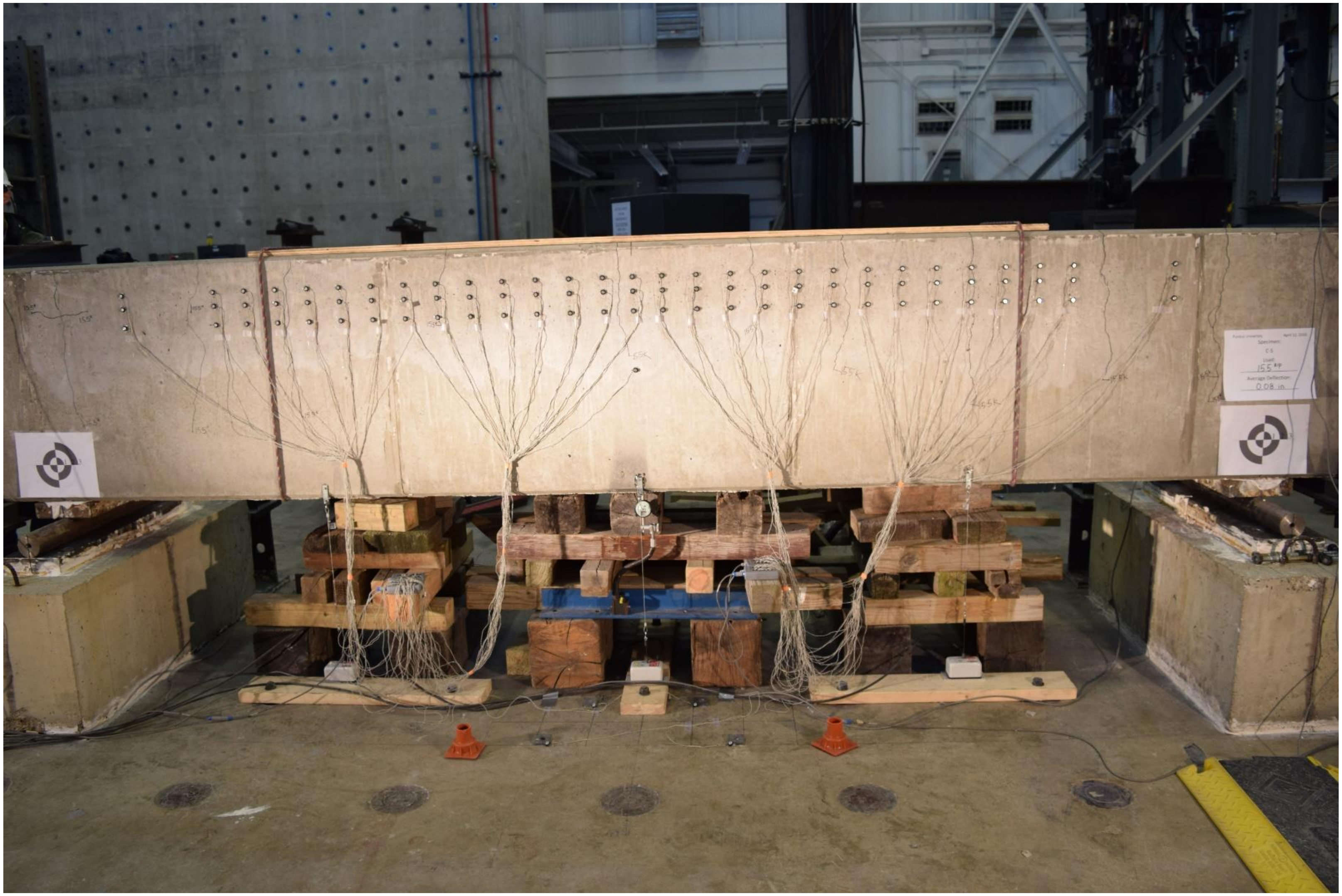

Figure 3-26: Spliced region of specimen C5 during testing

Figure 3-27: Splice failure of specimen C5. All beams in Series One failed in a similar manner

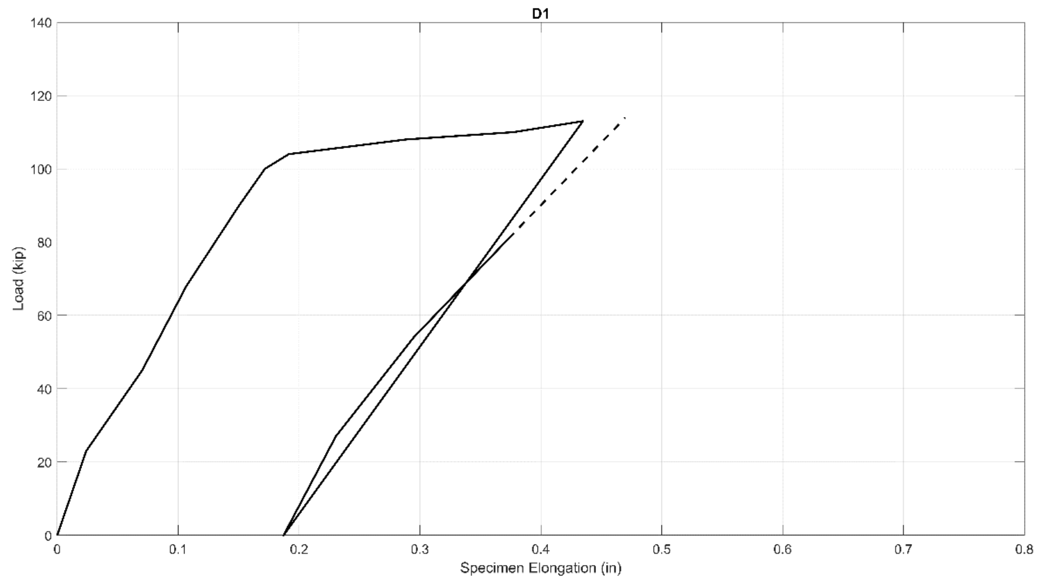

Figure 3-28: Specimen D1 load versus specimen elongation

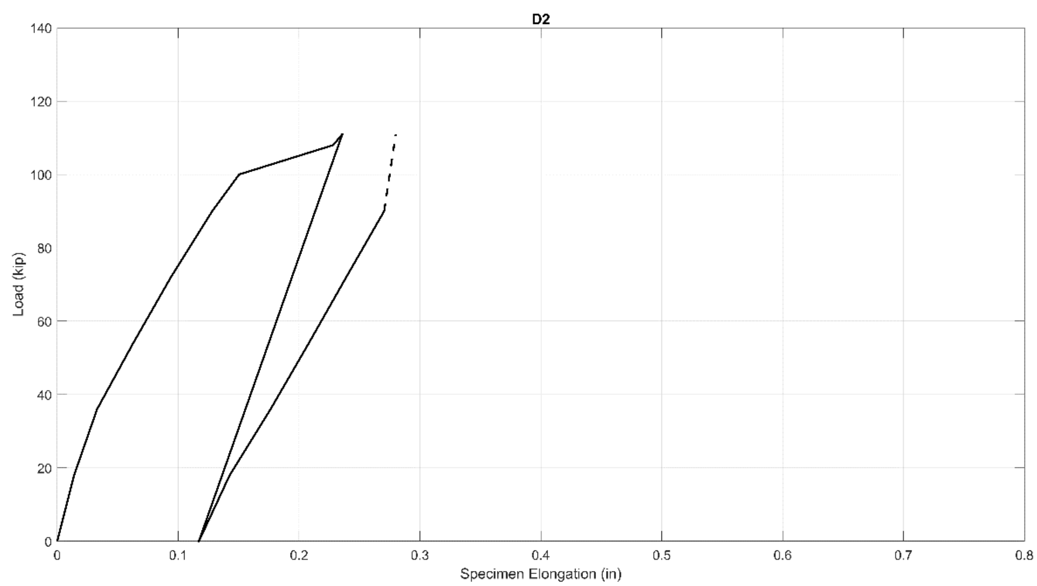

Figure 3-29: Specimen D2 load versus specimen elongation

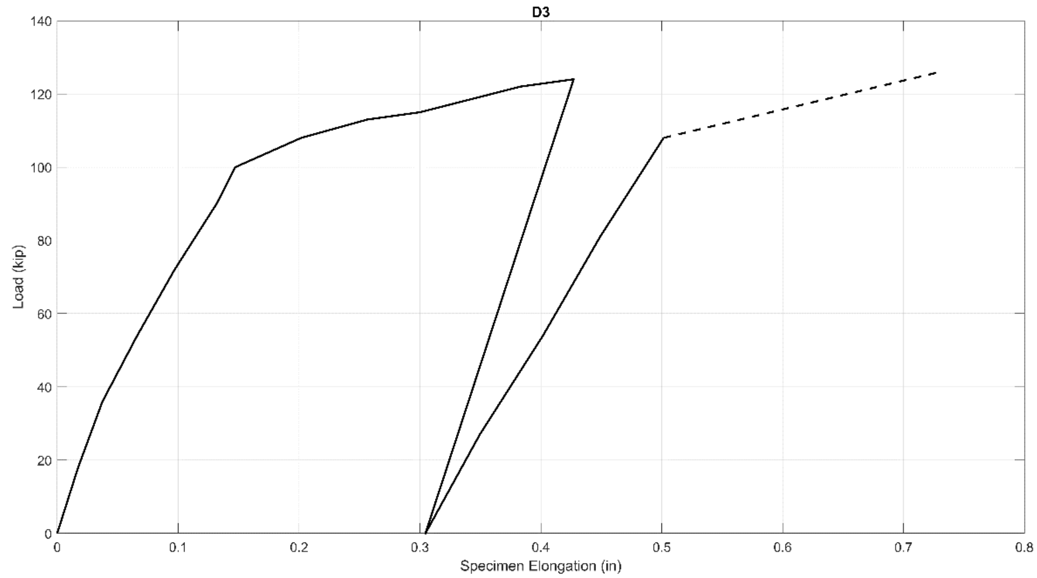

Figure 3-30: Specimen D3 load versus specimen elongation

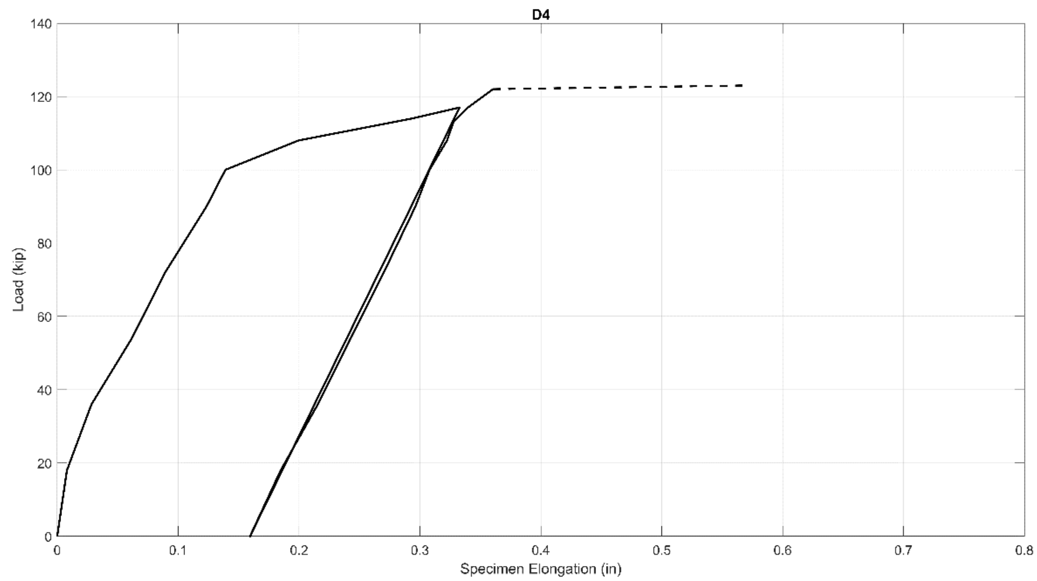

Figure 3-31: Specimen D4 load versus specimen elongation

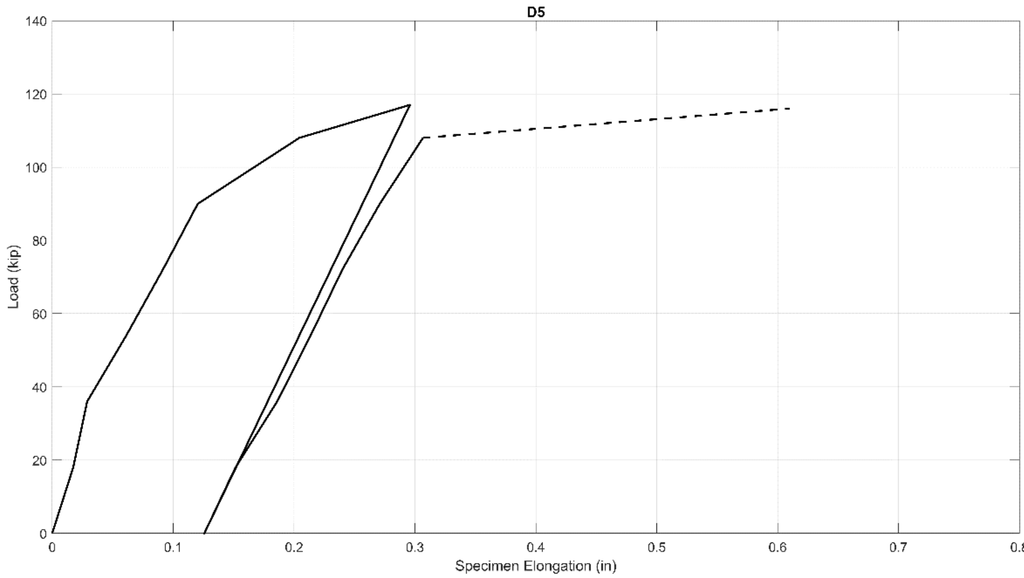

Figure 3-32: Specimen D5 load versus specimen elongation

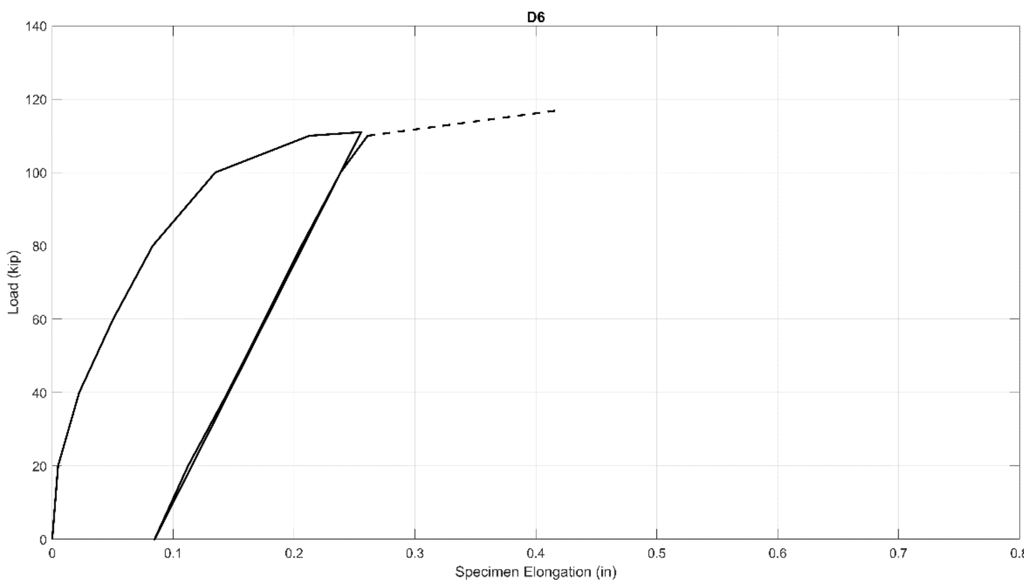

Figure 3-33: Specimen D6 load versus specimen elongation

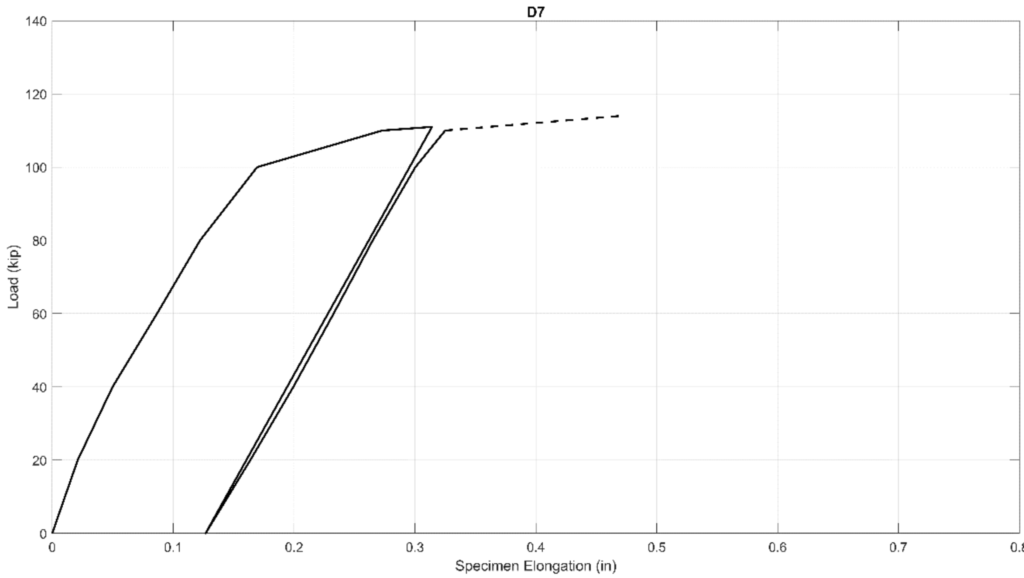

Figure 3-34: Specimen D7 load versus specimen elongation

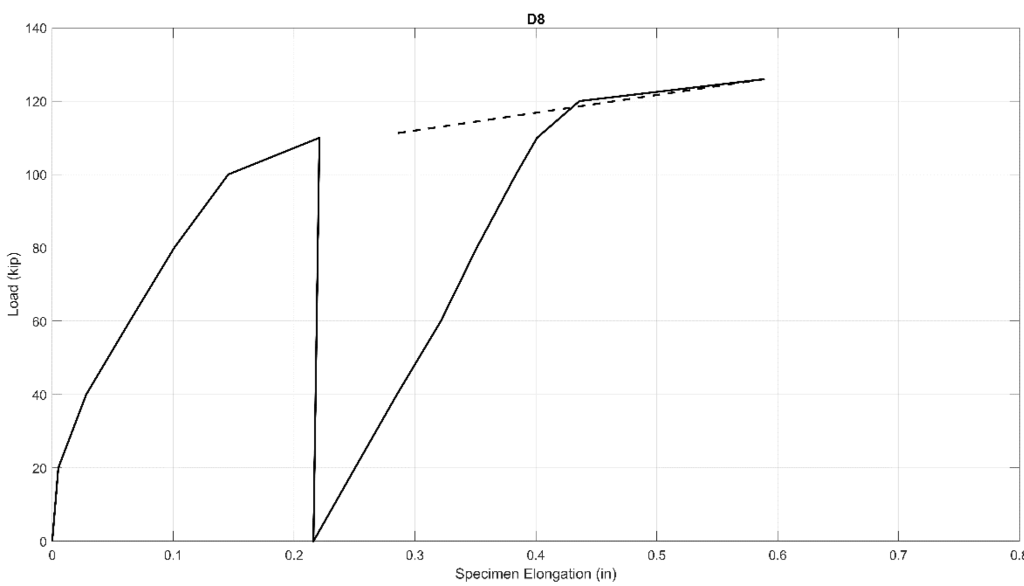

Figure 3-35: Specimen D8 load versus specimen elongation

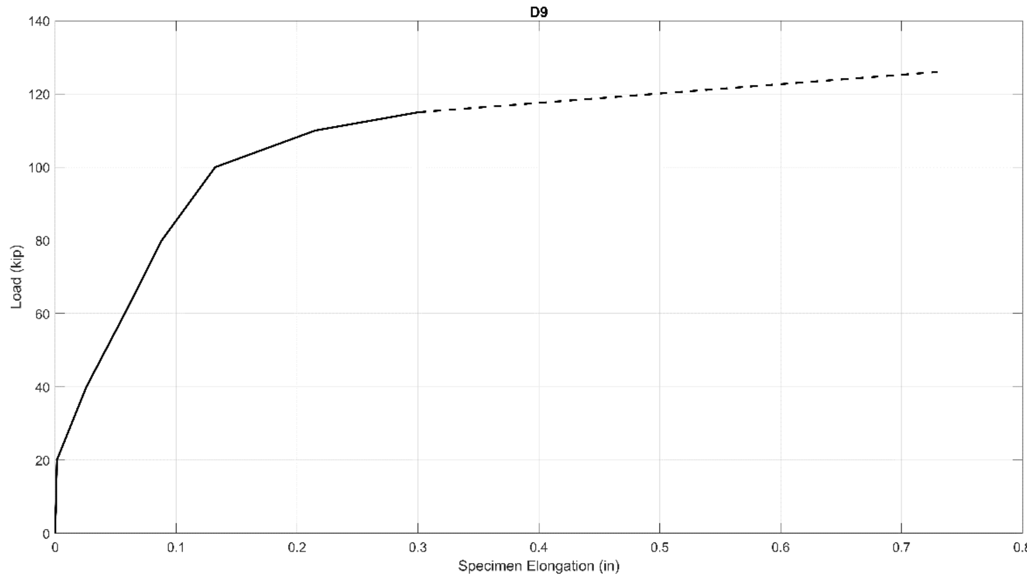

Figure 3-36: Specimen D9 load versus specimen elongation

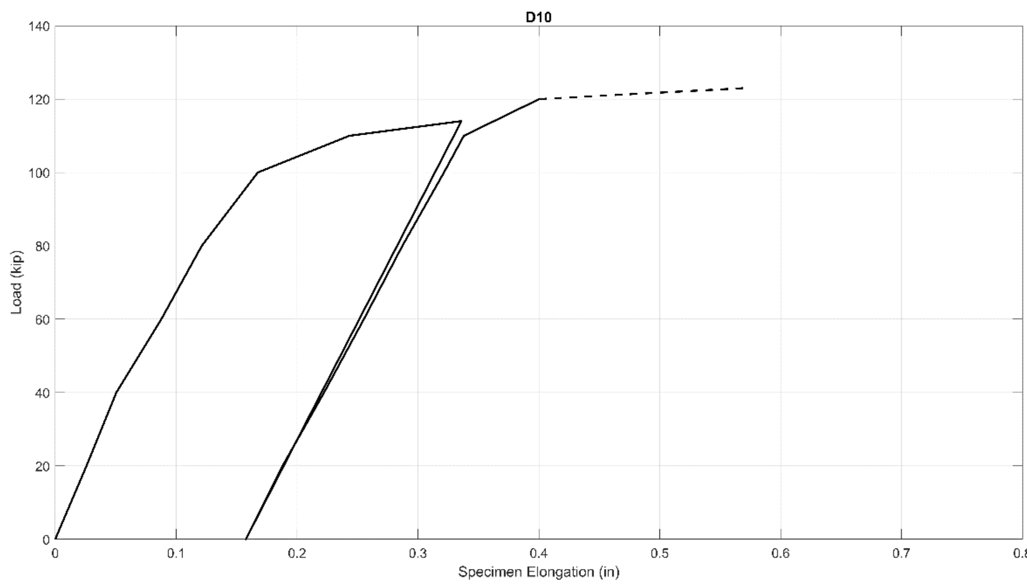

Figure 3 37: Specimen D10 load versus specimen elongation

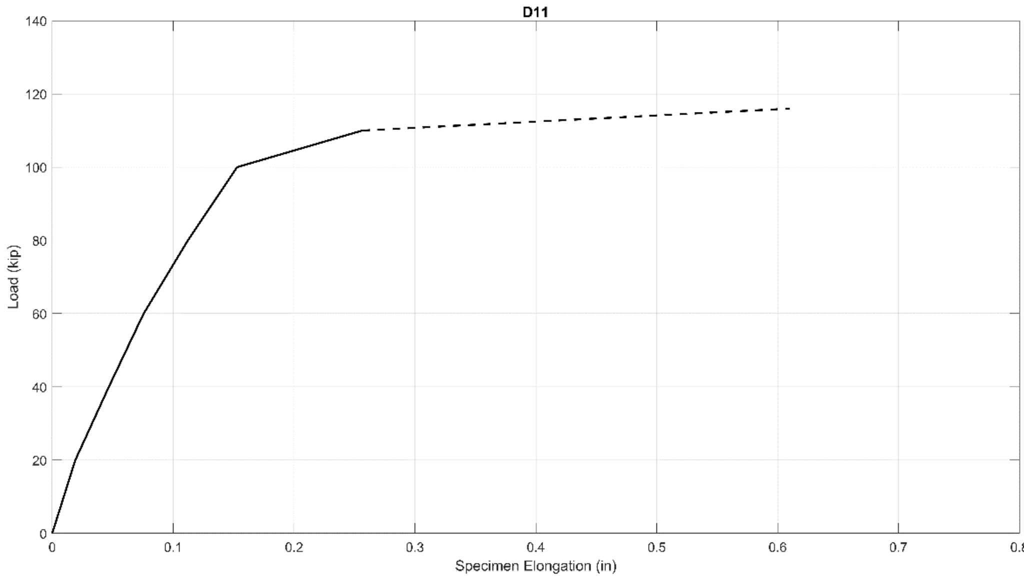

Figure 3-38: Specimen D11 load versus specimen elongation

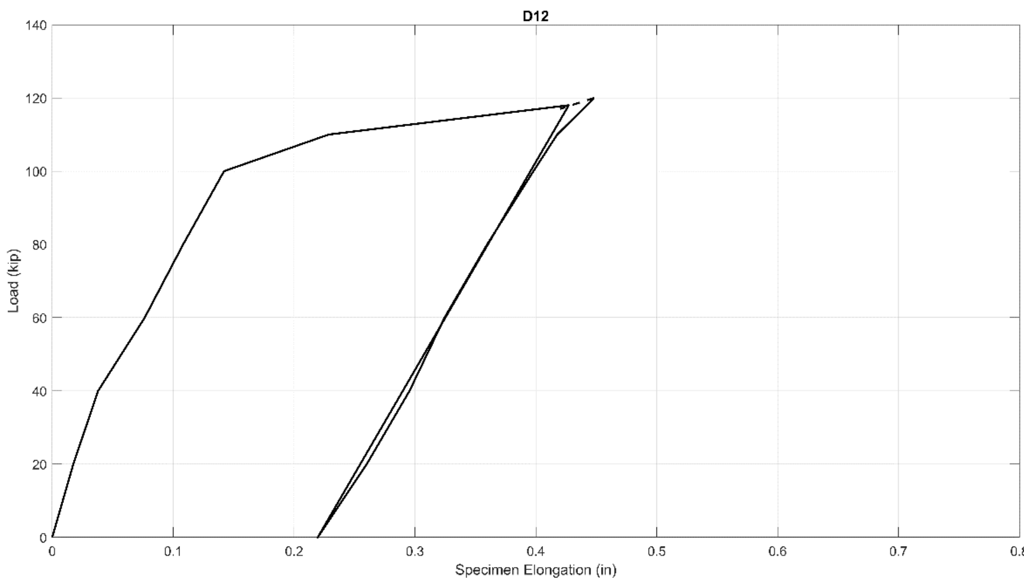

Figure 3-39: Specimen D12 load versus specimen elongation

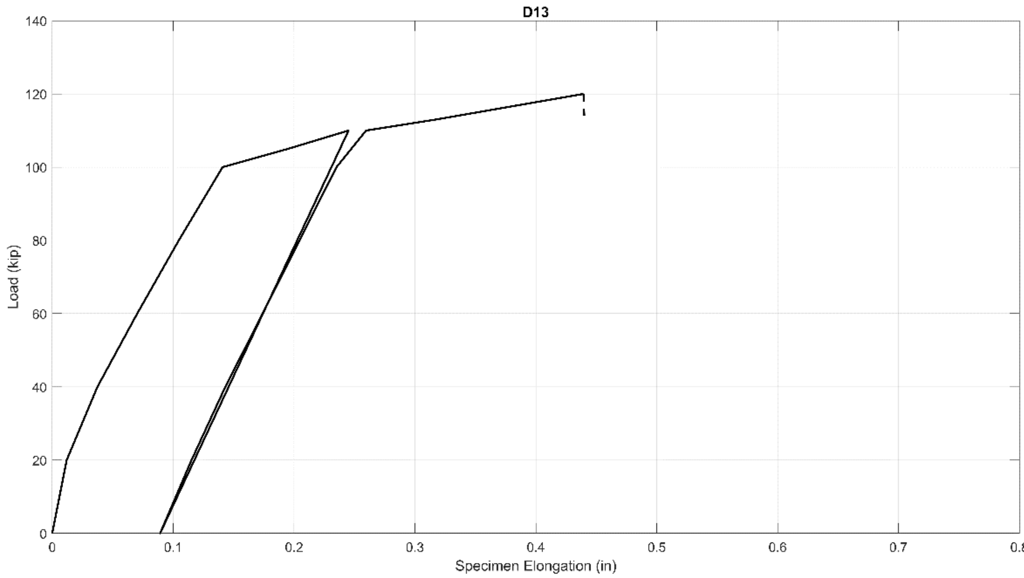

Figure 3-40: Specimen D13 load versus specimen elongation

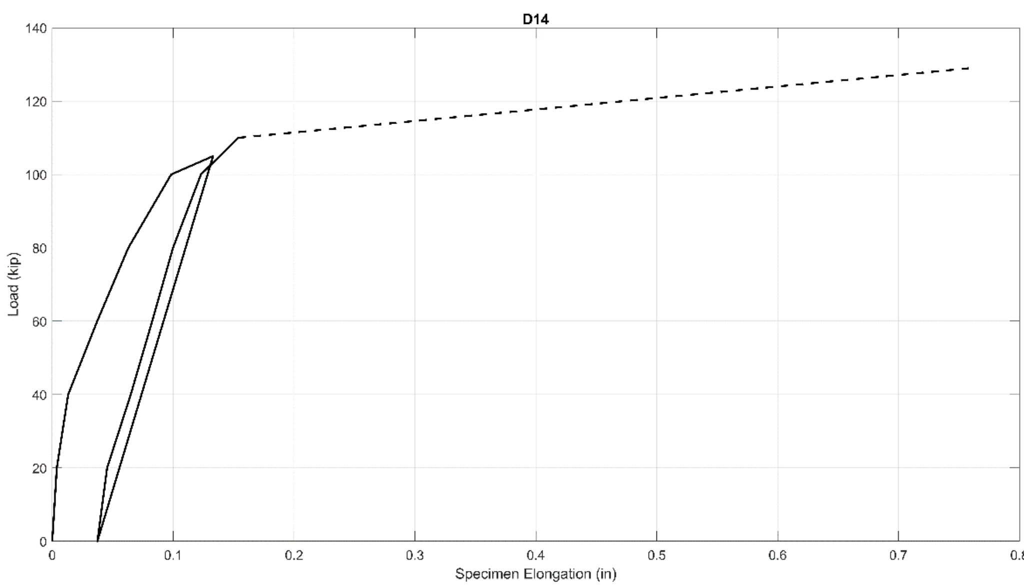

Figure 3-41: Specimen D14 load versus specimen elongation

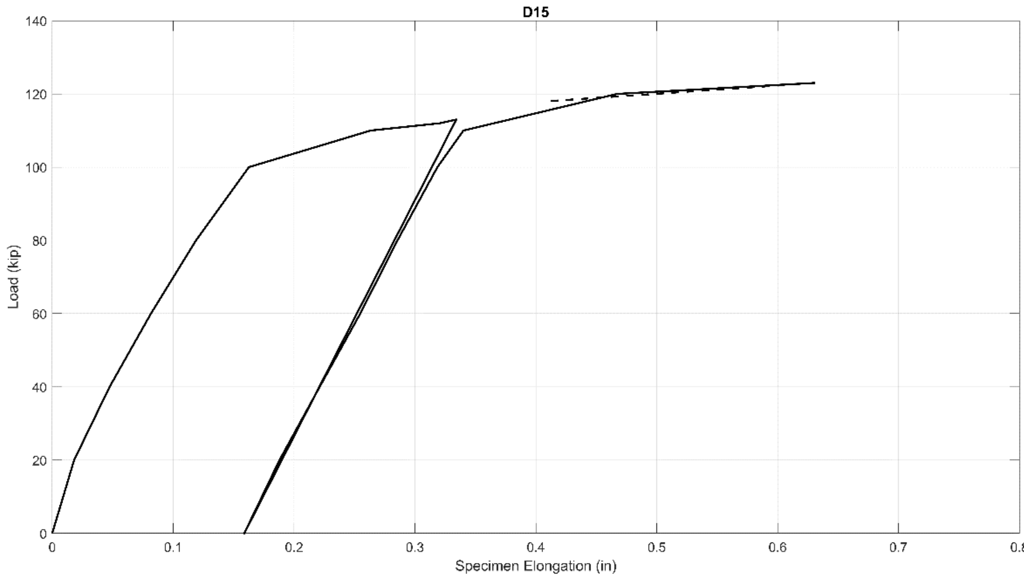

Figure 3-42: Specimen D15 load versus specimen elongation

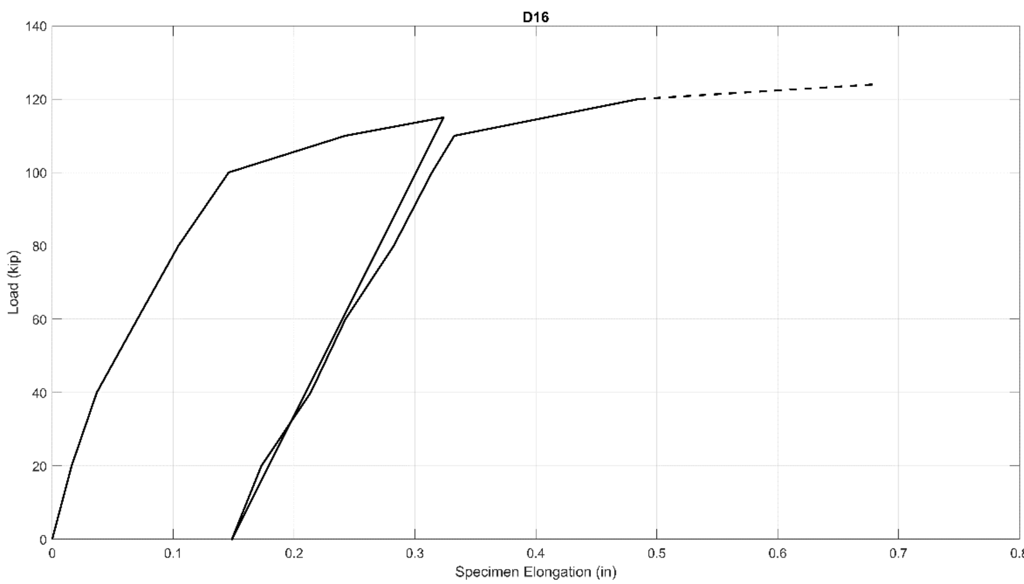

Figure 3-43: Specimen D16 load versus specimen elongation

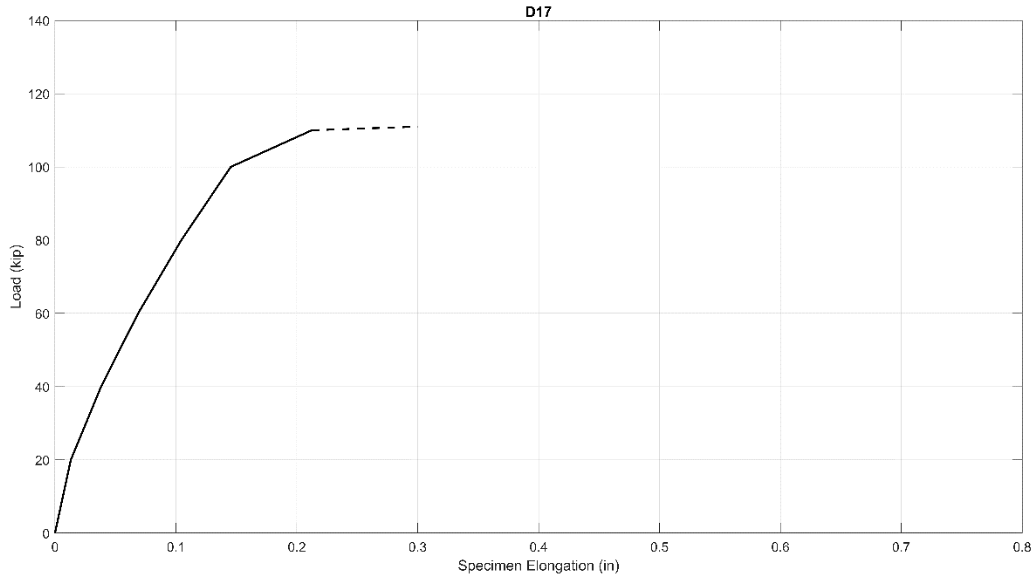

Figure 3-44: Specimen D17 load versus specimen elongation

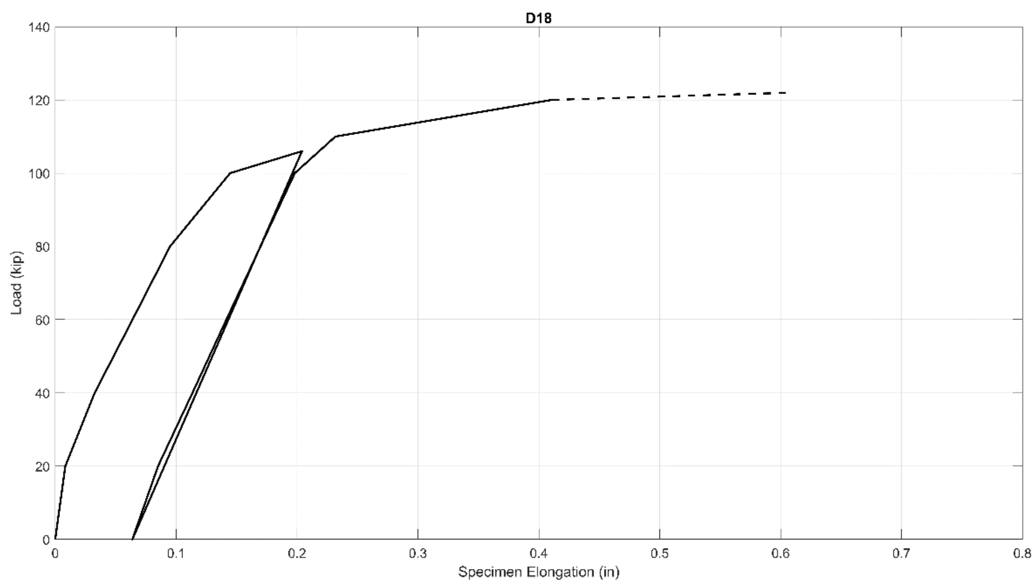

Figure 3-45: Specimen D18 load versus specimen elongation

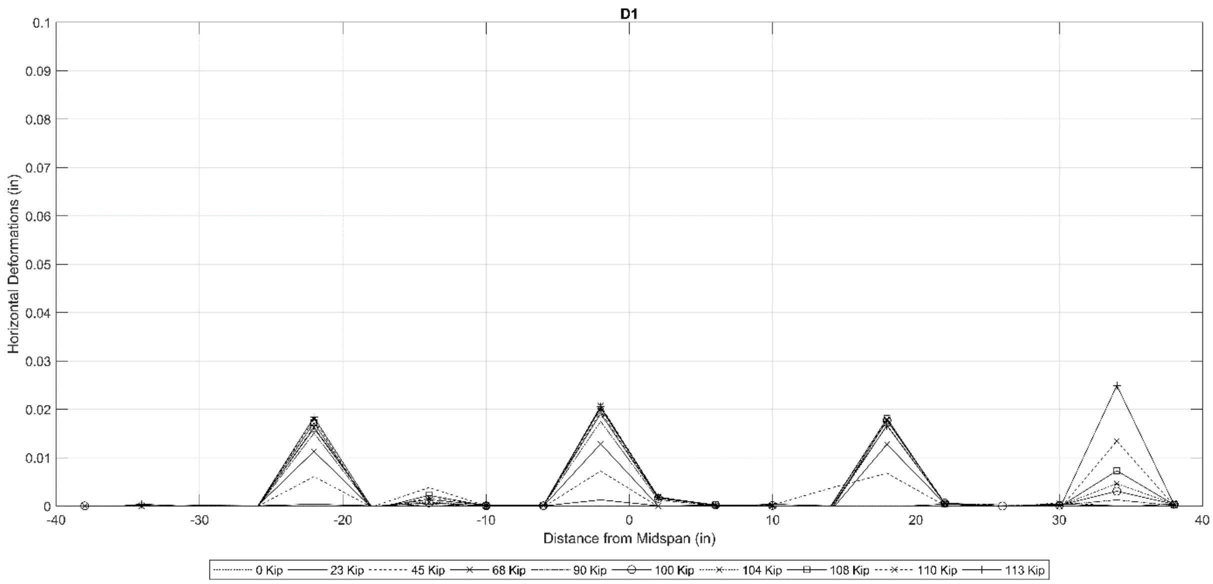

Figure 3-46: Horizontal deformations of concrete surface along splice length of specimen D1, initial loading (data series are label using the average load applied to the splice ends)

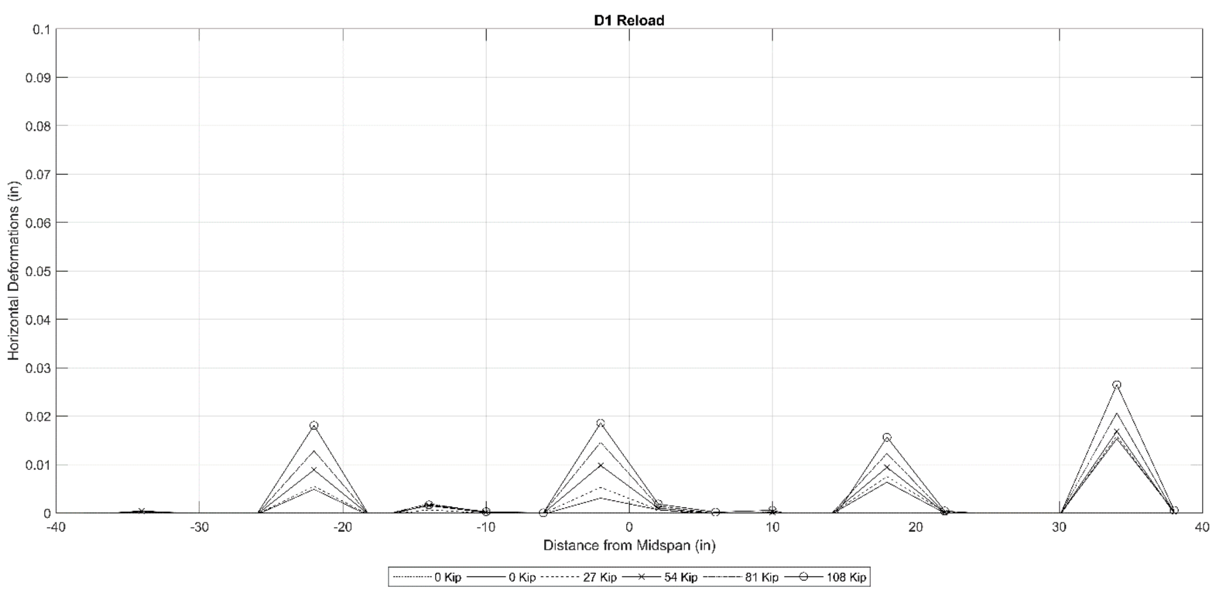

Figure 3-47: Horizontal deformations of concrete surface along splice length of specimen D1, reload (data series are label using the average load applied to the splice ends)

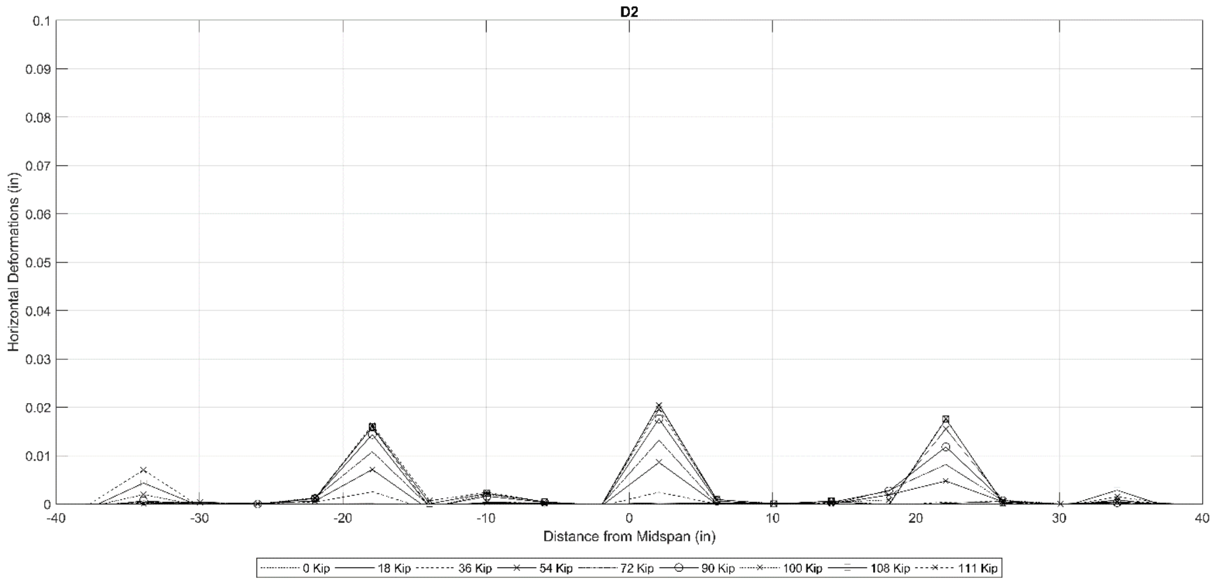

Figure 3-48: Horizontal deformations of concrete surface along splice length of specimen D2, initial loading (data series are label using the average load applied to the splice ends)

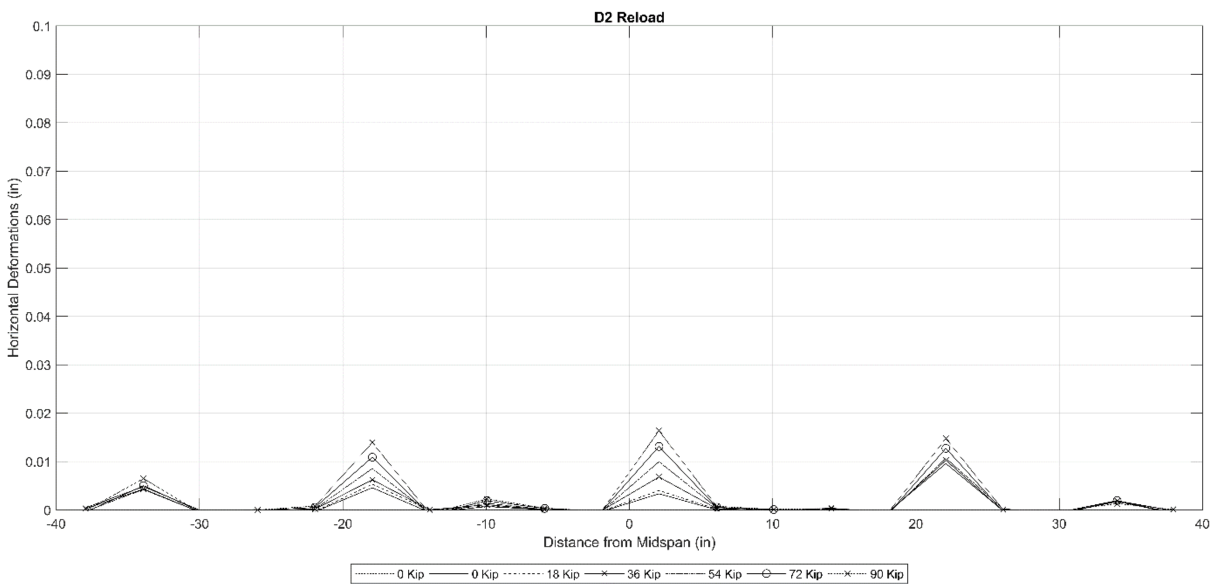

Figure 3-49: Horizontal deformations of concrete surface along splice length of specimen D2, reload (data series are label using the average load applied to the splice ends)

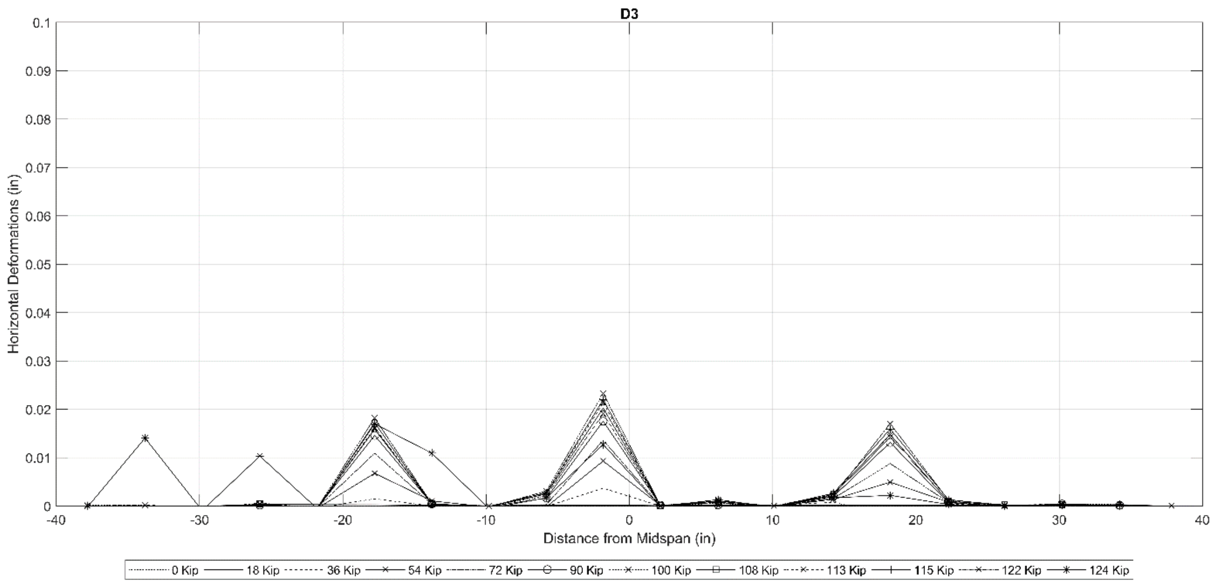

Figure 3-50: Horizontal deformations of concrete surface along splice length of specimen D3, initial loading (data series are label using the average load applied to the splice ends)

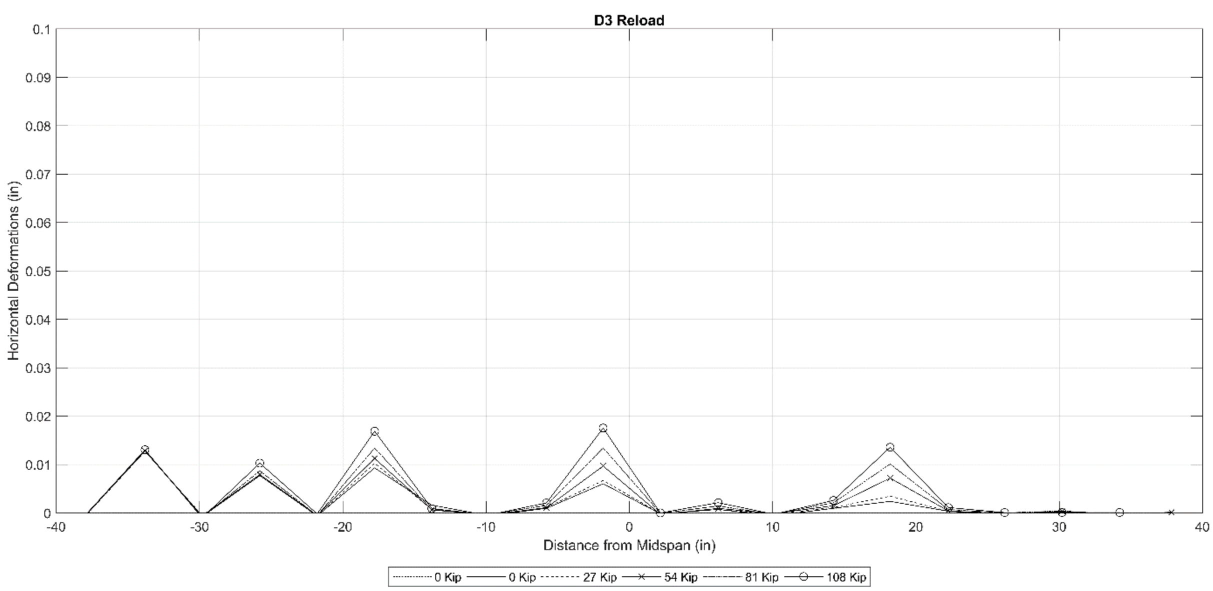

Figure 3-51: Horizontal deformations of concrete surface along splice length of specimen D3, reload (data series are label using the average load applied to the splice ends)

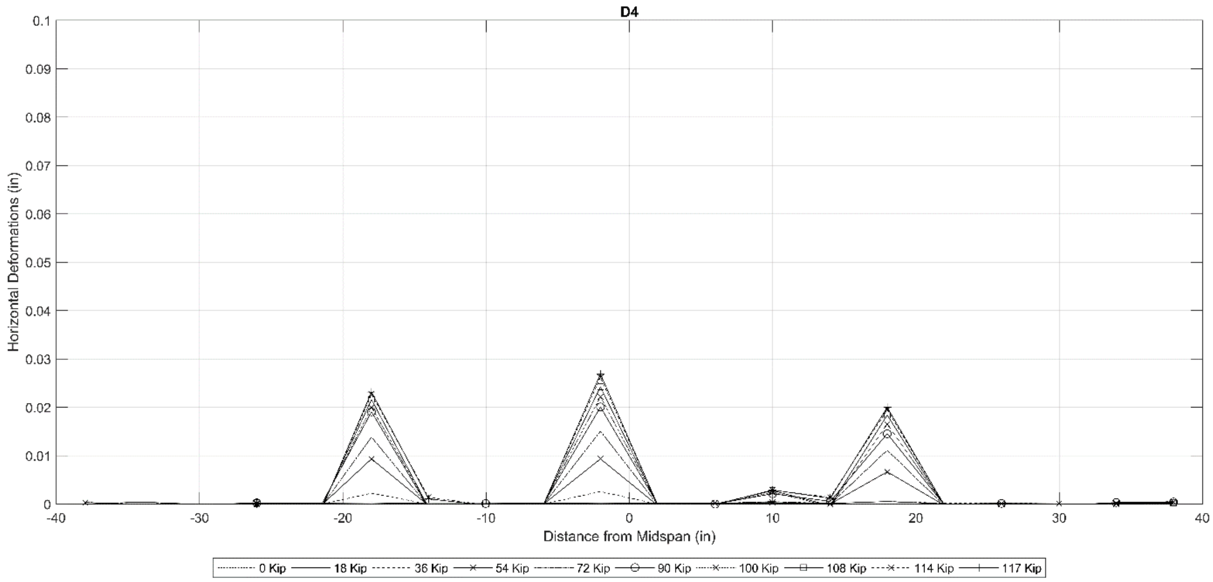

Figure 3-52: Horizontal deformations of concrete surface along splice length of specimen D4, initial loading (data series are label using the average load applied to the splice ends)

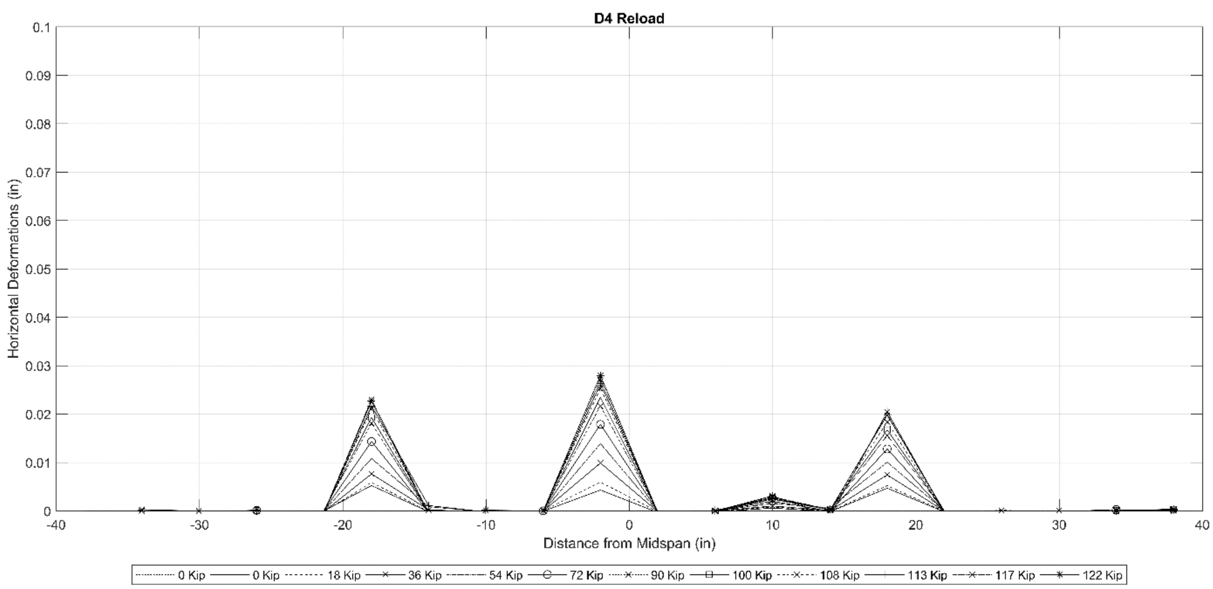

Figure 3-53: Horizontal deformations of concrete surface along splice length of specimen D4, reload (data series are label using the average load applied to the splice ends)

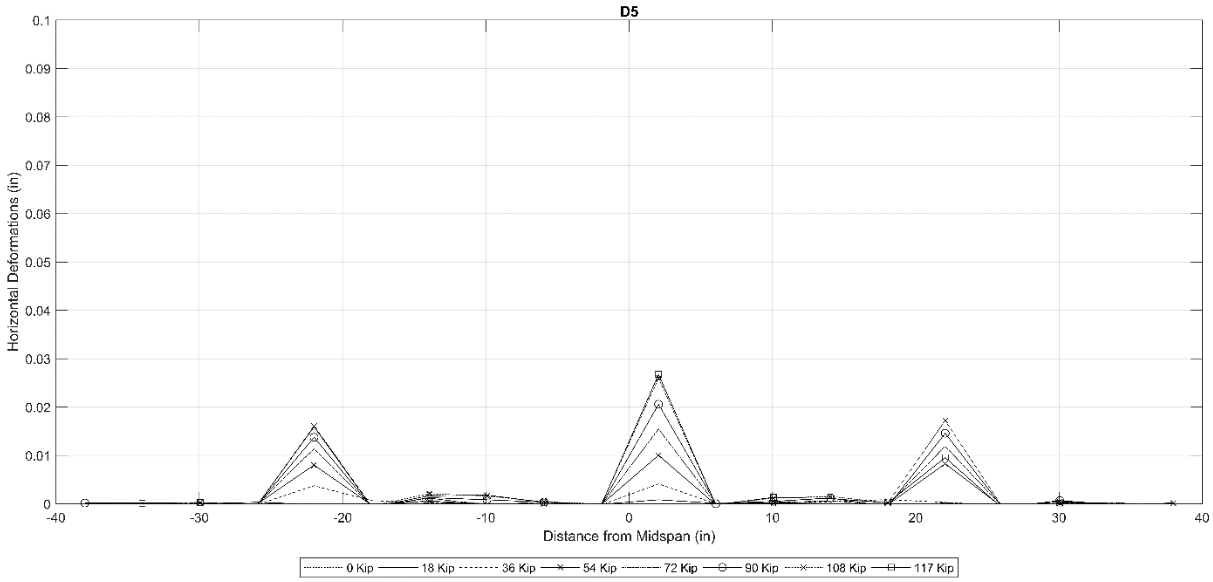

Figure 3-54: Horizontal deformations of concrete surface along splice length of specimen D5, initial loading (data series are label using the average load applied to the splice ends)

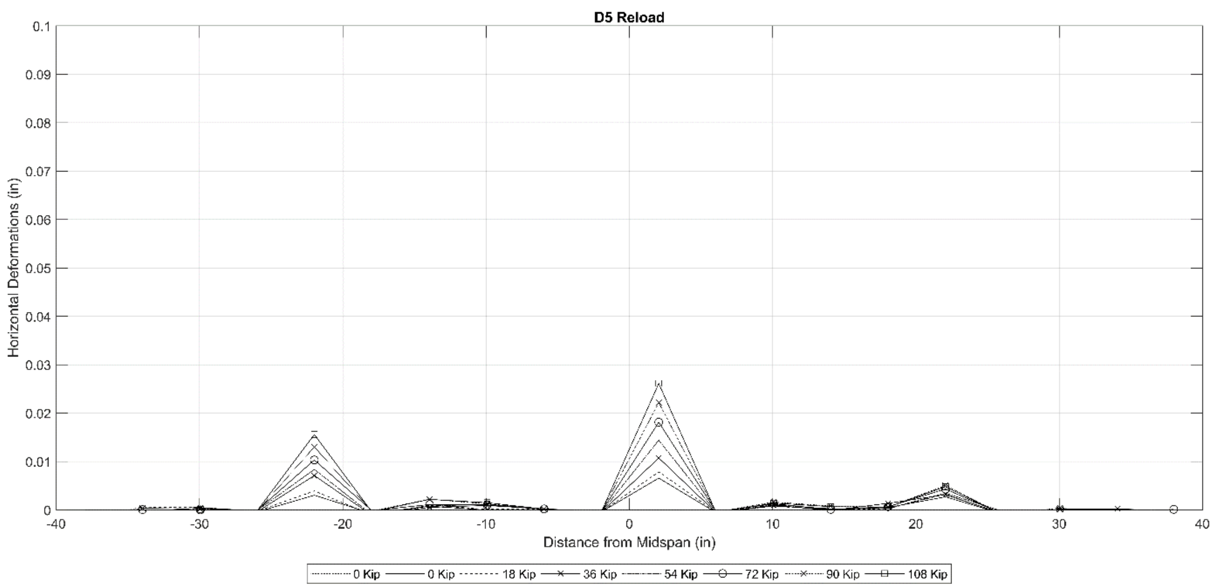

Figure 3-55: Horizontal deformations of concrete surface along splice length of specimen D5, reload (data series are label using the average load applied to the splice ends)

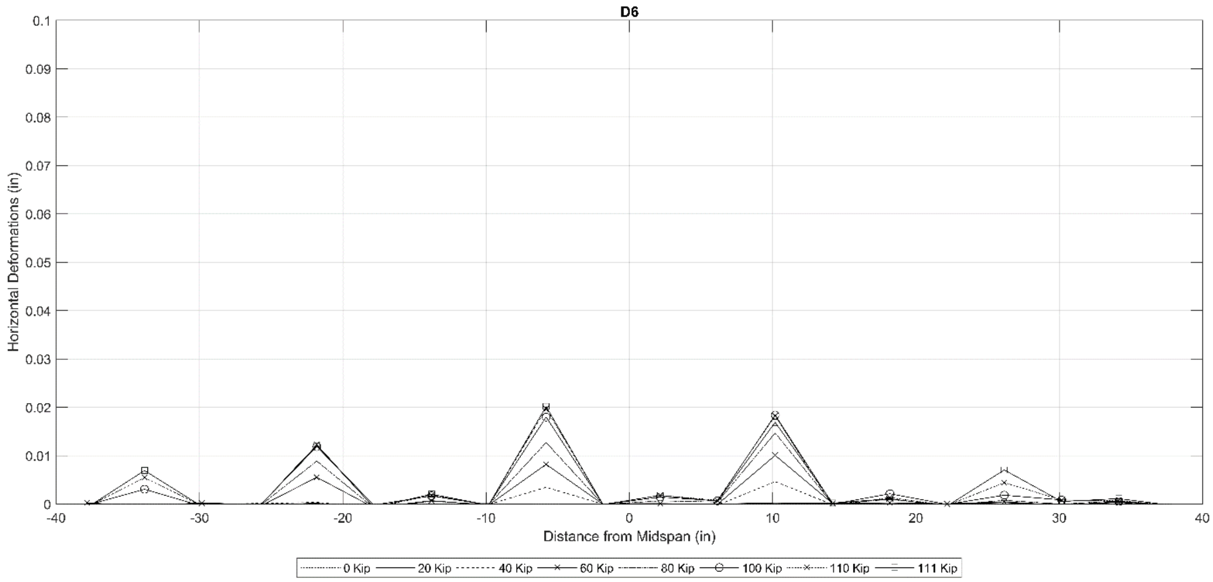

Figure 3-56: Horizontal deformations of concrete surface along splice length of specimen D6, initial loading (data series are label using the average load applied to the splice ends)

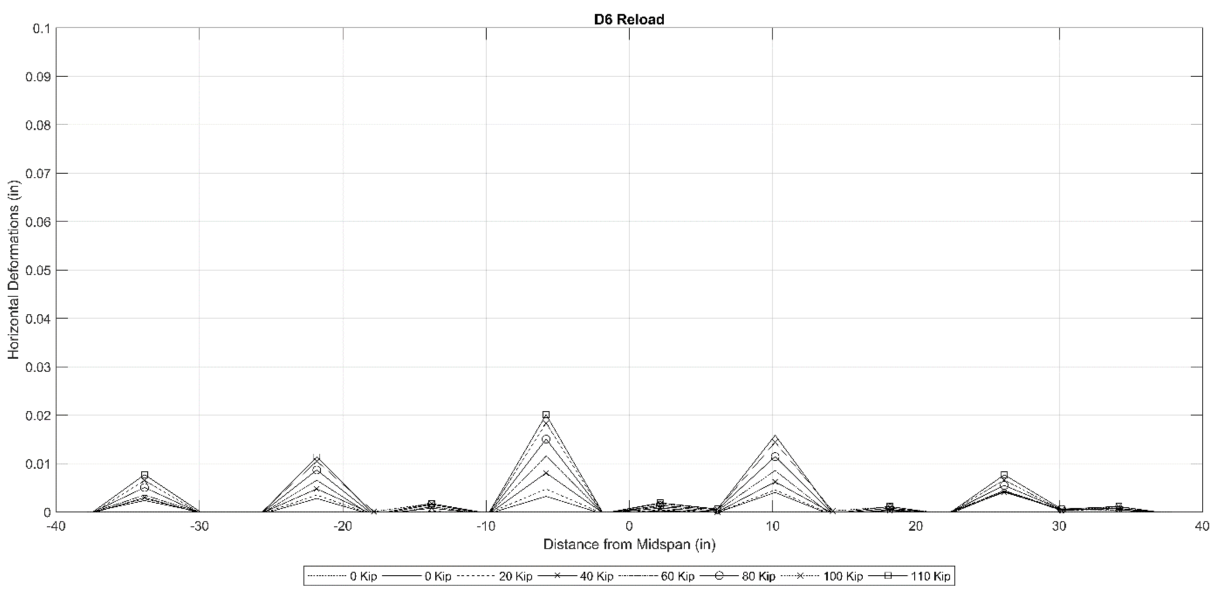

Figure 3-57: Horizontal deformations of concrete surface along splice length of specimen D6, reload (data series are label using the average load applied to the splice ends)

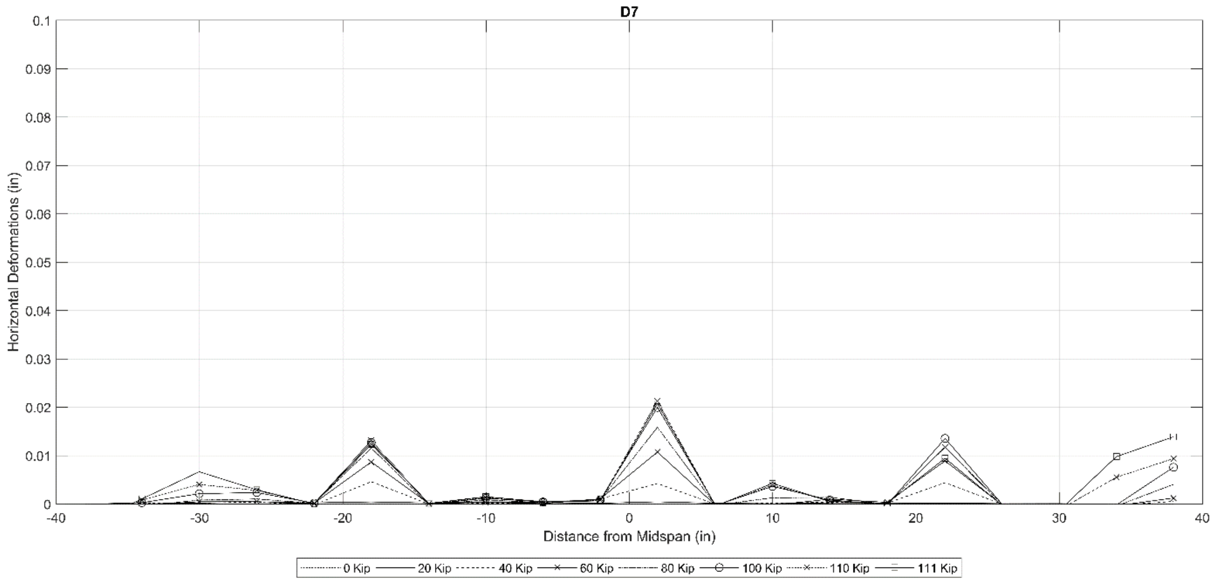

Figure 3-58: Horizontal deformations of concrete surface along splice length of specimen D7, initial loading (data series are label using the average load applied to the splice ends)

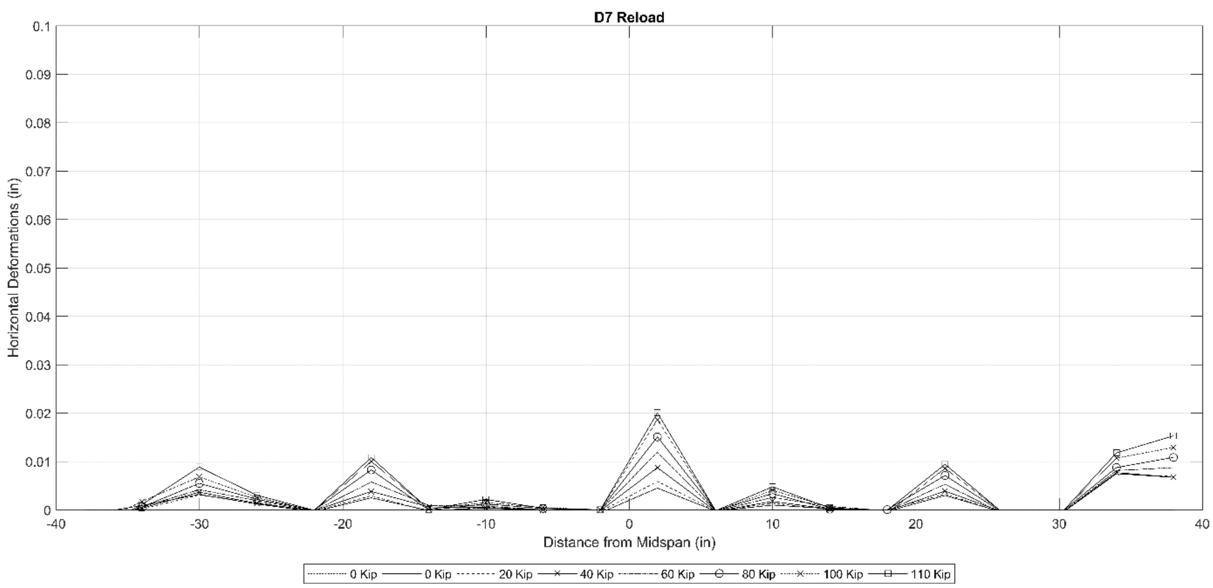

Figure 3-59: Horizontal deformations of concrete surface along splice length of specimen D7, reload (data series are label using the average load applied to the splice ends)

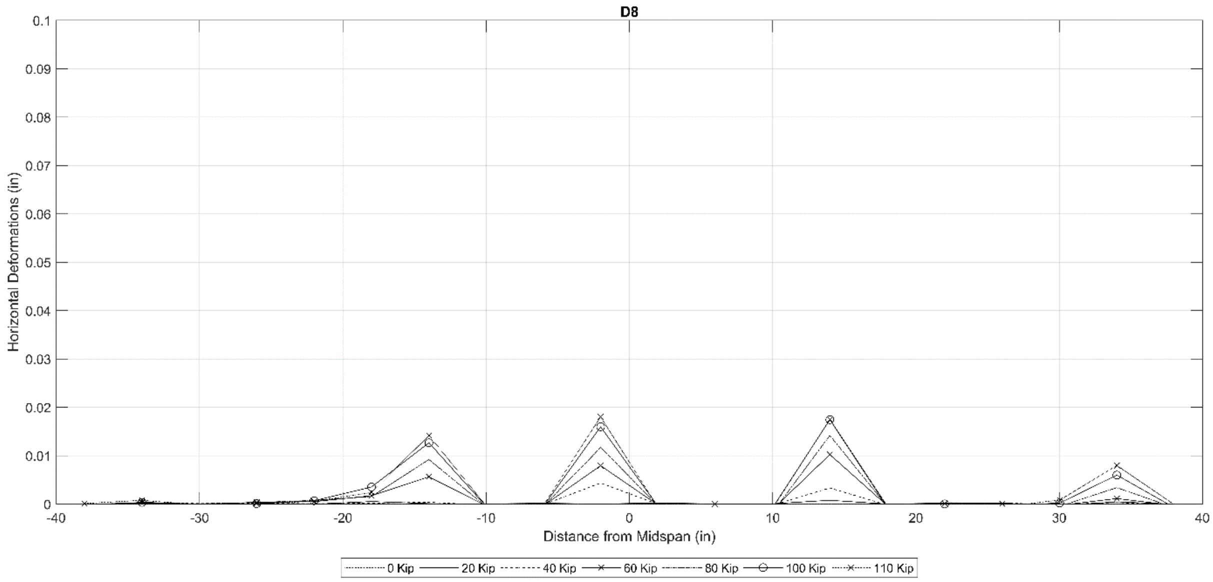

Figure 3-60: Horizontal deformations of concrete surface along splice length of specimen D8, initial loading (data series are label using the average load applied to the splice ends)

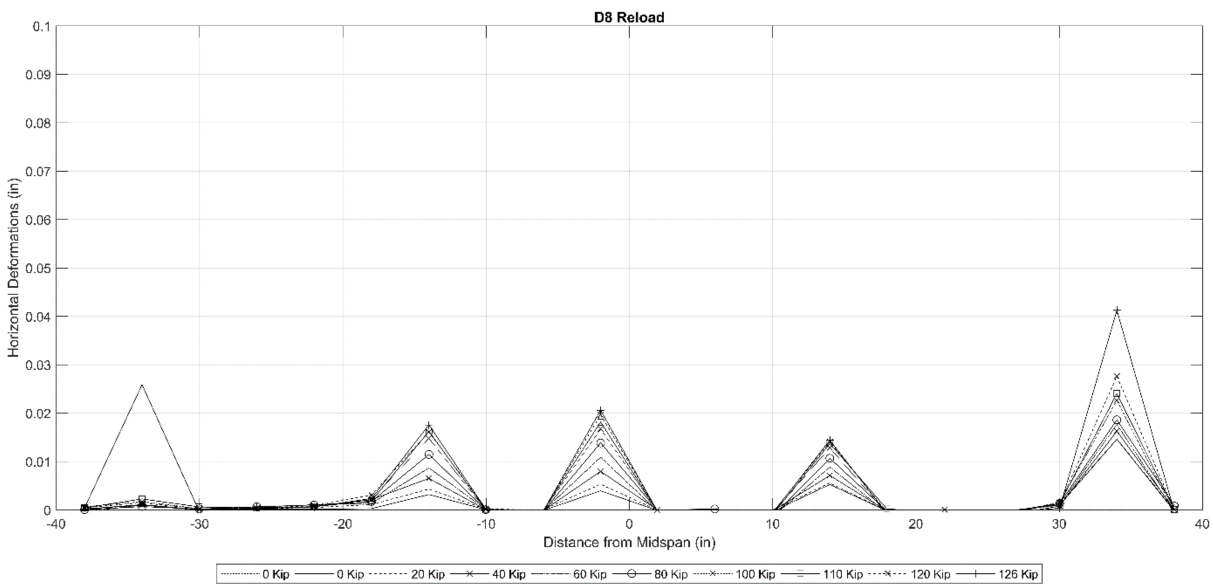

Figure 3-61: Horizontal deformations of concrete surface along splice length of specimen D8, reload (data series are label using the average load applied to the splice ends)

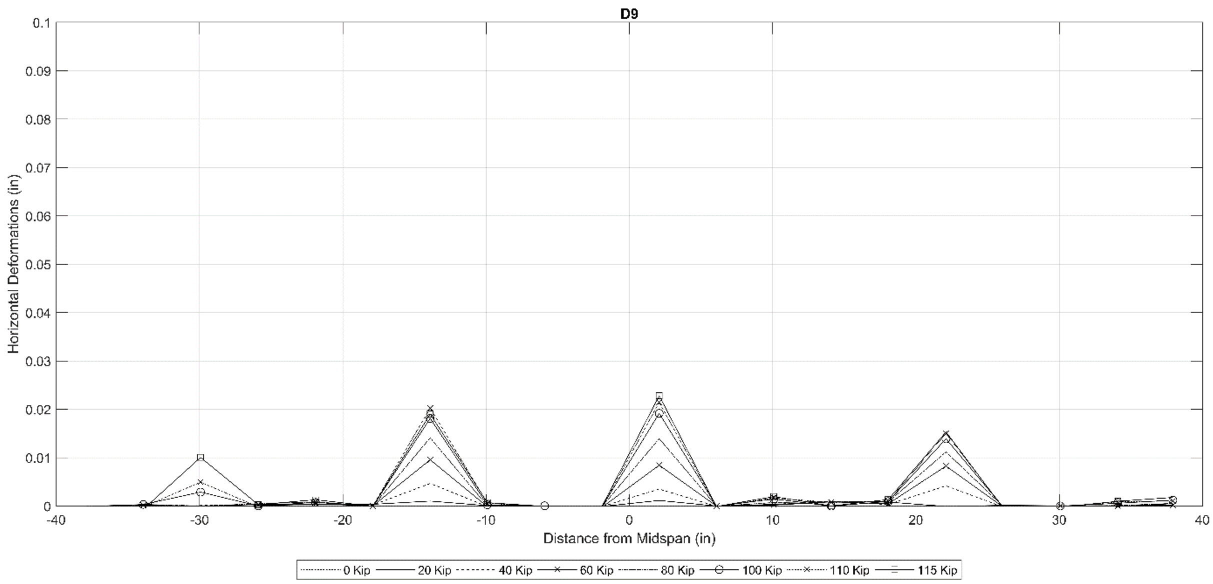

Figure 3-62: Horizontal deformations of concrete surface along splice length of specimen D9, initial loading (data series are label using the average load applied to the splice ends)

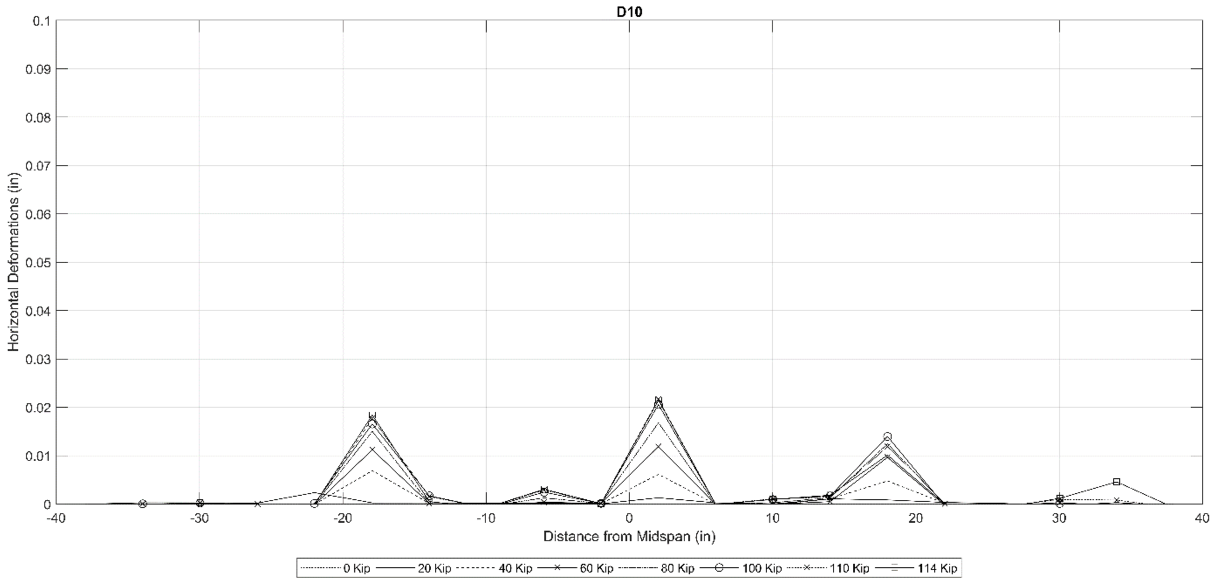

Figure 3-63: Horizontal deformations of concrete surface along splice length of specimen D10, initial loading (data series are label using the average load applied to the splice ends)

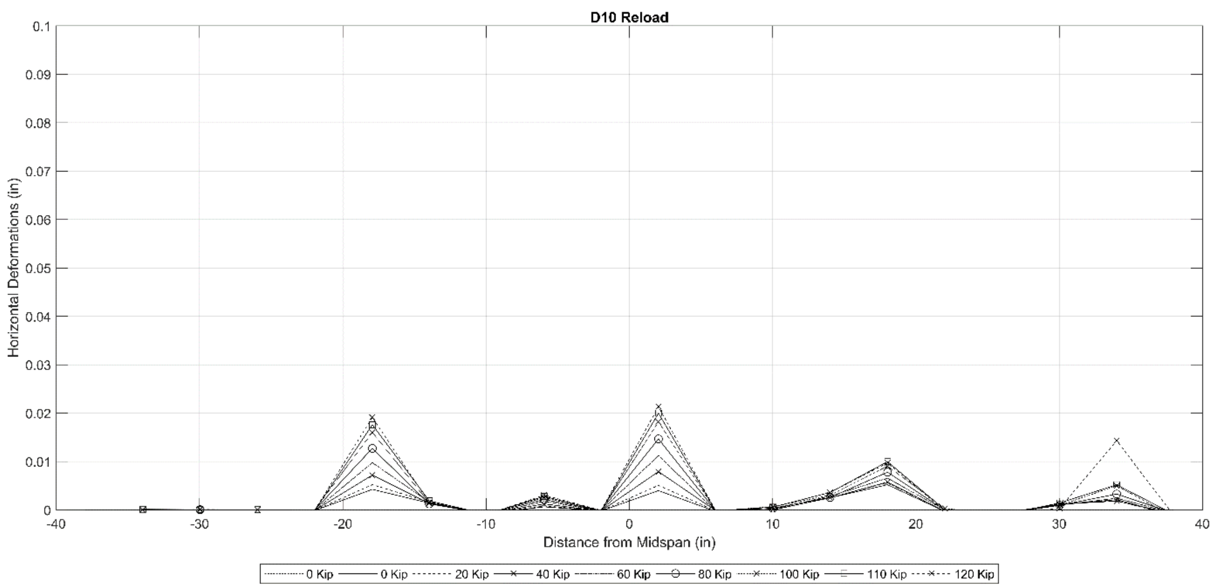

Figure 3-64: Horizontal deformations of concrete surface along splice length of specimen D10, reload (data series are label using the average load applied to the splice ends)

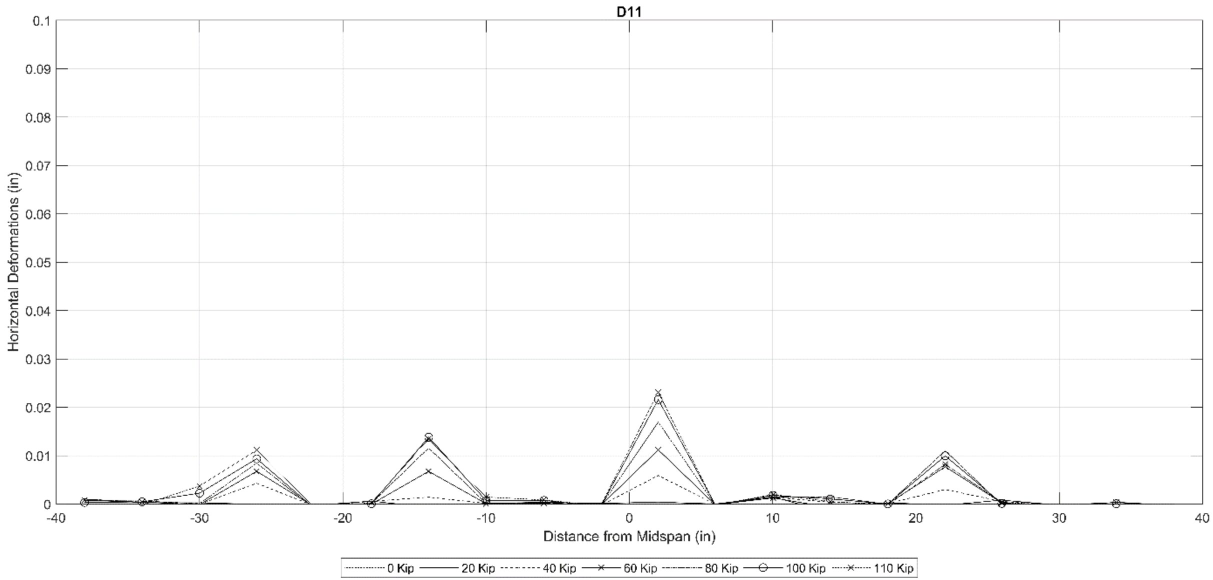

Figure 3-65: Horizontal deformations of concrete surface along splice length of specimen D11, initial loading (data series are label using the average load applied to the splice ends)

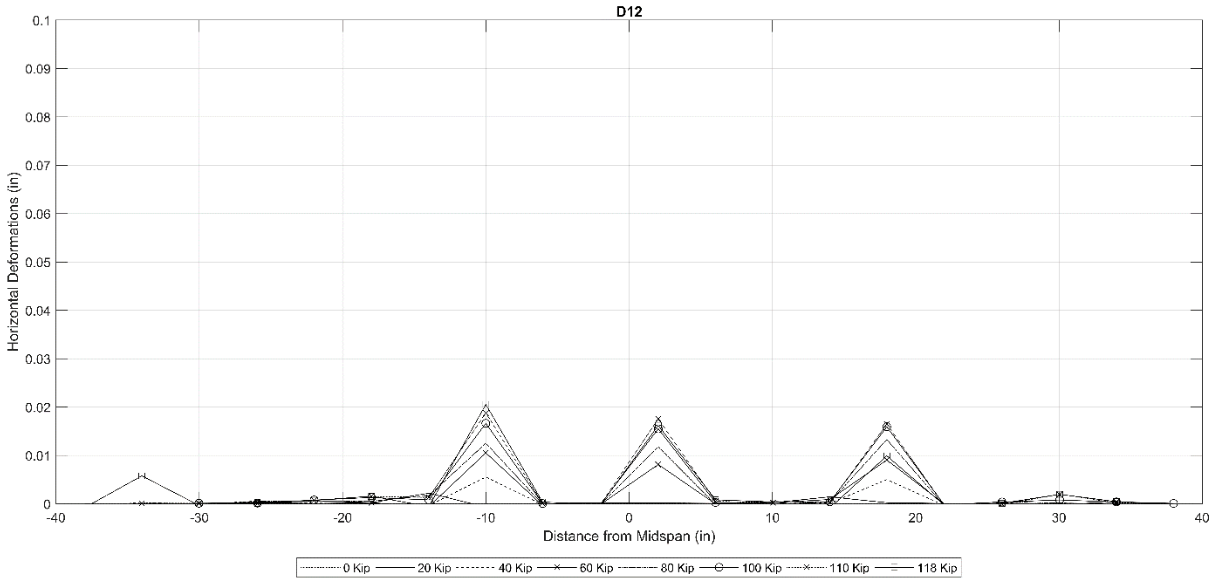

Figure 3-66: Horizontal deformations of concrete surface along splice length of specimen D12, initial loading (data series are label using the average load applied to the splice ends)

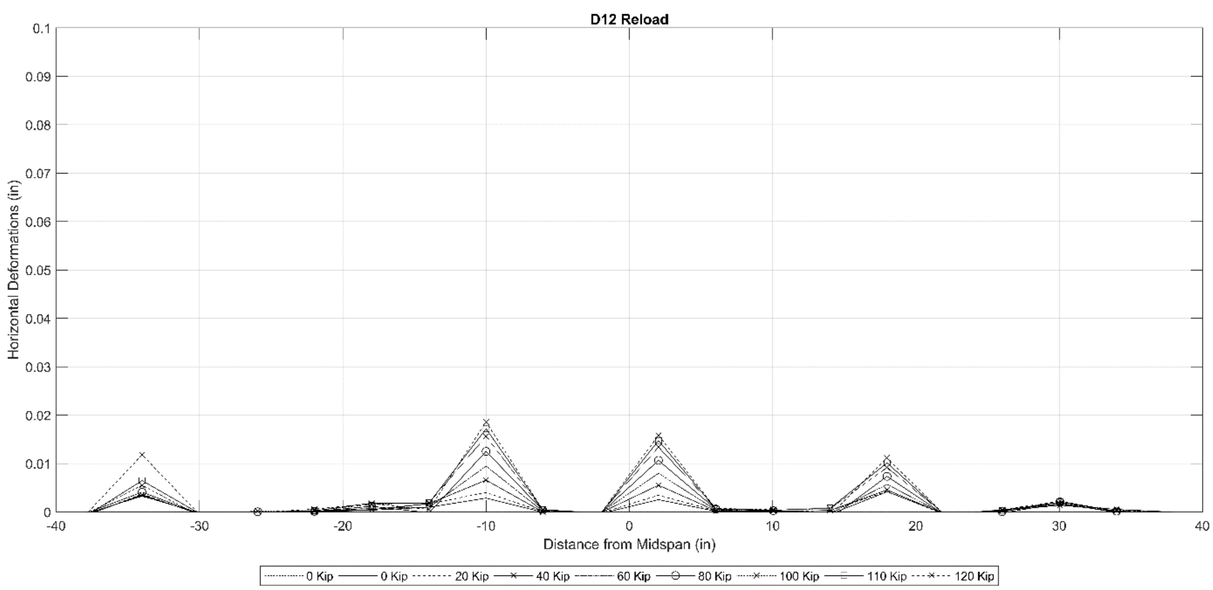

Figure 3-67: Horizontal deformations of concrete surface along splice length of specimen D12, reload (data series are label using the average load applied to the splice ends)

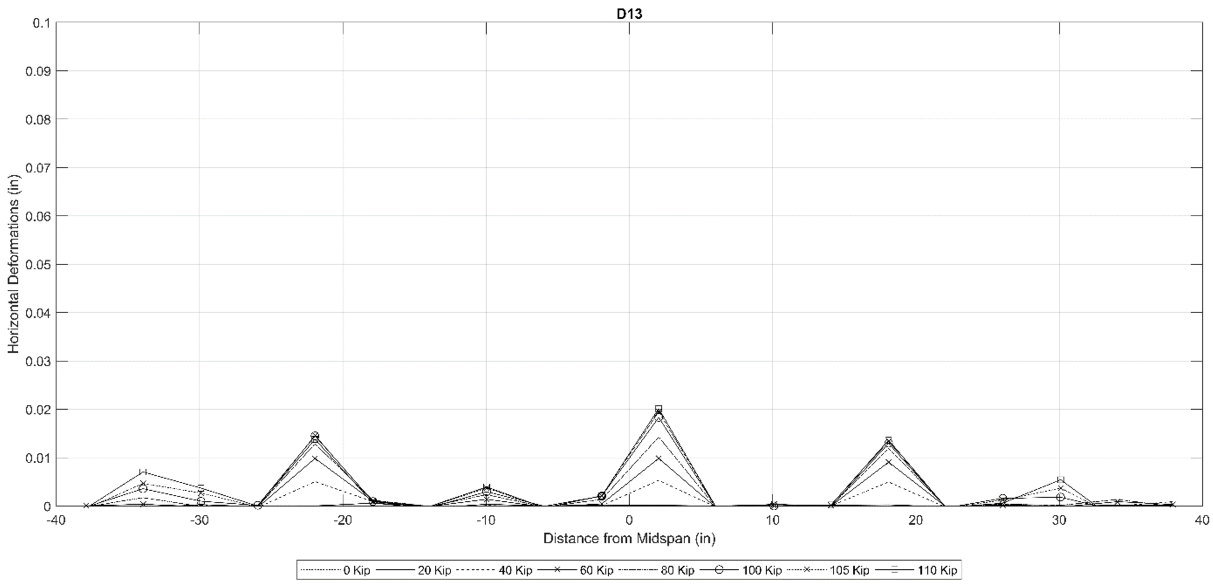

Figure 3-68: Horizontal deformations of concrete surface along splice length of specimen D13, initial loading (data series are label using the average load applied to the splice ends)

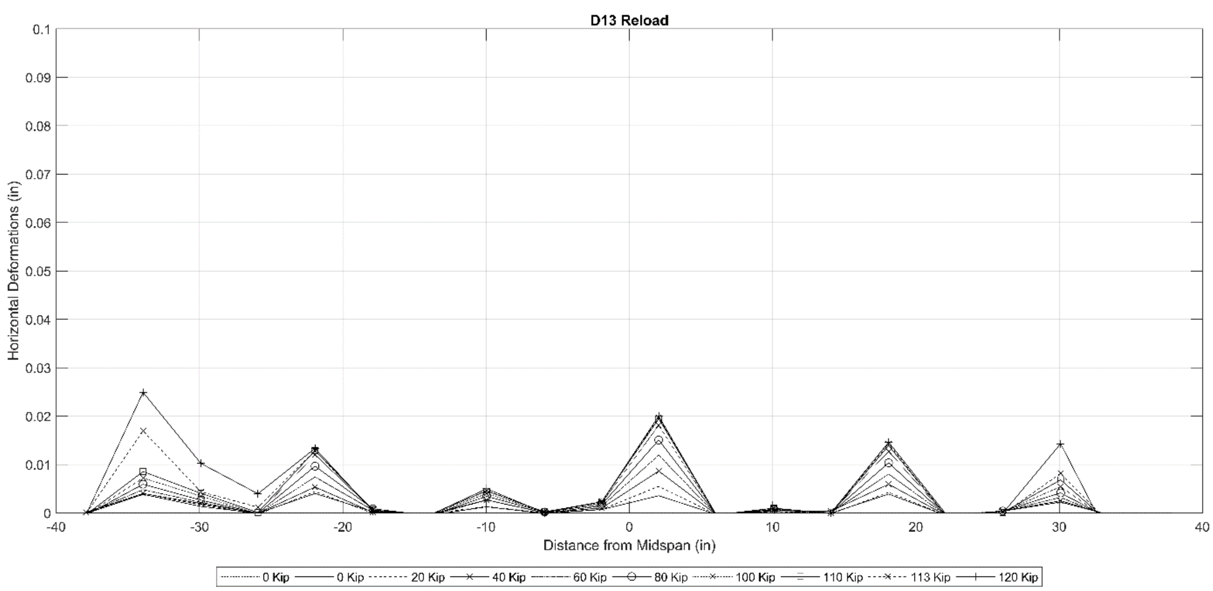

Figure 3-69: Horizontal deformations of concrete surface along splice length of specimen D13, reload (data series are label using the average load applied to the splice ends)

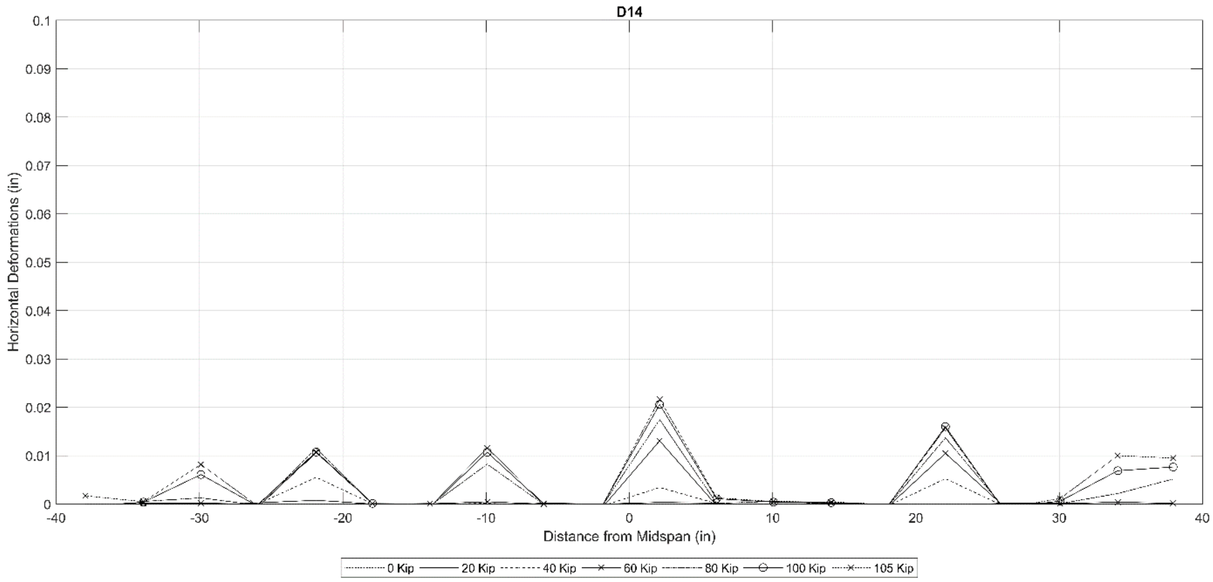

Figure 3-70: Horizontal deformations of concrete surface along splice length of specimen D14, initial loading (data series are label using the average load applied to the splice ends)

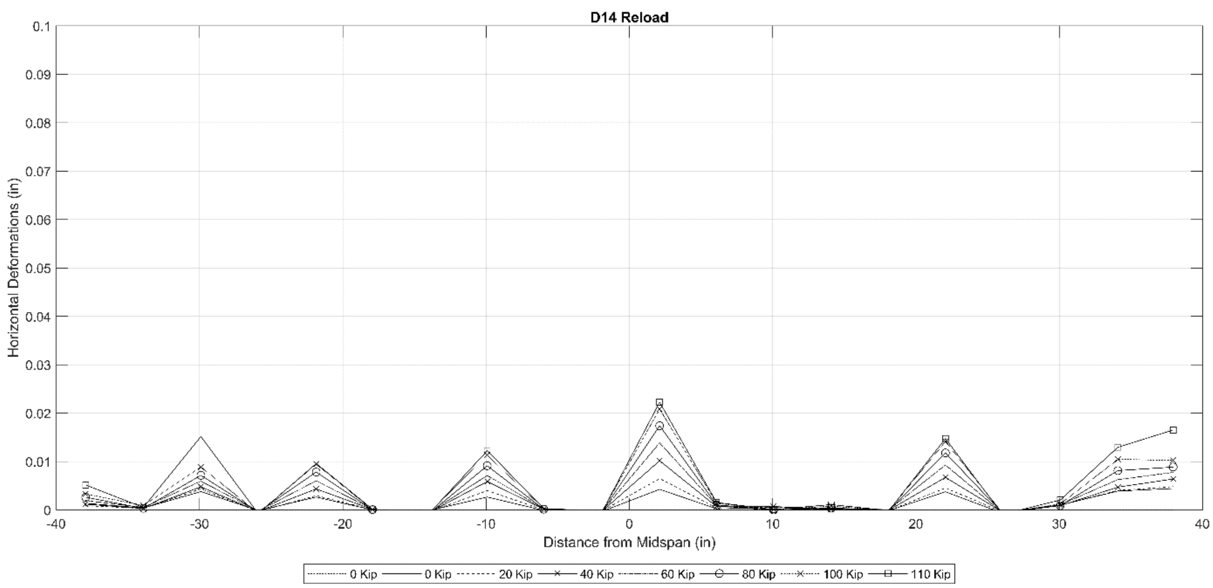

Figure 3-71: Horizontal deformations of concrete surface along splice length of specimen D14, reload (data series are label using the average load applied to the splice ends)

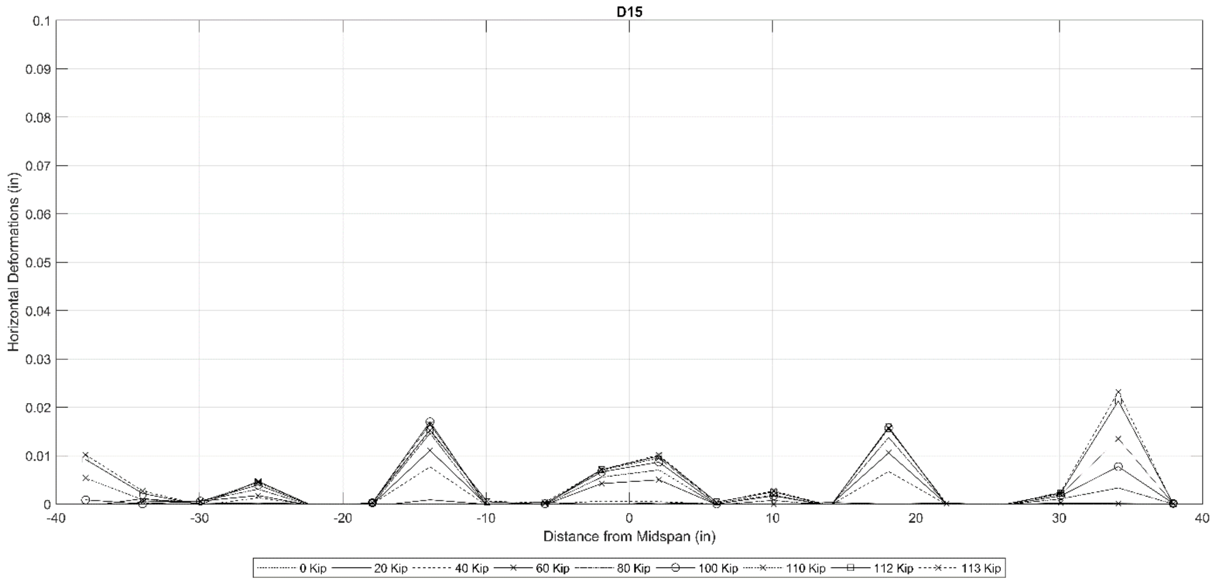

Figure 3-72: Horizontal deformations of concrete surface along splice length of specimen D15, initial loading (data series are label using the average load applied to the splice ends)

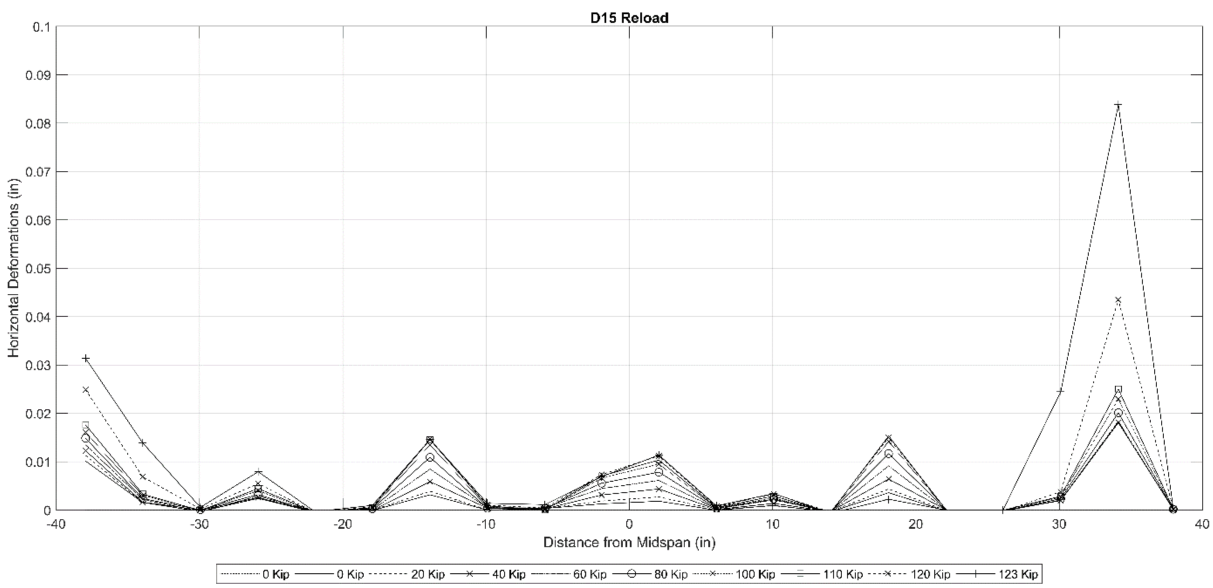

Figure 3-73: Horizontal deformations of concrete surface along splice length of specimen D15, reload (data series are label using the average load applied to the splice ends)

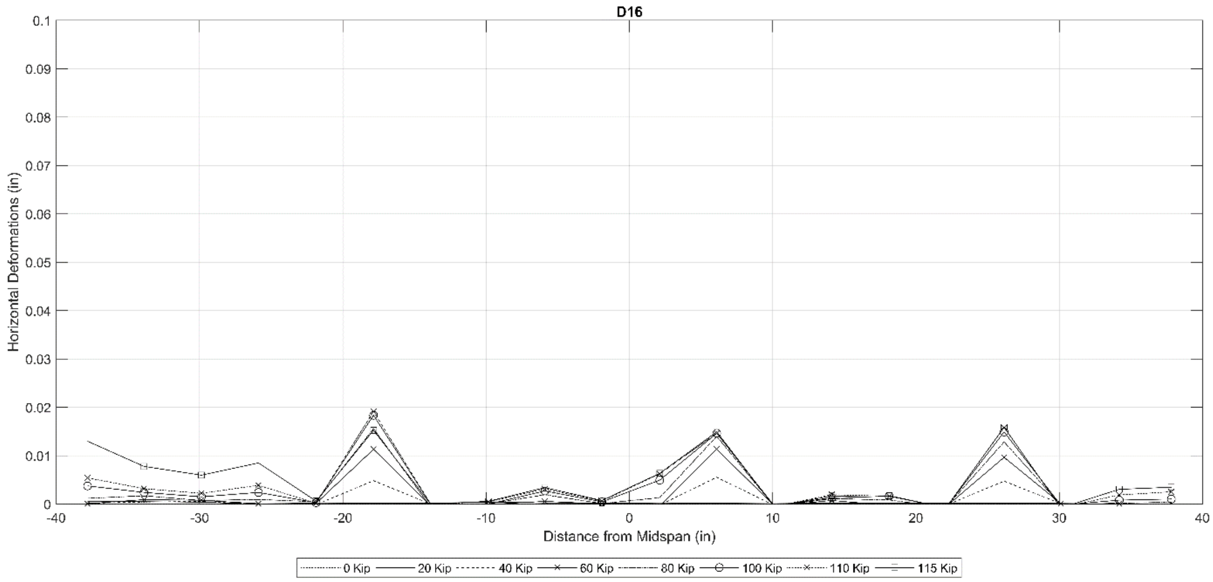

Figure 3-74: Horizontal deformations of concrete surface along splice length of specimen D16, initial loading (data series are label using the average load applied to the splice ends)

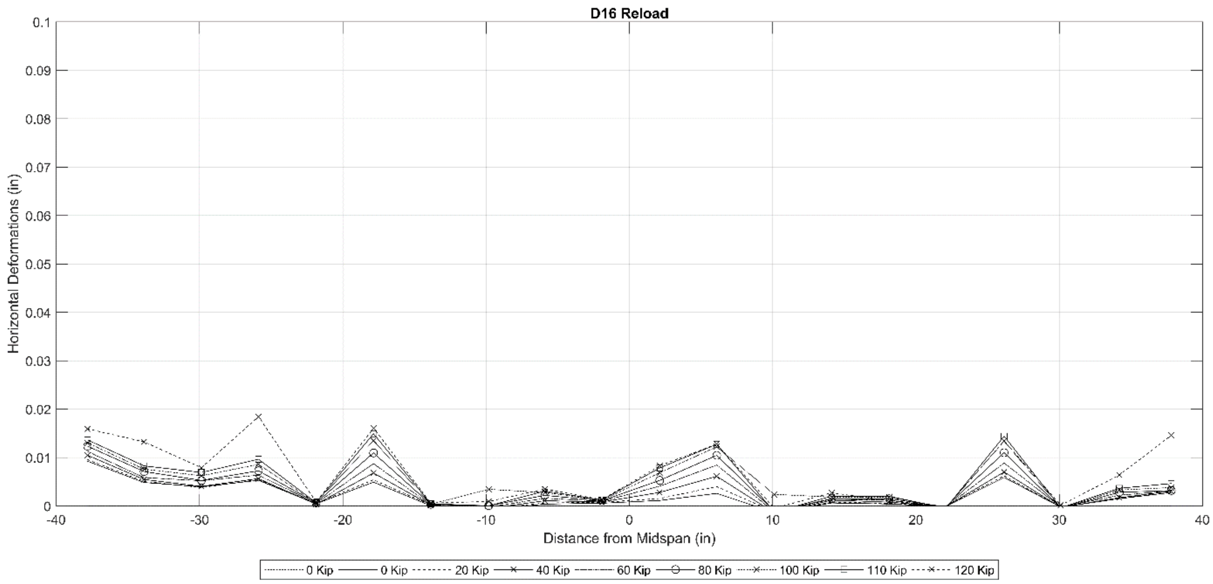

Figure 3-75: Horizontal deformations of concrete surface along splice length of specimen D16, reload (data series are label using the average load applied to the splice ends)

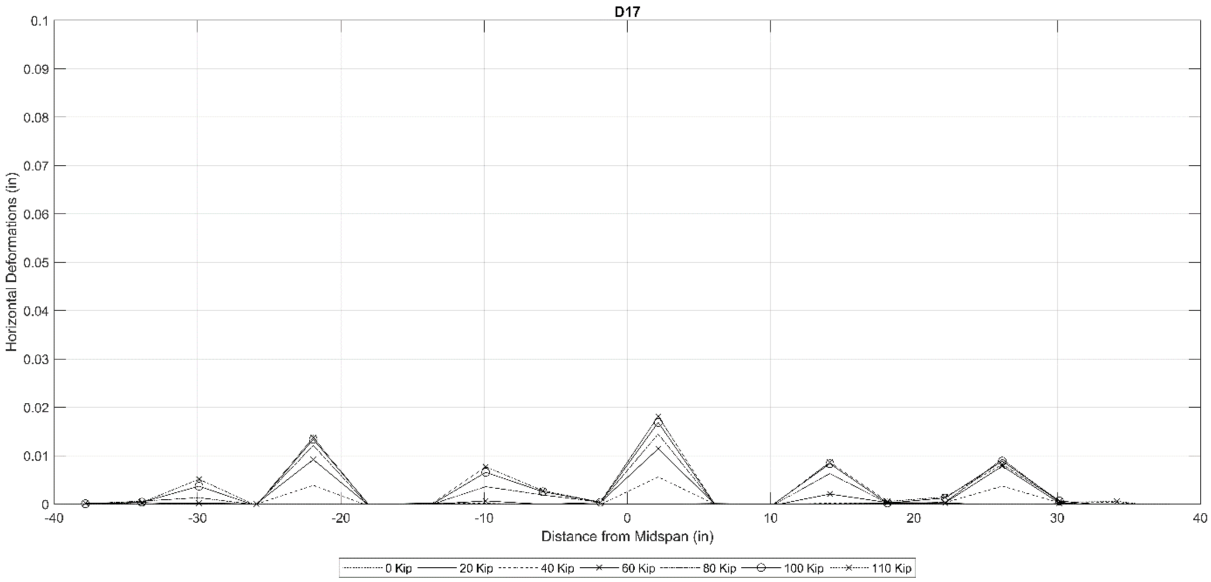

Figure 3-76: Horizontal deformations of concrete surface along splice length of specimen D17, initial loading (data series are label using the average load applied to the splice ends)

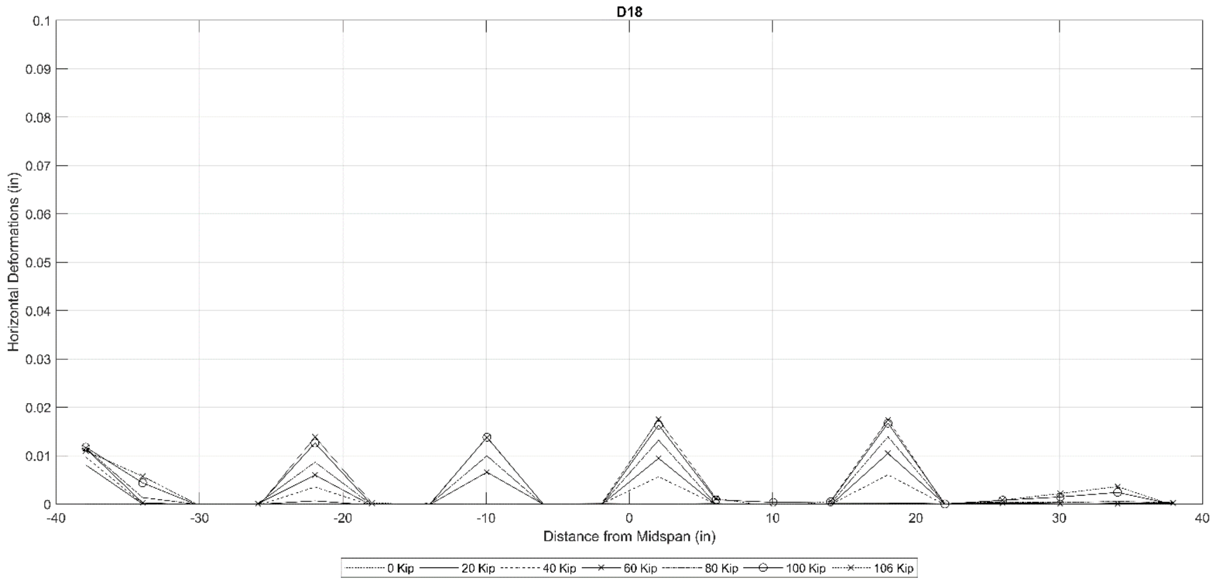

Figure 3-77: Horizontal deformations of concrete surface along splice length of specimen D18, initial loading (data series are label using the average load applied to the splice ends)

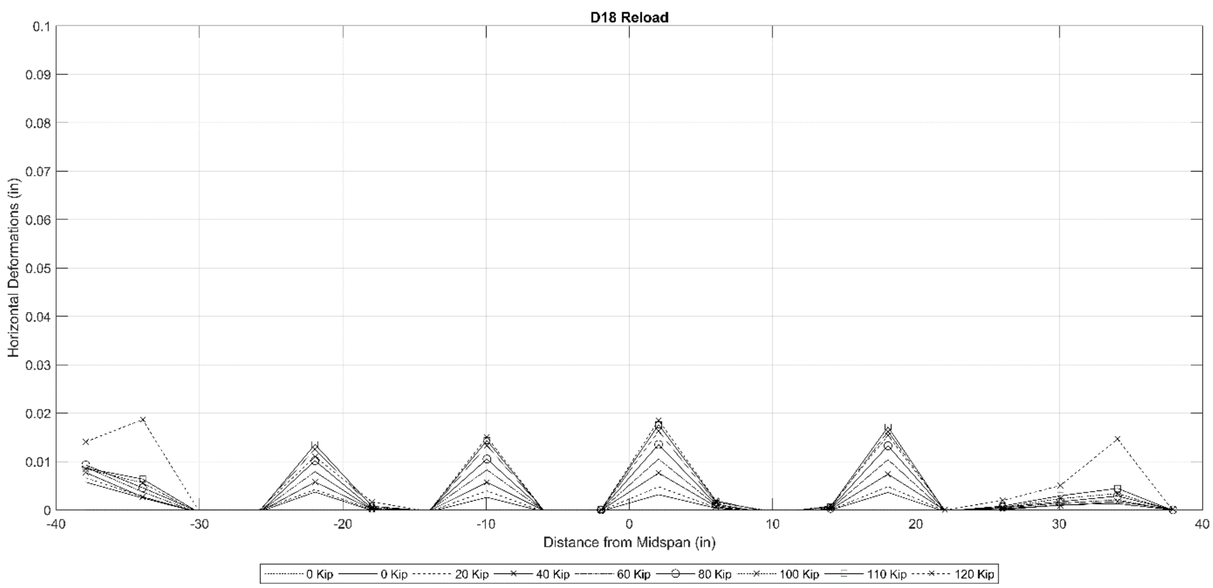

Figure 3-78: Horizontal deformations of concrete surface along splice length of specimen D18, reload (data series are label using the average load applied to the splice ends)

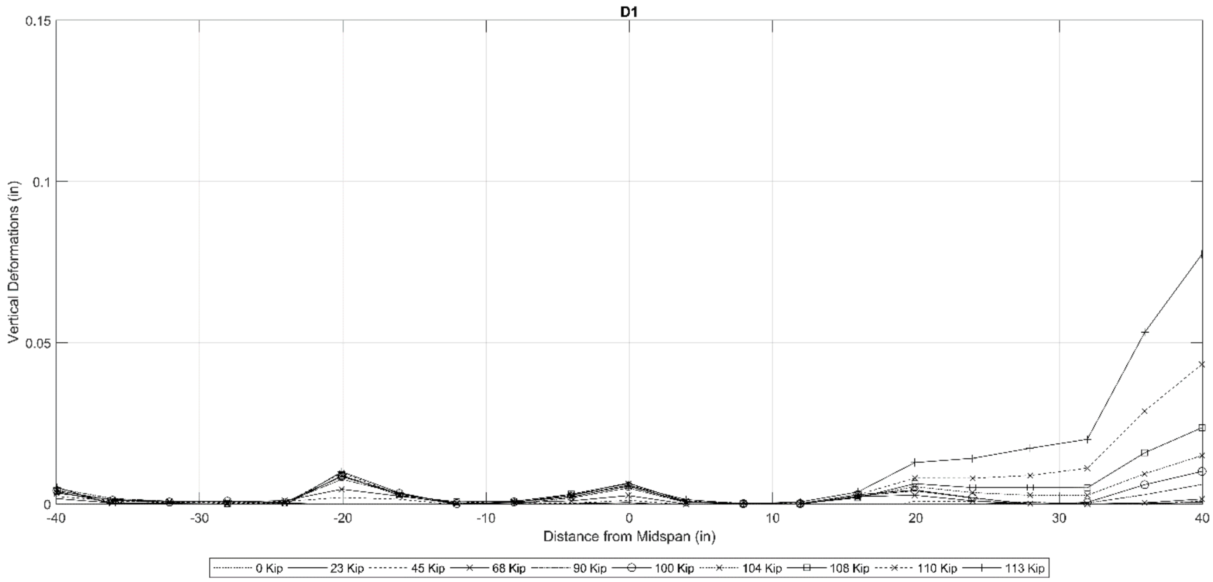

Figure 3-79: Vertical deformations of concrete surface along splice length of specimen D1, initial loading (data series are label using the average load applied to the splice ends)

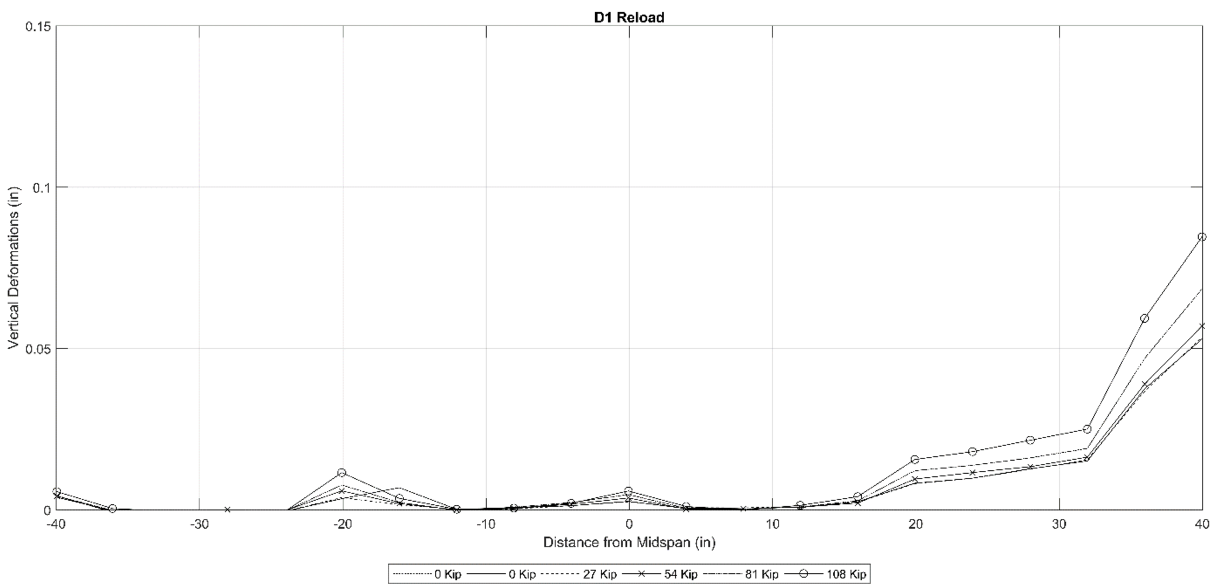

Figure 3-80: Vertical deformations of concrete surface along splice length of specimen D1, reload (data series are label using the average load applied to the splice ends)

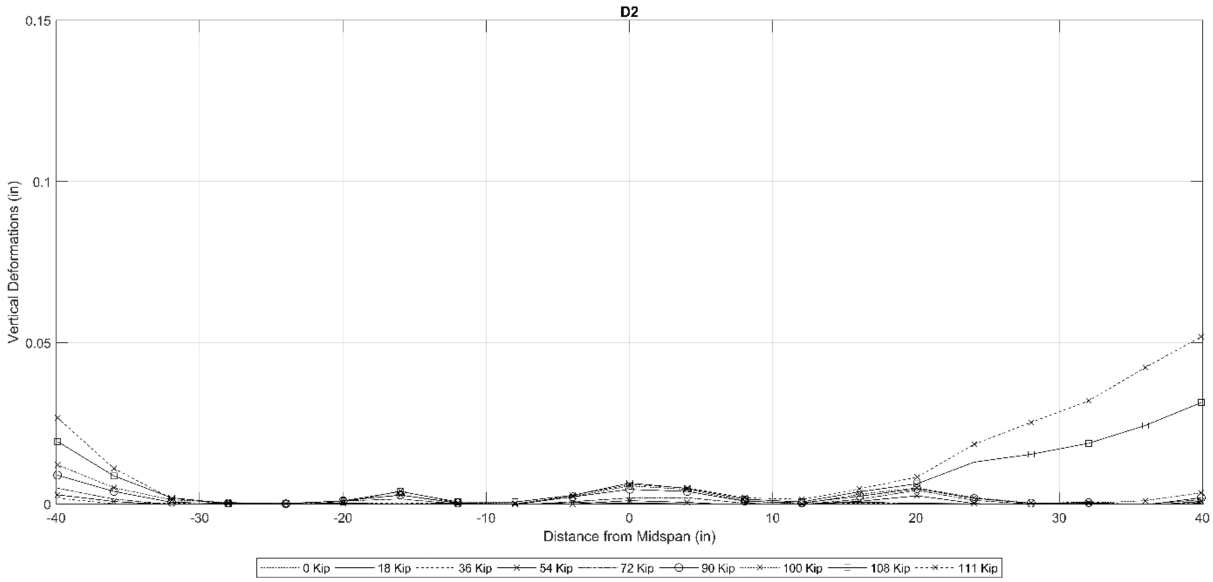

Figure 3-81: Vertical deformations of concrete surface along splice length of specimen D2, initial loading (data series are label using the average load applied to the splice ends)

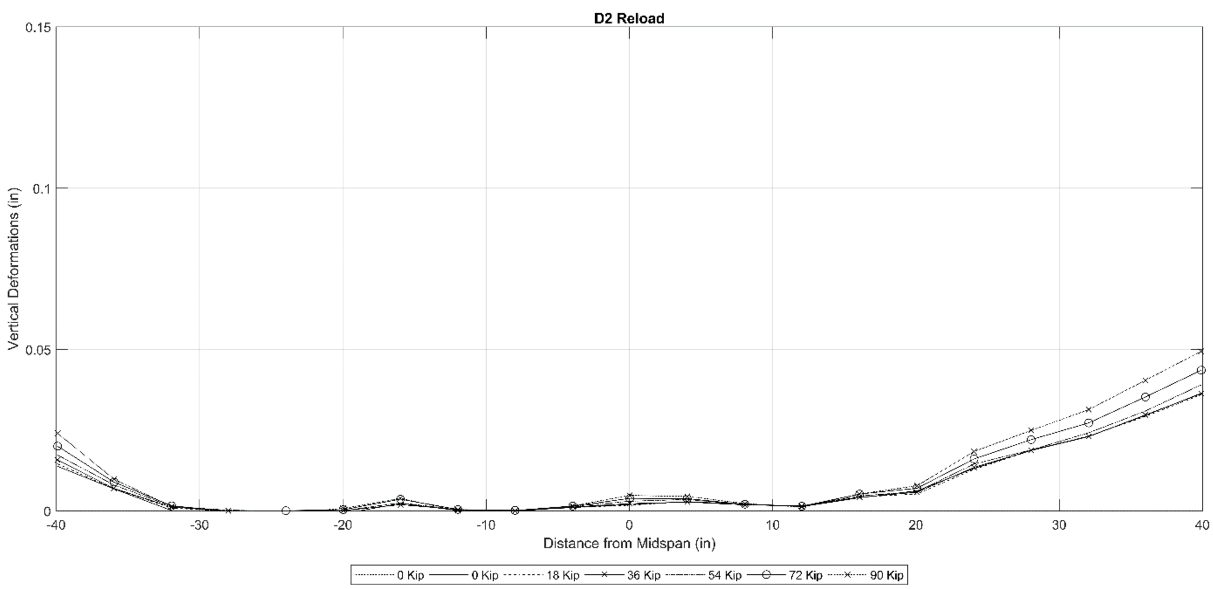

Figure 3-82: Vertical deformations of concrete surface along splice length of specimen D1, reload (data series are label using the average load applied to the splice ends)

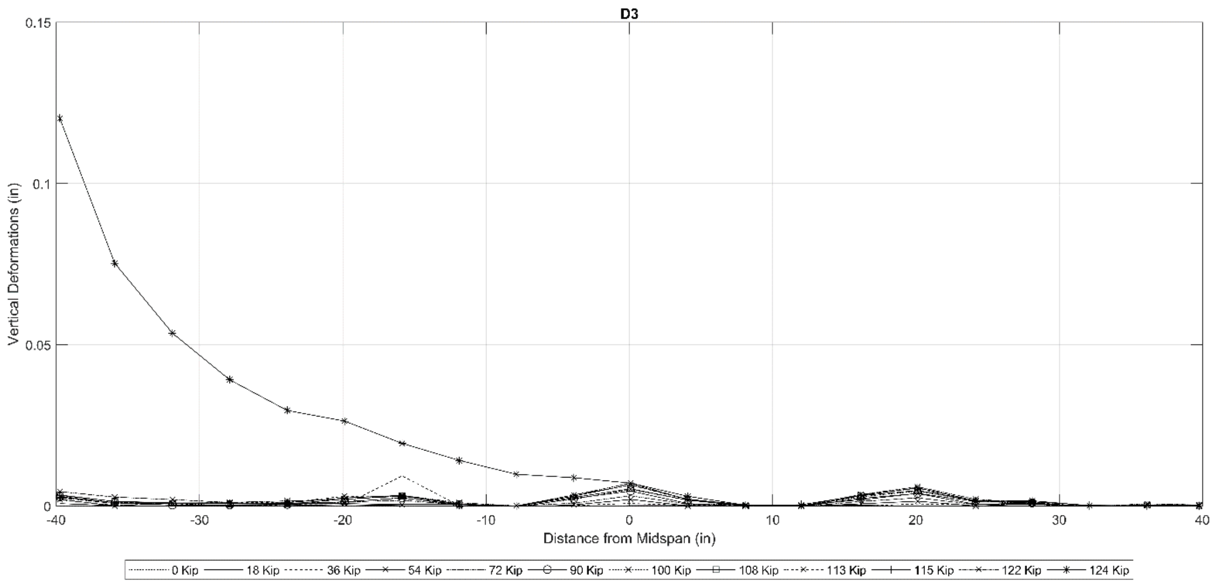

Figure 3-83: Vertical deformations of concrete surface along splice length of specimen D3, initial loading (data series are label using the average load applied to the splice ends)

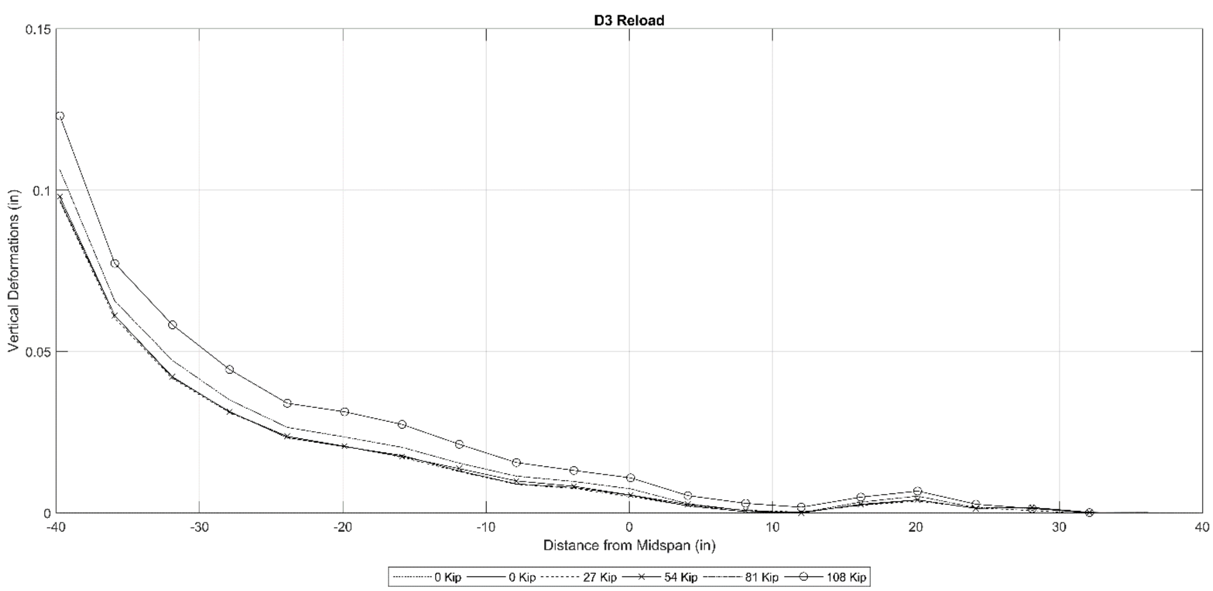

Figure 3-84: Vertical deformations of concrete surface along splice length of specimen D3, reload (data series are label using the average load applied to the splice ends)

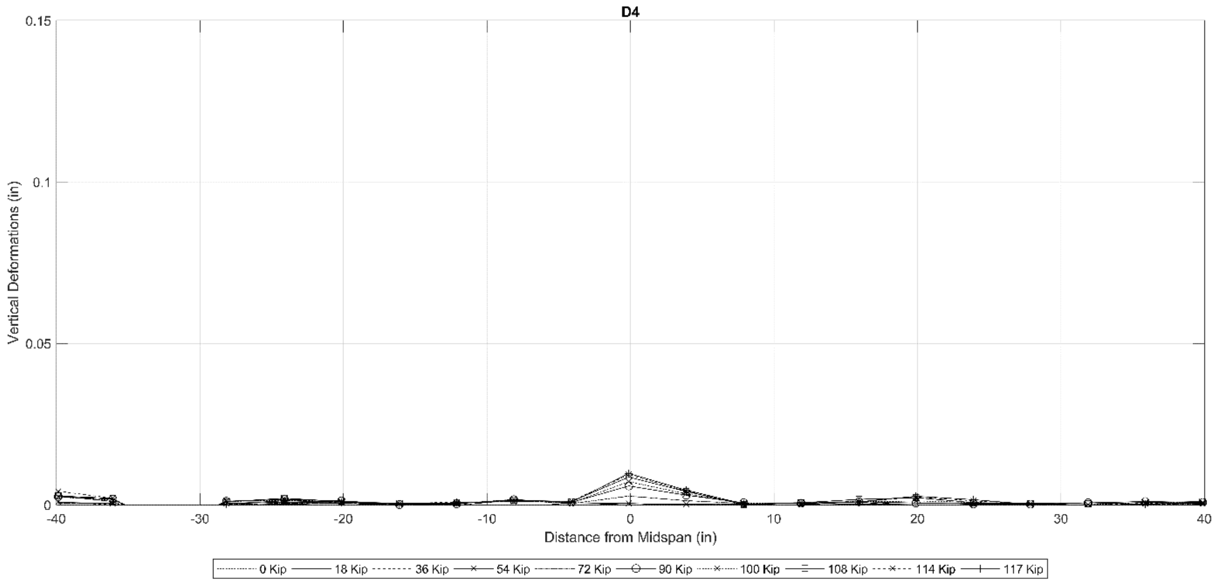

Figure 3-85: Vertical deformations of concrete surface along splice length of specimen D4, initial loading (data series are label using the average load applied to the splice ends)

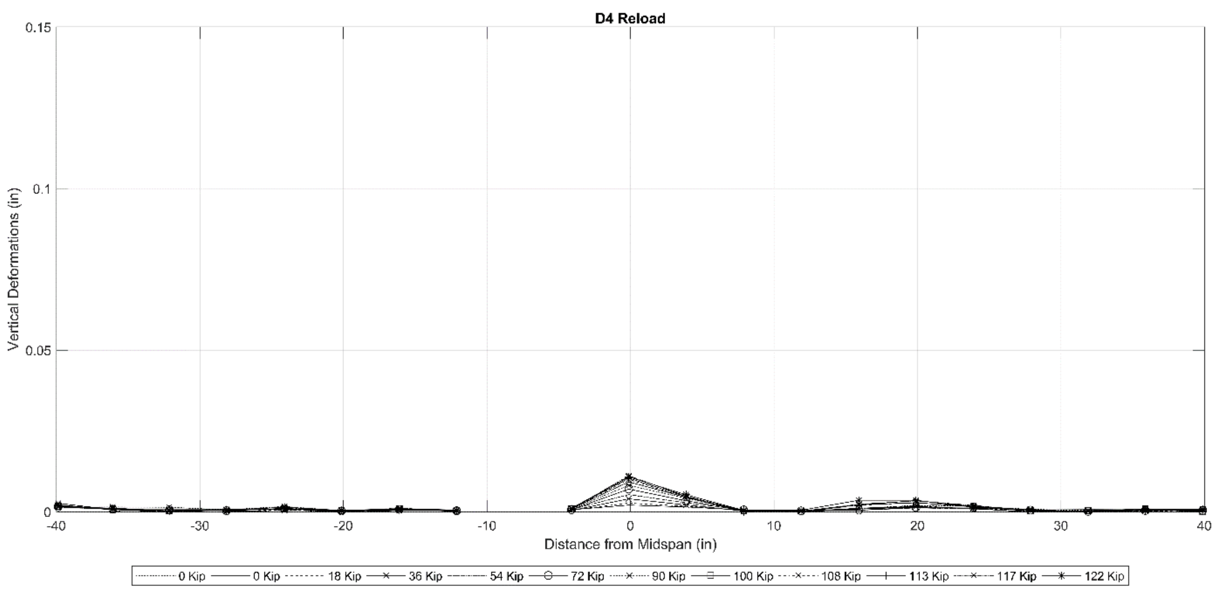

Figure 3-86: Vertical deformations of concrete surface along splice length of specimen D4, reload (data series are label using the average load applied to the splice ends)

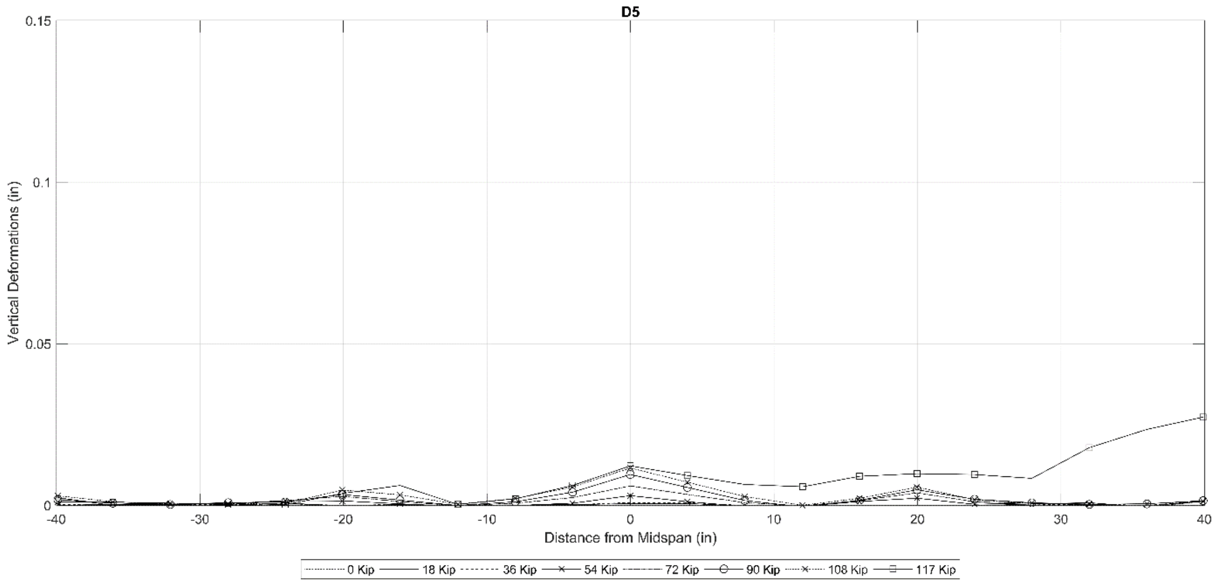

Figure 3-87: Vertical deformations of concrete surface along splice length of specimen D5, initial loading (data series are label using the average load applied to the splice ends)

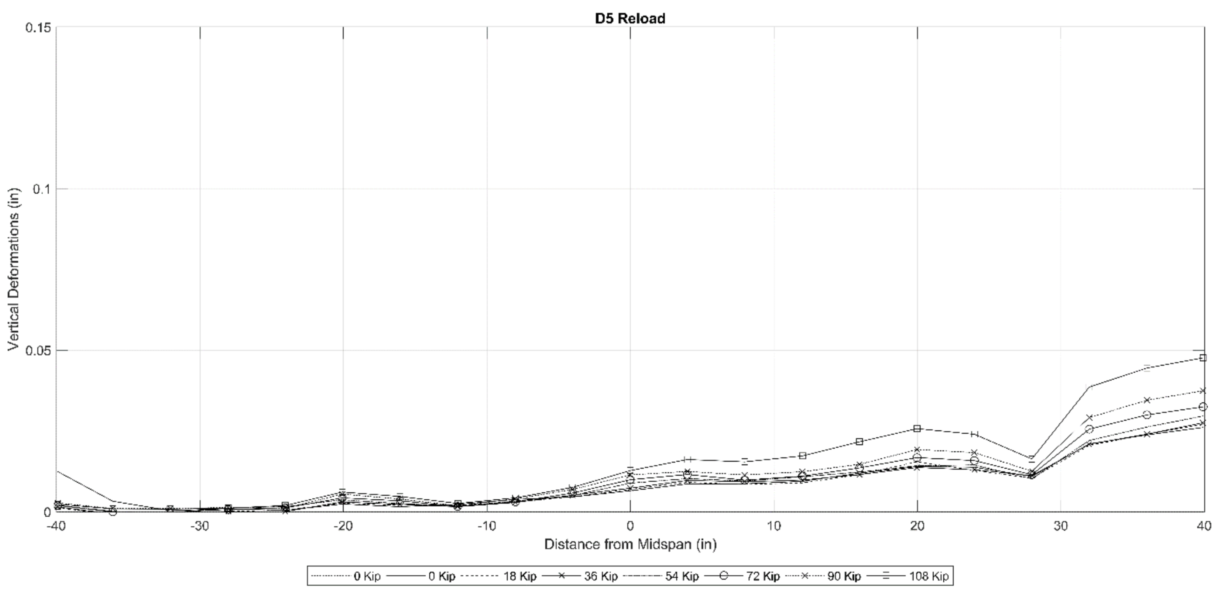

Figure 3-88: Vertical deformations of concrete surface along splice length of specimen D5, reload (data series are label using the average load applied to the splice ends)

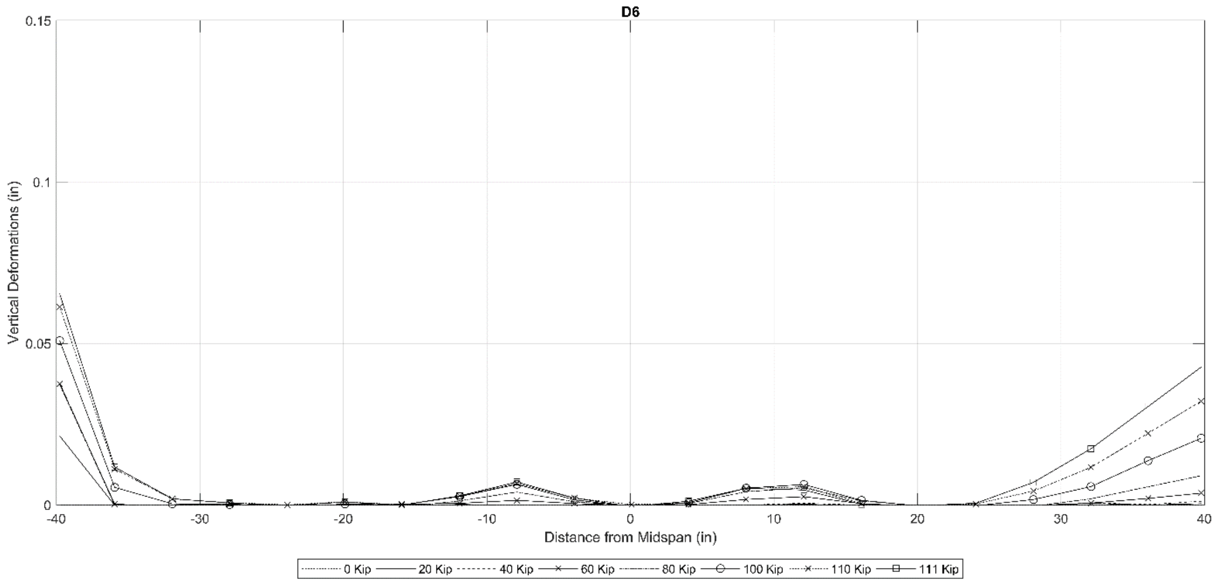

Figure 3-89: Vertical deformations of concrete surface along splice length of specimen D6, initial loading (data series are label using the average load applied to the splice ends)

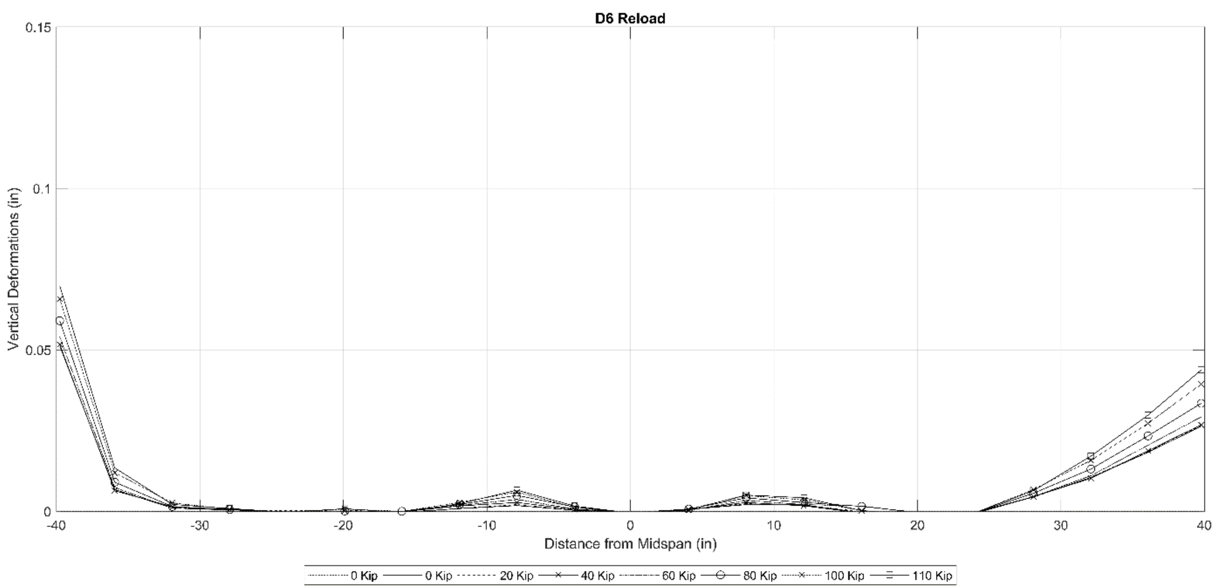

Figure 3-90: Vertical deformations of concrete surface along splice length of specimen D6, reload (data series are label using the average load applied to the splice ends)

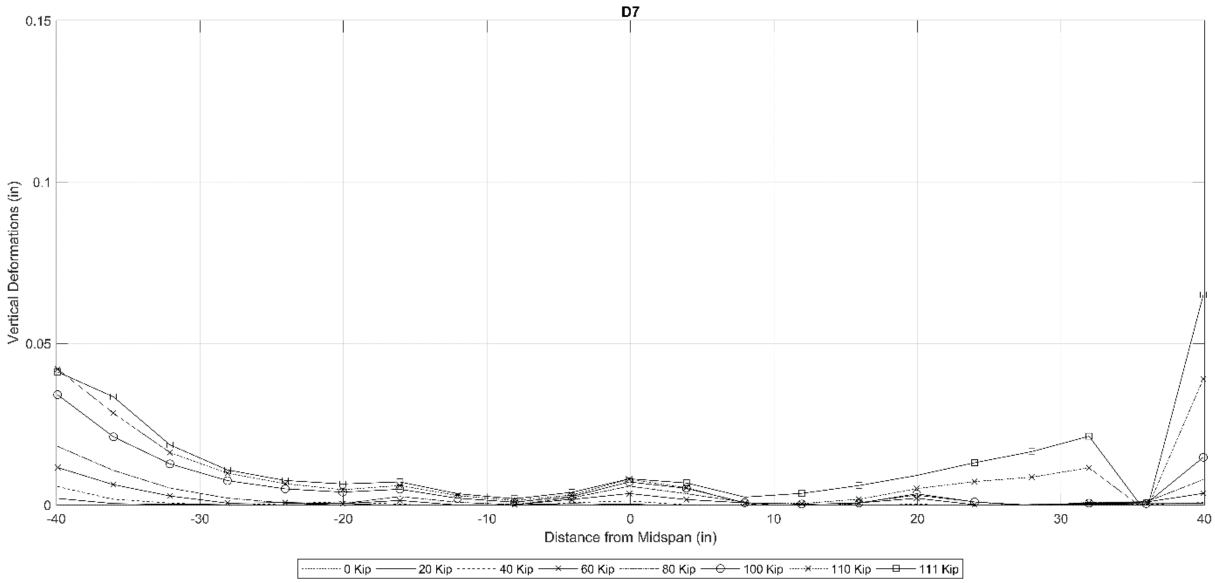

Figure 3-91: Vertical deformations of concrete surface along splice length of specimen D7, initial loading (data series are label using the average load applied to the splice ends)

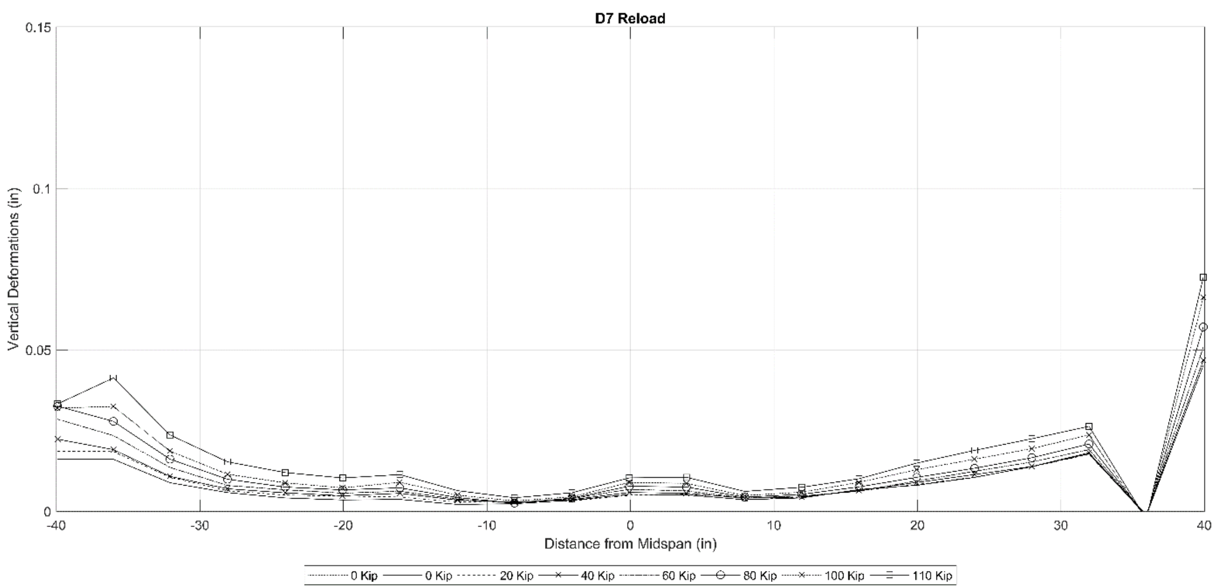

Figure 3-92: Vertical deformations of concrete surface along splice length of specimen D7, reload (data series are label using the average load applied to the splice ends)

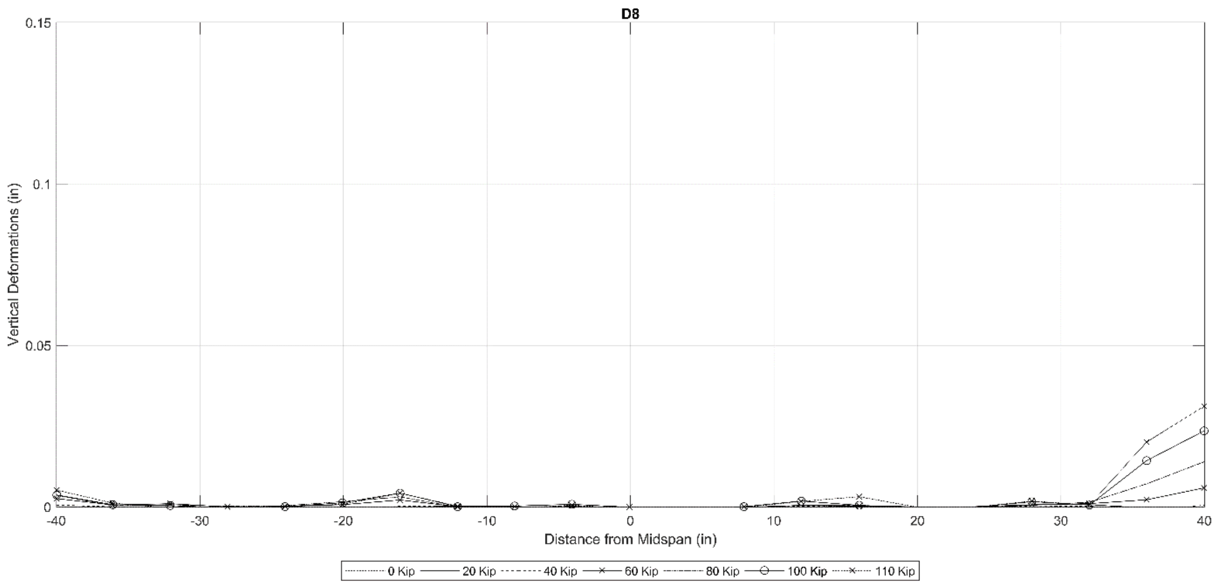

Figure 3-93: Vertical deformations of concrete surface along splice length of specimen D8, initial loading (data series are label using the average load applied to the splice ends)

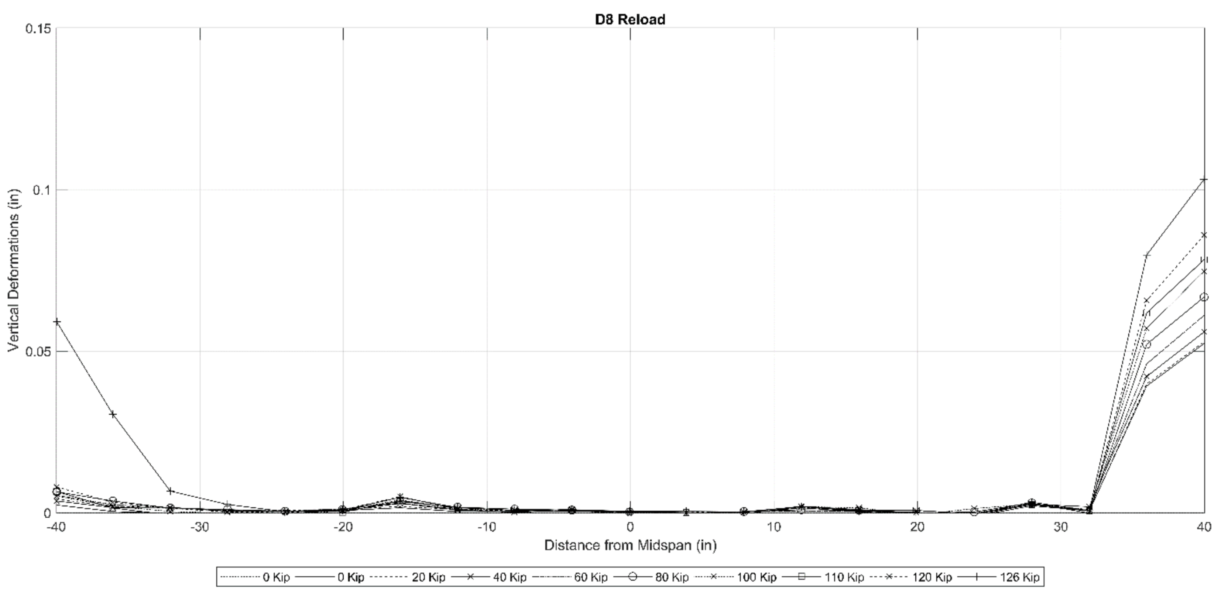

Figure 3-94: Vertical deformations of concrete surface along splice length of specimen D8, reload (data series are label using the average load applied to the splice ends)

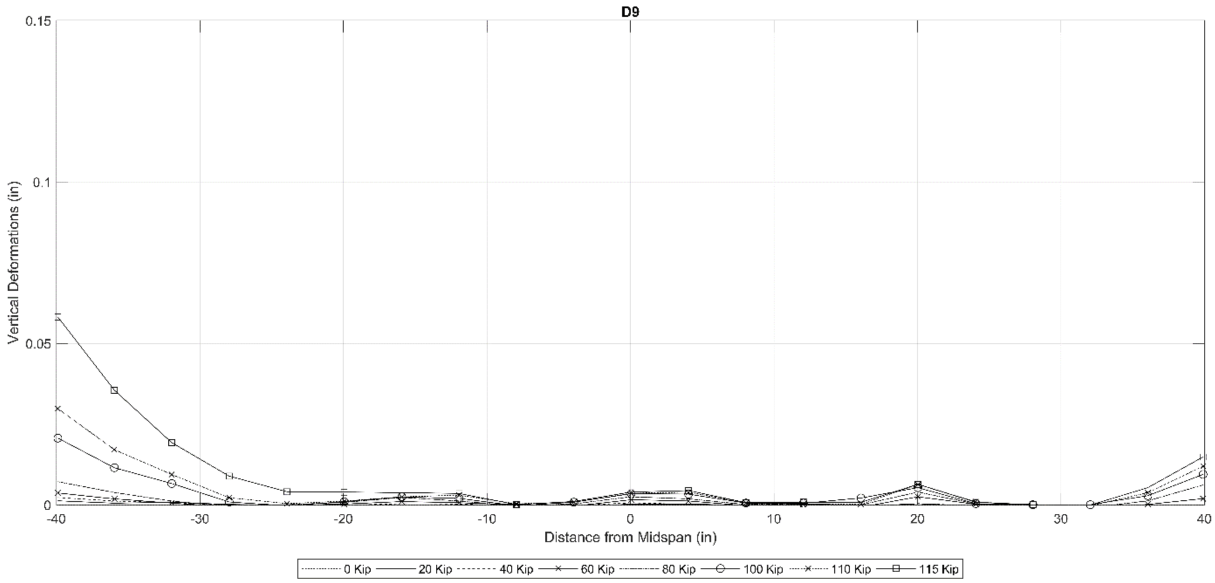

Figure 3-95: Vertical deformations of concrete surface along splice length of specimen D9, initial loading (data series are label using the average load applied to the splice ends)

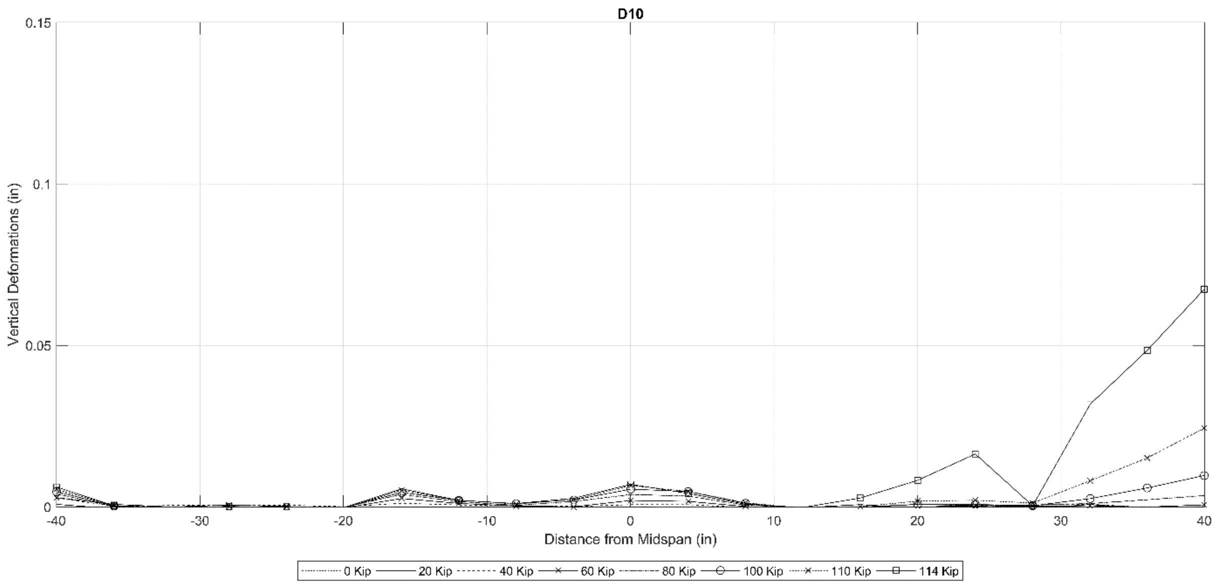

Figure 3-96: Vertical deformations of concrete surface along splice length of specimen D10, initial loading (data series are label using the average load applied to the splice ends)

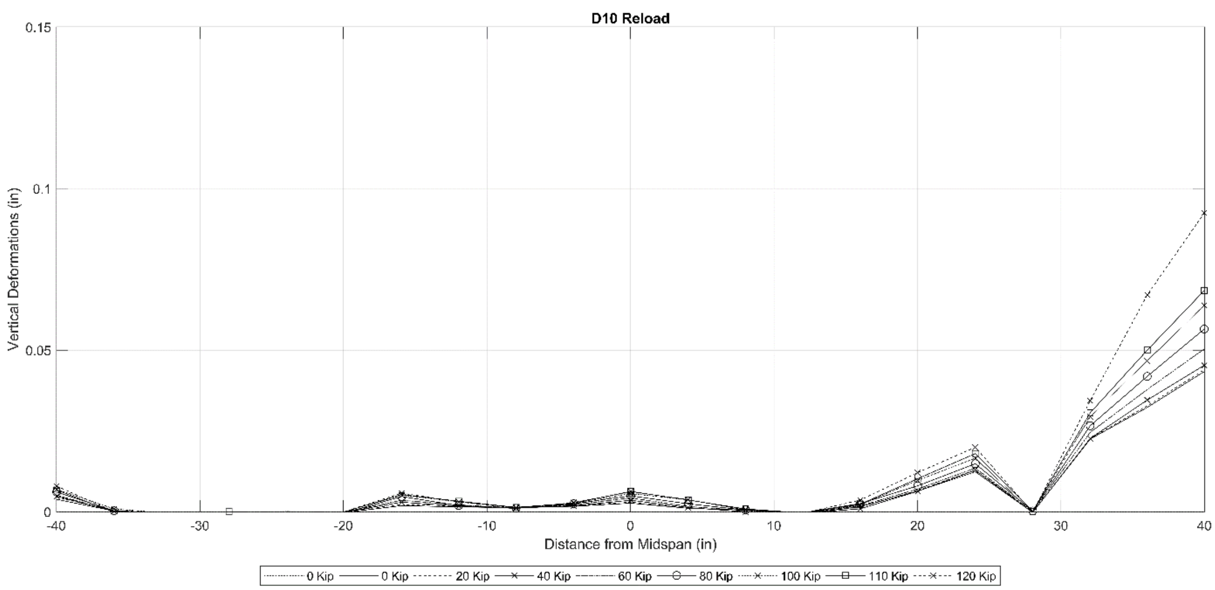

Figure 3-97: Vertical deformations of concrete surface along splice length of specimen D10, reload (data series are label using the average load applied to the splice ends)

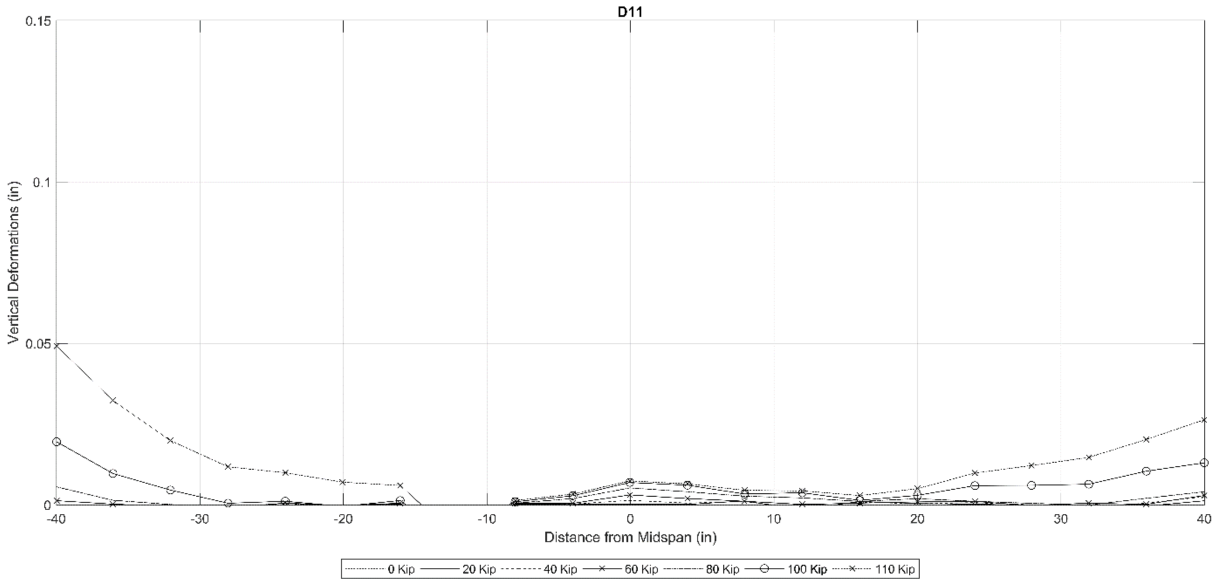

Figure 3-98: Vertical deformations of concrete surface along splice length of specimen D11, initial loading (data series are label using the average load applied to the splice ends)

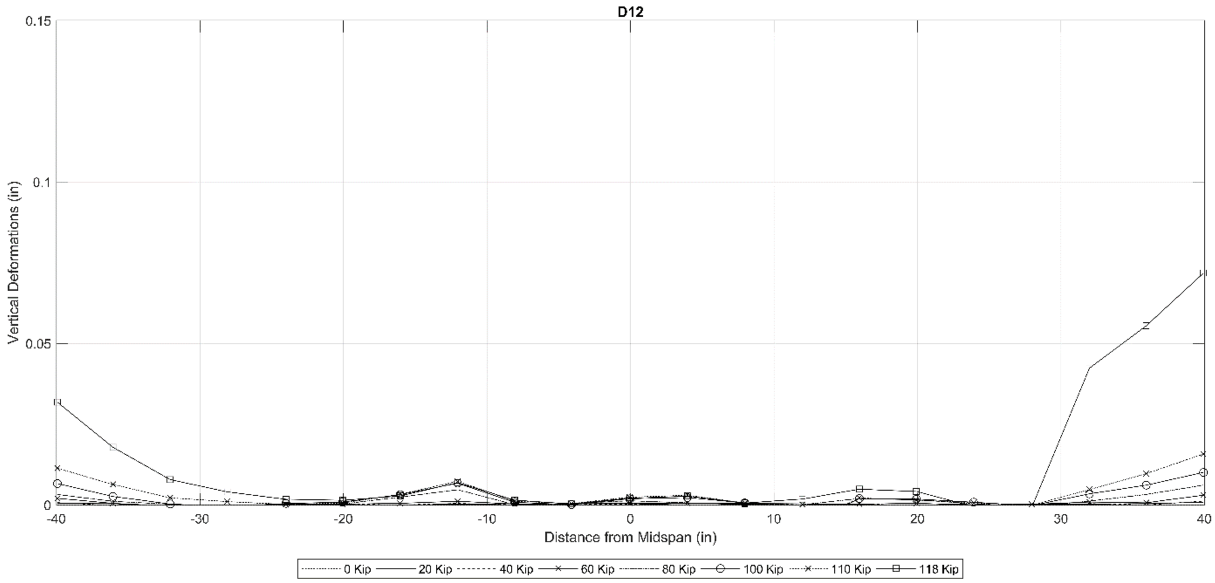

Figure 3-99: Vertical deformations of concrete surface along splice length of specimen D12, initial loading (data series are label using the average load applied to the splice ends)

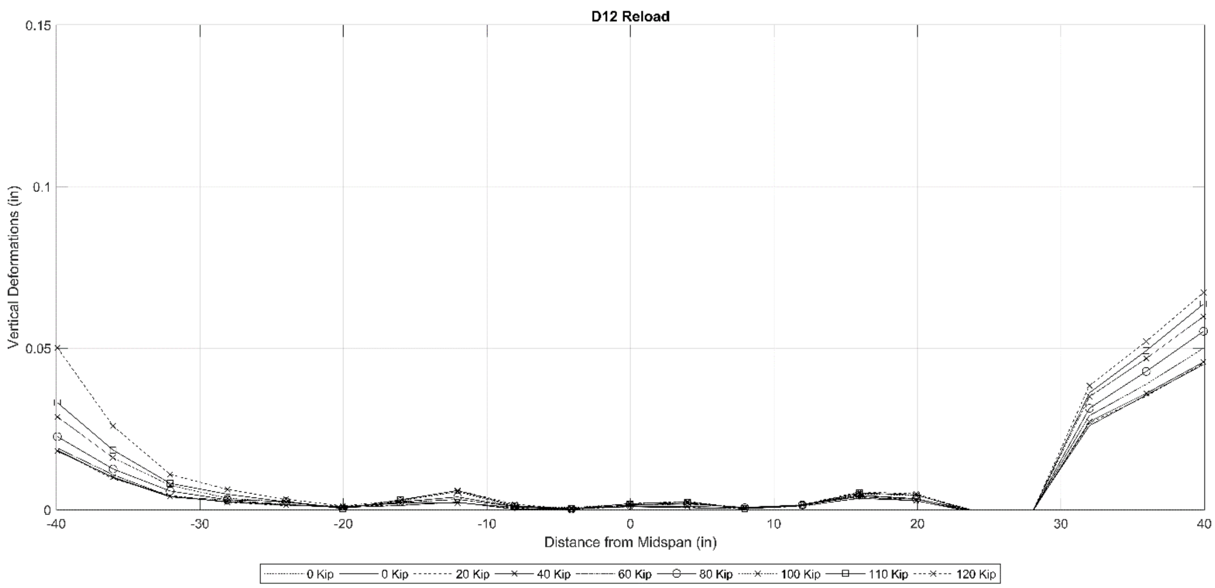

Figure 3-100: Vertical deformations of concrete surface along splice length of specimen D12, reload (data series are label using the average load applied to the splice ends)

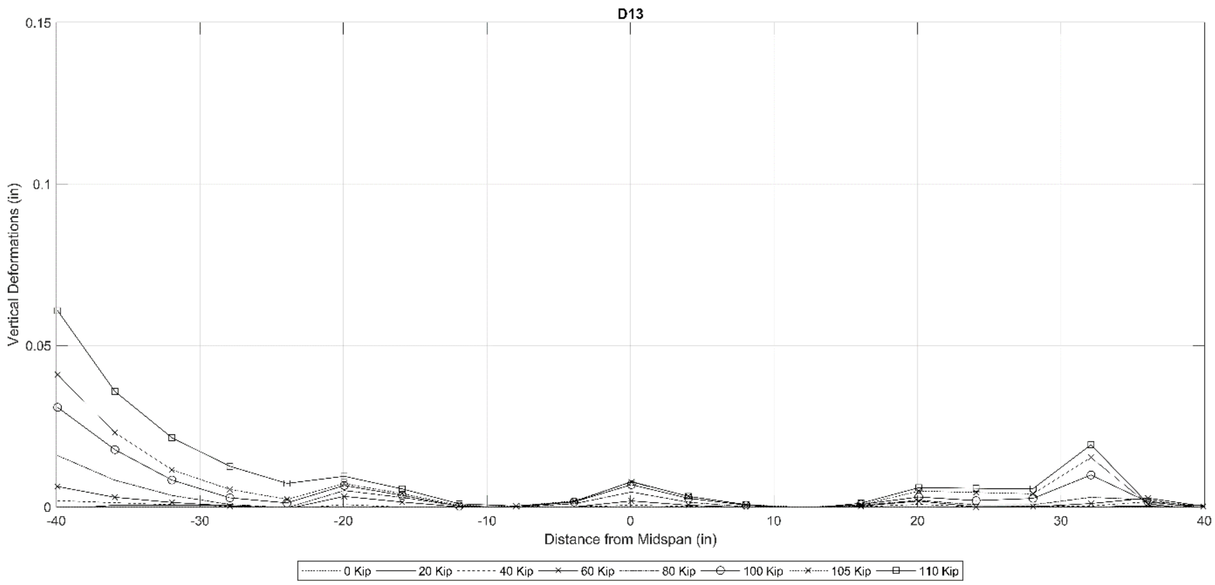

Figure 3-101: Vertical deformations of concrete surface along splice length of specimen D13, initial loading (data series are label using the average load applied to the splice ends)

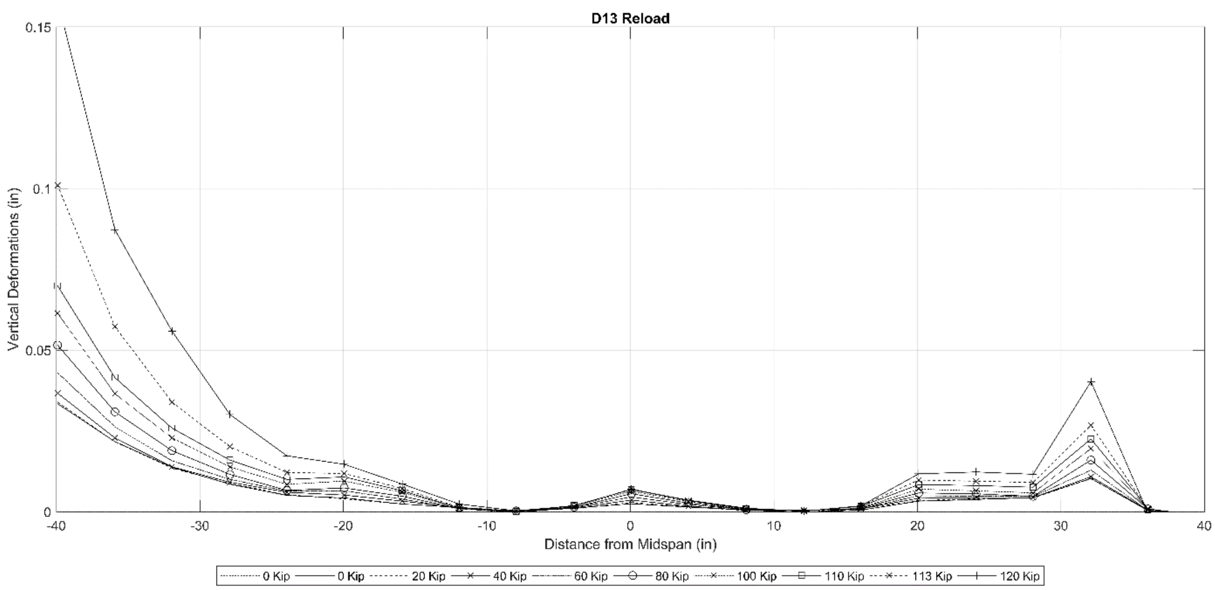

Figure 3-102: Vertical deformations of concrete surface along splice length of specimen D13, reload (data series are label using the average load applied to the splice ends)

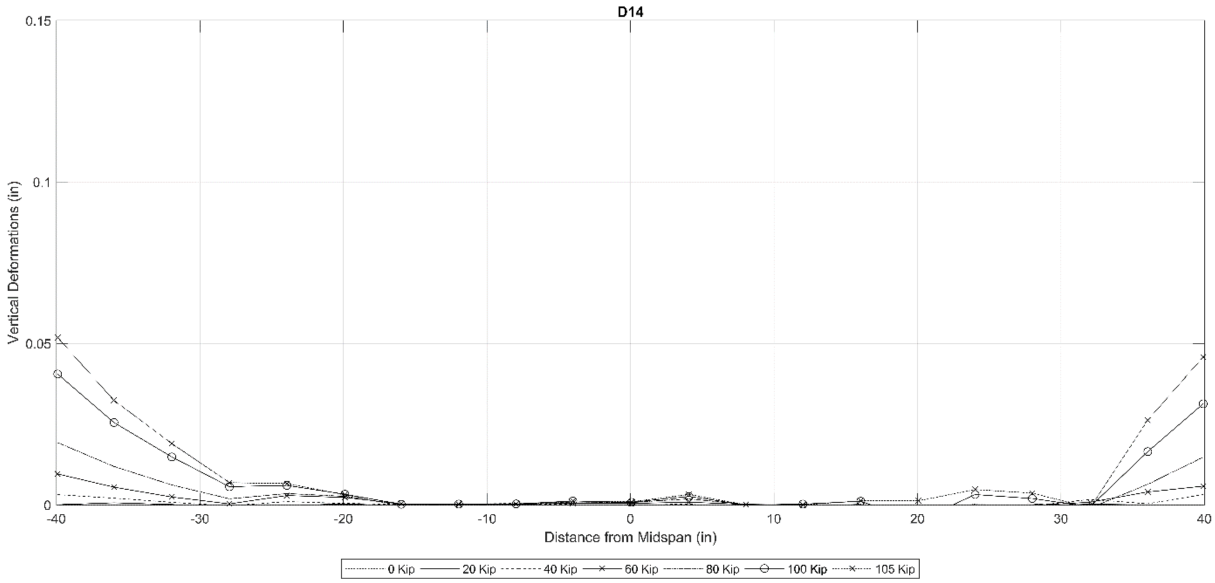

Figure 3-103: Vertical deformations of concrete surface along splice length of specimen D14, initial loading (data series are label using the average load applied to the splice ends)

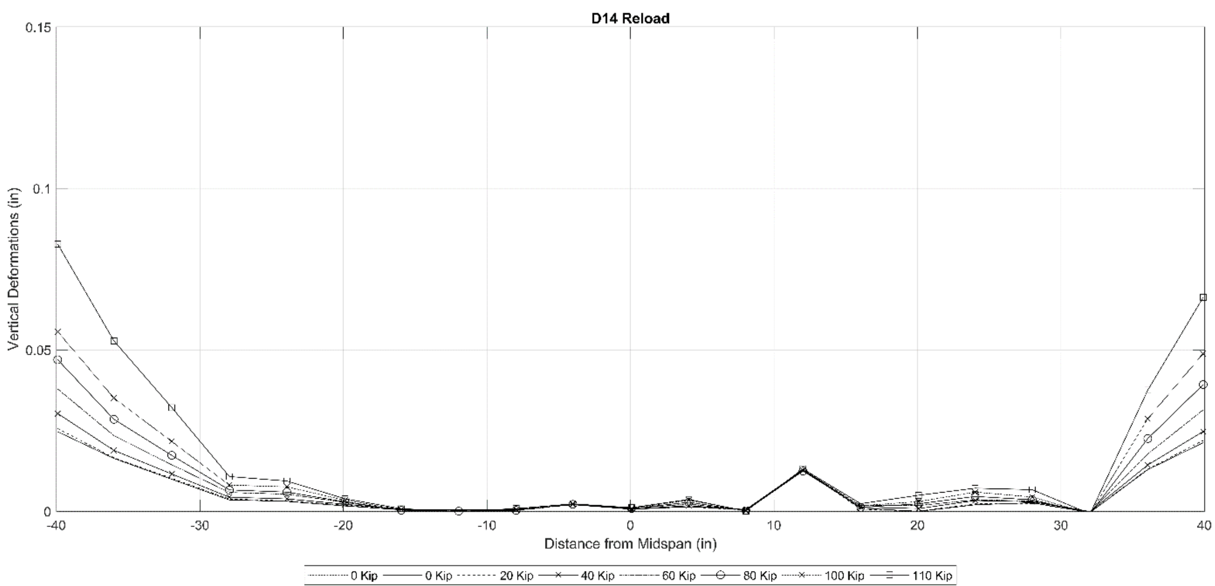

Figure 3-104: Vertical deformations of concrete surface along splice length of specimen D14, reload (data series are label using the average load applied to the splice ends)

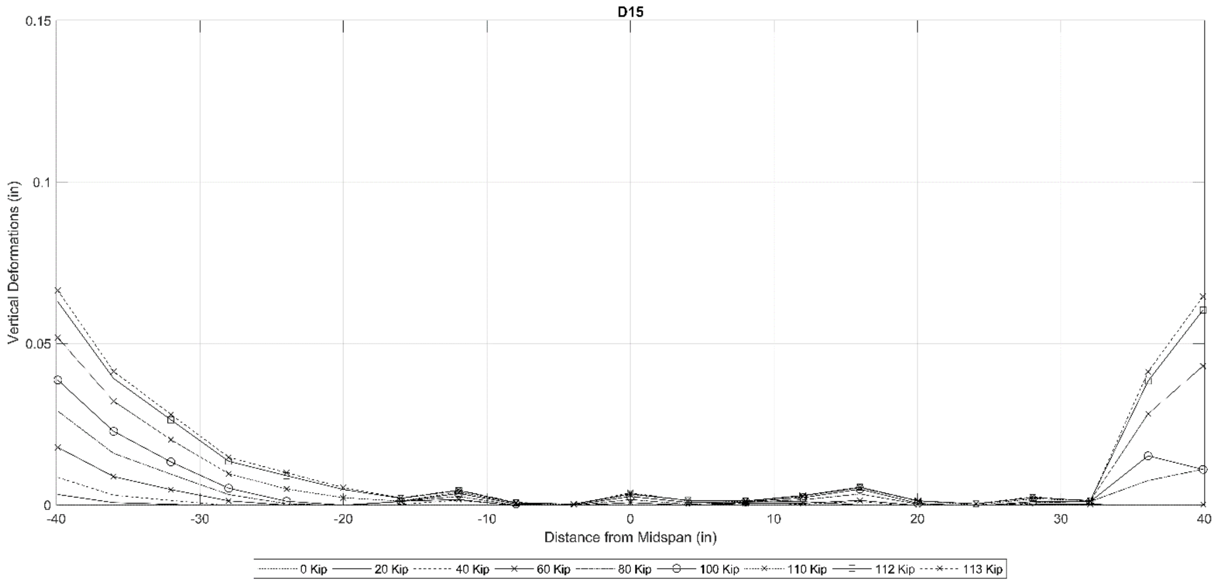

Figure 3-105: Vertical deformations of concrete surface along splice length of specimen D15, initial loading (data series are label using the average load applied to the splice ends)

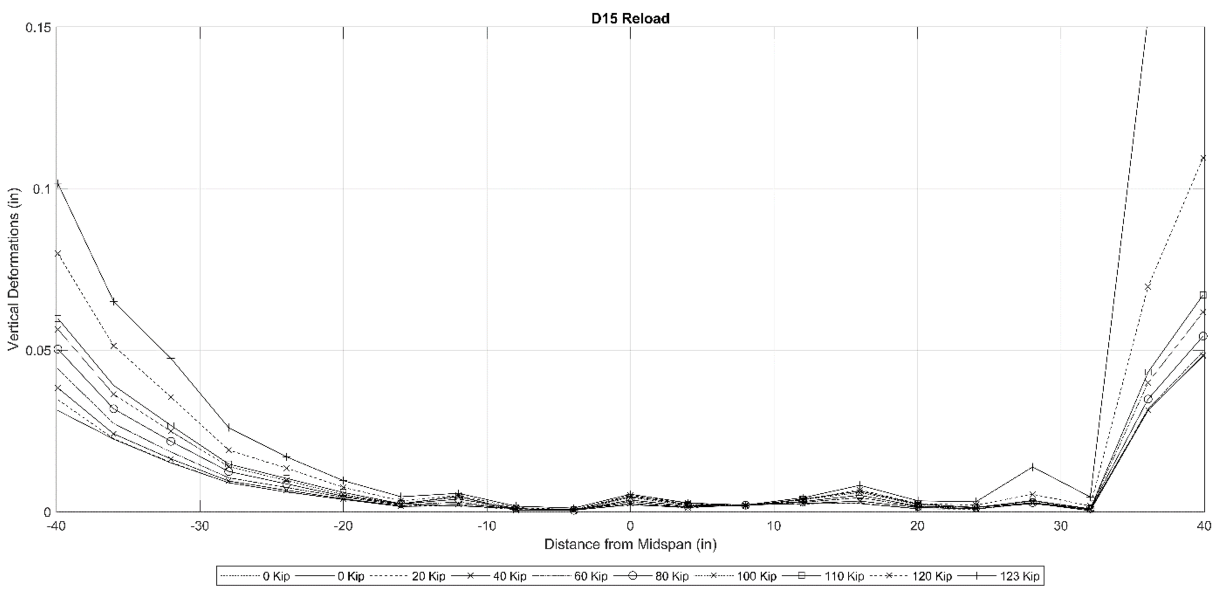

Figure 3-106: Vertical deformations of concrete surface along splice length of specimen D15, reload (data series are label using the average load applied to the splice ends)

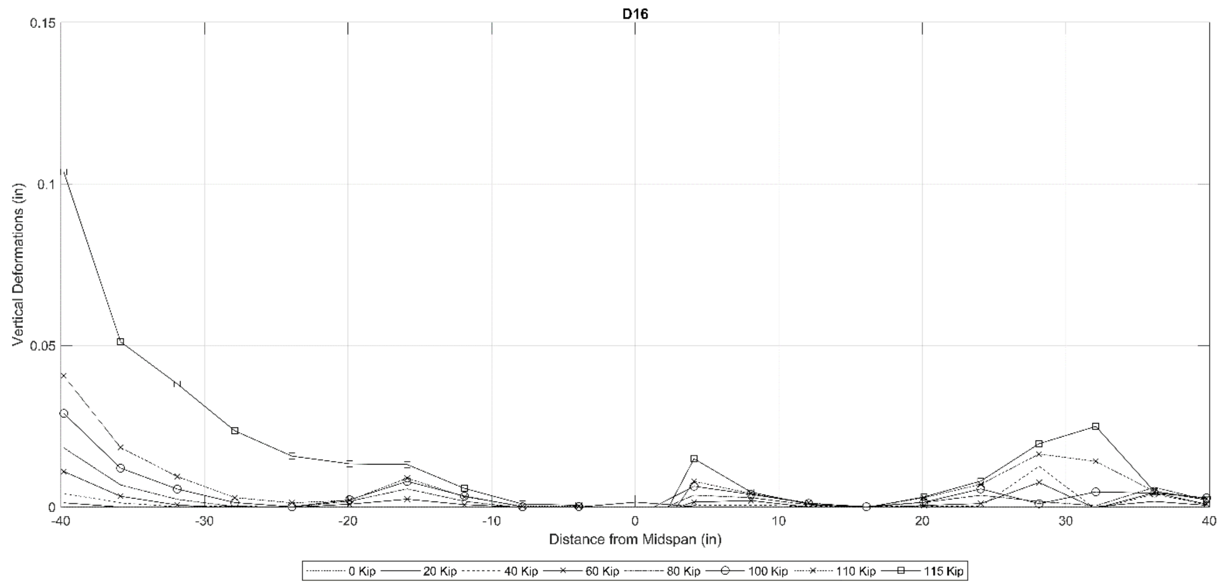

Figure 3-107: Vertical deformations of concrete surface along splice length of specimen D16, initial loading (data series are label using the average load applied to the splice ends)

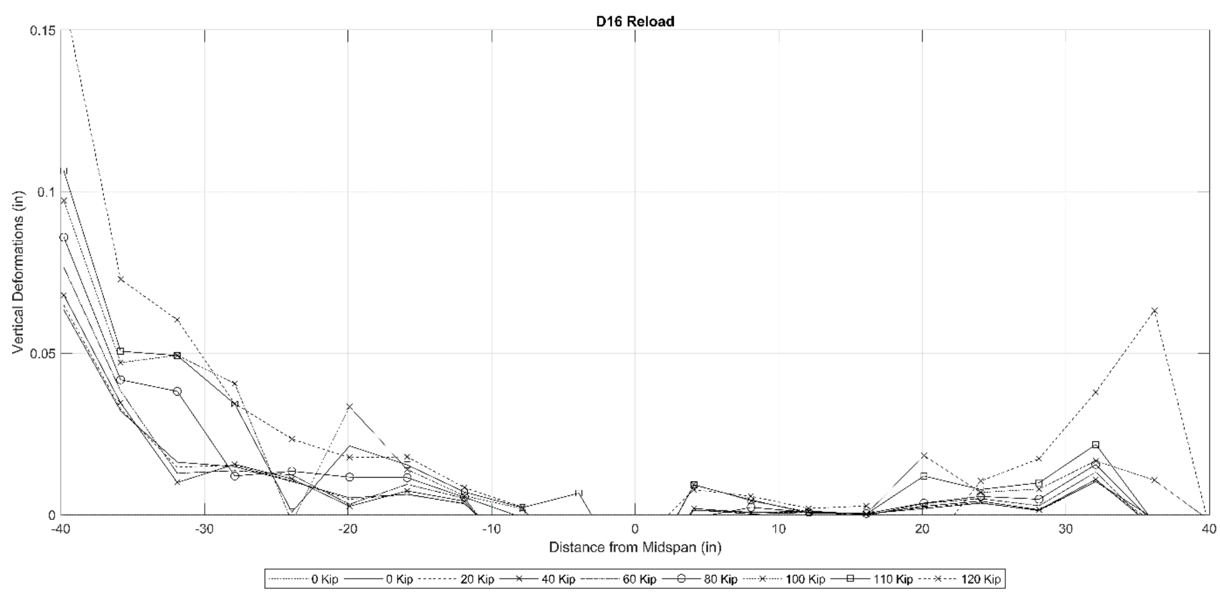

Figure 3-108: Vertical deformations of concrete surface along splice length of specimen D16, reload (data series are label using the average load applied to the splice ends)

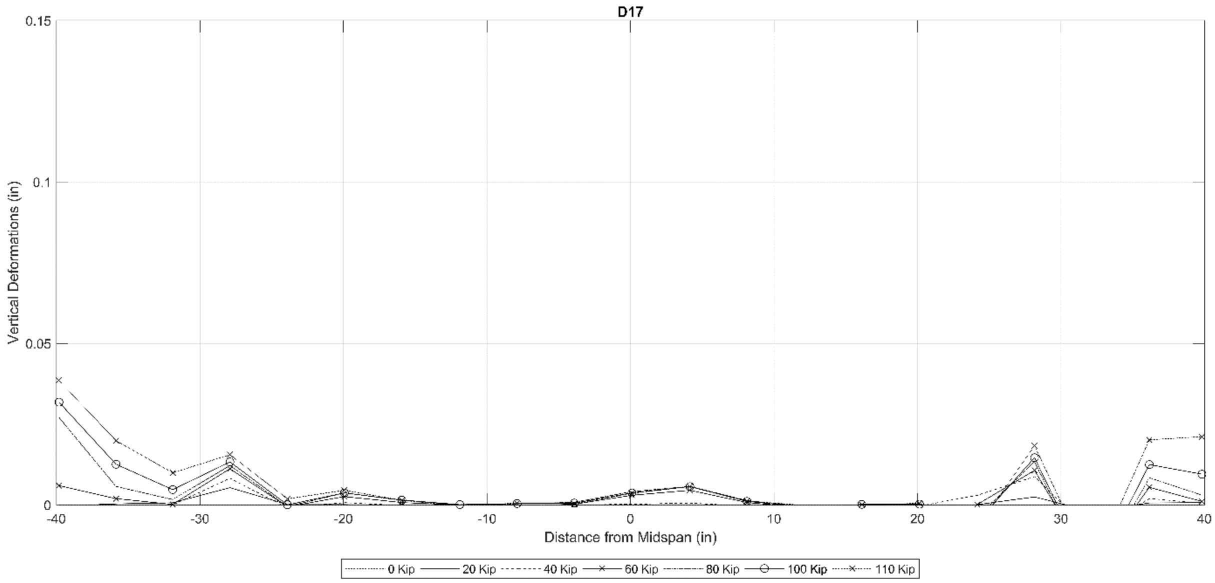

Figure 3-109: Vertical deformations of concrete surface along splice length of specimen D17, initial loading (data series are label using the average load applied to the splice ends)

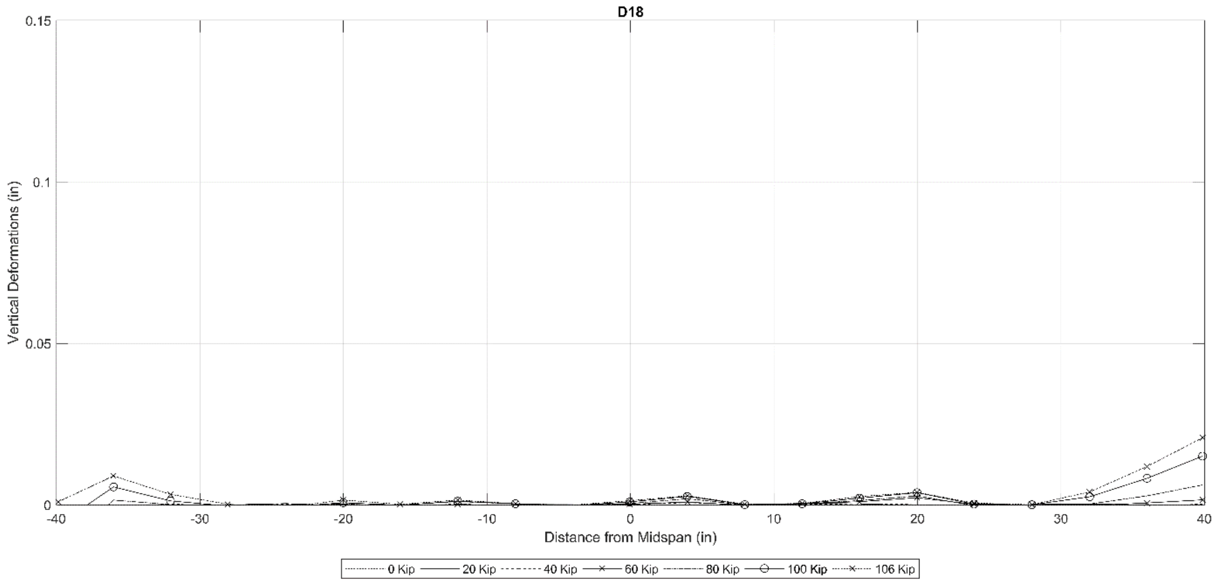

Figure 3-110: Vertical deformations of concrete surface along splice length of specimen D18, initial loading (data series are label using the average load applied to the splice ends)

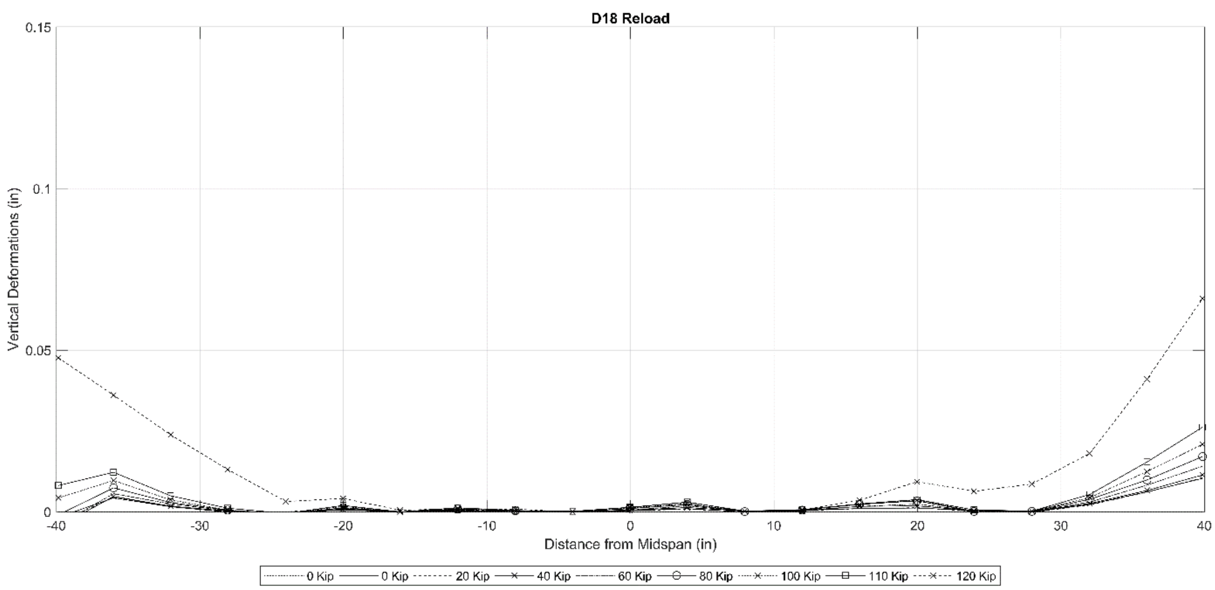

Figure 3-111: Vertical deformations of concrete surface along splice length of specimen D18, reload (data series are label using the average load applied to the splice ends)

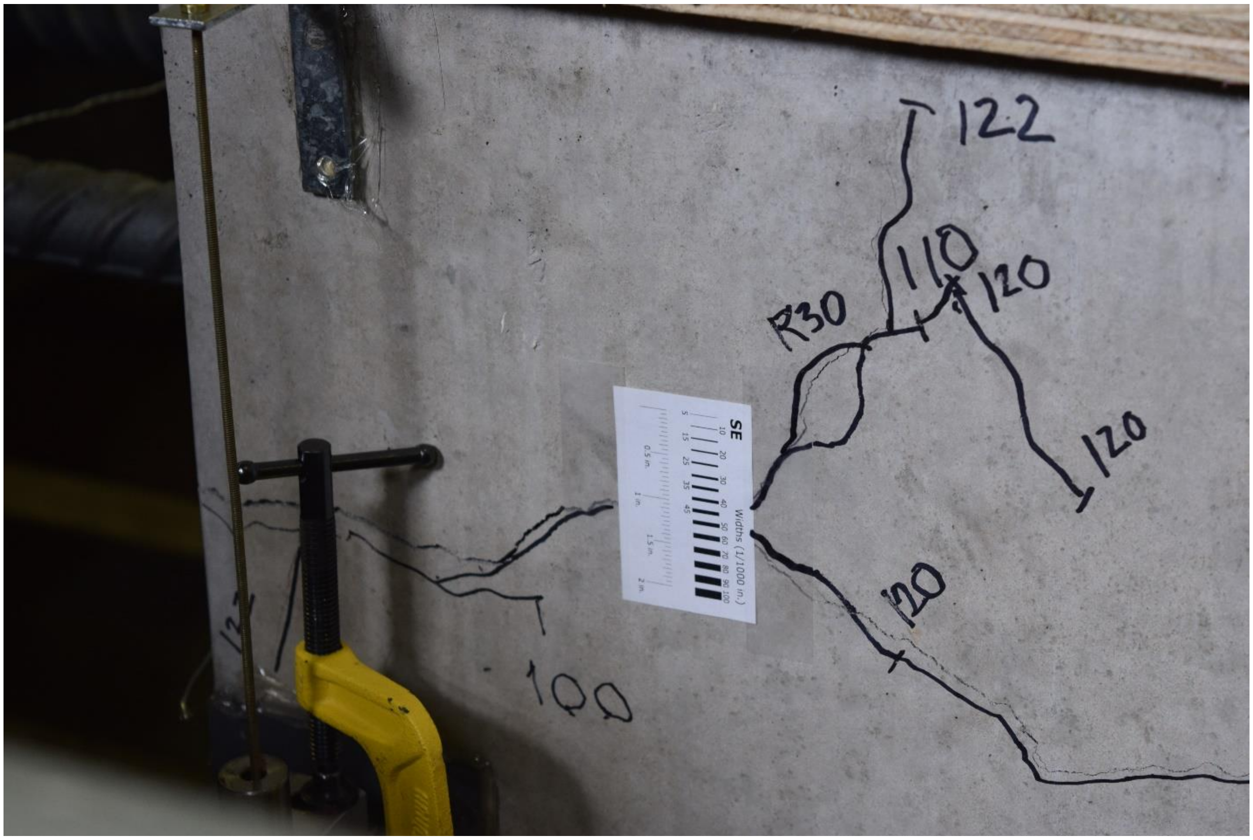

Figure 3-112: Crack pattern for specimen D1, southeast corner (average bar stress = 69 ksi)

Figure 3-113: Crack pattern for specimen D2, northeast corner (average bar stress = 58 ksi)

Figure 3-114: Crack pattern for specimen D3, northwest corner (average bar stress = 69 ksi)

Figure 3-115: Crack pattern for specimen D4, northwest corner (average bar stress = 78 ksi)

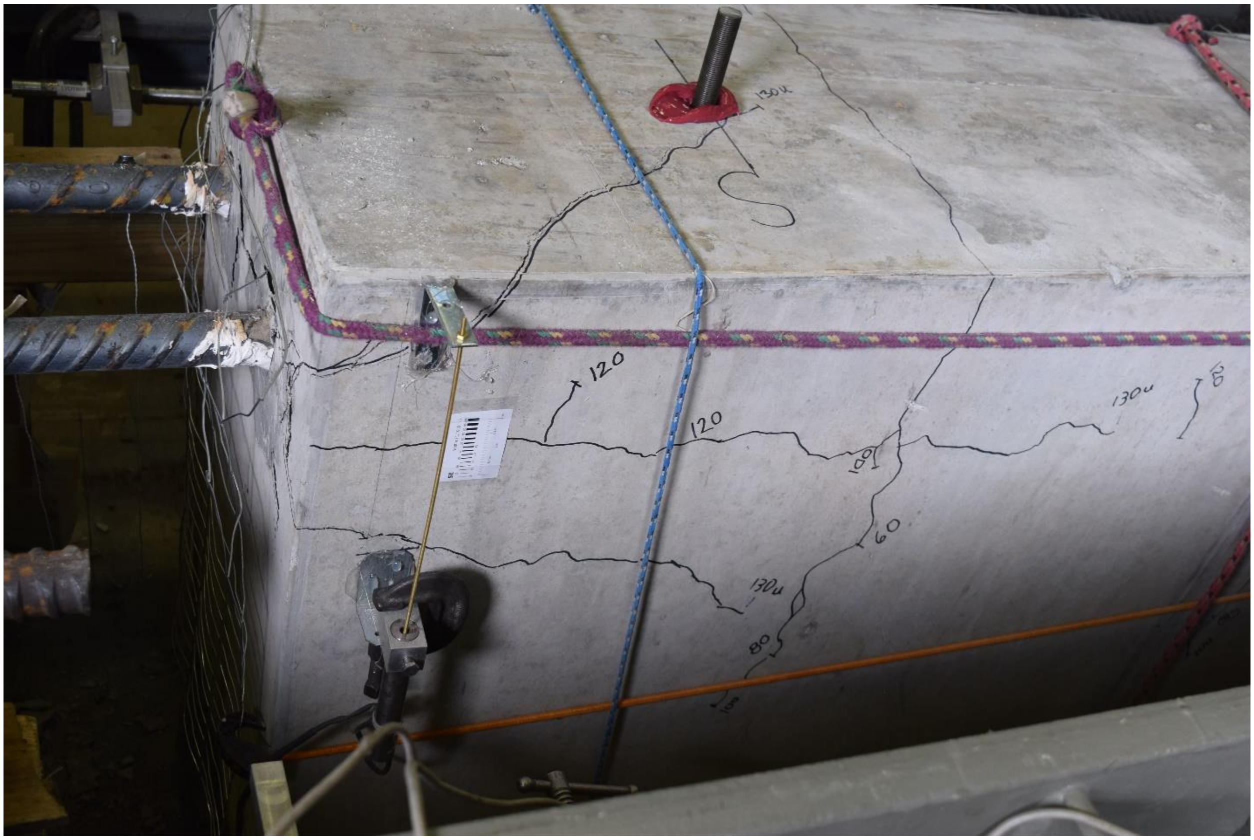

Figure 3-116: Crack pattern for specimen D5, southeast corner (average bar stress = 69 ksi)

Figure 3-117: Crack pattern for specimen D6, southwest corner (average bar stress = 70 ksi)

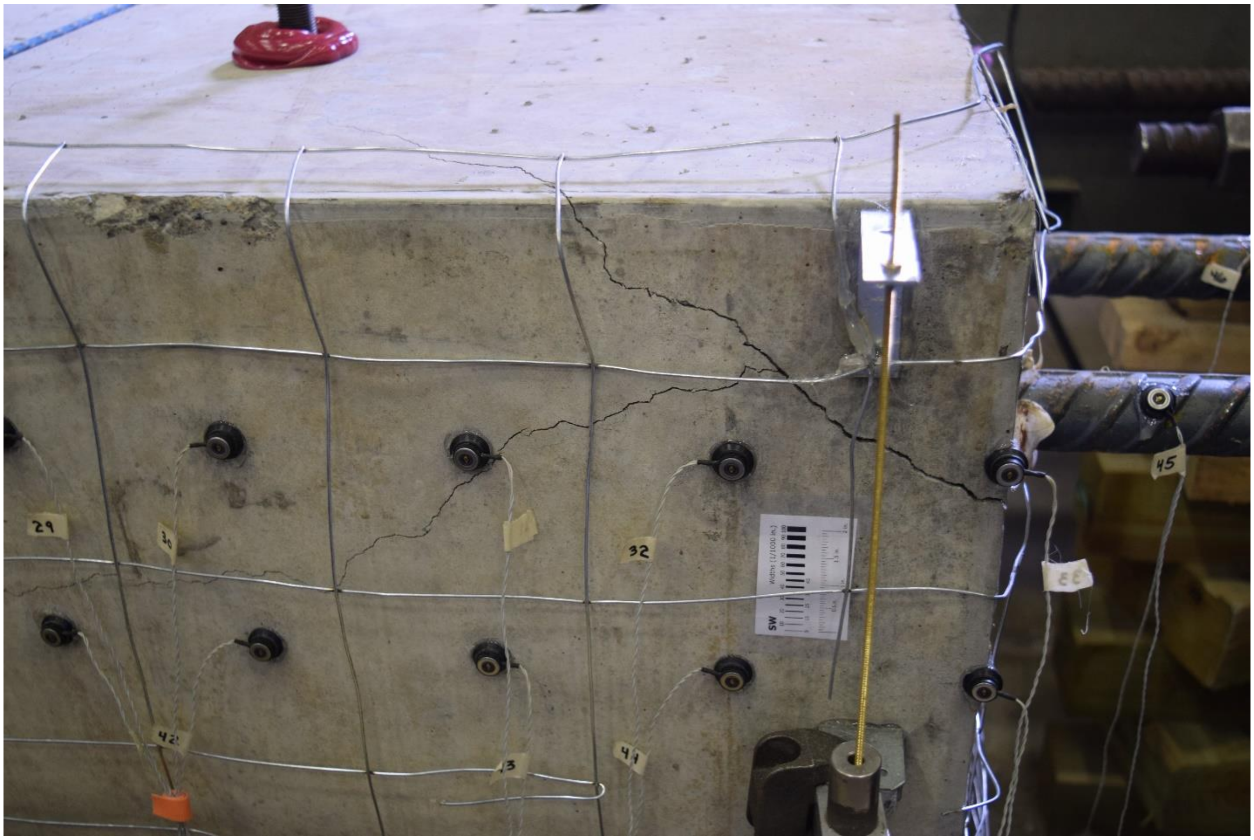

Figure 3-118: Crack pattern for specimen D7, southwest corner (average bar stress = 70 ksi)

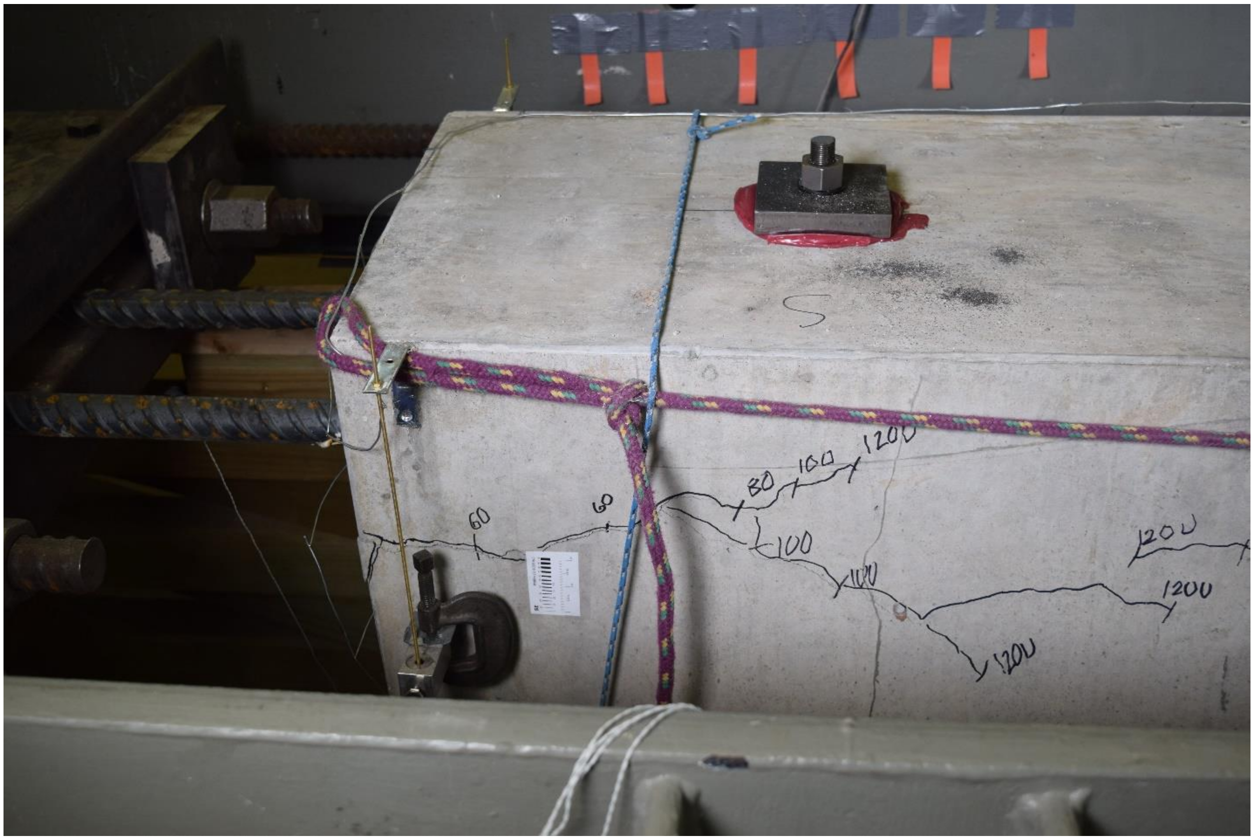

Figure 3-119: Crack pattern for specimen D8, southeast corner (average bar stress = 81 ksi)

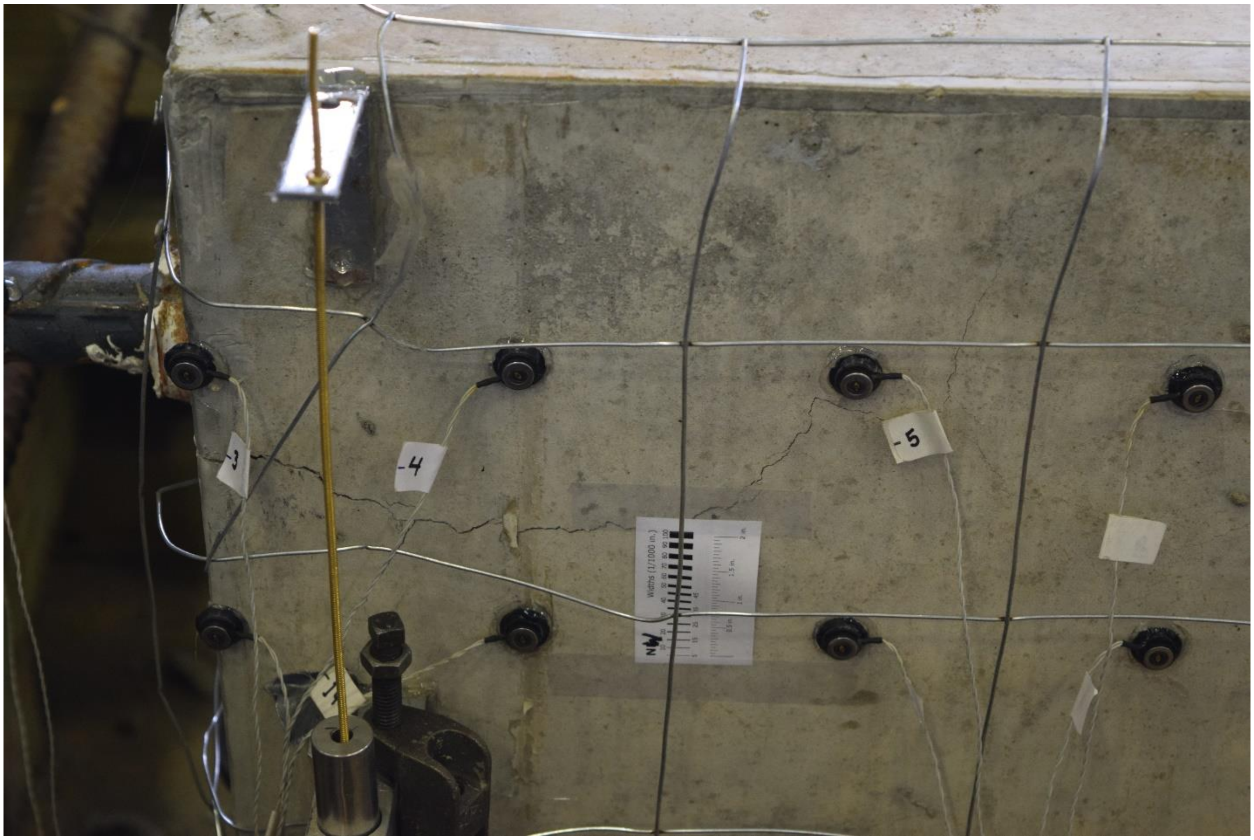

Figure 3-120: Crack pattern for specimen D9, northwest corner (average bar stress = 74 ksi)

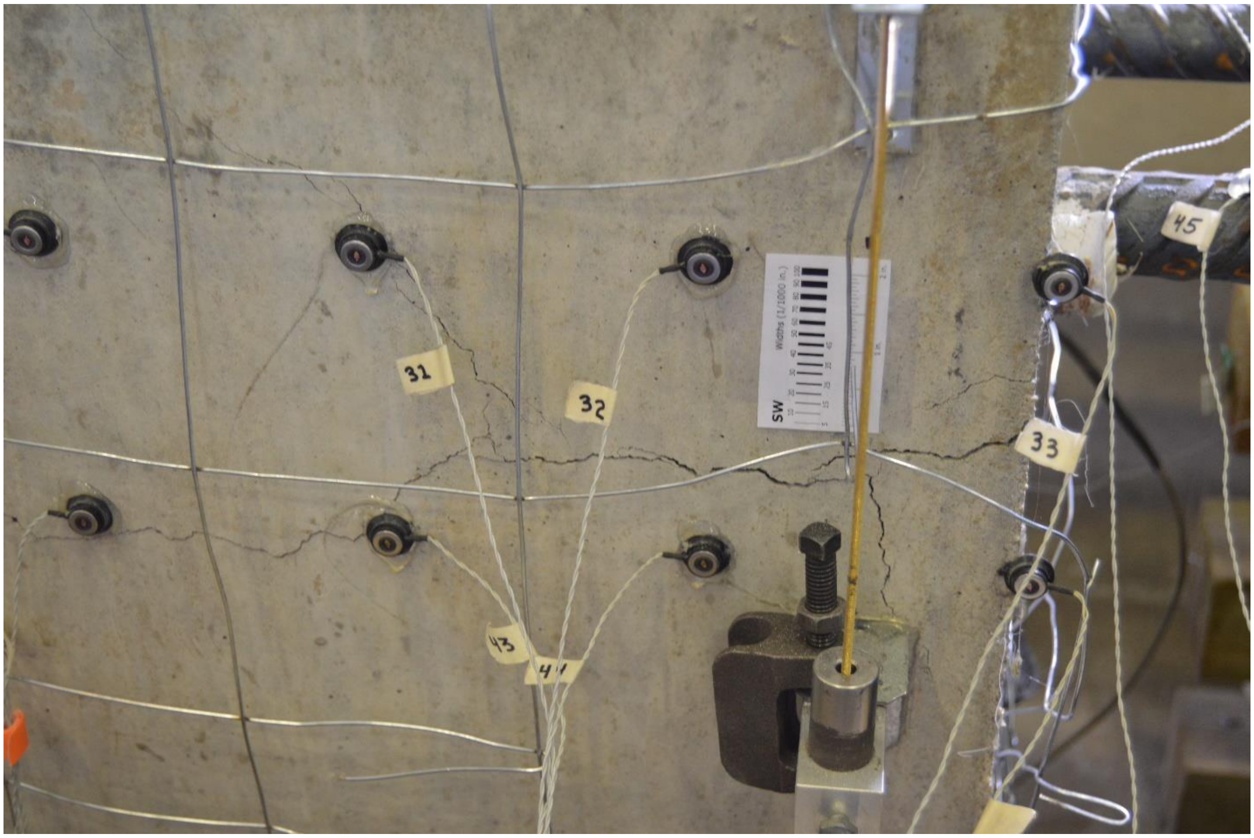

Figure 3-121: Crack pattern for specimen D10, southwest corner (average bar stress = 77 ksi)

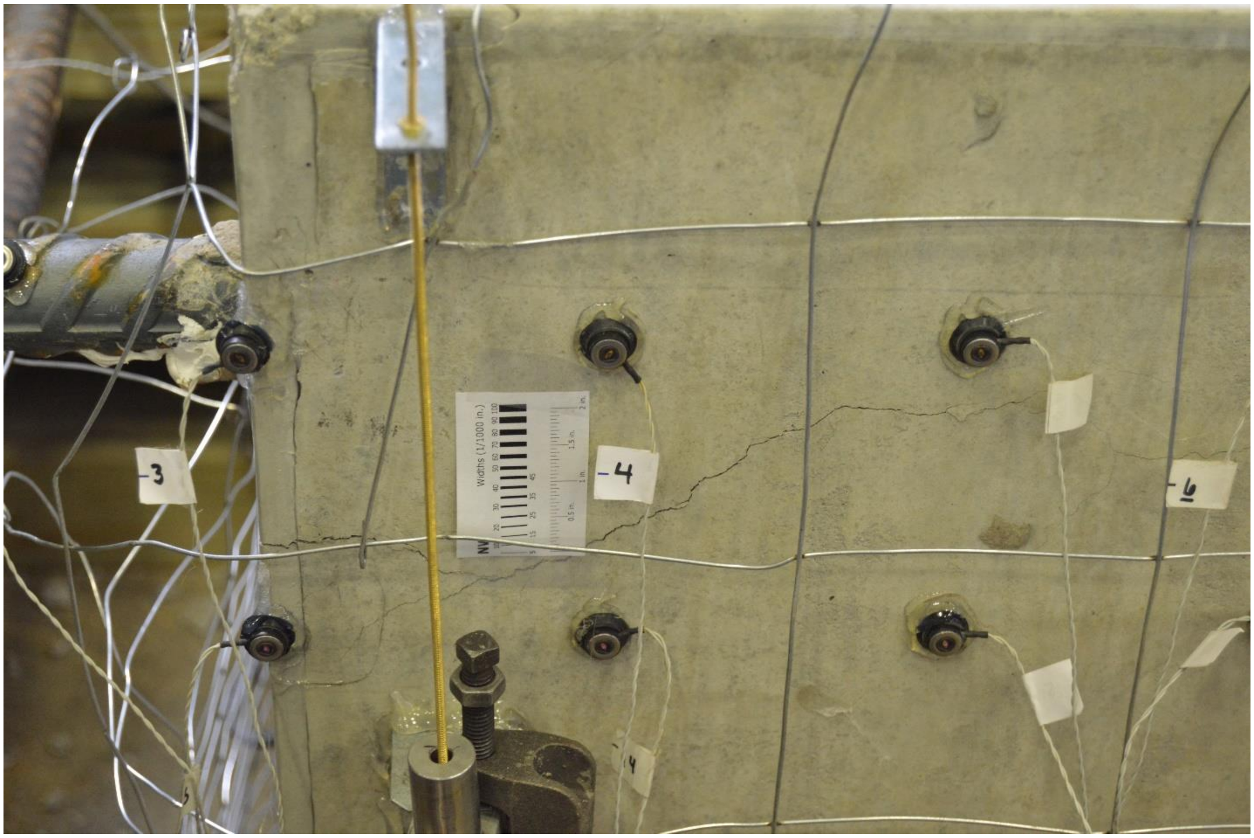

Figure 3-122: Crack pattern for specimen D11, northwest corner (average bar stress = 70 ksi)

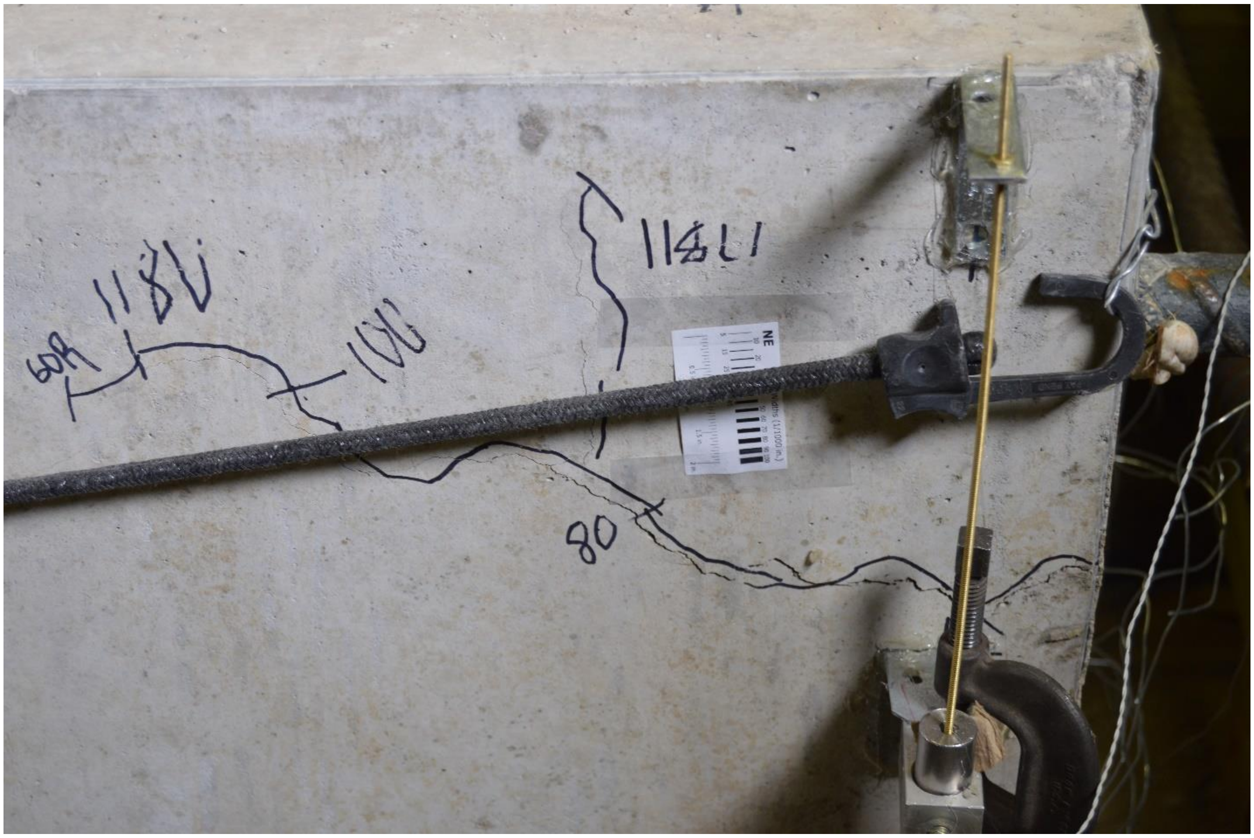

Figure 3-123: Crack pattern for specimen D12, northeast corner (average bar stress = 77 ksi)

Figure 3-124: Crack pattern for specimen D13, southwest corner (average bar stress = 77 ksi)

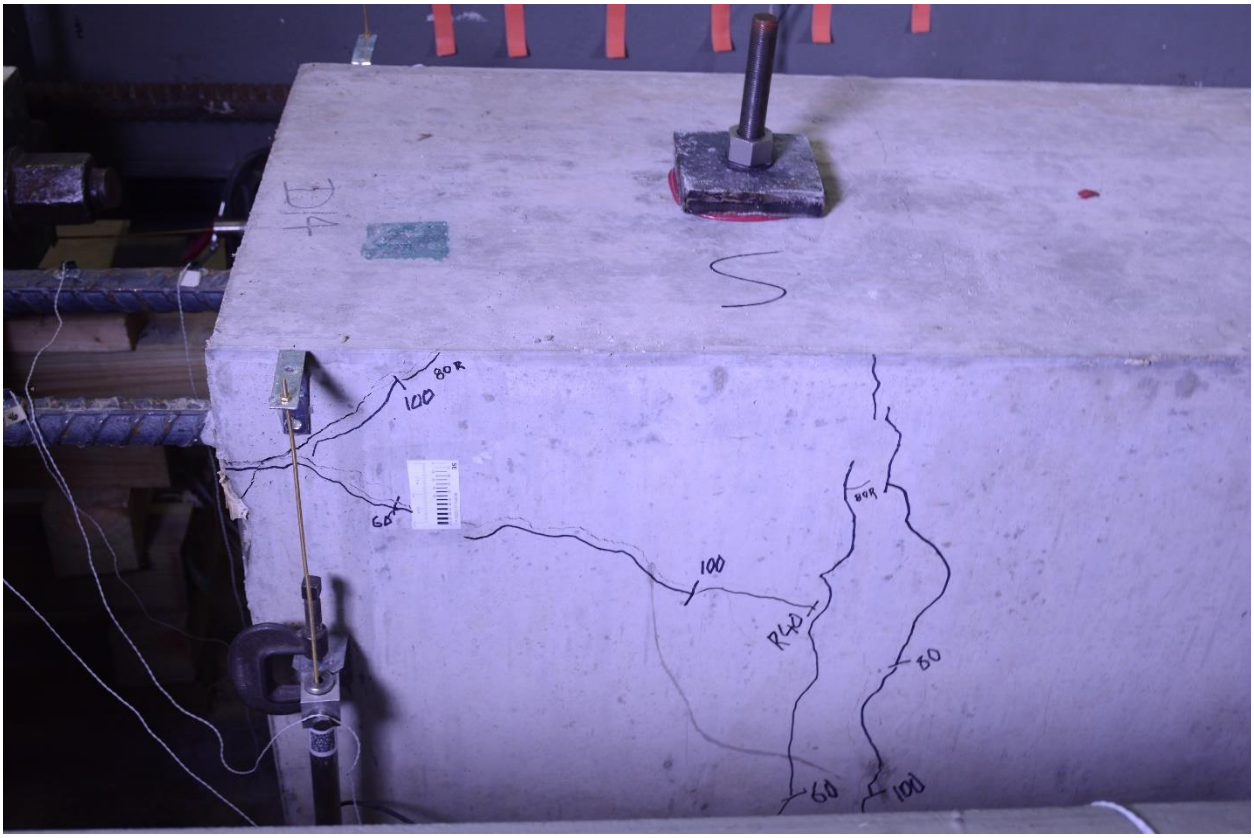

Figure 3-125: Crack pattern for specimen D14, southeast corner (average bar stress = 77 ksi)

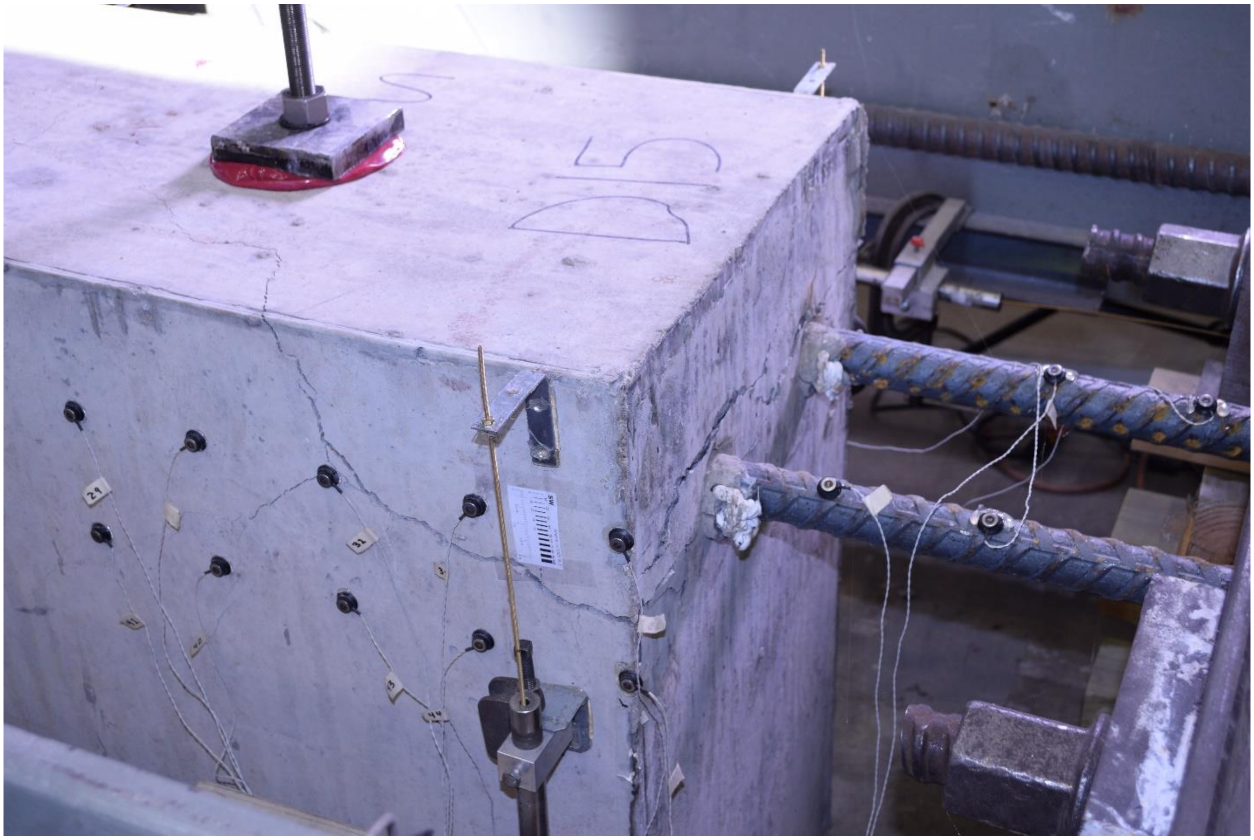

Figure 3-126: Crack pattern for specimen D15, southwest corner (average bar stress = 77 ksi)

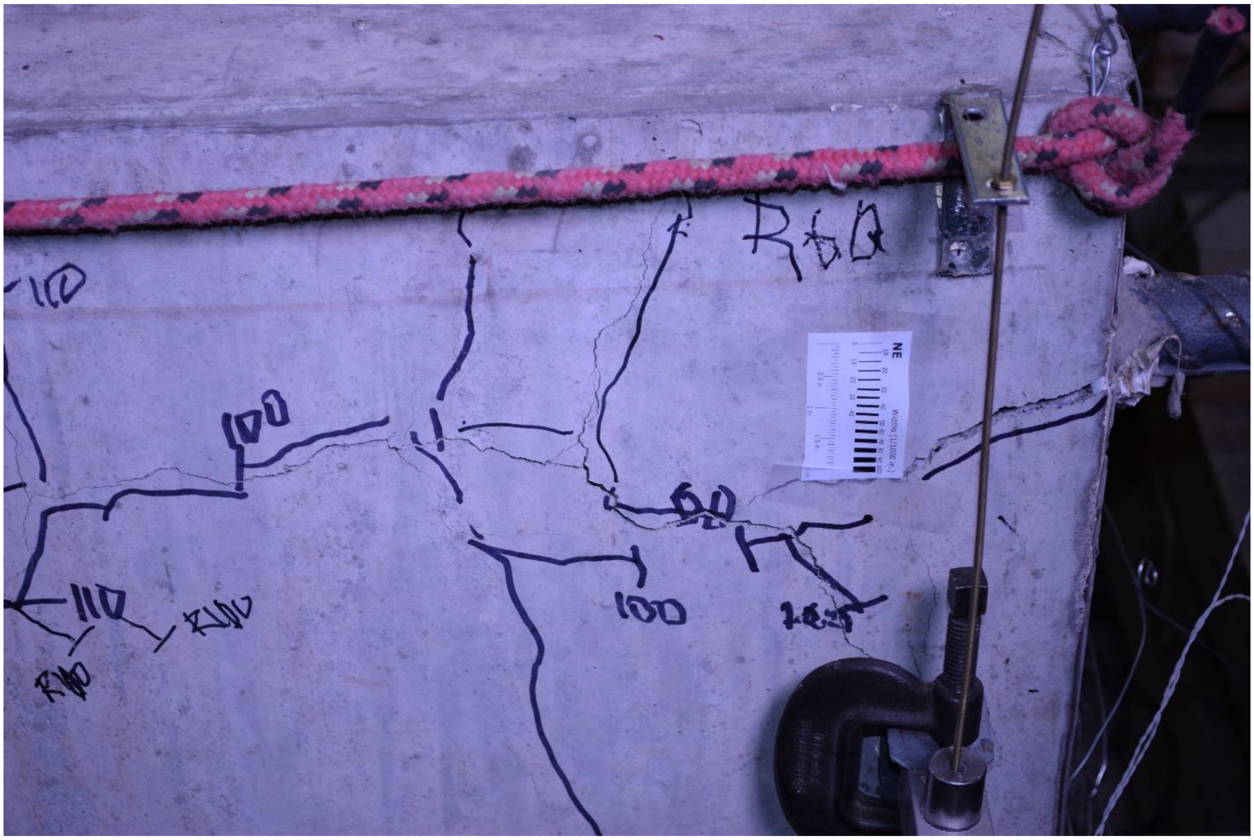

Figure 3-127: Crack pattern for specimen D16, northeast corner (average bar stress = 77 ksi)

Figure 3-128: Crack pattern for specimen D17, northeast corner (average bar stress = 70 ksi)

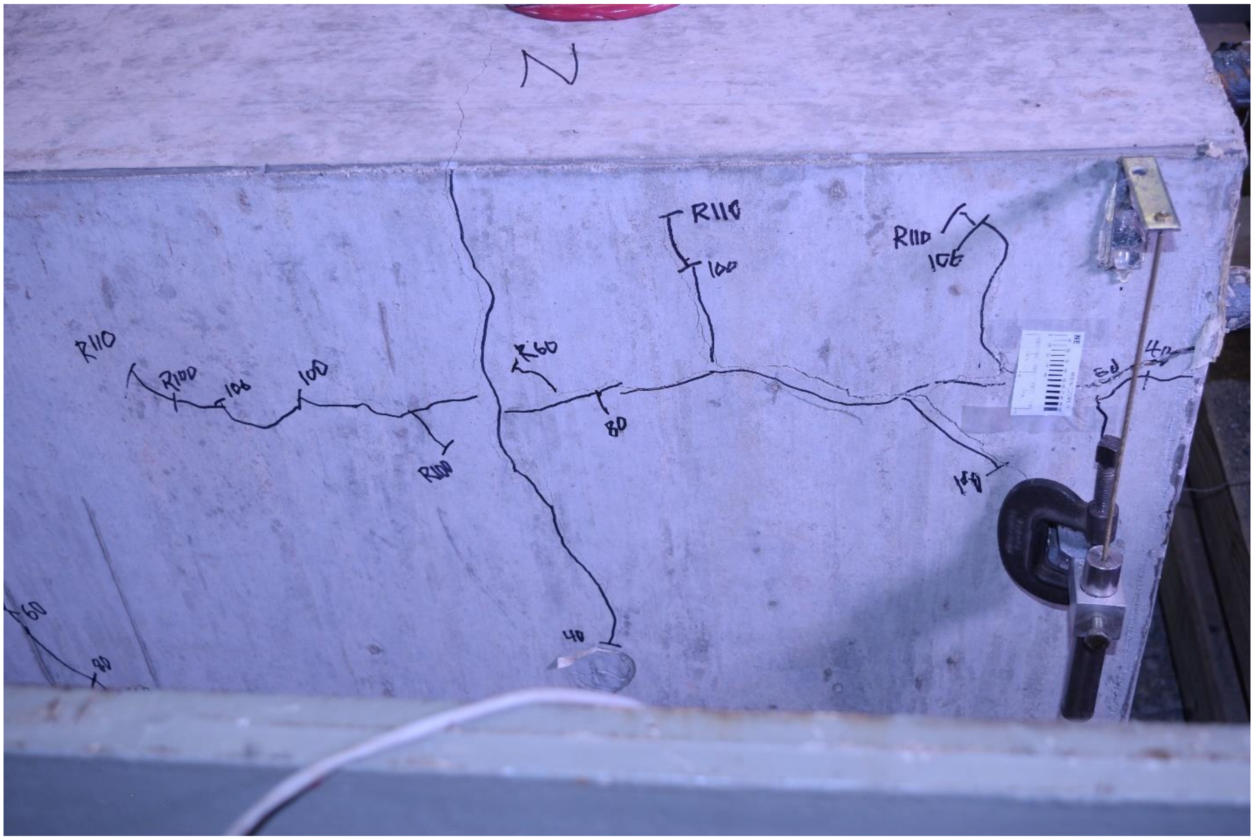

Figure 3-129: Crack pattern for specimen D18, northeast corner (average bar stress = 77 ksi)

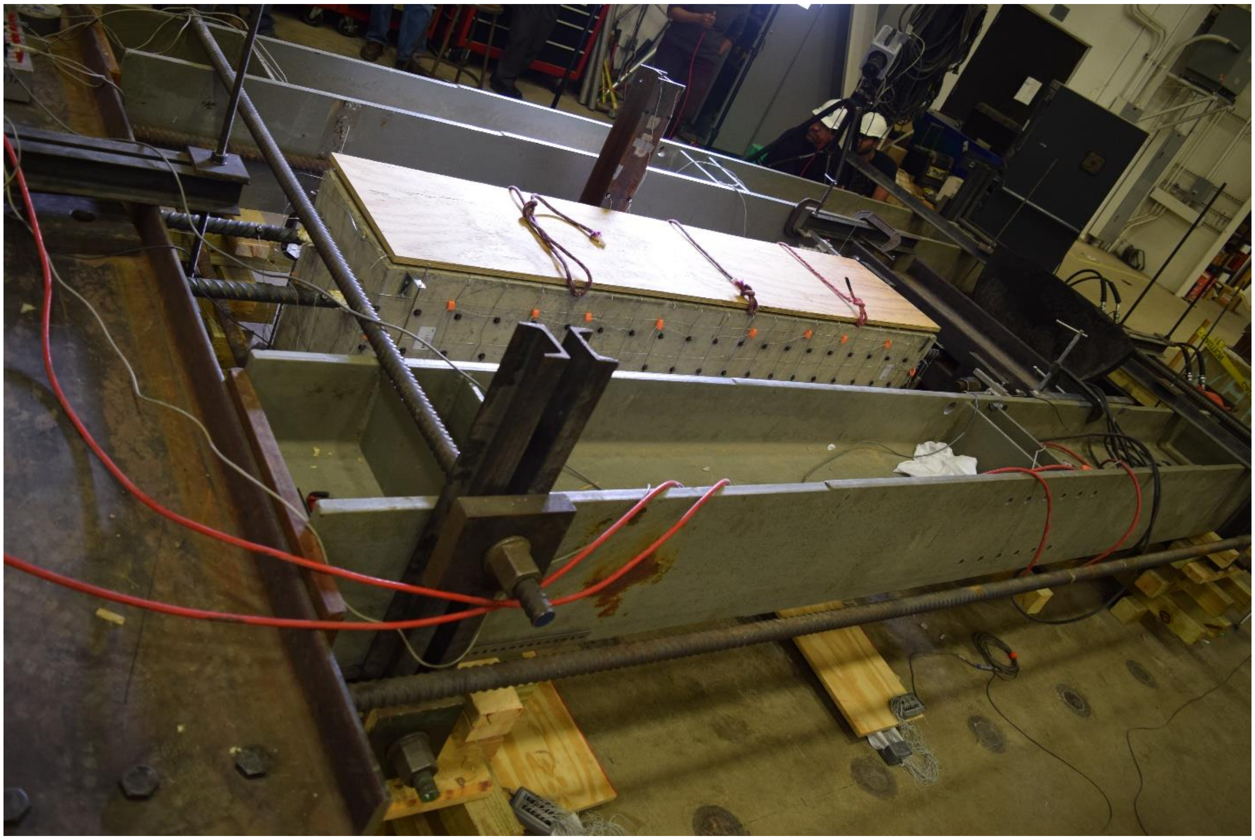

Figure 3-130: Unconfined specimen D1 during testing

Figure 3-131: Splice failure of specimen D1

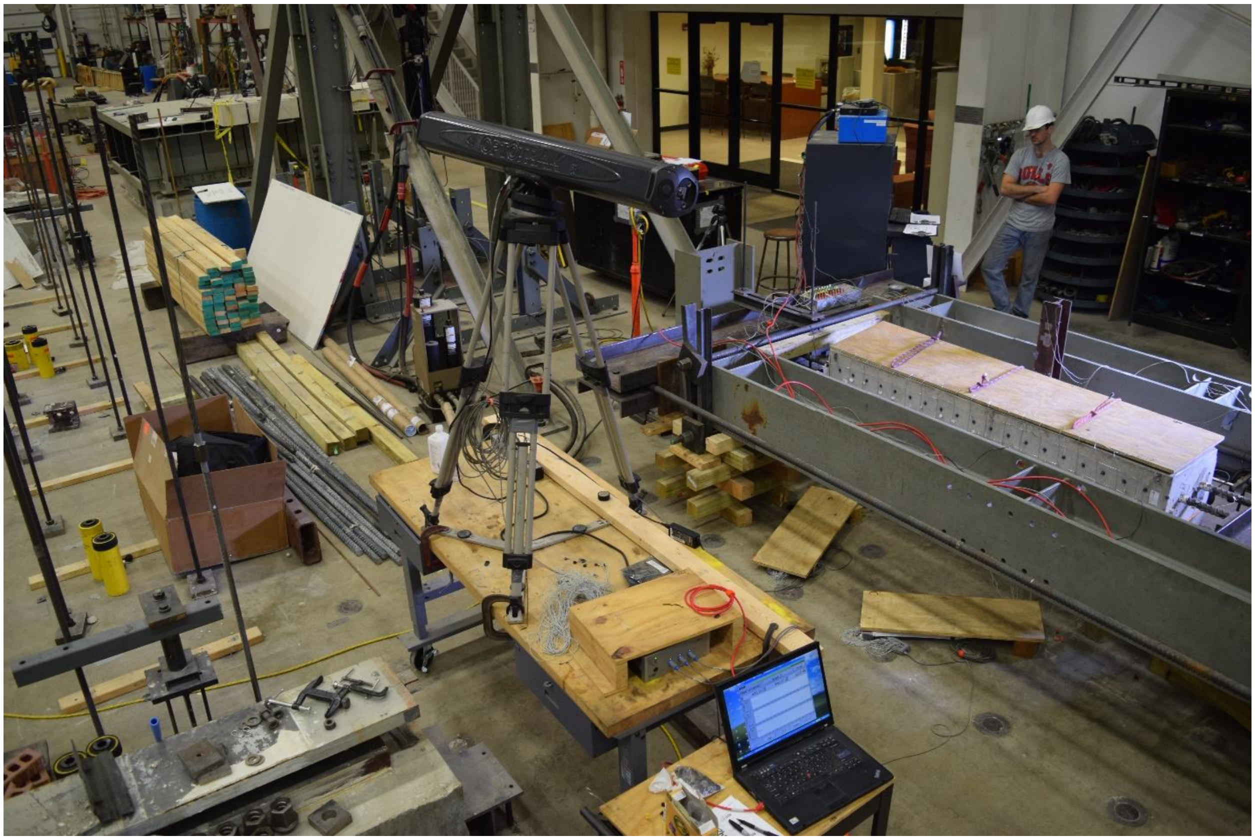

Figure 3-132: Confined specimen D4 (anchor configuration 1) during testing. Anchors under plywood cover which prevent concrete from damaging test equipment

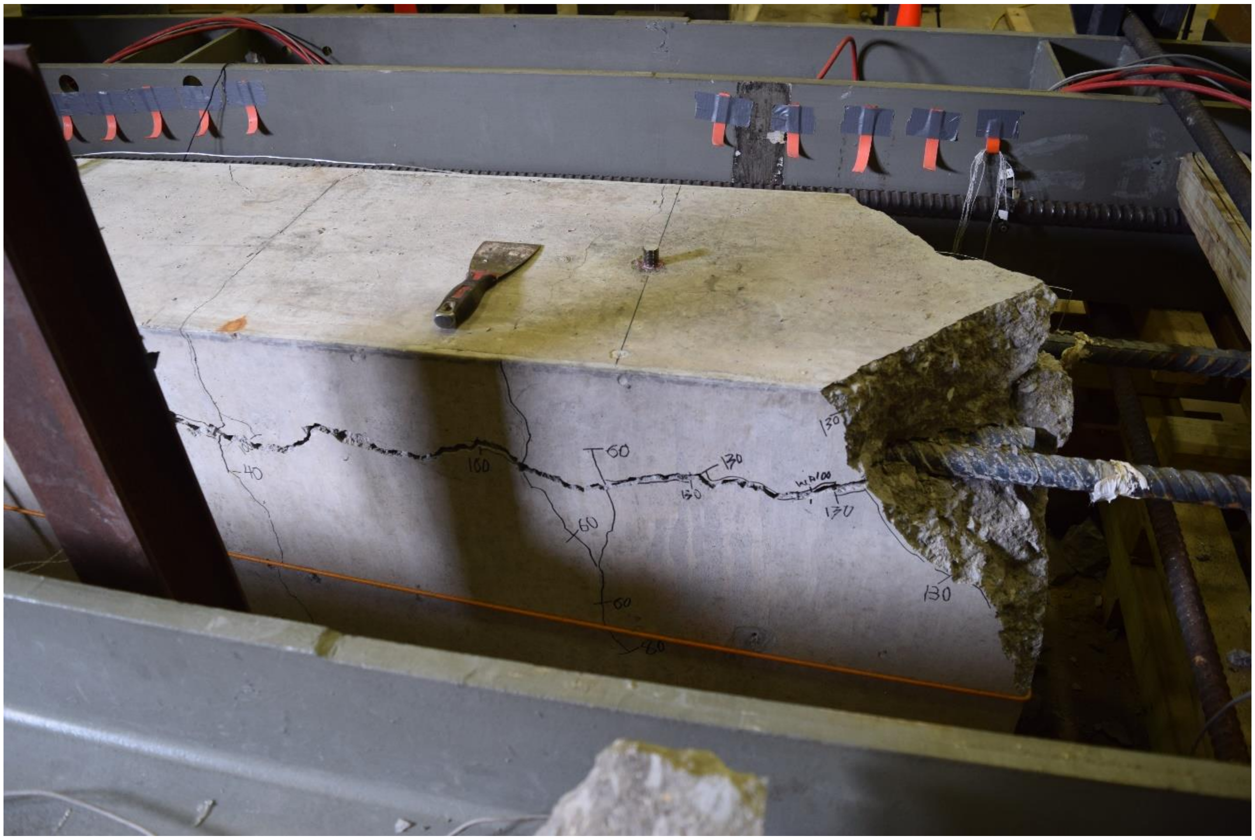

Figure 3-133: Splice failure of specimen D4 (plywood removed to show anchor)

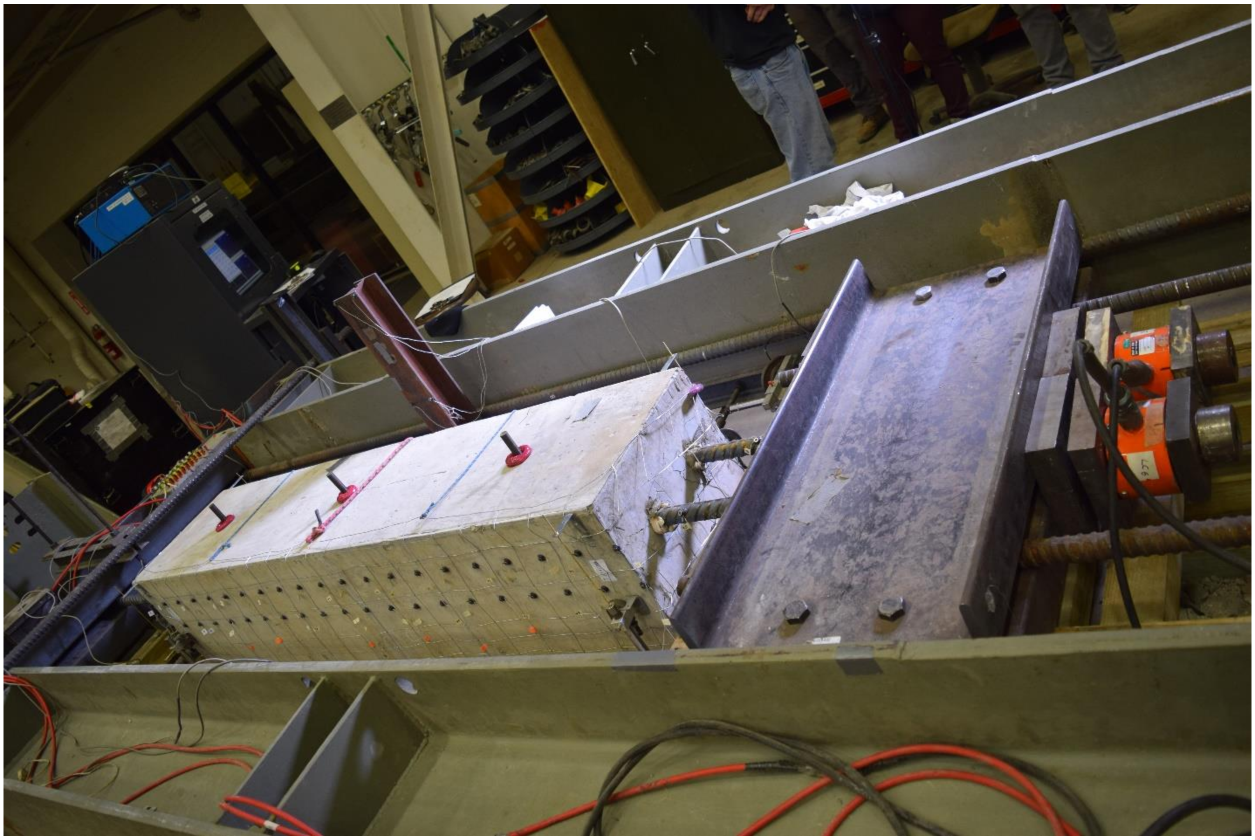

Figure 3-134: Confined specimen D7 (anchor configuration 3) during testing

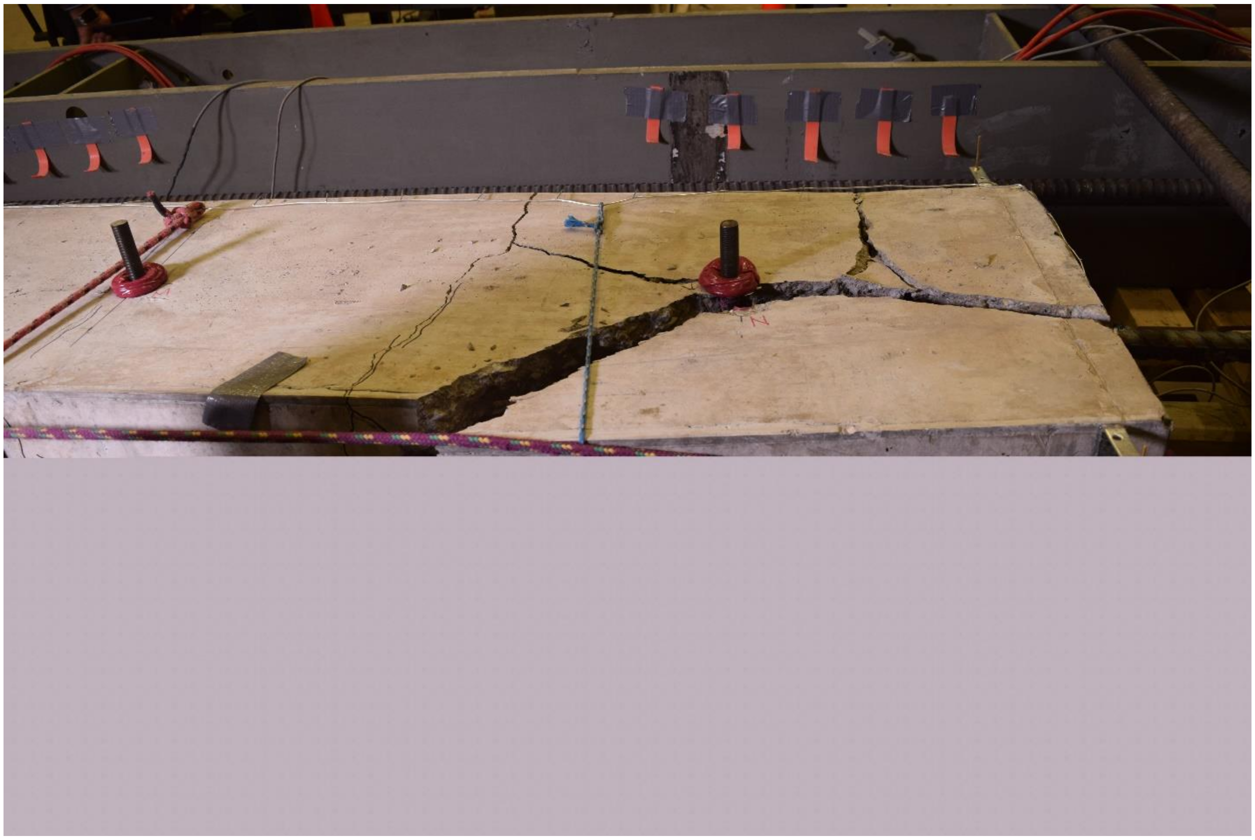

Figure 3-135: Splice failure of specimen D7

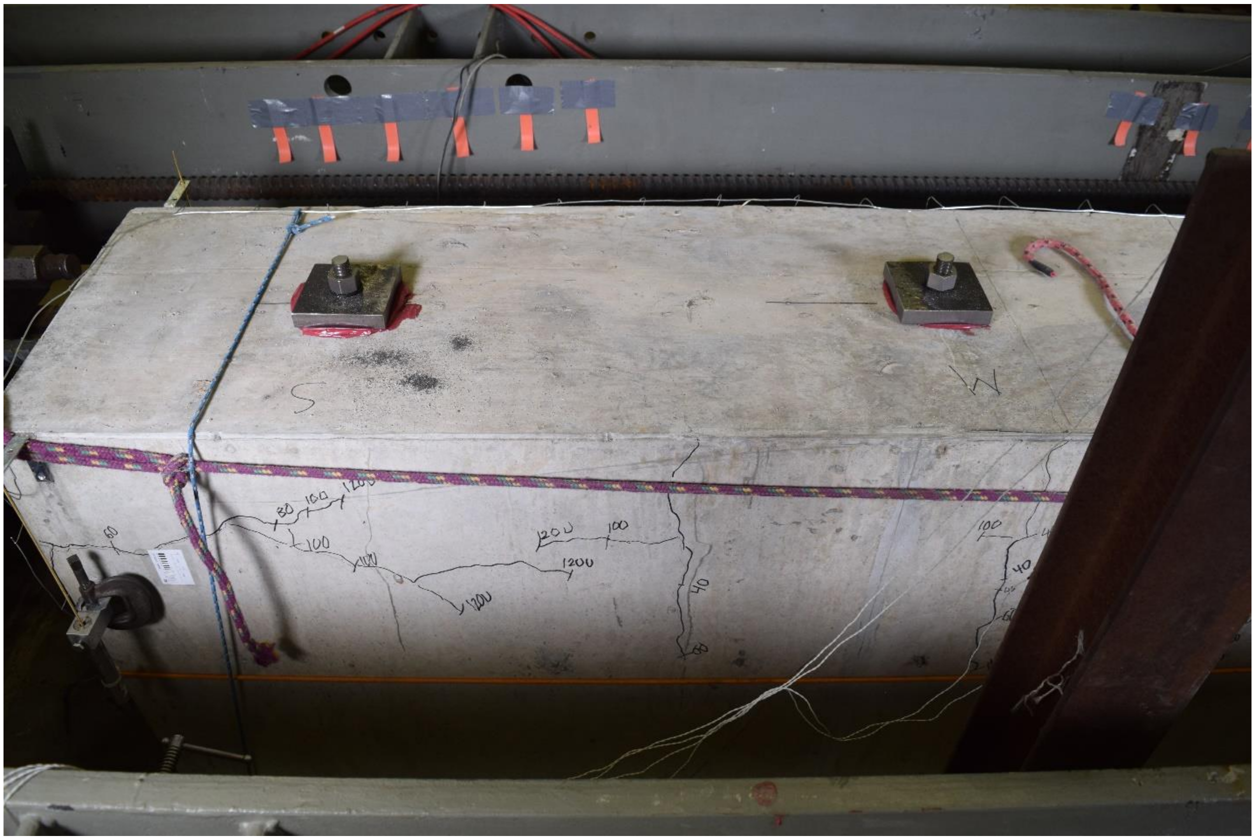

Figure 3-136: Confined specimen D8 (anchor configuration 4) during testing

Figure 3-137: Splice failure of specimen D8

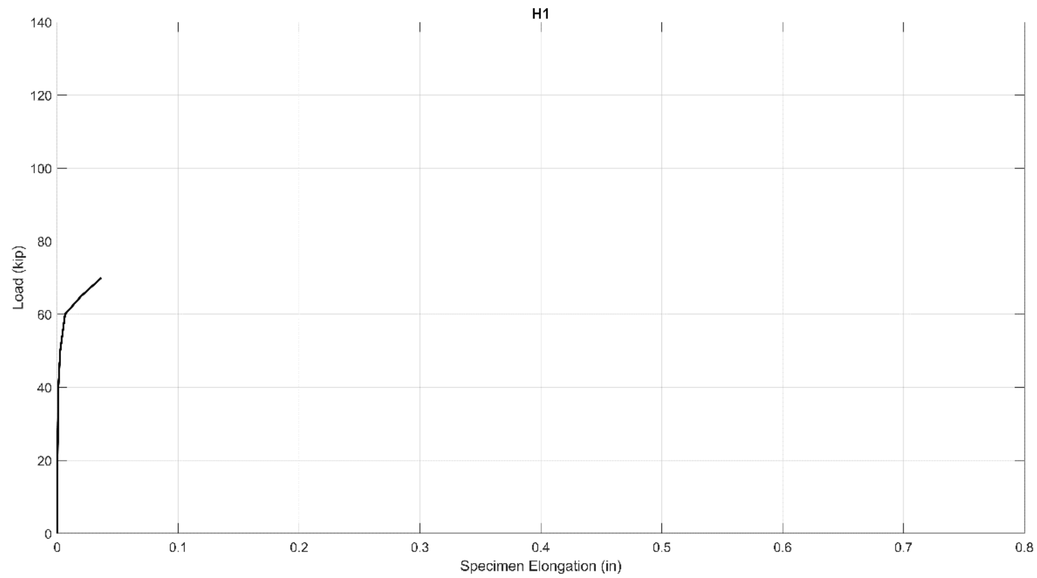

Figure 3-138: Specimen H1 load versus specimen elongation

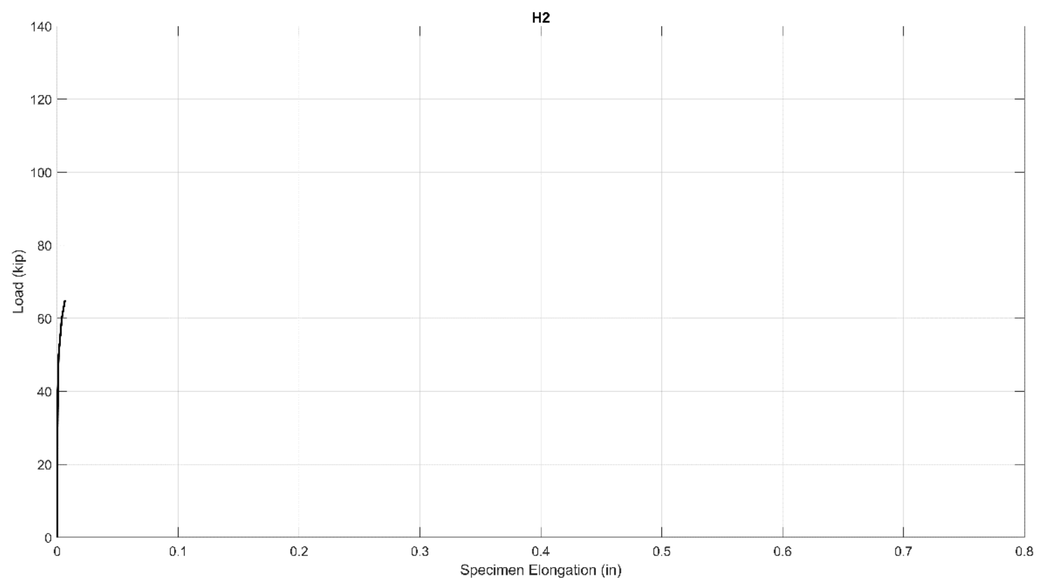

Figure 3-139: Specimen H2 load versus specimen elongation

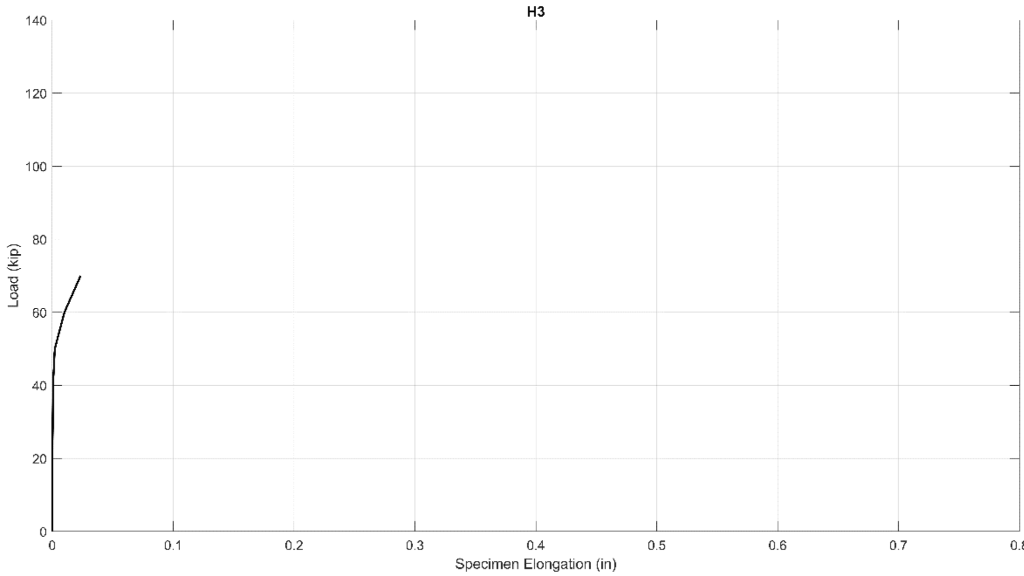

Figure 3-140: Specimen H3 load versus specimen elongation

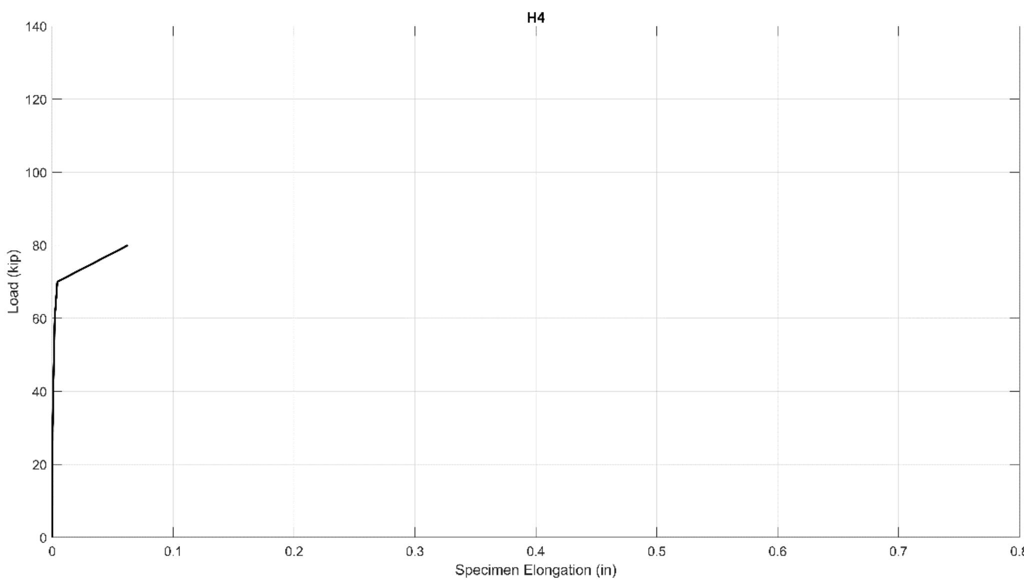

Figure 3-141: Specimen H4 load versus specimen elongation

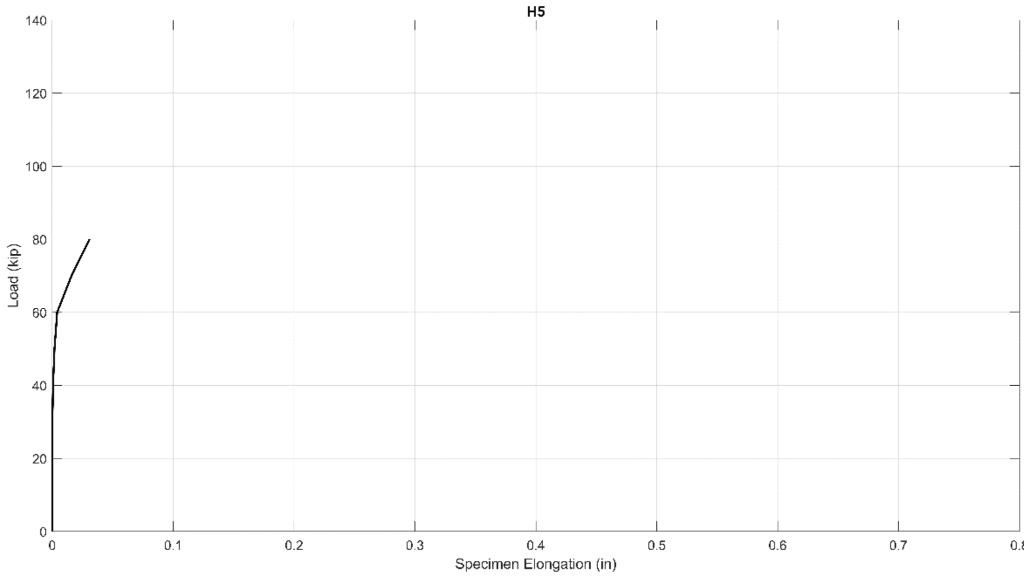

Figure 3-142: Specimen H5 load versus specimen elongation

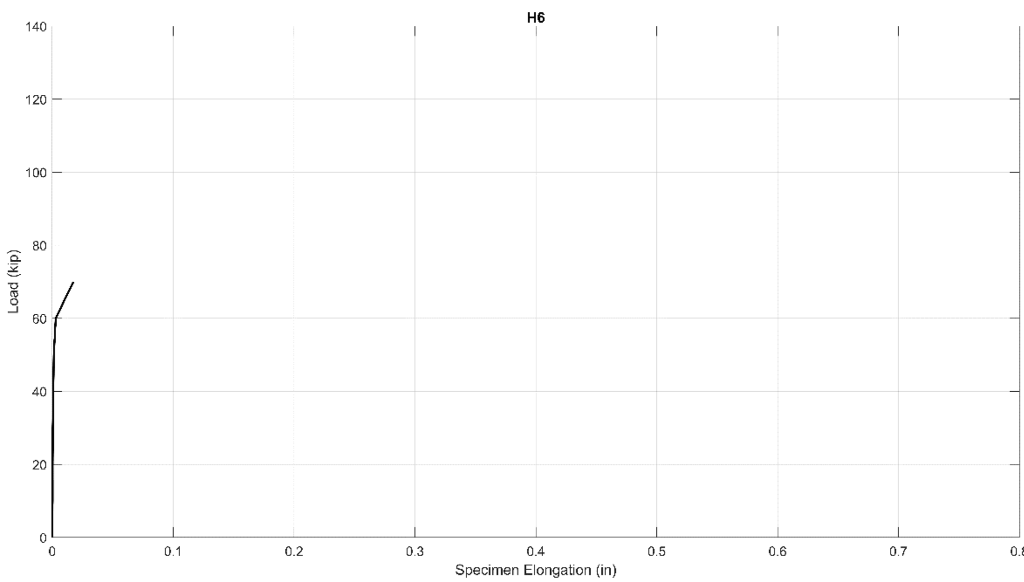

Figure 3-143: Specimen H6 load versus specimen elongation

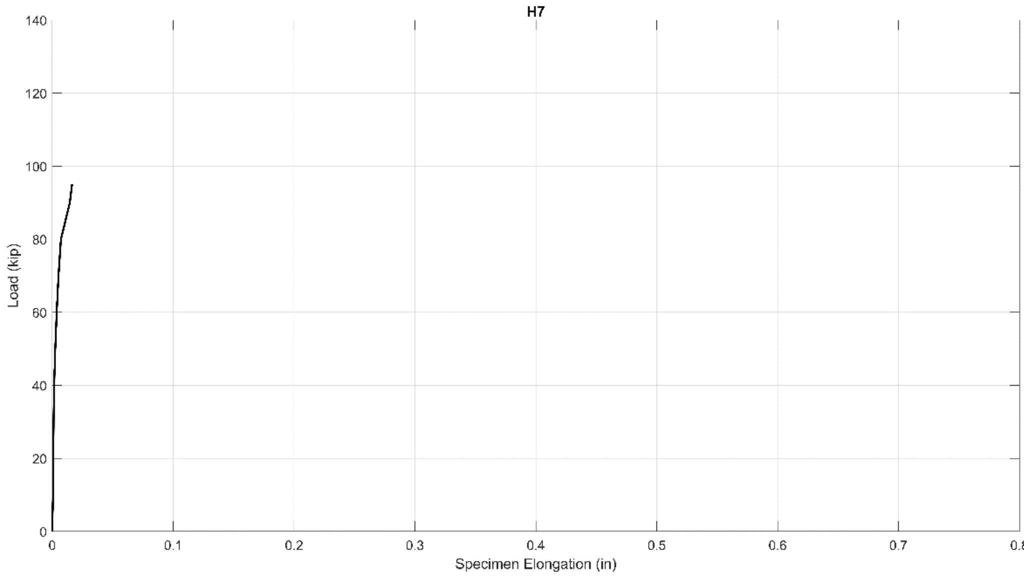

Figure 3-144: Specimen H7 load versus specimen elongation

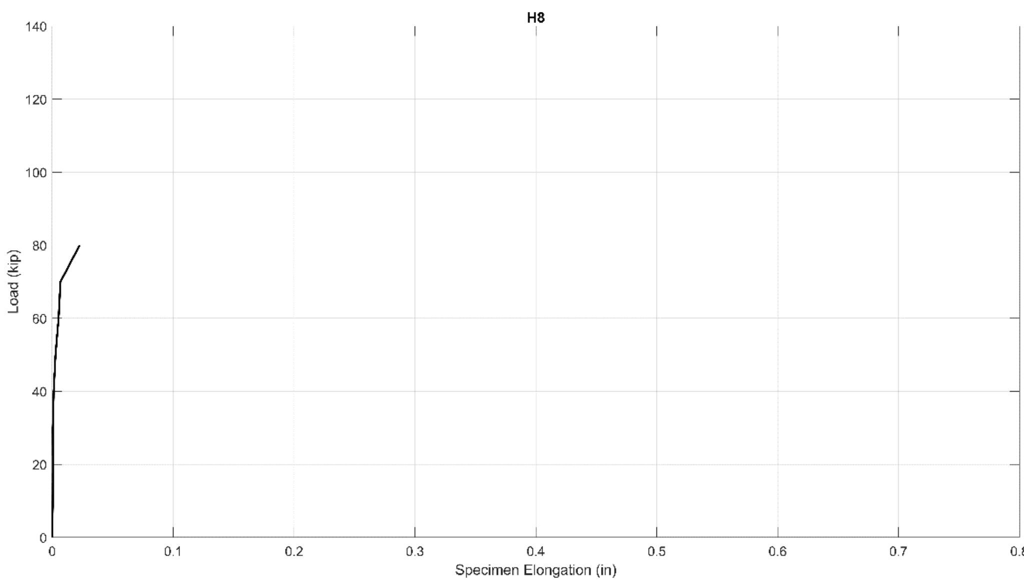

Figure 3-145: Specimen H8 load versus specimen elongation

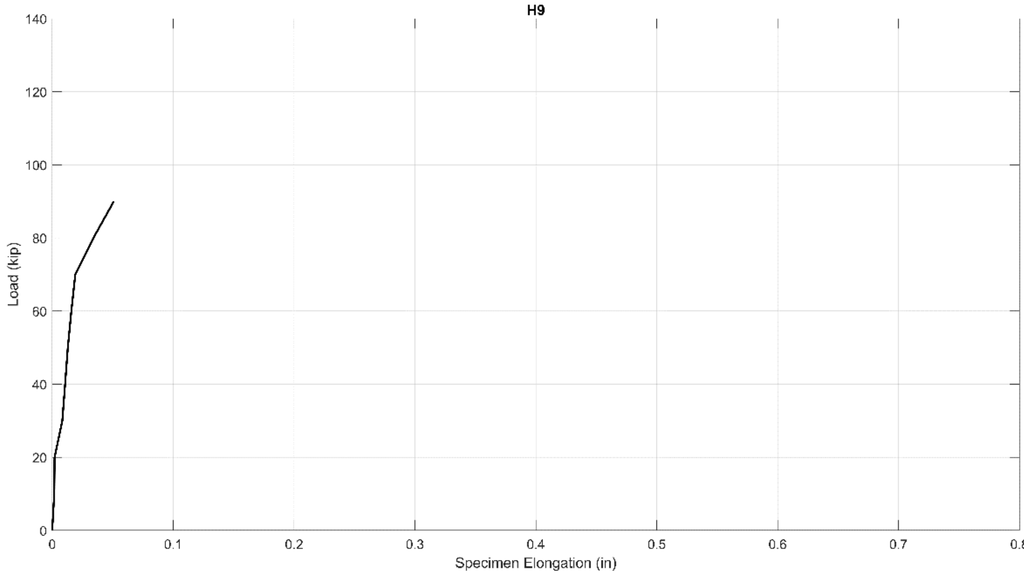

Figure 3-146: Specimen H9 load versus specimen elongation

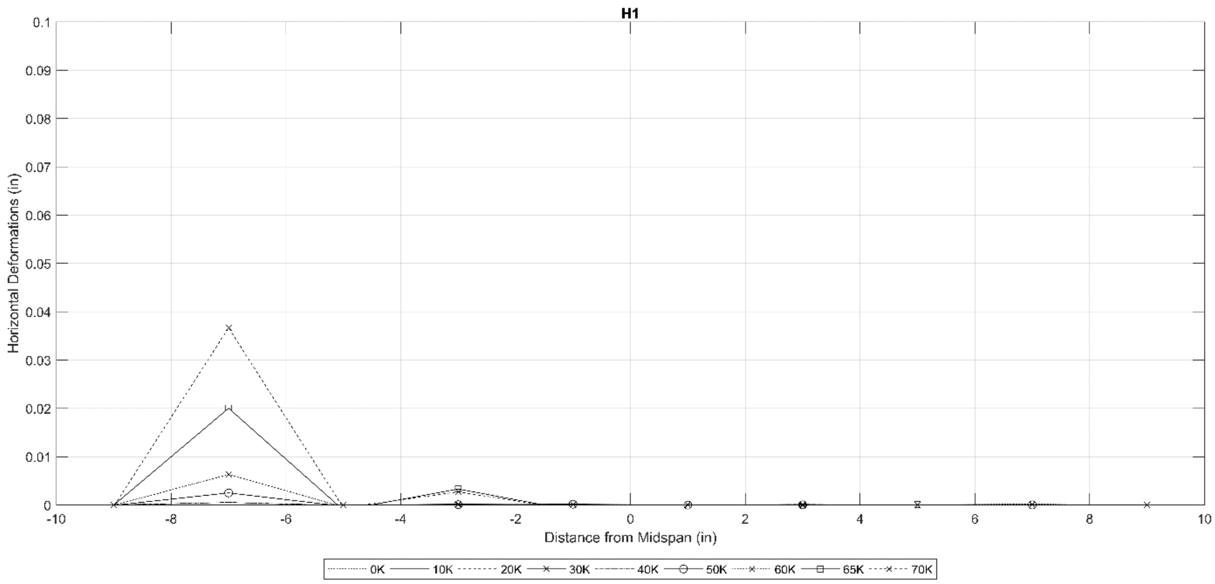

Figure 3-147: Horizontal deformations of concrete surface along splice length of specimen H1 (data series are label using the average load applied to the splice ends)

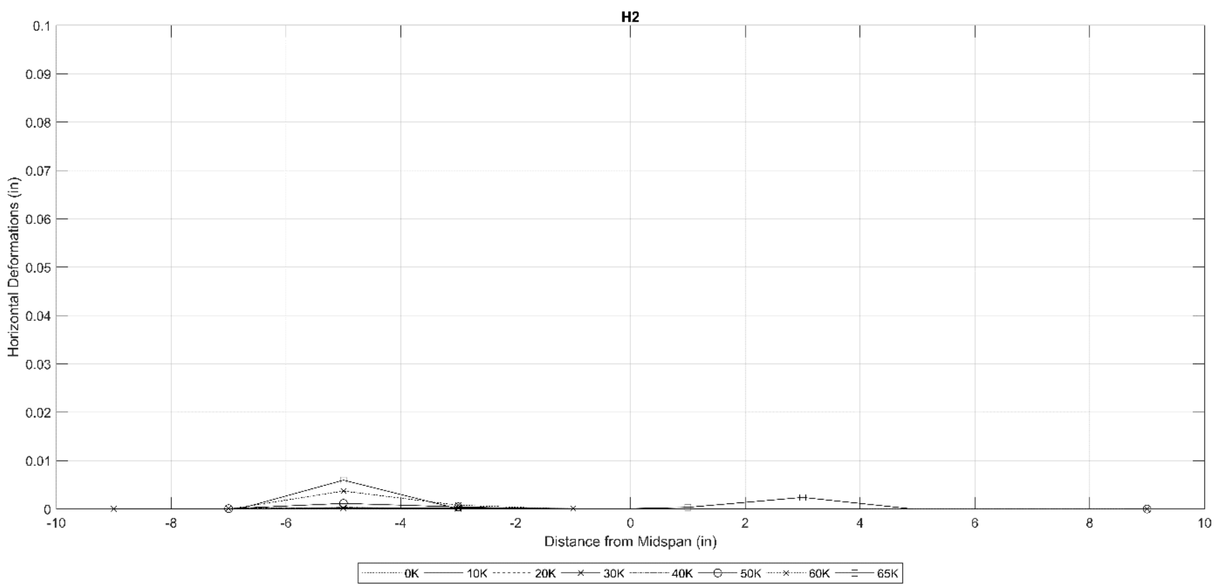

Figure 3-148: Horizontal deformations of concrete surface along splice length of specimen H2 (data series are label using the average load applied to the splice ends)

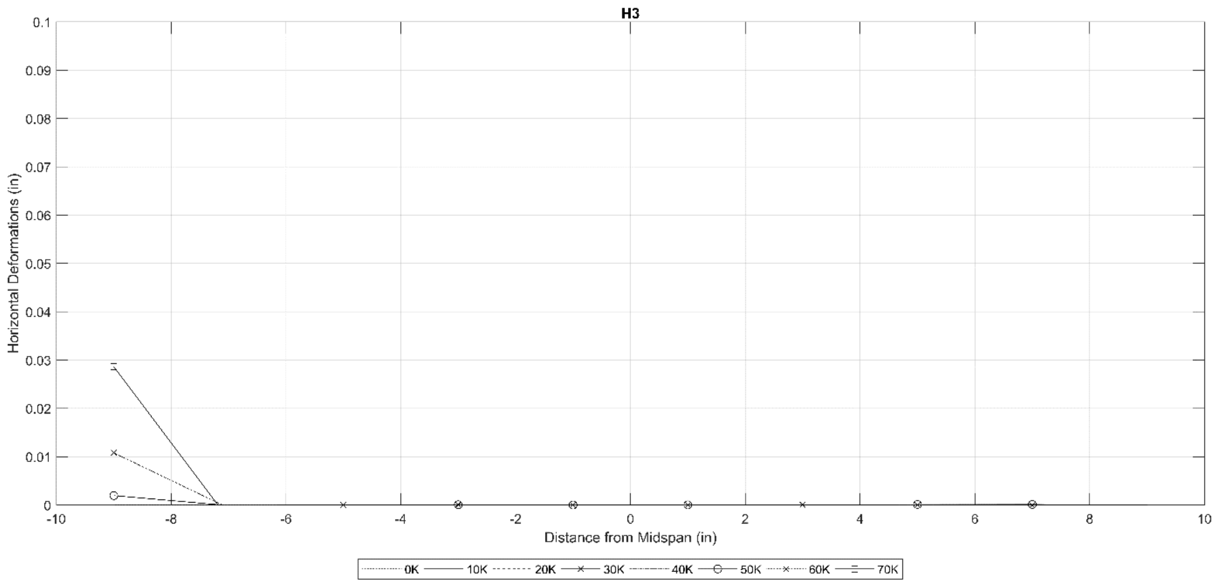

Figure 3-149: Horizontal deformations of concrete surface along splice length of specimen H3 (data series are label using the average load applied to the splice ends)

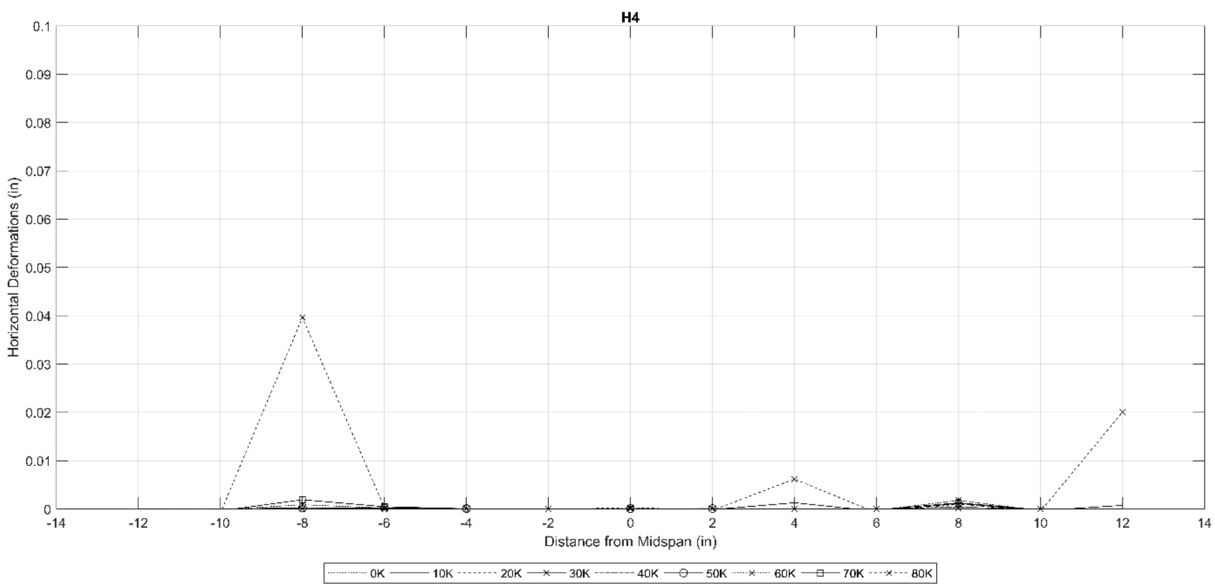

Figure 3-150: Horizontal deformations of concrete surface along splice length of specimen H4 (data series are label using the average load applied to the splice ends)

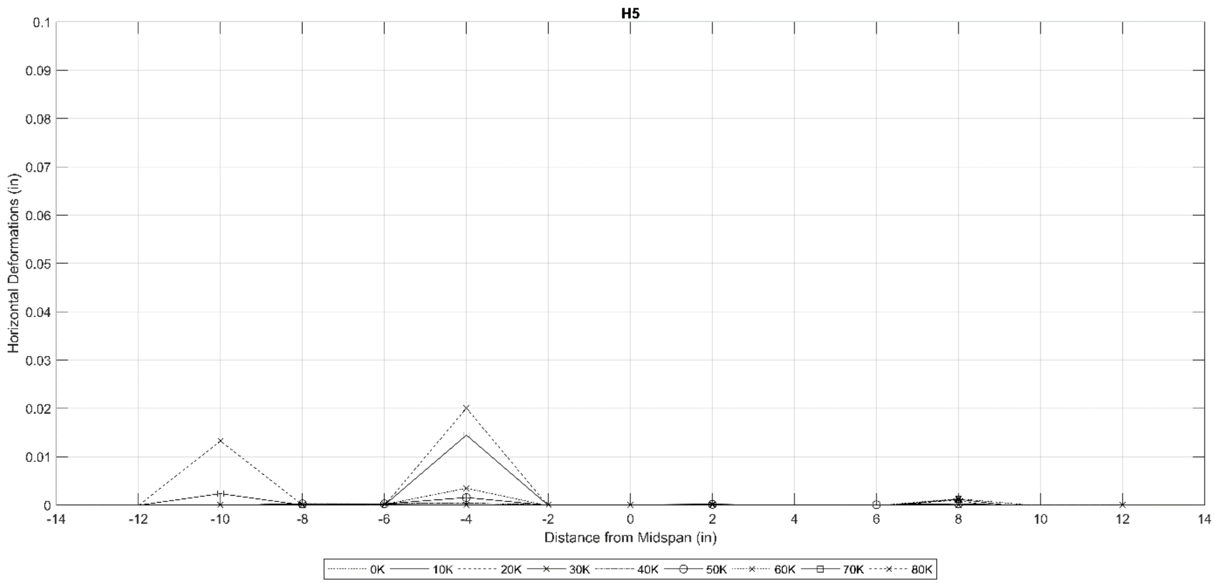

Figure 3-151: Horizontal deformations of concrete surface along splice length of specimen H5 (data series are label using the average load applied to the splice ends)

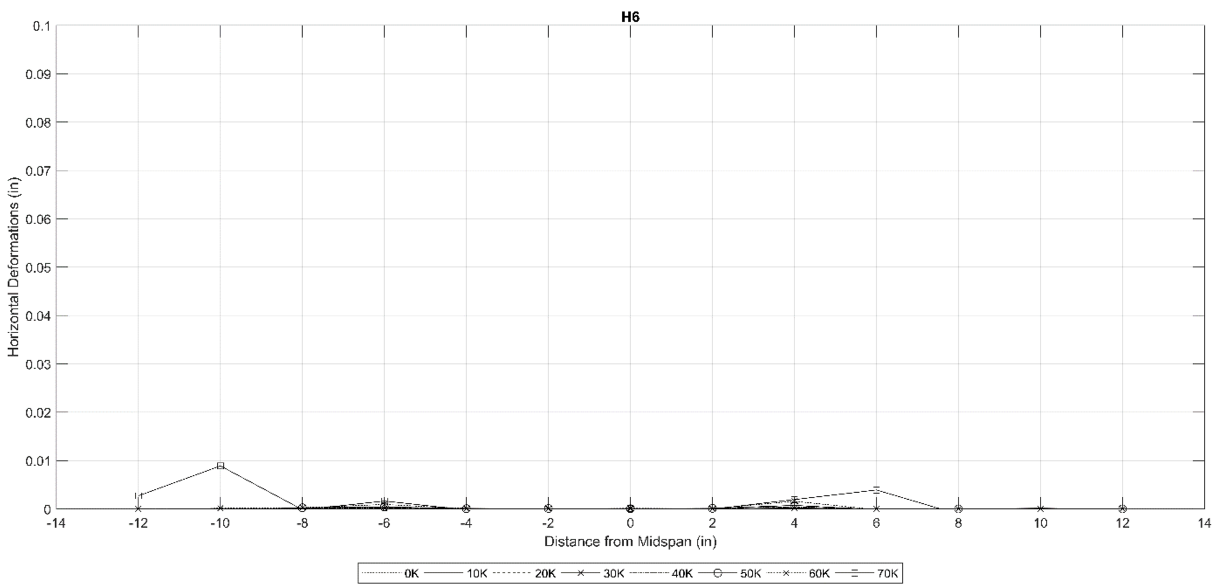

Figure 3-152: Horizontal deformations of concrete surface along splice length of specimen H6 (data series are label using the average load applied to the splice ends)

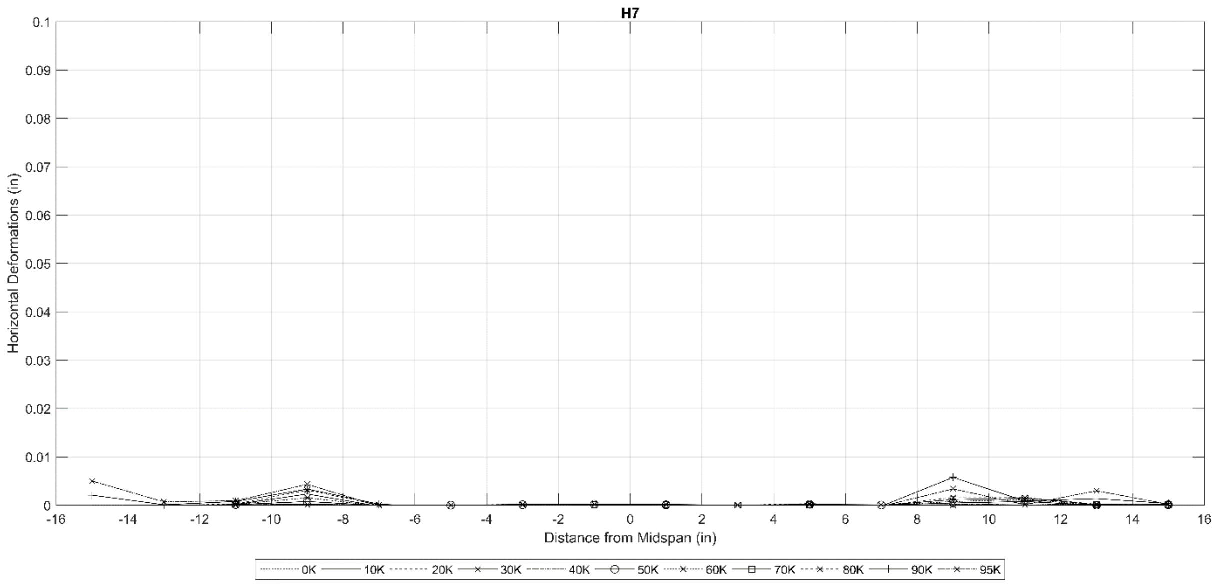

Figure 3-153: Horizontal deformations of concrete surface along splice length of specimen H7 (data series are label using the average load applied to the splice ends)

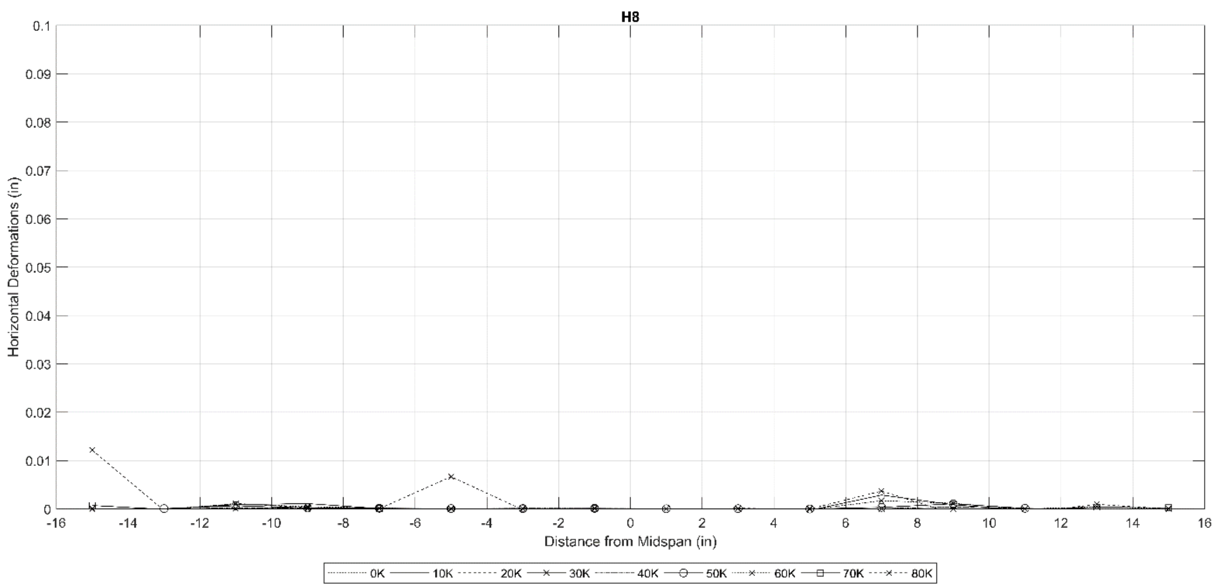

Figure 3-154: Horizontal deformations of concrete surface along splice length of specimen H8 (data series are label using the average load applied to the splice ends)

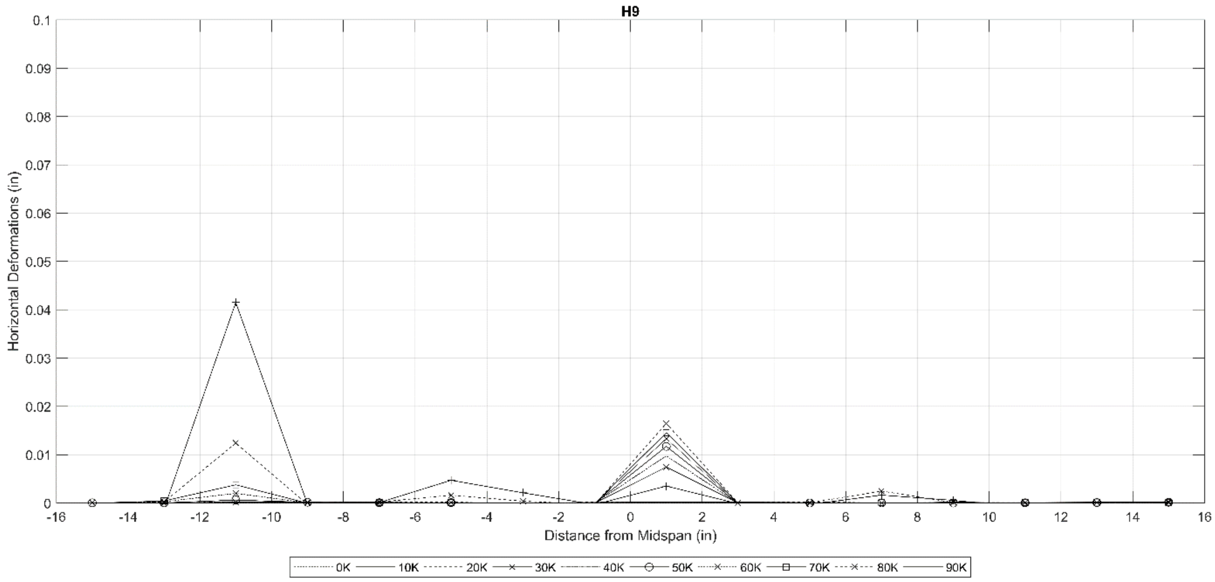

Figure 3-155: Horizontal deformations of concrete surface along splice length of specimen H9
(data series are label using the average load applied to the splice ends)

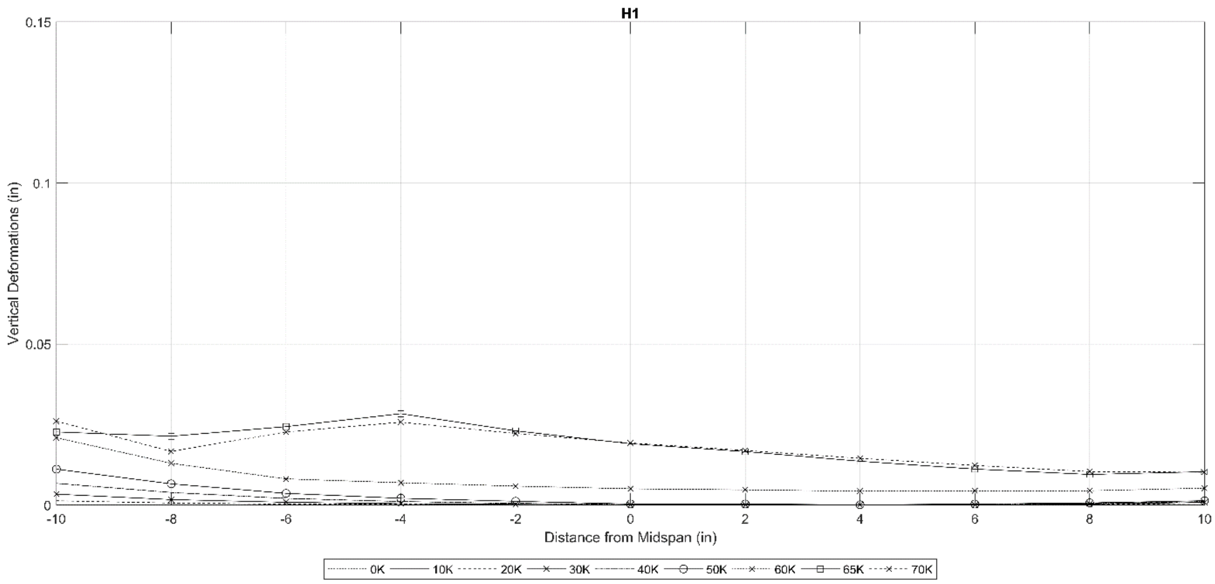

Figure 3-156: Vertical deformations of concrete surface along splice length of specimen H1 (data series are label using the average load applied to the splice ends)

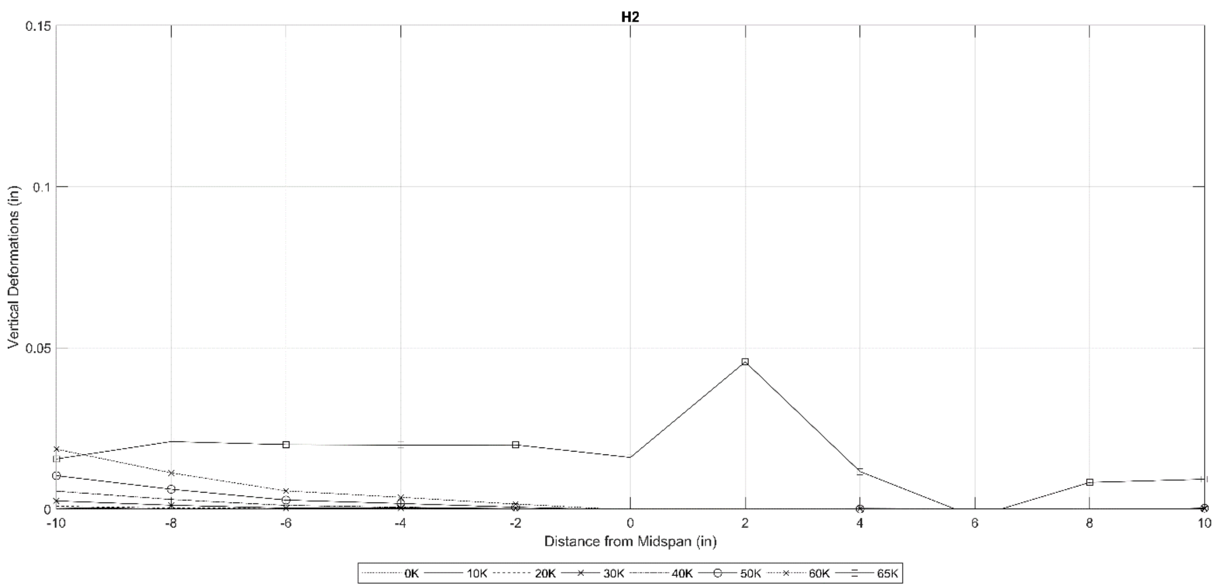

Figure 3-157: Vertical deformations of concrete surface along splice length of specimen H2 (data series are label using the average load applied to the splice ends)

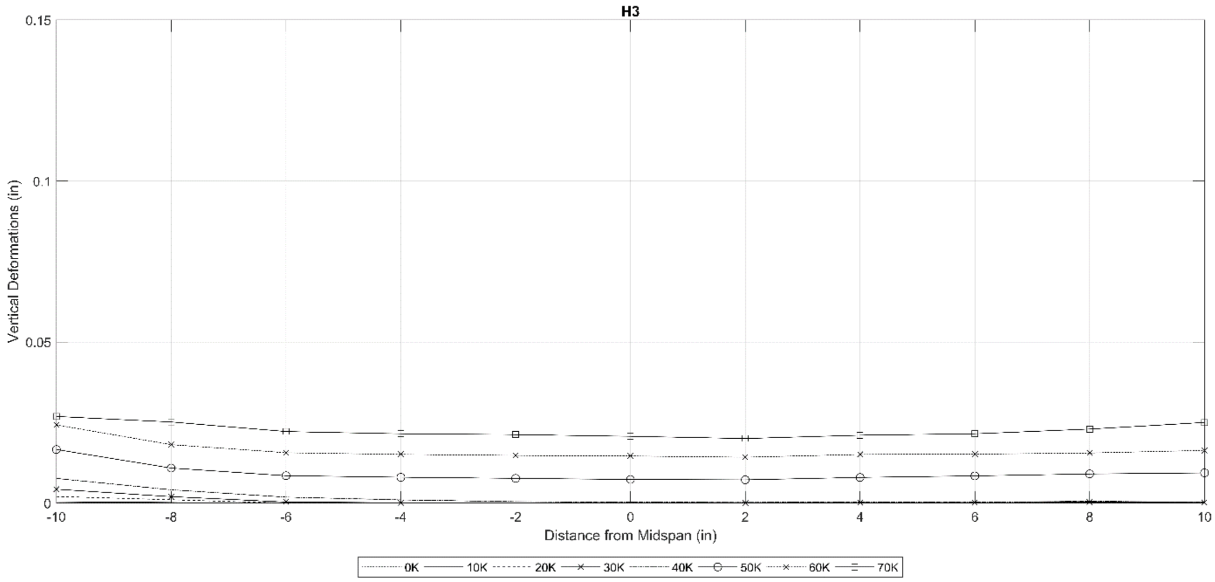

Figure 3-158: Vertical deformations of concrete surface along splice length of specimen H3 (data series are label using the average load applied to the splice ends)

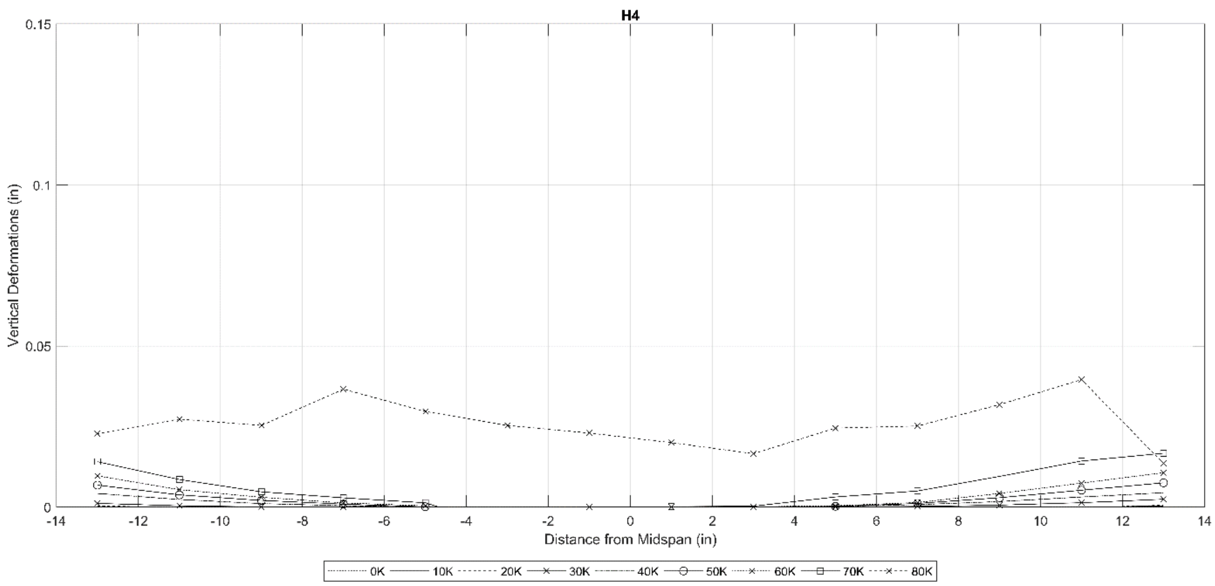

Figure 3-159: Vertical deformations of concrete surface along splice length of specimen H4 (data series are label using the average load applied to the splice ends)

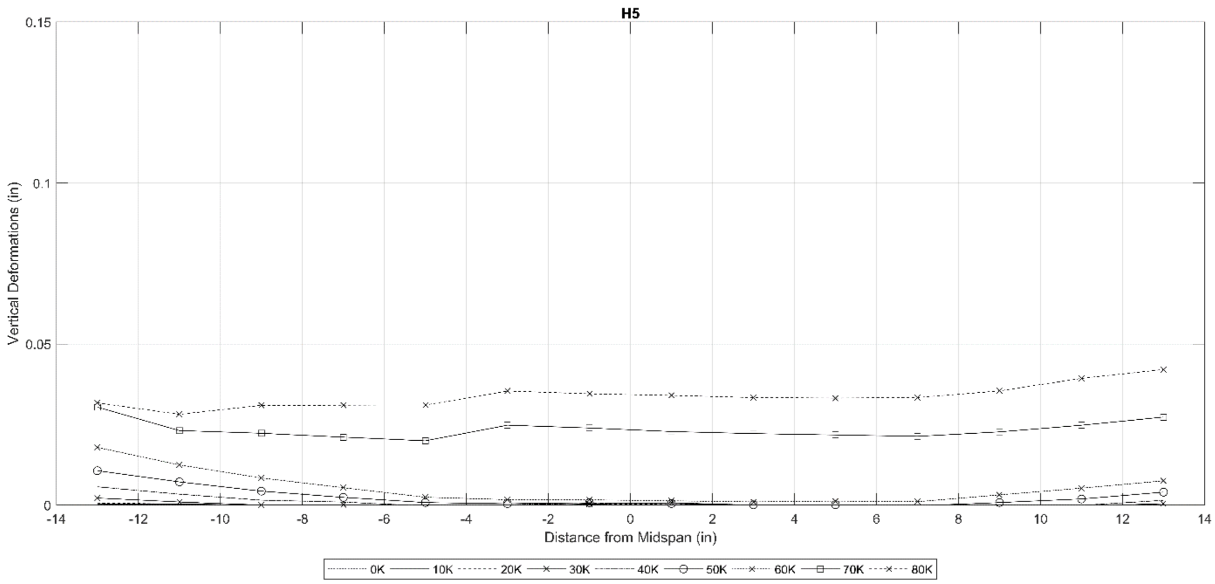

Figure 3-160: Vertical deformations of concrete surface along splice length of specimen H5 (data series are label using the average load applied to the splice ends)

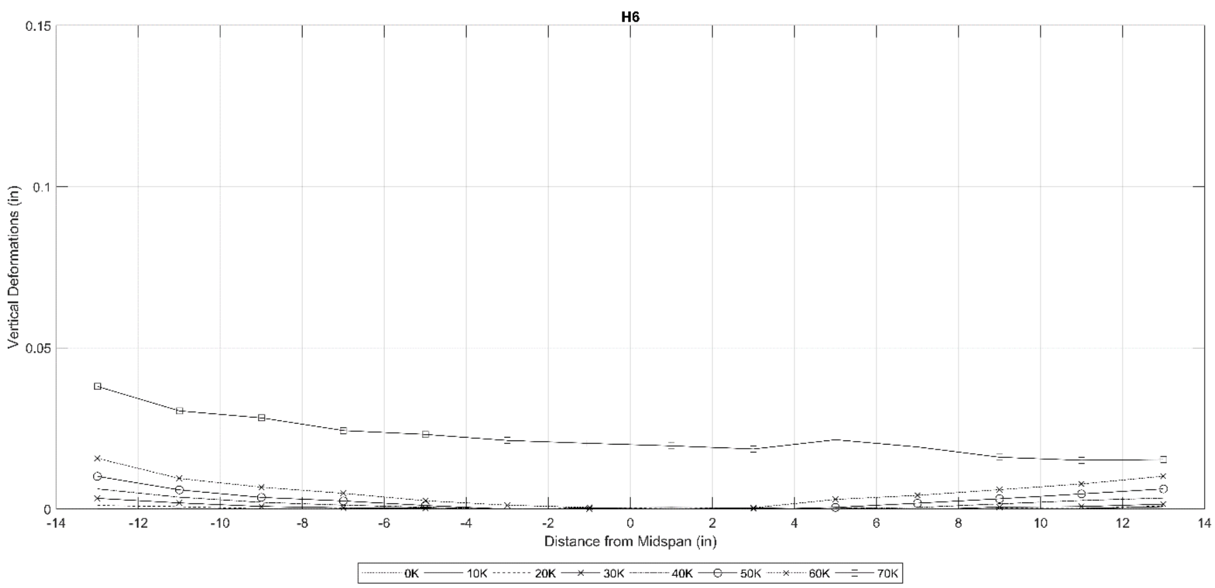

Figure 3-161: Vertical deformations of concrete surface along splice length of specimen H6 (data series are label using the average load applied to the splice ends)

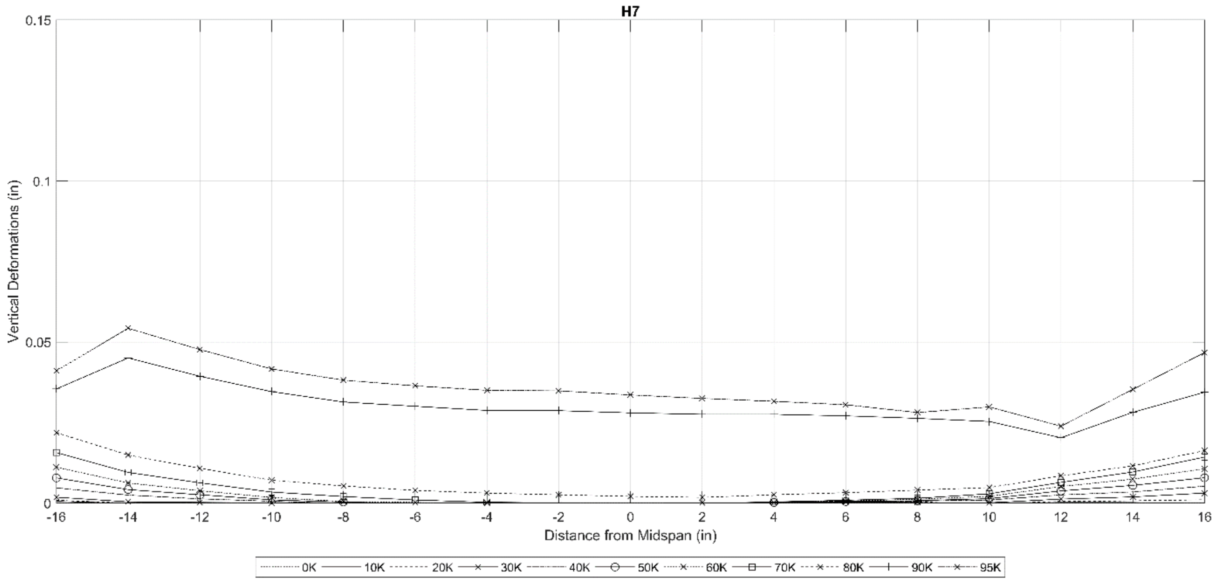

Figure 3-162: Vertical deformations of concrete surface along splice length of specimen H7 (data series are label using the average load applied to the splice ends)

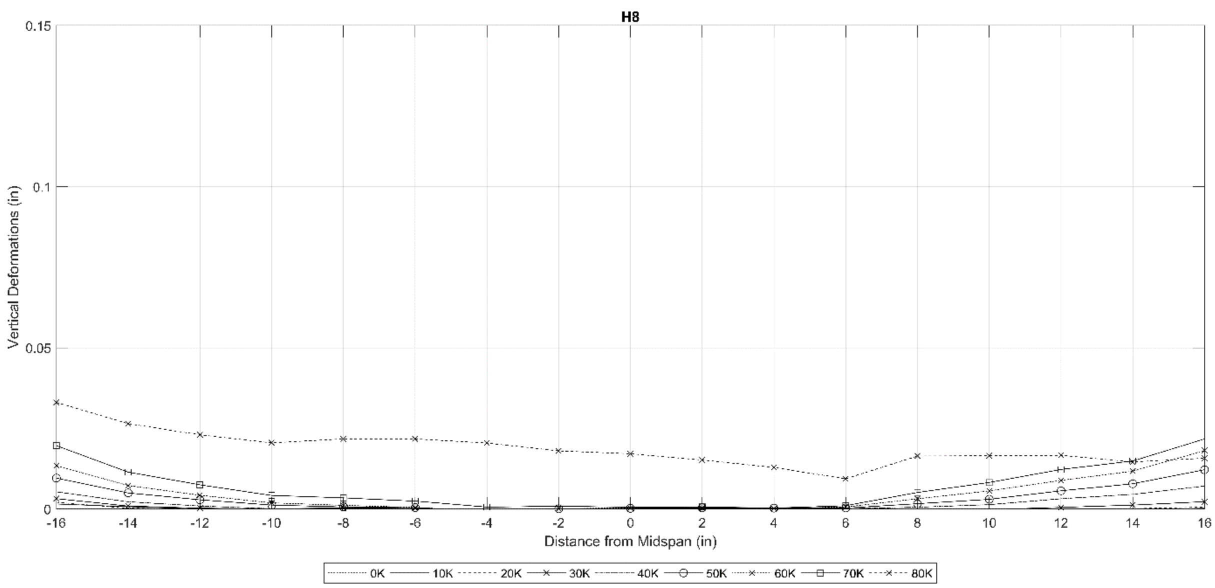

Figure 3-163: Vertical deformations of concrete surface along splice length of specimen H8 (data series are label using the average load applied to the splice ends)

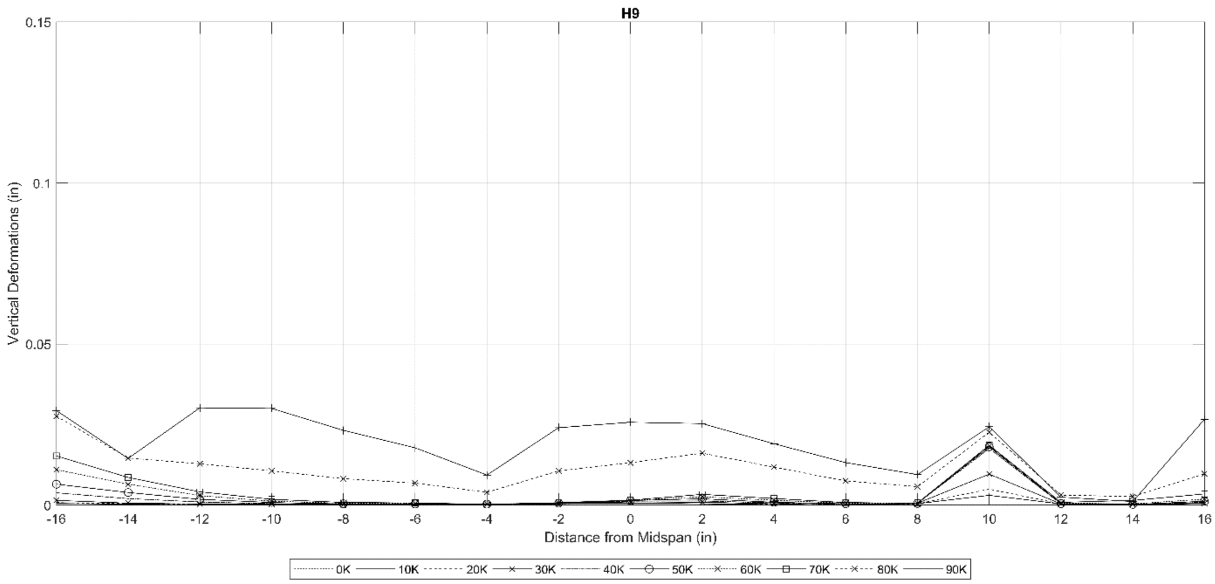

Figure 3-164: Vertical deformations of concrete surface along splice length of specimen H9 (data series are label using the average load applied to the splice ends)

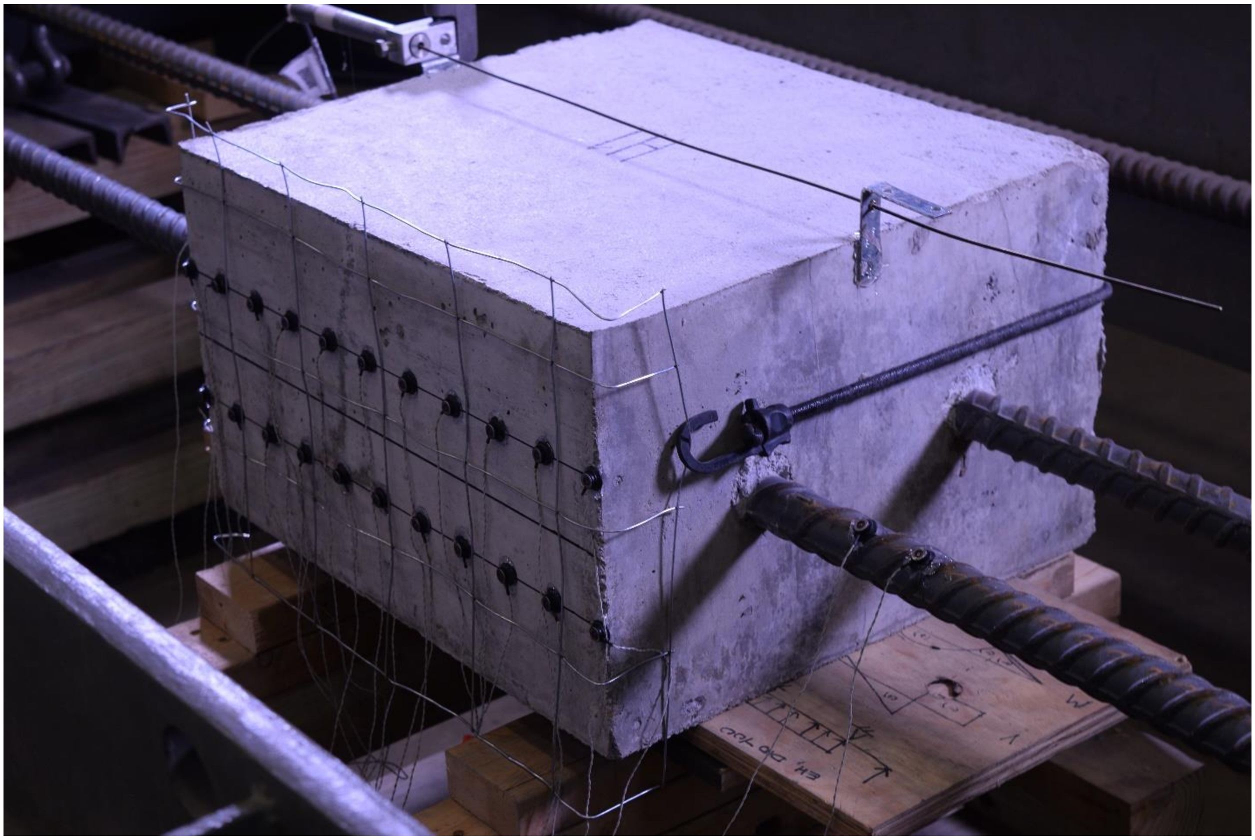

Figure 3-165: Specimen H1 during testing

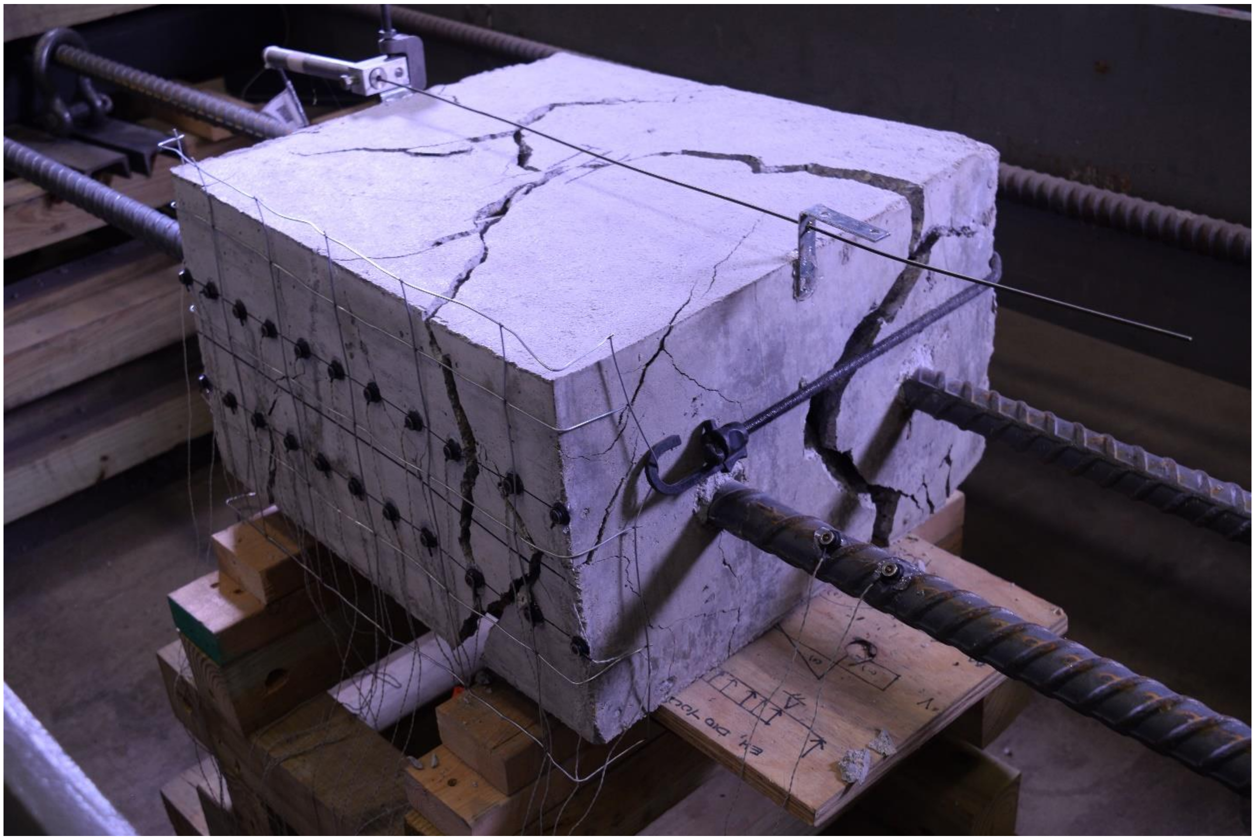

Figure 3-166: Splice failure of specimen H1

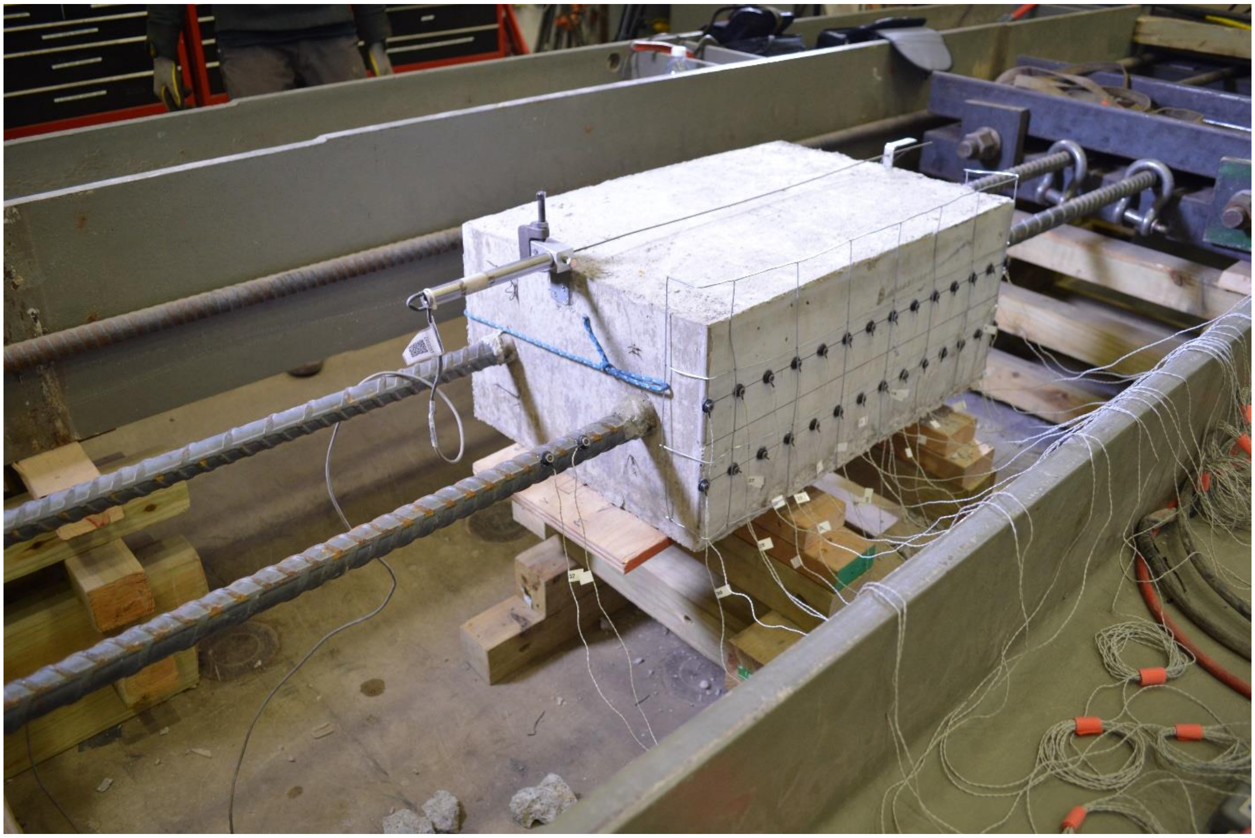

Figure 3-167: Specimen H4 during testing

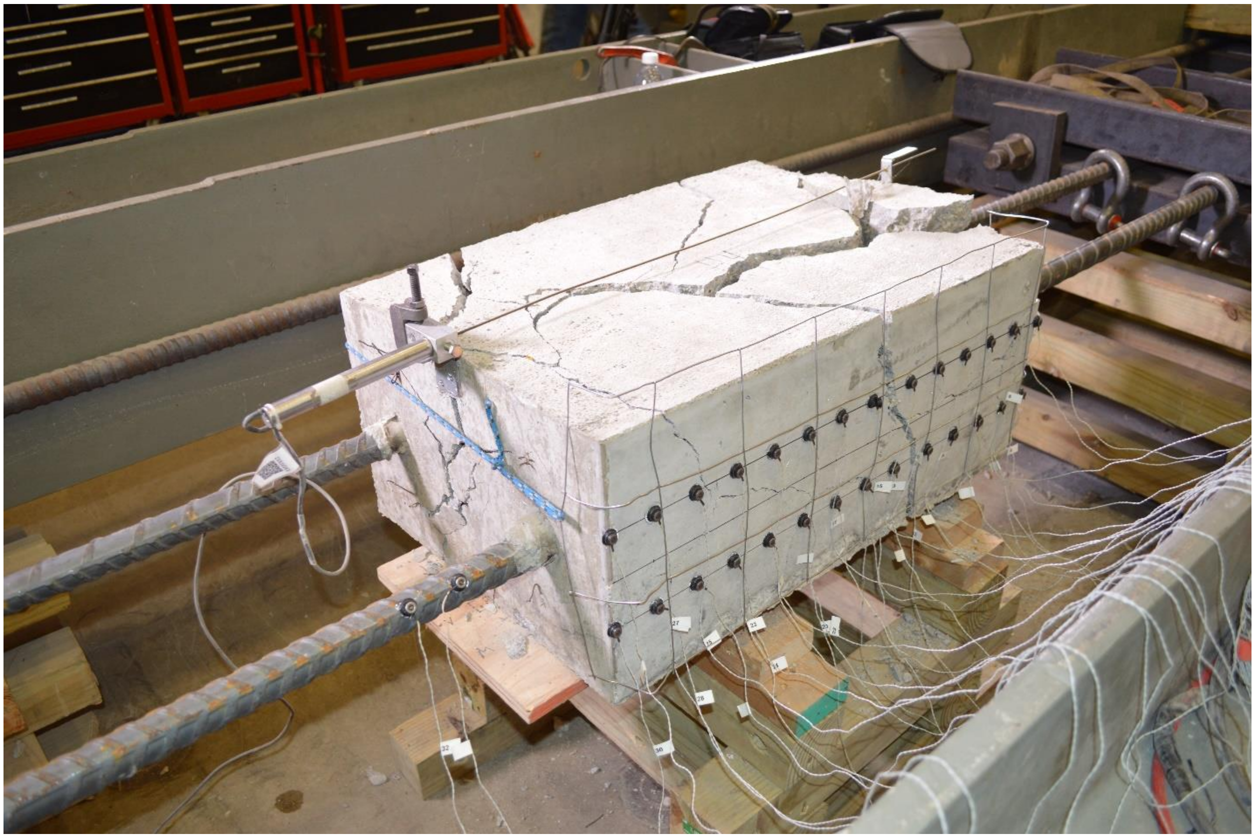

Figure 3-168: Splice failure of specimen H4

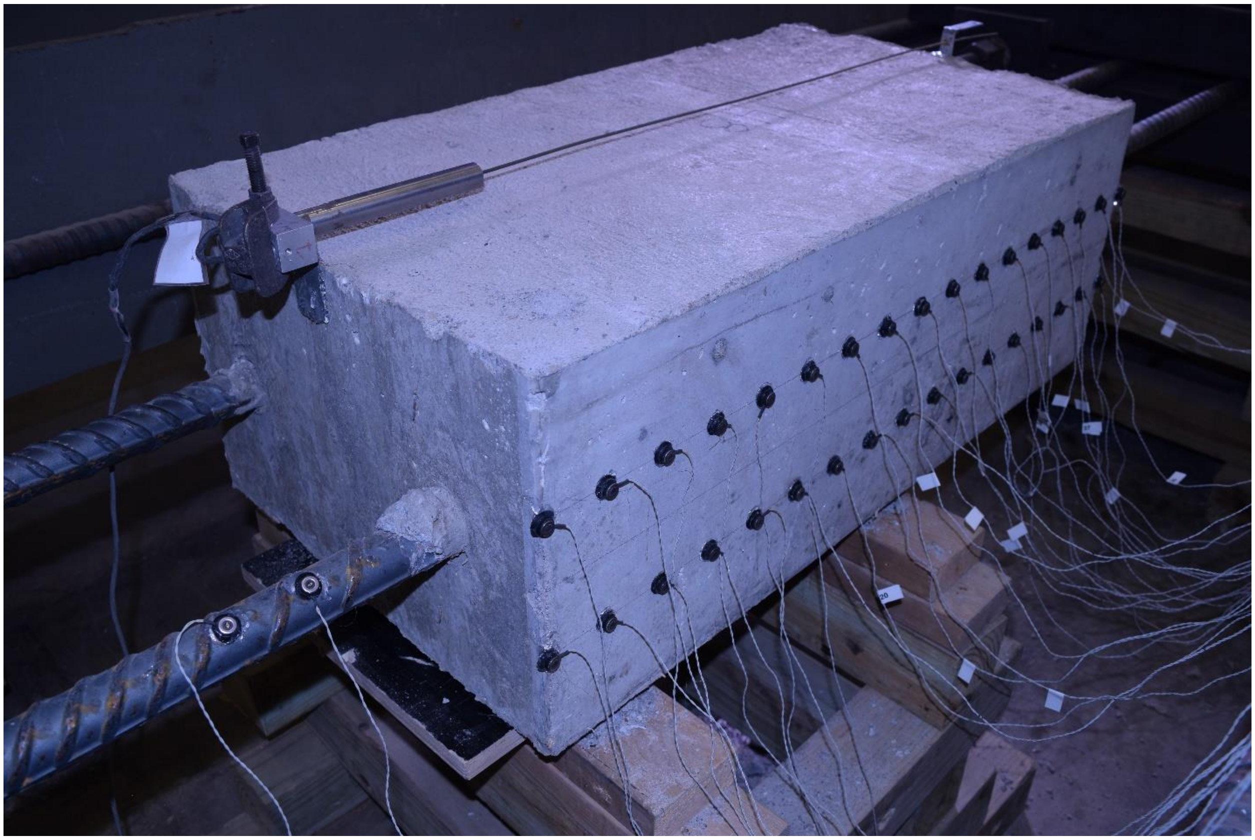

Figure 3-169: Specimen H8 during testing

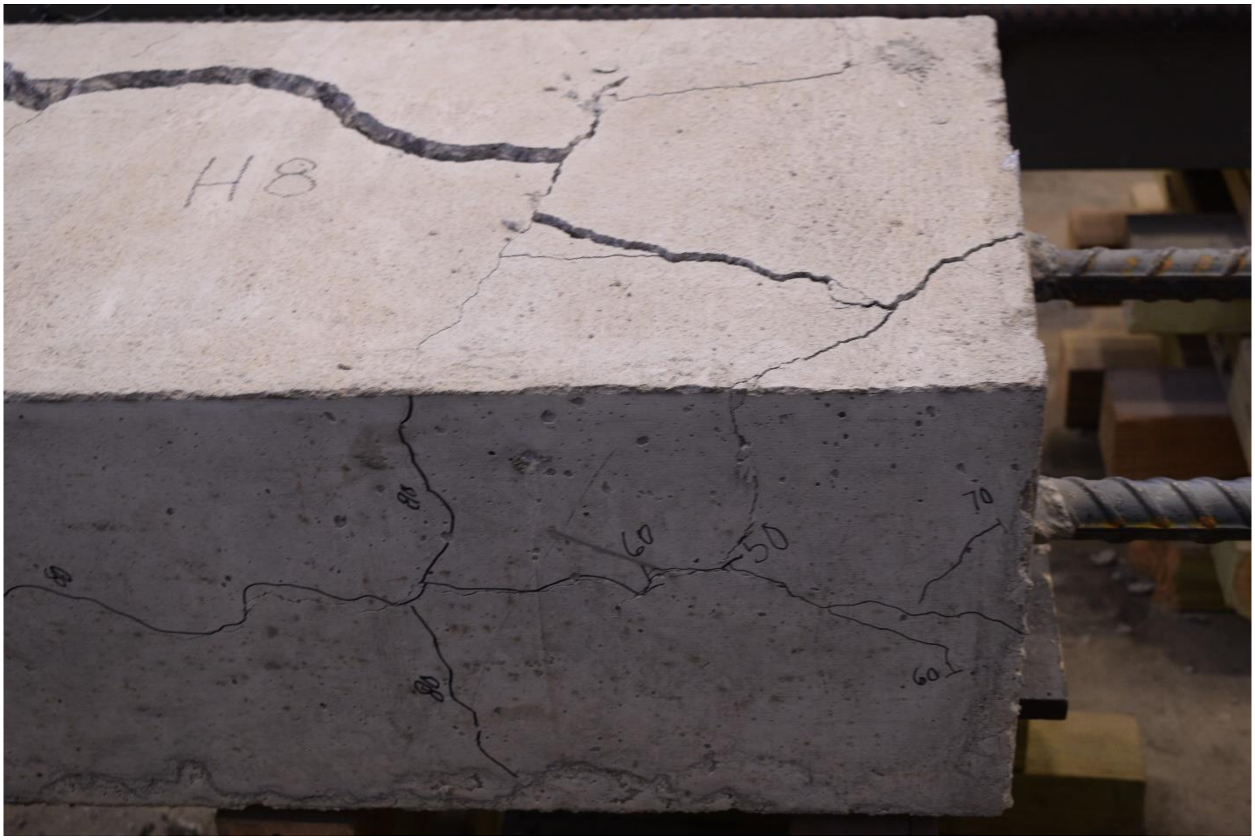

Figure 3-170: Splice failure of specimen H8

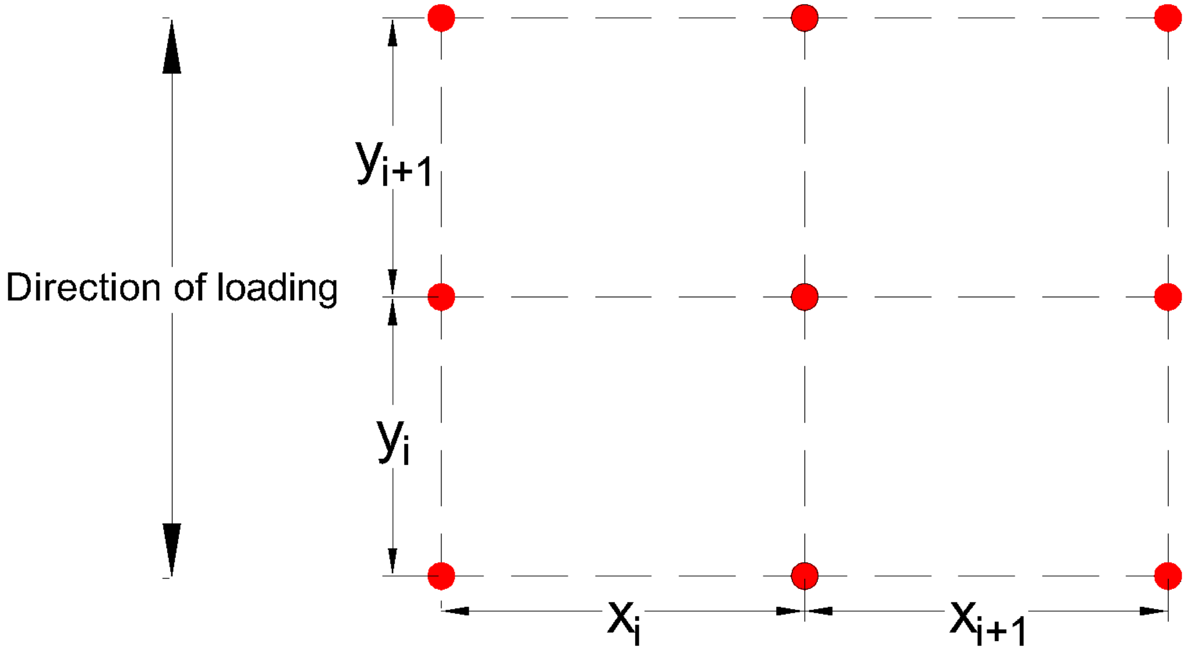

Figure 3-171: Grid station used for calculating vertical and horizontal deformations in Series-Four

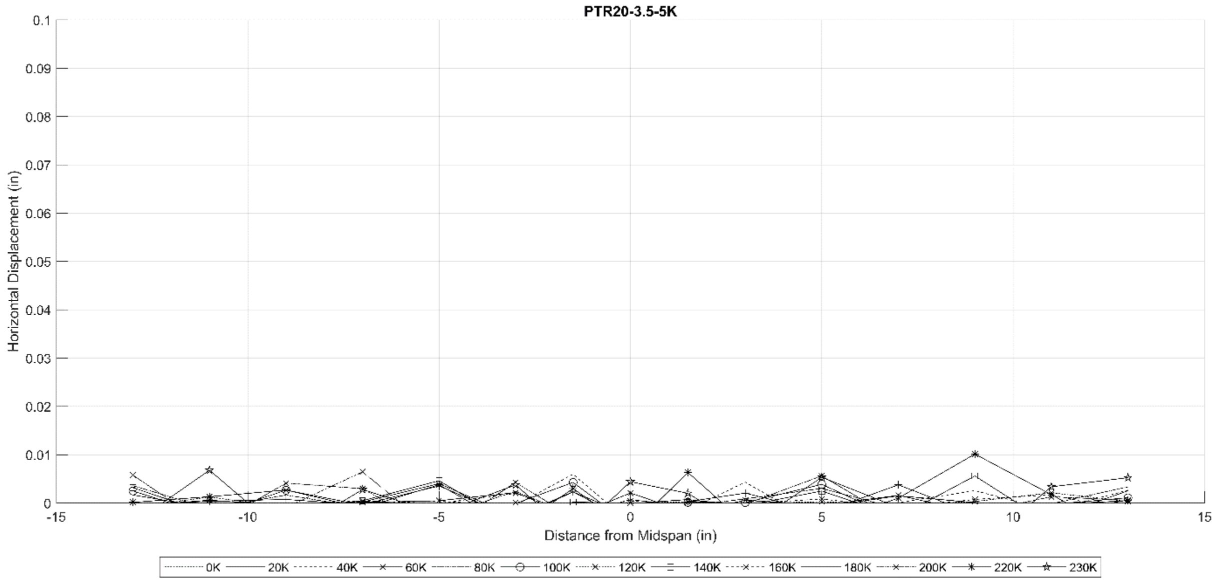

Figure 3-172: Horizontal deformations of concrete surface along splice length of specimen PTR20-3.5-5K (data series are label using the average load applied to the splice ends)

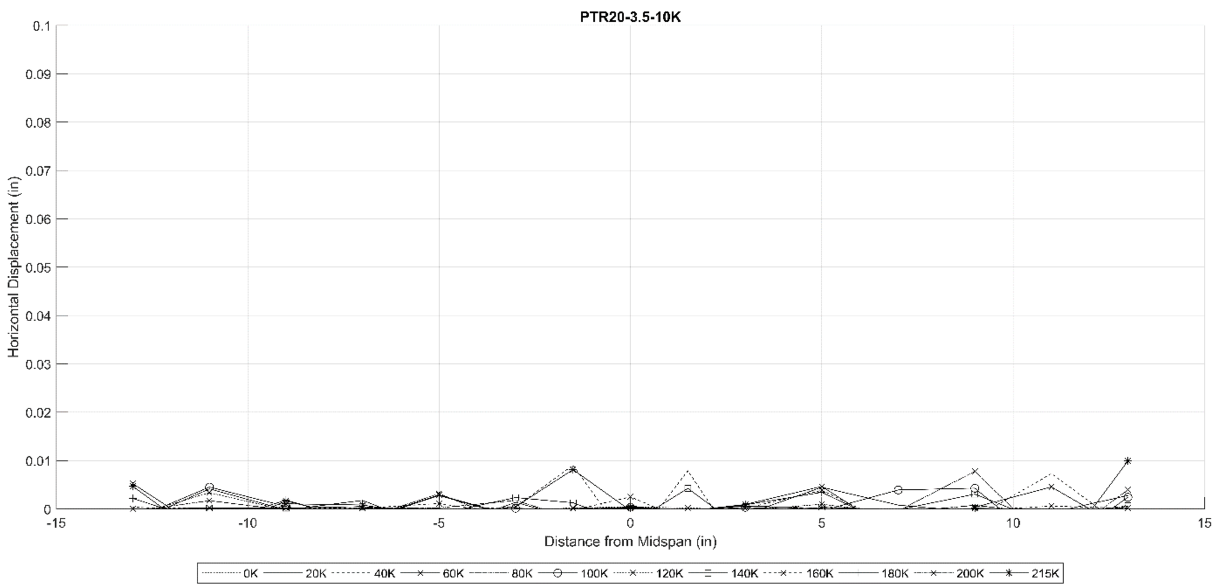

Figure 3-173: Horizontal deformations of concrete surface along splice length of specimen PTR20-3.5-10K (data series are label using the average load applied to the splice ends)

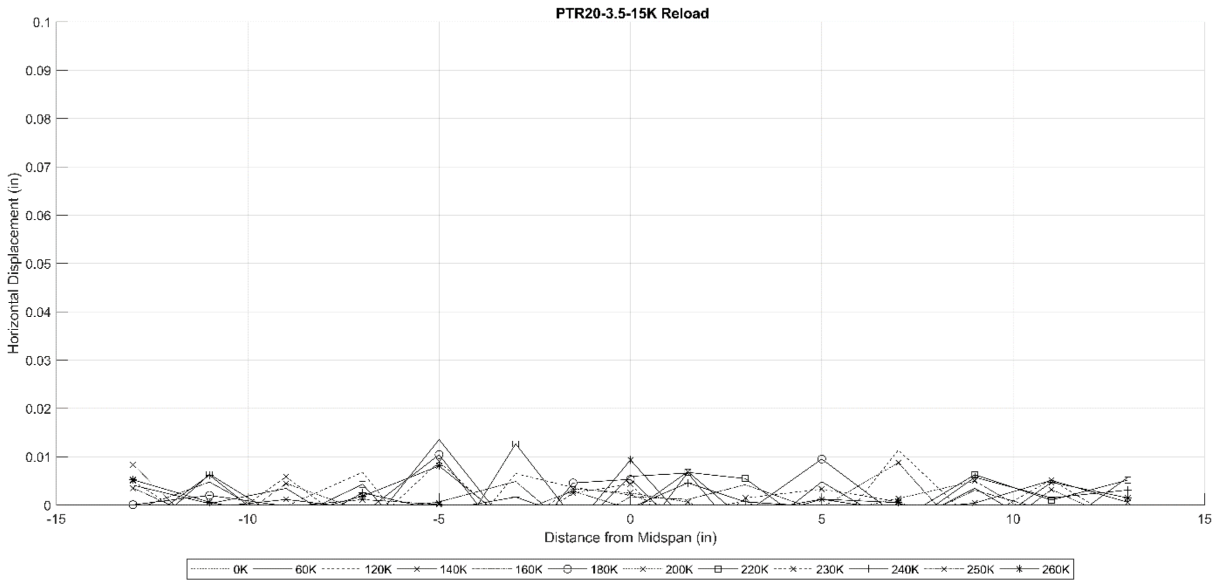

Figure 3-174: Horizontal deformations of concrete surface along splice length of specimen PTR20-3.5-15K (data series are label using the average load applied to the splice ends)

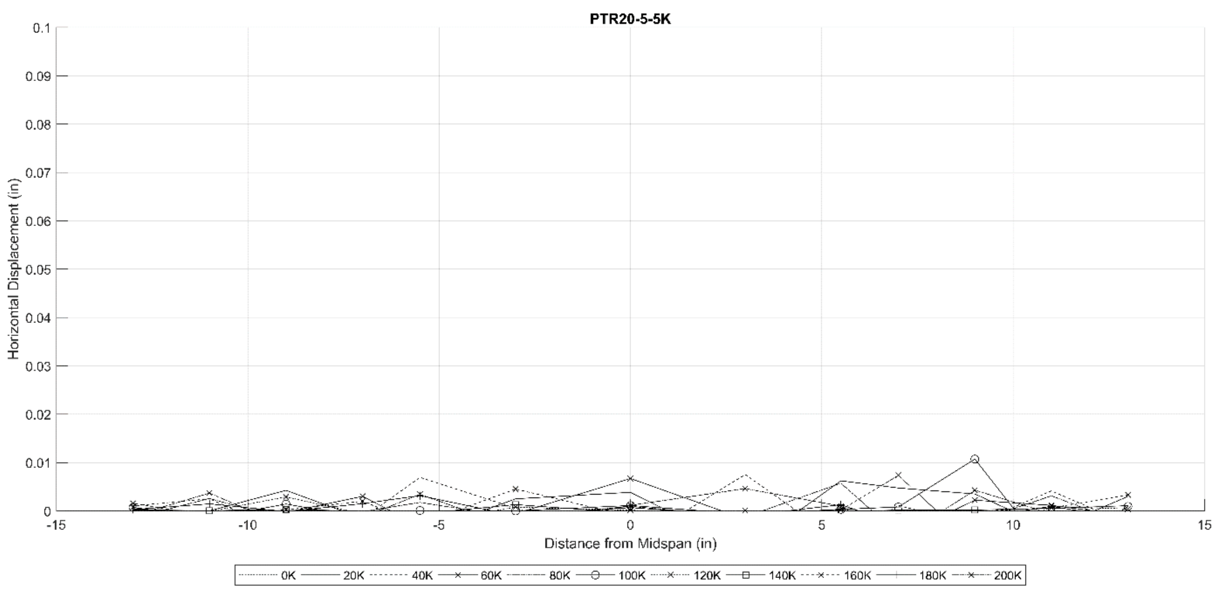

Figure 3-175: Horizontal deformations of concrete surface along splice length of specimen PTR20-5-5K (data series are label using the average load applied to the splice ends)

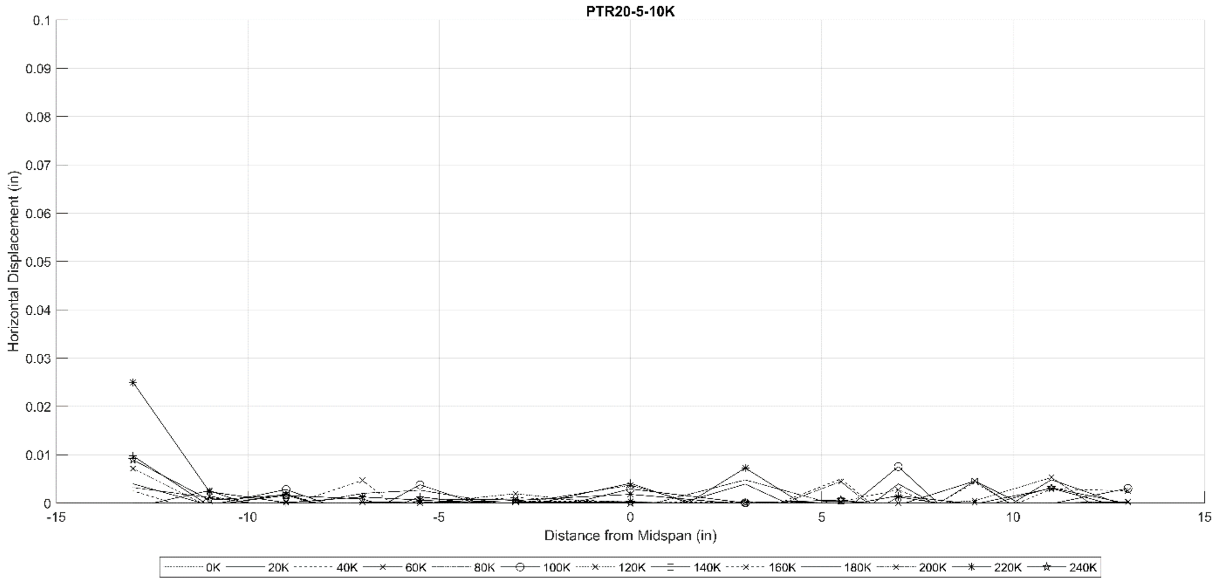

Figure 3-176: Horizontal deformations of concrete surface along splice length of specimen PTR20-5-10K (data series are label using the average load applied to the splice ends)

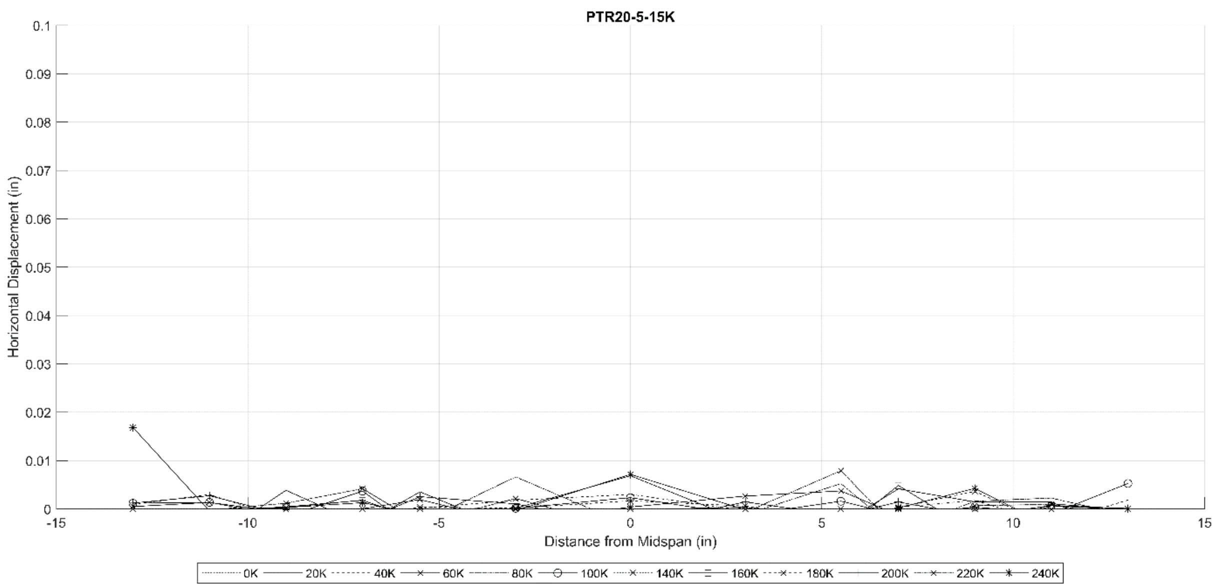

Figure 3-177: Horizontal deformations of concrete surface along splice length of specimen PTR20-5-15K (data series are label using the average load applied to the splice ends)

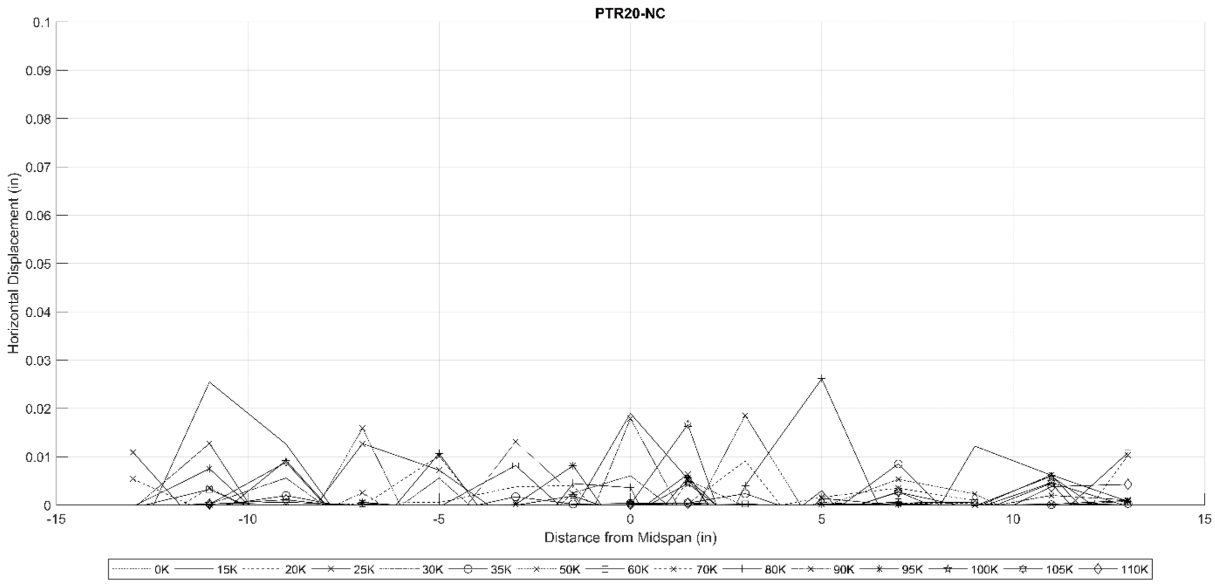

Figure 3-178: Horizontal deformations of concrete surface along splice length of specimen PTR20-NC (data series are label using the average load applied to the splice ends)

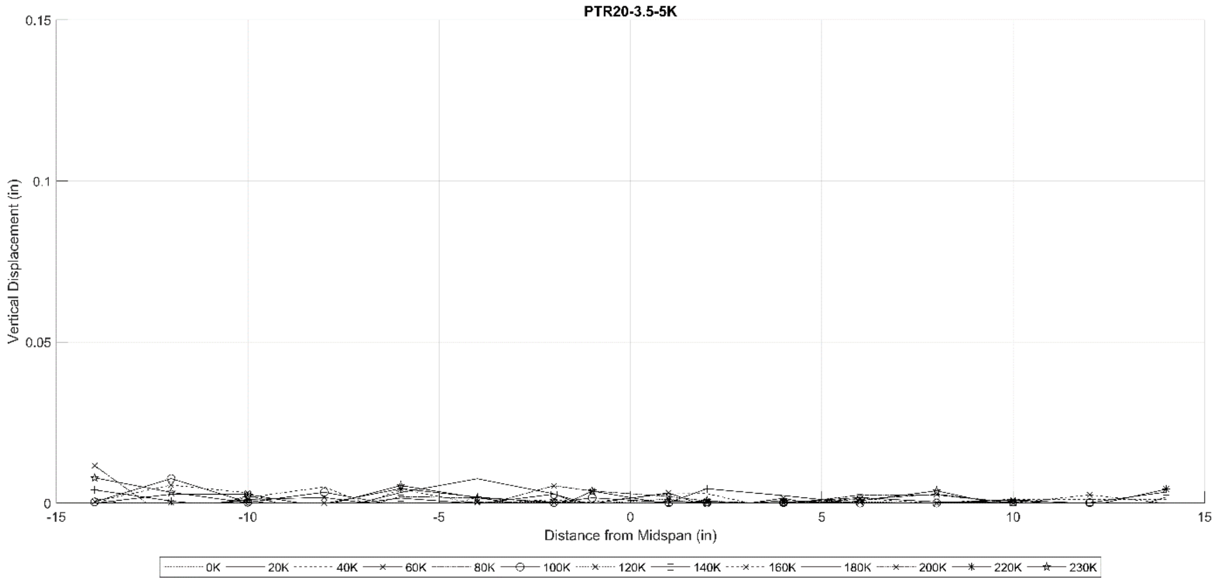

Figure 3-179: Vertical deformations of concrete surface along splice length of specimen PTR20-3.5-5K (data series are label using the average load applied to the splice ends)

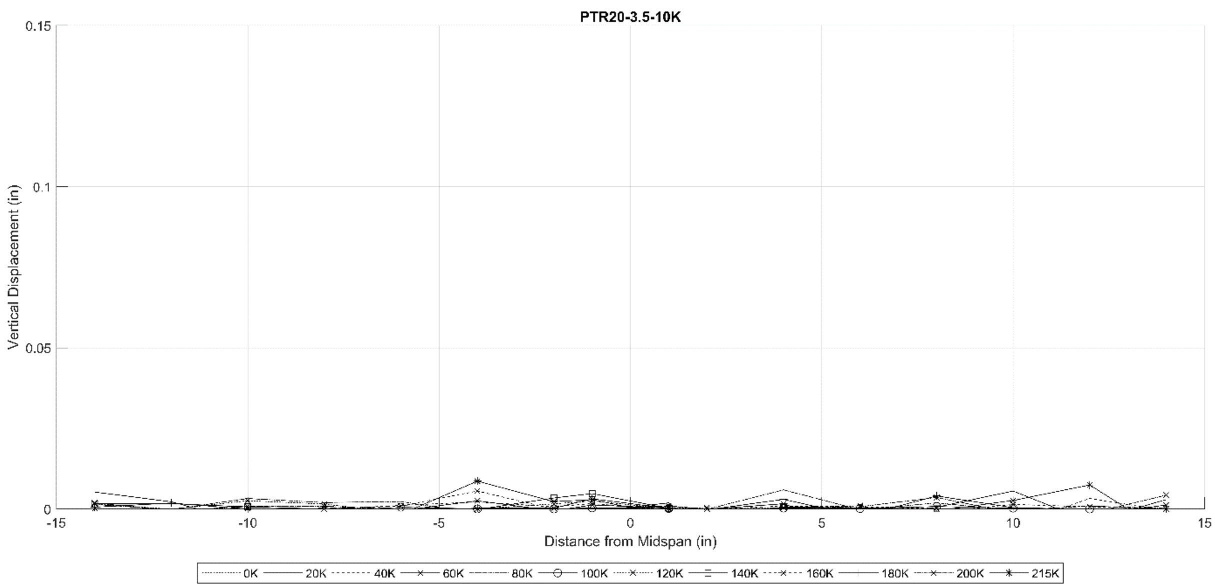

Figure 3-180: Vertical deformations of concrete surface along splice length of specimen PTR20-3.5-10K (data series are label using the average load applied to the splice ends)

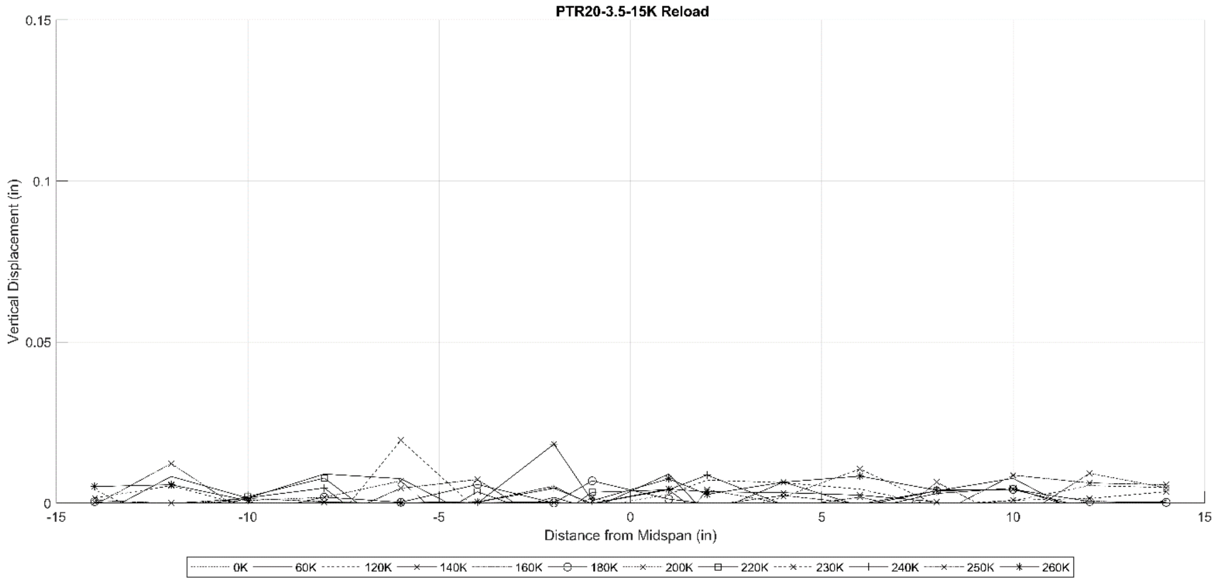

Figure 3-181: Vertical deformations of concrete surface along splice length of specimen PTR20-3.5-15K (data series are label using the average load applied to the splice ends)

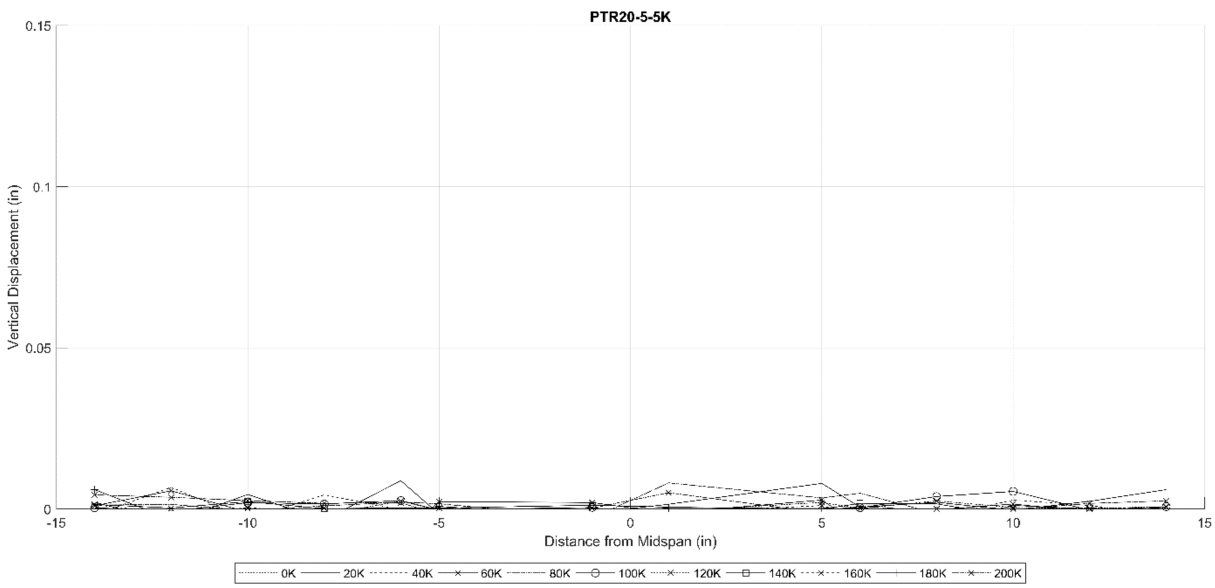

Figure 3-182: Vertical deformations of concrete surface along splice length of specimen PTR20-5-5K (data series are label using the average load applied to the splice ends)

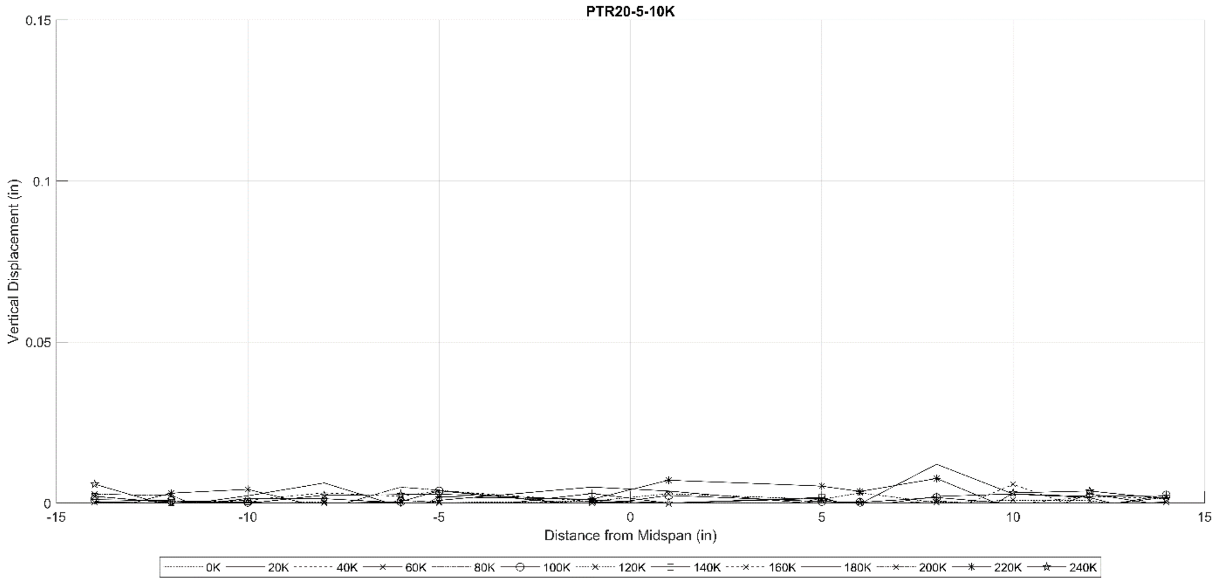

Figure 3-183: Vertical deformations of concrete surface along splice length of specimen PTR20-5-10K (data series are label using the average load applied to the splice ends)

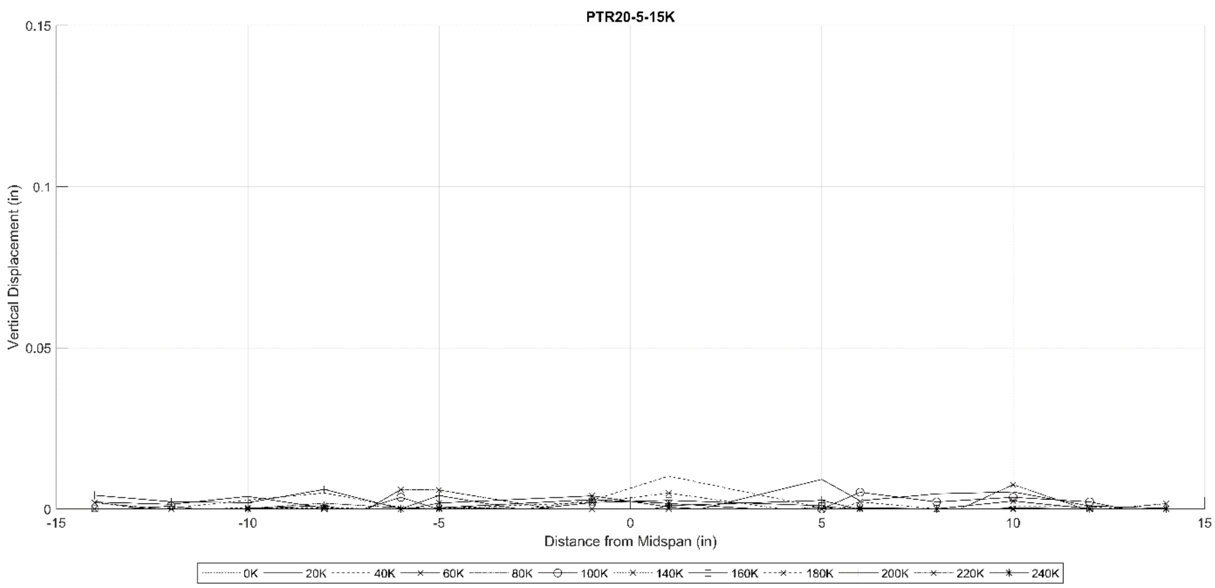

Figure 3-184: Vertical deformations of concrete surface along splice length of specimen PTR20-5-15K (data series are label using the average load applied to the splice ends)

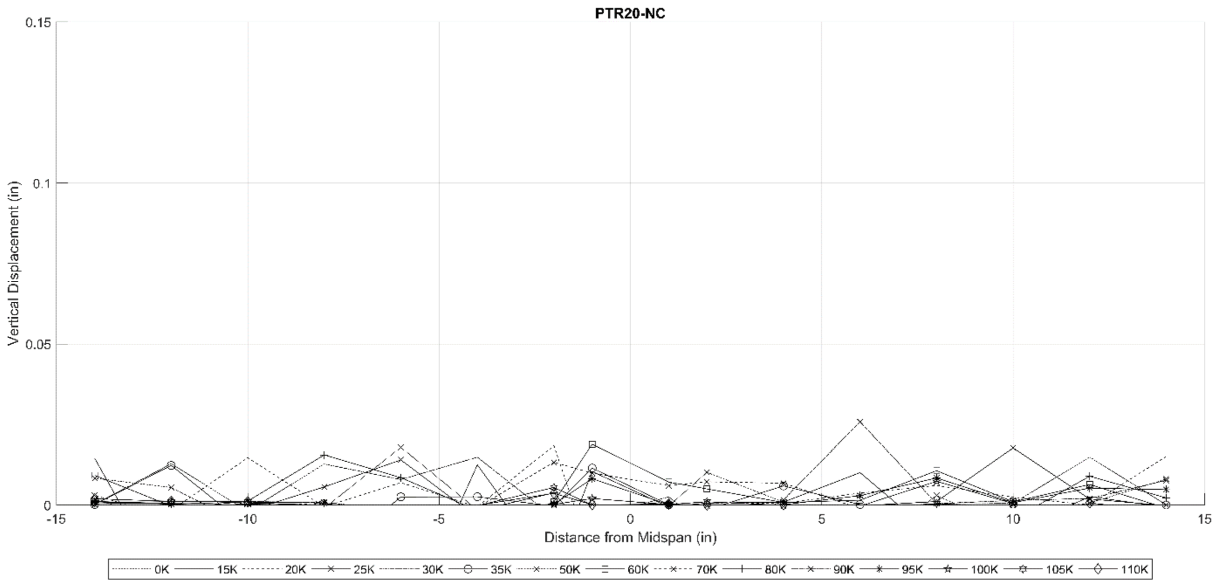

Figure 3-185: Vertical deformations of concrete surface along splice length of specimen PTR20-NC (data series are label using the average load applied to the splice ends)

Figure 3-186: Specimen PTR20-3.5-5K during testing

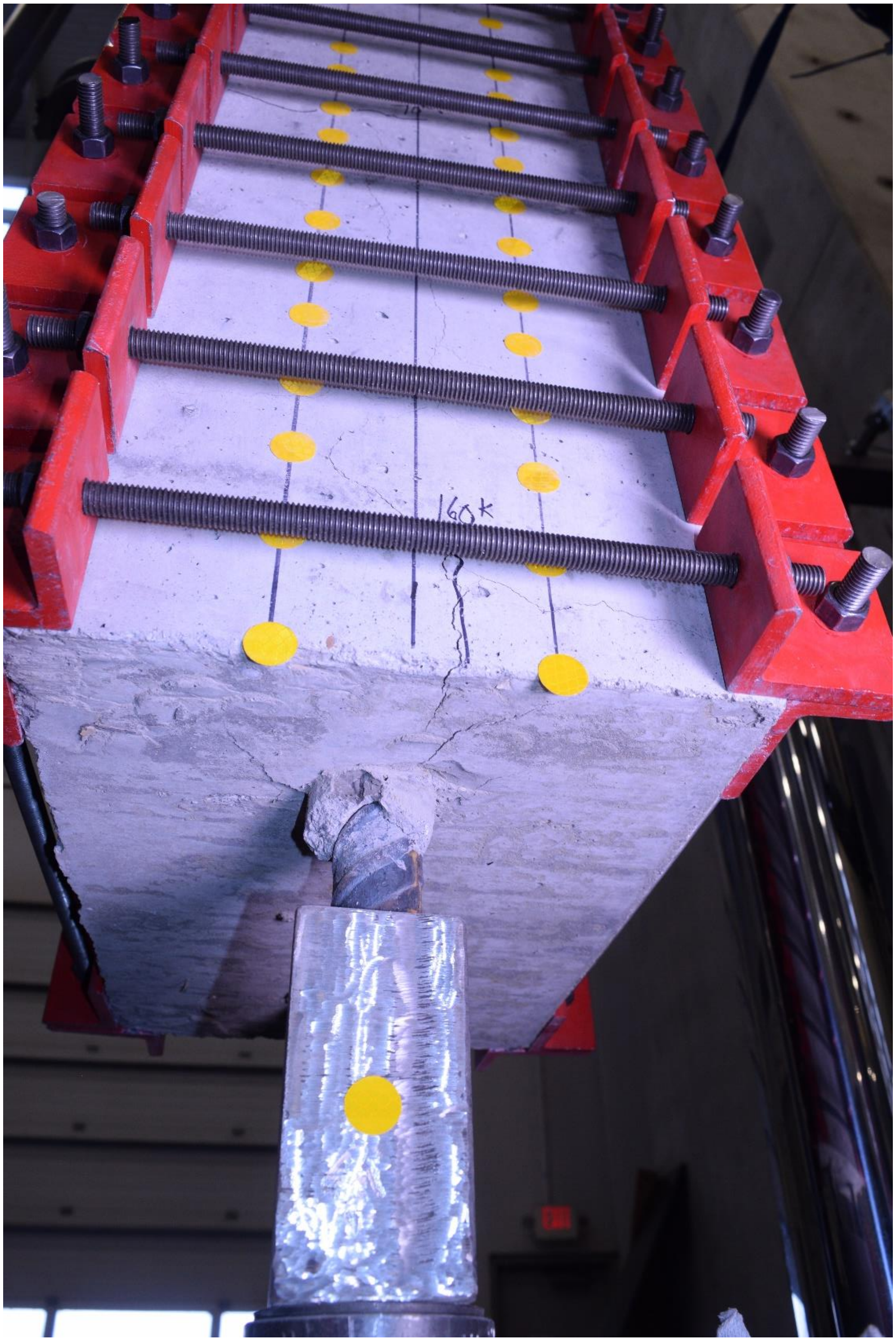

Figure 3-187: Splice failure of specimen PTR20-3.5-5K

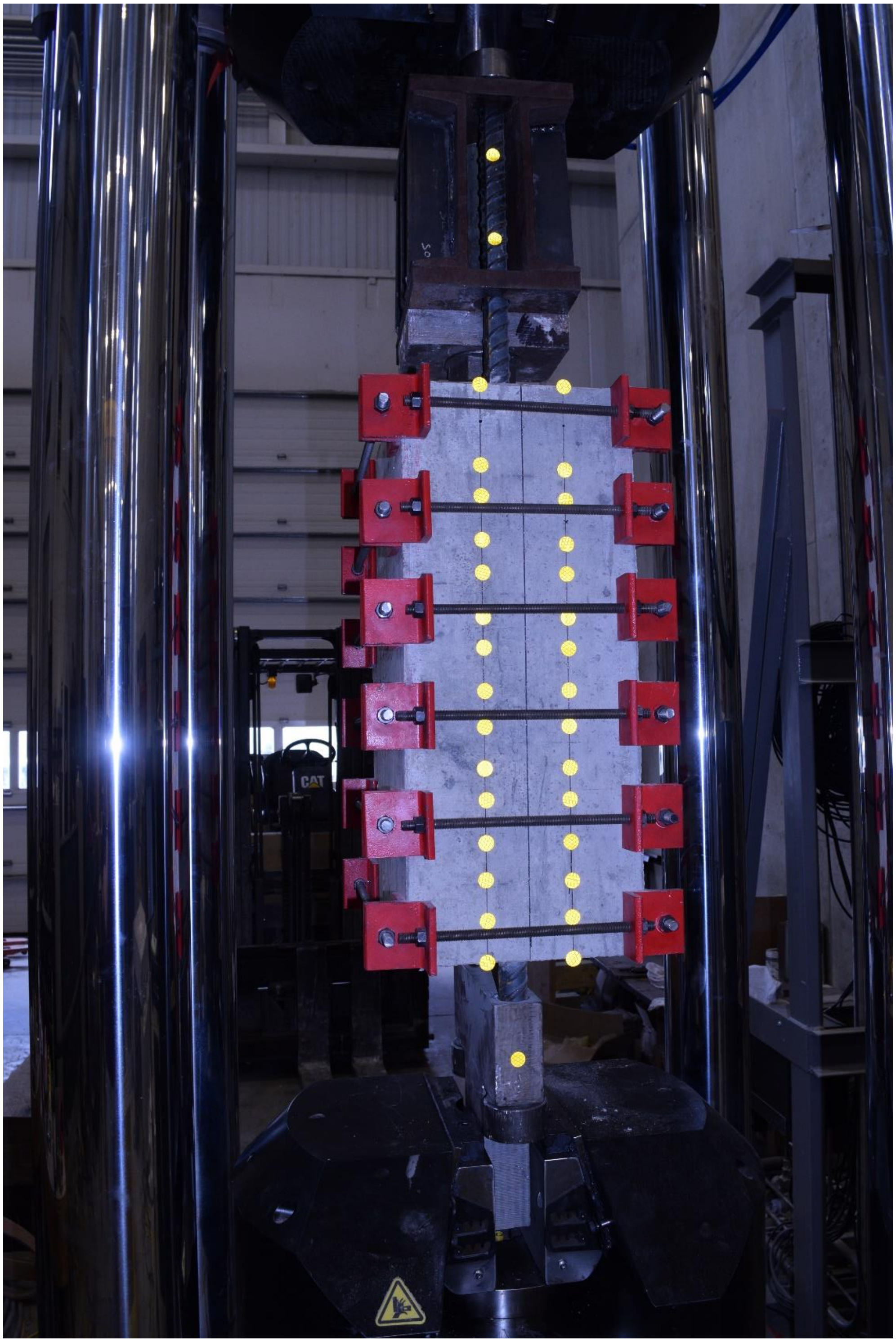

Figure 3-188: Specimen PTR20-5-10K during testing

Figure 3-189: Splice failure of specimen PTR20-5-10K

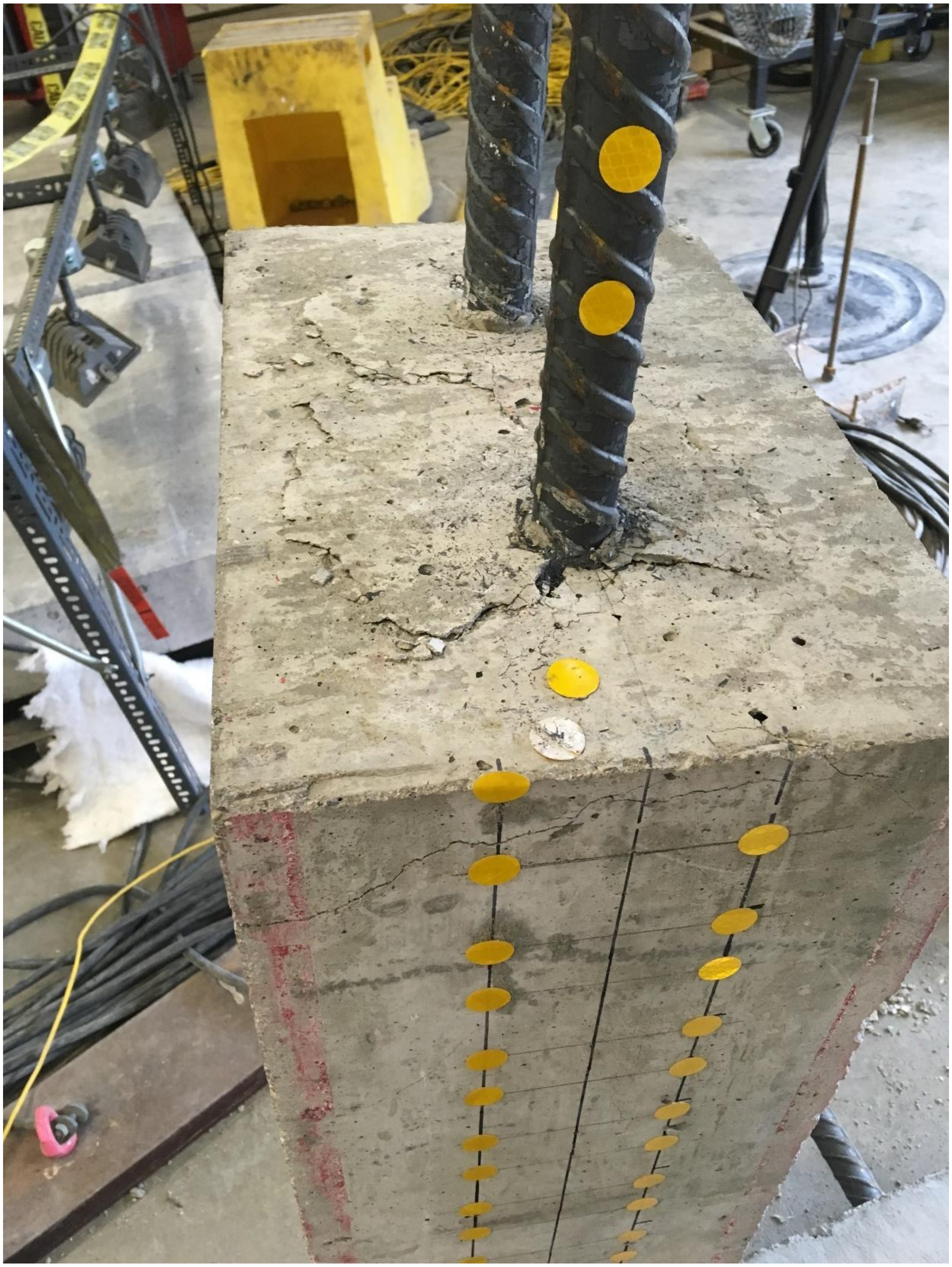

Figure 3-190: Shear cone failure of specimen PTR20-3.5-15K

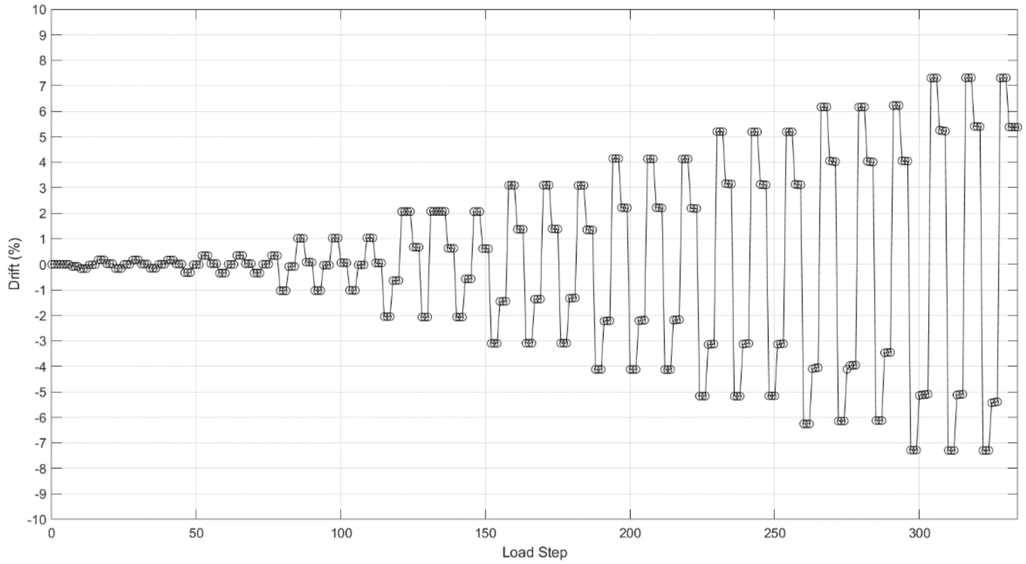

Figure 3-191: Column C1 loading history (markers indicate measurement recordings)

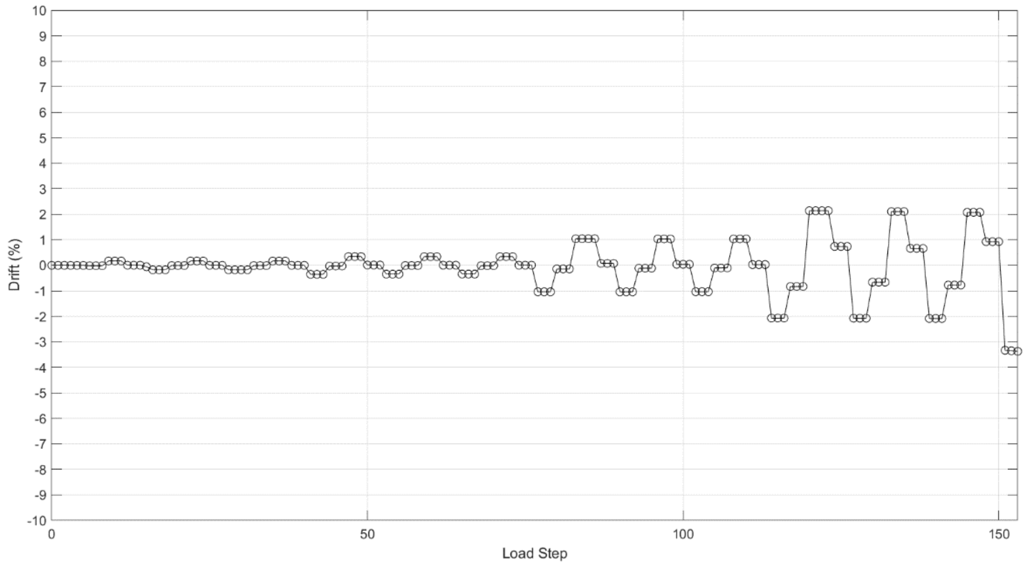

Figure 3-192: Column C2 loading history (markers indicate measurement recordings)

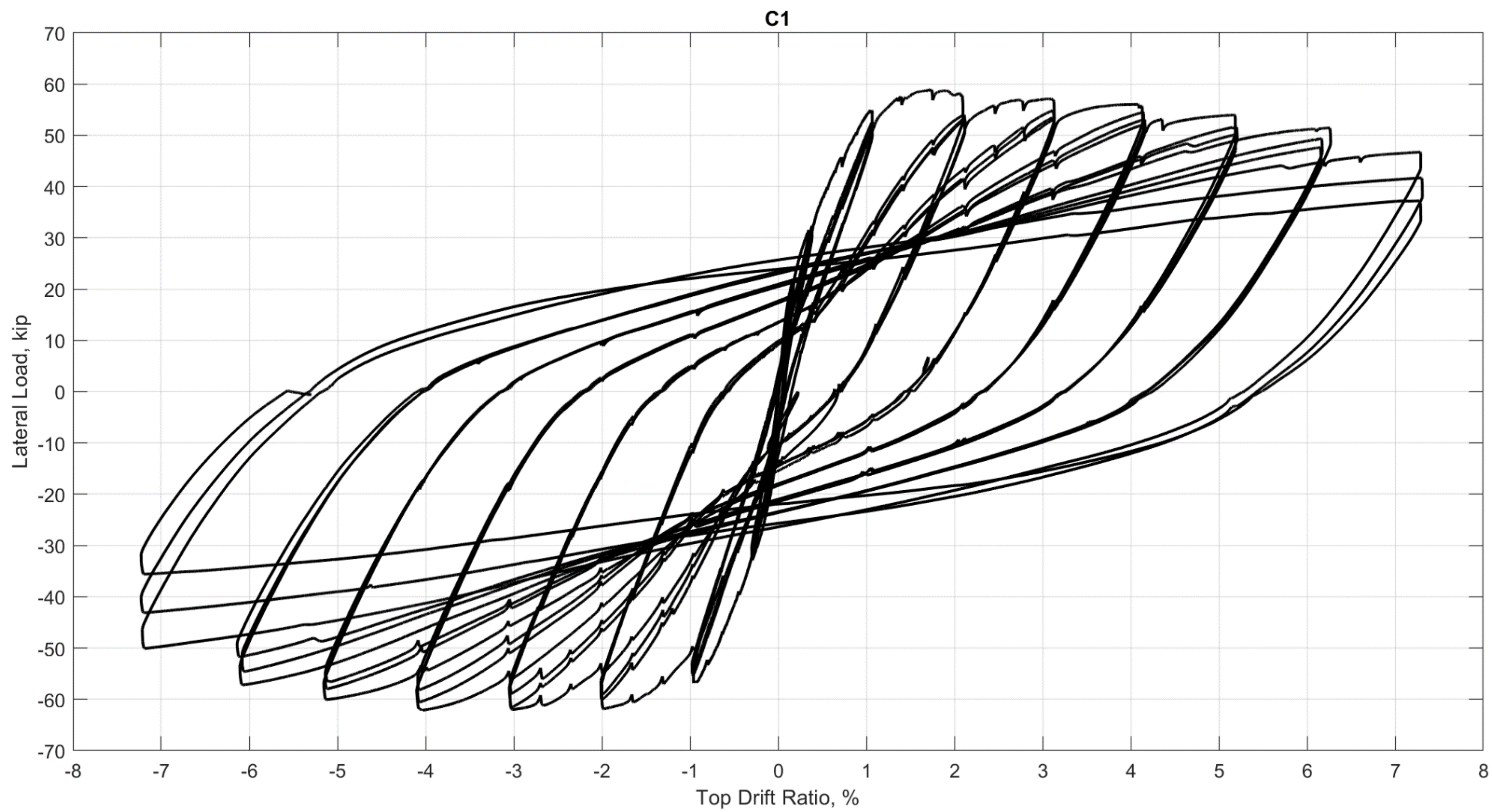

Figure 3-193: Lateral load versus top drift ratio for column C1.

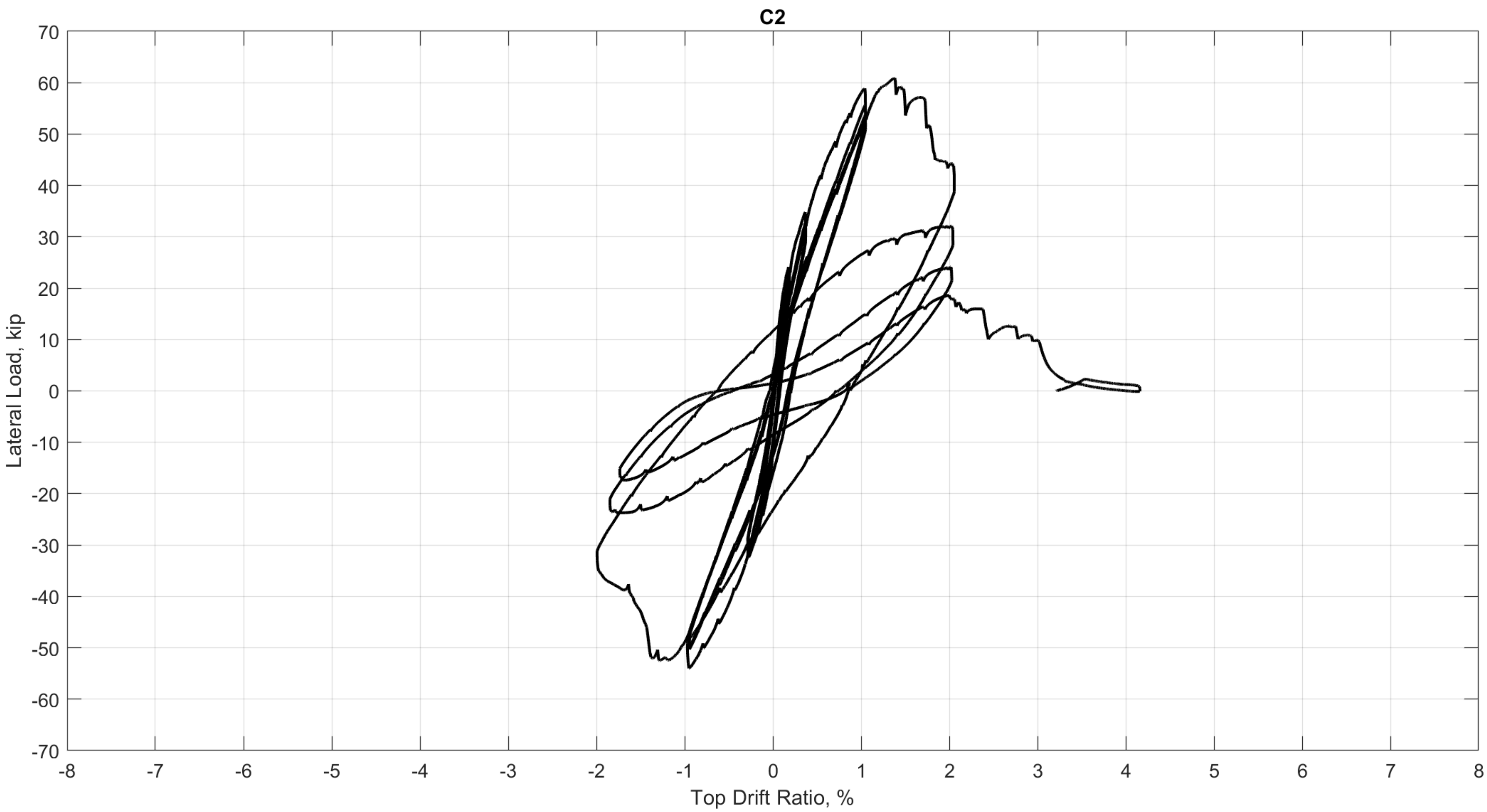

Figure 3-194: Lateral load versus top drift ratio for column C2.

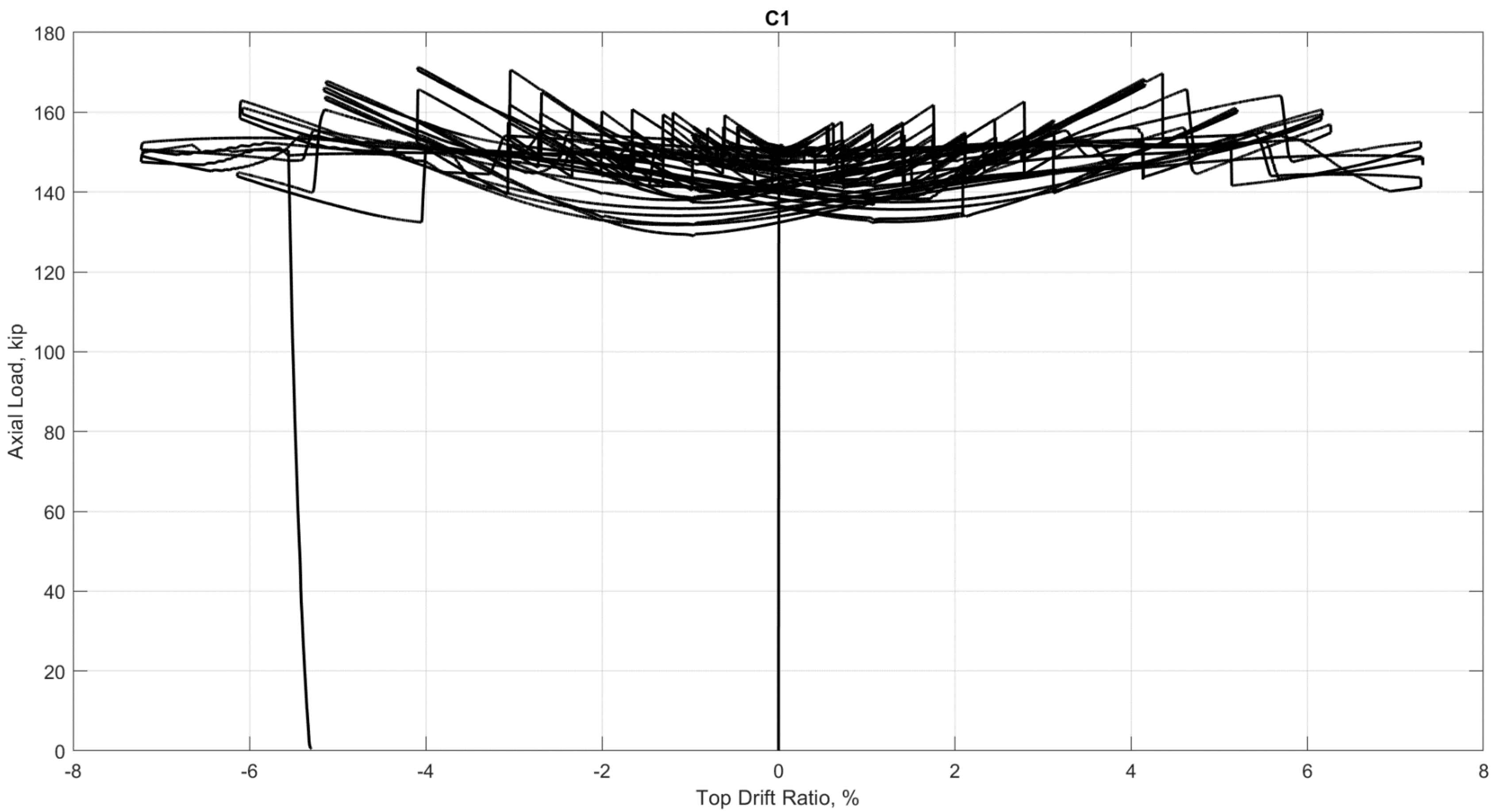

Figure 3-195: Axial load versus top drift ratio for column C1.

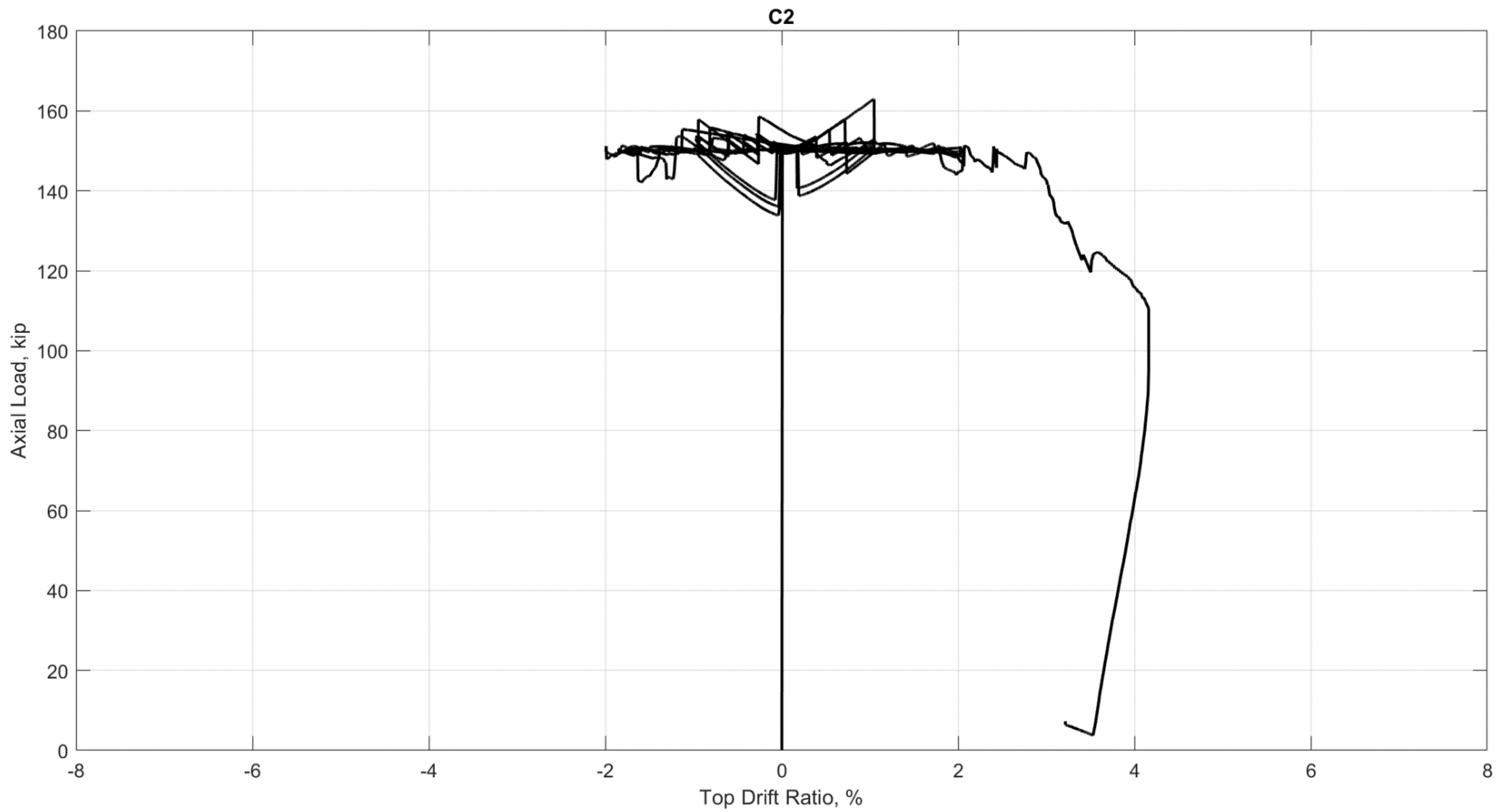

Figure 3-196: Axial load versus top drift ratio for column C2.

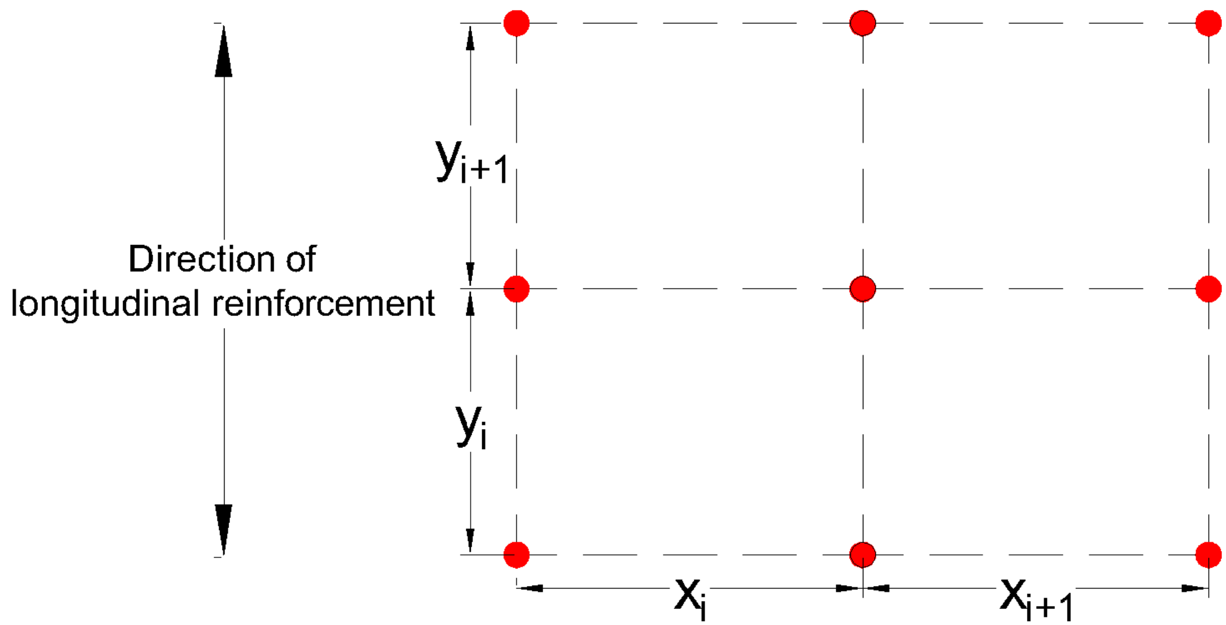

Figure 3-197: Grid station for calculating horizontal and vertical strains in series five.

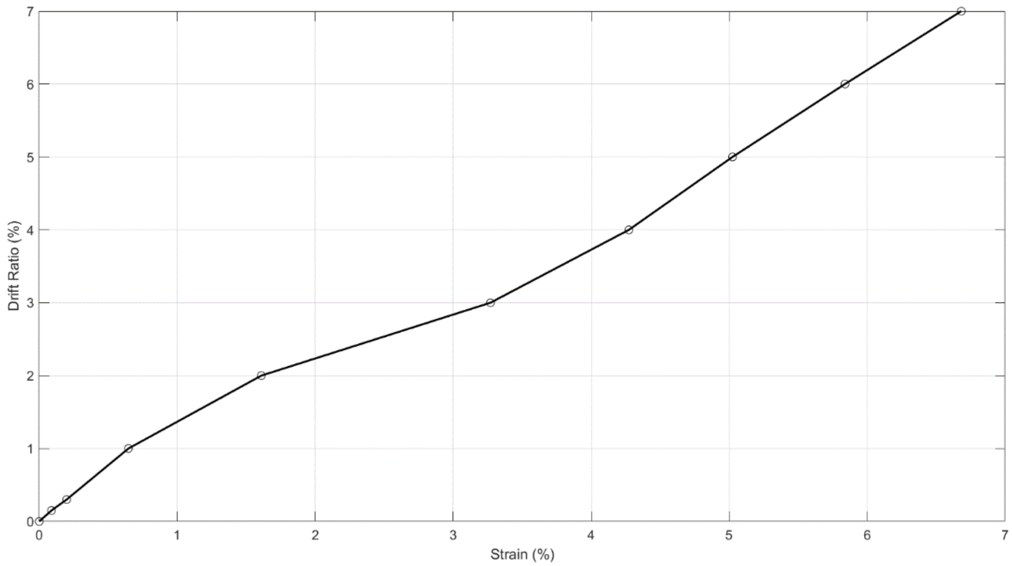

Figure 3-198: Column C1 drift ratio vs. tensile strain (recorded at the column base in the outermost layer of steel in tension)

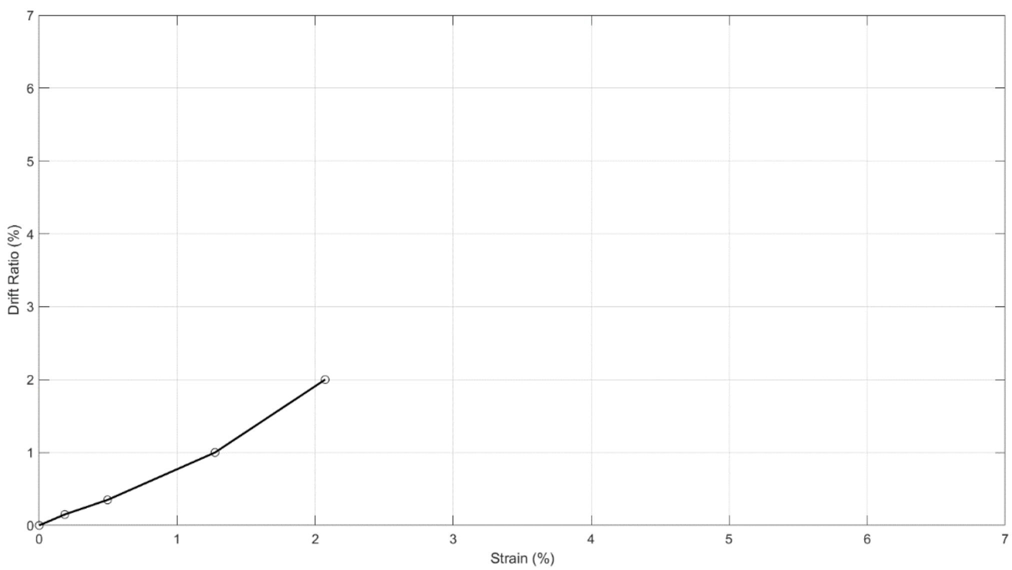

Figure 3-199: Column C2 drift ratio vs. tensile strain (recorded at the column base in the outermost layer of steel in tension)

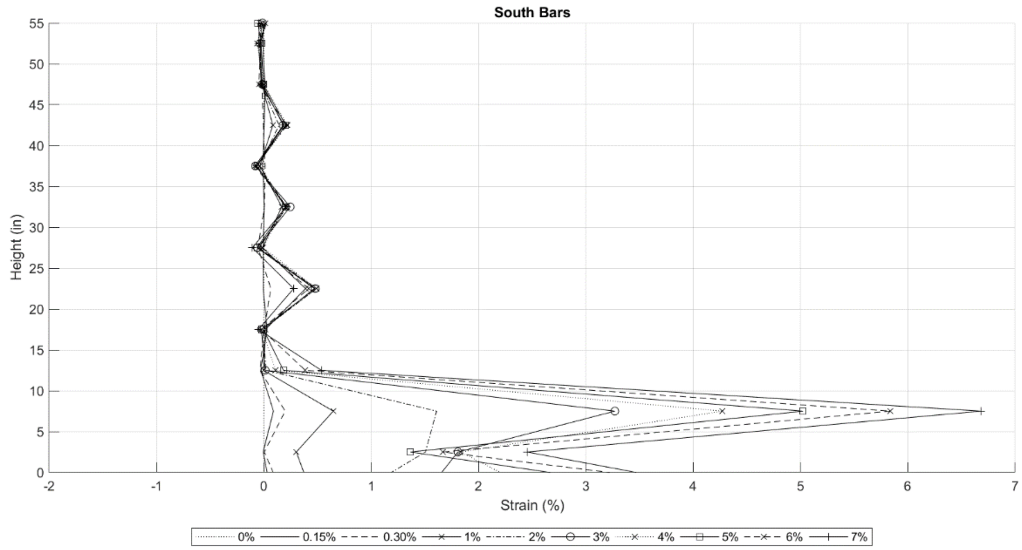

Figure 3-200: Reinforcement strain distribution over height of column C1 (south bars indicate outermost steel layer in tension, markers indicate the drift ratio when strain was recorded)

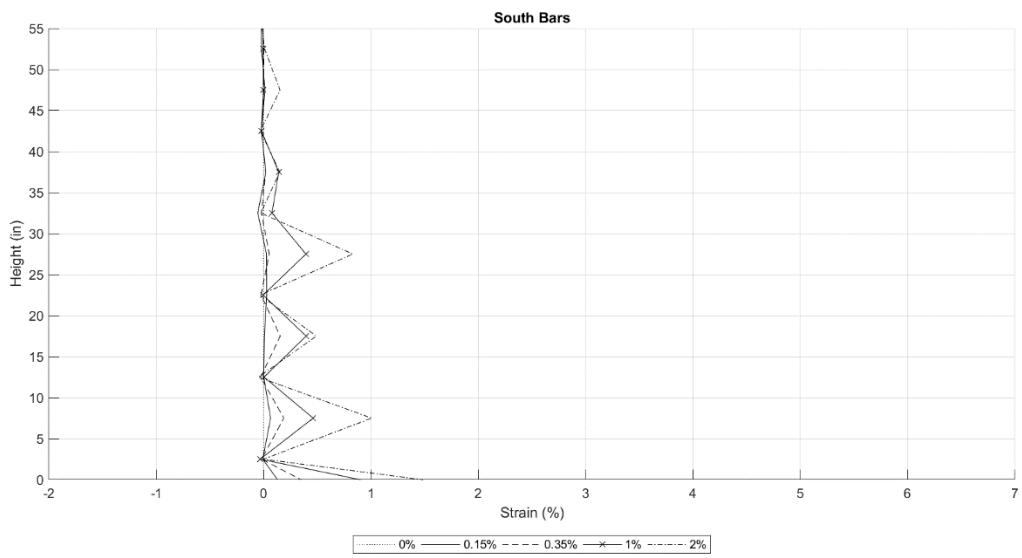

Figure 3-201: Reinforcement strain distribution over height of column C2 (south bars indicate outermost steel layer in tension, markers indicate the drift ratio when strain was recorded)

a) 0%

b) 0%

c) 1%

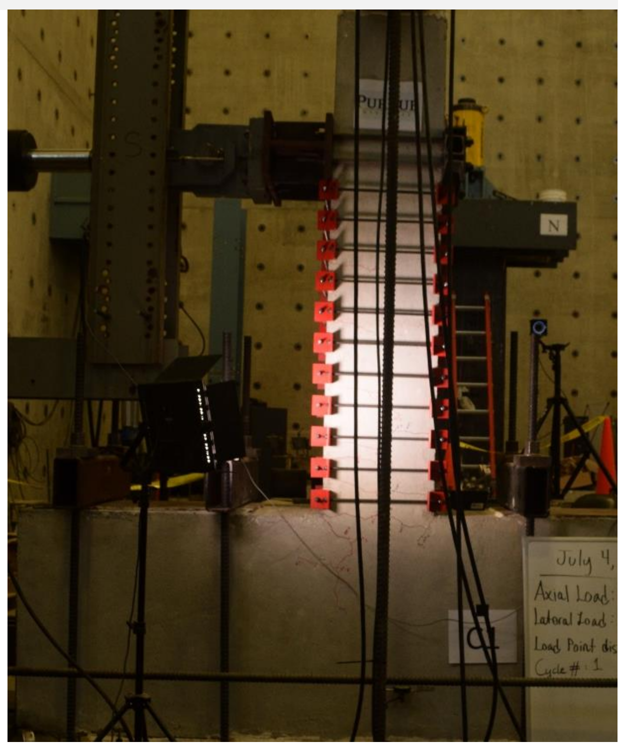

d) 1%

Figure 3-202: Comparisons of column C1 and C2 at the labeled drift ratio

a) 2%

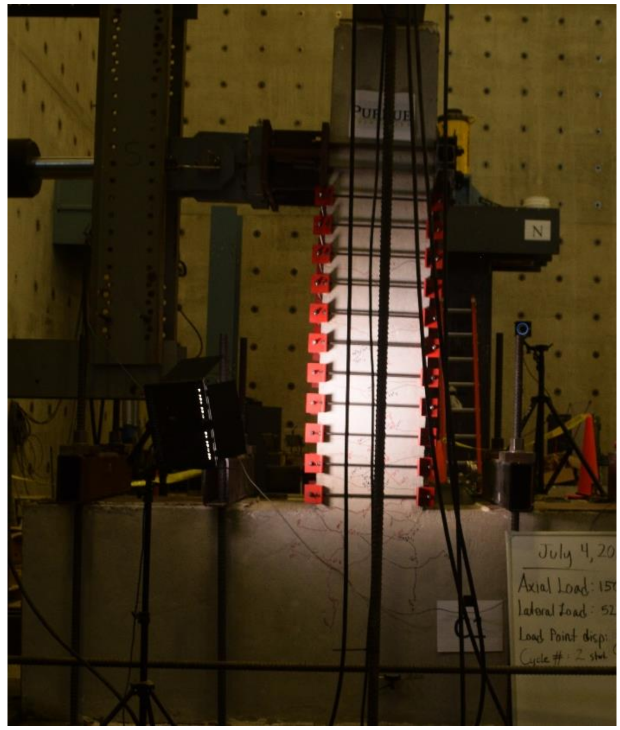

b) 2%

c) 3%

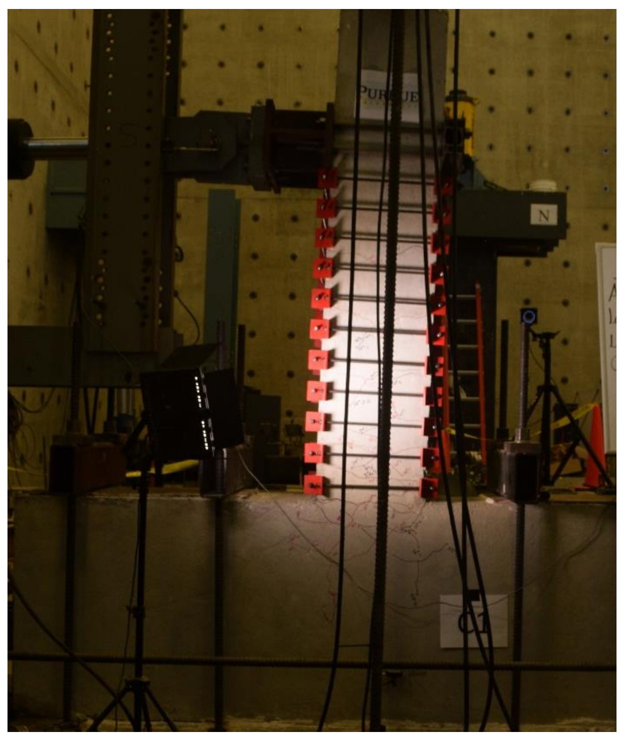

d) 3%

Figure 3-203: Comparisons of column C1 and C2 at the labeled drift ratio

 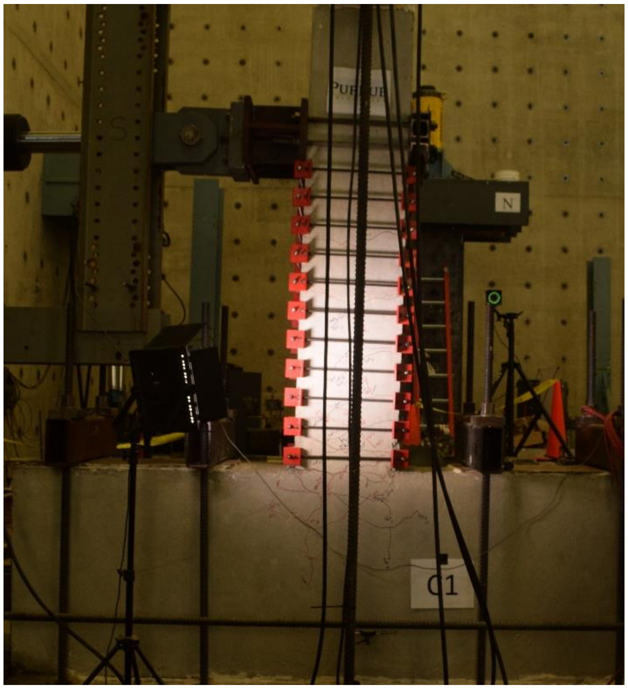

a) failed in shear b) 4%

 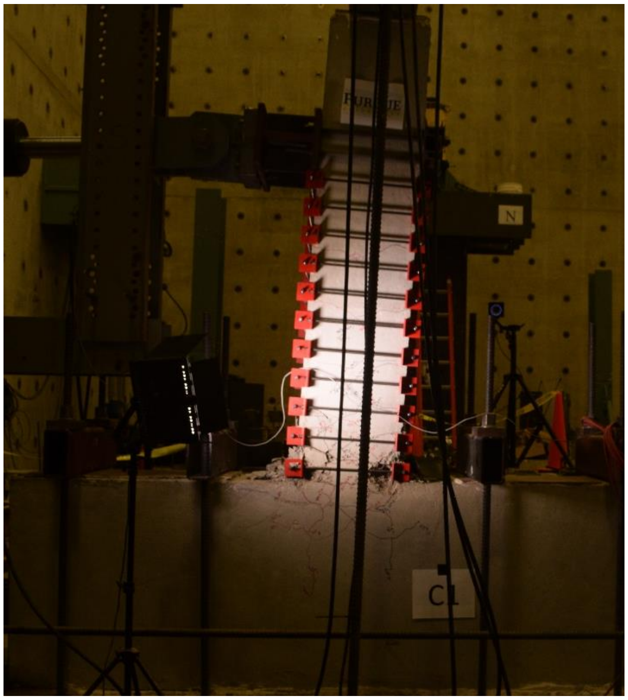

c) failed in shear d) 5%

Figure 3-204: Comparisons of column C1 and C2 at the labeled drift ratio

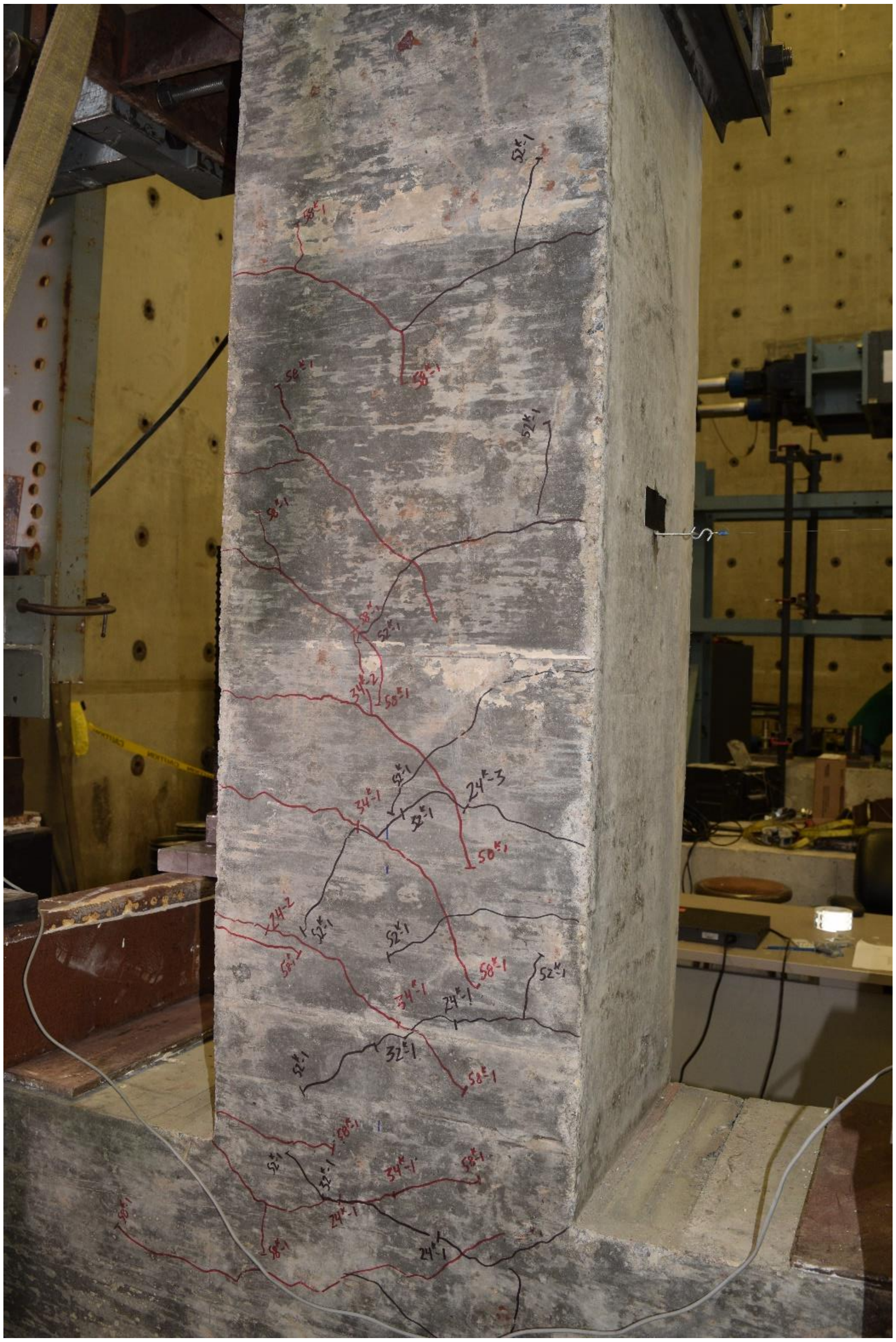

Figure 3-205: Inclined Shear cracking of column C2 at a drift ratio of 1%

Figure 3-206: Shear failure of column C2 resulting from large inclined crack

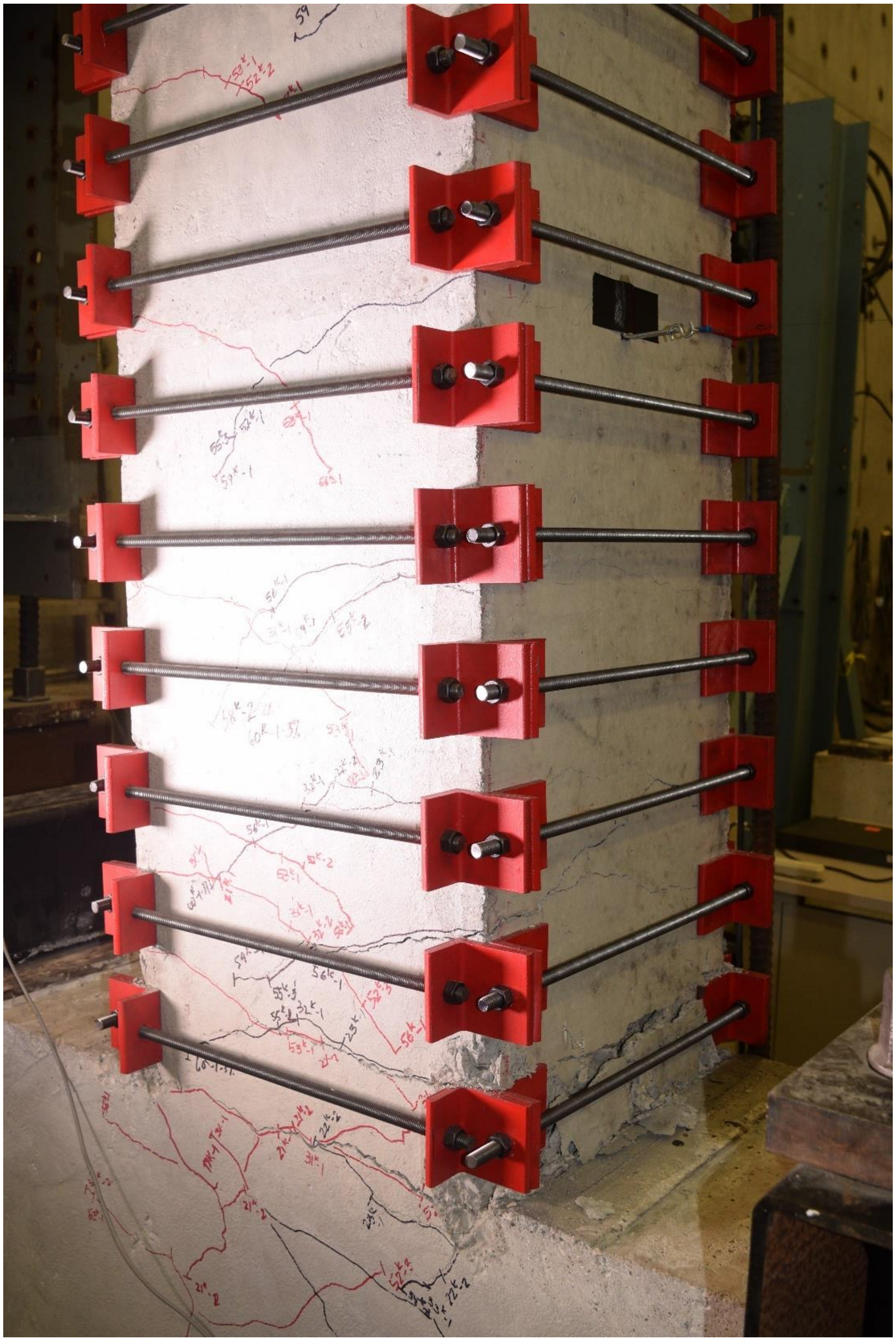

Figure 3-207: Concrete compression zone in column C1 at a drift ratio of 5%

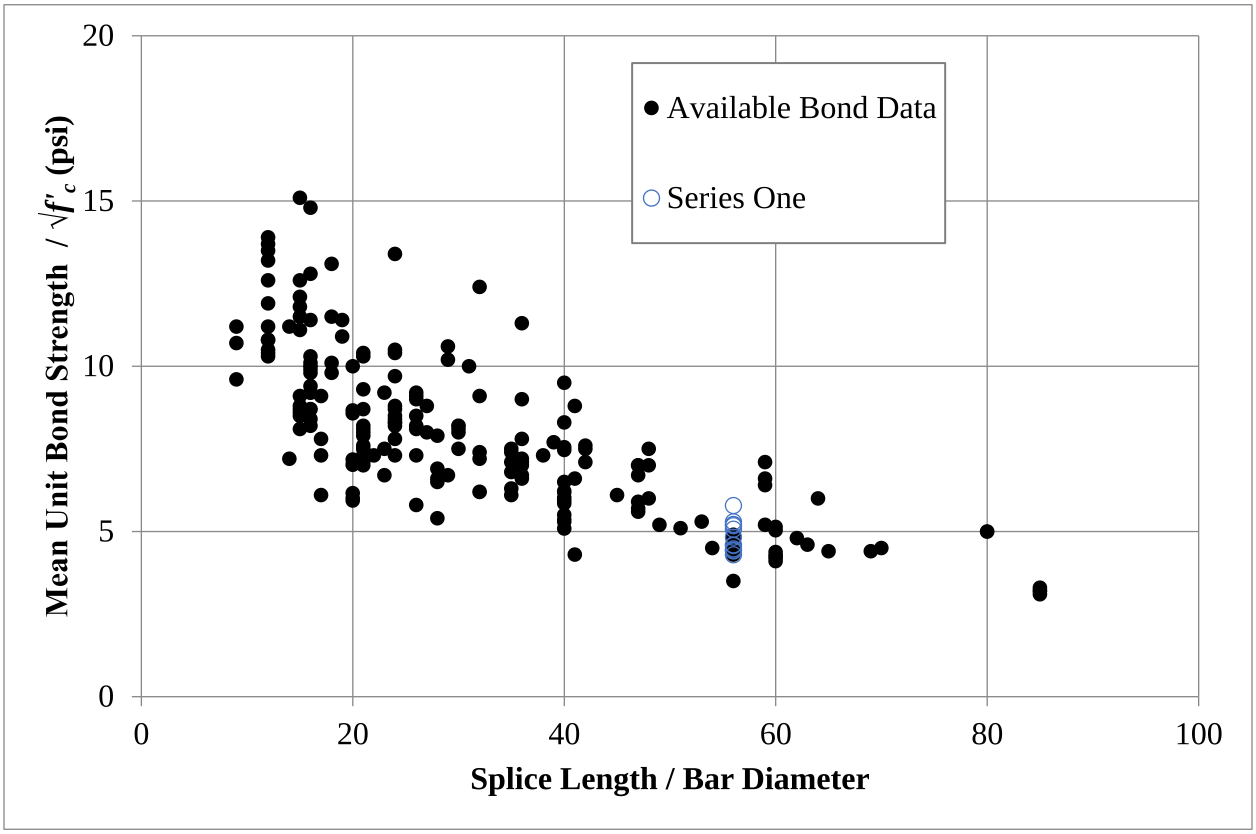

Figure 4-1: Mean bond strength versus splice length from unconfined lap splice tests

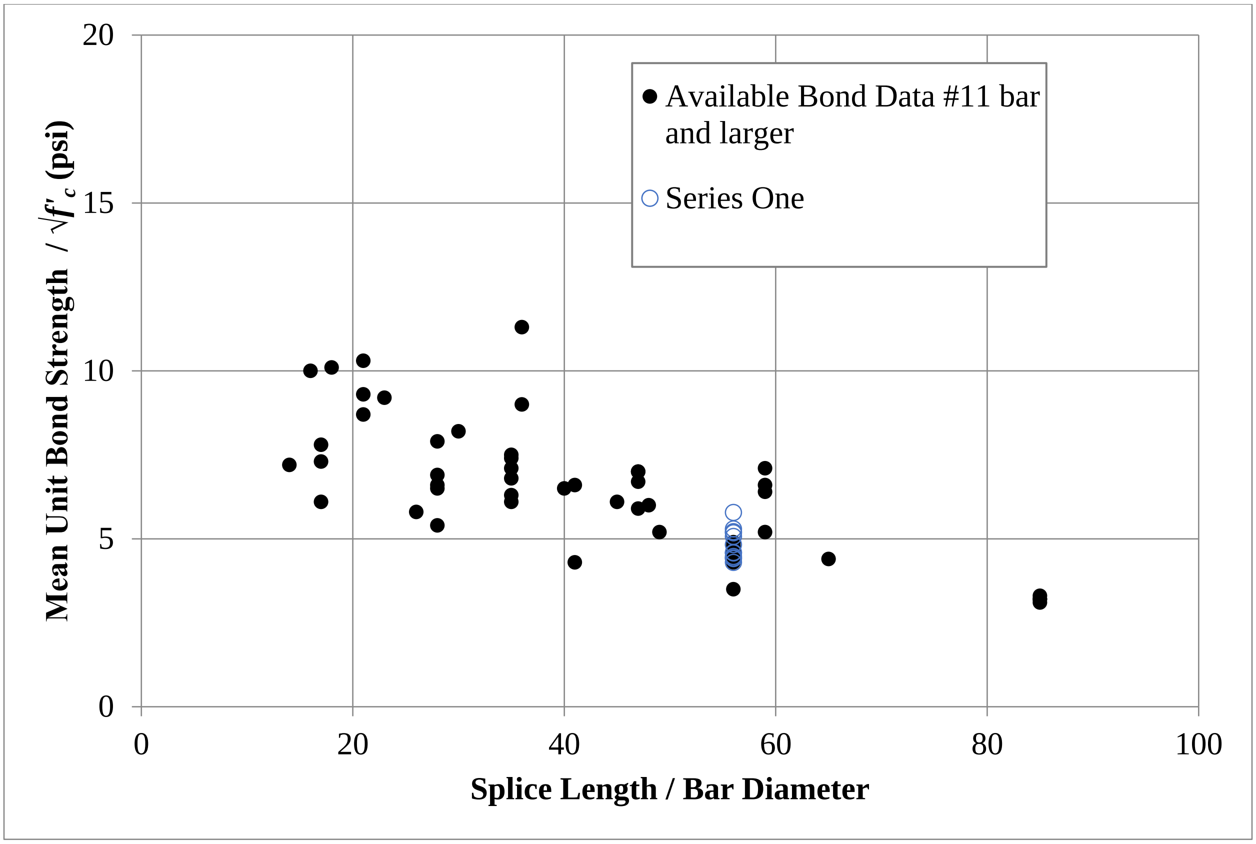

Figure 4-2: Mean bond strength versus splice length from unconfined lap splice tests containing #11 reinforcing bars and larger

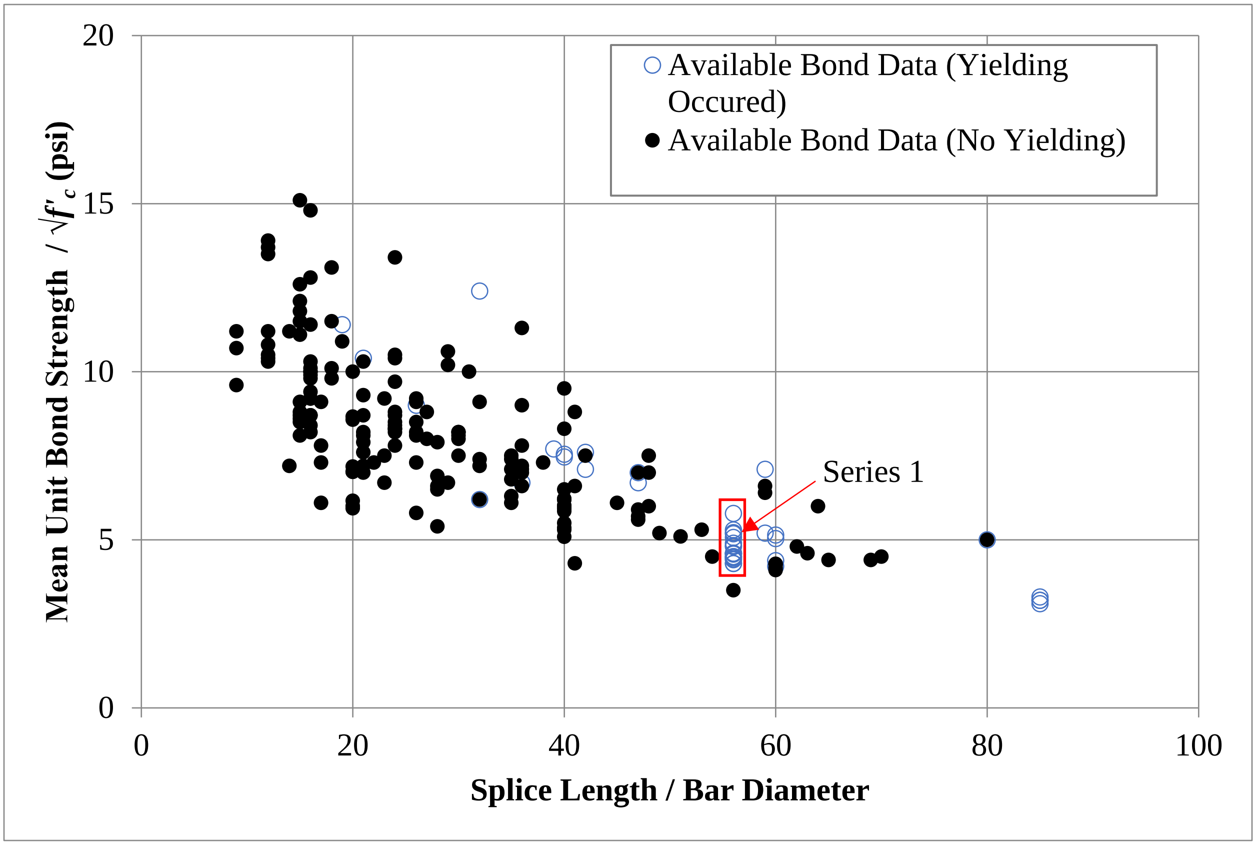

Figure 4-3: Mean bond strength versus splice length from unconfined lap splice tests with data representing yielding and no yielding

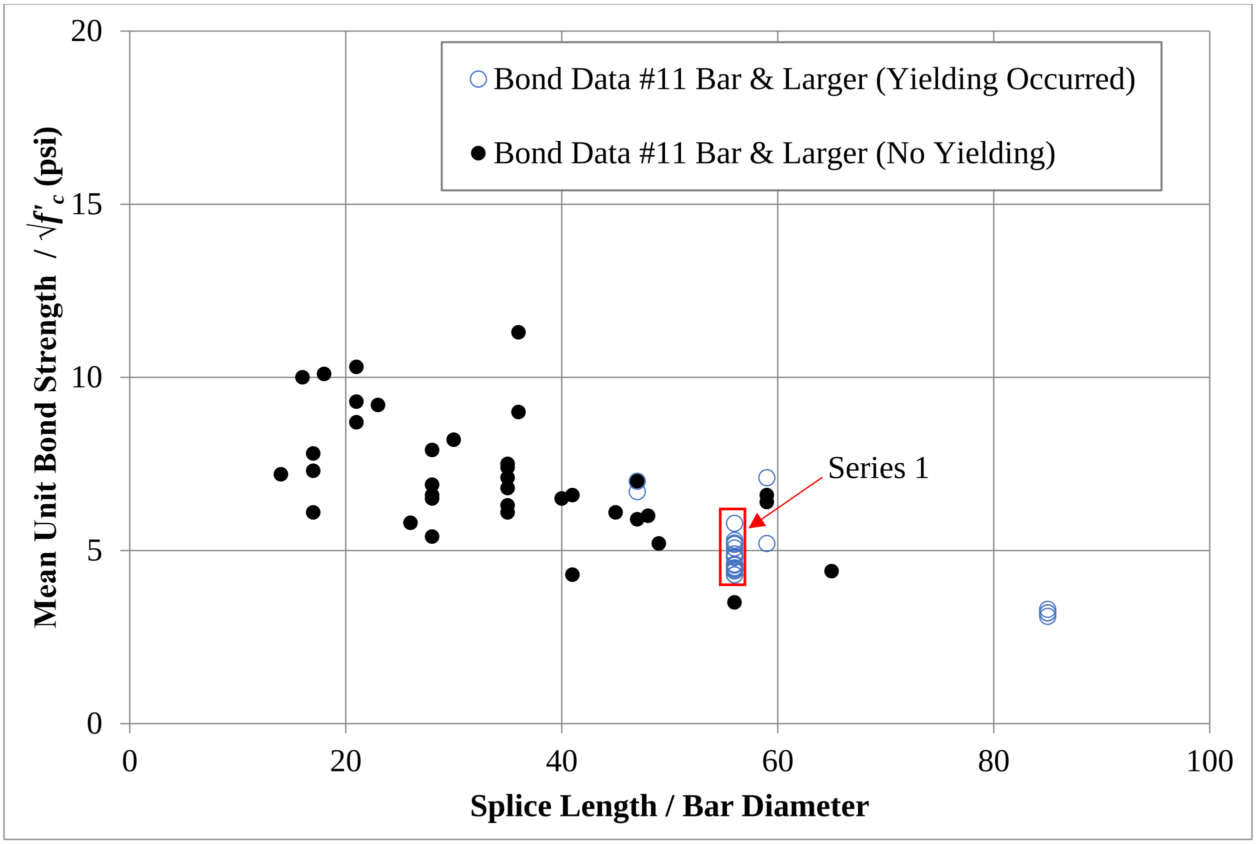

Figure 4-4: Mean bond strength versus splice length from unconfined lap splice tests containing #11 reinforcing bars and larger with data representing yielding and no yielding

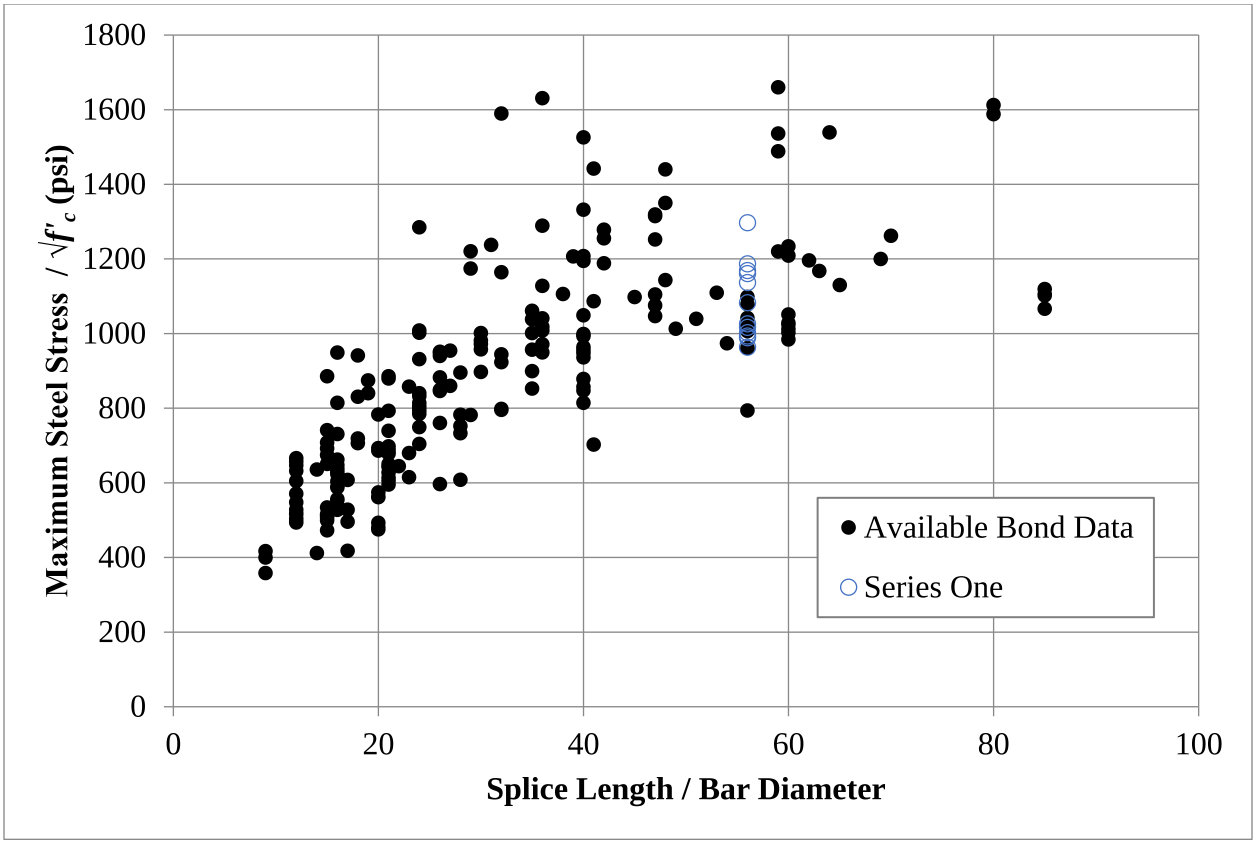

Figure 4-5: Maximum steel stress versus splice length from unconfined lap splice tests

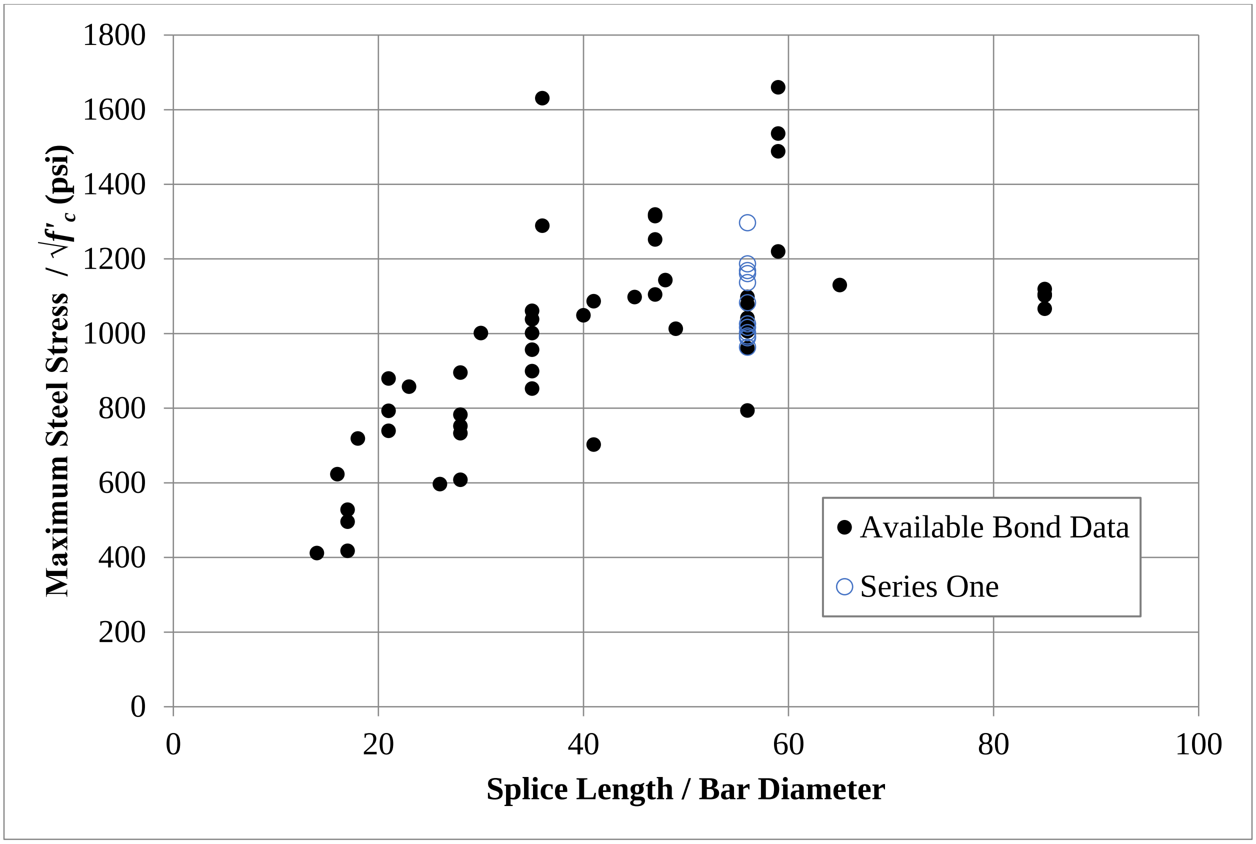

Figure 4-6: Maximum steel stress versus splice length from unconfined lap splice tests containing #11 reinforcing bars and larger

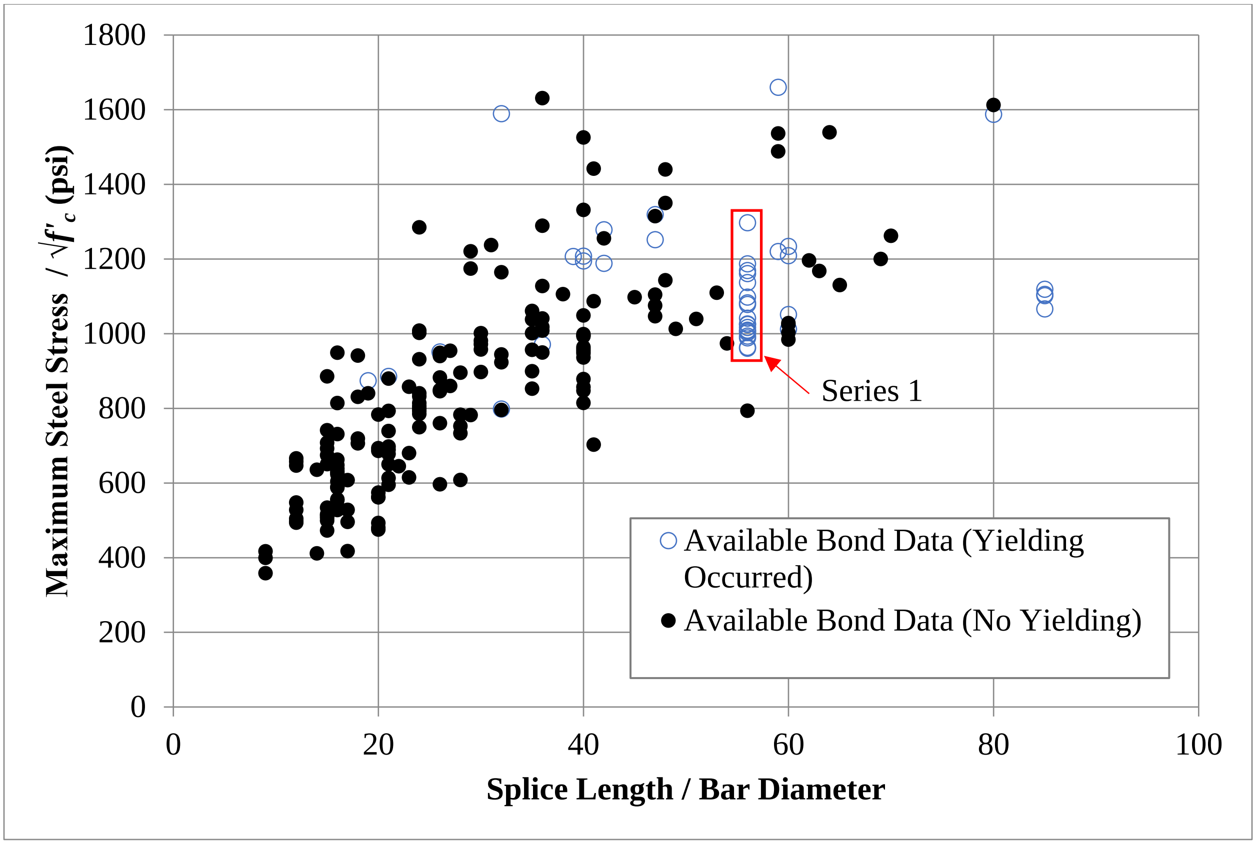

Figure 4-7: Maximum steel stress versus splice length from unconfined lap splice tests with data representing yielding and no yielding

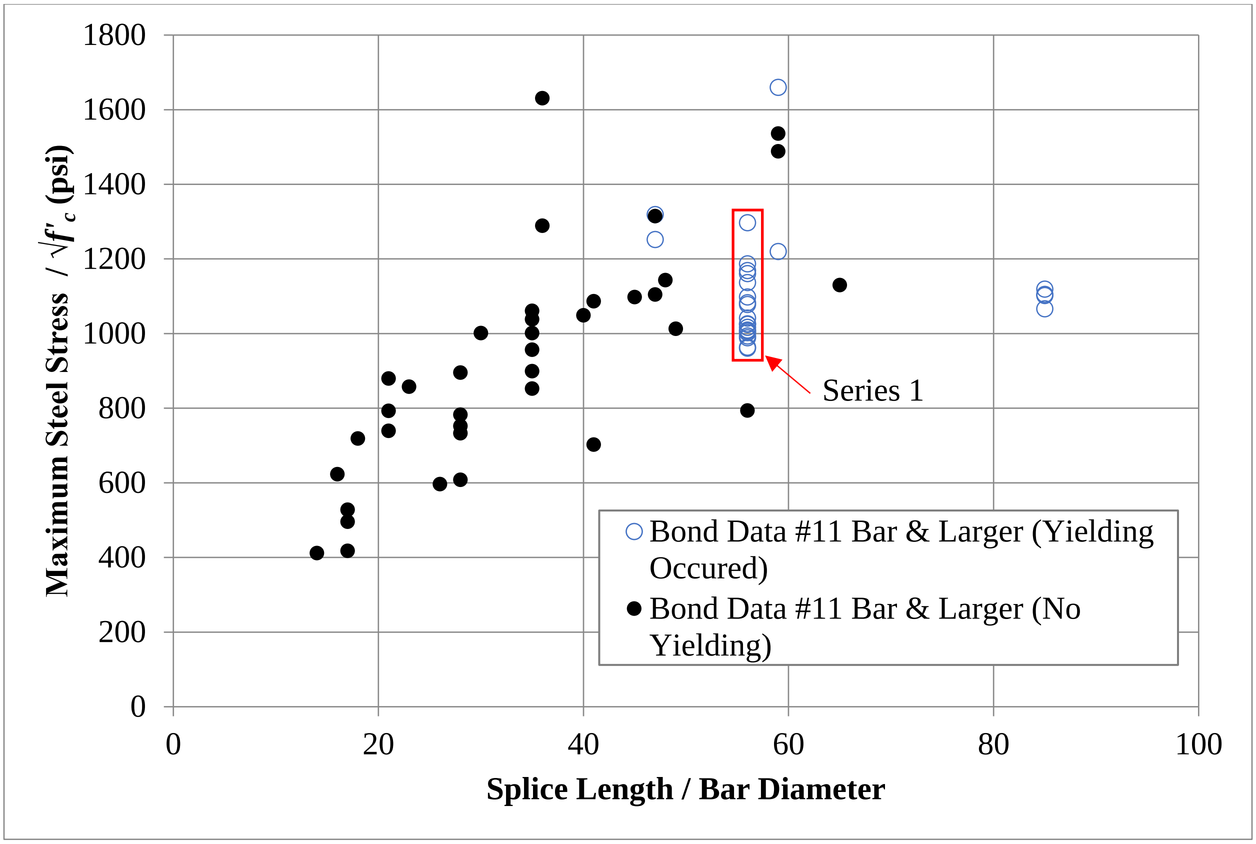

Figure 4-8: Maximum steel stress versus splice length from unconfined lap splice tests containing #11 reinforcing bars and larger with data representing yielding and no yielding

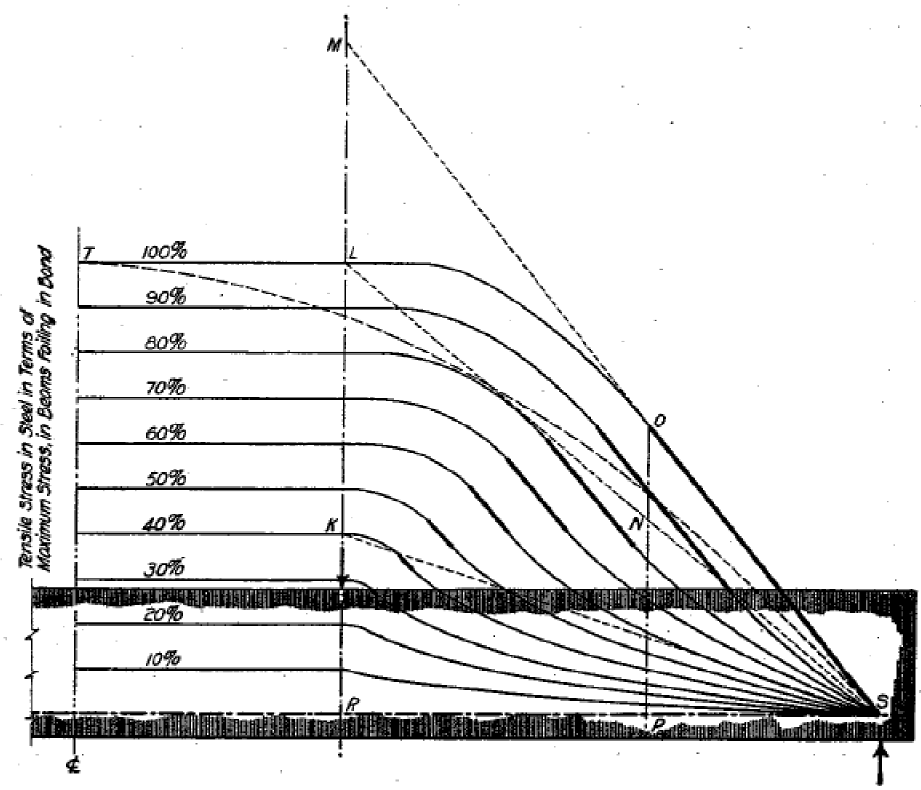

Figure 4-9: Idealized diagram showing the distribution of tensile and bond stresses in a simple reinforced concrete beam reprinted from Abrams (1913)

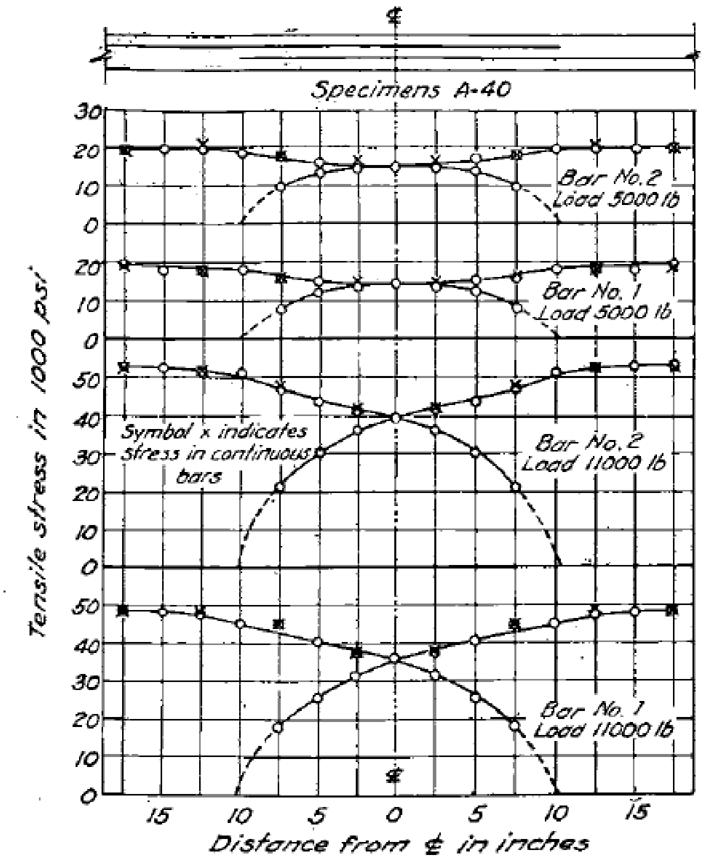

Figure 4-10: Distribution of bar stress along lapped bars reprinted from Kluge and Tuma (1945)

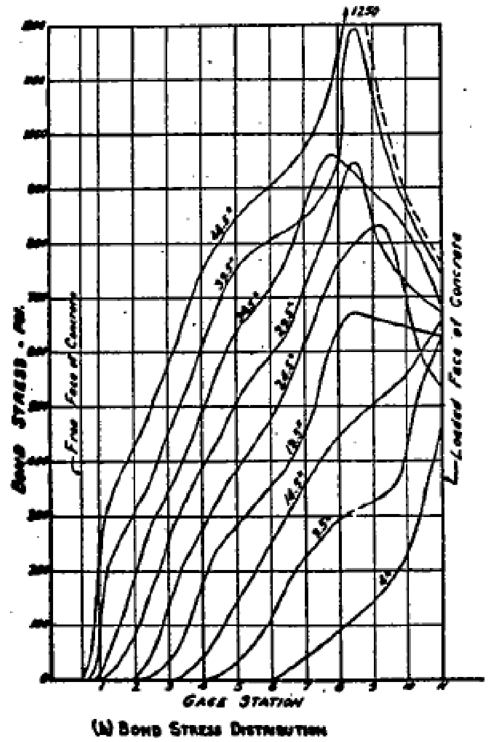

Figure 4-11: Force in bar and bond distribution reprinted from Mains (1951).

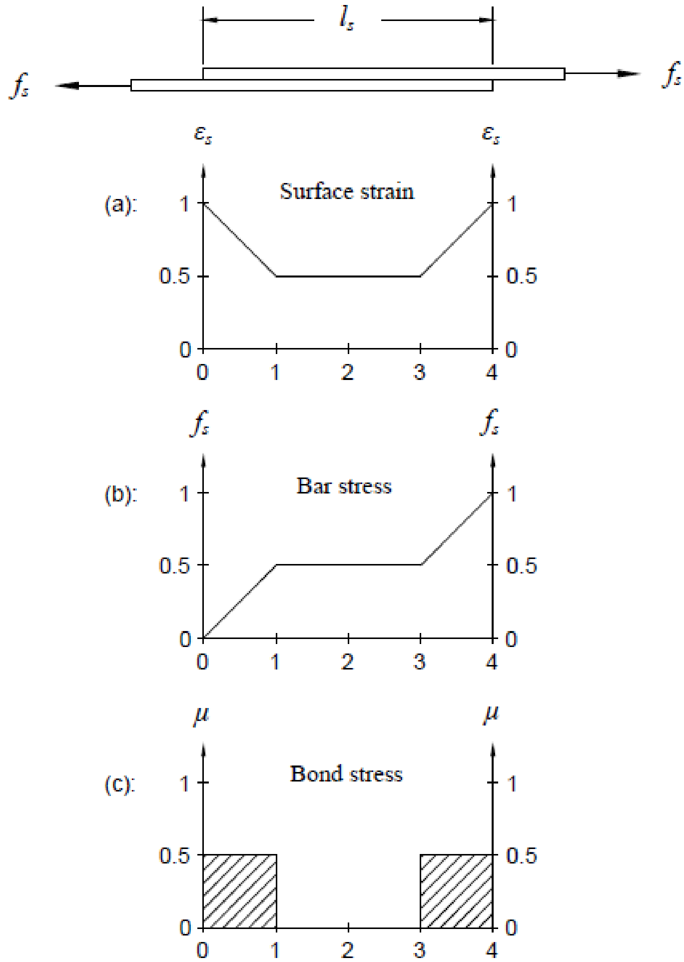

Figure 4-12: Idealized strain and stress distribution for unconfined lap splices reprinted from Richter (2012)

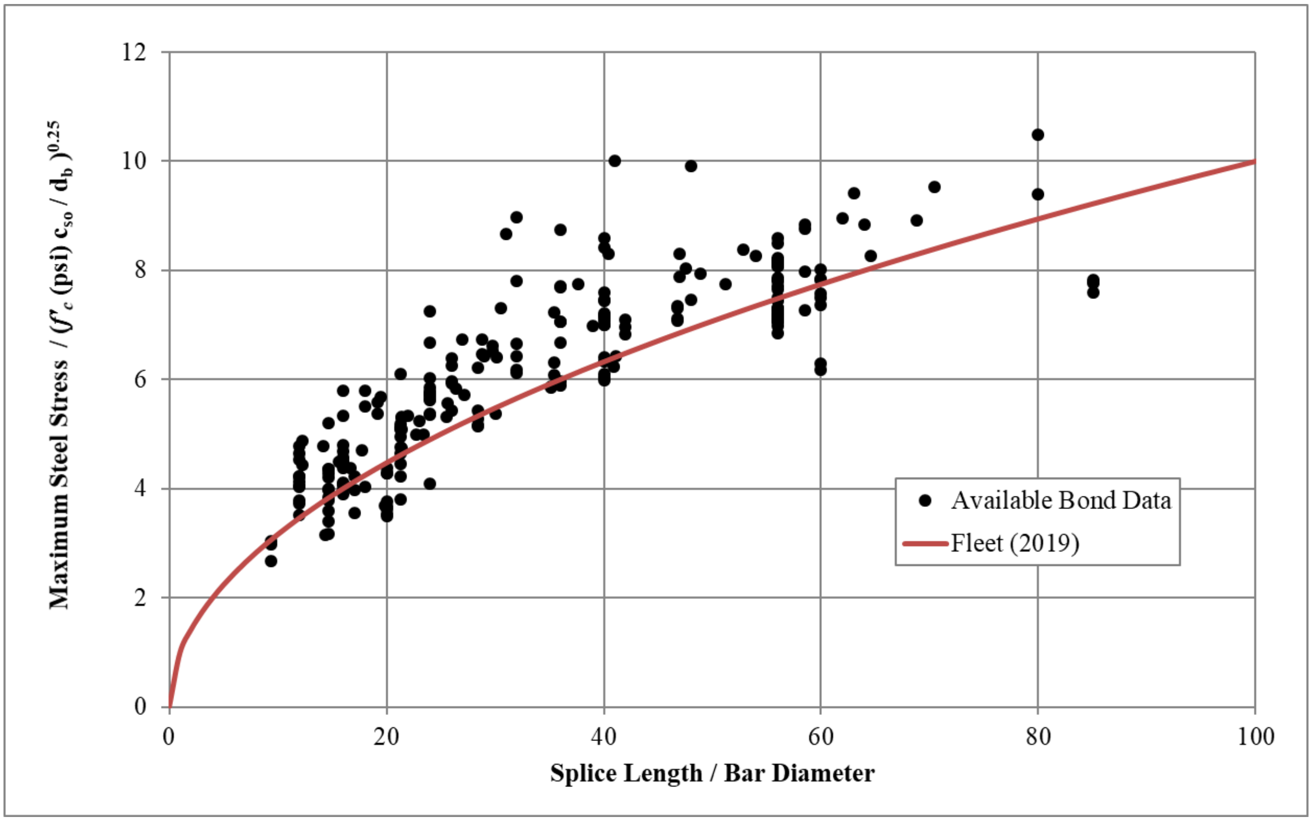

Figure 4-13: Trend of bar stress versus splice length for unconfined splice database proposed by Fleet 2019

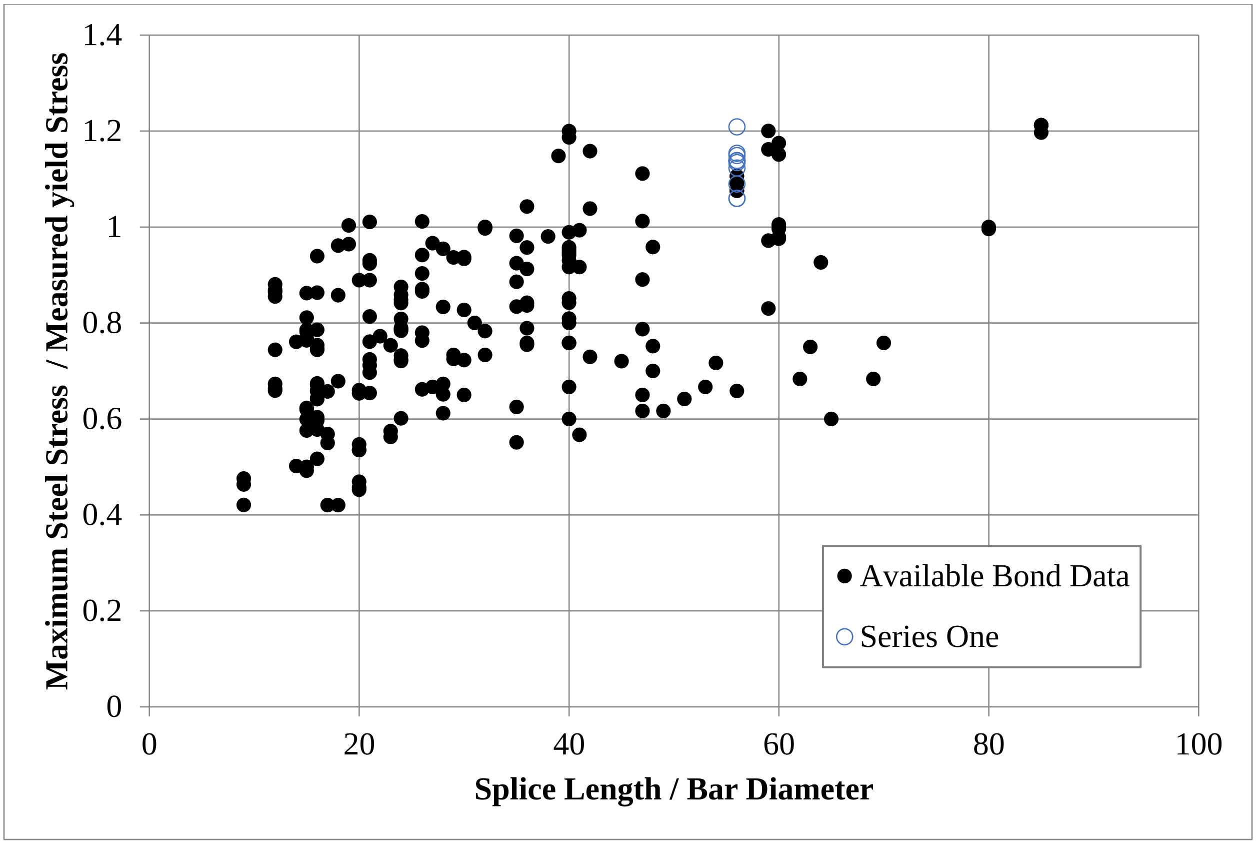

Figure 4-14: Ratios of measured steel stress to measured yield stress versus splice length

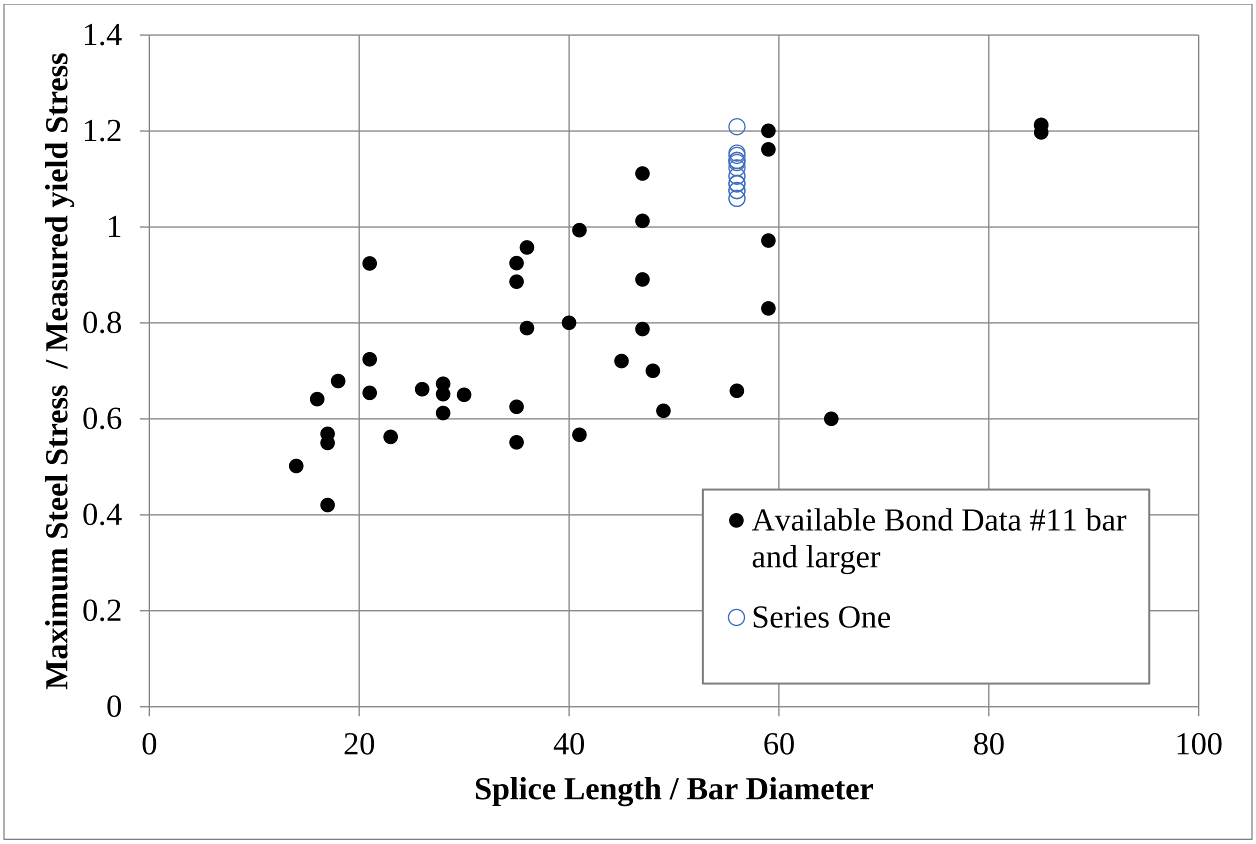

Figure 4-15: Ratios of measured steel stress to measured yield stress versus splice length of bars of #11 and larger

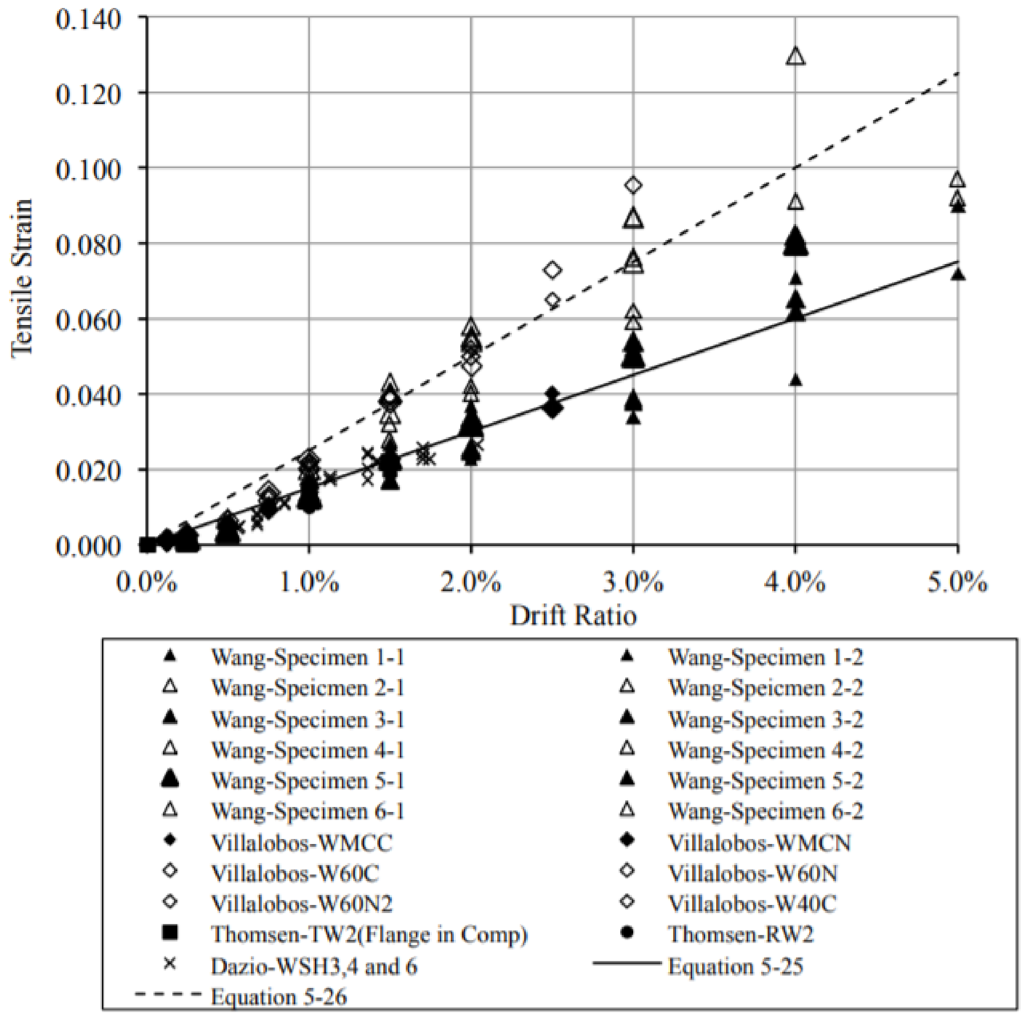

Figure 4-16: Surface tensile strain versus drift ratio adapted from Wang (2014)

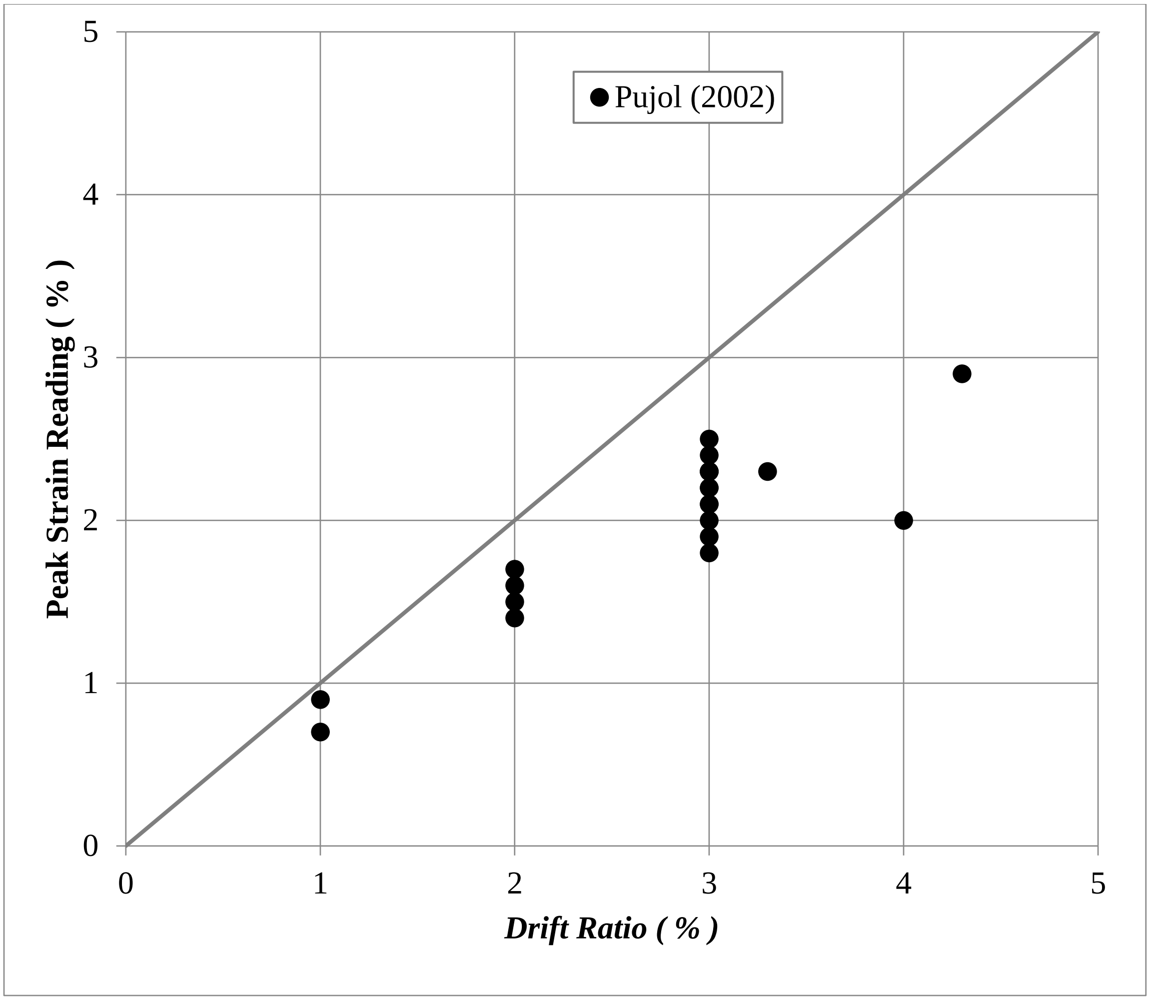

Figure 4-17: Measured bar strain versus drift ratio

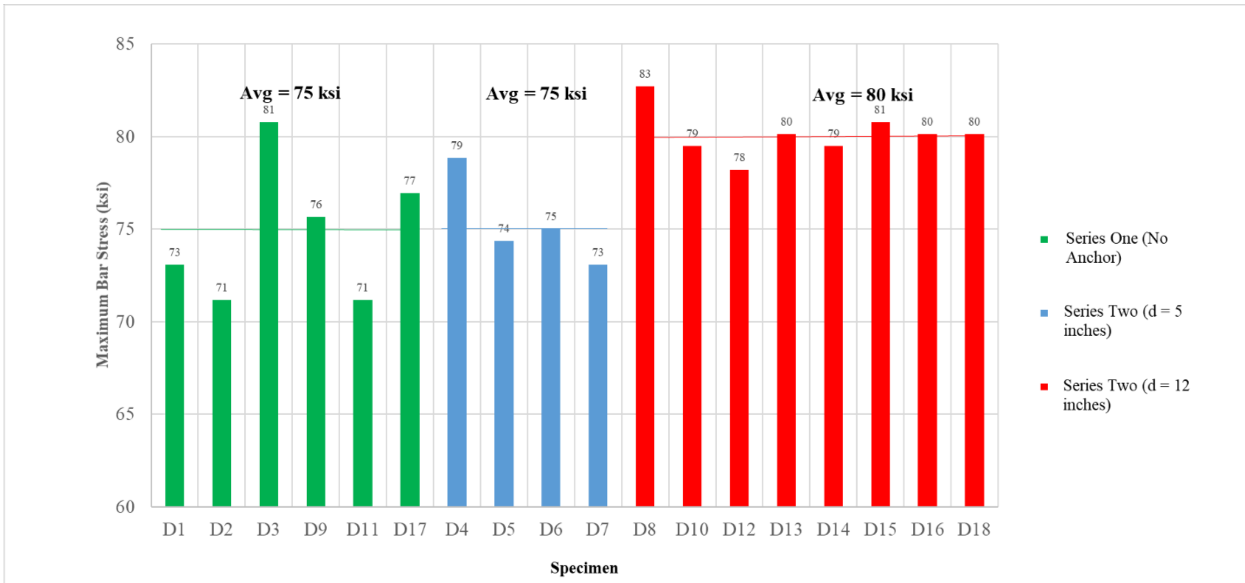

Figure 4-18: Peak bar stress values for Series One and Series Two coupon tests

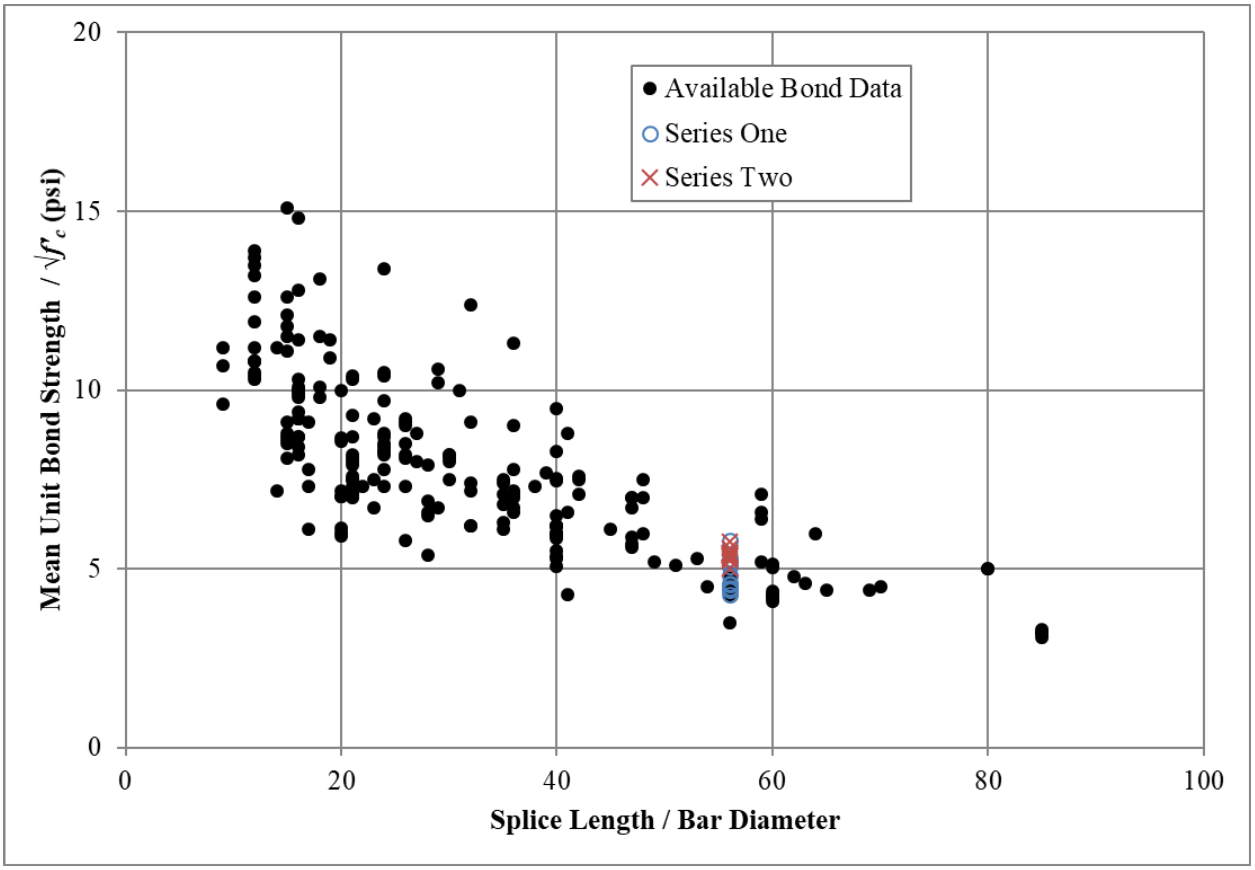

Figure 4-19: Mean bond strength versus splice length from Series Two

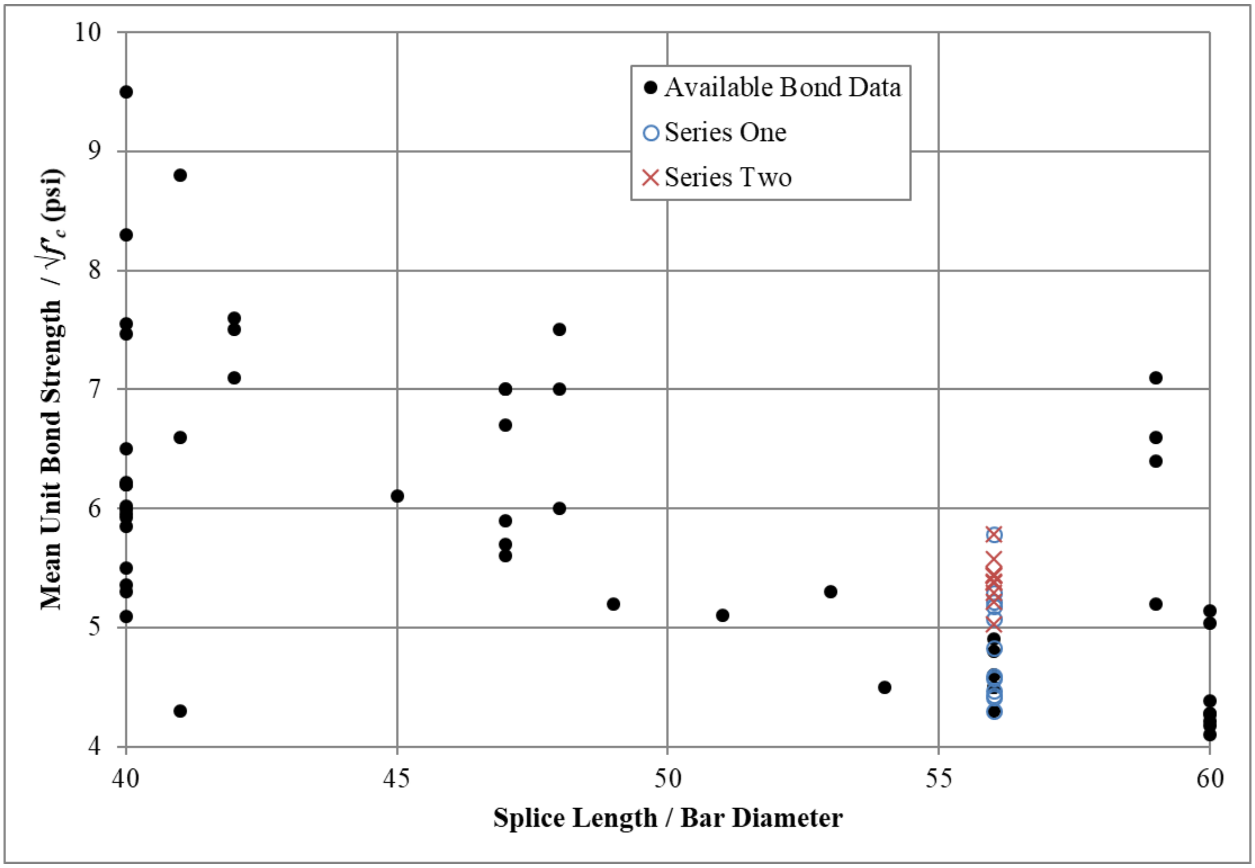

Figure 4-20: (Magnified view) Mean bond strength versus splice length from Series Two

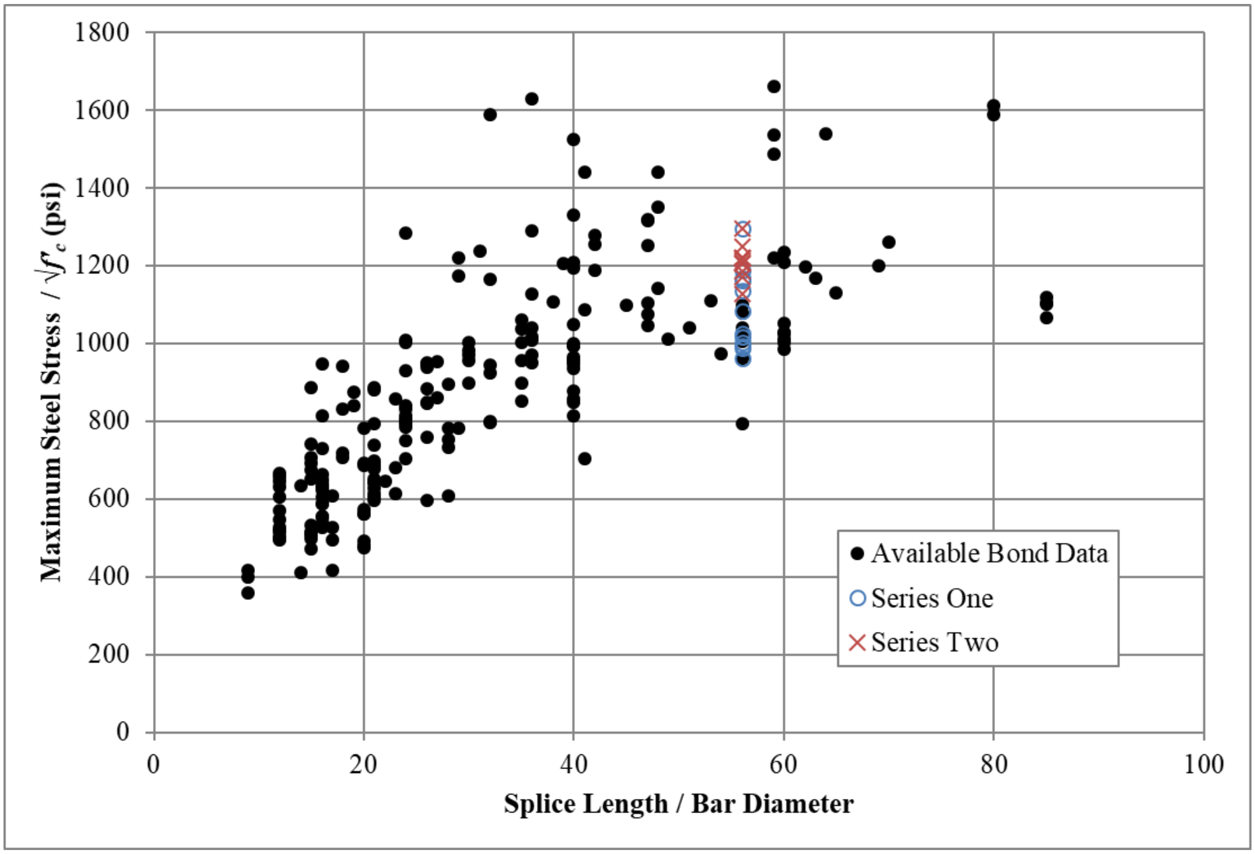

Figure 4-21: Maximum steel stress versus splice length from Series Two

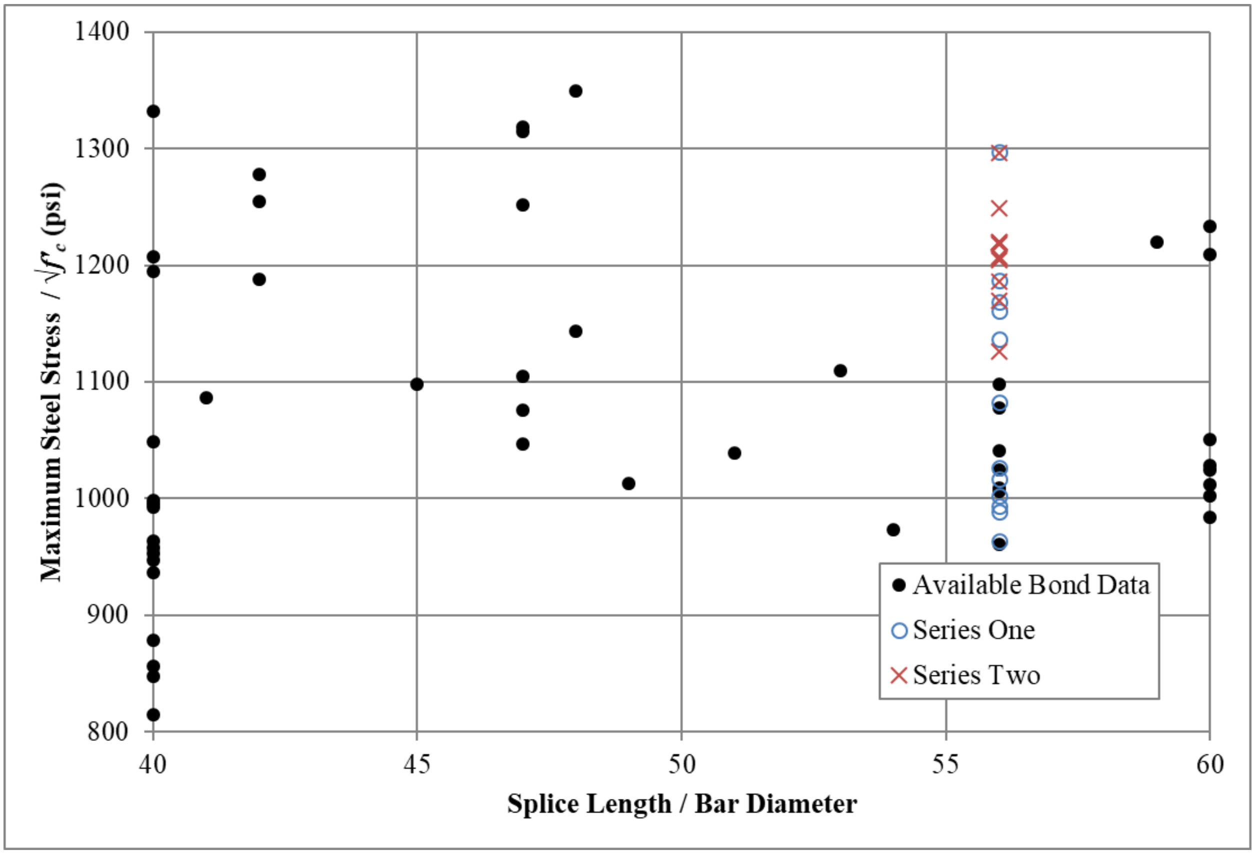

Figure 4-22: (Magnified view) Maximum steel stress versus splice length from Series Two

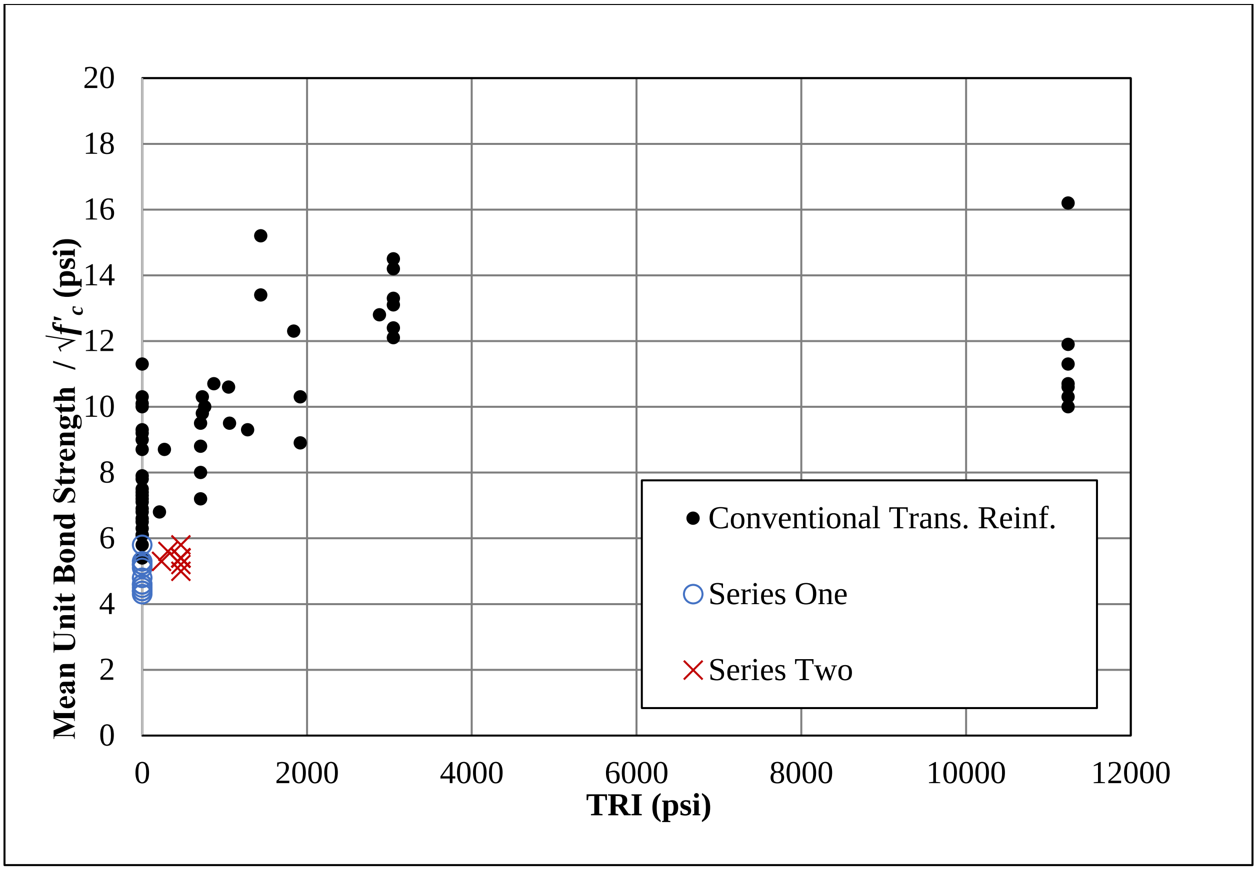

Figure 4-23: Mean bond strength versus TRI from Series One and Series Two

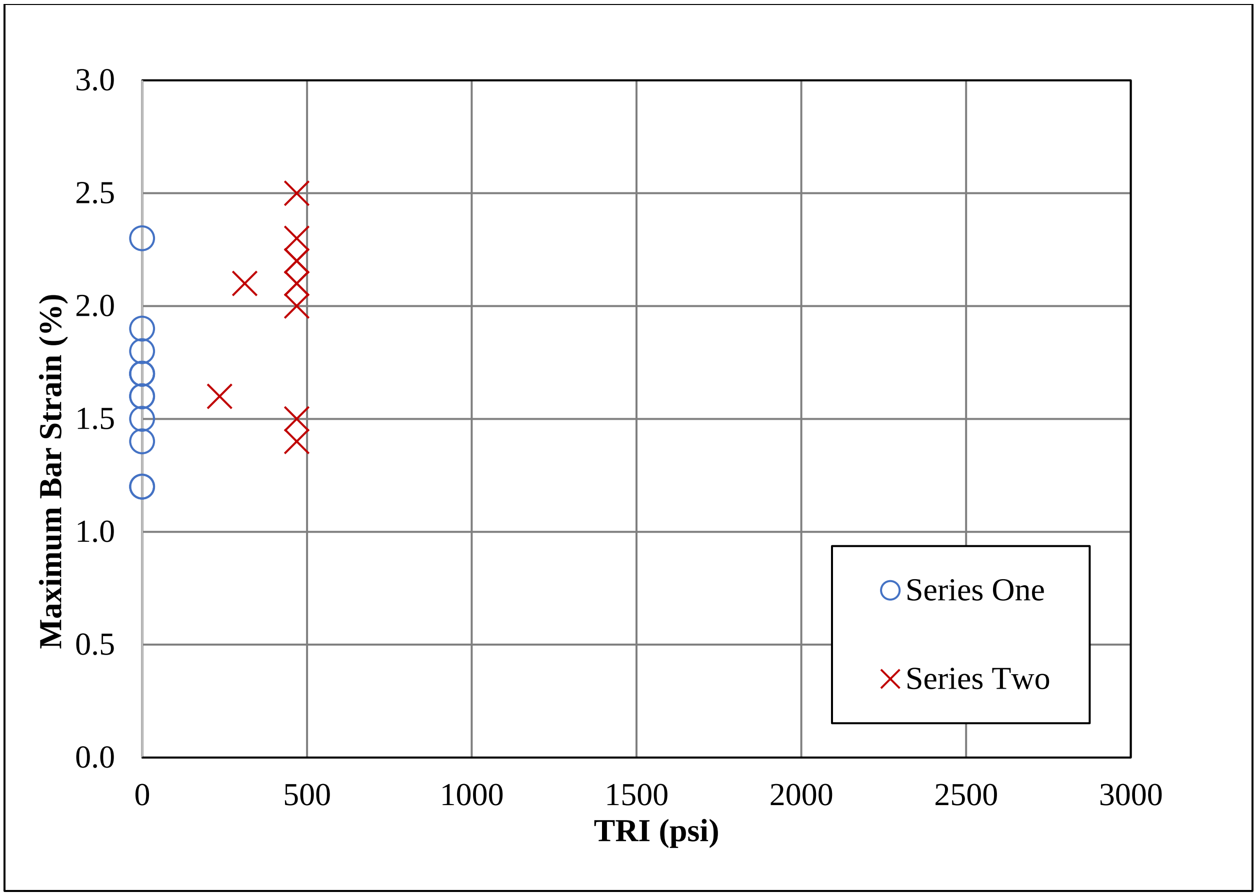

Figure 4-24: Maximum inferred bar strain versus values of TRI for Series One and Series Two

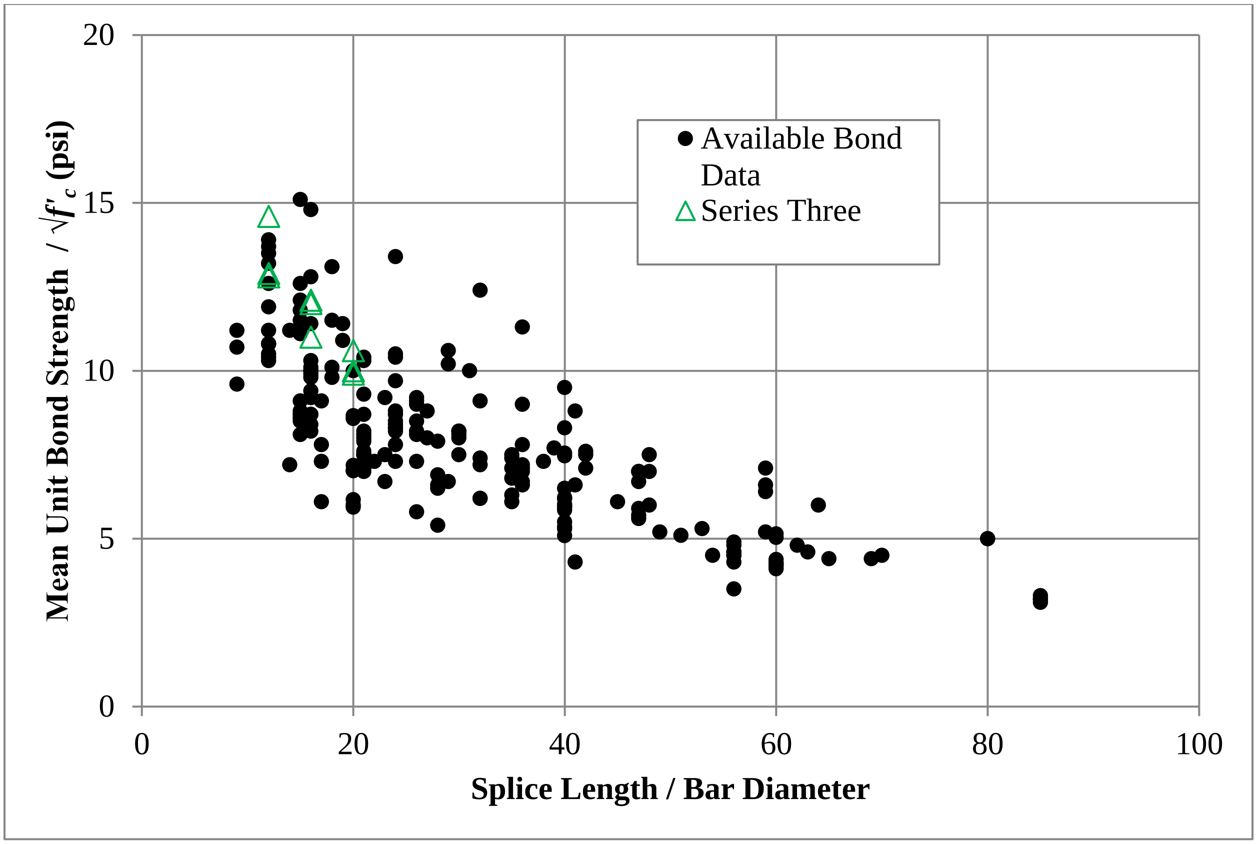

Figure 4-25: Mean bond strength versus splice length from Series Three

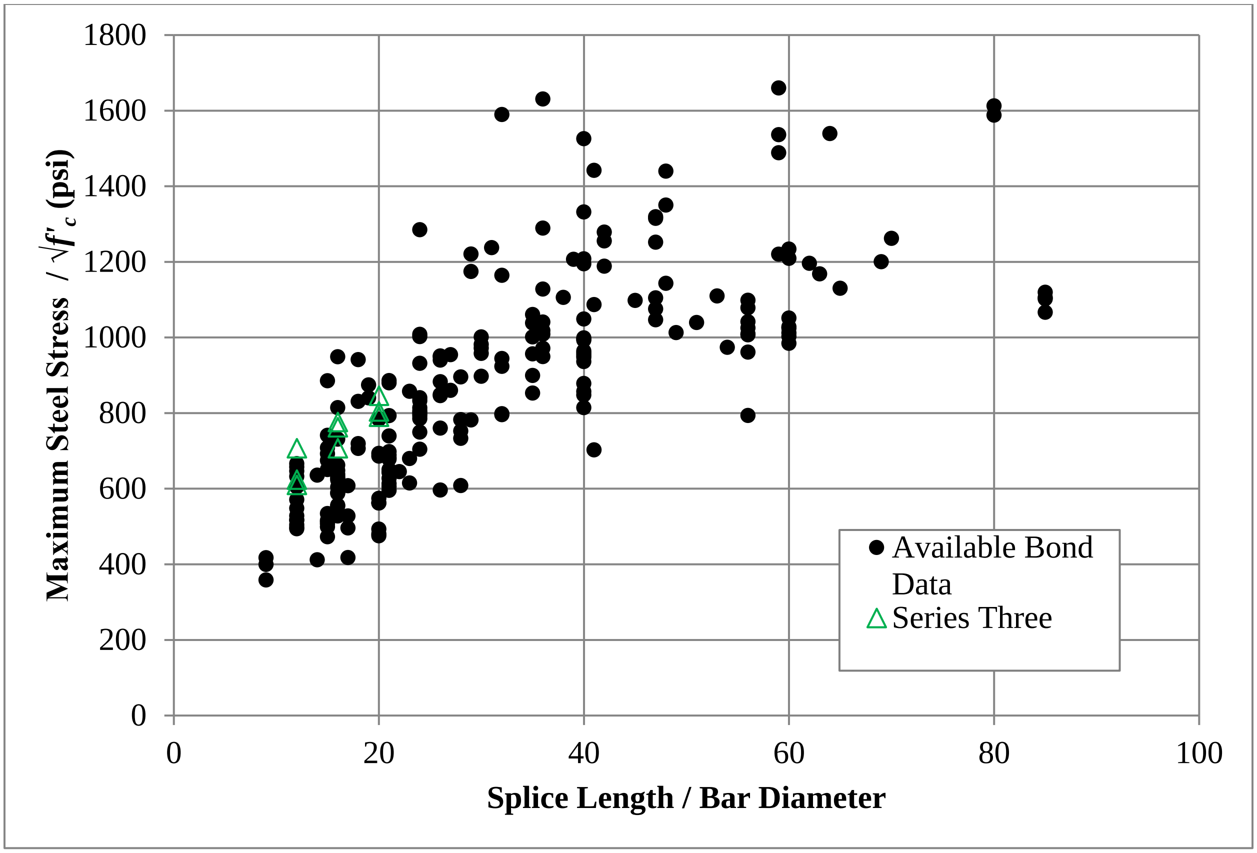

Figure 4-26: Maximum steel stress versus splice length from Series Three

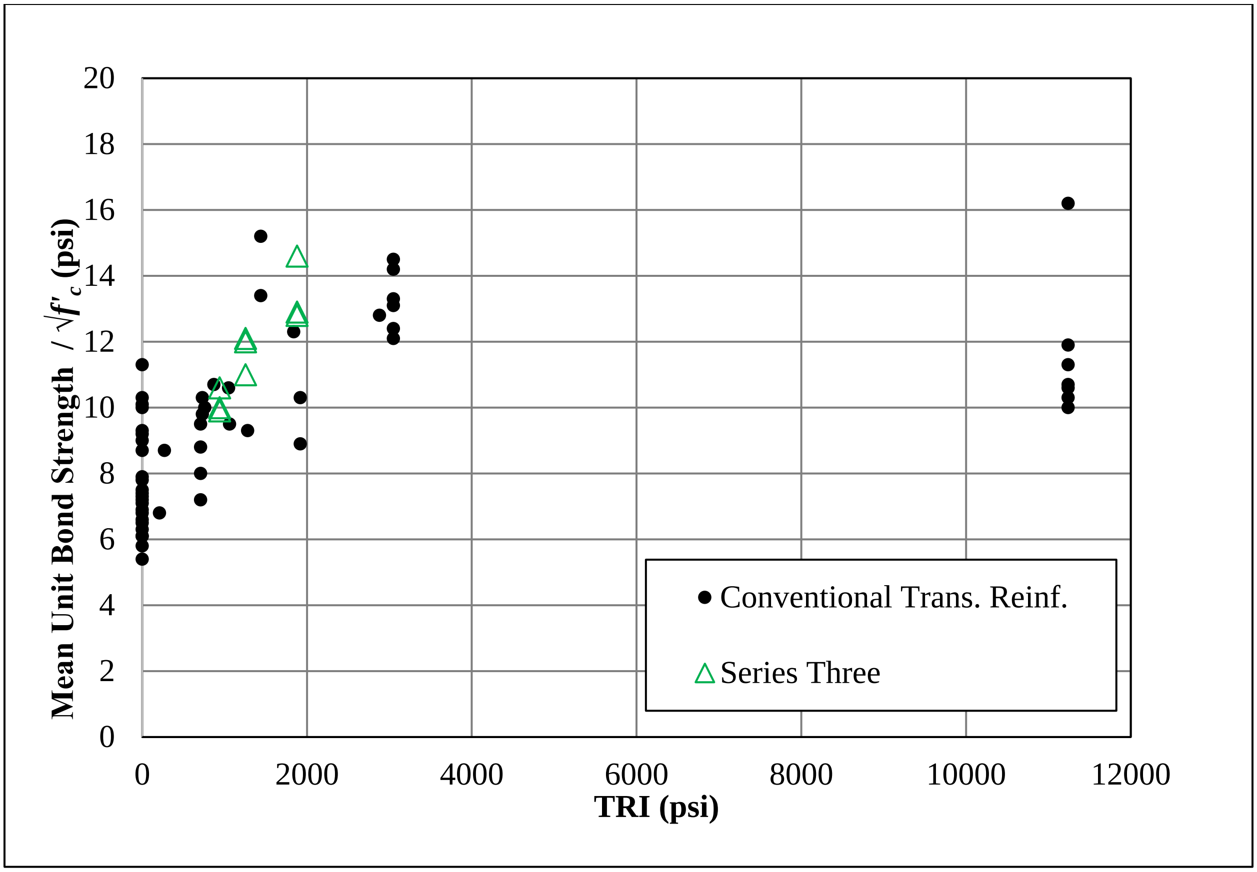

Figure 4-27: Mean bond strength versus TRI from Series Three

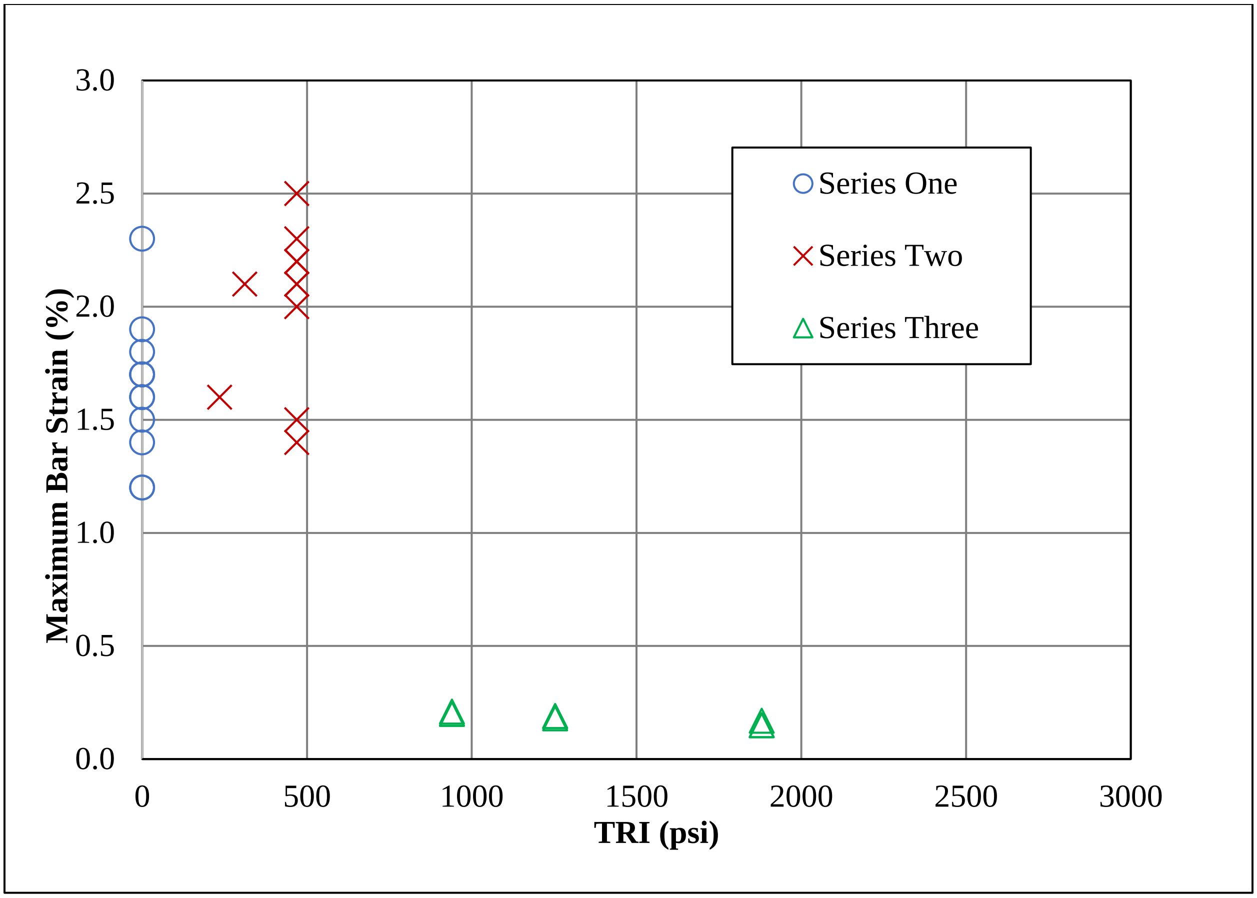

Figure 4-28: Maximum inferred bar strain versus values of TRI for Series One through Series Three

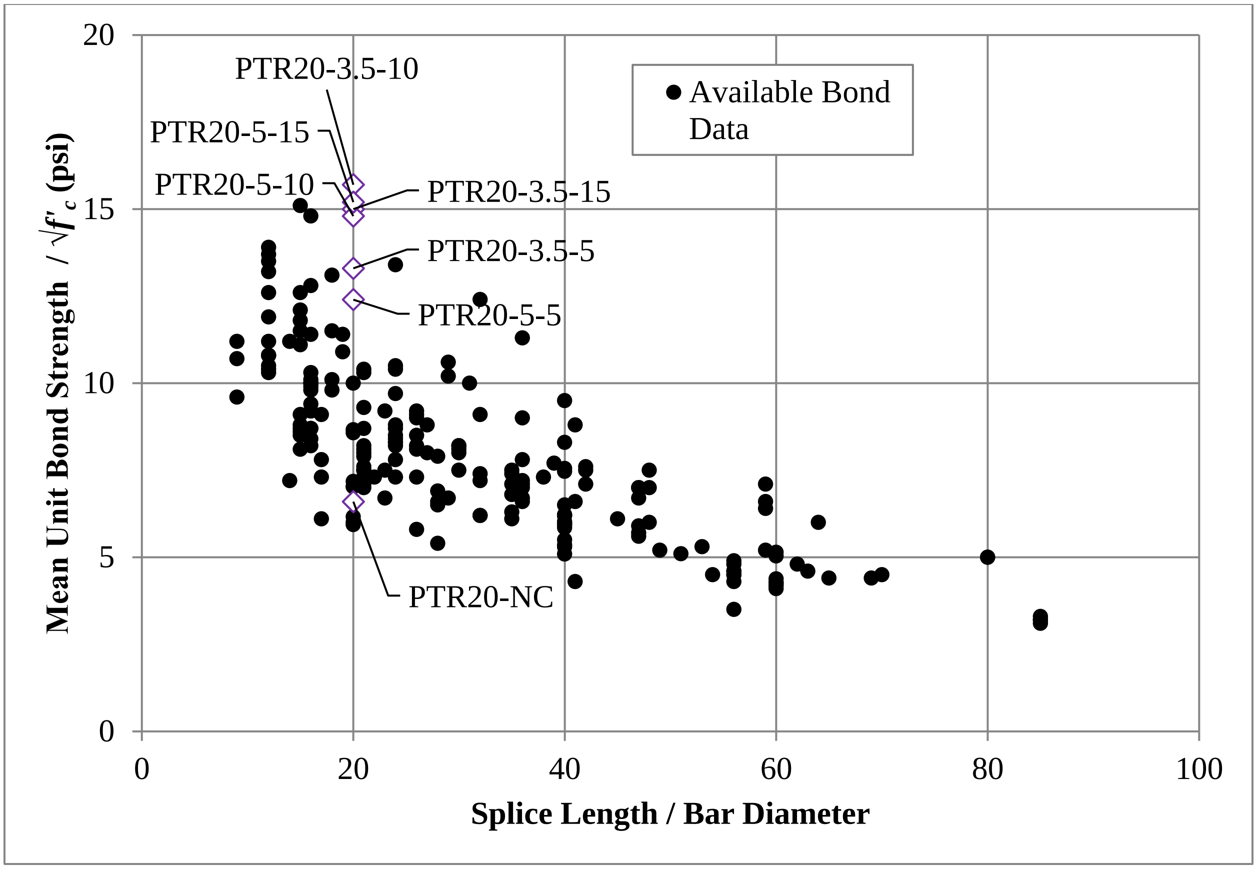

Figure 4-29: Mean bond strength versus splice length from Series Four

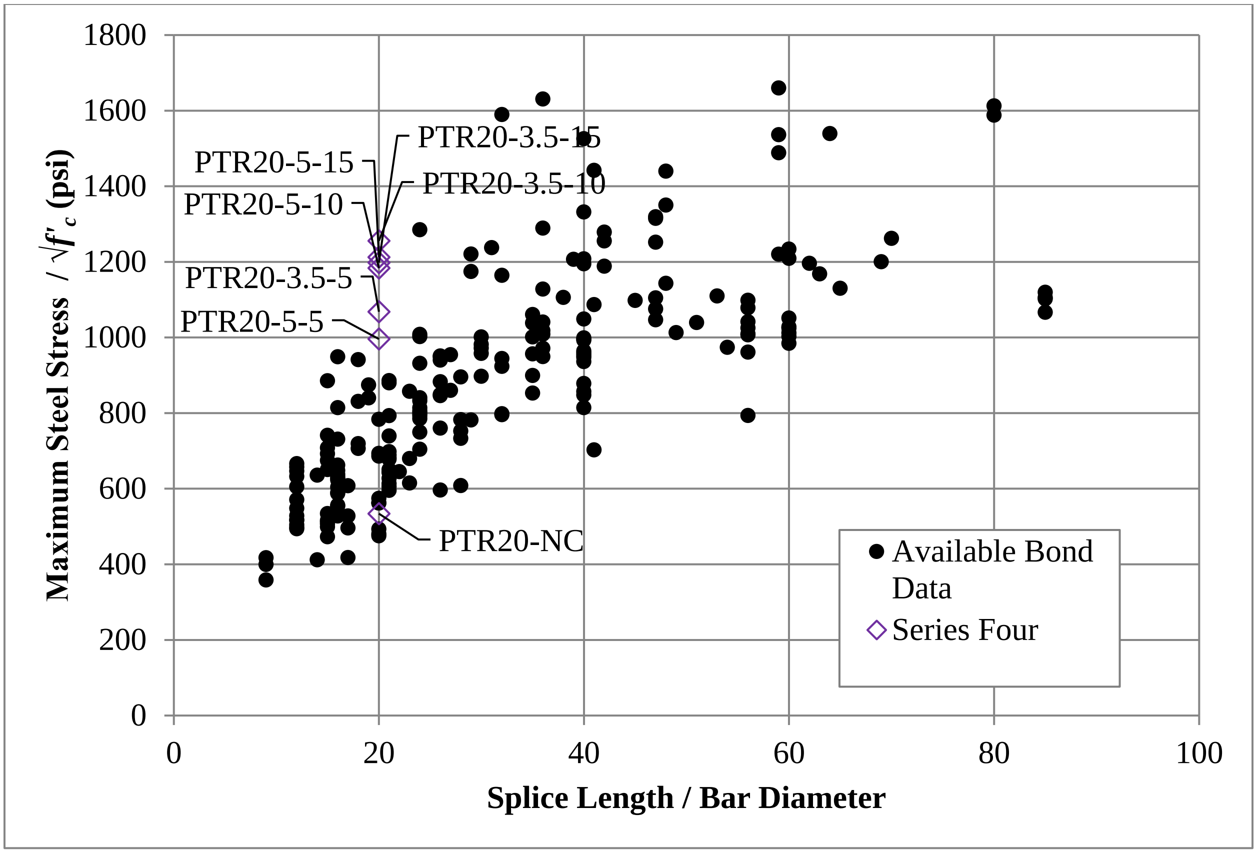

Figure 4-30: Maximum steel stress versus splice length from Series Four

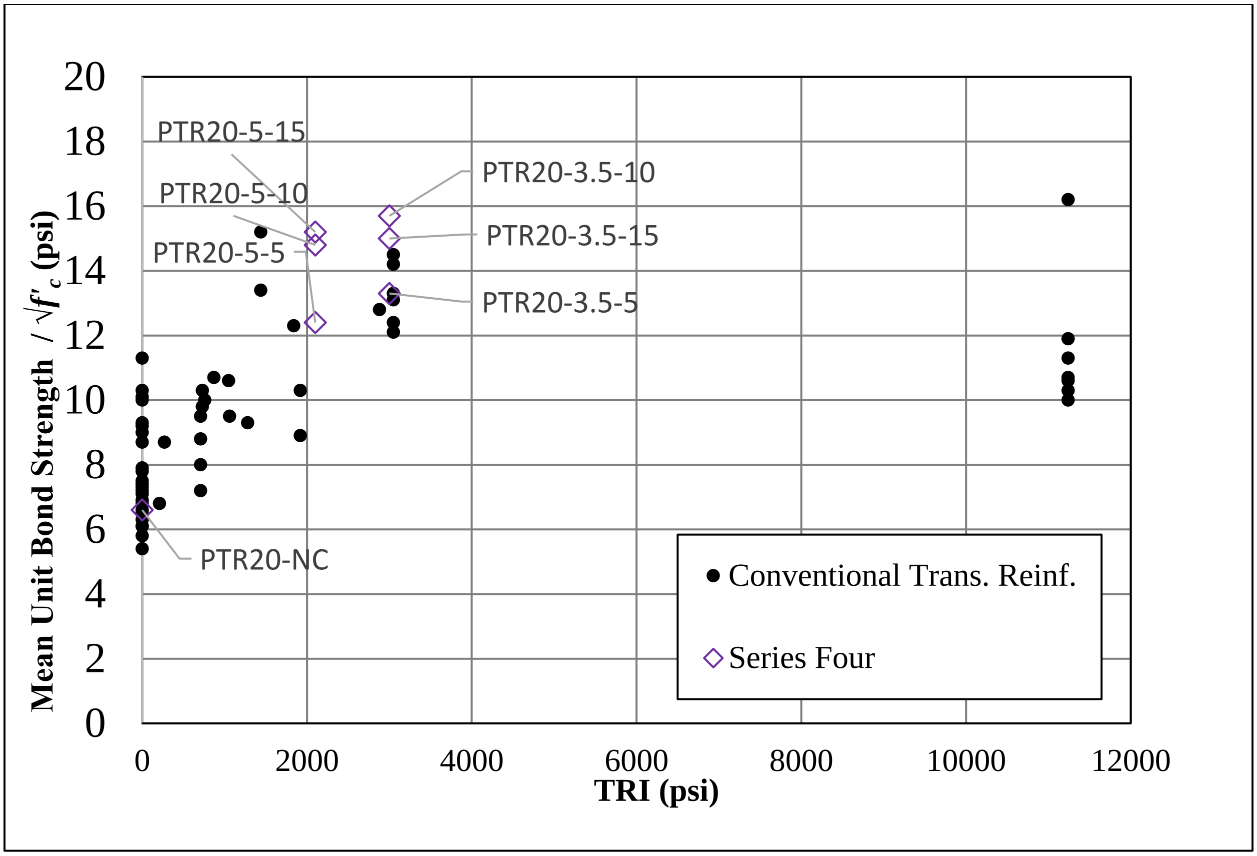

Figure 4-31: Mean bond strength versus TRI from Series Four

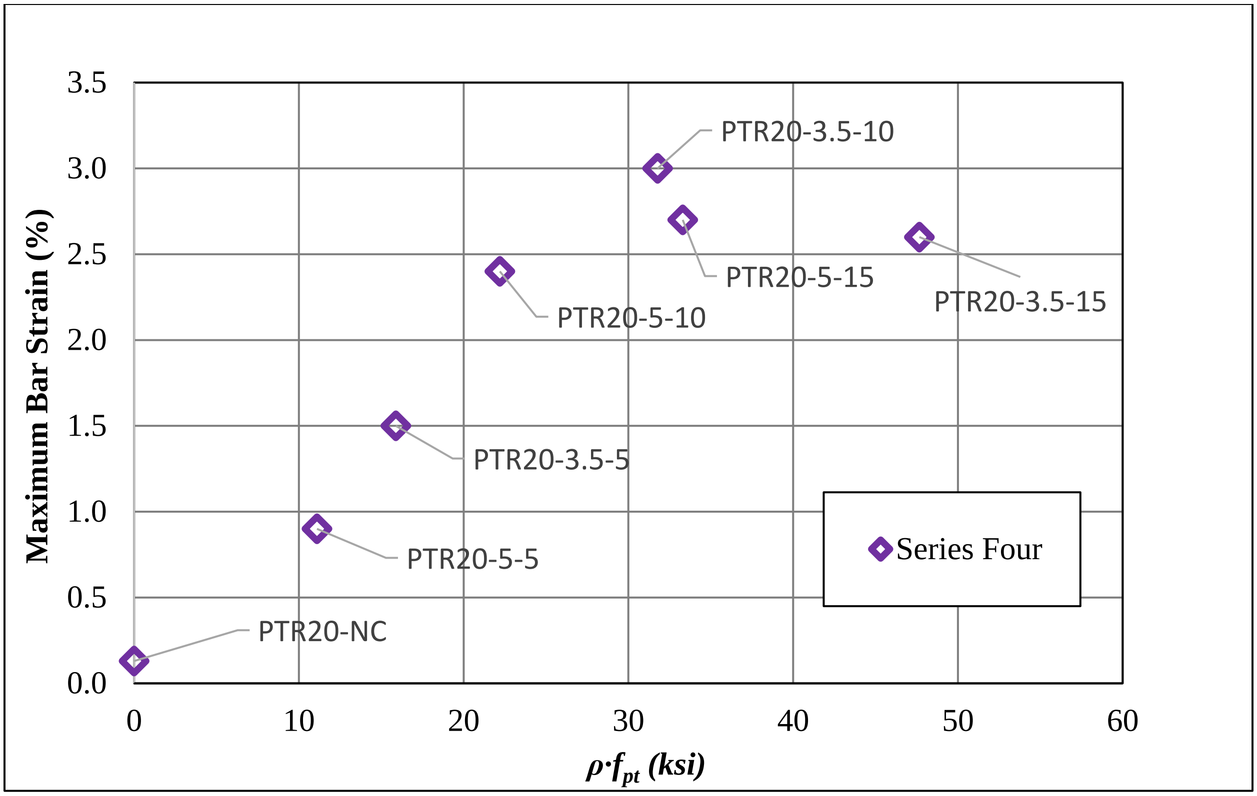

Figure 4-32: Maximum bar strain versus values of lateral confining pressure for Series Four

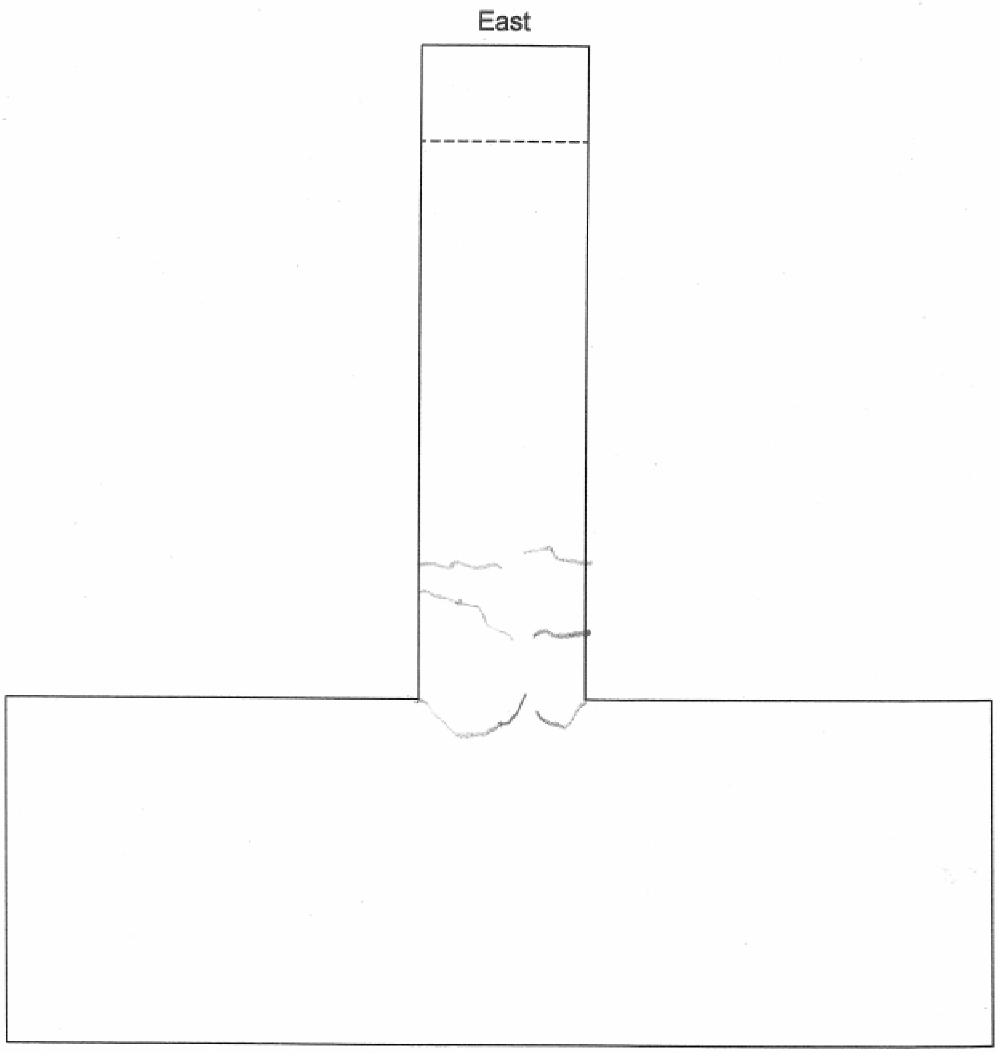

Figure 4-33: Crack map of column C2 at a drift ratio of 0.5%, Lateral load equal to 34.4 kips

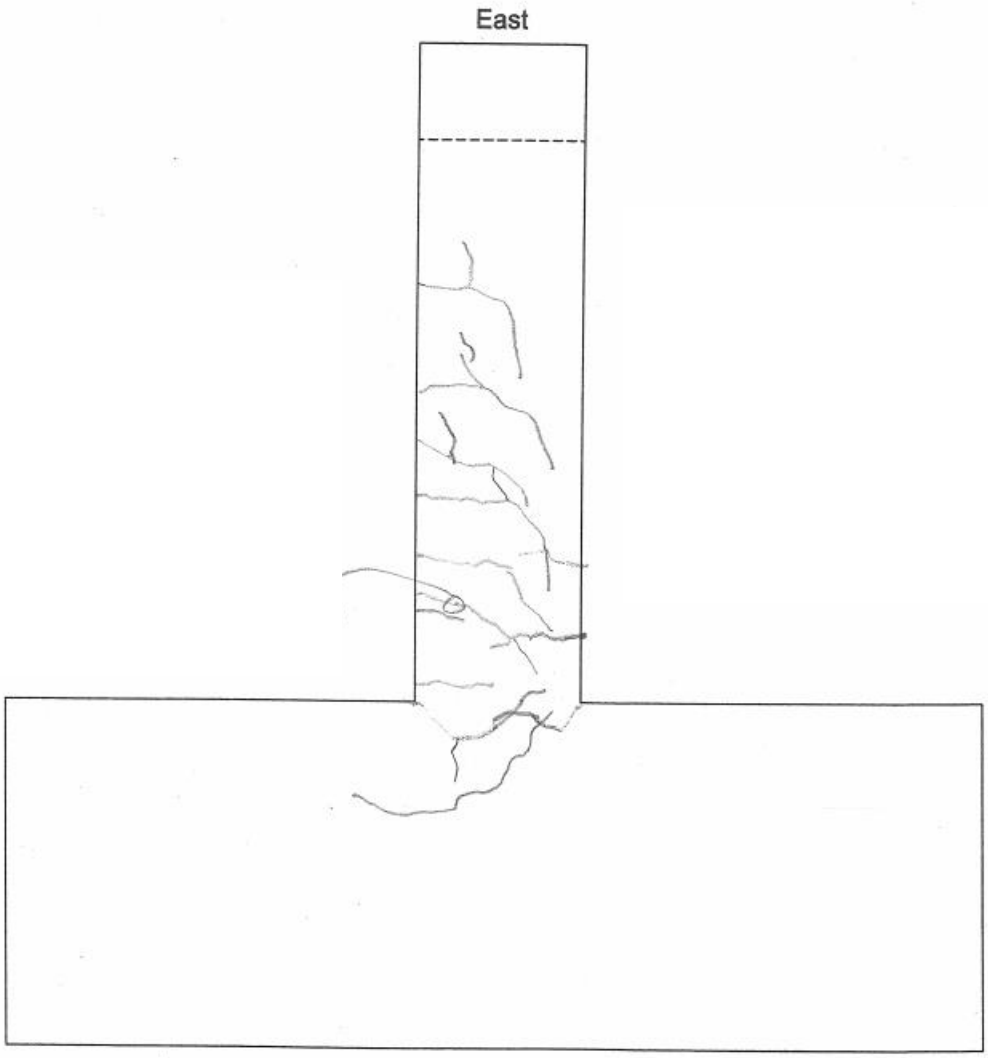

Figure 4-34: Crack map of column C2 at a drift ratio of 1%, Lateral load equal to 57.8 kips

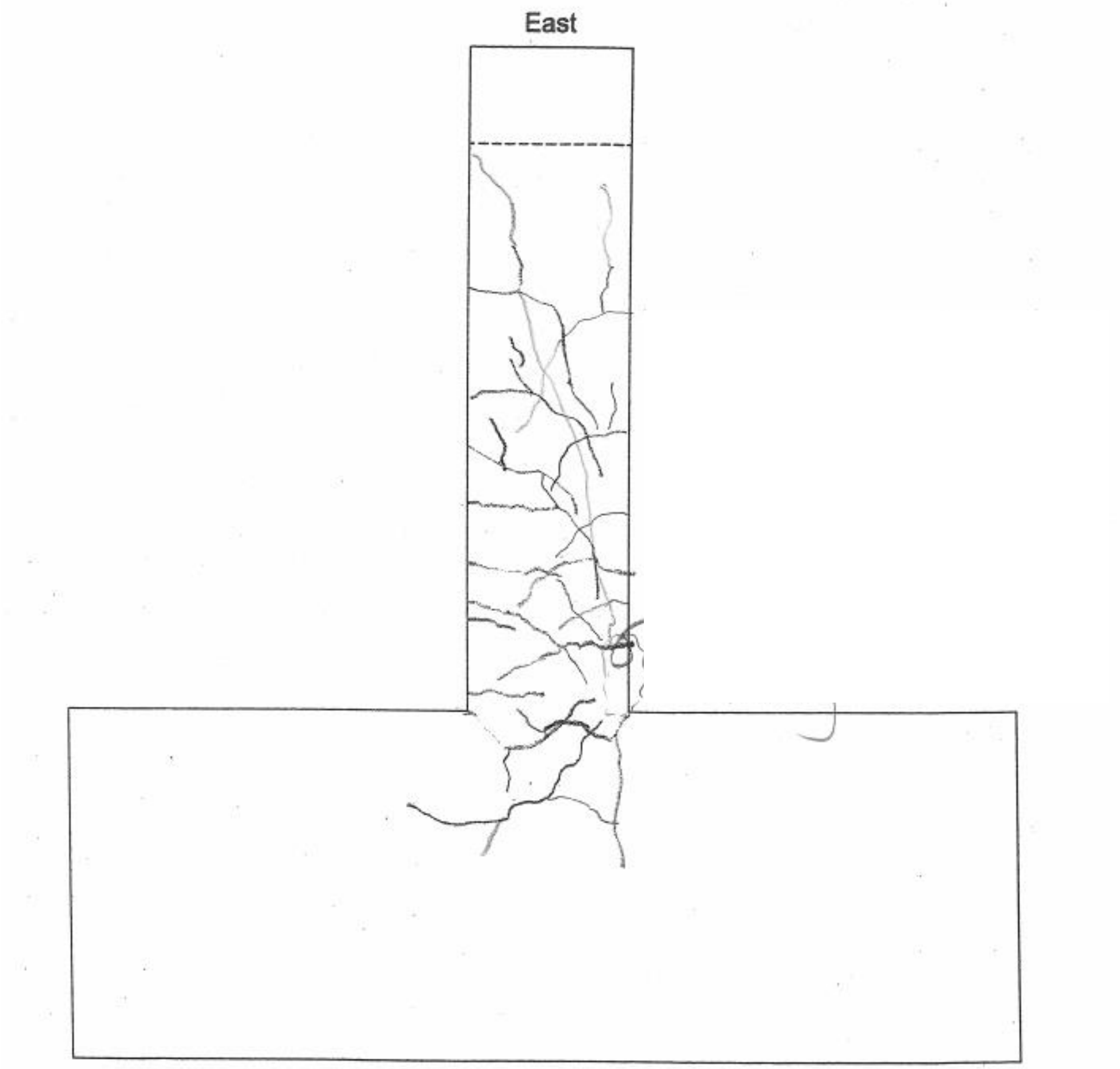

Figure 4-35: Crack map of column C2 at a drift ratio of 2%, Lateral load equal to 56.1 kips

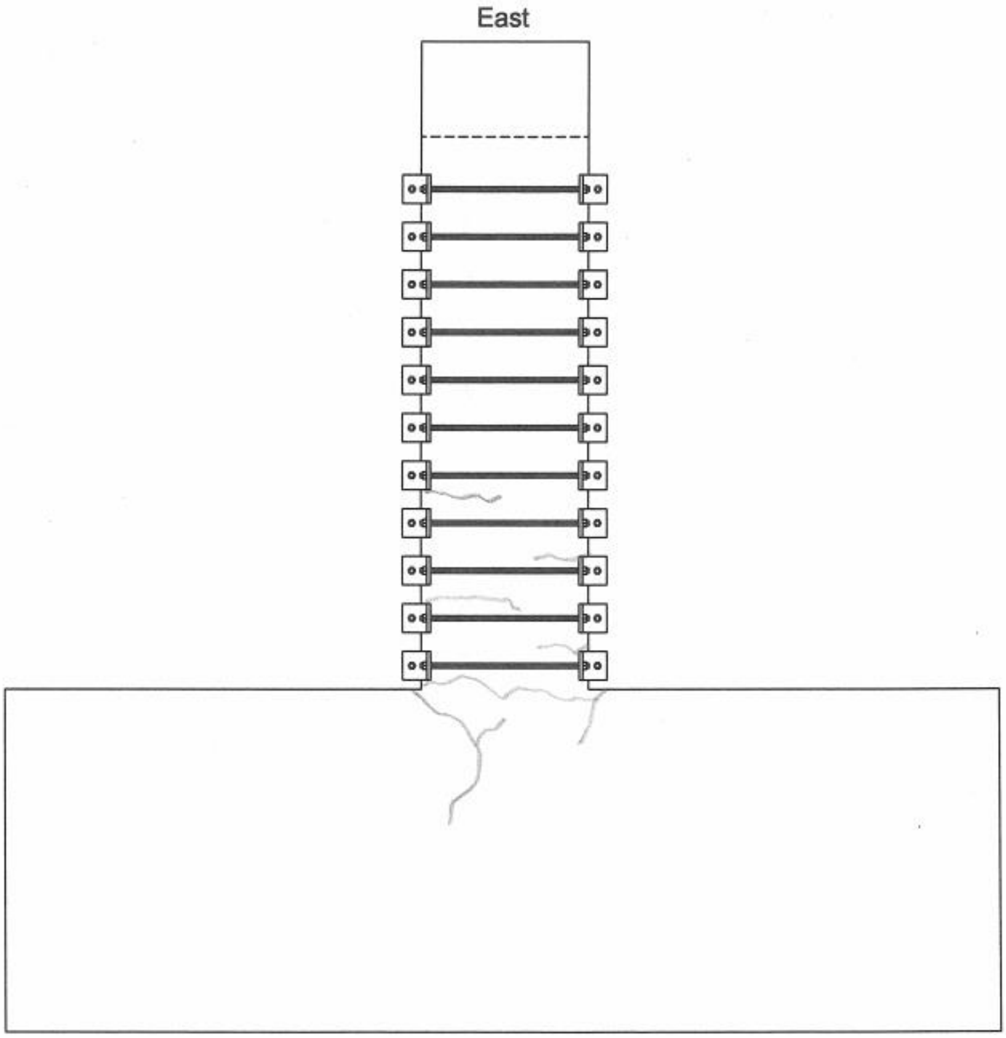

Figure 4-36: Crack map of column C1 at a drift ratio of 0.5%, Lateral load equal to 31.1 kips

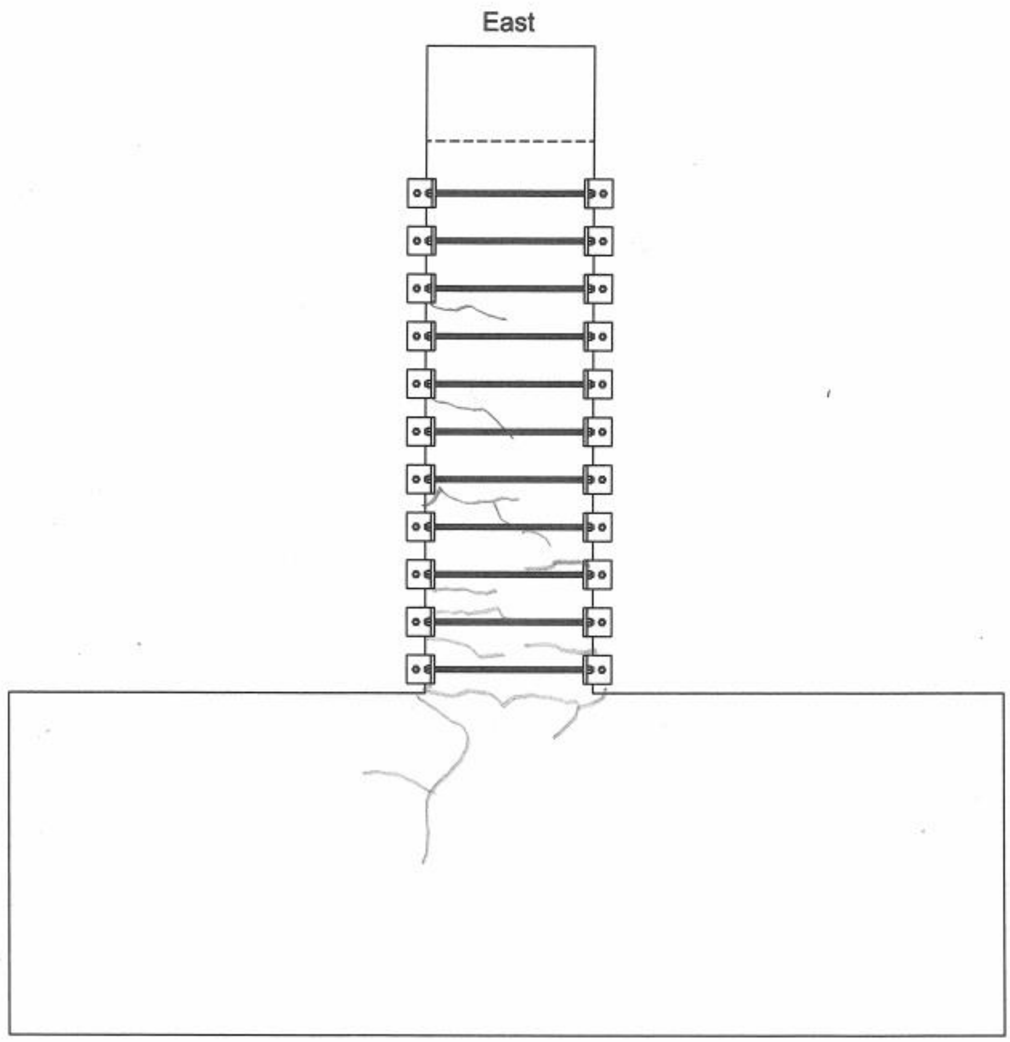

Figure 4-37: Crack map of column C1 at a drift ratio of 1%, Lateral load equal to 53 kips

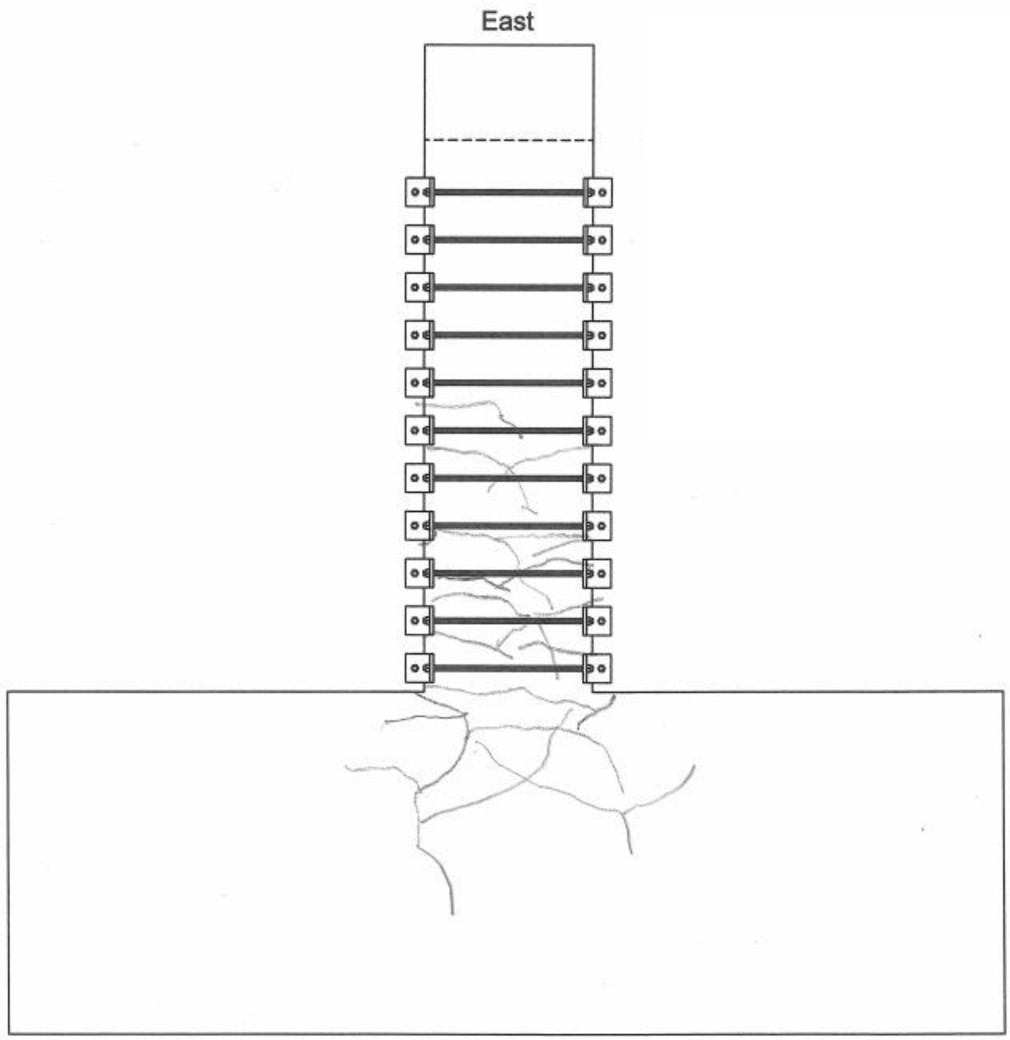

Figure 4-38: Crack map of column C1 at a drift ratio of 2%, Lateral load equal to 56 kips

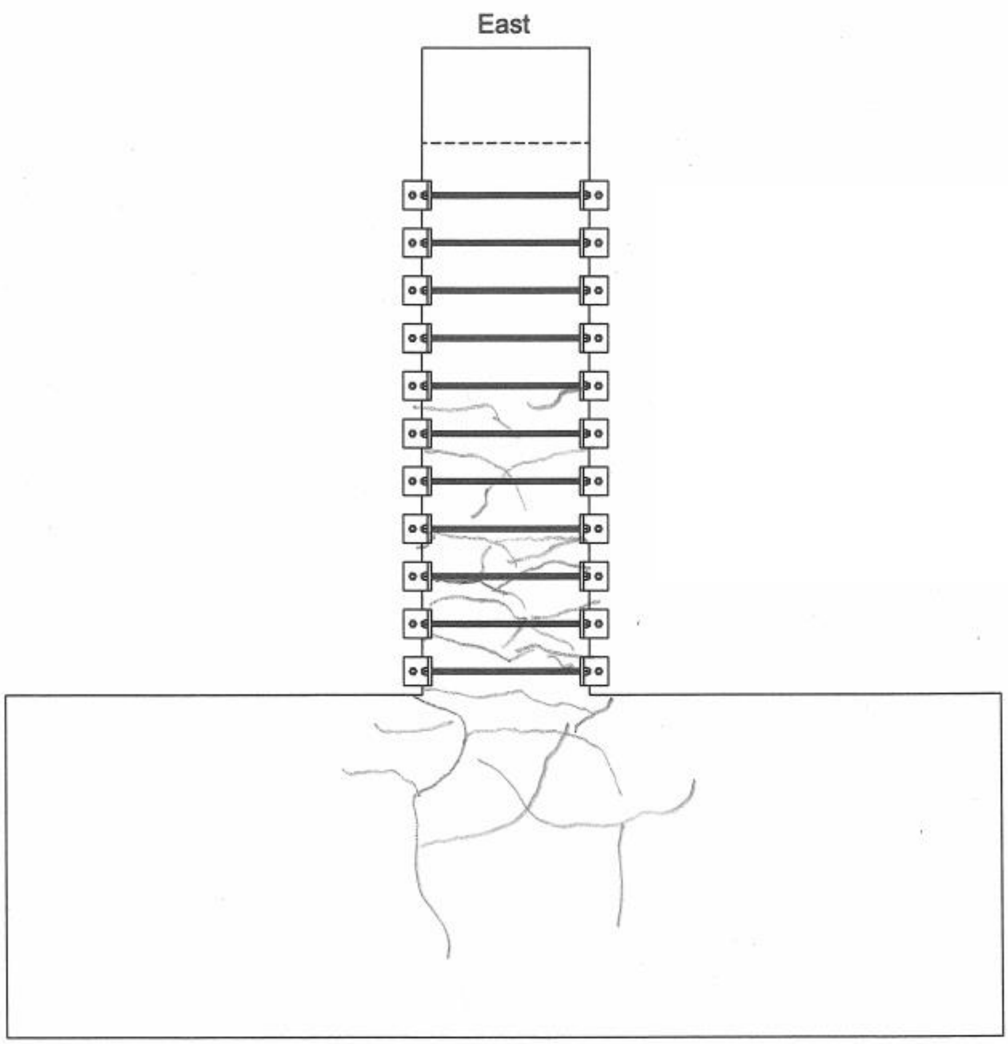

Figure 4-39: Crack map of column C1 at a drift ratio of 3%, Lateral load equal to 56.2 kips

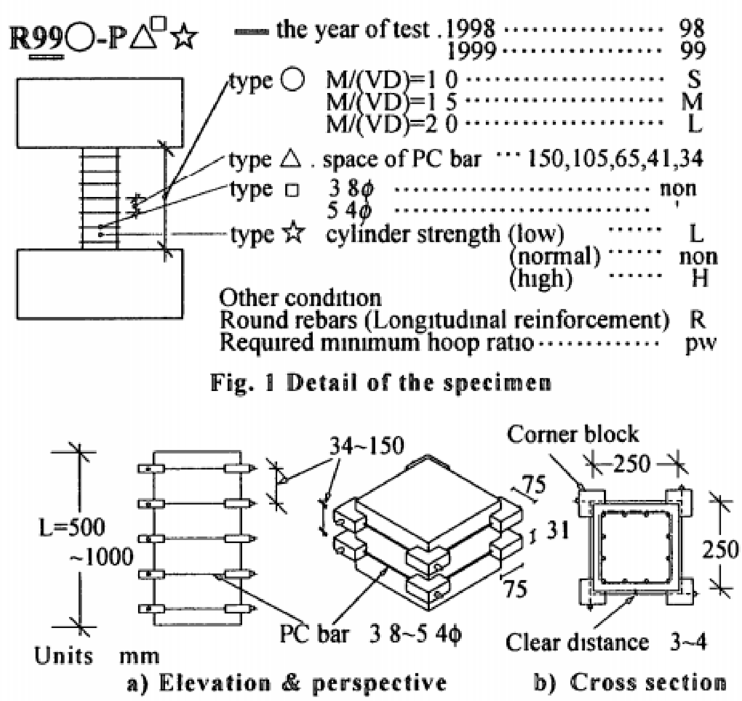

Figure 4-40: Geometry of specimens and post-tensioned transverse reinforcement adapted from (Yamakawa, 2000)

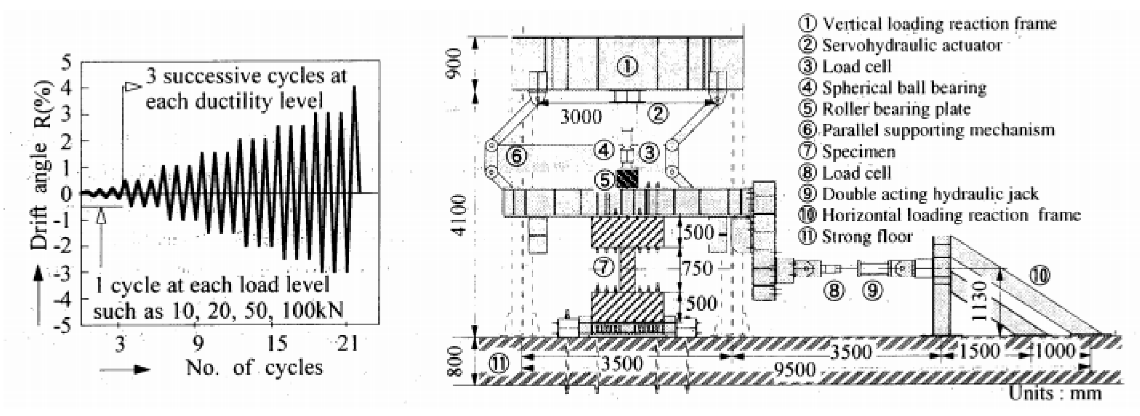

Figure 4-41: Testing protocol and loading setup used in column test by Yamakawa et al. (2000). Adapted from (Yamakawa, 2000)

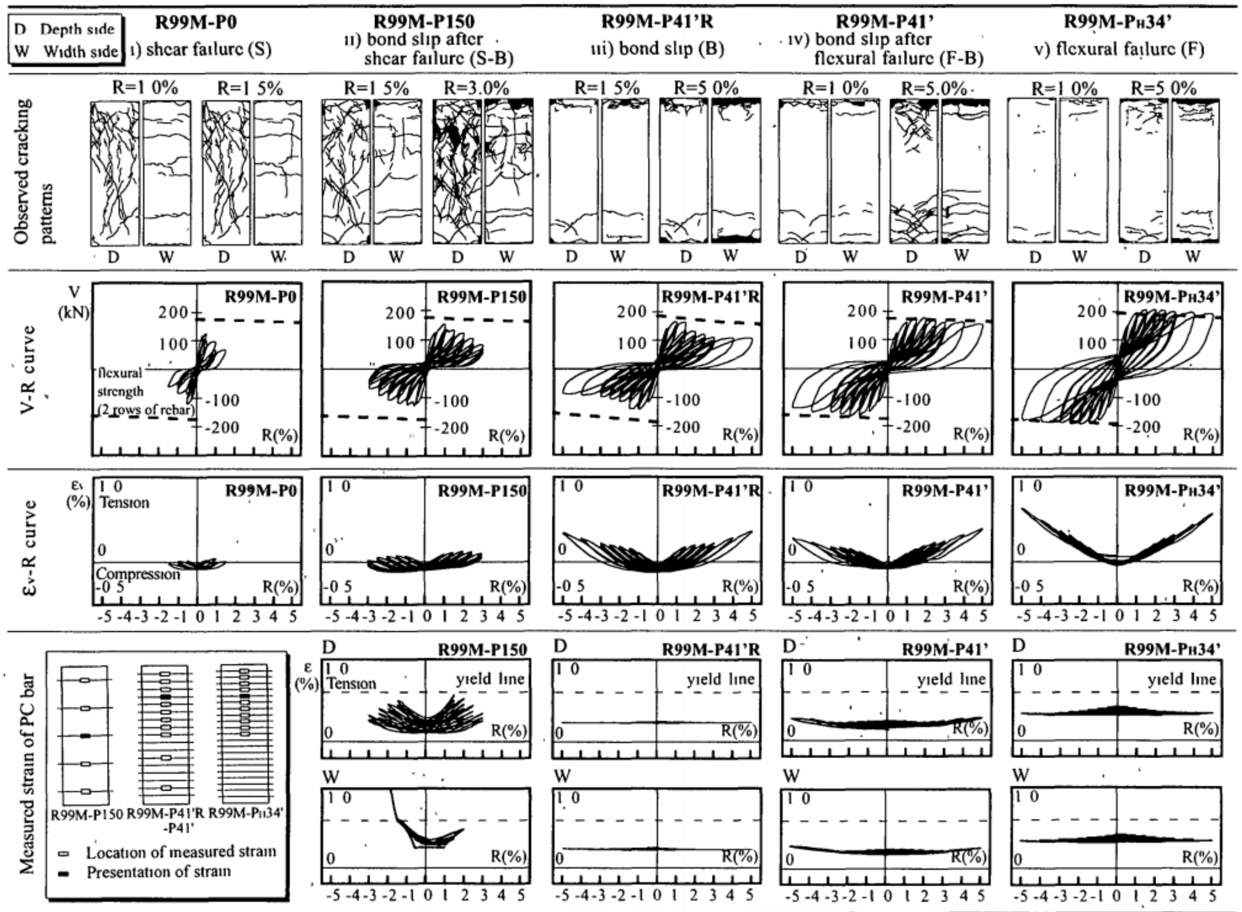

Figure 4-42: Summary of selected test specimens by Yamakawa et al. (2000). Adapted from (Yamakawa, 2000)

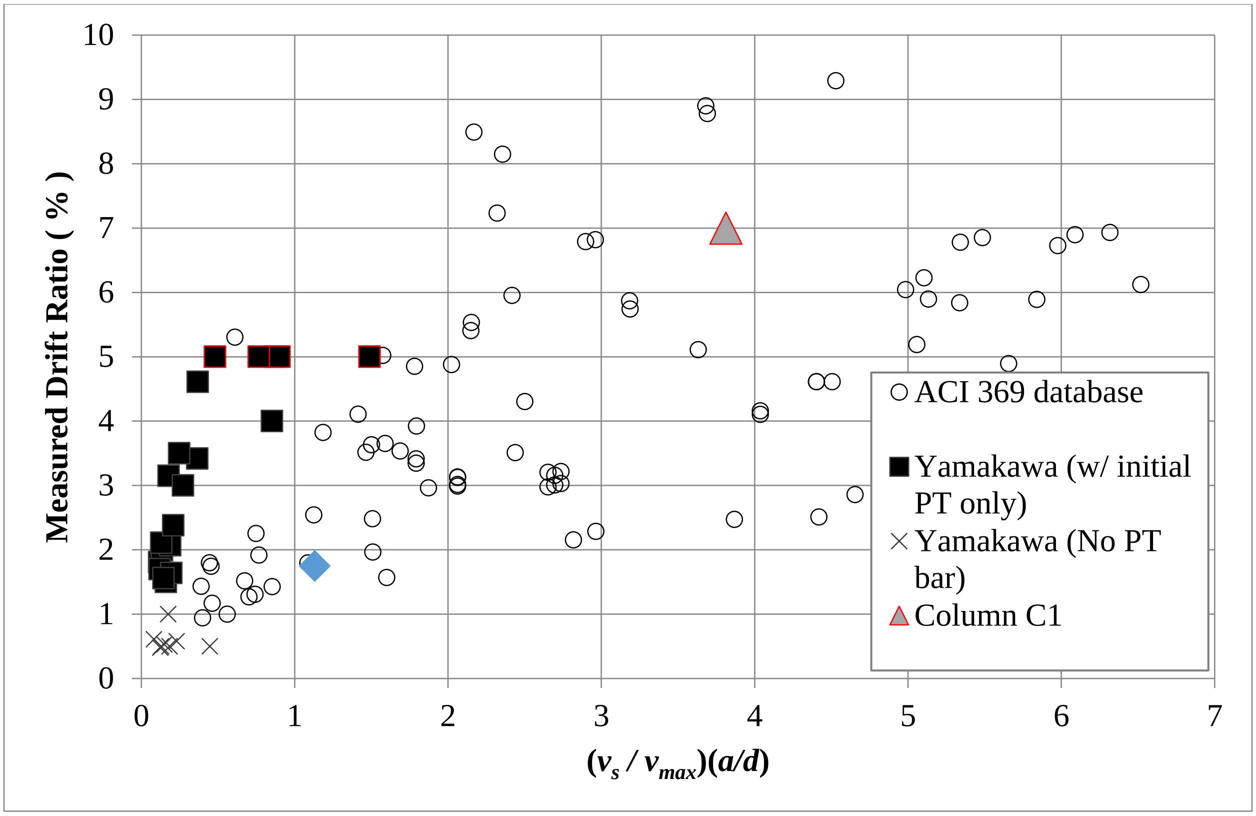

Figure 4-43: (Transverse reinforcement shear contribution / nominal shear demand)(shear span/effective depth) versus drift ratio for columns from Yamakawa et al. (2000), Series Five, and selected columns from the ACI 369 database. Data points with red border indicate specimens that did not failure in shear.

Note: data in Figure 4-43 through 4-48 are limited to the following parameters:

- Concrete compressive strengths $f_c{'}$ ranging from 2 ksi to 12 ksi
- Yield stress of longitudinal reinforcement f_y ranging from 46 to 74 ksi
- Yield stress of transverse reinforcement ranging f_{yt} from 36 to 95 ksi
- Longitudinal reinforcement ratios ranging ρ from 1.2% to 6.9%
- Conventional transverse reinforcement ratios ρ_{tr} ranging from 0.1% to 1.6%
- Aspect ratios *a/d* not exceeding 4
- *s/d* values less than 0.5
- s/d_b values less than 8
- No lap splices
- axial load less than $0.2f_c{`}A_g$

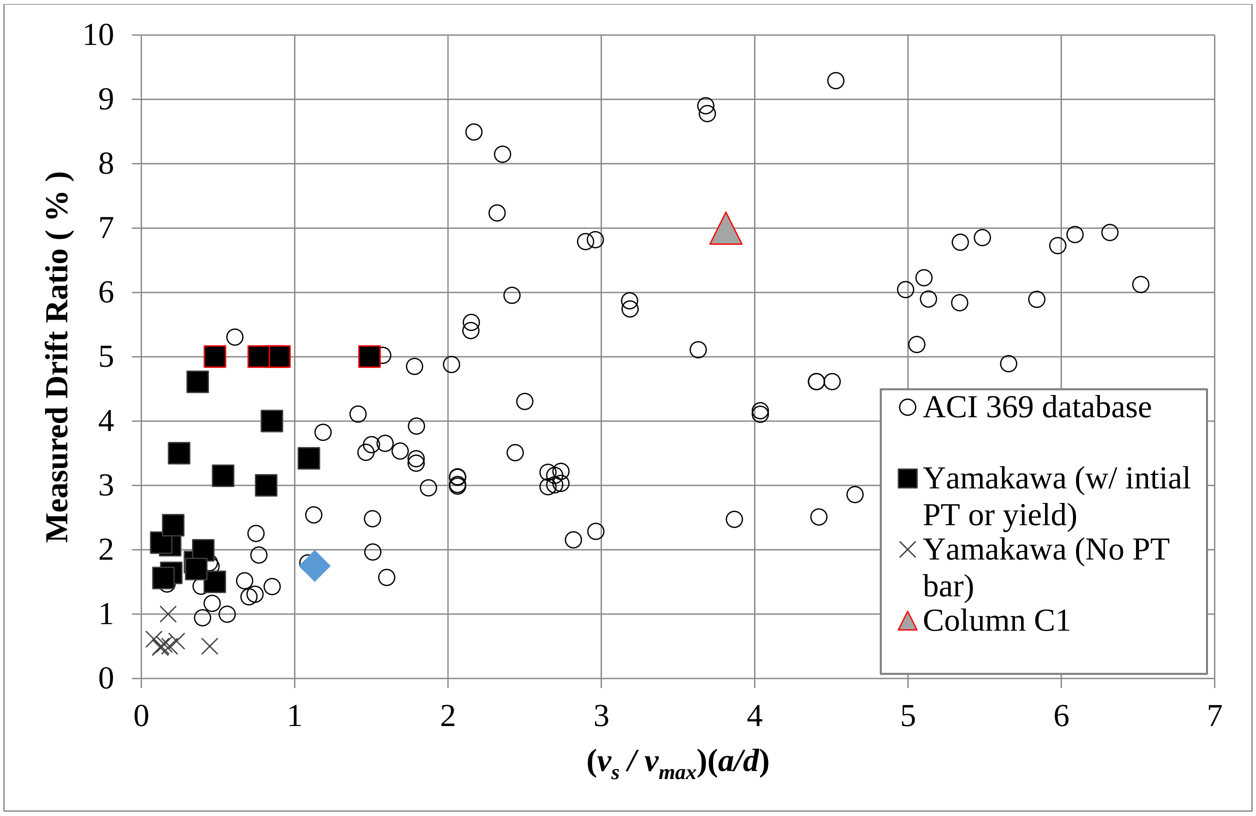

Figure 4-44: (Transverse reinforcement shear contribution / nominal shear demand)(shear span/effective depth) versus drift ratio for columns from Yamakawa et al. (2000), Series Five, and selected columns from the ACI 369 database. Data points with red border indicate specimens that did not failure in shear.

Note: Figure 4-44 differs from Figure 4-43 as the use of either the initial prestress (f_{pti}) or the yield stress (f_{pty}) is used in the determination of the shear strength contribution as reported by Yamakawa et al. (2000). In Figure 4-43 only the initial prestress (f_{pti}) is used.

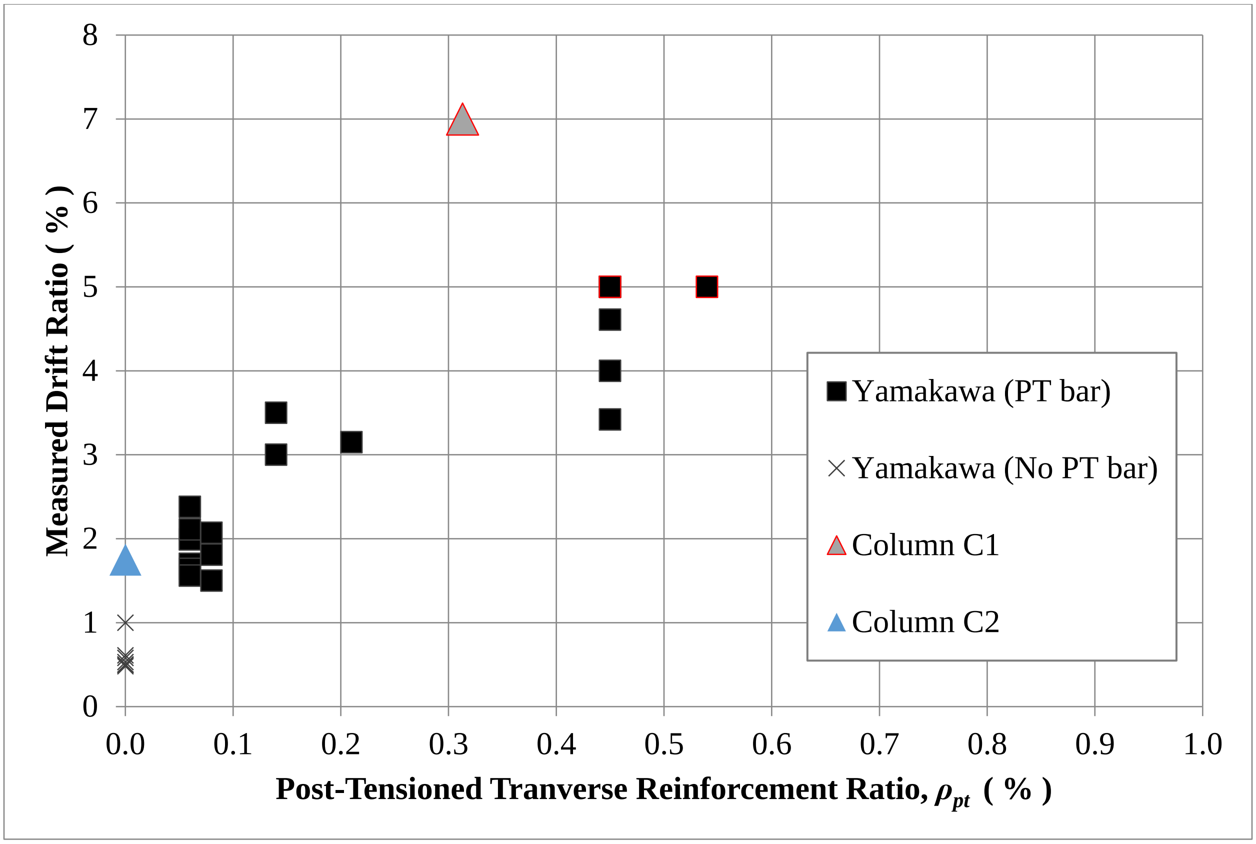

Figure 4-45: Post-tensioned transverse reinforcement ratio versus drift ratio for columns from Yamakawa et al. (2000) and Series Five

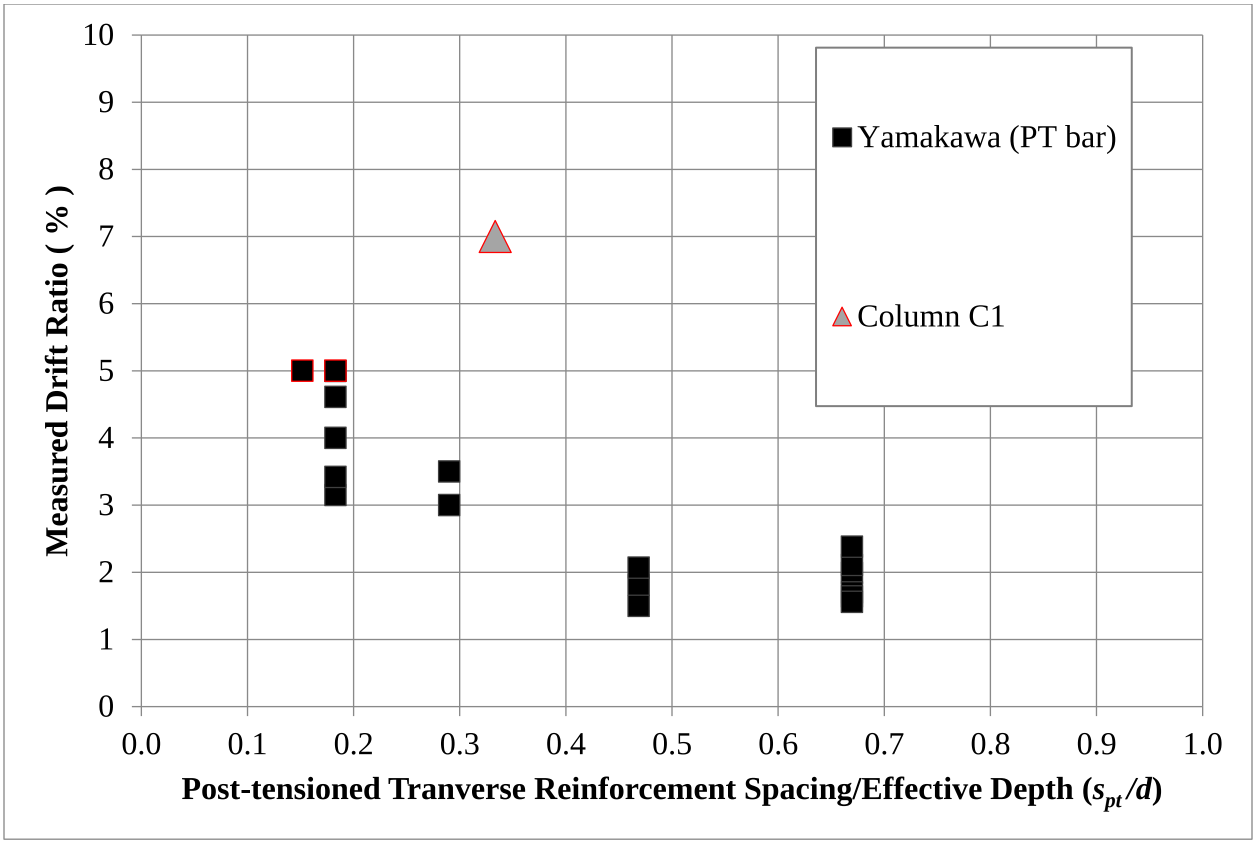

Figure 4 46: Post-tensioned transverse reinforcement spacing ratios versus drift ratio for columns from Yamakawa et al. (2000) and Series Five

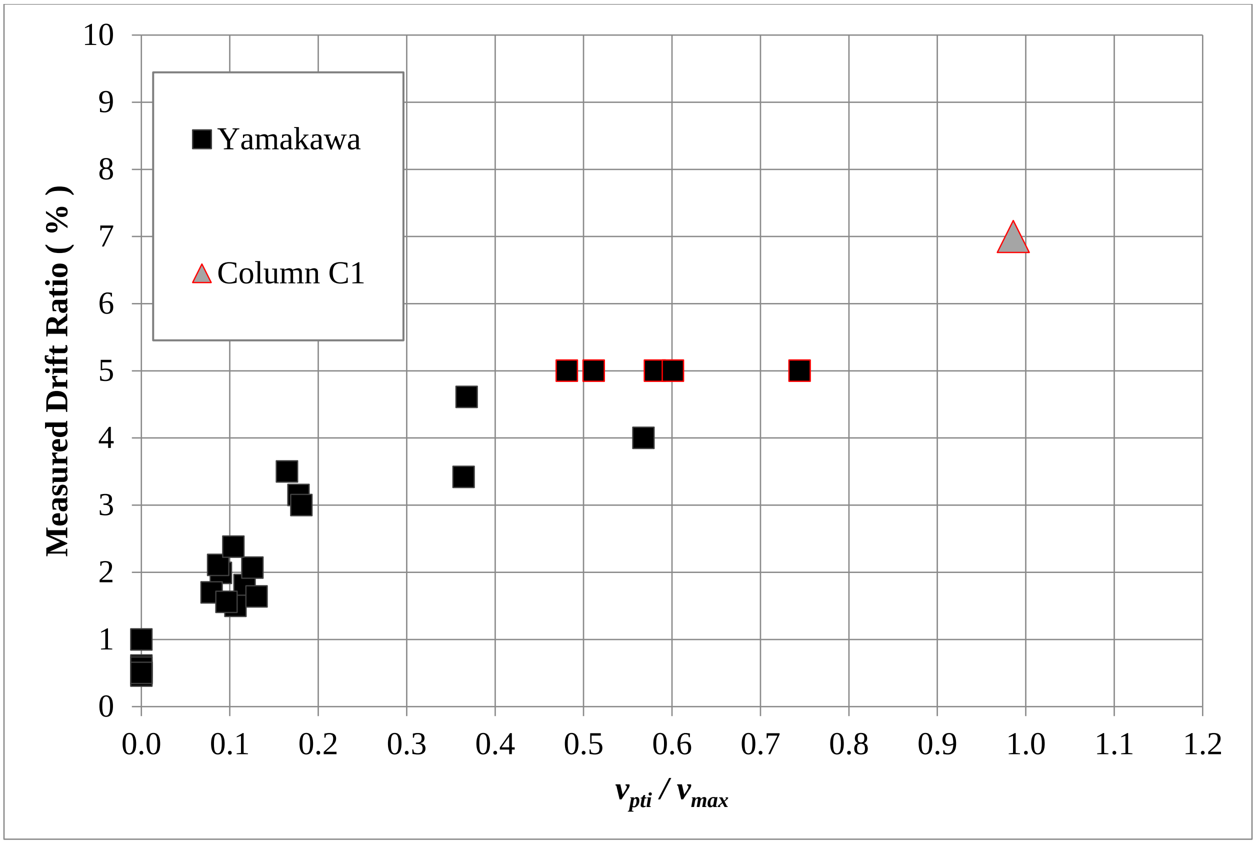

Figure 4-47: Shear strength contribution from initial post-tensioning stress to nominal shear demand versus drift ratio for columns from Yamakawa et al. (2000) and Series Five

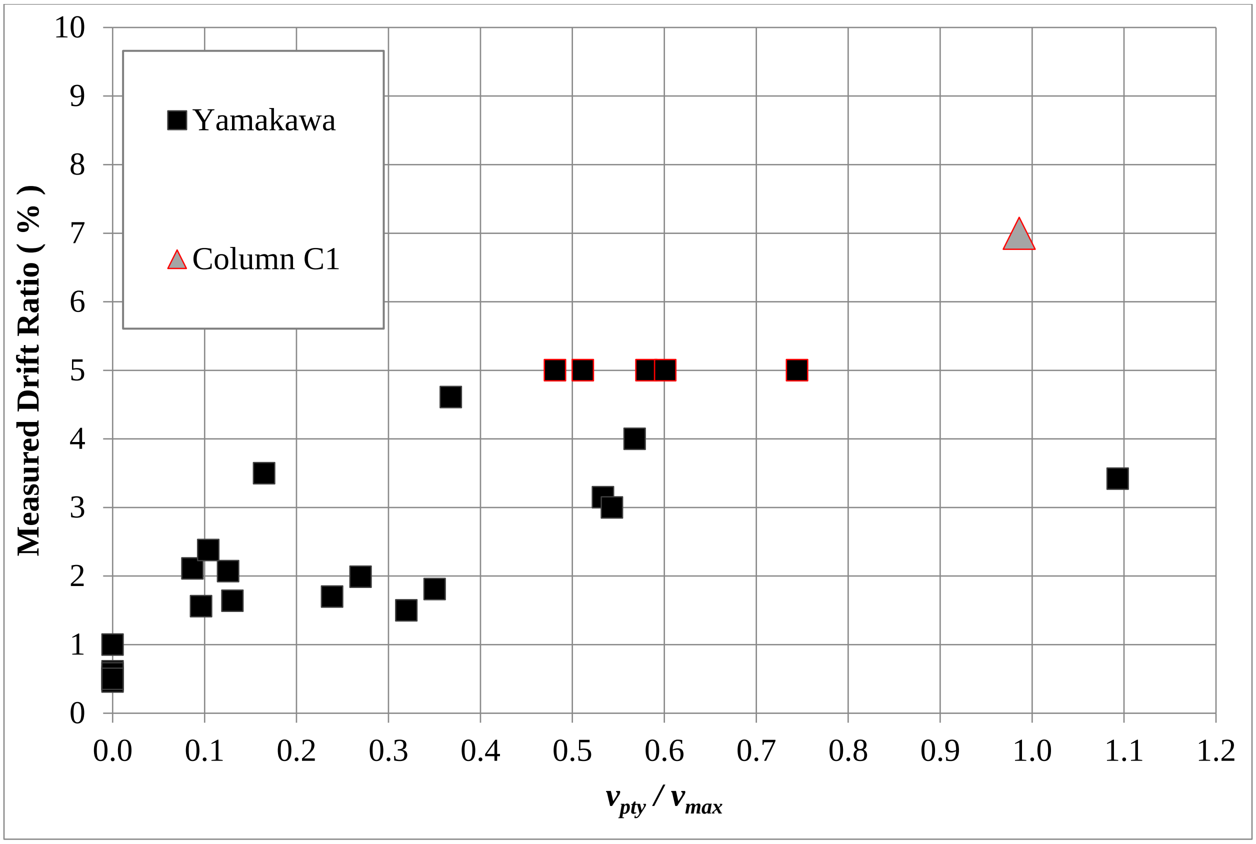

Figure 4-48: Shear strength contribution from post-tensioning stress equal at yield to nominal shear demand versus drift ratio for columns from Yamakawa et al. (2000) and Series Fi

REFERENCES

Aboutaha, R. S., Engelhardt, M. D., Jirsa, J. O., & Kreger, M. E. (1996). Retrofit of Concrete Columns with Inadequate Lap Splices by the Use of Rectangular Steel Jackets. *Earthquake Spectra*, 693-714.

Aboutaha, R. S., Engelhardt, M. D., Jirsa, J. O., & Kreger, M. E. (1999). Rehabilitation of Shear Critical Concrete Columns by Use of Rectangular Steel Jackets. *ACI Structural Journal*, 68-78.

Abrams, D. A. (1913). *Tests of Bond Between Concrete and Steel*. Urbana, IL: University of Illinois Bulletin.

ACI 408R-03. (2003). *Bond and Development of Straight Reinforcing Bars in Tension* . ACI.

ACI Committee 318. (1971). *Building Code Requirements for Structural Concrete.* Farmington Hills, MI: American Concrete Institute.

ACI Committee 318. (2019). *Building Code Requirements for Structural Concrete.* Farmington Hills, MI: American Concrete Institute.

ASCE. (2017). *ASCE/SEI 7-16: Minimum design loads and associated criteria for buildings and other sturctures.* Reston, Virginia: American Society of Civil Engineers.

ASCE/SEI. (2019). *Performance-Based Wind Design.* American Society of Civil Engineers.

ASTM C39. (2020). *Standard Test Method for Compressive Strength of Cylinderical Concrete Specimens.* Conshohocken, PA: ASTM International.

ASTM C496. (2017). *Standard Test Method for Splitting Tensile Strength of Cylinderical Concrete Specimens.* West Conshohocken, PA: ASTM International.

Berry, M. P., & Eberhard, M. O. (2003). *Performance Models for Flexural Damage in Reinforced Concrete Columns.* Berkeley: Pacific Earthquake Engineering Research Center Report.

Blume, J. A., Newmark, N. M., & Corning, L. H. (1961). *Design of Multistory Reinforced Concrete Buildings for Earthquake Motions.* Skokie: Portland Cement Association.

Comartin, C., Elwood, K., & Faison, H. (2004). *Reinforced Concrete Moment Frame Building without seismic Details.* World Housing Encyclopedia.

Daluga, D. (2015). *The Effect of Maximum Aggregate Size On The Shear Strength of Geometrically Scaled Reinforced Concrete Beams.* West Lafayette, IN: Purdue University.

Earthquake Engineering Field Investigation Team (EEFIT). (1994). *The Northridge, California Earthquake of 17 January 1994.*

Earthquake Spectra. (1996). *Northridge Earthquake Reconnaissance Report, Vol. 2.* Oakland, CA: Earthquake Engineering Research Insitute.

Elwood, K. J., & Moehle, J. P. (2005). Drift Capacity of Reinforced Concrete Columns with Light Transverse Reinforcement. *EERI*.

Fardis, M. N. (2018). Capacity Design - Early History. *Earthquake Engineering & Structural Dynamics*.

Ferguson, P. M., & Thompson, J. N. (1962). Development length for Large High-Strength Reinforcing Bars in Bond. *ACI Journal, Proceedings, Vol. 59, No. 7*, 887-992.

fib. (2003). *Seismic assessment and retrofit of reinforced concrete buildings.* Lausanne: International Federation for Structural Concrete.

Fleet, E. (2019). *Effecfive Confinement and Bond Strength of Grade 100 Reinforcement.* West Lafayette IN: Master Thesis.

Frosch, R., & Canbay, E. (2005). Bond Strength of Lap-Spliced Bars. *ACI Structural Journal, Vol. 102, No. 4*, 605-614.

Ghannoum, W., & A., M. (2014). Nonlinear Modeling Parameters and Acceptance Criteria for Concrete Columns. *ACI Symposium Publication*.

Harries, K. A., Ricles, J. R., Pessiki, S., & Sause, R. (2006). Seismic Retrofit of Lap Splices In Nonductile Square Columns Using Carbon Fiber-Reinforced Jackets. *ACI Structural Journal*, 874-884.

Henkhaus, K. W. (2010). *Axial Failures of Vulnerable Reinforced Concrete Columns Damaged by Shear Reversals.* West Lafayette, IN: Purdue University.

Hognestad, E. (1951). *A Study of Combined Beding and Axial Load in Reinforced Concrete Members.* Urbana: University of Illinois Experimentation Station.

Joint ACI-ASCE Committee 408. (2012). *Report on Bond of Steel Reinforcing Bars Under Cyclic Loads.* Farmington Hills, MI: American Concrete Institute.

Kilic, S. A., & Sozen, M. A. (2003). Evaluation of Effect of August 17, 1997, Marmara Earthquake on Two Tall Reinforced Concrete Chimneys. *ACI Structural Journal*, 357-364.

Kluge, R., & Tuma, E. (1945). *Lapped Bar Splices in Concrete Beams.* Detroit Michigan: American Concrete Institute.

Kunze, W. E., Sbarnounis, J. A., & Amrhein, J. E. (1965). The March 27 Alaskan Earthquake - Effects on Structures in Anchorage. *American Concrete Institute,* 635-649.

Laughery, L. A. (2016). *Response of High-Strength Steel Reinforced Concrete Structures to Simulated Earthquakes.* West Lafayette, IN: Purdue University.

Lepage, A. (1997). *A Method For Drift-Control In Earthquake-Resistant Design of RC Building Structures.* Urbana, IL: University of Illinois at Urbana-Champaign.

Low, K. S., Martinez, G. A., Wald, D. M., & Bayrak, O. (2018). Retrofit of Deficient Lap Splices Using Post-intalled Anchors. *ACI Structural Journal*, 1541-1550.

Lynn, A. C. (2001). *PhD Dissertation: Seismic Evaluation of Existing Reinforced Concrete Building Columns.* Berkeley, CA: University of California at Berkeley.

Lynn, A. C., Moehle, J. P., Mahin, S. A., & Holmes, W. T. (1996). Seismic Evaluation of Existing Reinforced Concrete Buildings. *Earthquake Spectra*, 715-739.

Mains, R. M. (1951). Measurement of the Distrubution of Tensile and Bond Stresses Along Reinforcing Bars. *American Concrete Institute*, 225-252.

Orangun, C. O., Jirsa, J. O., & Breen, J. E. (March 1977). A Reevaluation of Test Data on Development Length and Splices. *ACI Journal*, 114-122.

Pujol, S., & Pollalis, W. (2020). *Development and Splice Lengths for High-Strength Reinforcement.* Mclean Virginia: Charles Pankow Foundation.

Puranam, A. (2018). *Strength and Serviceability of Concrete Elements Reinforced with High-Strength Steel.* West Lafayette, IN: Purdue University .

Purdue University. (2018). *Buildings Surveyed after 2017 Mexico City Earthquakes.*

Richart, F. E., Brandtzaeg, A., & Brown, R. L. (1929). *The Failure of Plain and Spirally Reinforced Concrete In Compression.* Urbana: The University of Illinois.

Richter, B. P. (2012). *A New Perspective on the Tensile Strength of lap Splices in Reinforced Concrete Members.* West Lafayette, IN: Purdue University.

Rosenblueth, E., & Meli, R. (1986). *The 1985 earthquake: causes and effects in Mexico City.* Detroit, MI: Concrete International.

Seismic Safety Commission (SSC). (1994). *Holiday Inn. Northride Building Case Studies Project.*

Sezen, H., & Moehle, J. P. (2006). Seismic Tests of Concrete Columns with Light Transverse Reinforcment. *ACI Structural Journal*, 842-849.

Sim, C. (2014). *Structural and Corrosoin Performance of Concrete Bridge Decks Reinforced With corrosion-Resistant Reinforcing Steel.* West Lafayette IN: PhD Thesis.

Sozen, M. A. (1968). The Caracus Earthquake of July 29, 1967. *American Concrete Institute*, 394-401.

Sozen, M. A. (2003). *The Velocity of Displacement.*

Sozen, M. A. (2012, October 21). Oral Presentation - The Art of Designing Ductile Concrete in the Past 50 Years: The Impact of the PCA Book and Mete A. Sozen.

Sozen, M. A., & Moehle, J. P. (1990). *Development And Lap-Splice Lengths For Deformed Reinforcing Bars In Concrete.* Schaumberg: Portland Cement Association.

Tepfers, R. (1982). *Tensile Lap Splices With Confining Reinforcement.* Goteberg: Chamlers University.

Wang, Y. (2014). *Effects of Web Reinforcement Discontinuities on the Seisic Response of Structural Walls.* West Lafayette IN: PhD Thesis.

Wight, J. K., & Sozen, M. A. (1975). Strength Decay of RC Columns Under Shear Reversals. *Journal of the Structural Division*, 1053-1065.

Yamakawa, T., Kamogawa, S., & Kurashige, M. (2000). Seismic Performance and Design of RC Columns Retrofitted by PC Bar Prestressing As External Hoops. *Structural Construction Engineering*, 107-145.

Yarandi, M. S., Saatcioglu, M., & Foo, S. (2004). Rectangular Concrete Columns Retrofitted By External Prestressing For Seismic Shear Resistance. *13th World Conference on Earthqake Engineering.* Vancouver.

Zoppo, M. D., Ludovico, M. D., Balsamo, A., & Prota, A. (2017). FRP for seismic strengthening of shear controlled RC columns: Experience from earthquakes and experimental analysis. *Composites*, 47-57.

APPENDIX A

A.1 Introduction

The appendix contains information about the materials used, fabrication and casting test specimens, and instrumentation used.

A.2 Materials

A.2.1 Concrete

All specimens in Series One through Five used normal weight concrete. All specimens in each Series were cast together using the same mix proportions. Concrete mix proportions, casting date, and age at test day for all specimens are shown in Table A-1 through Table A-7. All batches of concrete were supplied by Irving Materials Inc. of West Lafayette, Indiana.

For all Series, 6x12 in. cylinders were cast and cured under the same conditions as the test specimens. Compressive strength for the cylinders was obtained by testing them in compression using the procedure described in ASTM C39 (ASTM C39, 2020). Tensile strength of the cylinders was obtained using the procedure described in ASTM C496 (ASTM C496, 2017). A 600-kip Forney F-60C-DFM/I compression testing machine with a nonlinearity of approximately 0.08% at full range was used to perform all concrete cylinder tests. Compression tests were performed at 3, 7, 14, 21 and 28 days after casting as well as on test day. Tensile tests were performed at 28 days and on test day.

A.2.2 Reinforcement

Reinforcement bars used in lap splices in Series One through Four consisted of #11 ASTM A615 Grade 60 deformed bars. All spliced reinforcing bars in Series One through Four were from the same heat of steel. In Series Three, ¼ in. ASTM C1018 smooth bars from the same heat were used as spiral reinforcement. In Series Five, longitudinal reinforcement in the column and base consisted of #8 ASTM A615 Grade 60 deformed bars whereas transverse reinforcement consisted of #3 ASTM A615 Grade 60 deformed bars. Reinforcing bars for the longitudinal and transverse reinforcement were from two different heats of steel.

Tensile tests of all reinforcing bars were performed using an MTS 220-kip universal testing machine with a nonlinearity of approximately 0.54% at full range. All tensile tests were performed using three feet long reinforcement samples with a two-foot clear distance between the grips of the MTS testing machine. Tensile strains were measured using an MTS extensometer (Model 634.25E-54) with a gage length of 2 in. and nonlinearity of approximately 0.09%. All tensile tests were performed at a strain rate of 0.006/min. Reinforcement details and yield stress for each heat of steel used are shown in Table A-8. Plots of stress-strain curves are shown in Figure A-1 through Figure A-8. Figure A-2 shows an idealized tri-linear stress strain relationship for tests in Series One through Series Four with parameters listed in Figure A-3.

A.2.3 Threaded Rods

In Series Two, anchors consisted of ¾ in. ASTM A193 B7 threaded rods. All threaded rods used in Series Two were form the same heat of steel. In Series Four and Five, post-tensioned transverse reinforcement consisted of ½ in. ASTM A193 B7 threaded rods. All threaded rods in Series Four and Five were from the same heat of steel. Tensile strength of threaded rods was obtained using the same procedure used to obtain tensile strength of reinforcing steel. Details of the threaded rods and yield stress are shown in Table A-8.

A.3 Specimen Fabrication

All specimens were constructed at the Robert L. and Terry L. Bowen Laboratory for Large-Scale Civil Engineering Research, Purdue University, West Lafayette, Indiana.

A.3.1 Fabrication

Formwork for beam tests in Series One was constructed using plywood as shown in Figure A-9 through Figure A-11. Reinforcement cage was constructed within the formwork. To prevent the formwork from prying open during casting, ¼ in. threaded rods were inserted transversely through the formwork and held tight using a set of wedges and nuts which reacted against two sets of two-by-fours. Threaded rods were placed at mid height of formwork with a spacing of approximately 24 in. Prior to casting, all formwork joints were sealed with caulk and the formwork was oiled using formwork oil.

Formwork for coupon tests in Series One, Two, Three and Four was constructed using plywood and is shown in Figure A-12 through Figure A-17. Specimens in Series Four were cast in the same formwork as Series Three formwork that was 20-bar diameters in length. Holes were drilled at the ends of each formwork to allow for reinforcing bars to protrude out. Proper reinforcement cover was achieved by suspending the lapped reinforcing bars using steel wires at a uniform spacing of 6 in. along the length of the splice. In addition, reinforcement bar protruding out of the formwork was supported using wooden supports which were fastened to the base of the formwork. Prior to casting, all formwork joints were sealed with caulk and the formwork was oiled using formwork oil.

Formwork for columns in Series Five was also constructed using plywood as shown in Figure A-18 through Figure A-20. Reinforcement cage was constructed outside the formwork and then lifted in place using an overhead crane. Proper reinforcement cover was maintained using steel chairs. Prior to placing the reinforcing cage in the formwork, all formwork joints were sealed with caulk and the formwork was oiled using formwork oil.

A.3.2 Casting and Curing

All concrete mixes were delivered within thirty minutes of batching. Upon delivery of the concrete, measured concrete mix proportions were checked and the slump was measured. Concrete was then placed into cylinders and formwork. For coupon specimens, concrete was placed in the formwork using a concrete bucket which was attached to an overhead crane. For beam and column specimens, concrete was directly poured into the formwork using the chute of the ready-mix truck. For cylinders, concrete was cast using handheld scoops. Electric vibrators were used to consolidate concrete during casting. All specimens and cylinders were cast using two lifts of concrete. Following casting, exposed concrete surfaces were leveled and finished using magnesium hand floats. Once the concrete set, it was cured by covering it with wet burlap and plastic sheets. Water was applied twice every day during the entire duration of the curing process. Following curing, specimens and cylinders were stored in the laboratory under room temperature until test day.

A.3.3 Dimensions and Tolerances

As-built locations of reinforcement were measured for all specimens before casting. The cover, spacing and length of reinforcement were measured to be within approximately 1/8 in. of nominal dimensions.

A.4 Instrumentation

A.4.1 Series One-Beam Instrumentation

For beams in Series One, applied load, displacements at midspan, overhangs, splice ends, and supports, and surface concrete deformations were measured. Applied load was measured using two 50-kip capacity load cells. Displacement at beam midspan, overhangs and splice ends were measured using 10 in. string potentiometers and 1 in. dial gages whereas displacements at supports were measured using 0.25 in. Linear Variable Displacement Transducers (LVDTs). Concrete surface deformations were measured using Optotrak Pro 6000, an optical displacement tracking system. Concrete surface deformations in the horizontal and vertical directions were measured using infrared targets that were installed above and below the place of the spliced reinforcing bars. All sensors were calibrated prior to testing of the beam specimens. Load cells were calibrated using a 120-kip Baldwin universal testing machine which had an accuracy of approximately 600 lbf. All displacement sensors were calibrated using a Fowler Trimos height gage (Model V1004+) which had an accuracy of 0.00025 in. Detailed information about all sensors used for the beam specimens in Series One are listed in

Sensor Type	Manufacturer	Model Number	Serial Number	Location	Range	Accuracy
Load Cell	Lebow	3175 50K	1176585	North Load Point	50 kip	80 lbf
		3175 50K	442	South Load Point		
String Potentiometer	Unimeasure	PA 20	36030715	North Overhang	20 in.	0.05 in.
		PA 20	45110640	South Overhang		
		PA 10	40010981	North Splice End	10 in.	0.02 in.
		PA 10	40010984	Mid-span*		

		PA 10	40010987			
		PA 10	40010979	South Splice End		
LVDT	Schaevitz	DC EC 250	22439	North Support	+/- 0.25 in.	0.001 in.
	Schaevitz	DC EC 250	22461	South Support		
Optotrak	Northern Digital Inc.	PRO Series 600	-	-	-	0.005 in.
Dial Gage	Federal	1 in. Dial Gage	-	North Overhang	1 in.	0.001 in.
			-	Mid-span		
			-	South Overhang		

Table A-9.

Voltage readings from load cells, potentiometers and LVDTs were acquired continuously during the entire duration of the test using National Instrument's SCXI 1000 data acquisition system at a sampling frequency of 10 Hz. Surface deformation measurements were only taken at load stops. At each load stop, surface deformation measurements were taken for approximately 10 seconds at a sampling frequency of 100 Hz.

A.4.2 Series One Through Series Three Coupons Instrumentation

For coupon specimens in Series One, Two and Three, applied load, laminar crack widths, bar strains and surface concrete deformations were measured. Applied load was measured using two 110-kip capacity load cells each placed next to the hydraulic jacks used to apply load. Laminar crack widths were measured using Linear Variable Displacement Transducers (LVDTs) that were installed across the plane of the lap splices near the ends of each splice at each of the four corners of the specimen. Reinforcing bar strains and concrete surface deformations were measured using Optotrak Pro 6000. Concrete surface deformations in the horizontal and vertical directions were measured using infrared targets that were installed above and below the plane of the spliced reinforcing bars. Bar strains were obtained using infrared targets that were attached directly to the exposed reinforcing bars. All sensors were calibrated prior to testing of the coupon specimens.

Load cells were calibrated using a 120-kip Baldwin universal testing machine which had an accuracy of approximately 600 lbf. LVDTs were calibrated using a Fowler Trimos height gage (Model V1004+) which had an accuracy of 0.00025 in. Detailed information about all sensors used for the coupon specimens in Series One, Two and Three are listed in Table A-10

Voltage readings from load cells and LVDTs were acquired continuously during the entire duration of the test using Vishay Measurements Group System 7000 data acquisition system at a sampling frequency of 10 Hz. Surface deformation measurements were only taken at load stops. At each load stop, surface deformation measurements were taken for approximately 10 seconds at a sampling frequency of 100 Hz.

A.4.3 Series Four Coupon Instrumentation

For coupon specimens in Series Four, applied load, specimen elongation and surface concrete deformations were measured. Applied load and specimen elongation were measured using load and displacement transducers of the 660-kip MTS universal testing machine that was used to test the coupon specimens. Load and displacement measurements were continuously recorded during the entire duration of the test using MTS's FlexTest controller software at a sampling frequency of 10 Hz. Surface concrete deformations were measured using Natural Point Inc.'s OptiTrack Motion Capture System, an optical displacement measurement system. Concrete deformations in both the horizontal and vertical directions were measured using reflective optical targets that were attached to the concrete surface on either side of the plane of spliced bars. Two Prime 41 cameras along with OptiTrack's Motive software were used to acquire concrete surface deformations at load stops. At each load stop, surface deformation measurements were taken for approximately 10 seconds at a sampling frequency of 100 Hz. Detailed information about all sensors used for the coupon specimens in Series Four are listed in Table A-11

A.4.4 Series Five Column Instrumentation

For column specimens in Series Five, applied axial and lateral load, lateral displacements at top of column, mid-height of column and base of column, and concrete surface deformations along the height of the column were measured. Applied axial load was measured using two 110-kip load cell placed in series with the two the hydraulic jacks used to apply axial load. Lateral load was measured using a 100-kip load cell placed in series with the actuator used to apply lateral load. Lateral displacement measurements were made at top of column, mid-height of column and base of column using 10 in. string potentiometers. All potentiometers were mounted on a steel column that was post-tensioned to the strong floor of the laboratory. In addition to string potentiometers, 1 in. dial gages were also used to measure the slip of the column base relative to the strong floor. All load cells and potentiometers were calibrated prior to testing of the column specimens. Load cells were calibrated using a 120-kip Baldwin universal testing machine which had an accuracy of approximately 600 lbf. LVDTs were calibrated using a Fowler Trimos height gage (Model V1004+) which had an accuracy of 0.00025 in. Voltage readings from load cells and potentiometers were acquired continuously during the entire duration of the test using Vishay Measurements Group System 7000 data acquisition system at a sampling frequency of 10 Hz.

Concrete surface deformations were measured using Natural Point Inc.'s OptiTrack Motion Capture System. Reflective optical targets were attached to the surface of the column along the height of the column at locations of longitudinal reinforcement. These surface deformations were also used to infer longitudinal strains in the reinforcing bar along the height of the column. Three Prime 41 cameras along with OptiTrack's Motive software were used to acquire concrete surface deformations at load stops. At each load stop, surface deformation measurements were taken for approximately 10 seconds at a sampling frequency of 100 Hz. Detailed information about all sensors used for the column specimens in Series Five are listed in Table A-12

Table A-1: Concrete mix design for Series One through Series Four

Component	Weight of Component / Weight of Cement
Cement	1
Fine Aggregate	2.4
Coarse Aggregate (max. size = 1¼ in.)	2.6
Water	0.55

Table A-2: Concrete mix design for Series Five

Component	Weight of Component / Weight of Cement
Cement	1
Fine Aggregate	4.9
Coarse Aggregate (max. size = 1¼ in.)	3.9
Water	0.53

Table A-3: Concrete properties for Series One beams

Specimen	Cast Date	Test Date	Concrete Compressive Strength (psi)	Concrete Splitting Cylinder Strength (psi)	Age of Specimen (days)
C1	2/2/2016	3/21/2016	5300	500	48
C2		3/28/2016	5200	450	55
C3		4/4/2016	5900	500	62
C4		4/11/2016	5700	500	69
C5		4/12/2016	5600	500	70
C6		4/14/2016	5300	400	72

Table A-4: Concrete properties for Series One and Series Two

Specimen	Cast Date	Test Date	Concrete Compressive Strength (psi)	Concrete Splitting Cylinder Strength (psi)	Age of Specimen (days)
D1	1/11/2017	2/13/2017	3900	450	33
D2		2/15/2017	3900	450	35
D3		2/15/2017	3900	450	35
D4		2/20/2017	4000	350	40
D5		2/22/2017	4000	350	42
D6		2/23/2017	4000	350	43
D7		2/26/2017	4200	400	46
D8		3/6/2017	4100	450	54
D9		3/10/2017	4100	400	58
D10		3/14/2017	4200	450	62
D11		3/17/2017	4300	400	65
D12		3/22/2017	4100	450	70
D13	4/27/2017	6/14/2017	4400	450	48
D14		6/19/2017	4300	450	53
D15		6/22/2017	4500	400	56
D16		6/29/2017	4300	400	63
D17		7/5/2017	4400	450	69
D18		7/6/2017	4300	450	70

Table A-5: Concrete properties for Series Three

Specimen	Cast Date	Test Date	Concrete Compressive Strength (psi)	Concrete Splitting Cylinder Strength (psi)	Age of Specimen (days)
H1	11/11/2017	12/15/2017	3900	450	34
H2		3/8/2018	3900	450	117
H3		3/14/2018	3900	450	123
H4		12/22/2017	4000	350	41
H5		3/15/2018	4000	350	124
H6		3/14/2018	4000	350	123
H7		12/27/2017	4200	400	46
H8		3/15/2018	4100	450	124
H9		3/16/2018	4100	400	125

Table A-6: Concrete properties for Series Four

Specimen	Cast Date	Test Date	Concrete Compressive Strength (psi)	Concrete Splitting Cylinder Strength (psi)	Age of Specimen (days)
PTR-NC	2/8/2019	4/18/2019	4800	500	69
PTR20-3.5-5K		4/19/2019			70
PTR20-3.5-10K		4/17/2019			68
PTR20-3.5-15K		4/22/2019			73
PTR20-5-5K		4/25/2019			76
PTR20-5-10K		4/26/2019			77
PTR20-5-15K		4/26/2019			77

Table A-7: Concrete properties for Series Five

Specimen	Cast Date	Test Date	Concrete Compressive Strength (psi)	Concrete Splitting Cylinder Strength (psi)	Age of Specimen (days)
C1	3/28/2019	7/4/2019	7000	650	98
C2		7/12/2019			106

Table A-8: Reinforcement summary for all test series

Reinforcement Type	Test Series	Measured Yield Stress (ksi)
#11 Gr. 60 A615	Series One Beams	65
	Series One Coupons	67
	Series Two	
	Series Three	
	Series Four	
#8 Gr. 60 A615	Series Five	70
#3 Gr. 60 A615		68
Gr. B7 Threaded Rod (1/2 in.)	Series Four	120
	Series Five	
Gr. B7 Threaded Rod (3/4 in.)	Series Two	125
C1018 smooth bar	Series Three	80

Table A-9: Sensors used in Series One beam tests

Sensor Type	Manufacturer	Model Number	Serial Number	Location	Range	Accuracy
Load Cell	Lebow	3175 50K	1176585	North Load Point	50 kip	80 lbf
		3175 50K	442	South Load Point		
String Potentiometer	Unimeasure	PA 20	36030715	North Overhang	20 in.	0.05 in.
		PA 20	45110640	South Overhang		
		PA 10	40010981	North Splice End	10 in.	0.02 in.
		PA 10	40010984	Mid-span*		
		PA 10	40010987			
		PA 10	40010979	South Splice End		
LVDT	Schaevitz	DC EC 250	22439	North Support	+/- 0.25 in.	0.001 in.
	Schaevitz	DC EC 250	22461	South Support		
Optotrak	Northern Digital Inc.	PRO Series 600	-	-	-	0.005 in.
Dial Gage	Federal	1 in. Dial Gage	-	North Overhang	1 in.	0.001 in.
			-	Mid-span		
			-	South Overhang		

Table A-10: Sensors used in Series One, Series Two and Series Three

Sensor Type	Manufacturer	Model Number	Serial Number	Location	Range	Accuracy
Load Cell	Tokyo Sokki	KCB-500KNA	ALU03006	East	112 kip	400 lbf
		KCB-500KNA	ALU03005	West		
LVDT	Schaevitz	DE EC 250	12838	NE	+/-0.25 in.	0.002 in.
		DC EC 500	23618	SE	+/-0.50 in.	0.001 in.
		DC EC 1000	8702*	NE	+/-1.00 in.	0.004 in.
		DC EC 1000	J4914*	SE		
		DC EC 1000	X00598	NW		
		DC EC 1000	J4913	SW		
Optotrak	Northern Digital Inc.	PRO Series 600	-	-	-	0.005 in.

Table A-11: Sensors used in Series Four

Sensor Type	Manufacturer	Model Number	Serial Number	Location	Range	Accuracy
Optical Target	OptiTrack	Prime^x 40	-	-	-	0.01 in.
Load	MTS	311.61	-	Splice ends	660 kip	800 lbf

Table A-12: Sensors used in Series Five

Sensor Type	Manufacturer	Model Number	Serial Number	Location	Range	Accuracy
Load Cell	Tokyo Sokki	KCB-500KNA	ALU03006	West	112 kip	400 lbf
		KCB-500KNA	ALU03005	East		
String Potentiometer	Unimeasure	PA 10	40010981	Top	10 in.	0.02 in.
		PA 10	40010984	Middle		
		PA 10	40010979	Base		
Optical Target	OptiTrack	Prime^x 40	-	-	-	0.01 in.

Figure A-1: Measured stress-strain curves for #11 Gr. 60 A615 bars used in Test Series One through Series Four

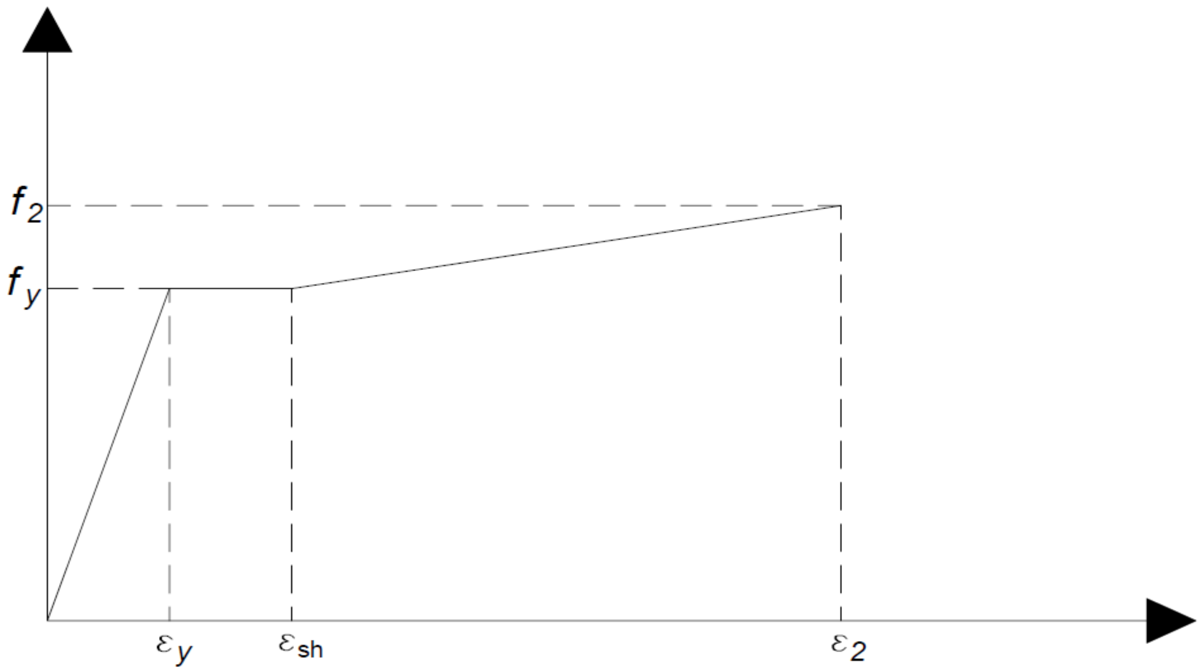

Figure A-2: Tri-linear stress strain curve used to estimate bar strains in Eq. 3-1 through Eq. 3-3

Test Series	f_y ksi	ε_{sh}	f_2 ksi	ε_2
1	65	0.0065	90	0.035
2-4	67	0.007	94	0.035

f_y	:	Steel stress at yield
ε_{sh}	:	Steel strain at onset of strain hardening
f_2	:	Steel stress at pt. used to define slope of strain hardening region
ε_2	:	Steel strain at pt. used to define slope of strain hardening region

Figure A-3: Parameters for stress-strain relationship for reinforcing steel in Series One through Series Four

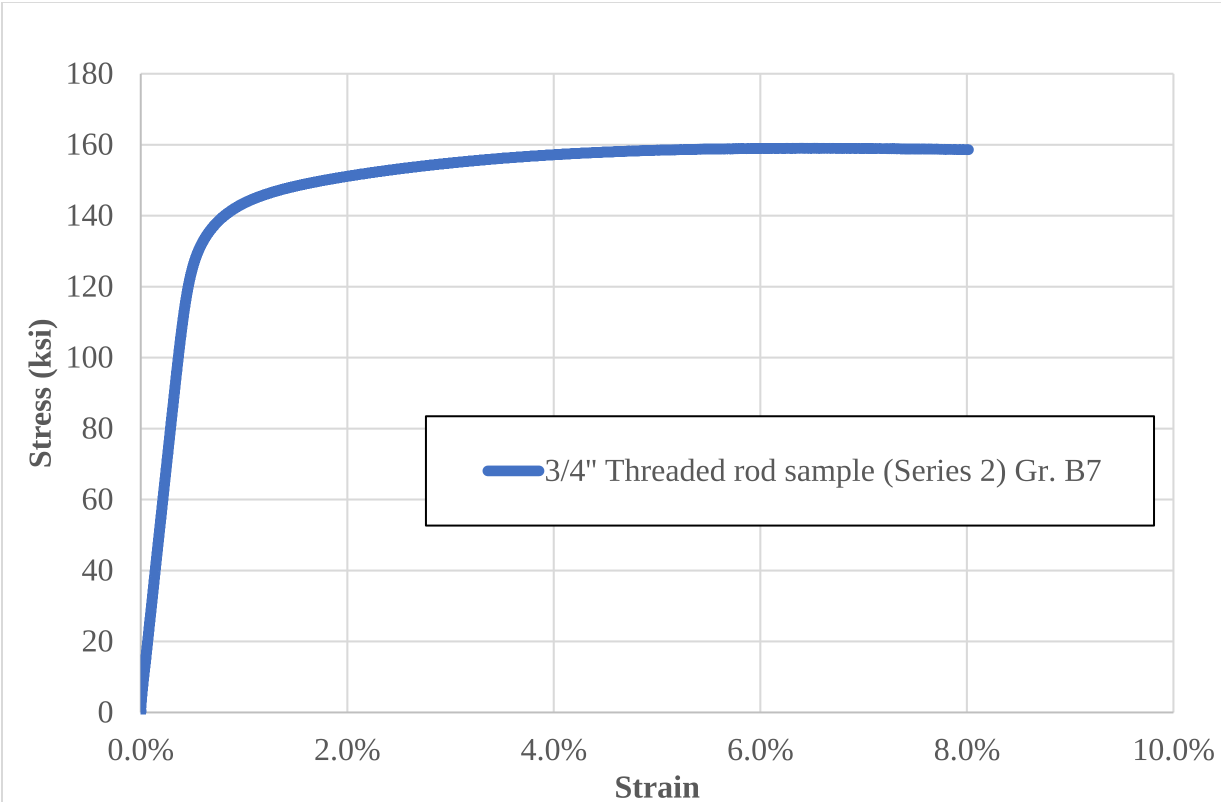

Figure A-4: Measured stress-strain curves for ¾ in. Gr. B7 threaded rod used as anchors in Series Two

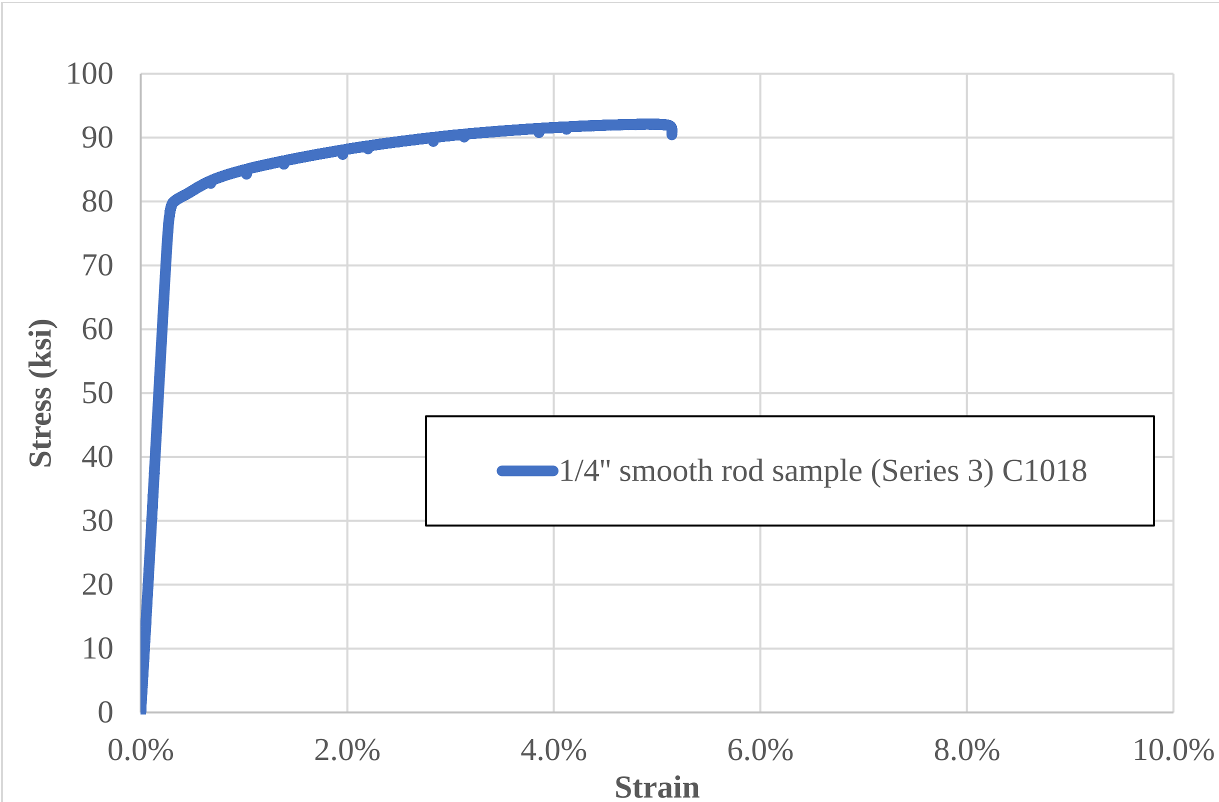

Figure A-5: Measured stress-strain curves for ¼ in. C1018 smooth rod used as spirals in Series Three

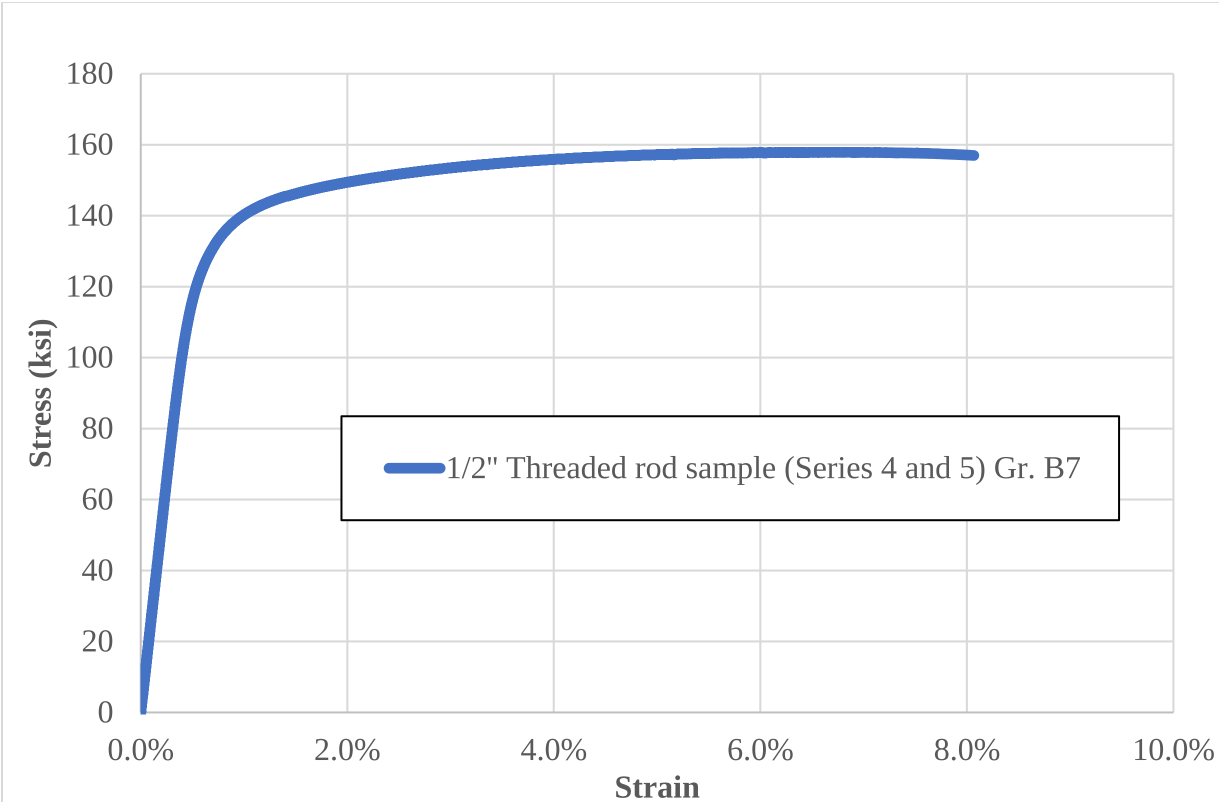

Figure A-6: Measured stress-strain curves for 1/2 in. Gr. B7 threaded rod used as post-tensioning rods in Series Four and Series Five

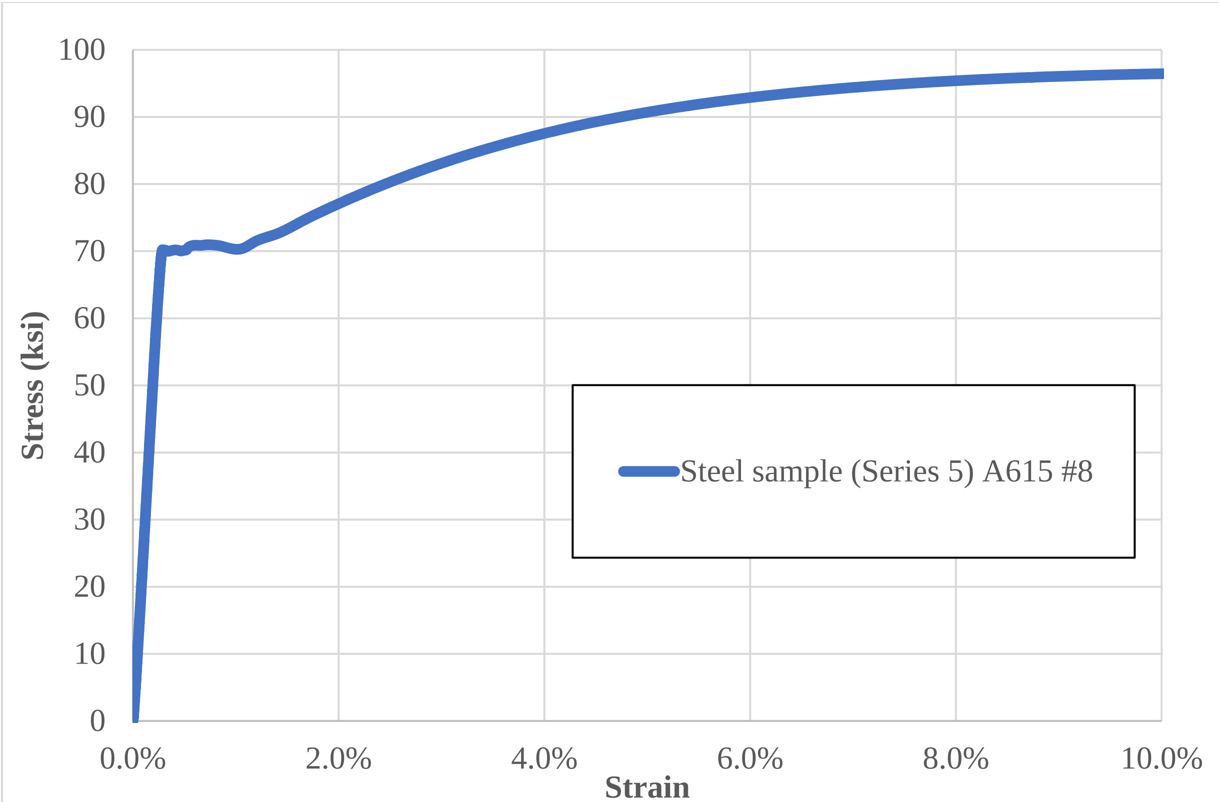

Figure A-7: Measured stress-strain curves for #8 Gr. 60 A615 bars used as longitudinal reinforcement in Series Five

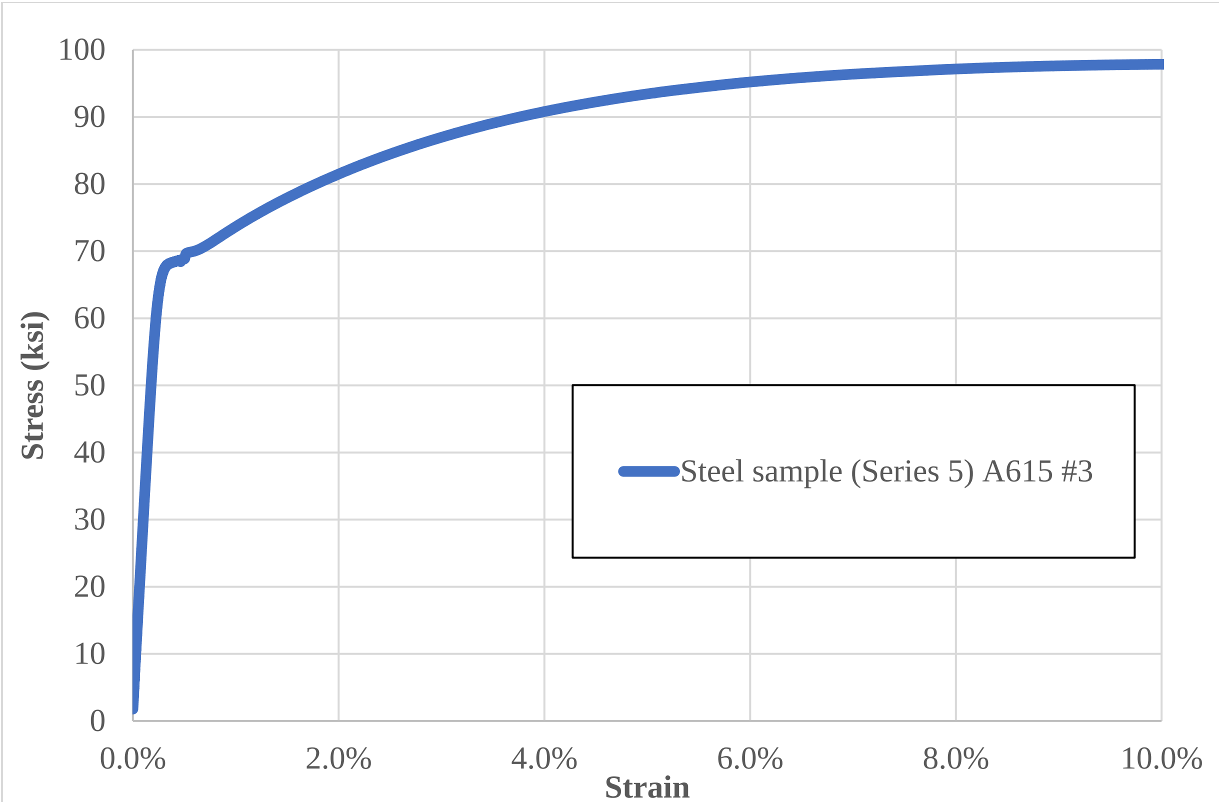

Figure A-8: Measured stress-strain curves for #3 Gr. 60 A615 bars used as transverse reinforcement in Series Five

Figure A-9: Series One formwork (beams)

Figure A-10: Spliced region prior to casting Series-One beams

Figure A-11: Placement of concrete in formwork for beams C1-C6

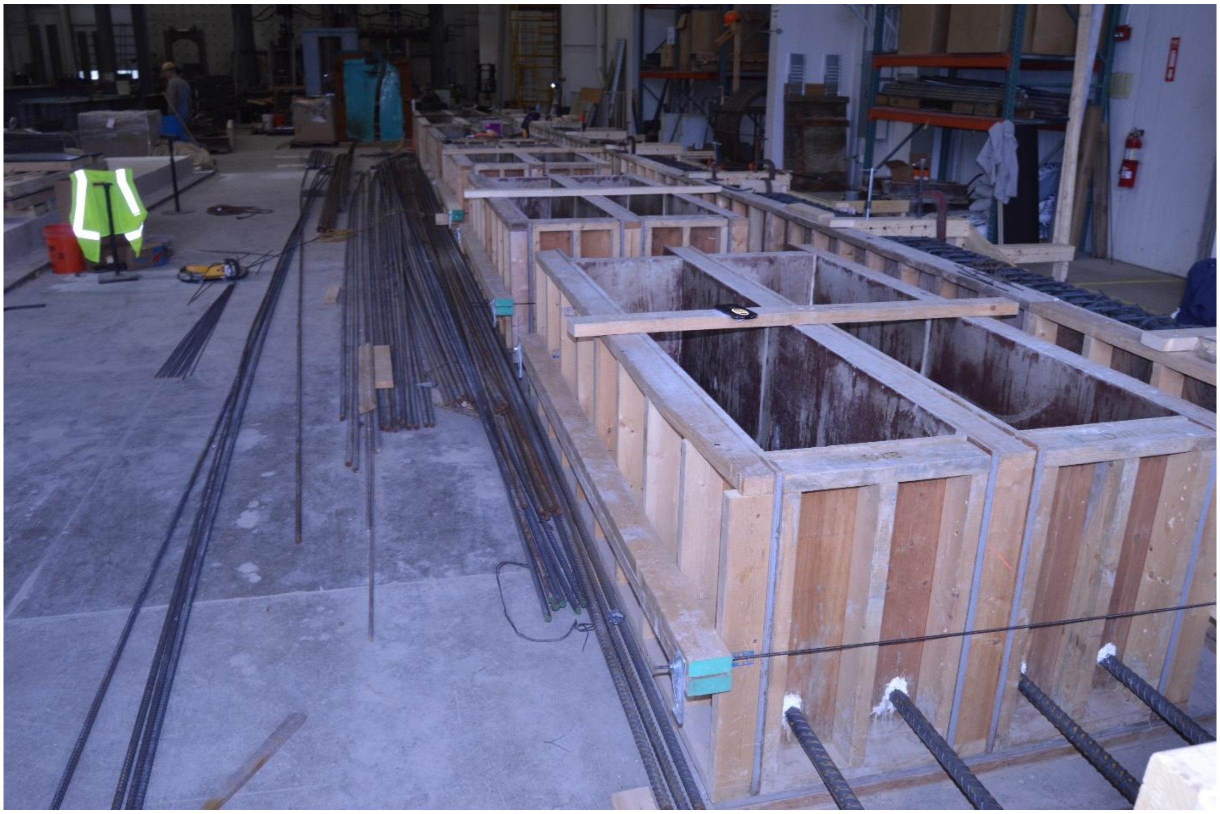

Figure A-12: Formwork used to cast coupons in Series One and Series Two

Figure A-13: Casting of coupons D13 and D14 tested in Series Two

361

Figure A-14: Series Three formwork

Figure A-15: Specimen H3 prior to casting (splice length = 18 in.)

Figure A-16: Specimen H6 prior to casting (splice length = 24 in.)

Figure A-17: Specimen H8 prior to casting (splice length = 30 in.)

Figure A-18: Reinforcing cage for specimens C1 and C2 in Series Five

Figure A-19: Spacing of ties along the shear span of specimens C1 and C2 (s=12in.)

Figure A-20: Depths to longitudinal bars in specimens C1 and C2